LIST OF SESSIONS

---

*For list of papers, see p. xxiii.

PROCEEDINGS

FIFTIETH ANNUAL MEETING

ELECTRON MICROSCOPY SOCIETY OF AMERICA

TWENTY-SEVENTH ANNUAL MEETING

MICROBEAM ANALYSIS SOCIETY

NINETEENTH ANNUAL MEETING

MICROSCOPICAL SOCIETY OF CANADA/
SOCIETE DE MICROSCOPIE DU CANADA

BOSTON, MASSACHUSETTS

16-21 August 1992

Editors
G. W. BAILEY
J. BENTLEY
J. A. SMALL

PUBLISHER'S NOTICE

ELECTRON MICROSCOPY SOCIETY OF AMERICA

Established 1942

OFFICERS 1992

Executive Council

President	Patricia G. Calarco
President Elect	Michael S. Isaacson
Past President	Charles E. Lyman
Secretary	Barbara A. Reine
Treasurer	Robert R. Cardell
Directors	C. Barry Carter
	Richard E. Crang
	Ulrich Dahmen
	M. Ann Goldstein
	James K. Koehler
	Ann LeFurgey
	Philip S. Sklad

Appointed Officers

Archivist	Frank B. Johnson
Bulletin Board System	Ron Anderson
Bulletin Editor	Joseph M. Harb
Certification Board	John J. Bozzola
Committee on Standards	Ray F. Egerton
Education Committee Chair	Richard L. McConville
Executive Secretary	Morton D. Maser
Expo	William T. Gunning
International Outreach	J. Alwyn Eades
Long-Range Planning	Ray W. Carpenter
Meeting Manager	Edward B. Ruffing
Membership	Michael Postek
Placement Office	John H. L. Watson
Proceedings Editor	G. William Bailey
Publications Committee Chair	David C. Joy
Sustaining Members Liaison	Joseph A. Mascorro
Technologists' Forum	John M. Basgen
1992 Local Arrangements Chair	Morton D. Maser
1992 Program Chair	James Bentley
1992 Program Vice Chair	Conly Rieder

1992 EMSA PROGRAM COMMITTEE

James Bentley, Chair
Conly Rieder, Vice Chair
David A. Agard
Ron Anderson
John Basgen
Joanna L. Batstone
M. Gracie Burke
Beth Burnside
Patricia Calarco
C. Barry Carter
Vinayak P. Dravid
Pat Echlin
Anthony J. Garratt-Reed
Laura Grabel
Mike S. Isaacson
David C. Joy
Ed A. Kenick

Jeanne Lawrence
Ann LeFurgey
Thomas Malis
Carmen Mannella
Laurie D. Marks
Richard L. McConville
Kent McDonald
John B. Posthill
Rose H. Roberts
Edward D. Salmon
Mehmet Sarikaya
David J. Smith
David L. Spector
Alasdair Steven
Jeffery Travis
Christopher Viney
Nestor J. Zaluzec

EMSA SUSTAINING MEMBERS

MICROBEAM ANALYSIS SOCIETY

OFFICERS 1992

Executive Council

President	David B. Williams
President Elect	Thomas G. Huber
Past President	John T. Armstrong
Secretary	John A. Small
Treasurer	Harvey A. Freeman
Directors	John J. Friel
	Dale E. Johnson
	Ryna B. Marinenko
	Joseph R. Michael
	John R. Porter
	Phillip E. Russell

Appointed Officers

Affiliated Groups Committee Chair .... V. E. Shull
Archivist .... C. Gordon Cleaver Jr.
Business Affairs Committee Chair .... Harvey A. Freeman
Corporate Liaison Officer .... Jon McCarthy
Computer Activities Committee Chair .... John F. Mansfield
Editor Micronews .... Arthur A. Chodos
Education Committee Chair .... Phillip E. Russell
International Relations .... K. F. J. Heinrich
Long-range Planning .... David B. Wittry
Meeting Arrangements Liaison .... Dale E. Newbury
Membership Chair .... Robert W. Warner
Microbeam Analysis Journal Editor .... Richard W. Linton
Speakers Tour Coordinator .... Paul F. Hlava
1992 Local Arrangements Chair .... Mary C. Finn
1992 Program Chair .... John A. Small

1992 MAS PROGRAM COMMITTEE

John A. Small, Chair
J. T. Armstrong, Co-Chair
G. F. Bastin
J. Bradley
S. Cvikevich
E. Etz
J. J. Friel
D. J. Gardiner
J. Geller
M. S. Germani
J. I. Goldstein
D. Golijanin
E. Jarosewich

P. Karduck
R. W. Linton
J. McCarthy
R. B. Marinenko
D. E. Newbury
J. R. Porter
G. Remond
A. D. Romig Jr.
E. B. Steel
R. R. Warner
D. B. Williams
D. B. Wittry

1992 CHAIRS FOR THE JOINT SYMPOSIA

R. Anderson
J. L. Batstone
R. Bolon
R. Leapman

I. H. Musselman
K.-R. Peters
P. E. Russell
S. Turner

MAS SUSTAINING MEMBERS

ADVANCED MICROBEAM SERVICES, INC.
AMRAY, INC.
CAMECA INSTRUMENTS, INC.
CHARLES EVANS & ASSOCIATES
DAPPLE SYSTEMS
ELECTRON MICROSCOPYY SCIENCES/DIATOME US
ELECTROSCAN CORPORATION
EMITECH USA, INC.
ENERGY BEAM SCIENCES
ETP-USA/ELECTRON DETECTORS, INC.
FEI COMPANY
FISONS INSTRUMENTS
GATAN, INC.
HESSLER TECHNICAL SERVICES
h•nu x•ray SYSTEMS, INC.
INSTRUMENTS S. A., INC.
JEOL USA, INC.
KRATOS ANALYTICAL
RJ LEE GROUP

LEICA INSTRUMENTS, INC.
MATERIALS ANALYTICAL SERVICES, INC.
WALTER C. McCRONE ASSOCIATES, INC.
MICRON, INC.
MICROSPEC CORPORATION
NSA/HITACHI SCIENTIFIC INSTRUMENTS
NORAN INSTRUMENTS, INC.
OVONIC SYNTHETIC MATERIALS, INC.
OXFORD INSTRUMENTS NORTH AMERICA, INC.
OXFORD INSTRUMENTS, INC.
PERKIN-ELMER, INC.
PHILIPS ELECTRONICS INSTRUMENTS, INC.
PRINCETON GAMMA-TECH, INC.
SEM/TEC LABORATORIES, INC.
SPI SUPPLIES DIVISION
SPECTRA-TECH, INC.
TOPCON TECHNOLOGIES, INC.
TOPOMETRIX CORPORATION
CARL ZEISS, INC.

MICROSCOPICAL SOCIETY OF CANADA
SOCIETE DE MICROSCOPIE DU CANADA

OFFICERS 1992

Executive Council

President	Gilles L'Espérance
First Vice President	Larry Arsenault
Second Vice President	Maria Neuwirth
Secretary	Douglas Craig
Treasurer	Ernest Spitzer
Past President	Peter Lea
Councillors	Jim Corbett
	Malkit Diocee
	Carolyn Emerson
	Lori Graham
	Michael Lalli
	Antonio Nanci
	David O'Neil
	Brian Robertson
	Lesley Smith

Appointed Officers

Bulletin Editor .... Frances Doane
Executive Secretary .... Nan Anderson

1992 MSC/SMC PROGRAM COMMITTEE

Larry Arsenault   James M. Corbett

MSC/SMC CORPORATE MEMBERS

ALCAN ARVIDA RESEARCH & DEVELOPMENT CENTRE
AMERSHAM CANADA LTD
ANALYCHEM CORPORATION LTD
BIO-RAD LABORATORIES (CANADA) LTD
C. Z. SCIENTIFIC INSTRUMENTS
CANBERRA PACKARD CANADA
CARSEN MEDICAL & SCIENTIFIC CO. LTD
DAWSON LAB SERVICES
DELAWARE DIAMOND KNIVES
EDWARDS HIGH VACUUM LTD
ELECTRON OPTIC SERVICES INC.
EMLAB EQUIPMENT INC.
ENERGY BEAM SCIENCES
J. B. EM SERVICES INC.
JEOL USA, INC.

KODAK CANADA LTD
LAB-6 INC.
LECO INSTRUMENTS LTD
LEICA CANADA INC.
MARIVAC LTD
NIKON CANADA INSTRUMENTS INC.
NISSEI SANGYO CANADA INC.
PELCO INTERNATIONAL
PHILIPS ELECTRONICS LTD
POLAROID CANADA INC.
SEMOPTICS LTD
SOQUELEC LTD
SPI SUPPLIES (CANADA)
VG INSTRUMENTS CANADA LTD
CARL ZEISS CANADA LTD

ELECTRON MICROSCOPY SOCIETY OF AMERICA

1992 DISTINGUISHED SCIENTIST AWARDS
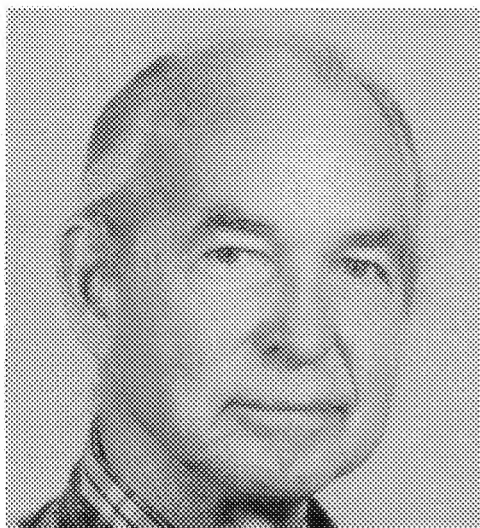
FRITIOF SJÖSTRAND
Biological Sciences

Fritiof S. Sjöstrand is a pioneer in electron microscopy whose contributions span almost 60 years, with significant developments continuing. He assisted M. Siegbahn in building one of the earliest electron microscopes (1930s-1940s); discovered double membrane disks of photoreceptor outer segment (1948); designed the first ultramicrotome (1952); and developed techniques for serial sectioning and 3-D reconstructions (1958), the low-denaturation embedding technique (1968), and the freeze-drying low-temperature embedding technique (1975). He discovered mitochondrial membranes (1952), the membranes of the Golgi apparatus (1954), the synaptic vesicles (1953), the chloroplast structure (1956), the connections extending from cones to rods and to bipolar cells connected to rods (1958), the gap junctions (1958), the ordered arrangement of enzyme molecules in mitochondrial cristae (1988), and the first elementary information-processing component in a neural center (1988). Dr. Sjöstrand recently developed an approach to the study of information processing in neural centers (1990), offering new conditions for neurophysiological studies of brain centers.
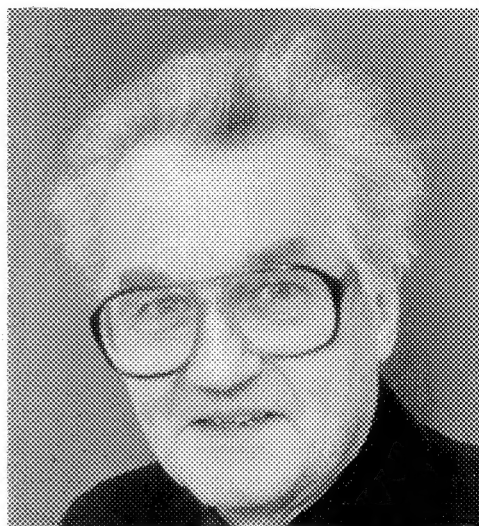
OLIVER WELLS
Physical Sciences

Oliver Wells is a graduate of the University of Cambridge, where he was a member of Professor Oatley's team that developed the scanning electron microscope (SEM). He was associated with an SEM project at Westinghouse Research and Development Center in Pittsburgh for several years, where he was the first to obtain an induced signal image from a semiconductor device (later called EBIC) and to demonstrate SEM-type registration during electron-beam exposure of photoresist. Since 1966 he has been occupied in full-time research into SEM theory and applications at IBM Thomas J. Watson Research Center, where (with others) he discovered the low-loss electron image and several other contrast mechanisms. He is at present working on in-lens methods in which the focusing magnetic field is also used to energy-filter the electrons scattered from the specimen.
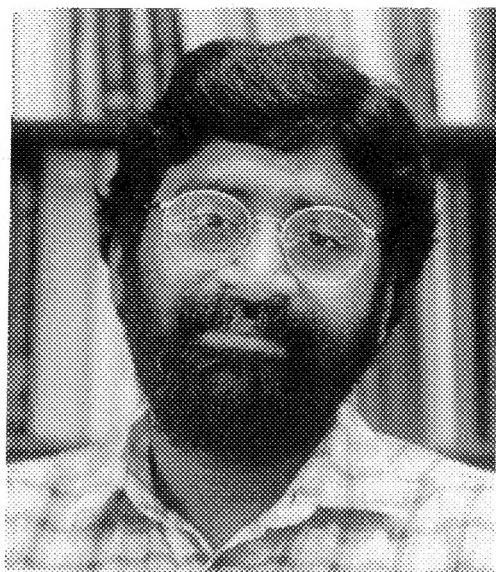
KANNAN M. KRISHNAN

Kannan M. Krishnan has been working at the Lawrence Berkeley Laboratory since completing the Ph.D. in materials sciences at the University of California in Berkeley in 1984, and is currently responsible for analytical electron microscopy at the National Center for Electron Microscopy at LBL. In addition, he is a Principal Investigator in the LBL Materials Sciences Division with a program on thin film structures and coatings. Dr. Krishnan's main research interests are centered around magnetic nanostructures, CVD synthesis of diamond films, phase transformations, and microanalytical electron microscopy and related spectroscopies. These programs involve materials synthesis, appropriate property measurements and their characterization by sophisticated application of electron microscopy, x-ray scattering, and other spectroscopic techniques. In electron microscopy, he has contributed to the development of channeling methods and spatially resolved EELS measurements for local electronic structure and bonding studies of materials. He is also responsible for the design and development of the Magnetic Materials Microscope, a dynamic laboratory for quantitative measurements of magnetic structures at the nanometer scale of resolution.

MICROBEAM ANALYSIS SOCIETY

1992 PRESIDENTIAL SCIENCE AWARDS


GRAHAM CLIFF

GORDON LORIMER
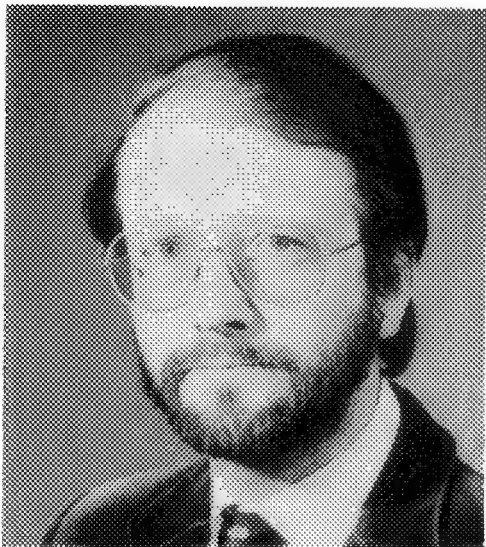
Graham Cliff graduated from the University of Manchester School of Physics and Electronic Engineering in 1971 and began his career in analytical electron microscopy with a two-year appointment in the Metallurgy Department of Manchester University to look after EMMA-4—an appointment that has now lasted 21 years. During much of that time he has been involved in establishing techniques for the quantitative analysis of thin specimens. He has been co-author of more than sixty papers dealing with the principles, practice, and problems of AEM. He has also lectured on RMS short courses in electron microscopy, and from 1982 until 1989 he lectured in Lehigh University's AEM courses. He co-authored, with Professors Williams and Goldstein, a chapter in *Principles of Analytical Electron Microscopy*; and with Professors Humphreys and Goodhew on software, in the Institute of Metals series. His current research interests lie in combining AEM with the surface-analysis techniques of SIMS and Auger/XPS.

Gordon Lorimer graduated from the University of British Columbia with a B.A.Sc. in Metallurgical Engineering in 1964. His Ph.D. research (on precipitation in aluminum alloys) was carried out in the Department of Metallurgy at the University of Cambridge. In 1986 he moved to the University of Manchester, where he is now professor of physical metallurgy and materials science. In 1970 the university took delivery of the first commercial analytical electron microscope, EMMA-4. Over the past twenty-two years his team has applied the AEM technique to the investigation of a wide range of problems in the physical sciences. His current research interests include solid-state phase transformations and oxidation, as well as analytical electron microscopy.
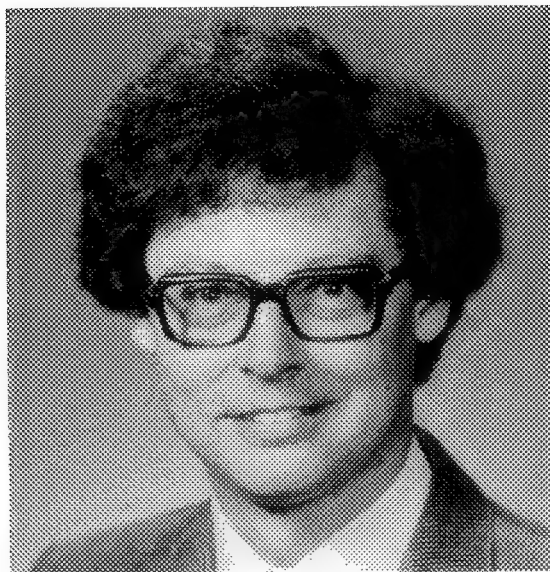
STEPHEN J. PENNYCOOK

Stephen J. Pennycook is leader of the Electron Microscopy Group in the Solid State Division of Oak Ridge National Laboratory (ORNL), Oak Ridge, Tennessee. He received the B.A., M.A., and Ph.D. in physics from the University of Cambridge. After completing his thesis research in 1978 he continued at the Cavendish Laboratory at Cambridge until 1982, when he joined the staff at ORNL to work on ion implantation in semiconductors. His main current research interests are the study of growth mechanisms and interfacial properties in semiconductors and superconductors through Z-contrast scanning transmission electron microscopy. The development of this technique earned him the U.S. Department of Energy award for outstanding scientific accomplishment in 1989, and, jointly with VG Microscopes, an R&D 100 award in 1990.

Patricia G. Calarco
EMSA President

David B. Williams
MAS President
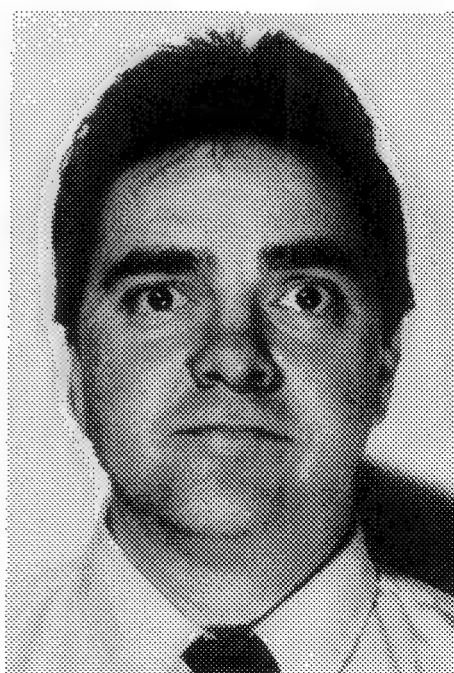
Gilles L'Espérance
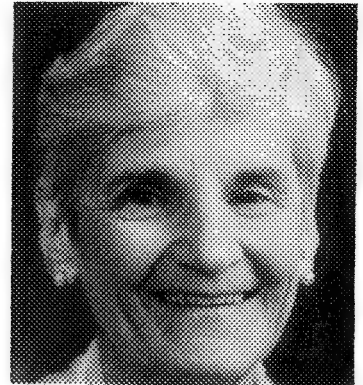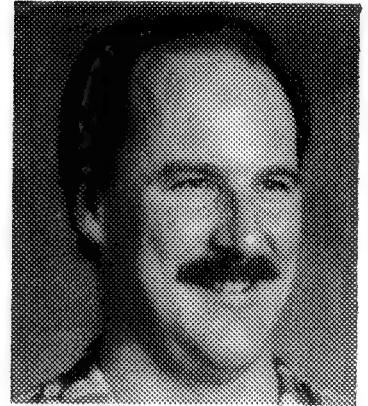MSC/SMC President

Morton D. Maser
EMSA Local Arrangements Chair

Mary Finn
MAS Local Arrangements Chair

James Bentley
EMSA Program Chair

Conly Rieder
EMSA Program Vice Chair

John A. Small
MAS Program Chair

James Corbett
MSC/SMC Liaison

1992 EMSA PRESIDENTIAL STUDENT AWARDS

Ian M. Anderson
Cornell University

Gerardo A. Bertero
Stanford University

S. J. Chen
University of California—Davis

R. Holland Cheng
Purdue University

Kirk J. Czymmek
Michigan State University

Rubai Ding
University of Colorado

Louis M. Holzman
University of Wisconsin

Stephen D. Jett
University of New Mexico

Amy C. Lam
Lehigh University

E. Naranjo
University of California—Santa Barbara

P. L. Ratnaparkhi
Carnegie Mellon University

Steven D. Toteda
Lehigh University

G. Waytena
North Carolina State University

1992 MAS DISTINGUISHED SCHOLAR AWARDS

Mark Backus
Duke University

Jean Baldwin
McGill University

J. P. Cassella
National Orthopaedic Hospital

W. Z. Chang
University of Southern California

Mark Denker
University of North Carolina

Thomas Fister
University of North Carolina

Consetta M. Helmick
Washington State University

Stephen Hoeft
Washington University

Pierre Hovington
Ecole Polytechnique de Montréal

Rollin E. Lakis
Lehigh University

T. D. Ly
University of California—Davis

Pamela A. Martoglio
Miami University

M. P. Mawn
University of North Carolina

C. B. Mooney
North Carolina State University

John G. Sheehan
University of Minnesota

Jim Vitarelli
North Carolina State University

Xinlei Wang
University of Tennessee

S. Wu
University of Antwerp

H. J. Zuo
University of Alabama—Birmingham

1992 MSC/SMC PRESIDENTIAL AWARDS

Gianluigi Botton
Ecole Polytechnique de Montréal

S. Ritchie
University of Waterloo

M. A. McCormick
Queen's University

PREFACE

Twenty-five years ago, on the occasion of the 25th anniversary meeting of the Electron Microscopy Society of America, the Executive Council decided that the proceedings of the annual meeting should be published in book form. Thus, along with EMSA now celebrating its 50th anniversary, the EMSA Proceedings is celebrating its 25th anniversary. That first Proceedings, edited by the late Claude J. Arceneaux, contained the 187 papers presented at that anniversary meeting in August 1967 in Chicago. As evidenced by the current two-volume Proceedings containing close to 900 papers, we have grown significantly in these 25 years.

Though EMSA has had many joint meetings with the Microbeam Analysis Society (MAS), this is the first year that all papers from both societies are contained in one Proceedings. Also included are the papers from the Microscopical Society of Canada (MSC), which makes this a truly complete Proceedings for this joint meeting of our three societies. The production of this Proceedings, as well as the entire meeting, is the result of a combined effort by many people. The co-editors would like to acknowledge the dedicated efforts of the members of the Program Committees of the three societies, with additional thanks to Neal Evans of the Oak Ridge Associated Universities for his assistance with the EMSA Program. We should also like to thank Mort Maser for his thorough and efficient handling of all papers received and for his assistance in the organization of the meeting program and of this Proceedings.

G. W. BAILEY
J. BENTLEY
J. A. SMALL

FOREWORD

PATRICIA G. CALARCO
President, Electron Microscopy Society of America

GILLES L'ESPERANCE
President, Microscopical Society of Canada

DAVID B. WILLIAMS
President, Microbeam Analysis Society

The Proceedings of this Annual Meeting contain nearly 900 papers representing the research interests of members from the three Societies. Our joint program in Boston is rich and varied, with seminal contributions from both the physical and the biological sciences. This year marks the 50th anniversary of EMSA. The EMSA Presidential Symposium, ''Microscopy then and now,'' features speakers who were part of the first electron microscopy efforts in North America, as well as speakers who represent a variety of new directions in imaging and microscopy. The MAS Presidential Symposium, ''Microanalysis at the atomic level,'' discusses how close we are to the ultimate in microanalytical spatial resolution and detectability limits, based on a variety of analytical techniques.

The excellence of our scientific program this year is due to the hard work of our combined Program Committees. We particularly acknowledge the contributions of EMSA Program Chair Jim Bentley, EMSA Vice Chair Conly Rieder, MSC Program Chairs Larry Arsenault and Jim Corbett, and MAS Program Chair John Small in making this year's meeting a success.

We congratulate our award recipients! The EMSA Distinguished Scientist Awards go to Fritiof Sjöstrand for the biological sciences and to Oliver Wells for the physical sciences; the EMSA Burton Award goes to Kannan Krishnan. The MAS Presidential Science Awards go to Graham Cliff and Gordon Lorimer; the MAS Presidential Heinrich Award, to Stephen J. Pennycook. They have made important contributions to the advancement of our science. We also award 13 EMSA Presidential Student Awards, 19 MAS Distinguished Scholar Awards, and 3 MSC Presidential Awards to students. We extend congratulations to all winners and participants.

We must also acknowledge the work of some of the other volunteers who have contributed to the success of this year's meeting. Special thanks go to EMSA Local Arrangements chair Mort Maser and his dedicated Local Arrangements Committee; to Mary Finn, the Local Arrangements chair for MAS; and to Jim Corbett, the MSC liaison officer.

This year also marks the 25th anniversary of the Proceedings. Our warmest thanks are due to Bill Bailey, who has seen to it that the two-part Proceedings for this anniversary years has stayed on schedule. (Thank you too, Bill, for keeping yet another EMSA President on track.) Our three societies extend an invitation to all to enjoy the excellent scientific program as presented in this two-part Proceedings.

August 1992

TUTORIALS

EMSA PHYSICAL SCIENCES TUTORIALS

HIGH-SPATIAL-RESOLUTION MICROANALYSIS IN THE ELECTRON MICROSCOPE

A. D. Romig Jr.

Materials and Process Sciences Center, Sandia National Laboratories, Albuquerque, NM 87185

Thin-film x-ray microanalysis via analytical electron microscopy (AEM) is proving to be a valuable tool in characterizing the composition of a material on a fine spatial scale. Depending on the size of the incident electron beam and certain characteristics of the specimen (thickness and average atomic number, weight, and density), x-ray spatial resolutions approaching 2 nm are possible. By deconvolution of compositional profiles measured across interfaces, *near* atomic resolution microanalysis is possible. Recently, it has been possible to perform these deconvolutions very quickly by use of Monte Carlo simulations run on massively parallel computers. The capability to perform high-spatial-resolution microanalysis concomitant with the capability to characterize the morphology and crystallography of the microstructure make AEM the most powerful technique for interpreting and understanding the microstructure of a material. A detailed understanding of microstructure is required to optimize the processing parameters of a material and to evaluate thoroughly the performance and reliability of that material. The tutorial reviews the basic principles of thin-film x-ray microanalysis in the AEM and describes the limitations of that analysis. Special emphasis is given to the limitations of quantification and spatial resolution for microanalysis. The utility of the technique is to be further demonstrated through a number of examples of studies of grain-boundary segregation and solid-state reaction kinetics.

FAILURE ANALYSIS METHODS FOR THE SEMICONDUCTOR INDUSTRY

Ron Anderson

IBM East Fishkill Facility, Hopewell Junction, NY 12533

The tutorial reviews the application of various analytical instruments and methods for failure analysis in the semiconductor industry. Emphasis is on the various microscopies, from light optical to high-resolution scanning-tip microscopy. The difference between construction analysis and failure analysis is explained. A statistical assessment of the actual cause of failure of many devices reveals that failure-analysis methods are not very efficient in finding the actual cause of failure. This problem can be attributed to the inability of preparing specimens properly or specimen loss during analysis. The concept of specimen-preparation spatial resolution is discussed.

FUNDAMENTALS OF CATHODOLUMINESCENCE IN THE SEM AND TEM

R. J. Graham

Center for Solid State Sciences, Arizona State University, Tempe, AZ 85287-1704

Cathodoluminescence (CL) is the process by which a material that has been excited by an electron beam can de-excite by the emission of light. All materials emit x rays on de-excitation, but only materials with the appropriate available energy states give CL. This tutorial deals with CL spectroscopy and imaging, which form a sensitive microanalytical technique capable of detecting and mapping impurities and defects in a variety of materials. Some account of basic theory is given and the details of typical systems for spectroscopy and mapping on SEMs are described. Also to be described is CL in TEM, which has the unique advantage of allowing direct correlation of CL with microstructure, such as the presence of faults. Applications of these techniques are illustrated by various examples including semiconductors, wideband-gap materials and ceramics, and geological specimens.

INTRODUCTION TO REFLECTION ELECTRON MICROSCOPY (REM) OF CRYSTAL SURFACES

Tung Hsu

Department of Materials Science and Engineering, University of Utah, Salt Lake City, UT 84112

In REM, electrons reflected from the surface of a bulk specimen at a glancing angle are used to form an image of the surface. The image-forming process is almost the same as the dark-field method of transmission electron microscopy (TEM), except that in REM the specimen is semi-infinite and the electron beam enters and reflects from the same surface of the specimen. This particular geometry results in some special features and applications of REM that are quite different from TEM. In this tutorial we discuss the basic imaging principle and image interpretation through the basic geometrical optics and kinematical diffraction theory. Also to be discussed is the operation of the microscope and specimen preparation. Surface atomic steps, dislocations, reconstructions, and other features observed on Pt, GaAs, sapphire, and other crystals are used for illustration. In situ treatment of specimens, dynamical theories, and the combination of REM and other surface techniques are also presented.

EMSA BIOLOGICAL SCIENCES TUTORIALS

FLUORESCENCE IN SITU HYBRIDIZATION MICROSCOPY IN BIOMEDICAL RESEARCH

J. W. Gray, D. Pinkel, O. Kallioniemi, A. Kallioniemi, M. Sakamoto, and F. Waldman

Department of Laboratory Medicine, University of California, San Francisco, CA 94143-0808

The combined use of fluorescence in situ hybridization and computer-assisted microscopy is proving to be particularly useful for analysis of genetic aberrations in single-interphase nuclei associated with human genetic disease. This technique now permits ready detection of aneusomies involving chromosomes 21, 18, and 13 in cells taken prenatally, as well as aneusomies in human cancer cells. In addition, this technique allows detection and quantitative characterization of structural aberrations such as deletions that "uncover" recessive mutant tumor suppressor genes such as Rbl and p53, and gene amplification events that lead to activation of oncogenes such as ERBB2 and CMYC. The advantages of this approach include applicability to small number of cells (even from paraffin-embedded samples), the ability to exclude normal cells from analysis, and the ability to assess cell-to-cell heterogeneity. These techniques are now sufficiently advanced to make it possible to consider their application to disease diagnosis, prognostication, and residual or metastatic cell detection.

MICROPROBE ANALYSIS IN CLINICAL DIAGNOSIS

J. D. Shelburne

MICROCHEMICAL IMAGING IN BIOMEDICAL RESEARCH

P. Ingram

Research Triangle Institute, Research Triangle Park, NC 27709

It is well established that one can obtain unique physiological information by rapidly freezing cells in various functional states and analyzing the cell element content and distribution by electron probe x-ray microanalysis. (The other techniques of microanalysis that are amenable to imaging, such as electron energy loss spectroscopy, secondary ion mass spectroscopy, particle induced x-ray emission, etc., are not addressed in this tutorial.)   However, the usual processes of data acquisition are labor intensive and lengthy, requiring that x-ray counts be collected from individually selected regions of each cell in question and that data analysis be performed subsequent to data collection. A judicious combination of quantitative elemental maps and static raster probes adds not only an additional overall perception of what is occurring during a particular biological manipulation or event, it substantially increases data productivity.

THREE-DIMENSIONAL CONFOCAL MICROSCOPY IN LIVING CELLS: HISTORICAL DEVELOPMENT, PRACTICAL APPLICATION, AND LIMITATIONS

B. R. Masters

Uniformed Services University of the Health Sciences, Department of Anatomy and Cell Biology, Bethesda, MD 20814

Confocal microscopy is a rapidly evolving technique that is solving problems in the biological and material sciences. This tutorial focuses on the confocal microscopy of living cells. Both in vivo and in vitro applications of confocal microscopy are reviewed. The historical development of instrumentation and novel applications in the biological sciences is discussed. Various designs of confocal microscopes are illustrated and a critical review of their features is presented. The physics of image formation, microscope objective design, and digital deconvolution is analyzed. The limitations of confocal microscopy are reviewed and practical solutions are illustrated. Fluorescence and backscattered light confocal microscopy are compared. Three-dimensional and four-dimensional microscopy are discussed in terms of image fidelity and image aberrations. Video animations are used to illustrate examples of three-dimensional image reconstruction.

EMSA JOINT PHYSICAL-BIOLOGICAL SCIENCES TUTORIALS

SECONDARY ION MASS SPECTROMETRY (SIMS) IN THE BIOLOGICAL AND MATERIALS SCIENCES

R. W. Linton

Department of Chemistry, University of North Carolina, Chapel Hill, NC 27599-3290

The SIMS technique is based on energetic ion bombardment of surfaces that results in the emission of sputtered particles, including both atomic and molecular ions. The use of mass-spectrometric detection provides a highly versatile and sensitive tool for solids characterization with analysis modes including (1) molecular monolayer analysis (static SIMS), (2) lateral imaging (ion microscope or microprobe analysis), (3) elemental depth profiling (dynamic SIMS), (4) image depth profiling (combination of modes 2 and 3), and (5) postionization (laser ionization of sputtered neutrals). Analytical principles and advances in the above areas are reviewed, with special emphases on time-of-flight instruments for static SIMS or SIMS incorporating laser postionization, sector field instruments for dynamic SIMS, and ion microprobes or microscopes for microchemical imaging studies. Applications are to be illustrated for a diverse range of materials: organic (polymer and self-assembled films), electronic (conductive polymer arrays, electronic devices), and biological (tissue sections, phospholipid model membranes). New developments in image processing, such as volume rendering and pattern recognition, are discussed briefly as means to facilitate the interpretation of complex multidimensional SIMS data.

ATOMIC-FORCE MICROSCOPY IN BIOLOGICAL AND MATERIALS SCIENCES

K. A. Fisher

Departments of Anatomy and of Biochemistry and Biophysics, and Proctor Foundation,
University of California, San Francisco, CA 94143-0944

The atomic-force microscope is one of a new generation of machines called scanned-probe microscopes that are capable of producing atomic-resolution images of surfaces. This tutorial briefly describes the history of scanned-probe microscopes, from the development of the scanning tunneling microscope in the early 1980s to the subsequent development of the atomic-force microscope in 1986. In contrast to the tunneling microscope, the force microscope does not require electrical conductivity and can image insulating surfaces. The basic instrumentation of scanned-probe microscopes and the special characteristics of the scanned-force microscope are discussed. Components include the piezoelectric scanner, cantilever and tips, force-detection systems, electronics to detect and amplify signal and to control scanning and height, data acquisition, and image processing. The applications of force microscopy to imaging surfaces of biological and nonbiological materials is discussed, as are limitations associated with image production and considerations important for image interpretation.

MAS TUTORIALS

BASIC IMAGE PROCESSING FOR THE MICROSCOPIST

D. S. Bright

PARTICLE PREPARATION FOR MATERIALS SCIENCE

C. J. Zeissler

SCANNING AUGER MICROSCOPY: AN EXTENSION OF SEM/EDS AND EPMA

J. D. Geller

Geller MicroÅnalytical Laboratory, 1 Intercontinental Way, Peabody, MA 01960

Scanning Auger electron microscopy (SAM) is a complementary technique to scanning electron microscopy with x-ray analysis and electron-microprobe analysis. The primary difference between the techniques is in the *depth and spatial resolution*. Under "typical" conditions, the x-ray excitation volume is about 1 μm^3 (with the depth and width approximately equal). The depth resolution for SAM is 3-10 Å (0.0003-0.001 μm); spatial resolution is nearly equal to the beam diameter, about 500 Å (0.05 μm). This tutorial introduces scanning Auger microscopy from the viewpoint of the SEM/EDS analyst, and serves as preparation for the MAS session (pp. 1780-1785) on Surface Analysis (or, What You Have Been Missing with Your EDS/SPMA). We review the fundamentals of the excitation process, the vacuum requirements, and the use of sputter ion guns; and we compare data from the same specimens using SEM/EDS or EPMA and SAM.

TITLES AND ORDER OF SESSIONS

Part I

EMSA PRESIDENTIAL SYMPOSIUM
MICROSCOPY THEN AND NOW

METALS AND ALLOYS

HIGH-T_C SUPERCONDUCTORS

HIGH-RESOLUTION ELECTRON MICRSOCOPY

ROLE OF EM IN THE DEVELOPMENT OF MATERIALS

Composites

High-temperature Alloys

Al Alloys and Polymers

Alloys and Magnetic Materials

INTERFACES

MICROSCOPY OF SMALL-MOLECULE AND POLYMERIC LIQUID CRYSTALS

SURFACES AND SMALL PARTICLES

CERAMICS AND MINERALS

RADIATION-SENSITIVE MATERIALS AND POLYMERS

PHYSICAL SCIENCES SPECIMEN PREPARATION

FRONTIERS OF LIGHT MICROSCOPY

HREM OF BIOLOGICAL MEMBRANES

NUCLEIC ACID-PROTEIN COMPLEXES AND INTERACTIONS

MICROSCOPY OF NEURONAL SYSTEMS

IMAGING AND THE EYE

THE CELL NUCLEUS REVISITED:
ADVANCED TECHNIQUES TO EXAMINE ITS MOLECULAR ORGANIZATION

HIGH-RESOLUTION IMAGING OF MACROMOLECULAR ASSEMBLIES

NEW WAYS OF LOOKING AT CELLS

CORRELATIVE LIGHT AND ELECTRON MICROSCOPY FOR DETERMINING STRUCTURE/FUNCTION RELATIONSHIPS

RECONSTRUCTION AND ANALYSIS FROM LIGHT AND ELECTRON MICROSCOPY

STRUCTURAL CORRELATES IN DEVELOPMENTAL SYSTEMS

PATHOLOGY

MICROBIOLOGY

MEMBRANES AND TRANSPORT

BIOLOGICAL SPECIMEN PREPARATION

CYTOCHEMISTRY AND IMMUNOCYTOCHEMISTRY

PHYTOMORPHOLOGY

MICROBIOLOGY

CELL SURFACE AND EXTRACELLULAR MATRIX

3-D RECONSTRUCTION FROM SERIAL SECTIONS

DEVELOPMENTAL BIOLOGY

CYTOPLASMIC ORGANELLES

Part II

NEW INSTRUMENTATION

Noncommercial

Commercial

IMAGE ANALYSIS, PROCESSING, AND RECONSTRUCTION

MICROSCOPY OF SELF-ASSEMBLED MATERIALS AND BIOMIMETICS

INSTRUMENTATION AND 3-D VISUALIZATION

TECHNOLOGISTS' FORUM

Recollections of the Masters

BIOMATERIALS

EMSA TUTORIALS

SCANNED-PROBE MICROSCOPIES

THE SECOND BOSTON TEA PARTY: MICROSCOPY AND ANALYSIS

QUANTITATIVE ELECTRON DIFFRACTION AND CRYSTALLOGRAPHY

ANALYTICAL ELECTRON MICROSCOPY

Electron Spectroscopic/Spectrum Imaging

Interfacial Segregation

Dark-field STEM and X-ray Microanalysis

Electron Energy Loss Spectroscopy

SCANNING ELECTRON MICROSCOPY

High-resolution SEM

Environmental and Biological SEM

New Directions

General

ELECTRONIC MATERIALS

Novel Experiments with Group IV Semiconductors

Metal/Semiconductor Contacts

Compound Semiconductors and Device Characterization

General

DIFFRACTION AND DIFFRACTION CONTRAST

OPTICAL SPECTROSCOPIC ANALYSIS

MICROPROBE MASS SPECTROSCOPY

BIOLOGICAL MICROANALYSIS
Electron-beam Instrumentation

Microprobe Mass Spectrometry

COMPOSITIONAL IMAGING AND QUANTITATIVE MICROSCOPY

QUANTITATIVE MICROPROBE ANALYSIS

Light-element Analysis

Fundamental Parameters

Analytical Methods

Monte Carlo

APPLICATIONS TO MATERIALS SCIENCE: MICROANALYSIS OF ELECTRONIC MATERIALS AND DEVICES

ENVIRONMENTAL APPLICATIONS

INTERPLANETARY DUST AND INTERSTELLAR GRAINS

NEW AND REEMERGING PROBE TECHNOLOGIES

GEOSCIENCES

MICRO X-RAY DIFFRACTION AND FLUORESCENCE

MICROANALYSIS OF CERAMICS

SURFACE ANALYSIS

MAS TUTORIALS

ELECTRON MICROSCOPY SOCIETY OF AMERICA
E M S A
FOUNDED 1942

MAS
MICROBEAM
Analysis Society

MSC
SMC

THE ORIGINS OF ELECTRON MICROSCOPY IN NORTH AMERICA AT THE UNIVERSITY OF TORONTO

John H. L. Watson

652 Hupp Cross Rd., Bloomfield Village, MI 48301

On the North American continent, electron microscopy had its genesis due to the foresight of Professor E. F. Burton, Chairman of the University of Toronto Physics Department from 1932 to 1948. The realization of the 1938 electron microscope was a direct result of earlier episodes which involved Burton, his friend W.H. Kohl and his first graduate student in electron optics Cecil E. Hall. Burton was a colloid physicist anxious to observe directly the physical properties of colloidal particles and was well aware of the two physical principles which might make this possible, viz. deBroglie's hypothesis of the dual nature of electrons and Busch's thesis where axially symmetric magnetic and electric fields were shown to act as lenses upon electron beams. Kohl, often referred to as a "catalyst" for the development of the 1938 microscope, was a German research physicist immigrant to Canada, interested in the deflection of electron beams by magnetic and electric fields. Burton and Kohl met at Physics Department seminars and "catalyst" or not their friendship, coupled with Kohl's frequent lectures and demonstrations on electron optics, strongly influenced Burton to initiate the electron microscope project. Hall began his work in the autumn of 1935, building an emission microscope of the electrostatic type and obtaining micrographs of hot cathodes. In his second year he successfully completed a two-stage emission microscope with magnetic lenses and took photographs of emitting surfaces at X3000. Subsequently, Hall planned to build an instrument to obtain micrographs of objects placed in the path of the beam but funding ran out and he had to leave the project. Hall's work at Toronto deserves special recognition because it was the basis upon which the construction of the 1938 transmission magnetic electron microscope by James Hillier and Albert Prebus was built. Hillier and Prebus accomplished this feat successfully in April 1938, although working drawings had not been ready until the end of the Christmas vacation and shop work not begun until January 1938. The instrument, designed and built by the two Canadian students was remarkable not only for the speed of its construction but for the facts 1) that it was applied immediately for practical purposes with resolution 10 to 30 times that of the light microscope, and 2) that it was the first such to be built and operated anywhere in the world. Bill Ladd and I began our work with Professor Burton in the autumn of 1939 and I used the 1938 instrument until the autumn of 1943. Hillier, Prebus and Ladd had each left the laboratory by 1940 and Dr. L. T. Newman and Dr. Beatrice Deacon had come on staff. Later Glen Ellis and still later Frank Boswell, Tom McLaughlan and R. S. Sennett with Dave Scott joined the Burton group in electron microscopy. I had left in 1943, returning briefly in the summer of 1944 to assist in setting up the 1944 model Toronto microscope, the design of which had been part of my 1943 thesis.

Most work done with the '38 instrument was related to the World War II effort. The filtration efficiency of masks of many types was studied extensively, relating it to the particle sizes of particulates, the particles having been gathered on collodion films in an altered thermal precipitator. A whole array of substances both biological and physical was studied: including polished glass, carbon blacks, diatoms, polishing powders, vacinnia virus, the vole, tubercle and typhoid bacilli and Rickettsia typhi. The effect of growing streptococcus hemolyticus in the presence of sulphathiazole was investigated. The soap

components of lubricating greases and the helical nature of lime-based soaps were demonstrated, and, well before the days of ultrathin sectioning, an attempt was made to visualize the fine structure of human, pathological tissue by examining tissue pieces macerated in a blender. Contiguous with these studies, the 1944 model Toronto electron microscope was designed and built. With it Boswell did his precise determinations of lattice constants in small crystallites.
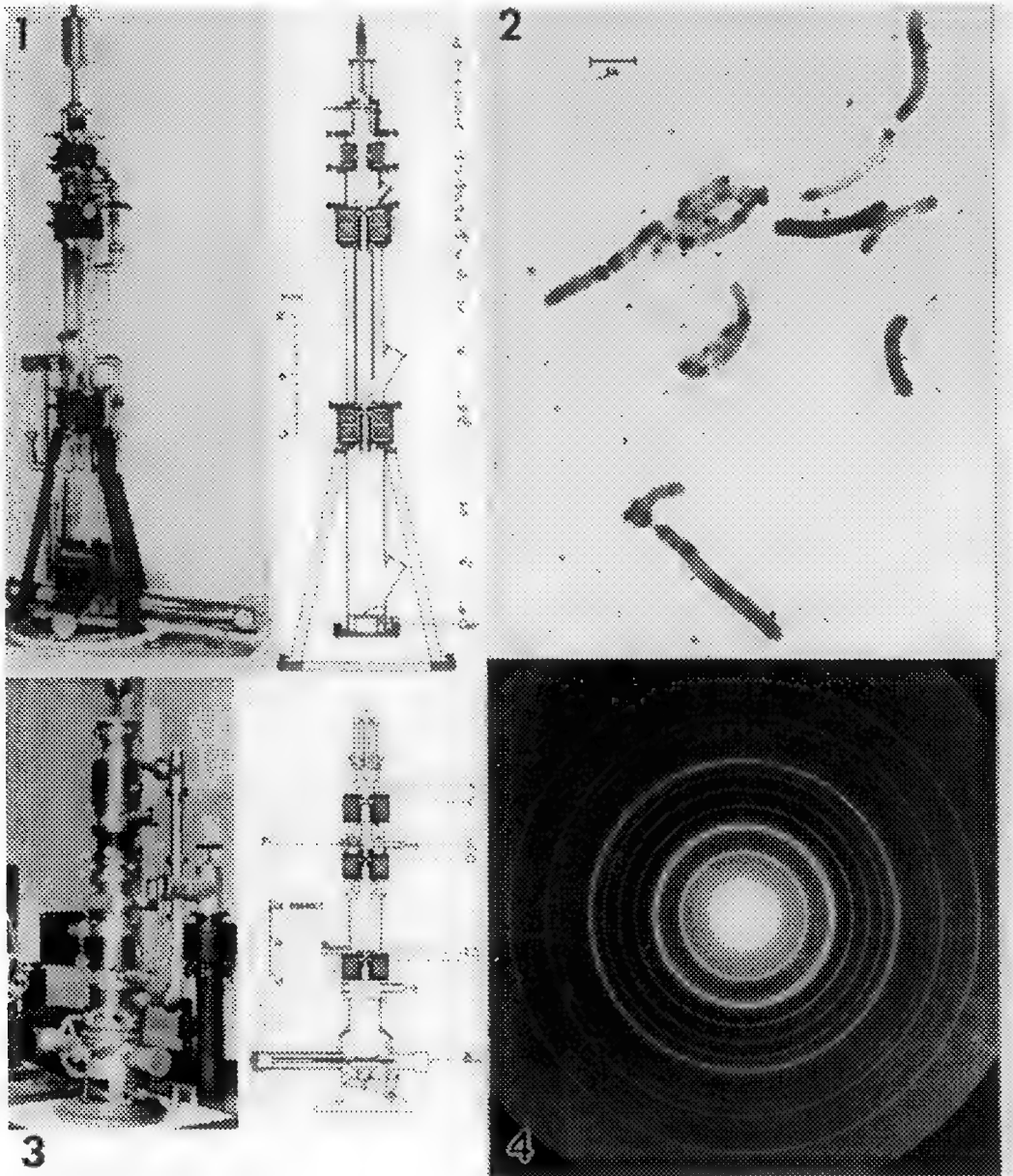
Fig. 1. The 1938 Toronto electron microscope. **Fig. 2.** A micrograph of vole bacilli, with the 1938 instrument. **Fig. 3.** The 1944 Toronto model. **Fig. 4.** A diffraction pattern of a TlCl vacuum-evaporated film, with the 1944 instrument.

EARLY ELECTRON MICROSCOPY REMEMBERED THROUGH THE CANDLE LIGHT OF HISTORY

Sterling Newberry

CBI Labs, 11 S. Westcott Road, Schenectady, NY 12306-9405

As nearly as we have been able to ascertain, three very early programs to make a true Electron microscope arose in this hemisphere independently and concurrently.[1] That is to produce instruments with demountable vacuum systems and means for interchanging specimens. Washington University in St. Louis was one of the three. The author is grateful for this opportunity to describe the Washington University work.

Washington University was a likely place for a beginning in electron microscopy. In the first quarter of the century it had risen to prominence in many fields especially physics, biology and medicine and close communication existed between them.[2] The physics department had direct lineage from J. J. Thompson and W. H. Bragg and close ties with Chicago and Berkeley. The biology department had strong connections with Woods Hole, while the medical school staff included "people from the four corners of the earth" and it had a close association with the Rockefeller Medical Institute.

Gordon Scott had been at Rockefeller the year before coming to WU in 1928. Scott began an orderly study of the location and role of soluble ions in the cell turning to the newest physical equipment and methods then available. He employed freeze drying, optical spectroscopy, and microincineration. The freeze drying set-up we used is shown in fig. 1. J. Howard McMillen joined him as a resident physicist in August 1935. They must have quickly hit upon the idea of trying to activate an oxide cathode of an emission microscope using the minerals in the cell, for they had such a microscope operating before the end of the year. The activation, up to three orders of magnitude over the background activation, was surprisingly good. Why they did not send a note off to Physical Review is hard to understand, but the first publication we know of was in 1937.[3] They built a second version which is the one shown with Scott and McMillen in fig. 2. McMillen obtained a teaching position at Kent State and was followed by David Packer who made several improvements during the year 37-38.

By 1937, Scott had received reports of resolution well beyond the optical microscope in Europe and his hopes that the emission microscope could distinguish between elements was fading. Thus when I started with him in the fall of 1938, he was determined that we should now make as high quality an instrument as we could from the parts of the second instrument. By spring of '39 we had the new microscope finished as shown in fig. 3. Our work was known in the biological community and we were on our way to becoming a center for Electron microscopy when our support was ended in favor of a global plan by the head of the medical school to win the Rockefeller grant to build a Medical Cyclotron.[1]

The microscope effort was not totally lost. Francis Schmitt who had become a close friend of the project, prepared a generation of biologist to be ready for the electron microscope when it should appear and was then taken by MIT where he built one of the first academic microscope facilities. He brought two graduate students with him from WU, Marie Jakus and David Waugh. Scott lost out to the Johnson foundation on a grant to build the higher voltage version of the emission microscope but was hired by them as a consultant in its construction. He also worked on the committee under NSF which sponsored the landmark application program masterfully executed by Anderson at RCA. He then became Head of Anatomy at UCLA and obtained one of the Early microscopes for them. There he started Dan Pease in the field of Electron Microscopy. He thence moved on to become dean of Wayne State University Medical school. It was my fate to be side tracked to applied physics during the war which greatly broadened my technology base. At wars end, my work returned to electron microscopy and related fields continuing even today. The highlights of this part of my career are well known to you.[1,4]

1. J. H. Reisner, Adv. Elect. & Electron Phys. (1989)73, 143.
2. F. O. Schmitt "The Never-Ceasing Search" Am. Phil. Soc. Memoirs Series (1990)188, 118.
3. J. H. McMillen, G. H. Scott, RSI (1937)8, 288.
4. S. P. Newberry, EMSA Bulletin (1985)15-1, 39; (1985)15-2, 39; (1986)16-1, 44.
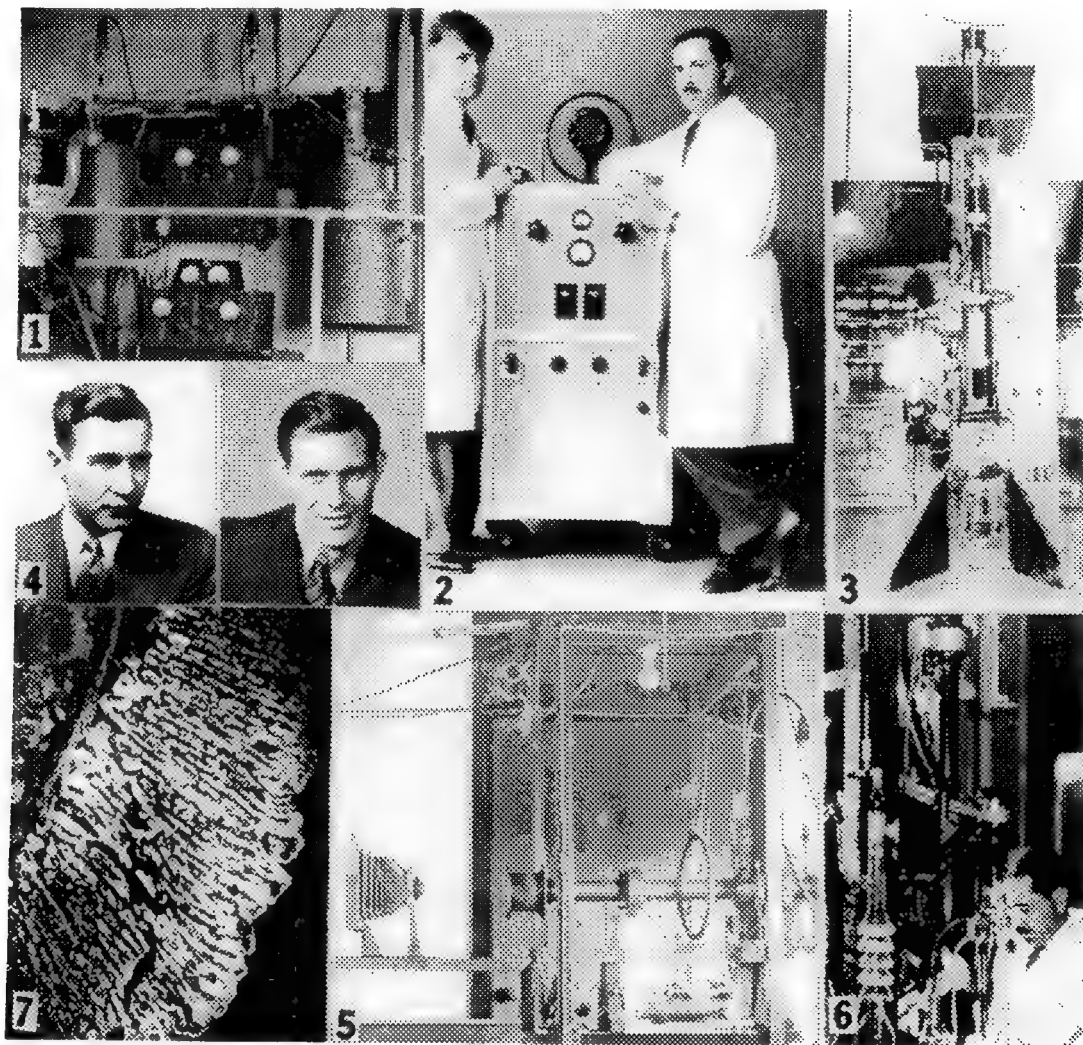
Fig. 1.--Freeze-drying setup in Scott's lab. Copies were built for other laboratories.

Fig. 2.--Scott and McMillen with the second version of the microscope.

Fig. 3.--The microscope of Scott and Newberry taken by the author.

Fig. 4.--Donald Packer left, and Sterling Newberry taken at different times. There are no pictures of them with the equipment.

Fig. 5.--The first version as modified by Packer and then Newberry. Apparently no one thought to take a picture of this first instrument until this one taken by the author.

Fig. 6.--Scott at the microscope of fig. 5 as taken by St. Louis Post photographer, copy supplied by Scott for 25th EMSA meeting historical Poster.

Fig. 7--Representative micrograph, mucous lining of monkey stomach magnification unknown.

ELECTROSTATIC OPTICS AND ABERRATION CORRECTION IN THE 1940s AND TODAY

Gertrude F. Rempfer

Department of Physics, Portland State University, Portland, OR 97207

I became involved in electron optics in early 1945, when my husband Robert and I were hired by the Farrand Optical Company. My husband had a mathematics Ph.D.; my degree was in physics. My main responsibilities were connected with the development of an electrostatic electron microscope. Fortunately, my thesis research on thermionic and field emission, in the late 1930s under the direction of Professor Joseph E. Henderson at the University of Washington, provided a foundation for dealing with electron beams, high vacuum, and high voltage.

At the Farrand Company my co-workers and I used an electron-optical bench to carry out an extensive series of tests on three-electrode electrostatic lenses, as a function of geometrical and voltage parameters. Our studies enabled us to select optimum designs for the lenses in the electron microscope. We early on discovered that, in general, electron lenses are not "thin" lenses, and that aberrations of focal point and aberrations of focal length are not the same. I found electron optics to be an intriguing blend of theory and experiment. A laboratory version of the electron microscope was built and tested, and a report was given at the December 1947 EMSA meeting. The micrograph in fig. 1 is one of several which were presented at the meeting. This micrograph also appeared on the cover of the January 1949 issue of Journal of Applied Physics. These were exciting times in electron microscopy; it seemed that almost everything that happened was new. Our opportunities to publish were limited to patents because Mr. Farrand envisaged a commercial instrument. Regrettably, a commercial version of our laboratory microscope was not produced.

At the time of our arrival at the Farrand Company, Professor Reinhold Rüdenberg was serving as an electron optics consultant for the electron microscope project. Rüdenberg held the basic patent on the electron microscope in Germany and also in the United States. His U. S. patent had been taken over by the Alien Property Custodian during World War II, but was regained with Farrand's help. Rüdenberg was interested in promoting the hyperbolic electron lens, because he believed that the hyperbolic potential field was free of spherical aberration. Actually, a converging hyperbolic lens, either with or without the effects of the apertures in the outer electrodes, exhibits spherical aberration of the same sign as do conventional electrostatic or magnetic electron lenses (i.e., undercorrected aberration). On the other hand a diverging hyperbolic lens (with a positive center electrode and foil windows) has spherical aberration of the opposite sign, (i.e., overcorrected aberration). This property led me to design a spherically-corrected combination of a converging lens with a diverging corrector having either one or two foil-windows. Figure 2, taken from a patent for a spherically-corrected doublet, illustrates the cancellation of the undercorrected spherical aberration of the converging component by the overcorrected aberration of the diverging component. The second drawing shows the electrode shapes for a hyperbolic lens. I left the Farrand Company in 1951; my husband had left a year earlier. A more detailed description of the Farrand electron microscope development is included in Reisner's account of the early history of electron microscopy in the United States [1].

Since the Farrand years I have continued my involvement in electron optics, most recently in emission microscopy and related low-energy electron microscopies, in collaboration with Professor O. H. Griffith of the University of Oregon. For a review of the history of these microscopies see ref. [2]. Today we are developing a

new method of using the hyperbolic field to correct aberrations, this time by means of a hyperbolic mirror, which can, in principle, simultaneously compensate both the chromatic and the spherical aberrations of electron lenses [3].

References

1. J. Reisner, in P. W. Hawkes, Ed., Advances in Electronic and Electron Physics, New York: Academic Press 73(1989)115.
2. O. H. Griffith and W. Engel, Ultramicroscopy 36(1991)1.
3. G. F. Rempfer, J. Appl. Phys. 67(1990)6027.
4. This work was supported by NSF Grant No. DIR 8907619.
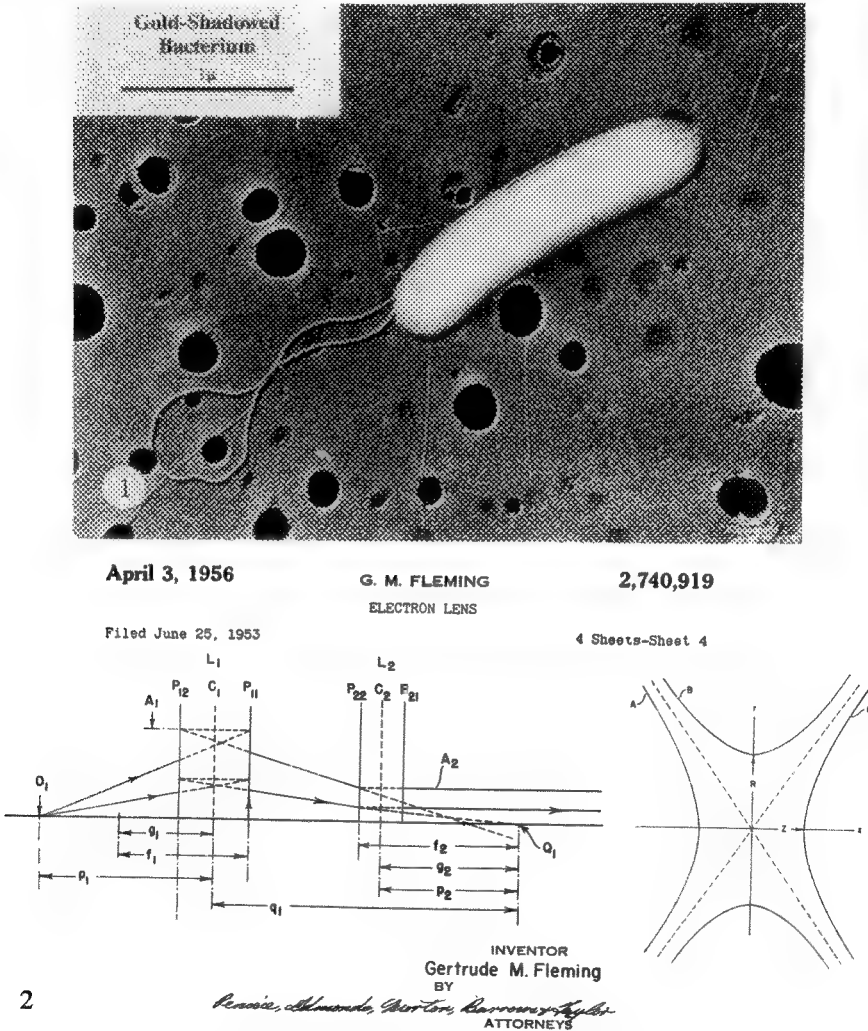
Fig. 1.--Electron micrograph taken with the Farrand electrostatic electron microscope in 1947. Acceleration voltage, 30kV; no objective aperture stop.
Fig. 2.--Diagrams from corrected lens patent illustrating cancellation of spherical aberration (left) and hyperbolic electrodes (right). Patent under maiden name.

ELECTRON MICROSCOPY AND CELL BIOLOGY IN THE 20TH CENTURY

Keith R. Porter

Department of Biology, University of Pennsylvania, Philadelphia, PA

The recent history of cell biology cannot be recorded without generous reference to electron microscopy. After all, it was this instrument and the enormous increase in resolution it provided that gave cell biologists access to information that even the most imaginative of investigators had not submitted to the printed page. This paper will record highlights that a few investigators introduced into specimen preparation. This pursuit has contributed more to the progress, i.e. history, of the field than is generally recognized. The first images of cells that can be said to reveal something new were published in 1945.[1] They were micrographs of thinly spread cells grown in tissue culture on surfaces coated with formvar and thence with evaporated carbon. .After the suitability of a cell or group of cells had been established by light microscopy, they were freed of culture medium with balanced salt solution and fixed with OsO4. Thereafter, and before drying, the selected cells were washed in distilled water, and to get the cells onto a grid, a small flap of the formvar film was separated from the glass surface and floated over the grid. Subsequently, the preparation was drained of H_2O on filter paper and allowed to dry. Cells that resided in open areas between the wires of the grid were available for examination.[2]

The first images of the cultured cells showed a lacework of strands and vesicles too small for resolving with the light microscope. We could see from its density and morphology that it comprised a unit system; and after additional studies it became evident that the whole was membrane-limited.[3] In calling it as we did we were influenced by the nomenclature of the Protozoologists. Just where they came from with their endoplasm and ectoplasm, I do not know, but it was evident that this new structure was part of the endoplasm and that it was reticular in general form.[4]

It can be argued that cultured cells have a few advantages over thin sections, e.g. there is more of the cell in the preparation. However, not every cell type can be cultured and most are too thick in the region of the cell center for satisfactory microscopy. Thus the pressure to design a microtome capable of cutting very thin sections was intense. Several models were constructed and tested, but none was totally satisfactory. Some got lost in trying to modify available microtomes for the task. It has to be said that one, more than all the others, was simple in design and effective in cutting thin sections.[5] Advance of the embedded tissue to the knife was obtained by heating a horizontal bar with a reading lamp. This crude device for advancing the specimen was soon replaced by a mechanical one, which proved in all respects to be superior to the original.[5]

It is possible to identify several additional technics which in combination with the above have contributed greatly to the growth of cell biology over the decades since the 1950s.

References

1. K.R. Porter, A. Claude and E.F. Fullam, J. Exp. Med.(1945)81, 233.
2. A. Claude, K.R. Porter and E.G. Pickels, Cancer Res.(1947)7, 421.
3. K.R. Porter and H.P. Thompson, J. Exp. Med.(1948)88, 15.
4. K.R. Porter and F.J. Kallman, Exp. Cell Res.(1953)4, 127.
5. K.R. Porter and J. Blum, Anat. Rec.(1953)117, 685.
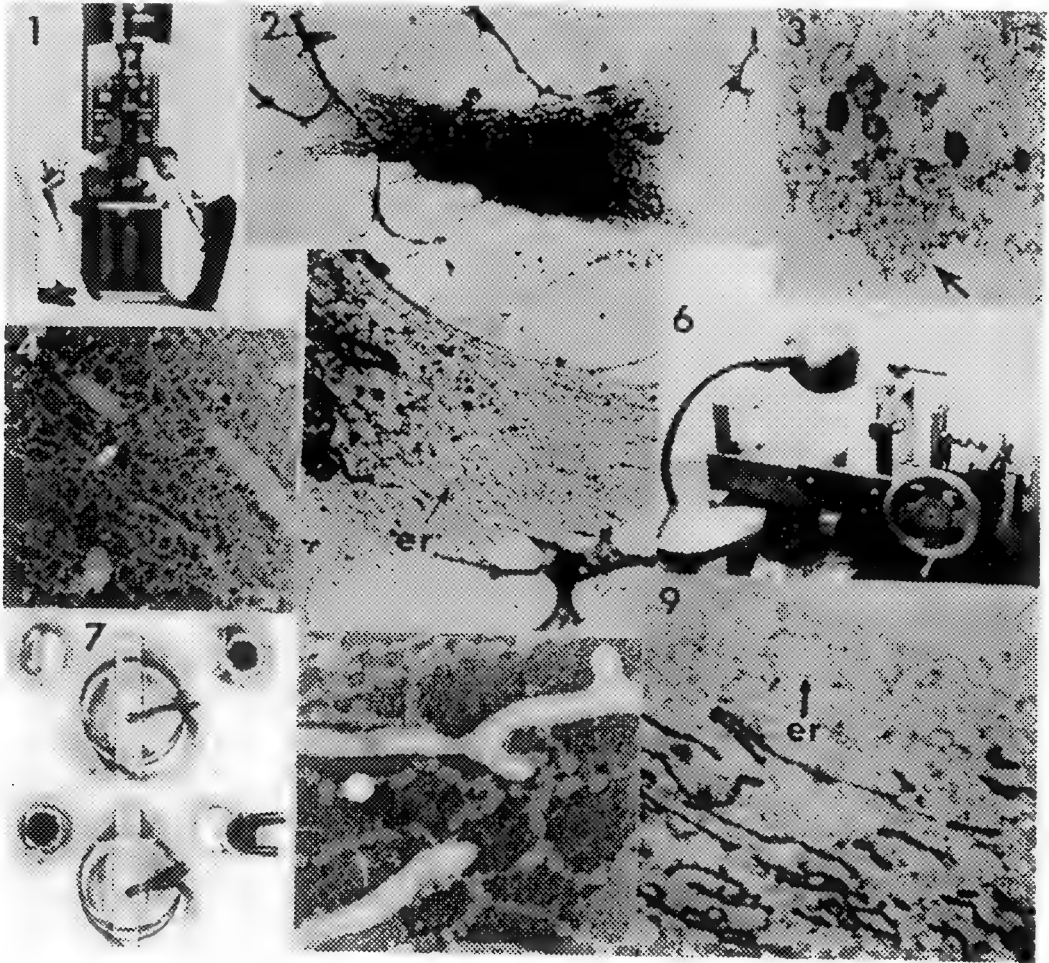
FIG. 1.--RCA type B electron microscope used in early studies.
FIG. 2.--The first image of a chick fibroblast.
FIG. 3.--Chicken tumor 10 cell showing virus-like particles.
FIG. 4.--Part of thin edge of cell from mouse mammary tumor.
FIG. 5.--Margin of cell in Fig. 1. See endoplasmic reticulum (ER).
FIG. 6.--Earliest microtome for thin sectioning (left hand version!).
FIG. 7.--Drawings of steps in getting cells onto grids.
FIG. 8.--Normal rat fibroblast showing strands of ER vesicles.
FIG. 9.--Endoplasmic reticulum (ER) in thin margin of fibroblast
after prolonged exposure to OsO_4.

PROBING THE SPATIAL ORGANIZATION OF NUCLEIC ACIDS WITHIN CELLS BY NON-ISOTOPIC IN SITU HYBRIDIZATION

Jeanne Bentley Lawrence

Dept. of Cell Biol., U. of Mass. Med. Center, Worcester MA 01655

In situ hybridization is a powerful experimental approach that directly couples molecular and cytological information in a visual context. Advances in hybridization procedures over recent years, coupled with previously described non-isotopic labelling methods developed in a number of laboratories, now provide a way to detect nucleic acids within cells with a high degree of resolution and sensitivity. Adaptations of this technology allow either DNA or RNA to be detected and visualized either with the light microscope, using fluorescence or colorimetric methods, or with the electron microscope using antibodies conjugated to gold or peroxidase. The potential applications of this technology are relevant to numerous areas of biomedical research and range from the more straightforward study of differential gene expression in single cells within a population to the precise localization of individual genes or RNAs within the cytoplasm or nucleus of a cell.

In order to bring the practical application of this technology closer to its theoretical potential, Lawrence and Singer[1] began quantitative analytical work a number of years ago to identify key parameters which would allow greater sensitivity and efficiency of hybridization. This initial work focused on the optimization of procedures which significantly increased the preservation and detection of cytoplasmic mRNAs, resulting in the demonstration that some mRNAs show discrete localizations near the site of function for the corresponding protein[2]. Further developments in electronmicroscopic detection of in situ hybridization using 5nm and 10nm gold-labelled antibodies have allowed direct visualization of the association of actin mRNA with specific elements of the cytoskeleton[3] (see abstract by R.H. Singer). Although initially done in triton-extracted whole mounts, ultrastructural in situ hybridization has been extended to studies of mRNA molecules within sectioned material of non-extracted muscle[4].

In other work, quantitative analysis of procedures for high sensitivity hybridization to double-stranded DNA within the nucleus led to the fluorescence detection of single-copy genes within metaphase chromosomes and interphase nuclei[5]. This non-statistical gene detection technology has far-reaching impact in a number of areas, including human genetics, clinical cytogenetics, virology and studies of nuclear organization[6-9]. The power of this approach has been further enhanced by the ability to detect multiple sequences simultaneously using two and three-color detection schemes. Analysis can be done using inexpensive dual and triple-band microscope filters or more sophisticated digital imaging procedures that allow detailed three-dimensional analyses.

In addition to the visualization of single genes within cells, the localization of intranuclear RNAs by fluorescence hybridization has

produced exciting results. Since the initial visualization of highly localized accumulations or "tracks" of RNA from an integrated viral genome[10], we have undertaken several studies to investigate the site of transcription, transport, and processing of individual gene transcripts or classes of RNA. Our analyses indicate that these processes are highly organized and compartmentalized within the nuclear interior (see abstracts by Lawrence et al. and Carter et al.). We are currently developing and applying approaches which integrate biochemical fractionation, immunohistochemistry for specific proteins, and hybridization to both DNA and RNA to obtain a more in depth view of genome and nuclear organization[11,12].

Future application and development of this technology for light and electron microscopy will allow still more precise and sophisticated questions to be addressed, providing a powerful approach for visualizing the spatial localization of nucleic acids within cells.
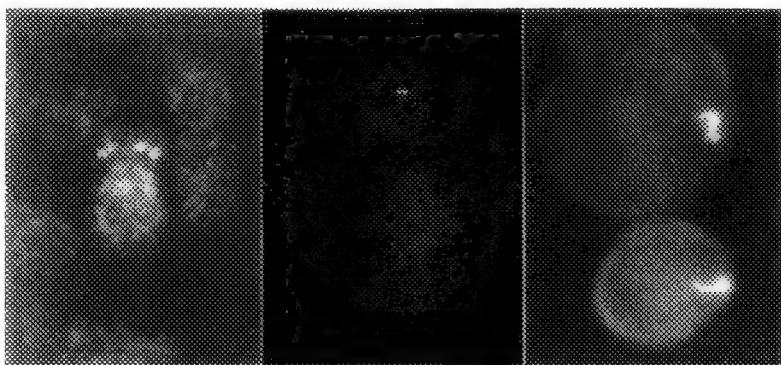
Left: Detection of two 10kb sequences from the human dystrophin gene, separated by 1Mb resolved across the width of metaphase chromosomes. Middle: Extremely high visualization of sequnces separated by 50-100kb can be obtained by hybridization to interphase nuclei. Right: A nuclear track of specific viral RNA.

References

1.   JB Lawrence and RH Singer (1985) Nucl Acids Res 13:1777.
2.   JB Lawrence and RH Singer (1986) Cell 45:407.
3.   RH Singer, GL Langevin, and JB Lawrence (1989) J Cell Biol 108:2343.
4.   ME Pomeroy et al. (1991) Dev. Biol. 143:58.
5.   JB Lawrence, Villnave CA and Singer RH (1988) Cell 57:51.
6.   JB Lawrence in Genome Analysis Volume 1: Genetic and Physical Mapping Cold Spring Harbor NY: Cold Spring Harbor Press, 1990, p. 1-38.
7.   P Lichter et al. (1991) Genetic Analysis Techniques and Applications 8:24.
8.   BJ Trask (1991) Methods in Cell Biology 35:3.
9.   JA McNeil, et al. (1991) Genetic Analysis Techniques and Applications 8:41-58.
10. JB Lawrence, RH Singer, LM Marselle (1989) Cell 57:493.
11. Y Xing, JB Lawrence (1991) J. Cell Biol. 112:1055-1063.
12. KC Carter, KL Taneja, JB Lawrence (1991) J. Cell Biol. 115:1191.

IMAGING CELLULAR DYNAMICS USING SCANNING LASER CONFOCAL MICROSCOPY

M. S. Cooper

Department of Zoology, University of Washington, Seattle, WA 98195

In recent years, the ability to image morphological dynamics and physiological changes in living cells and tissues has been greatly advanced by the advent of scanning laser confocal microscopy. Confocal microscopes employ optical systems in which both the condenser and objective lenses are focused onto a single volume element of the specimen.[1] In practice, galvanometer-driven mirrors or acousto-optical deflectors are used to scan a laser beam over the specimen in a raster-like fashion through an epifluorescence microscope. The incident laser beam, as well as the collected fluorescent light, are passed through pinhole or slit apertures in image planes that are conjugate to the plane of the specimen. This method of illumination and detection prevents fluorescent light which is generated above and below the plane-of-focus from impinging on the imaging system's photodetector, thus rejecting much of the fluorescent light which normally blurs the image of a three-dimensional fluorescent specimen.[2]

In living specimens, the rapid movement of the confocal microscope's scanning laser beam dramatically improves the imaging of rapidly moving particles and organelles which are displaced in cells by Brownian movement or active transport. As the scanning laser beam passes rapidly over the specimen in single sweeps, an effective stroboscopic illumination is produced which allows sub-micron particles, moving at rates on the order of 1 micron/second, to be imaged without motional blurring. Motional blurring normally poses a limitation to imaging systems which employ frame averaging techniques to increase signal/noise levels within video images. In general, the enhanced constrast that is generated by confocal microscopy improves both the resolution of cytological structures and the detectability of objects which are defined by a limited number of pixels.

When confocal images are constructed within video frame buffers, great flexibility exits in transferring time-lapse sequences to and from digital image files or optical memory disk recorders, which serve as analog storage devices for video images. Using image-reconstruction software, stacks of confocal images taken as a vertical series of x-y planes through the specimen (a z-series) can be rendered into 3-dimensional images. By acquiring a set of z-series at sequential timepoints, 3-dimensional time-lapse recording becomes feasible.

Time-lapse confocal microscopy is ideally suited to exploit the wide variety of fluorescent probe molecules which are available to stain organelles or report the concentrations of ions in living cells. Recent applications of confocal microscopy in living cells include: observation of vesicles emerging from the Golgi apparatus[3]; Ca-waves[4] and endoplasmic reticulum dynamics[5] in sea urchin eggs after fertilization; in situ imaging of neurotransmitter-induced Ca-oscillations within glial cells embedded in brain slices.[6] Time-lapse photobleaching-recovery with a laser confocal microscope has also been used to detect membrane fusion between organelle membranes within cells.[3] Several examples of time-lapse confocal recordings of living cells and tissues will be shown in this presentation.

The ability to monitor two channels of fluorescence simultaneously in confocal microscopy opens a wide number of experimental opportunities, especially in the area of resonance energy transfer[7], where close proximity between donor and acceptor fluorophore probe molecules can be detected. In addition to fluorescence, confocal microscopes can be configured to generate

images from laser light which is either transmitted through or reflected from the specimen. In many biological situations, it is extremely useful to acquire a brightfield or differential interference constrast (Nomarski) image from laser light transmitted through a stained specimen at the same time that an epifluorescence image of the object is being obtained.[2]

Confocal microscopy, like all fluorescence imaging, is constrained by the physics and photochemistry that is associated with the production of fluorescent light. Due to the presence of oxygen in living specimens, fluorophores have a statistical lifetime, measured in the average number of times they can be excited before they become photolyzed from reactions with singlet oxygen molecules. As fluorophores become bleached, free radicals byproducts are generated which are toxic to cells. Due to such constraints, success in imaging living specimens requires experimental trade-offs between a variety of factors including temporal resolution, spatial resolution, detectability, illumination intensity, saturation of a fluorophore response with increasing laser illumination, loss of fluorescence signal associated with fluorophore photobleaching, and loss of biological viability due to phototoxicity.[8] In computer-controlled confocal microscopy, the choice of photon acquistion rate necessary to obtain a desired signal/noise level in a given image is faciliated by the ability to rapidly change laser scanning speeds and photodetector integration time-constants electronically.

References

1. S. Inoue, Video Microscopy, Plenum Press, New York (1987).
2. A. Fine, B. Amos, R.M. Durbin and P.A. McNaughton, Trends in Neurosci. (1988) 11, 346.
3. M.S. Cooper, A.H. Cornell-Bell, A. Chernjavsky, J.W. Dani, and S.J. Smith, Cell. (1990) 61, 135.
4. S. Stricker, V.E. Centonze, S.W. Paddock, and G. Schatten, Dev. Biol. (1992) 149, 370.
5. M. Terasaki and L.A. Jaffe, J. Cell Biol. (1991) 114, 929.
6. J.W. Dani, A. Chernjavsky, J. Buchanan and S.J. Smith, Soc. Neurosci. Abstr. (1991) 17, 56.
7. R. E. Pagano, M. A. Sepanski, and O. C. Martin, J. Cell Biol. (1989) 109, 2067.
8. D.L. Taylor and E.D. Salmon, Methods in Cell Biol. (1989) 29, 207.
9. This work was supported by a NSF Presidential Young Investigator Award (DCB-9157132) and an Alfred P. Sloan Foundation Research Fellowship. The author gratefully acknowledges instrumental support from the Bio-Rad, Universal Imaging, and Meridian Instruments Corporations through the NSF PYI program.

SOLVING THE MECHANISMS RESPONSIBLE FOR ORGANELLE BEHAVIOR *IN VIVO* BY SAME-CELL CORRELATIVE LIGHT AND ELECTRON MICROSCOPY

Conly L. Rieder

Biological Microscopy and Image Reconstruction Biotechnological Resource Facility,
Wadsworth Center for Laboratories and Research, P.O. Box 509, Albany, New York 12201;
and Dept. of Biomedical Sciences, State University of New York, Albany, New York 12222

The behavior of many cellular components, and their dynamic interactions, can be characterized in the living cell with considerable spatial and temporal resolution by video-enhanced light microscopy (video-LM). Indeed, under the appropriate conditions video-LM can be used to determine the real-time behavior of organelles ≤ 25-nm in diameter (e.g., individual microtubules--see [1]). However, when pushed to its limit the structures and components observed within the cell by video-LM cannot be resolved nor necessarily even identified, only detected. Positive identification and a quantitative analysis often requires the corresponding electron microcopy (EM).

Same-cell correlative LM\EM provides a particularly powerful approach for elucidating the mechanisms responsible for the behavior of cell components. This method involves following the event of choice *in vivo* by video-LM, and then fixing the cell at a critical time during observation for a subsequent immunofluorescent (IMF) and\or 3D EM analysis. With this approach the past history of a particular event or response can then be correlated with the 3D ultrastructure underlying the behavior. Although technically demanding same-cell LM\EM eliminates the uncertainties inherent in "blind" studies and is an absolute requirement for obtaining convincing answers to many structure/function questions.

Over the past several years we have used same-cell LM\EM (in particular HVEM) to answer numerous questions regarding the behavior of spindle poles (i.e., centrosomes) in marine zygotes.[2-4] More recently we have used this approach to determine why chromosomes behave the way they do during the early stages of mitosis in vertebrate somatic cells, and why asbestos fibers become concentrated around the nucleus of interphase cells. Both studies are good examples of how same-cell LM\EM can provide data not obtainable by LM or EM alone.

Study #1. Chromosome Motion During the Early Stages of Mitosis

Background and Behavior: During spindle formation in vertebrates chromosomes usually attach first, and move rapidly toward, the closest spindle pole prior to forming a bipolar connection and slowly moving to the spindle equator. The order in which chromosomes attach is dictated by their distance from the pole at the time of nuclear envelope breakdown--those closest attach prior to those more distal. Chromosome attachment involves the formation of a kinetochore fiber (K-Fiber), composed primarily of microtubules (MTs), that firmly connects the one of the kinetochores on the chromosome to the pole. K-Fibers are also responsible for generating and/or transmitting the force for chromosome motion.

Explanation for Behavior: Our video-LM observations on newt lung epithelial cells (NLCs)

directly demonstrate that chromosomes become attached to a spindle pole when a dynamically unstable MT growing from that pole contacts one of the kinetochores on the chromosome[5]. This observation solves a century-old debate regarding the origin of K-Fiber MTs. Moreover, it offers a straightforward explanation for chromosome behavior during this spindle formation. Since MT density within the radial array of growing polar-nucleated MTs rapidly decreases as a function of distance from the pole, chromosomes should attach first to the closest pole, and those closer to the pole should attach prior to those more distal. Concurrent same-cell video-LM/IMF/EM studies on attaching chromosomes further reveal that: a) all Brownian motion is arrested 1-2 seconds after NLCs are contacted by 1% glutaraldehyde (in PO_4 buffer), b) individual pole-nucleated MTs are faithfully preserved by our fixation protocol, and c) the initial rapid poleward movement of an attaching kinetochore often occurs along the *surface* of a single MT[6]. From these observations it can be concluded that glutaraldehyde fixation rapidly and faithfully preserves dynamically unstable MTs within cell monolayers, and that the force-producers for poleward chromosome motion are located on the surface of the kinetochore.

Study #2. Crocidolite Asbestos Fibers in Interphase NLCs

Background and Behavior: The carcinogenic properties of asbestos fibers are related to their size and shape, not composition--long, thin fibers are more tumorigenic than shorter thicker ones. The primary working hypothesis for how asbestos transforms cells is that it physically interferes with chromosome distribution during mitosis to promote aneuploidy. Asbestos fibers are incorporated into cells by phagocytosis, and ultimately become highly concentrated around the nucleus. Why asbestos becomes positioned in the perinuclear region of cells is unknown.

Explanation for Behavior: NLCs incorporate asbestos fibers within 18 hours by endocytosis. Our video-LM observations reveal that fibers less than 5 μm long undergo rapid saltatory transport within the cell, whereas fibers over 5-μm long rarely exhibit such motions. Over time all of the fibers become preferentially located around the nucleus. Depleting the cell of MTs by Nocodazole treatment does not inhibit phagocytosis, but inhibits the saltatory motion of fibers and their perinuclear accumulation. Same-cell correlative LM/EM reveals that fibers exhibiting saltatory behavior are enclosed within a membrane[7]. It can be concluded from these observations that the perinuclear accumulation of asbestos fibers is MT-dependent. A hypothesis for this behavior, that is consistent with our results and those of others, is that upon endocytosis asbestos fibers are transported along MTs as endosomes, and eventually ac-cumulate within secondary lysosomes located near the nucleus (the perinuclear location of which is known to be maintained by the cytoplasmic MT network). The affinity of asbestos fibers for MTs, and the inability of the longer fibers to move along MTs, provides a possible mechanism for why the carcinogenic properties of fibers are linked to their dimensions.

References

1) L. Cassimeris, N.K. Pryer and E.D. Salmon. J. Cell Biol. (1988)107, 2223.
2) G. Sluder and C.L. Rieder. J. Cell Biol. (1985)100, 897.
3) G. Sluder, R. Miller and C.L. Rieder. J. Cell Biol. (1986)103, 1873.
4) G. Sluder, R. Miller, R. Cole and C.L. Rieder. J. Cell Biol. (1990)110, 2025.
5) J. Hayden, S.S. Bowser and C.L. Rieder. J. Cell Biol. (1990)111, 1039.
6) C.L. Rieder and S.P. Alexander. J. Cell Biol. (1990)110, 81.
7) R. Cole, J.G. Ault, J.H. Hayden and C.L. Rieder. Cancer Res. (1991)51, 4942.

ELECTRON PROBE X-RAY MICROANALYSIS OF SUBCELLULAR ION TRANSPORT *IN SITU*

Avril V. Somlyo, Ph.D. and Andrew P. Somlyo, M.D.

Department of Physiology, University of Virginia, Charlottesville, Virginia 22908

Electron probe x ray microanalysis [EPMA] provides quantitative information within a single spectrum about elements of biological interest with atomic number of 11 or greater. Therefore, the transport of ions and their accompanying co and counter ions across organelle membranes can be studied *in situ* by sampling within and adjacent to the intracellular organelle of interest under resting and stimulated conditions.

EPMA is based on the fact that the ionization of atoms by fast electrons generates x rays having energies characteristic of the excited atoms. The interaction of incident fast electrons with atomic nuclei generates a background of continuum x rays. Elemental quantitation of ultra thin sections with EPMA is generally based on the linear relationship between elemental concentrations and the ratio of the number of characteristic/continuum.[1-3] The use of this principle, together with the appropriate standards for calibration, has been the most successful approach for quantitative biological EPMA. The spatial resolution of EPMA at present is better than 10 nm and the practical limit of sensitivity for detecting calcium, (albeit with high electron dose), is approximately 0.3 mmol/kg dry wt.[4]. Two modes of data collection are utilized: fixed probe analysis of a region of interest or a scanning probe mode, where an x ray spectrum is collected at each picture point, to obtain quantitative elemental x ray maps. To preserve the morphology and the *in vivo* distribution of diffusible elements, we prepare specimens by rapid freezing in sub cooled Freon or, more recently with a Lifecell CF100 metal are mirror device; thin sections cut at -130 °C to -160 °C on a Reichert cryoultramicrotome. Msec time resolution of physiological are events can be achieved by freeze trapping.

Subcellular translocation of calcium, modulated via intracellular messengers, is a major mechanism of signal transduction. The following examples illustrate how the application of EPMA to problems involving calcium translocation in a variety of cells has provided new insights into intracellular Ca^{2+} transport:

1) Ca^{2+} has been quantitated within individual *terminal cisternae* of the sarcoplasmic reticulum (SR), where most of the Ca^{2+} is stored in resting striated muscle.[5] During a 1.2 sec tetanus, ~ 60% of the Ca^{2+} content of the TC is released, accompanied by the uptake of Mg^{2+} and K^+. In frog muscle, about 80% of the released Ca^{2+} is bound to parvalbumin, a cytosolic Ca-binding protein, as first directly shown by EPMA through changes in total cytoplasmic Ca^{2+} [5]. Measurements of Ca^{2+} and Mg^{2+} movements across the SR of muscles frozen at intervals following a tetanus showed that the half-time of the return of the total calcium released into the cytoplasm during a tetanus was 1.1 sec, comparable to the slow K_{off} rate of Ca^{2+} from parvalbumin and consistent with the hypothesis that the return calcium to the *terminal cisternae* is rate limited by the Ca^{2+} off rate from parvalbumin [6]. The delayed post tetanic return of Mg^{2+} from the TC into the cytoplasm was significantly slower than the time course of the calcium movements, suggesting that the Mg^{2+} permeability of the SR *in situ* is low, and may be transiently increased during tetanic stimulation.[6]

2) The morphology of the SR in mammalian myocardium differs from that of skeletal muscle: apart from *terminal cisternae* (junctional SR), the network contains corbular SR, which resemble *terminal cisternae*, but are not closely apposed to either the sarcolemma or the transverse tubule [7]. Both terminal cisternae and corbular SR stores calcium, but whether and how calcium is released from the corbular SR remains to be determined.[8,9] X-ray maps of atrial muscle revealed a previously unrecognized intracellular store of cardiac calcium: atrial-specific granules that store the

atrial natriuretic prohormone.[10]

3) Smooth, like cardiac, muscles are activated both by calcium influx and by calcium release from the SR. Calcium has been localized with EPMA to both the central SR and to the junctional SR that forms surface couplings with the plasma membrane.[11-13] These studies also showed that norepinephrine can release Ca^{2+} form the junctional and the central SR in depolarized, or in normally polarized smooth muscles, both in the presence and absence of extracellular Ca^{2+}. Approximately 50% of the Ca^{2+} stored in the central SR of the rabbit main pulmonary artery is released by maximal stimulation with norepinephrine.

4) EPMA measurements of mitochondrial composition in resting and in activated muscles, liver, brain, and retina demonstrated unequivocally that mitochondria do not regulate cytoplasmic Ca^{2+} [14,15]. Mg^{2+}, but not Ca^{2+}, increased in mitochondria in hormone stimulated liver.[16] This increase in [Mg^{2+}] may modulate the Mg^{2+} sensitive mitochondrial dehydrogenases. EPMA has shown unambiguously that, rather than mitochondria, the endoplasmic reticulum (ER) is the physiological store of calcium in non muscle cells. Hormones released Ca^{2+} from hepatic ER.[16] The honey bee photoreceptors contain large sacs of ER, allowing the probe to be positioned in the lumen: these measurements showed that 50% of the Ca content was released from the ER during light stimulation of dark adapted photoreceptors, and was accompanied by a highly significant increase in the Mg content of the ER.[17] Unlike the *terminal cisternae* of skeletal muscle, where K is the major counter ion accompanying Ca release in the photoreceptor, Mg^{2+} uptake can nearly balance the charge movement by Ca^{2+}.

The use of fluorescent Ca^{2+} indicators in a variety of cell types and identification of $InsP_3$ and ryanodine receptor/channels, suggest that different intracellular Ca releasing messengers may not access the same Ca storage pool, whereas other evidence suggests that Ca influx may be modulated by the amount of Ca stored in junctional ER; both spot mode EPMA and x ray mapping will be suitable for spatially resolving some of these storage sites and their interactions.

References

1. Hall, T.A.: Physical Techniques in Biological Research, G.P. Oster, (Ed), Academic Press, New York: 1A (1971), 257.
2. Shuman, H., et al: Ultramicroscopy 1 (1976) 317.
3. Kitazawa, T., et al: Ultramicroscopy 11 (1983) 262.
4. Somlyo, A.P. and Shuman, H.: Ultramicroscopy 8 (1982) 219.
5. Somlyo, A.V., et al.: J. Cell Biol. 90 (1981) 577.
6. Somlyo, A.V., et al.: J.Biol. Chem. 260 (1985) 6801.
7. Sommers, J.R. and Jennings, R.B.: The Heart and Cardiovascular System. H.A. Fozzard et al (Eds), Raven Press, New York (1986) p.61.
8. Moravec, C.S. and Bond, M.: Am. J. Physiol. 260 (1991) H989.
9. Jorgensen, A.P., et al: Circ. Res. 63 (1988) 1060.
10. Somlyo, A.V., et al: Proc. Natl. Acad. Sci. USA 85 (1988) 6222.
11. Bond, M., et al: J. Physiol. [Lond] 355 (1984) 677.
12. Kowarski, D., et al : J. Physiol. [Lond] 366 (1985) 153.
13. Somlyo, A.P., et al: J. Cell Biol. 81 (1979) 316.
14. Somlyo, A.P., et al: Nature 314 (1985) 622.
15. Moravec, C.S. and Bond, M.: J. Biol. Chem. 267 (1992): In Press.
16. Bond, M., et al: J. Biol. Chem. 262 (1987) 15630.
17. Baumann, O., et al : Proc. Natl. Acad. Sci. USA 88 (1991) 741.

SCANNED PROBE MICROSCOPY: PAST, PRESENT, AND FUTURE

Knute A. Fisher

Departments of Anatomy and Biochemistry & Biophysics, and Francis I. Proctor Foundation, University of California, San Francisco, CA 94143-0944

In the past decade a new family of image-forming devices has been developed, machines that do not use lenses and are collectively called scanned probe microscopes (SPM). The SPM family evolved from the scanning tunneling microscope (STM) developed by Binnig and Rohrer in the early 1980s. The tunneling microscope and subsequent probe microscopes, such as the atomic force microscope (AFM), are based on the precise positioning and scanning of a probe within nanometer distances of a surface. Sub-nanometer precision is accomplished using piezoelectric ceramics that change shape with applied electrical potential allowing probes to be moved laterally with less than 0.1-nm resolution and vertically with less than 0.01-nm resolution. This method of positioning has been routinely used with SPM over the past 10 years, during which time many different probes have been developed. These probes measure signals from a variety of physical phenomena such as electron tunneling, atomic force, electrical conductivity, temperature gradients, light absorption, ion currents, and magnetic properties. A significant difference between SPM and conventional light and electron microscopes is that the probes can operate in a wide range of environments including pressures that range from ultrahigh vacuum to ambient pressure, temperatures that range from liquid helium to hundreds of degrees Kelvin, and physical states that include immersion in hydrophobic liquids such as oil and hydrophilic liquids such biological buffers. The probes are usually scanned in either a constant signal mode or in a constant height mode. Signals are amplified and can be used to control the probe's vertical position. The signal is recorded digitally and displayed on a computer screen and thus can be manipulated by image-processing tools to generate topographic maps of the surface. The references at the end of this article cite several of the major reviews of probe microscopy.[1-13]

Despite the relatively recent invention of tunneling microscopy the STM has been increasingly widely used in the physical sciences, especially surface science. The STM has been used to study the silicon (111) 7 x 7 reconstruction, to visualize surface charge density, and to analyze the processes of atomic adsorption and growth of metal islands. As a non-averaging microscopic method the STM has uniquely contributed to studies of grain boundary and crystal surface defects. Numerous dynamic processes including electrochemical and corrosive phenomena have been studied. The STM has also been used in remarkable nanofabrication and micro-machining applications. It has been used to position and write on planar crystal surfaces with single atoms. Despite the requirement for electrical conductivity, the STM has been used to image organic polymers and liquid crystals with submolecular resolution. It has also been used to image single biological molecules such as DNA, actin, collagen, cellulose, enzymes, storage proteins, and antibodies. For most biological studies, however, highly oriented pyrolytic graphite (HOPG) has been used as the electrically conductive substrate. Unfortunately, HOPG alone can generate structures that resemble linear or globular molecules. There is a

saying that if you've invented a new hammer, everything looks like a nail! And that thought can be applied to many early STM images of samples mounted on HOPG that purported to show molecules and sub-molecular structure. Nevertheless some striking images of metal-coated molecules and supramolecular assemblies have been published. The force microscope has been used to image a wide variety of biological structures ranging from 10-nm particles to whole cells.

What is happening at the present? The SPM, especially tunneling microscopes, have become increasingly common tools in surface science and continue to be applied to studies of the atomic organization of surfaces. On the industrial side the STM is widely used for metrology and evaluating and quantifying surface characteristics, for example of data storage devices such as compact discs. There are currently dozens of companies worldwide that produce commercial SPMs. The force microscopes are increasingly used to study hydrated biological samples under physiological conditions, hydrated planar lipid bilayers and monolayers, and have even begun to be used in biomedical studies. From the standpoint of technology development, there are two areas that are being currently investigated actively. First, probes are being developed that are appropriate for sub-nanometer studies, and second, the interactions between the tip and the sample, especially soft organic samples, are being investigated. Several laboratories and companies worldwide are addressing the issue of producing high resolution tips. Soft or biological sample stabilization is also being investigated with focus on high-resolution coatings and/or stabilization by freezing and scanning at cryogenic temperature.

And what about the future of SPM? This question was addressed at the tenth anniversary meeting of STM in Interlaken, Switzerland last summer, by Rohrer who in 1986 with Binnig received the Nobel Prize for their invention of the STM. Rohrer noted that new combination microscopes such as an STM/AFM will continue to be developed. In addition it is likely that SPMs will be used experimentally rather than solely as imaging tools. In the biological sciences sample and probe preparation techniques will be developed that allow routine sub-molecular imaging and especially imaging of dynamic processes in a physiologically relevant milieu. The future of scanned probe microscopy appears exciting indeed.

References (reviews)
1. G. Binnig and H. Rohrer, *Sci. Amer.* (1985) **253**, 50.
2. G. Binnig and H. Rohrer, *IBM J. Res. Dev.* (1986) **30**, 355.
3. J. A. Golovchenko, *Science* (1986) **232**, 48.
4. C. Quate, *Phys. Today* (1986) **39**, 26.
5. P. Hansma and J. Tersoff, *J. Appl. Phys.* (1987) **61**, R1.
6. P.K. Hansma et al., *Science* (1988) **242**, 209.
7. B. Drake et al., *Science* (1989) **243**, 1586.
8. K.A. Fisher, *J. Elect. Microsc. Tech.* (1989) **13**, 355.
9. J.P. Rabe, *Angew. Chem.* (1989) **101**, 117.
10. H.K. Wickramasinghe, *Sci. Amer.* (1989) **Oct**, 79.
11. E.P. Stoll, *IBM J. Res. Dev.* (1991) **35**, 67.
12. A. Engel, *Annu. Rev. Biophys. Biophys. Chem.* (1991) **20**, 79.
13. D. Sarid, *Scanning Force Microscopy*, (1991) New York: Oxford Univ. Press
14. Supported by a grant from NIDA, number DA05043.

AN ATOMIC RESOLUTION STUDY OF A CARBIDE PHASE IN PLATINUM

M.J. Witcomb*, M.A. O'Keefe, C.J. Echer, C. Nelson, J.H. Turner, U. Dahmen and K.H. Westmacott

National Center for Electron Microscopy, University of California, LBL, Berkeley, CA 94720
*Electron Microscope Unit, University of the Witwatersrand, Johannesburg, South Africa

Under normal circumstances, Pt dissolves only a very small amount of interstitial carbon in solid solution. Even so, an appropriate quench/age treatment leads to the formation of stable Pt_2C {100} plate precipitates[1,2]. Excess (quenched-in) vacancies play a critical role in the process by accommodating the volume and structural changes that accompany the transformation. This alloy system exhibits other interesting properties. Due to a large vacancy/carbon atom binding energy[3], Pt can absorb excess carbon at high temperatures in a carburizing atmosphere[4]. In regions rich in carbon and vacancies, another carbide phase, Pt_7C, which undergoes an order-disorder reaction[5] was formed. The present study of Pt carburized at 1160°C and aged at 515°C shows that other carbides in the Pt_xC series can be produced.

Figure 1a is a bright field micrograph of a typical field of precipitate plates with a {001} habit, formed when Pt was carburized at 1160°C and subsequently aged at 515°C. Corresponding μ-μ-diffraction patterns taken along a <100> zone axis are shown for an individual precipitate variant and the nearby matrix in Figure 1b and c. Weaker superlattice reflections bisecting the fundamental Pt spots were observed in all the patterns, as found in earlier studies of ordered Pt_7C[5].

Direct atomic resolution imaging of the precipitate structure was performed on the JEOL ARM-1000 at 800keV for a series of defocus and thickness values. One member of a through-focus series showing an edge-on precipitate plate in a <110> zone axis is given in figure 2. It is seen that the image characteristics change along the length of the precipitate as the foil becomes thicker. To parallel these observations, image simulations were performed, using the NCEMSS[6] HREM images simulation programs to produce computed image-thickness-focus maps[7]. When the model for Pt_7C, deduced from earlier work was used, no satisfactory match with experiment could be found. On the other hand, images computed using the sub-stoichiometric Pt_3C_{1-x} model, shown in figure 3, resulted in a very satisfactory match as a function of increasing thickness (see figure 4). These preliminary results suggest that, as a function of foil thickness, high resolution images are sensitive to subtle changes in structure, even when the constituent atoms include light elements[8]. The sensitivity of these high resolution images to the stoichiometry of the carbide is currently being investigated in more detail.

References
1. M.J. Witcomb et al., Acta Met., **31** (1983) 743, 749, 755.
2. ibid Proc. EMSSA **11**, (1981) 45.
3. U. Dahmen et al., Proc. Int'l. Conf. on Solute/Def. Interactions, Kingston, Ontario (1986) 91.
4. P. Fergusson et al., Mat. Sci & Techn. **1** (1985) 53.
5. K.H. Westmacott et al., Met. Trans., **A17** (1986) 807.
6. R. Kilaas, Proc. *45th Ann. Meeting EMSA, Baltimore* (1987) 66.
7. M.A. O'Keefe et al., Mat. Res. Soc. Symp. Proc. **159** (1989) 453.
8. This work was supported by the Director, Office of Energy Research, Office of Basic Energy Sciences, Chemical Sciences Division of the U.S. Department of Energy, under contract No. DE-AC03-76SF00098.
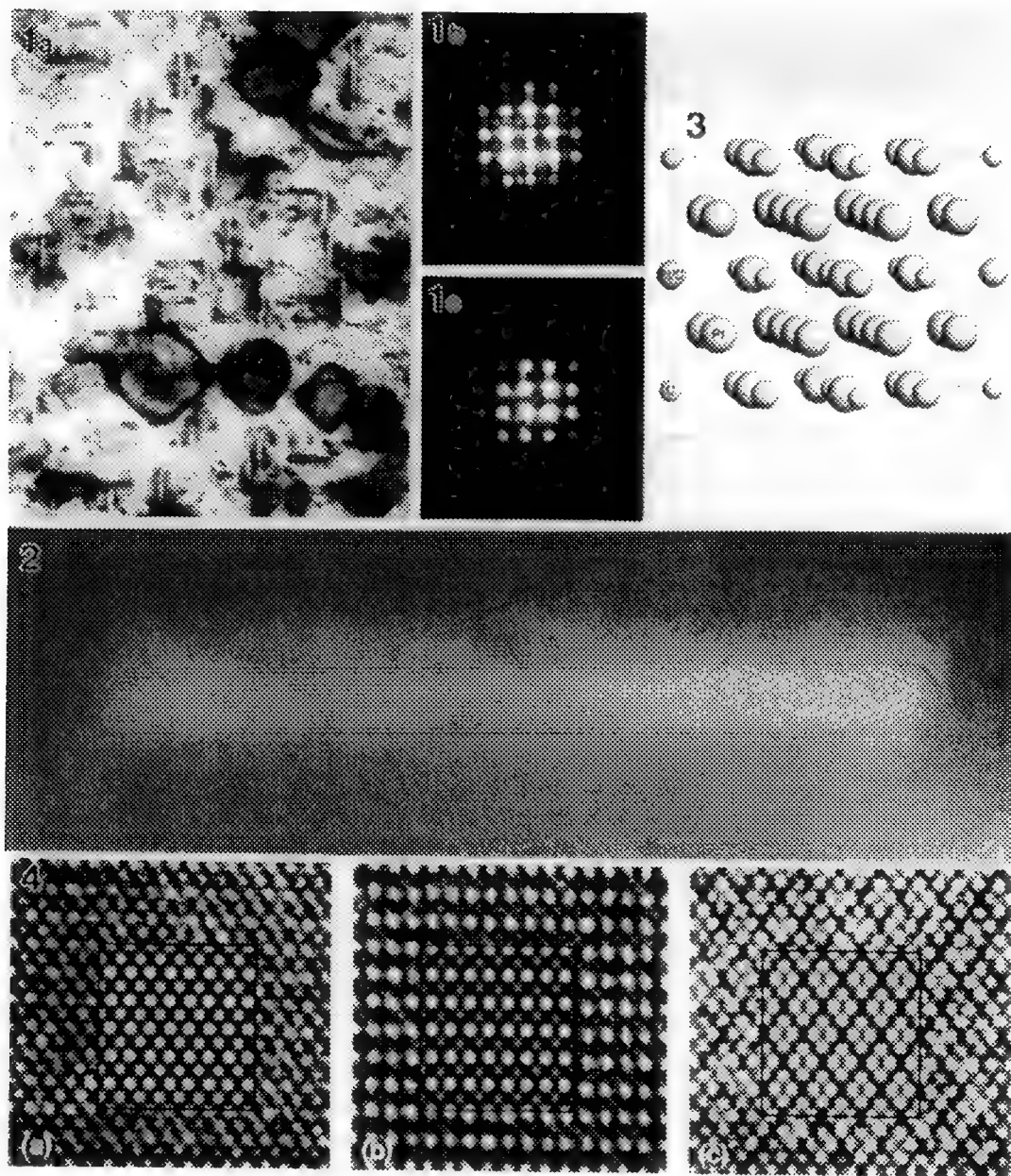
Fig.1 Bright-field micrograph of {001} carbide precipitate plates (a). μ-μ-diffraction pattern from single variant (b), and nearby lattice (c).

Fig.2 {001} plate imaged at high resolution in the JEOL ARM-1000 at 800keV.

Fig.3 Structural model of Pt_3C_{1-x} for simulation, showing Pt sites, C sites and mixed Pt/C sites.

Fig.4 Comparison of simulated and experimental images as a function of foil thickness for (a) 22Å, (b) 33Å, and (c) 44Å. Microscope conditions were 800keV, C_S=2.0mm, defocus=-1400Å, convergence semi-angle of 0.6mrad, spread of focus of 140Å halfwidth.

THE EFFECT OF THERMAL EXPOSURE ON PRECIPITATION OF $Ti_3Al(C,N)$ IN Ti-48Al-1V-0.2C

W.T. Donlon, W.E. Dowling, C.E. Cambell, and J.E. Allison

Ford Motor Company, Research Laboratory, SRL S-2065, Dearborn, MI 48121-2053

Titanium aluminides are attractive candidates for high temperature structural applications because of their high strength to weight ratio at elevated temperatures. The microstructure of these alloys consists of γ-TiAl (distorted Ll_0 structure), plus α_2-Ti_3Al (ordered DO_{19} structure). Varying the heat treatment temperature and cooling rate of these alloys alters the volume fraction and distribution of the γ and α_2 phases. This has significant effects on the room temperature ductility.[1] In addition, precipitation of carbides has been observed during high temperature exposure.[2] The effect of these precipitates on the mechanical properties has yet to be determined.

Figure 1 shows the general microstructure that was used for this investigation. TEM foils were prepared by electropolishing using 5% perchloric, 35% 1-butanol, 60% methanol at -40°C. No precipitates were found following heat treatment in the $\gamma+\alpha$ phase field. Samples approximately 20 mm square were thermally exposed to temperatures between 625° and 1000°C for times between 1 and 2000 hours.

Thermal exposure to temperatures between 675° and 775°C produces fine spherical or ellipsoidal precipitates in the γ-TiAl matrix (Figures 2 & 3). Precipitate free zones are observed around dislocations, at γ/α_2 and most γ/γ grain boundaries. Some regions were observed to contain large number of precipitates while other regions contained no precipitates, suggesting variations in chemistry of the γ-TiAl matrix. Diffraction patterns from areas containing these precipitates exhibit diffuse extra reflections in the positions of the forbidden {100} γ-TiAl reflections. Thermal exposure to temperatures of 825 to 925°C results in precipitates occurring only on grain boundaries and on pre-existing dislocations (Figure 4). Diffraction intensity due to these precipitates consists of sharp discrete extra reflections, but is otherwise identical to that observed from the precipitates formed at lower temperatures. Figure 5 shows precipitate reflections observed in the [010], [01$\bar{1}$], and [111] γ-TiAl zone axis. Analysis of these diffractions shows that the position and intensity of the extra reflections is consistent with the Perovskite $Ti_3Al(C,N)$ structure. Temperatures and times for which these precipitates were observed were plotted to generate a precipitation curve (Figure 6). Reversion experiments are currently in progress to determine the solvus temperature of the $Ti_3Al(C,N)$ precipitates.

The effect of these precipitates on the room temperature mechanical properties was determined by machining tensile samples from material which was thermally exposed at 775°C for 100 hr and 825°C for 100 hr to introduce high densities of each morphology of precipitate. No change in the tensile properties were observed for either exposure condition when compared to material which had not been thermally exposed.

1. W.E. Dowling et al., Proceedings on Microstructure/Property Relationships in Titanium Aluminides and Alloys, ed. Y.W. Kim & R.R. Boyer, TMS, (1991), 123.
2. P.L. Martin et al., Proceedings of the Fourth International Conference on Creep and Fracture of Engineering Materials and Structures, Inst. of Metals, (1990), 265.
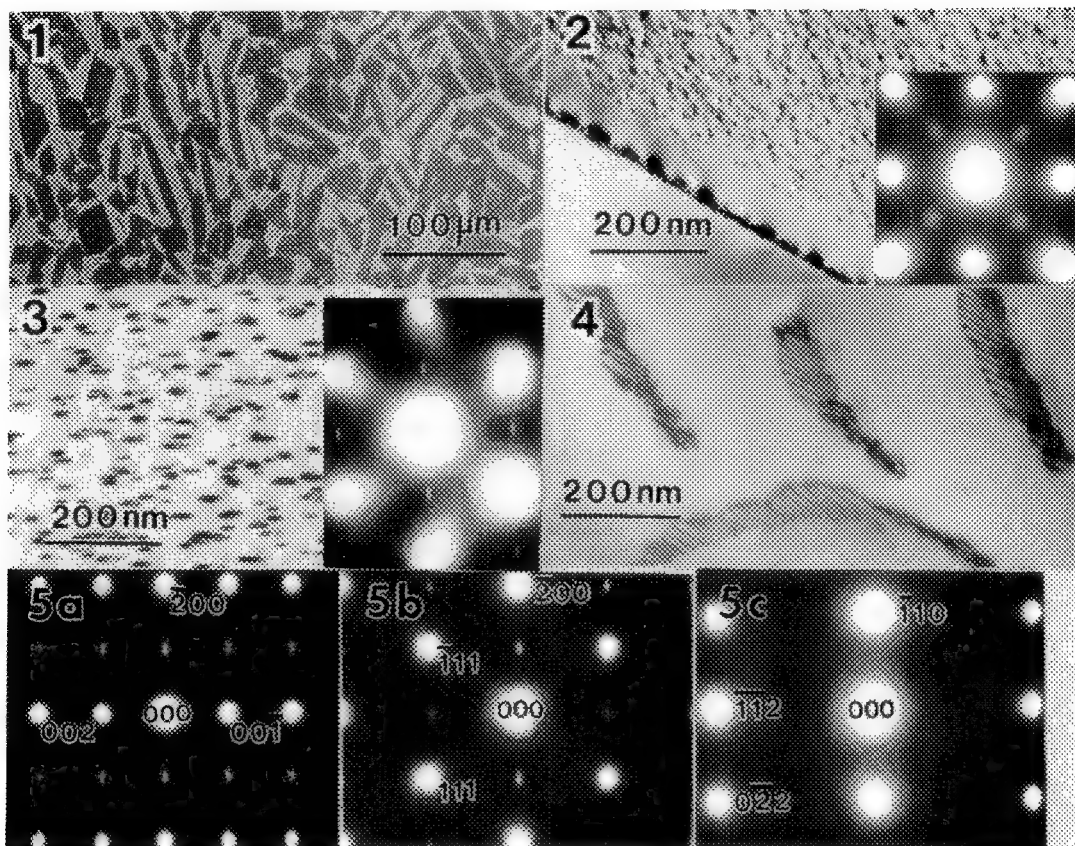
Fig. 1-Backscattered electron image of Ti-48Al-1V-0.2C alloy. White phase is Ti₃Al.
Fig. 2-Bright-field (BF) image of γ-TiAl grain in sample aged at 675°C for 500 hr.
Fig. 3-BF image of γ-TiAl grain in sample aged at 725°C for 500 hr.
Fig. 4-BF image of γ-TiAl grain in sample aged 850°C for 10 hr.
Fig. 5-SAED patterns of the [010], [0$\bar{1}$1], and the [111] γ-TiAl zone axis obtained from precipitates similar to those shown in Fig.4.
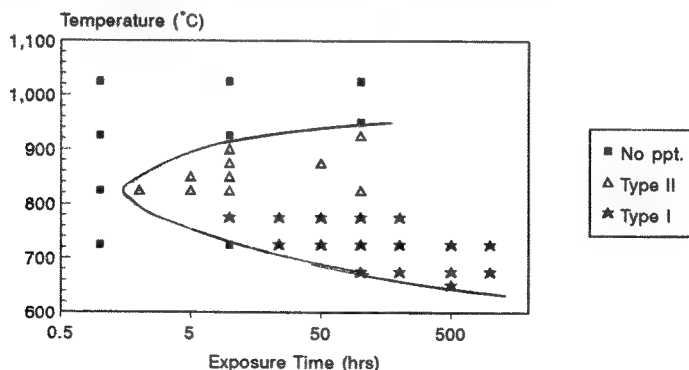
Fig. 6-Temperatures and times for which Ti₃Al(C,N) precipitates were observed. Type I precipitates are shown in Fig. 2 & 3, Type II precipitates are shown in Fig. 4.

TEXTURED CRYSTALLIZATION OF GERMANIUM TELLURIDE

M. Libera
Dept. of Materials Science and Engineering
Stevens Institute of Technology, Hoboken, New Jersey

Phase-change optical storage uses a focused laser to locally switch a chalcogenide film between the crystalline and amorphous states.[1] Data bits are stored as amorphous spots in a crystal matrix. They can be erased by laser annealing, but applications require fast crystallization during the erase. The crystallization kinetics are not well understood. A recent study of germanium telluride (GeTe) used time-resolved optical measurements and TEM to show that crystallization in $Ge_{48}Te_{52}$ films is dominated by the 2-D growth of crystallites in the film plane.[2] Current work relates the complex crystallite morphology to the operative transformation kinetics.

Fig. 1a shows a bright-field image of a 75nm $Ge_{48}Te_{52}$ film crystallized by furnace annealing.[2] The mottled contrast has been observed previously.[3] The SAD pattern of fig. 1b shows rings characteristic of a polycrystal. The odd reflections are weak and the even reflections are strong confirming that the film has NaCl ordering. $\{1,1,1\}$, $\{2,2,0\}$, and higher-order peak splitting is consistent with the GeTe rhombohedral distortion ($\alpha \sim 88°$).[4,5] Fig. 2a shows a bright-field image of one crystallite in a partially-crystallized 75nm $Ge_{48}Te_{52}$ film. The sequence of SAD patterns in figs. 2b–d were taken with progressively larger apertures centered on the crystallite center. The $\{211\}$ pattern in fig. 2b uses an aperture sampling a 0.2µm diameter region. This symmetry is preserved when the selected area is broadened to 0.8µm diameter (fig. 2c), but additional $\{220\}$ reflections appear with 6-fold symmetry. Fig. 2d uses an aperture sampling an area 4.5µm in diameter including the entire crystallite and some surrounding amorphous matrix. This pattern displays strong 6-fold symmetry with intense $\{220\}$-type reflections. The crystallite clearly adopts a strong texture with $\{111\}$ planes generally lying in the film plane.

Similar analysis of other crystallites indicates that all assume a general $\{111\}$ texture beyond the initial stages of growth. The discrete arcs of intensity in these patterns are consistently observed. These indicate that the sub-grains within each particle are all related to some parent orientation. Microdiffraction experiments are underway to relate the subgrains to the crystallite texture. In-situ annealing experiments are also underway to relate the isothermal growth rate to the observed crystallite morphology.[6]

1. M. Libera and M. Chen, MRS Bulletin XV, 40-45 (April, 1990).
2. M. Libera and M. Chen, submitted to J. Appl. Phys.
3. K.L. Chopra and S. Bahl, J. Appl. Phys. 40, pp. 4171-4178 (1969).
4. J. Goldak et al., J. of Chem. Phys. 44, 3323-3325 (1966).
5. M. Libera, M. Chen, and K. Rubin, J. Matls. Res. 6, 2666 (1991).
6. Thanks are due to M. Chen of IBM and H.C. Lee of Stevens for help in preparing the films. This work used the ATC-SEM TEM Facility at Stevens funded by the State of NJ and NSF grant #DMR-9109274.

Fig. 1 - a) bright-field TEM image of a fully-crystallized 75nm $Ge_{48}Te_{52}$ film; b) large-aperture SAD pattern showing peak splitting and intensity modulations characteristic of GeTe.
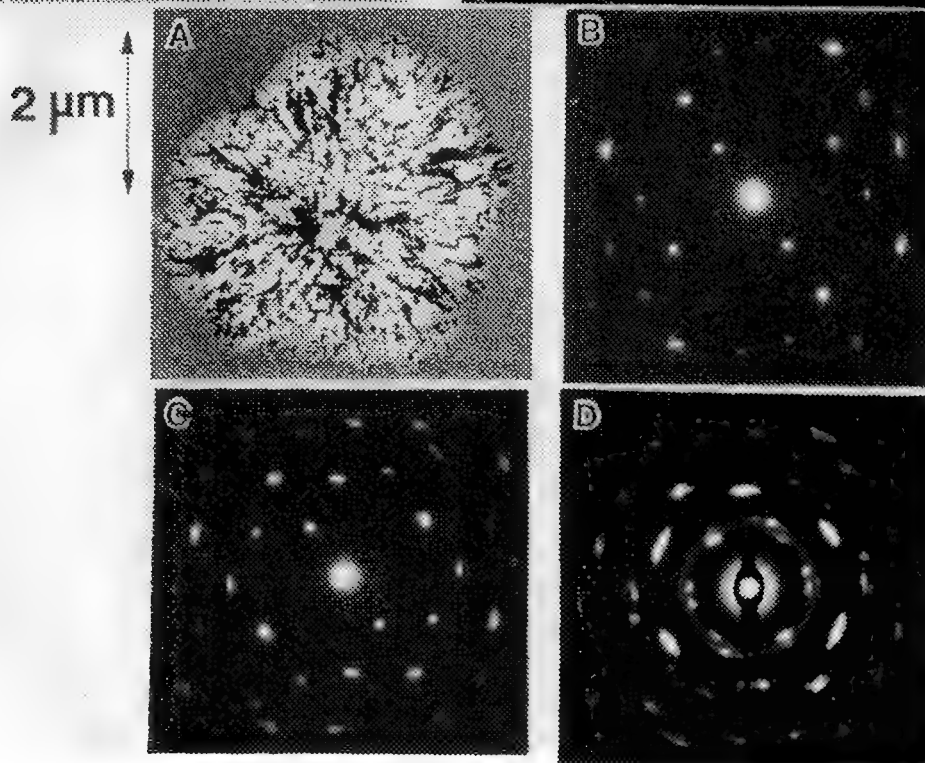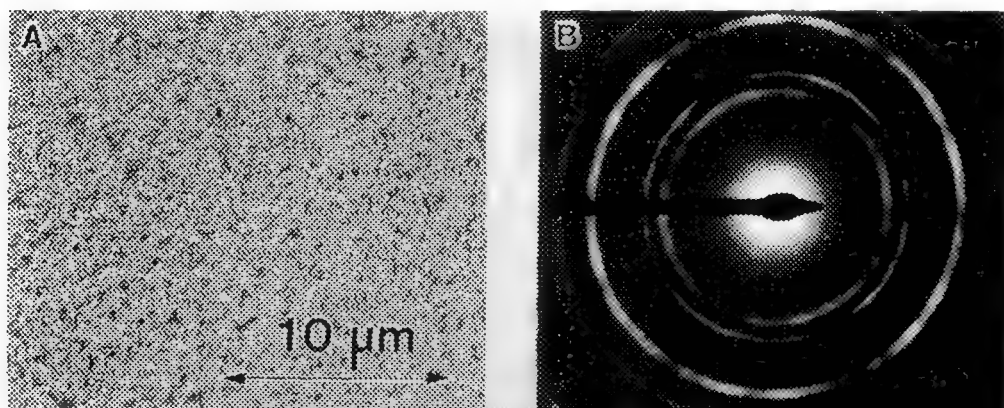
Fig. 2 - a) bright-field image of a single crystallite in a partially crystallized 75nm $Ge_{48}Te_{52}$ film; b-d) SAD patterns from the center of the crystallite with SAD apertures sampling 0.2μm (b), 0.8μm (c), and 4.3μm (d) centered on the crystallite center.

LAMELLAR MICROSTRUCTURE OF DISCONTINUOUS PRECIPITATION REACTION FRONT IN Cu-7.5%In

I. G. Solorzano[1] and M. Audier[2]

[1] Departamento de Ciencia dos Materiais e Metalurgia, PUC/Rio, 22453 Rio de Janeiro, Brasil
[2] Laboratoire de Thermodynamique et Physicochimie Metallurgique, CNRS/INPG, Grenoble, France

There is an increasing body of evidence for discontinuous precipitation (DP) as a general solid state phase transformation in materials[1,2]. The understanding of the DP phenomenon, however, requires to establish its energy balance. The lamellar microstructure at the grain boundary reaction front (RF) is of particular interest since it results from the optimization of, at least, chemical, capillary and interfacial energy terms coupled with the boundary mobility at a given undercooling[3]. Our investigation into this field has lead us to the conclusion that an additional term reflecting the residual stresses in the transformed product should be incorporated. In the present paper, microstructural features focused at the lamellar growth front are illustrated and discussed supporting the idea that DP is a non-equilibrium reaction.

The alloy used for this study, Cu-7.5at.%In, was prepared at the Max-Planck-Institut, Stuttgart, from high purity components by induction melting under argon atmosphere and chill cast. After homogenization at 600°C/300h samples were directly aged isothermally at different temperatures and quenched. The parent FCC matrix α decomposes into depleted α' lamellae and tetragonal Cu_3In β lamellar precipitates.

Fig. 1 represents a reaction front typical of a DP growth process under constant driving force characterized by regularly spaced lamellae following the $(311)\alpha//(133)\beta$ orientation. The concave-forward curvature of the α/α' grain boundary indicates that the chemical driving force overcomes capillarity. Sample tilting operations in the TEM reveals local distortions between neighbor α' lamellae, Fig. 2, and also dislocations that have been incorporated in the transformed product during aging, Fig. 3. In some cases, the dislocation dynamics gives rise to twinning in the FCC lamellae which is favored at higher aging temperatures, Fig. 4. These microstructural features are caused by the internal (residual) stresses generated by the transformation being thereby capable of storing extra energy at the DP colonies. This energy term added to the α'/β interfacial energy has been interpreted as a possible driving force for the recrystallization phenomenon at the DP colonies observed in this alloy upon dissolution[4]. On the other hand, the dynamical force balance at the growth RF can be inferred from the TEM micrograph of Fig. 5 where a grain boundary that has come to rest imposes a more stable morphological configuration to the β precipitates.[5]

References

1. D. B. Williams and P. Buttler, (1981), Int. Met. Rev., 3, 158
2. G. R. Purdy, in "Phase Transformations' 87" , (1988) Inst. of Metals, London, 1988
3. I. G. Solorzano and G. R. Purdy, Metall. Trans. (1984), 15A, 1055
4. I. G. Solorzano J. A. Cohn and R. M. de Andrade, Mater. Sc. and Tech. (1991), 7, 565
5. One of the authors (I.G.S.) is indebted to the EEC (Brussels) for an European Fellowship award. Thanks are due to Prof W. Gust, MPI, Stuttgart, for providing the alloy.
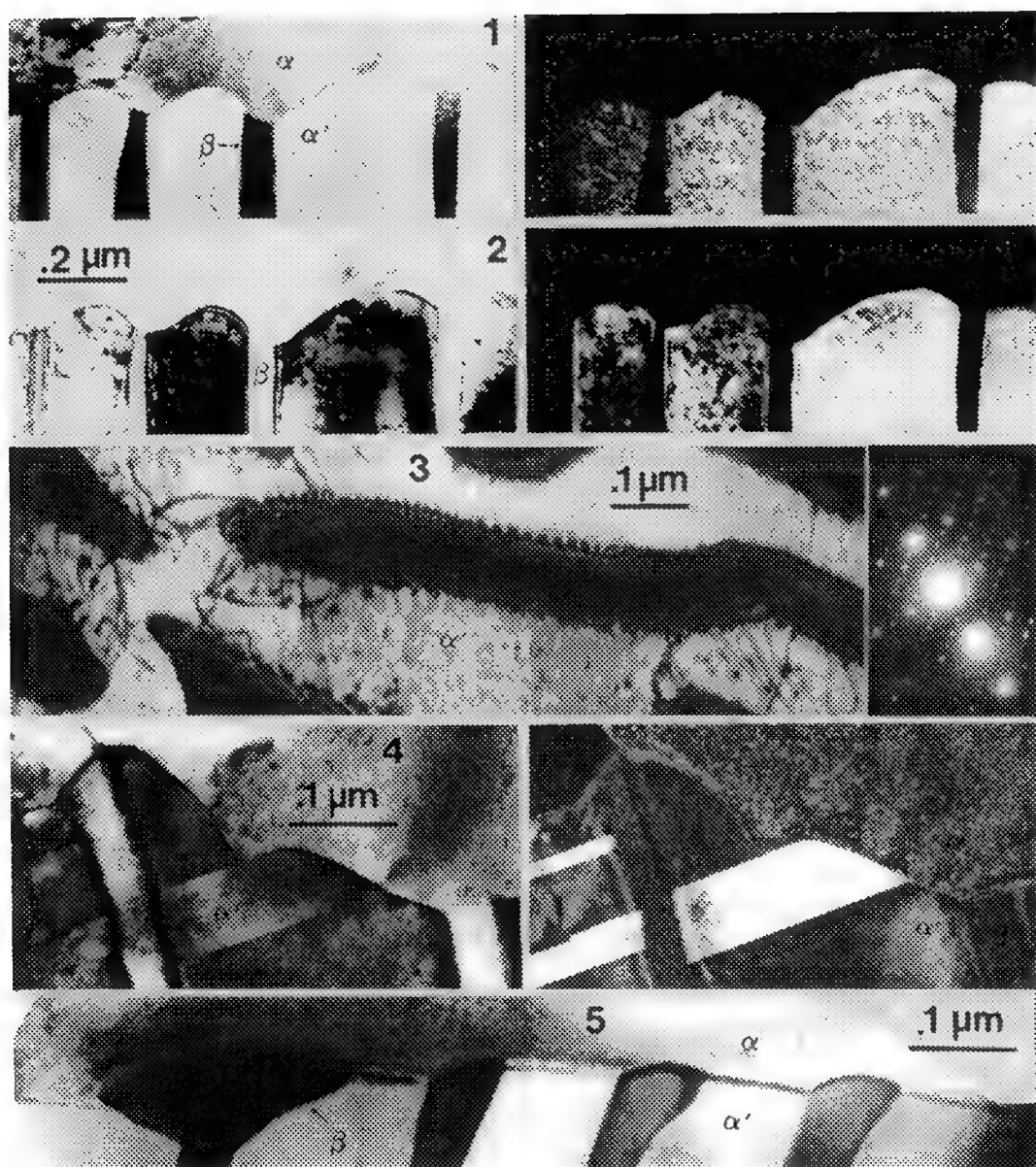
Fig. 1.- TEM bright field (left) and dark field (right) of a grain boundary growth front at 345°C

Fig. 2.- Same reaction front of Fig. 1 under different diffraction conditions showing misorientations between α' lamellae.

Fig. 3.- Misfit dislocations at α'/β interfaces and extended dislocations in a DP product at 390°C

Fig. 4.- Twinning of α' depleted lamellae aged at 390°C

Fig. 5.- Morphological accommodation of β precipitates at a grain boundary that has stop migrating during aging at 390°C

STRUCTURAL ANALYSIS OF ω-LIKE DIFFUSE SCATTERING FROM QUENCHED Cr-Ti ALLOYS

W. Sinkler and D. E. Luzzi

University of Pennsylvania, Department of Materials Science and Engineering, Phila. PA 19106-6272

Incommensurate diffuse scattering is seen in electron diffraction from the quenched-in body centered cubic phase (β phase) of alloys composed of titanium or zirconium with other early transition metals. Such diffuse scattering is related to the commensurate ω phase, a high pressure equilibrium phase of pure titanium [1], which also forms in dilute quenched alloys after annealing [2]. The present study concerns ω-like diffuse scattering in the quenched β phase of the Ti-Cr system. It is shown that the diffuse scattering in concentrated alloys consists of ω diffraction maxima which have undergone ordered displacements from commensurate ω reciprocal lattice positions. The displacement magnitude increases with solute content (see figure 1). A general expression in reciprocal space for the dependence of the diffuse peak shift on (hkl)ω was found. A model based on this expression correctly predicts the location of all diffuse peaks. The peak shifts of the model are characterized by a high degree of regularity, which is of fundamental importance to the determination of the structure giving rise to the diffuse scattering. A schematic of a $Ti_{0.6}Cr_{0.4}$ [$0\bar{1}\bar{1}$]β zone axis based on the reciprocal space model is shown in figure 2. In the figure, the line segments representing the streaked diffuse maxima from two of the four ω orientation variants are labeled using the indices of the corresponding commensurate ω Bragg reflections.

The continuous shifting of diffuse maxima in reciprocal space is explained by a faulty periodicity in the ω-phase. The present model proposes the existence of distinct higher-order ω structures, whose unit cell geometries differ from commensurate ω. In diffuse ω, unit cells of higher order ω are increasingly substituted at random into the ω structure as solute content is increased. This causes the observed continuous shifting of diffuse peaks.

The effect on the diffraction trace along [111]β due to a random planar mixing of two distinct ω structures along this direction has been simulated. The experimental trace is seen in figure 1, and consists of the two diffuse [001]$ω_1$ and [002]$ω_1$ maxima which are shifted symmetrically toward each other from the commensurate positions at $\frac{1}{3} \times k_{222(\beta)}$ and $\frac{2}{3} \times k_{222(\beta)}$ respectively. For the case of a planar random substitution of two structures in a diffracting array, the kinematical diffraction trace along the direction of disorder was derived, and is given by the square of S, where:

$$S = \left(xf_1 + (1-x)f_2\right) \times \sum_{k=0}^{N-1} \sum_{j=0}^{k} \frac{k!}{(k-j)!\,j!} x^j (1-x)^{k-j} e^{2\pi i\left[u(ja_1 + (k-j)a_2)\right]}$$

In this equation N is the number of unit cells in the array, f_1 and f_2 are the one-dimensional structure factors along the array of unit cells 1 and 2, x represents the molar fraction of unit cell type 1 in the array, a_1 and a_2 are the lengths of unit cells 1 and 2 and u is the independent reciprocal space variable. A simulated trace from a mixture of commensurate ω with the higher order ω structure using this expression is shown in figure 3. By adjusting the peak shift magnitude to agree with the experimental trace, quantitative information is obtained on the structure of diffuse ω. The present model is capable of simulating the very large peak shifts seen in concentrated quenched Ti-Cr. An earlier model developed to explain diffraction from quenched β Zr-Nb [3] is not capable of reproducing such large peak shifts. The generalization of the present model to two dimensions will be presented.

In addition to the structural analysis, the significance of ω-like diffuse scattering for β phase

stability will be discussed. Anomalously large shifts of ω-like diffuse maxima are seen in systems characterized by a large atomic size difference, such as Ti-Cr and Ti-Mn [4]. This suggests a relationship between large reciprocal space shifts of ω-like diffuse scattering and a destabilization of the β phase. Recent results from low temperature irradiation of β Ti-Cr will be used to discuss the significance of large peak shifts and chemical ordering for β phase stability.
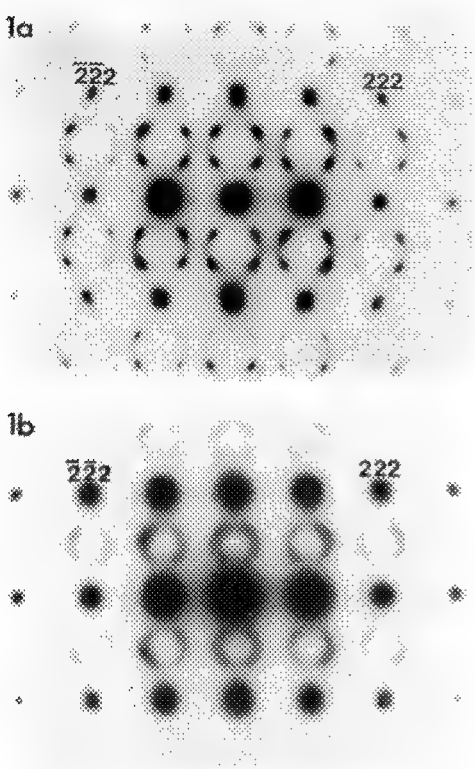
Fig. 1 $[0\bar{1}\bar{1}]\beta$ patterns. a) $Ti_{0.87}Cr_{0.13}$: ω-like diffraction maxima are close to the commensurate ω positions. b) $Ti_{0.6}Cr_{0.4}$: the ω-like maxima are both diffuse and shifted, giving the impression of rings which have contracted relative to a). Along $[111]\beta$, ω reflections are shifted toward the $(111)\beta$ reciprocal lattice position away from commensurate ω positions at $\frac{1}{3}k_{222(\beta)}$ and $\frac{2}{3}k_{222(\beta)}$.
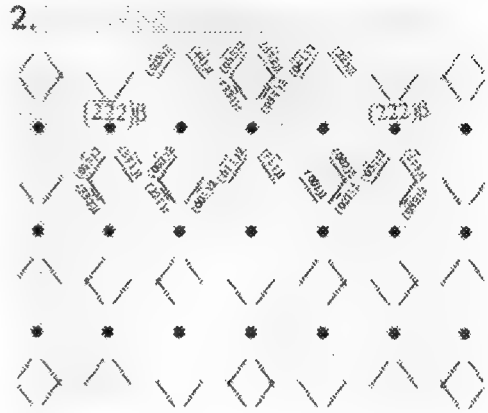
Fig. 2 Schematic of Fig. 1b constructed by systematic displacement and disk-like broadening of commensurate ω Bragg reflections. Diffuse maxima appear as line segments. Indices refer to corresponding commensurate ω Bragg reflection.
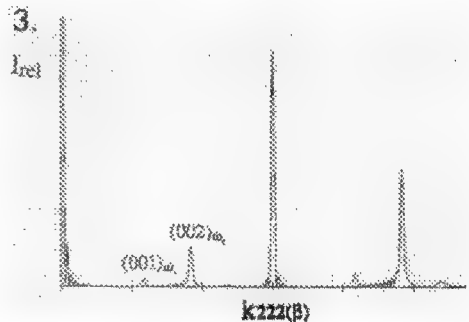
Fig. 3 Simulated $[111]\beta$ diffraction trace from equation 1, using mixture of commensurate ω and high order ω structure. Note displacements of $(001)\omega_1$ and $(002)\omega_1$ maxima toward $(111)\beta$.

1. B. Horovitz, J. L. Murray and J. A. Krumhansl, *Phys. Rev. B* 18, 7 (1978) p.3549

2. B. S. Hickman, *Trans. AIME* 245 (1969) p.1329

3. B. Borie, S. L. Sass and A. Andreasson, *Acta. Cryst.* A29 (1973) p.585

4. N. N. Aparov, I. V. Lyasotskiy and Yu. D. Tyapkin, *Fiz metal. Metalloved.* 40, (5) (1975) p.187

HVEM OF CRYSTALLIZATION OF AMORPHOUS TiNi SHAPE MEMORY FILMS

Warren J. Moberly*, John Busch** & David Johnson**

*Department of Materials Science & Engineering, Stevens Institute of Technology, Hoboken, NJ 07030
**TiNi Alloy Company, 1144 65th Street, Oakland, CA 94608

TiNi alloys, well-known for their shape memory properties that arise due to a martensitic transformation, have recently been considered for application as thin film actuators [1, 2, 3]. Although various methods of thin film preparation have been considered, deposition via d.c. magnetron ion sputtering provides for reproducible film formation as well as possible integration of a TiNi film as a micromachine with a semiconductor device. When sputter deposited at room temperature, the as-deposited films have an amorphous structure. These films can be bent into a particular macroscopic shape prior to crystallization, thereby setting the parent (memory) shape. When used as thin film actuators, TiNi shape memory alloys are quite cost efficient, as compared to the prohibitive manufacturing costs typical when producing bulk shape memory devices. In addition, thin film shape memory devices may be cooled much more quickly than a bulk part, and reversible transformation cycles are achieved in only milliseconds. Applications being considered for these shape memory thin films are as microactuators in optical storage devices and as microvalves in portable gas chromatographs [1, 2].

In order to make use of the shape memory properties resulting from the martensitic transformation from the cubic B2 structure to the monoclinic B19' structure, the as-deposited amorphous TiNi thin films must be crystallized to form the B2 structure. Differential scanning calorimetry scans of films having thicknesses ranging from 5 to 30 μm determine the crystallization temperature to be ~490°C. All films which are crystallized in an annealing furnace exhibit a nominal grain size of 1-2 μm, independent of film thickness. No preferred grain orientation has been observed. When annealing occurs with the film attached to a substrate, interfacial reactions must be considered. (For example, when thin TiNi films are deposited on Si and subsequently annealed, the titanium silicide that forms at the interface may have undesirable electrical and mechanical properties.) Annealing must also be conducted in vacuum to prevent oxidation of the TiNi films. The precipitation of oxides significantly lowers the martensitic transformation temperature in shape memory thin films. For films which exhibit only the B2 phase after annealing, a martensitic transformation temperature (M_S) of ~60°C is achieved [1, 2]. Electron diffraction determines the formation of the B2 structure upon crystallization and reveals the transformation from B2 to rhombohedral R phase, prior to the martensitic transformation upon cooling (FIG.3).

In situ high voltage (1500KeV) TEM (and video recording) has been the primary means of characterizing the crystallization of these thin films. Films of thicknesses ranging from 100 nm to 2 μm were prepared by deposition on amorphous SiO and C substrates, as well as prepared from thicker films by electropolishing. The spherulitic microstructure that develops upon crystallization is similar to that which has been observed in other thin film compound materials [4 - 6]. Crystallization occurs slower (and/or at a higher temperature) in thinner regions of an amorphous film (FIG.1). The crystallization occurs in films of 100 nm thickness at temperatures in excess of 540°C, as compared to the 490°C crystallization temperature in films of > 1 μm thickness. This "easier" crystallization in thicker films is consistent with the observation that crystallites homogeneously nucleate. The nucleation component of the crystallization process is more temperature dependent than the growth regime. Thus once a critical-size nuclei forms, it quickly grows spherically until it consumes the thickness of the film. Two-dimensional growth then continues at a constant rate. Nucleation is quite sluggish; therefore grains can undergo extensive 2-D radial growth before grain impingement occurs. Whereas further nucleation is essentially terminated by lowering the temperature to <450°C, grains that have already been nucleated will continue to grow at measurable rates. It is quite common for grains to radially grow to a size many times the thickness of the film, with some grains growing to >10 μm in regions of film that are 1 - 2 μm thick. A second difference related to nucleating crystallites in thin films, as compared to thicker films, is the radial bending that develops during crystallization (see FIG.2), presumably as a consequence of thin film stresses.

References
1. W. Moberly, J. Busch, D. Johnson & M. Berkson, Proceedings of 1991 Spring MRS, Anaheim, CA.
2. A. D. Johnson, J. Micromech. Microeng., 1991, 1, p34-41.
3. C. Hu-Simpson, L. Chang, & D. S. Grummon, Proceedings of 1990 Fall MRS, Boston, MA.
4. A.F. Marshall, Y.S. Lee & D.A. Stevenson, J. Non-Cryst. Sol., 1984, 64, p399-419.
5. J. L. Batstone & D. A. Smith in Proc. EMSA, 1990, p524-525.
6. J. J. Kim, P. Moine & D. A. Stevenson, Scripta Met., 1986, 20, p.243.
7. The NCEM at LBL, Berkeley, CA is acknowledged for its financial support and use of the HVEM.
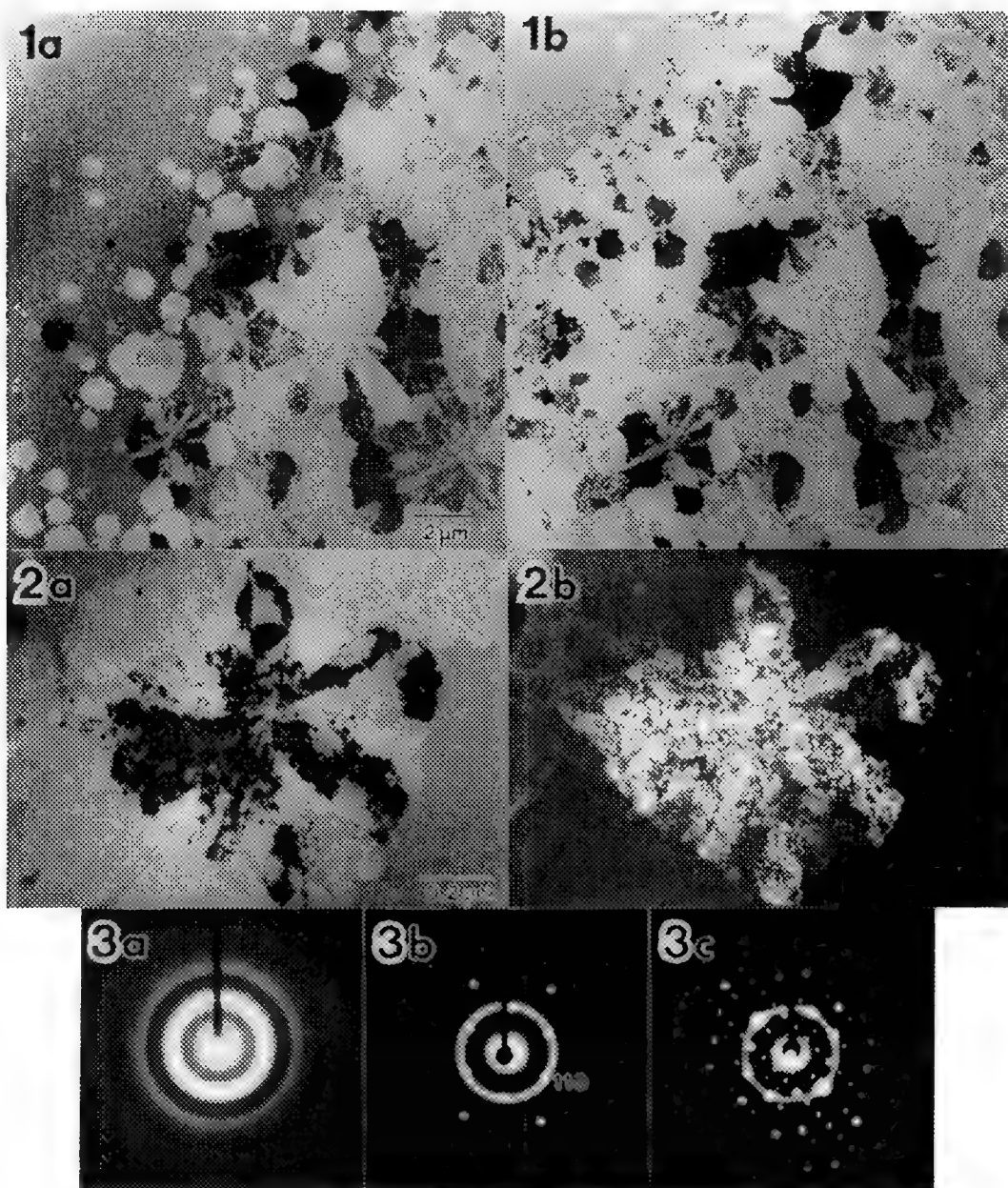
FIG.1.--TEM micrographs of crystallization of amorphous TiNi thin film during *in situ* heating at 540°C. Bright field images were acquired within a time span of ~5 minutes and indicate spherulitic growth occurs until grains impinge. FIG.2.--BF and DF micrographs acquired with a 2-beam condition of **g= <011>**. Diffraction contrast indicates the presence of undulated bending in the B2 crystallites. FIG.3a.--Electron diffraction indicates the as-sputter-deposited thin films are amorphous. FIG.3b.--<111> zone axis SAD pattern acquired of a B2 grain crsytallizing in an amorphous matrix. FIG.3c.--SAD pattern acquired of a crystallite upon subsequent cooling to room temperature exhibits 1/3 <110> refections indicating the R phase has formed prior to the martensitic transformation to the B19' structure.

NEW PHASES IN THE Al-Co-Cu ALLOY SYSTEM : MARKED VARIATIONS FROM THE "TRUE" DECAGONAL PHASE

Atul S. Ramani, Lucille A. Giannuzzi, Altaf H. Carim, William R. Bitler and Paul R. Howell

Dept. of Mat. Sci. and Eng., Pennsylvania State University, Univ. Park, PA 16802

The decagonal phase in the Al-Co-Cu alloy system was first discovered by He et al [1]. We shall call this phase the "true" decagonal phase (TD) phase because it is the one most commonly observed in the Al-Co-Cu alloy system [2, 3]. It is well known that quasicrystalline phases such as the TD phase contain the phason defect peculiar to incommensurate phases that causes subtle variations from perfect decagonal symmetry. In this paper we report on the existence of new phases in the Al-Co-Cu alloy system, that are related to the TD phase but yet show marked variations from the TD phase. These variations are too drastic to be caused by phason defects alone.

Figure 1(a) is a selected area diffraction pattern (SADP) recorded from a TD phase single "crystal" showing near perfect decagonal (tenfold) symmetry. This SADP agrees very well with the first published SADP of the TD phase in Al-Co-Cu [1] that also shows almost perfect decagonal symmetry. In a previous paper [2] we have reported several kinds of deviations from perfect decagonal symmetry, but none of these deviations involved the observation of perfect pentagonal (fivefold) symmetry. Figure 1(b) is an SADP recorded from a phase in Al-Co-Cu that exhibits perfect pentagonal symmetry instead of the expected decagonal symmetry. This breakdown of true tenfold symmetry into true fivefold symmetry is caused by unequal intensities of equal and opposite reflections. This example is a clear violation of Friedel's law, which states that the intensities of equal and opposite diffraction vectors must be equal.

Figure 2(a) is an SADP recorded from a TD phase single "crystal" down the 2(P)-fold axis (arrowed in Figure 1(a)). This SADP shows the 0.4 nm periodicity along the tenfold axis that is characteristic of the TD phase [1]. He et al [1] have also reported the occurrence of phases with 0.8, 1.2 and 1.6 nm periodicities along the tenfold axis in phases in Al-Co-Cu. Figure 2(b) is an SADP also recorded down the 2(P)-fold axis that indicates a new phase with 0.6 nm periodicity along the tenfold axis. Thus it is clear that the decagonal phases in Al-Co-Cu consist of different types of stacking sequences of two-dimensional Penrose tiling layers. An approach similar to that of Yamamoto and Ishihara [4] is necessary in order to explain diffraction patterns from layered Penrose tilings and thus ultimately from the decagonal phases in Al-Co-Cu.

A final and interesting occurrence is that of a new periodic phase that mimics several of the characteristic features of the TD phase. Figure 3(a) is an SADP recorded down the pseudo-fourfold axis of the TD phase. It shows the characteristic inter-reciprocal layer diffuse sheets (arrowed) and a pseudo-fourfold arrangement of a lattice of main reflections. Note the quasiperiodic arrangement of satellite reflections between the main reflections. Figure 3(b) is an SADP recorded from a periodic phase that mimics the inter-reciprocal layer diffuse sheets and the lattice of main reflections in Figure 3(a), however the arrangement of reflections between the main reflections is clearly periodic.

Detailed studies of the Al-Co-Cu alloy system are being carried out in order to investigate the possibility of formation of further new phases related to the TD phase.

References
1. L.X. He et al, J. Mater. Sci. Lett. (1988)7, 1284.
2. A.S. Ramani et al, Proceedings of the 49th Annual Meeting of the Electron Microscopy Society of America, p. 914, ed. G. W Bailey , San Francisco Press, San Francisco (1991).
3. A.R. Kortan et al, Phys. Rev. Lett. (1990)64, 200.
4. A. Yamamoto and K.N. Ishihara, Acta Cryst. (1988)A44, 707.
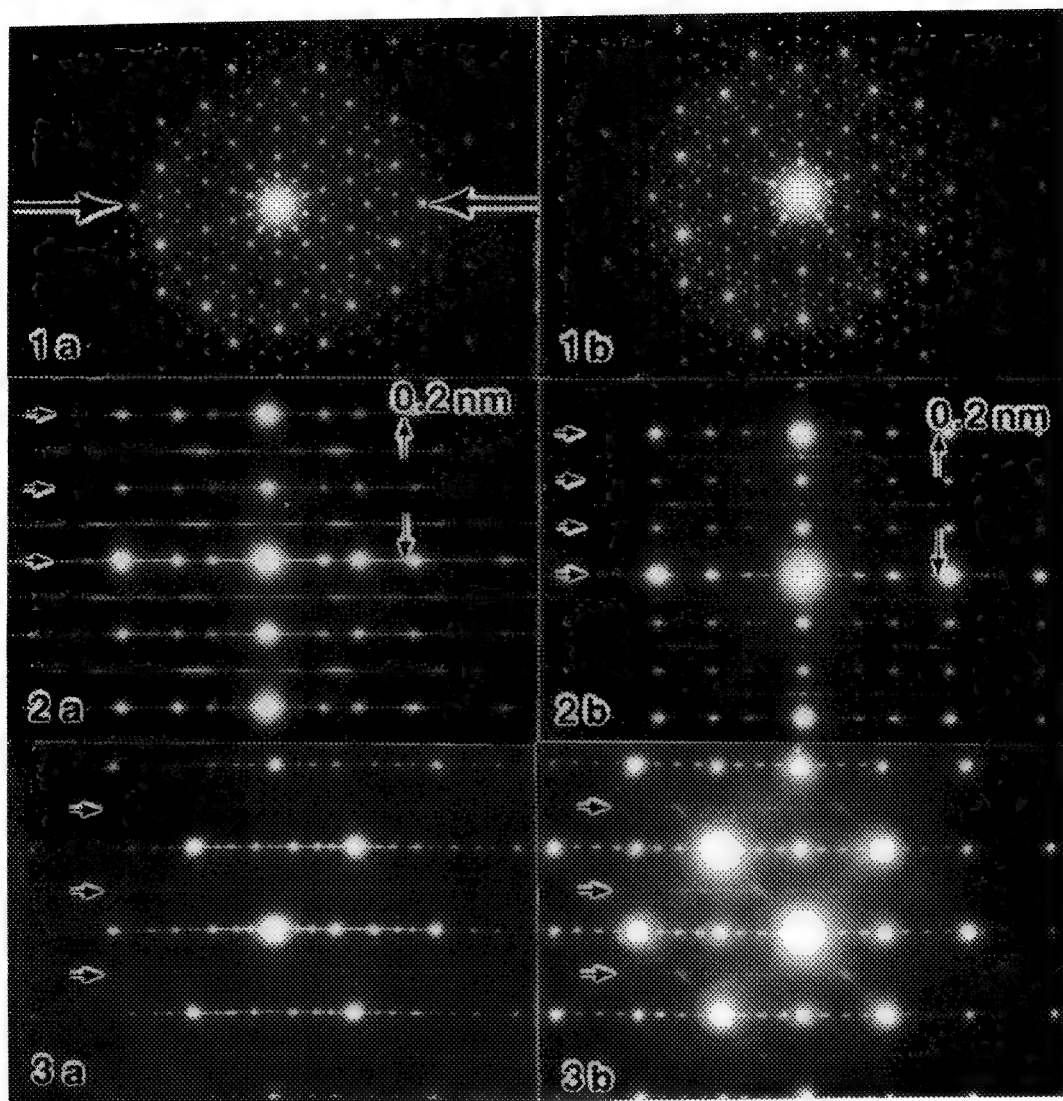
Figure   1(a) -- "True" decagonal (TD) phase SADP showing perfect decagonal (10-fold) symmetry.
           1(b) -- SADP from new phase showing perfect pentagonal (5-fold) symmetry in clear
                 violation of Friedel's law.
Figure   2(a) -- 2(P)-fold SADP from the TD phase showing 0.4 nm periodicity along tenfold axis.
           2(b) -- 2(P)-fold SADP from new phase showing 0.6 nm periodicity along tenfold axis.
Figure   3(a) -- Pseudo-fourfold SADP from the TD phase. Note the occurrence of diffuse sheets and
                 the lattice of main reflections. The arrangement of satellite reflections is quasiperiodic.
           3(b) -- SADP from new phase that mimics the occurrence of diffuse sheets and the lattice of
                 main reflections as in the case of the TD phase. However the arrangement of satellite
                 reflections is periodic

TEM CHARACTERIZATION OF A NEW CHROMIUM HYDRIDE PHASE

Y. Pan, M. Takeo and J. Dash

Environmental Science and Resources-Physics, Portland State
University, Portland, Oregon 97207

Single crystal, body centered cubic (bcc) Cr thin films were
prepared by epitaxial growth on newly cleaved optical grade rock
salt substrates (Figure 1). With a vacuum of 6-8 x 10^{-7} torr and the
substrate at about 500 °C, the deposition of the thin film was
almost instantaneously completed by rapidly evaporating Cr powder
(99.996%) in a tungsten basket. These films were exposed to
hydrogen gas (99.999%) at high temperature (close to the melting
point of Cr) and 550 atm pressure in a ballistic compressor (BC)[1,2]
for about 1 millisecond. The cooling rate of the compressed gas is
higher than 10^5°C/s. This process was repeated several times to
enhance the interaction of Cr with H_2.

Using the transmission electron microscope (TEM), second phase
particles of superhexagonal (sh) structure, which has lattice
constant A=4.77Å and C/A=1.84, are found in the H_2-exposed films.
Selected area diffraction (SAD) from the films exposed in the BC
shows the original bcc patterns with new patterns from sh structure
superimposed (Figures 2 and 3). Figures 2c and 3c show the
schematic patterns analyzed to obtain the crystallographic
information. An electronic camera device and a computer program[3]
were used to analyze the electron diffraction patterns.

The sh is used to refer to the new hexagonal structure since it
has a larger crystallographical period than the hcp CrH structure.[4]
One unit cell of the sh consists of 6 hcp units (12 chromium atoms).
Inside the sh unit some chromium atoms are shifted so that the
symmetry of the original hcp would be distorted, but the hexagonal
structure is retained in the larger unit cell. The sh has a
definite orientation relationship with the bcc matrix: $[021]_{sh}$ //
$[001]_{bcc}$ and $(2\bar{1}2)_{sh}$ // $(\bar{1}10)_{bcc}$. The superhexagonal structure is quite
stable in air and at room temperature, but decomposes to bcc Cr when
bombarded by the electron beam in the TEM.

No such particles were observed in Cr films exposed to pure
argon under similar conditions in the BC. No changes in the
composition of the films were found by comparing the characteristic
x-ray spectra of the same film before and after exposures to hot,
dense hydrogen in the BC. By high-temperature vacuum extraction in a
discharge tube, the hydrogen spectrum was observed, and the
intensity of electron diffraction spots from superhexagonal
structure decreased.[5]

References

1. M. Takeo et al., J. Appl. Phy. **38**, 3544 (1967).
2. J. Dash et al., Metallurgical Applications of Shock-Wave and
High-Strain-rate Phenomena, Marcel Dekker (1986) 1051.
3. A. Trzynka and M. Takeo, Rev. Sci. Instr. **59**, 434 (1988).
4. C. A. Snavely, Trans. Electrochem. Soc. **92**, 537 (1947)
5. This is Environmental Sciences and Resources Publication No. 279.
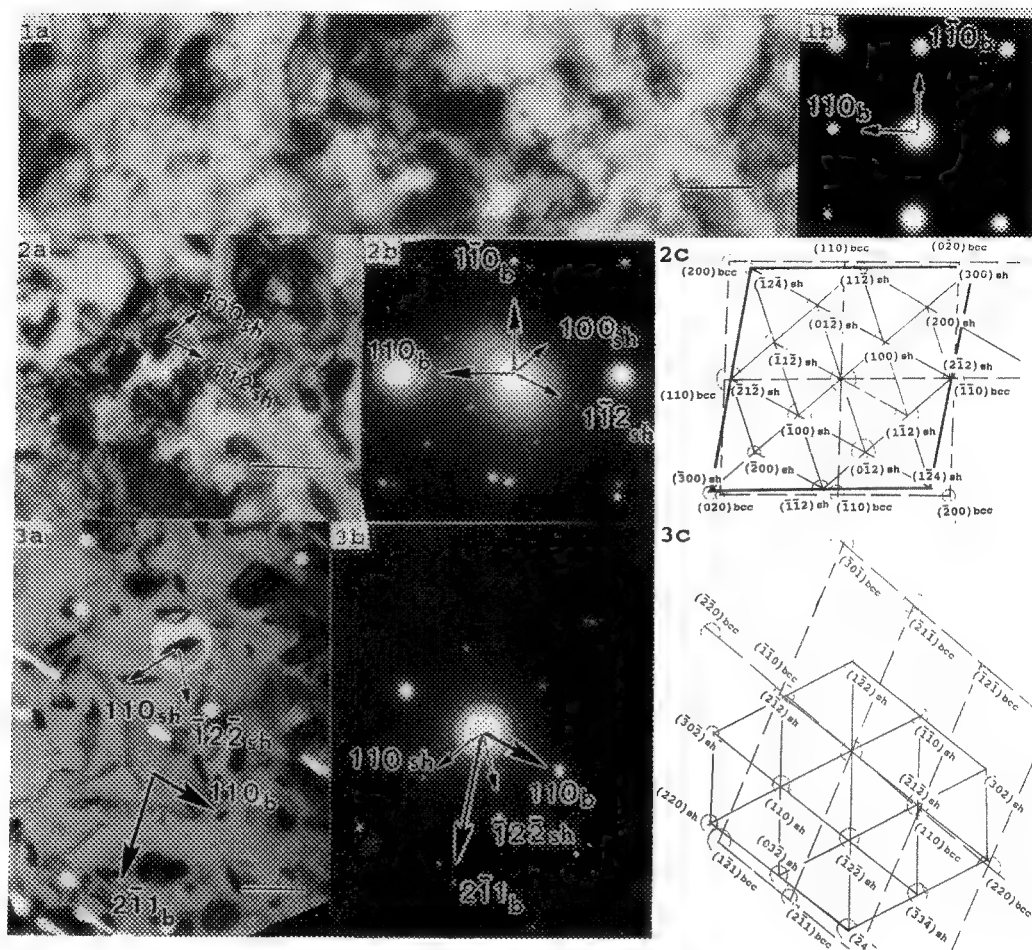
Fig.1. Single crystal Cr thin film, (a) micrograph and (b) SAD in [001]$_{bcc}$. bar=0.1μm.

Fig.2. (a) Micrograph, (b) SAD of [021]$_{sh}$ superposed with [001]$_{bcc}$, and (c) schematic pattern of (b). bar=0.25μm.

Fig.3. (a) Micrograph, (b) SAD of [$\bar{2}$23]$_{sh}$ superposed with [$\bar{1}$13]$_{bcc}$, and (c) schematic pattern of (b). bar=0.25μm.

OBSERVATION OF PSEUDO 10-FOLD SYMMETRY IN THE ORDERED IRON-ZINC DELTA PHASE

L. A. Giannuzzi, A. S. Ramani, P. R. Howell, H. W. Pickering and W. R. Bitler

Dept. of Materials Science and Eng., The Pennsylvania State University, University Park, PA 16802

The δ phase is a Zn-rich intermetallic, having a composition range of ~ 86.5 - 92.0 atomic percent Zn, and is stable up to 665°C [1]. The stoichiometry of the δ phase has been reported as $FeZn_7$ [2] and $FeZn_{10}$ [3]. The deviation in stoichiometry can be attributed to variations in alloy composition used by each investigator. The structure of the δ phase, as determined by powder x-ray diffraction, is hexagonal ($P6_3mc$ or $P6_3/mmc$) with cell dimensions a = 1.28 nm, c = 5.76 nm, and 555±8 atoms per unit cell [3]. Later work suggested that the layer produced by hot-dip galvanizing should be considered as two distinct phases which are characterized by their morphological differences, namely: the iron-rich region with a compact appearance (δ_k) and the zinc-rich region with a columnar or palisade microstructure (δ_p) [4]. The sub-division of the δ phase was also based on differences in diffusion behavior, and a concentration discontinuity across the δ_p/δ_k boundary [4]. However, work utilizing Weisenberg photographs on δ single crystals reported that the variation in lattice parameters with composition was small and hence, structurally, the δ_k phase and the δ_p phase were the same and should be thought of as a single phase, δ [5]. Bastin et al. [5] determined the average cell dimensions to be a = 1.28 nm and c = 5.71nm, and suggested that perhaps some kind of ordering process, which would not be observed by x-ray diffraction, may be responsible for the morphological differences within the δ phase.

Amelinckx et al. [6] have reviewed a number of instances in which electron diffraction combined with high resolution electron microscopy (HREM) has revealed modulated structures in ordered alloys, previously interpreted by x-ray diffraction as structures with large unit cells. The modulation may result from the periodic arrangement of planar defects (interface modulated) or local composition changes (composition modulated). Modulated structures may produce commensurate or incommensurate diffraction patterns, depending on the ratio of the modulation wave vector to the underlying basic reciprocal lattice.

Daulton and Kelton [7] observed that HREM images along the 10-fold axis of a decagonal phase contained large unit cell crystalline phases that were decorated with 10-fold symmetric atomic clusters. After long term annealing of this phase, a crystalline approximant showing Kikuchi bands and selected area diffraction pattern (SADP) spot modulations with a pseudo 10-fold symmetry similar to those from the true decagonal phase, was observed. They also suggested that convergent beam electron diffraction "Kikuchi bands and intensity modulations of the diffraction spots do not reflect the symmetry of the crystalline lattice, but rather the 10-fold symmetry of the dominant scattering cluster within the unit cell, unlike the case for small unit cell crystals" [7].

Fig. 1a is a lattice image of the δ phase, obtained using a Philips EM420T transmission electron microscope operating at 120kV. The lattice fringes correspond to the {0001} planes. The {0001} lattice images are easily resolved even by the EM420T due to the large d-spacing of the {0001} planes (d = 5.71 nm). However, due to the limited resolution of the EM420T, local defects causing variations in the distance between the lattice images are not readily characterized. Fig. 1b is a [$2\bar{1}\bar{1}0$] SADP corresponding to the image in fig. 1a. The dense reciprocal space is evident in the SADP. In addition, there are some intriguing characteristics of the SADP. Firstly, there is an intensity modulation within the close-packed rows of diffraction spots. Secondly, and more interestingly, is the apparent 10-fold arrangement of the most intense reflections, as indicated by the arrows in fig. 1b. These intense reflections can be indexed in terms of the hexagonal unit cell dimensions. The high intensity reflections are arranged in a pseudo 10-fold arrangement with a calculated angle of 36 ± 0.5° between them. This may be an example of a crystalline approximant (with a hexagonal lattice) of a quasicrystalline phase that could possibly exist in this system.

Fig. 2a shows a [0001] SADP from the δ phase and fig. 2b shows a [111] αFe SADP. Both diffraction patterns are at the same camera length. The interesting item to note in this δ diffraction pattern is that the positioning of the most intense reflections {$\bar{6}330$} (d = 0.214 nm) correspond closely to the positions of the {$\bar{1}01$} (d = 0.202 nm) αFe reflections from the [111] αFe zone axis pattern. Hence, it appears that the δ phase may be an ordered version of the αFe. HREM images of the δ phase reported by Lin et al. [8] did not touch on the observations we have presented here. It is suggested that the δ phase may be ordered, modulated, and a crystalline approximant to a quasicrystal, however, additional work is needed to confirm these observations [9].

References

1. O. Kubaschewski, Iron-Binary Phase Diagrams, Springer-Verlag, Berlin, (1982), 173.
2. M. Hansen and K. Anderko, Constitution of Binary Alloys, McGraw-Hill, NY, (1958), 739.
3. H. Bablik, F. Gotzl, and F. Halla, Z. Metallkde, 8, (1938), 249.
4. M. Ghoniem and K. Lohberg, Metall, 26, (1972), 1026.
5. G. F. Bastin, F. J. J. van Loo, and G. D. Rieck, Z. Metallkde, 68, (1977), 359.
6. S. Amelinckx, J. Van Landuyt, and G. Van Tendeloo, in Modulated Structure Materials, ed. T. Tsakalakos, (1984), Martinus Nijhoff, 183.
7. T.L. Daulton and F. Kelton, Phil. Mag. Letters, 63, (1991), 257.
8. Yuli Lin, Wen-An Chiou and M. Meshii, Proceedings of the 49th Annual Meeting of the Electron Microscopy Society of America, ed. G. W. Bailey, San Franscisco Press, (1991), 568.
9. This work was supported by AESF Research Project 76 and Inland Steel Company.
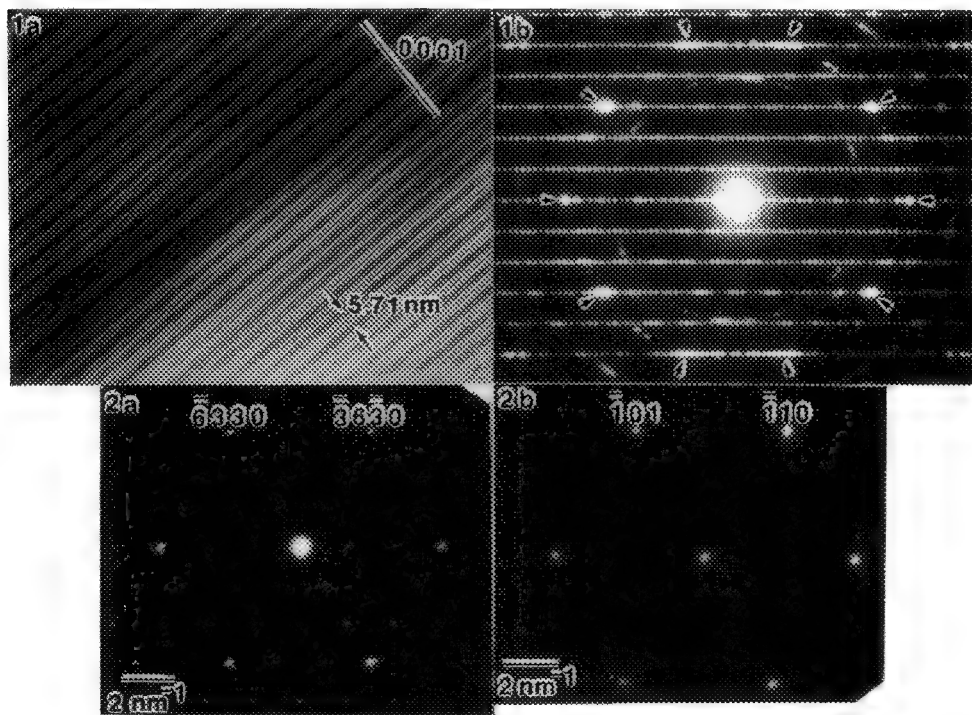
FIG. 1.--a) Lattice image of the δ phase. b) δ [2$\bar{1}\bar{1}$0] SADP from the image in fig. 1a.
FIG. 2.--δ [0001] SADP and αFe [111] SADP.

DEFECT STRUCTURES OF $Nb_{1+\alpha}S_2$ SULFIDATION SCALES

Chuxin Zhou and L. W. Hobbs

H. H. Uhlig Corrosion Laboratory, Massachusetts Institute of Technology, Cambridge, MA 02139

One of the major purposes in the present work is to study the high temperature sulfidation properties of Nb in severe sulfidizing environments. Kinetically, the sulfidation rate of Nb is satisfactorily slow[1,2], but the microstructures and non–stoichiometry of $Nb_{1+\alpha}S_2$ challenge conventional oxidation/sulfidation theory and defect models of non–stoichiometric compounds. This challenge reflects our limited knowledge of the dependence of kinetics and atomic migration processes in solid state materials on their defect structures.

Figure 1 shows a high resolution image of a platelet from the middle portion of the $Nb_{1+\alpha}S_2$ scale. A thin lamellar heterogeneity (about 5nm) is observed. From X–ray diffraction results, we have shown that $Nb_{1+\alpha}S_2$ scale is principally rhombohedral structure, but $2H-NbS_2$ can result locally due to stacking faults, because the only difference between these 2H and 3R phases is variation in the stacking sequence along the c axis. Following an ABC notation, we use capital letters A, B and C to represent the sulfur layer, and lower case letters a, b and c to refer to Nb layers. For example, the stacking sequence of 2H phase is AbACbCA, which is a ~12Å period along the c axis; the stacking sequence of 3R phase is AbABcBCaCA to form an ~18Å period along the c axis. Intergrowth of these two phases can take place at stacking faults or by a shear in the basal plane normal to the c axis.

Faulting of these stacking sequences is relatively easy because of the weak bonding between S–S layers and the weak communication between neighboring Nb layers which are separated by two sulfur layers. In addition to continued stacking of 3R structure AbABcBCaC|AbA, three other stacking faults may be created; for example, AbABcBCaC|AcA corresponds to a simple fault, AbABcBCaC|BaB to the intergrowth of 2H structure (CaCBaB), and AbABcBCaC|BcB to a twin (BcBCaCBcB). If more extended stackings of the trigonal prismatic S–Nb–S slabs are considered, a combination of these faults may form very complicated structures. The following three kinds of faults are possible in the 3R structure:

fault plane
↓
(1) AbAB̲c̲B̲C̲a̲C̲|B̲c̲B̲C̲a̲C̲AbA   Nb, S faults, $\vec{u} = 1/3 < 11\bar{2}0 >$
↑
twin plane

(2) AbABcBCaC|AcABaBCbC   Nb fault, $\vec{u} = 1/3 < 11\bar{2}0 >$
↑
fault plane
↓
(3) AbABcBCaC|A̲c̲A̲B̲c̲B̲CaC   Nb fault, $\vec{u} = 1/3 < 11\bar{2}0 >$
2H
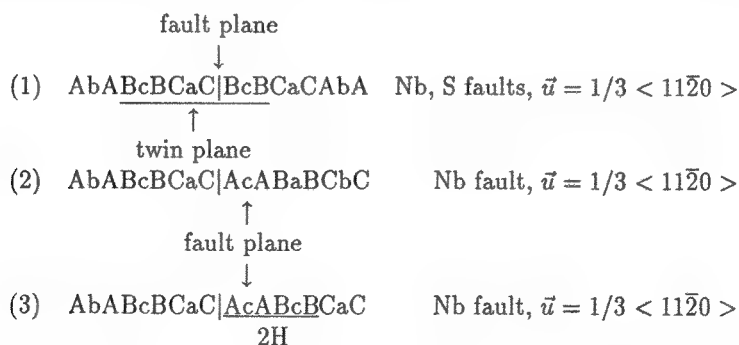
The first represents a shear $\vec{u} = 1/3 < 11\bar{2}0 >$ between adjacent S planes and faults both the S and Nb stacking sequence. In the second, all Nb layers are shifted by the same

38
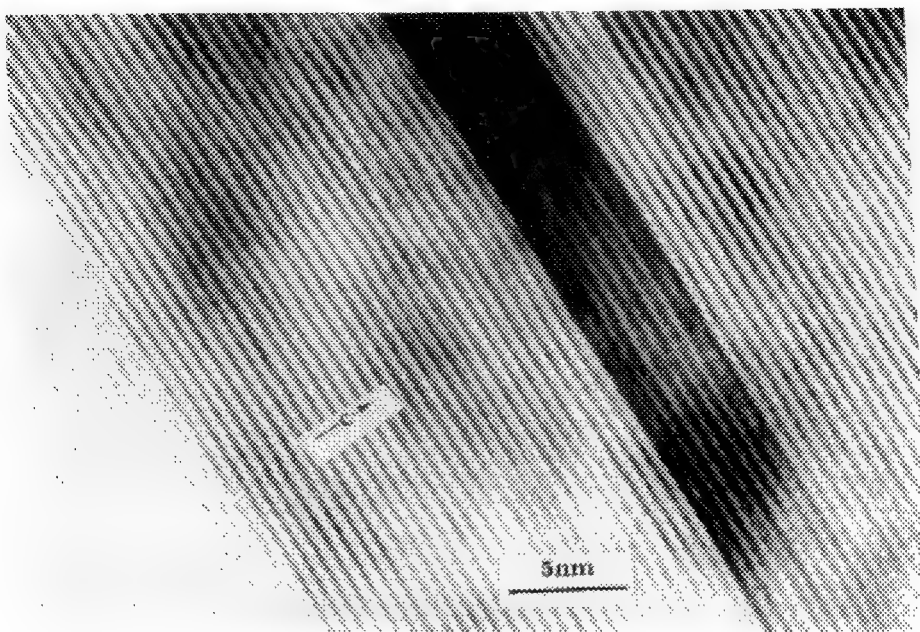
Figure 1: HREM image of a platelet from the middle of NbS_2 scales formed on polycrystalline Nb in $H_2 - H_2S$ gas mixtures ($P_{S_2} = 10^{-4.62} atm$) at 900^0C(1173K) for 100 min, showing a lamellar heterogeneity of 5 nanometer width. The average lattice spacing of adjacent 3R material is d=5.97–6.05Å with a maximum value d=6.35Å.

$\vec{u} = 1/3 < 11\bar{2}0 >$ shear vector within a rigid S sublattice resulting in a fault only in the Nb layer sequencing. The third represents a shift in a single Nb layer. Faults (2) and (3) are likely to be of similar energy, because the cation layers are well insulated from each other and of higher energy than the sulfur fault. Multiple admixtures of these fault layers is, of course, possible. Further planar anomalies can be constructed by arranging alternative stacking sequences.

The octahedral sites between two S–Nb–S slabs provide accommodation for extra Nb or foreign atoms. The large non–stoichiometry of NbS_2 is closely related to this octahedral coordination. If Nb atoms are inserted into all the octahedral sites, we obtain the niobium monosulfide (NbS). These octahedral Nb cations increase the bonding between the slabs by a strong interaction with their neighboring atoms and defects. Our marker experiments indicated that minority vacancies on the sulfur sublattice are free to move[3], and we suggest they are the dominant mobile defects for the growth of $Nb_{1+\alpha}S_2$ scale. This interpretation is consistent with our experimental observations.

References

1. K. N. Strafford and J.R. Bird, J. Less-Common Metals (1979)**68**, 223
2. C. Zhou and L. W. Hobbs, *Heat–Resistant Materials*, ed. K. Natesan (ASM, 1991) p.225
3. C. Zhou and L. W. Hobbs, MRS Proceedings (1991)**222**, 321

DISLOCATION STRUCTURES AND TWINNING IN TUNGSTEN <110> SINGLE CRYSTALS

Raja Subramanian and Kenneth S. Vecchio

Department of Applied Mechanics and Engineering Sciences, University of California-San Diego, La Jolla, CA 92093

Tungsten single crystals are brittle due to predominant twinning and crack formation at twin-twin intersections. Twinning and its influence on crack nucleation have been studied in detail[1]. Despite the twinning, significant plastic deformation takes place by the generation and glide of dislocations. Hitherto uninvestigated dislocation structures and twin boundaries in tungsten <110> single crystals deformed quasistatically in compression have been studied using transmission electron microscopy.

In compressed samples, cracks nucleate at twin-boundary intersections. Such a crack is indicated by an arrowhead in Figure 1 which shows an optical image of twin boundaries. Figure 2 shows a bright field (BF) image of a twin boundary (marked by an arrowhead). The inset in Figure 2 is the microdiffraction pattern taken at the twin boundary which shows a $\Sigma 3$ coincidence site lattice (CSL) symmetry.

The dislocation substructures produced in the samples deformed in compression are shown in Figure 3 (a) to (d), obtained using different g-reflections under two-beam dynamical conditions. The dislocation structures consists primarily of two sets of perfect disloction that run from side to side and top to bottom in Fig. 3(a). The contrast results of these dislocations are given in Table 1.

TABLE 1. Contrast Results for Dislocations in Figure 3 (a-d).

| g-reflection | dislocation in contrast | | $g \cdot \frac{a}{2}[1\bar{1}1]$ | $g \cdot \frac{a}{2}[\bar{1}\bar{1}1]$ |
	vertical set	horizontal set		
[200]	visible	visible	1	-1
[$\bar{2}1\bar{1}$]	visible †‡	invisible	-2	0
[$\bar{2}\bar{1}1$]	invisible	visible ‡	0	2
[$21\bar{1}$]	invisible	visible †‡	0	-2

† indicates image taken with large ω   ‡ indicates dislocation double image.

The Burger's vectors of the horizontal and vertical set of dislocations are a/2[$\bar{1}\bar{1}1$] and a/2[$1\bar{1}1$], respectively. There was no residual contrast for g•b = 0, then g•b^u = 0 and is an indication that the dislocations are near screw in character. Trace analysis confirmed that the dislocations are screw type and the slip plane as (011).

Using tilting experiments in TEM, small cusps (marked by arrowheads in Figure 3(a)) of edge character have been observed on an otherwise long, straight screw dislocations. In Figure 3(b), the main screw segment is out of contrast (g•b=0) while the small dislocation cusps (marked by arrowheads) of edge character are in residual contrast (g•b^u ≠ 0). Tungsten is isotropic[2] having an elastic anisotropic ratio of 0.98. As such, the elastic strain energy of the dislocation does not vary with the line direction. The wavy nature of the dislocations is an indication of the instability of the screw orientation.

References
1. U. E. Wolff, *Trans. Met. Soc. AIME*, **224**, 327, (1962).
2. D. I. Bolef and J. de Klerk, *J. Appl. Phys.*, 33, 2311, (1962).
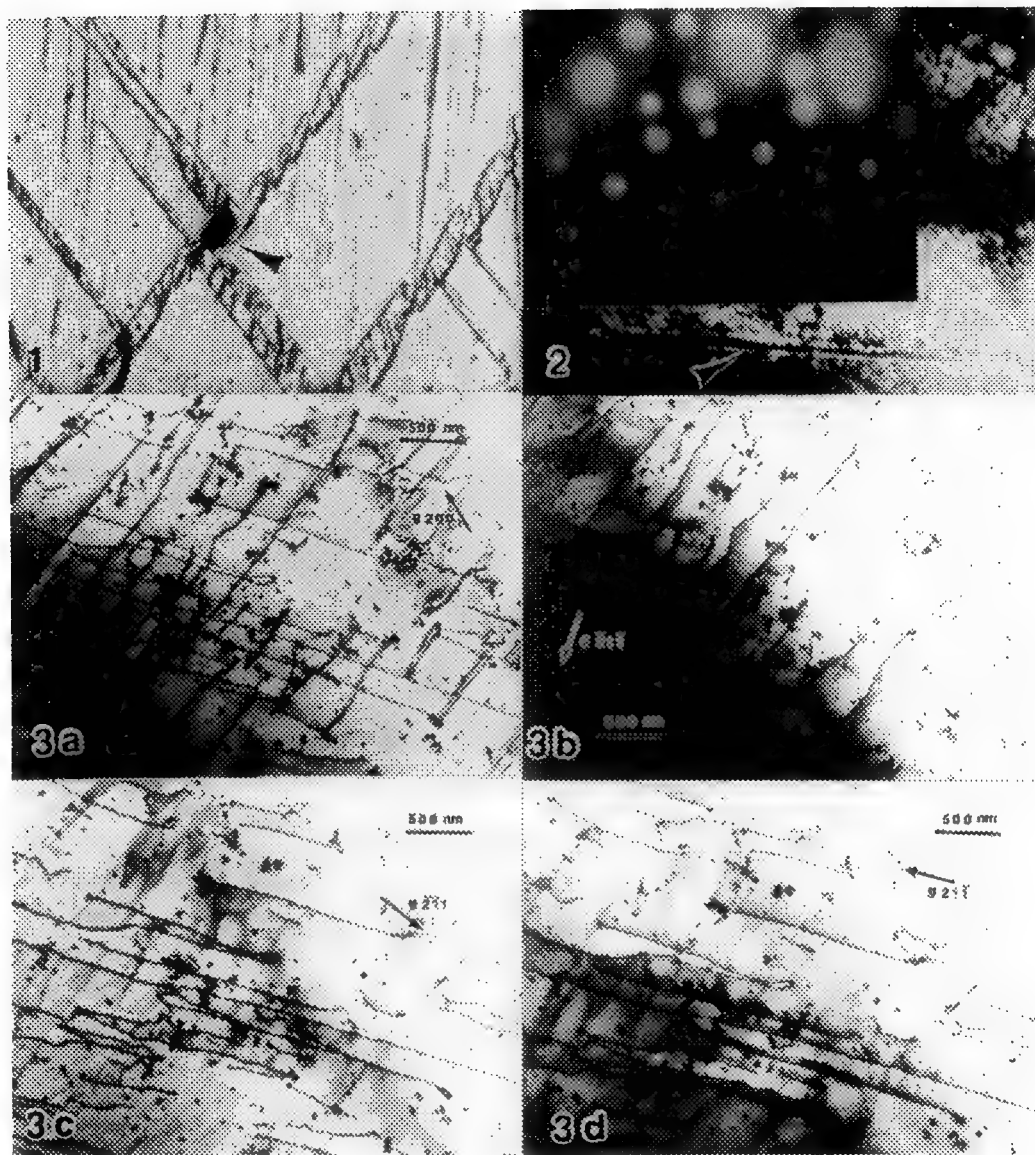
Figure 1--Optical micrograph of crack (marked by arrowhead) at twin intersections.

Figure 2--BF image of a twin boundary (marked by arrowhead); microdiffraction pattern (inset) taken from twin boundary shows Σ3 CSL symmetry.

Figure 3--(a) BF image of dislocations taken using g= [200], (b) BF image of dislocations taken using g= [$\bar{2}$1$\bar{1}$] with large ω, (c) BF image of dislocations taken using g=[$\bar{2}\bar{1}$1], (d) BF image of dislocations taken using g= [21$\bar{1}$] with large ω.

41

MICROSTRUCTURE IN SHAPED CHARGE CONES AND ITS RELATIONSHIP TO PLASTIC INSTABILITY AND JET PERFORMANCE

A. C. Gurevitch L. E. Murr, C-S. Niou, A. H. Advani, J. R. Grieves, and L. Zernow*

Department of Metallurgical and Materials Engineering, The University of Texas at El Paso, El Paso, TX 79968 and *Zernow Technical Services, Inc., San Dimas, CA 91773

When a plane wedge of relatively thin plates of metal or a cone of sheet metal is backed up on the outside with explosive and detonated, the walls of these wedge-type geometries are caused to collapse so that the metal is forced to concentrate on the corresponding axis. In the case of a plane wedge a planar jet of metal is formed which conceptually approximates the blade of a sword moving at speeds up to 30,000 ft./sec. (~ 9 km/s). When strategically placed on structural girders of a building, demolition can be achieved in a remarkable collapse process which can be carried out in the midst of a city. As a metal cone, the ensuing axial jet can punch a hole the size of a U.S. quarter in more than a meter of steel armor.[1] These shaped charge jets, especially those originating from explosively collapsed metal cones, also exhibit remarkable mechanical behavior: metals such as copper are stretched nearly 900 percent (in the solid state) before necking into small particulates like a non-viscous fluid breaking up into small droplets. As it turns out this jet breakup, and its corresponding armor penetrating ability, seems to be dependent upon the initial metallurgical processing of the cone, especially the initial grain size in the case of copper.[2] However since the jet break up for copper seems to occur over a very narrow range of grain sizes (between about 35 and 45 μm), more subtle features of the cone microstructure could be controlling the jet performance.[2]

In the present investigation, the microstructures of the interior wall portions of shaped charge metal cones - which essentially produce the jet during explosive detonation - are being examined by transmission electron microscopy (TEM). Metallurgically deformed and annealed cone micro-structures have been compared for both copper (fcc) and tantalum (bcc). Using a novel technique developed by Zernow[3], individual jet particulates have been recovered corresponding to these different fabrication regimes and initial cone microstructures. A novel technique for examining recovered jet fragments in the TEM is also being utilized.[4]

Figure 1 shows a schematic representation of a shaped charge cone and the residual slug and jet which are formed upon complete collapse by the detonating explosive. Figure 2 shows a few representative plane views parallel to the inside surface for deformed and annealed tantalum cones (Fig. 1a). While the optical microscope views of the grain structure (Fig. 2 a & b) show a dramatic difference in grain size and morphology, the corresponding TEM views show a rather dramatic microstructural difference which is further exemplified on comparing the associated SAD patterns (Fig. 2 e & f). This difference manifests itself in a sub-grain microstructure where the boundary misorientations average 4°, and provide a unique grain refinement which is absent in the larger-grain, annealed cone microstructure. The unique structure and energy of these sub-grain boundaries and their relationship to the more general grain size shown in Fig. 2a and 2b may hold the key to the narrow microstructural regime which apparently influences the jet breakup.[2]

1. W. P. Walters and J. A. Zukas, Fundamentals of Shaped Charges, Wiley, New York (1989).
2. M. L. Duffy and S. K. Golaski, Effect of Liner Grain Size on Shaped Charge Jet Performance and Characteristics, Tech. Report BRL-TR-2800, U. S. Army Ballistic Res. Lab., April 7 (1987).
3. L. Zernow, Metallurgical, XRD, and SEM Studies of Individual Shaped Charge Jet Particles Captured by Soft Recovery, Int. Conf. on Ballistics, Nanjing, China, Oct. (1988).
4. A. C. Gurevitch, et al, Chap. 47 in Shock Wave and High-Strain Rate Phenomena in Materials, Eds. M. A. Meyers, L. E. Murr, and K. P. Staudhammer, Marcel Dekker, N.Y. 1992, p. 521.
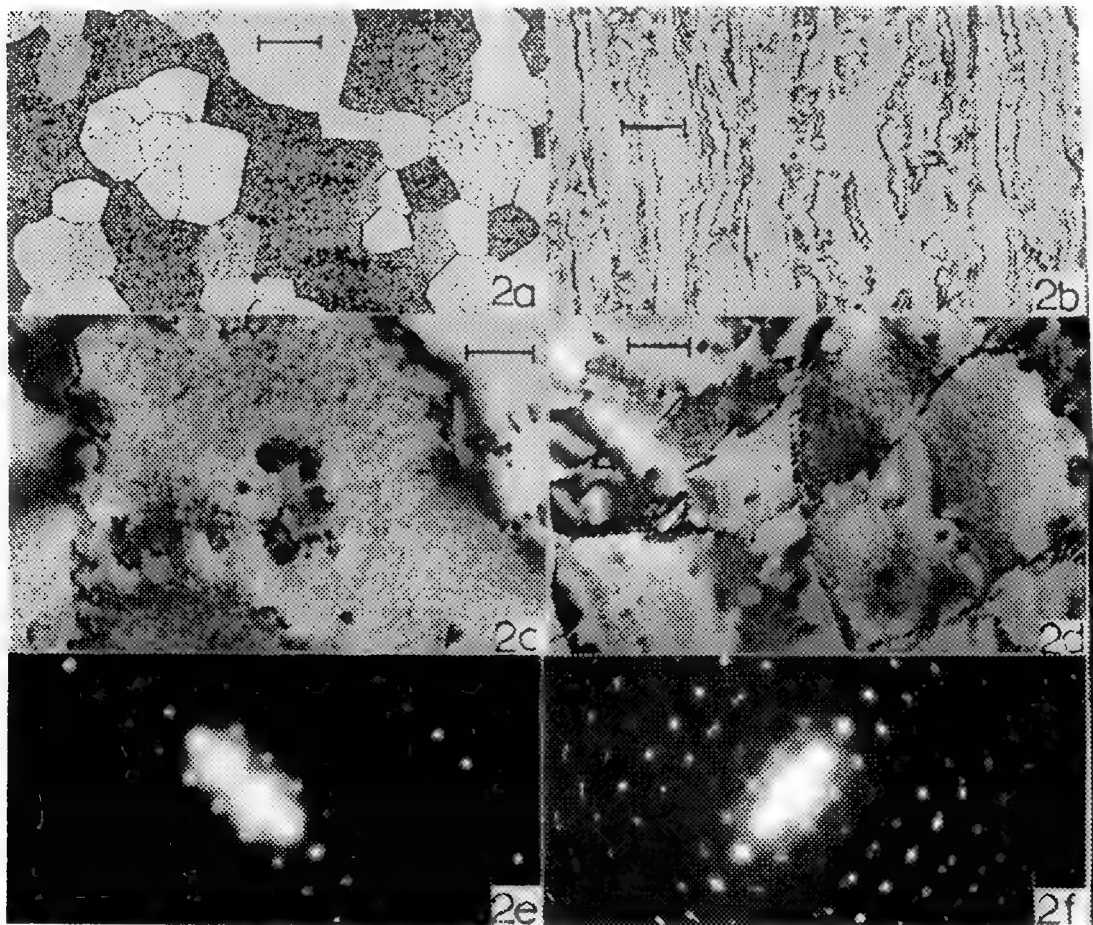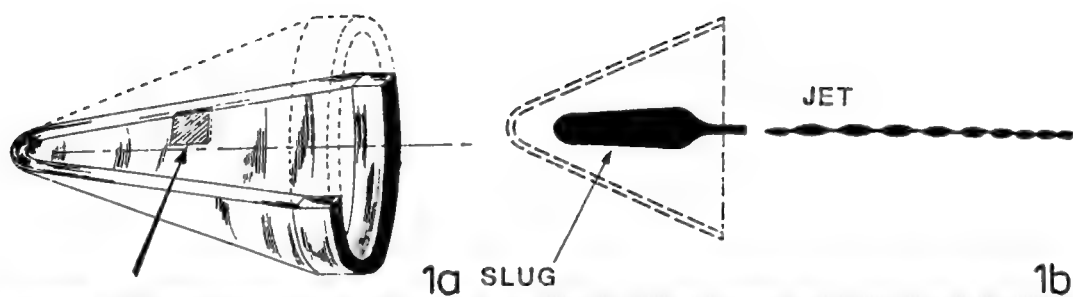
FIG. 1: Schematic representation of shaped charge cone (showing inside wall section shaded) (a) and slug and jet formation after explosive collapse of the cone (b).

FIG. 2: Optical microscope views of grain structure in annealed tantalum cone (a) and deformed tantalum cone (b) as in the shaded region in Fig. 1a. (c) and (d) compare corresponding TEM views in the same plane while (e) and (f) show corresponding SAD patterns. The arcing of diffraction spots in (f) provides an average measure for the misorientations of sub-grain boundaries shown in (d). Markers in (a) and (b) equal 30 μm; in (c) and (d) equal 0.1 μm.

43

ANALYTICAL ELECTRON MICROSCOPY OF RAPIDLY SOLIDIFIED Pt-Co-B ALLOYS

J.E. Wittig, N. Qiu, and N.D. Evans[*]

Dept. of Materials Science and Engineering, Vanderbilt University, Nashville, TN 37235
* Oak Ridge Associated Universities, P.O. Box 117, Oak Ridge, TN 37831

Compared to binary Pt-Co materials, the ternary $Pt_{42}Co_{45}B_{13}$ (at.%) alloy exhibits major improvements in hard magnetic behavior[1,2]. Although rapid solidification processing (RSP) of the Pt-Co-B alloy is necessary to produce a refined distribution of the boron, this RSP condition does not constitute a strong magnetic material. To achieve the optimum hard magnetic properties requires subsequent annealing steps. Upon annealing the RSP ternary alloy, boron combines with Co to form magnetically anisotropic Co-borides and the presence of boron has been observed to increase the rate of the transformation from the disordered FCC Pt-Co phase to the $L1_0$ superlattice[2,3]. Understanding these phase transformations and their influence on the magnetic properties demands characterization of both the metastable RSP and annealed conditions.

Rapid solidification of $Pt_{42}Co_{45}B_{13}$ was achieved by melt spinning ribbons 5 mm wide and 60 mm thick. Discs punched from the ribbons were prepared for AEM by mechanical dimpling and ion beam thinning with cryogenic cooling. The samples were analyzed by energy dispersive spectroscopy (EDS) for their Pt and Co compositions with an EDAX 9800 spectrometer and standard Be window detector in a Philips CM20T TEM/STEM operated in the STEM mode at 200kV. The Co $K\alpha$ and the Pt $L\alpha$ peaks were selected for quantification of the spectral data since their symmetrical shapes and background levels facilitate intensity extraction, Fig. 1. An experimental Cliff-Lorimer k factor was determined by using reference spectra from a homogeneous binary alloy of 53 at% Pt and 47 at% Co (Fig. 1). Foil thickness was always maintained within the "thin film criterion". For boron composition determination, these samples were analyzed in a Philips EM400T-FEG at 100 kV with a Gatan 666 PEELS system using a 2 nm dia. probe size, 2 mrad convergence angle, and 8 mrad collection angle.

The bright field image of the melt spun ribbon in Fig. 2 depicts the dendritic microstructure. Electron diffraction experiments determined the structure of the dendrites as disordered FCC Pt-Co (a = 0.378 nm) and the interdendritic phase to be orthorhombic (a = 0.489 nm, b = 0.541 nm, and c = 0.717 nm). The Pt/Co ratio of the interdendritic phase, measured by EDS (Fig. 3), is 1.17 whereas the dendritic phase has a slightly Co rich Pt/Co ratio of 0.96. These data have an estimated accuracy of +/- 9% owing to counting statistics and error in the k factor determination. PEELS analysis of the interdendritic phase revealed a distinct B K edge as shown in the insert on Fig. 3. Quantification of the PEELS data indicates a B/Co ratio of 0.3 +/- 0.1. Although the thickness of the sample was significantly less than a mean free path as determined by an I_p/I_0 ratio of about 0.1, the accuracy of the boron composition is severely limited by the background subtraction routine. The present curve fitting routine permits only an exponential fit to the background, whereas in this energy range a polynomial fit would be more appropriate. PEELS spectra from the dendrites did not detect boron and the dendrite composition was virtually equiatomic Pt-Co (49 at% Pt and 51 at% Co).

Fig. 4 shows a BF image of the RSP material after annealing for 30 minutes at 650°C. The matrix has ordered into the FCT $L1_0$ superstructure with a composition of 55 at% Pt and 45 at% Co (Pt/Co = 1.22) and the interdendritic phase has transformed into the equilibrium orthorhombic Co_3B phase (a = 0.409 nm, b = 0.532 nm, and c = 0.627 nm). Comparison of the lattice parameters from the metastable interdendritic phase and Co_3B suggests that this interdendritic material transformed directly into the Co-boride. The changes in composition upon annealing and the relative volume fractions of the phases are consistent with the interdiffusion of Pt out of the interdendritic regions into the matrix and Co diffusion from the dendrites into the Co-borides[4].

References
1. J. Teubert, J.E. Wittig, and T. Overfelt, Matls. Sci. Forum, Trans.Tech. Pub.,vol. 50 (1989) 197
2. N. Qiu et al, J. of Appl. Phys., 70 (1991) 6137
3. N. Qiu and J.E. Wittig, Proc. Ann. EMSA Meeting 49 (1991) 784
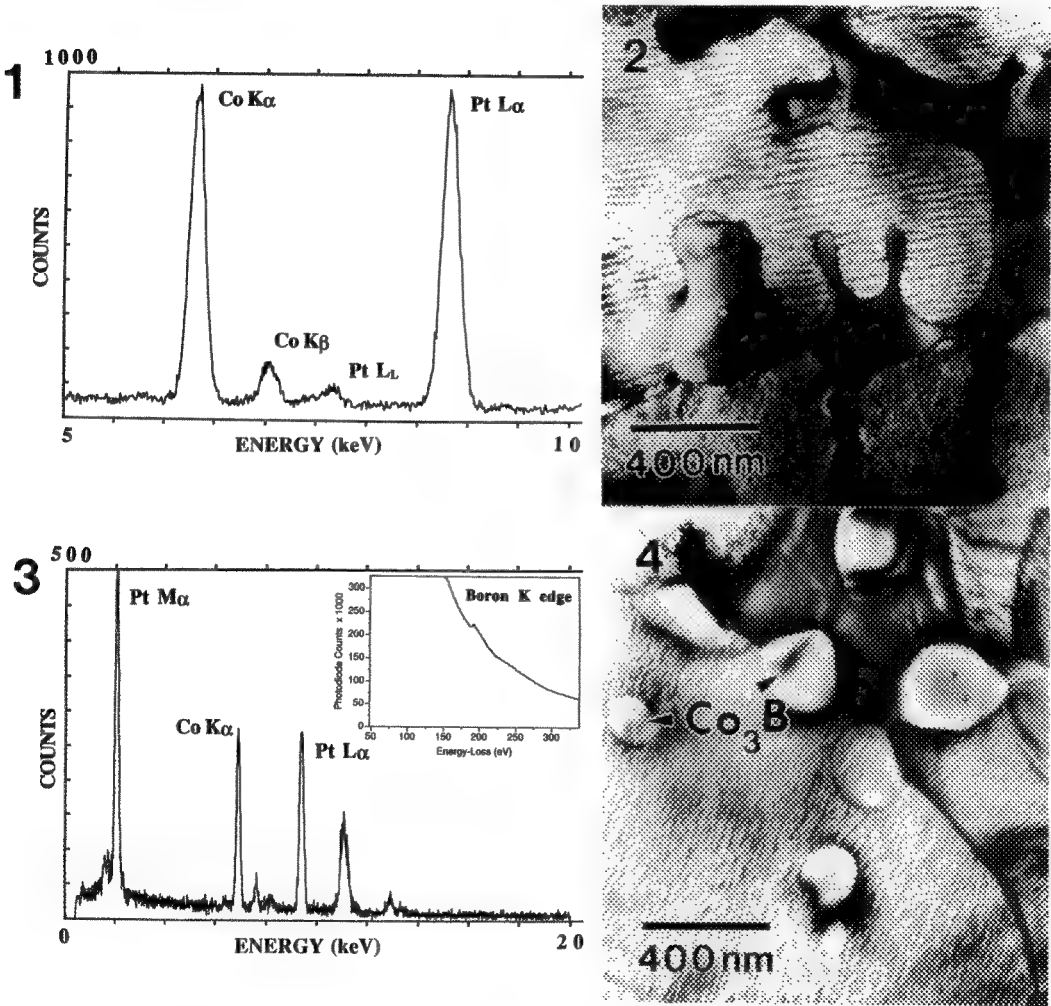
FIG. 1. Reference EDS spectrum from a binary 53 at% Pt and 47 at% Co alloy.
FIG. 2 Bright field image of the rapidly solidified $Pt_{42}Co_{45}B_{13}$ alloy.
FIG. 3 EDS spectrum and PEELS boron K edge from the interdendritic phase.
FIG. 4 Bright field image of the RSP $Pt_{42}Co_{45}B_{13}$ alloy annealed for 30 min at 650°C.

45

RAISED FERRITE: YET ANOTHER AUSTENITE DECOMPOSITION PRODUCT IN MICROALLOYED STEEL

T.F. Malis[*], B. Dogan[**], and J.D. Boyd[***]

[*] Metals Technology Laboratories, CANMET, Ottawa, K1A 0G1, CANADA
[**] GKSS Forschungszentrum, D-2054 Geesthacht, GERMANY
[***] Materials and Metallurgical Engineering, Queen's University, Kingston K7L 3N6, CANADA

In a recent study of microstructural evolution in a Ti-V microalloyed steel[1] it was observed that a significant proportion of the ferrite showed a slower etching response and appeared in relief in secondary electron SEM images. Figure 1 shows 2 examples of this "raised ferrite" constituent. Figure 1a is a Ti-V microalloyed steel controlled rolled and quenched from above the Ar_3 temperature. The ferrite (66%) is a mixture of polygonal ferrite (PF) and raised ferrite (RF). The rest of the microstructure is bainite (22%), pearlite (7%) and martensite-austenite (5%). Figure 1b is the same steel rolled and quenched from the 2-phase ($\alpha+\gamma$) region, and the microstructure comprises deformed ferrite-DF (62%), raised ferrite (24%) and martensite-austenite (14%). Two-surface SEM examination shows that a raised ferrite grain stands in relief on both surfaces, i.e. there is no orientation dependence. Also, no preferred orientation of the raised ferrite grains were detected in the TEM analysis. It was further determined that the hardness of the raised ferrite (235 ± 10 VPH) is higher than polygonal ferrite (182 ± 3 VPH) or deformed ferrite (204 ± 3 VPH), and that it fractures preferentially at low and ambient temperatures (Fig. 2). The literature contains numerous micrographs similar to Figures 1 and 2 which show raised ferrite, yet the structure and origin of this constituent have not been discussed. It is clearly distinguishable from other ferritic phases, and it can influence the fracture properties of steels by acting as a brittle crack-initiating phase[2].

In TEM examination, EELS measurements of local foil thickness[3] indicate that raised ferrite also exhibits a different thinning rate in electropolished samples. The foil thicknesses given on Figure 3a show that raised ferrite grains are thicker by 30-100nm than adjacent constituents. For more complex microstructures, such as the steels rolled in the $\alpha+\gamma$ region, this technique is invaluable for delineating the raised ferrite, deformed ferrite, and M-A constituents. It is then evident that deformed ferrite contains an unrecovered substructure with many long, straight dislocations and dipoles (Fig. 3b). Carbide particles, approximately 1 μm in length, occur along boundaries between regions of deformed ferrite and raised ferrite. When tempered 1h at 700°C, SEM examination indicates recovery and coarsening of the substructure in deformed ferrite and carbide formation in M-A. Yet there is no change in the appearance of the raised ferrite. TEM of tempered specimens confirms that deformed ferrite has a completely recovered subgrain structure, whereas the dislocation substructure of the raised ferrite is essentially unchanged.

These results identify and characterize a distinct ferrite constituent which seems to fall between the current descriptions of polygonal ferrite and acicular ferrite. It can have a polygonal or slightly elongated grain morphology, but it contains a partially-recovered dislocation substructure which is stable up to 700°C. However, the dislocation density is less than that generally found in acicular ferrite. We have tentatively christened this phase "raised ferrite", and postulate that it forms in a temperature range between that for polygonal ferrite and acicular ferrite.

REFERENCES

1.   B. Dogan, L.E. Collins and J.D. Boyd, Met. Trans. (1988) 19A, 1221.
2.   B. Dogan and J.D. Boyd, Met. Trans. (1990) 21A, 1177.
3.   T.F. Malis, S.C. Cheng and R.F. Egerton, J. Elec. Micros. Techniques (1988), 8, 193.
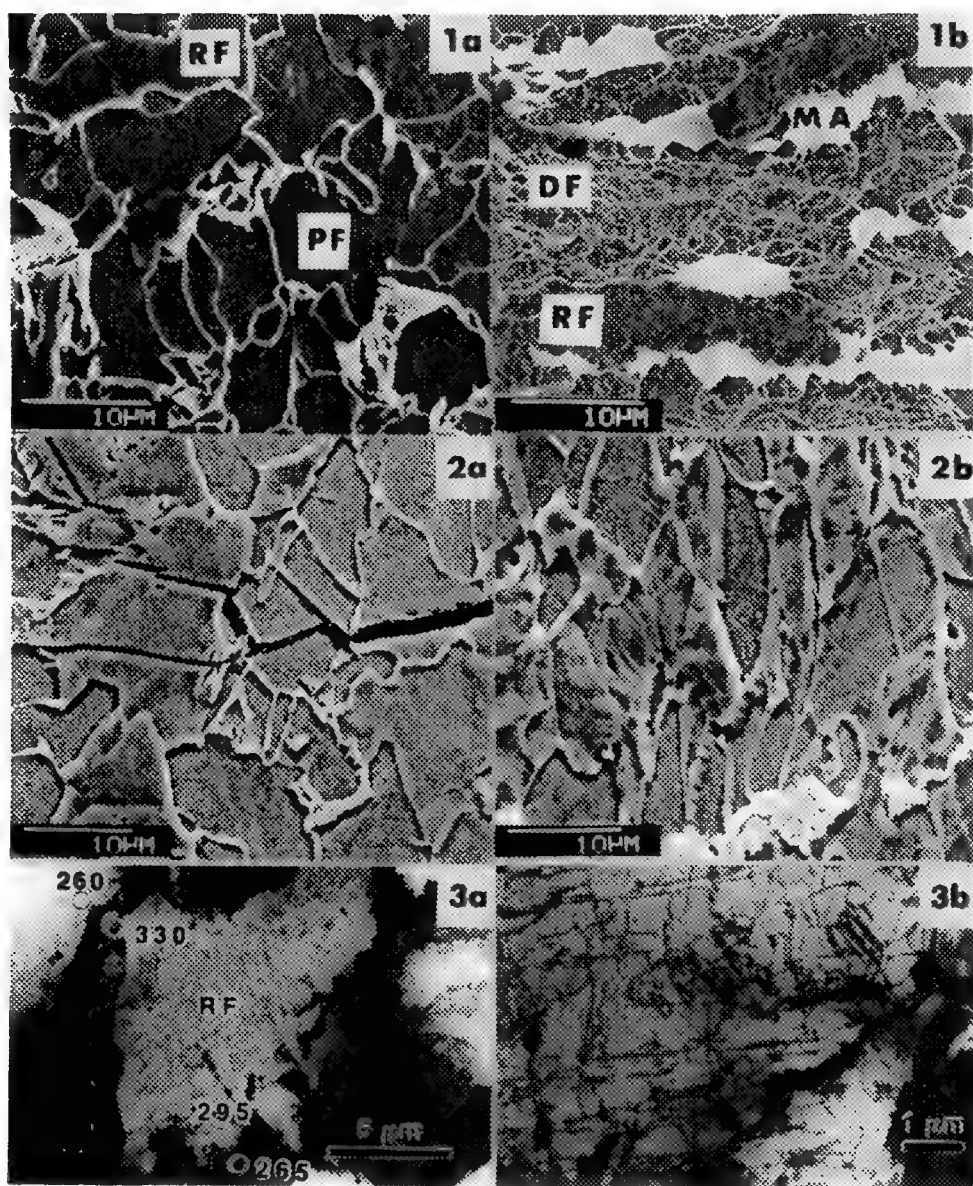
FIG. 1 a) Ti-V microalloyed steel, controlled rolled and quenched from 830°C. b) Controlled rolled and quenched from 700°C.

FIG. 2 Same condition as 1a, sections near fracture surface of through-thickness tensile specimens a) -196°C test temperature. b) 20°C test temperature.

FIG 3 Same condition as 1a. a) Local foil thickness measurements of raised ferrite grain and adjacent grains. b) Detail of dislocation substructure in raised ferrite.

STRUCTURAL MODIFICATIONS IN H-IMPLANTED AND LASER DESORBED Si

P.Zheng, R.G. Saint-Jacques, R. Boivin and B. Terreault

INRS-Energie et matériaux, Varennes, Qc, Canada, J3X 1S2

Near-surface microstructural modifications of silicon which occur in hydrogen ion implantation and classical thermal desorption have already been reported [1]. Our work is related to desorption using an intense and pulsed laser. The particularity of this technique is only the surface ($\approx$2μm) heated [2-3]. We report results of transmission electron microscopy (TEM) of the microstructural modifications in H-implanted and laser desorbed silicon.

Silicon [001] oriented has been implanted with 5 keV H to a dose of 10^{17}cm^{-2} and desorbed with a ruby laser (694.3 nm, 30 ns). It received an energy of 0.9 J.cm^{-2} and its surface temperature reached the melting point. This sample was totally desorbed as indicated by mass spectroscopy and checked by Elastic Recoil Detection [3]. Plan-view [001] and cross-sectional [110] TEM samples were mechano-chemically thinned (10% HF + 90% HNO$_3$). TEM dynamic imaging conditions (imaging vector g=220, w$\approx$0) were used to observe the defects.

Defect clusters (5-10nm) created by H-implantation (Fig.1a) were not completly annealed during the laser desorption (Fig.1b) because the Si was not heated during a sufficiently long time (50 ns). But some of them have been regrouped as dislocation loops ($\approx$20nm) by laser desorption (Fig.1b).
Gas bubbles are observed in plan-view dark-field images of as-implanted areas (Fig.2a). This formation of microbubbles is responsible of the pronounced volume expansion observed in H-implanted silicon [4]. After the laser desorption, residual voids are visible in TEM image (Fig.2b). We believe that those voids are imprints of emptied hydrogen bubbles. These voids (20-40nm) are three times smaller than the gas bubbles. This fact explains the volume retraction already measured in desorped areas [3].
Second phase precipitates (20-60nm) appear in bright-field images and microdiffraction patterns from the laser desorped areas (Figs.3,4). A dark-field image (Fig.4c) taken from "g$_2$" of the diffraction shows the second phase grains. This spot "g$_2$" has been indexed as ($1\bar{2}10$) of the hexagonal structure SiO$_2$ (a=0.500nm, c=0.545nm). The oxide precipitates were found to extend much deeper ($\approx$2μm) in cross-section than the implanted region (R$_p$ = 80 nm). This depth of 2μm corresponds to the layer heated to a high temperature by the laser. On the contrary the clusters and the voids are only seen in plan-view samples which means that they are located in the implanted layer. These precipitates are related to surface carbon or oxygen contamination. Reduction of C and O adsorbates on Si under laser irradiation have been previously observed and attributed to desorption and diffusion of the impurities into the substrate. They may react with Si and precipitate. Future work is needed to understand the possible role played by these microstructural changes in the process of laser-induced thermal desorption.

References
1. J.K.G. Panitz, D.J. Sharp, C.R. Hills, J. Vac. Sci. Technol. A3 (1985) 1
2. B. Terreault, J.Appl.Phys. 62 (1987) 152-158.
3. R. Boivin, Ph.D. Thesis, INRS-Energie-matériaux (1992).
4. K. Wittmaack, G. Staudenmaier, J. Nucl. Mater. 93&94 581-587
5. V.M. Bermudez, J. Vac. Sci. Technol. 20 (1982) 51-56.
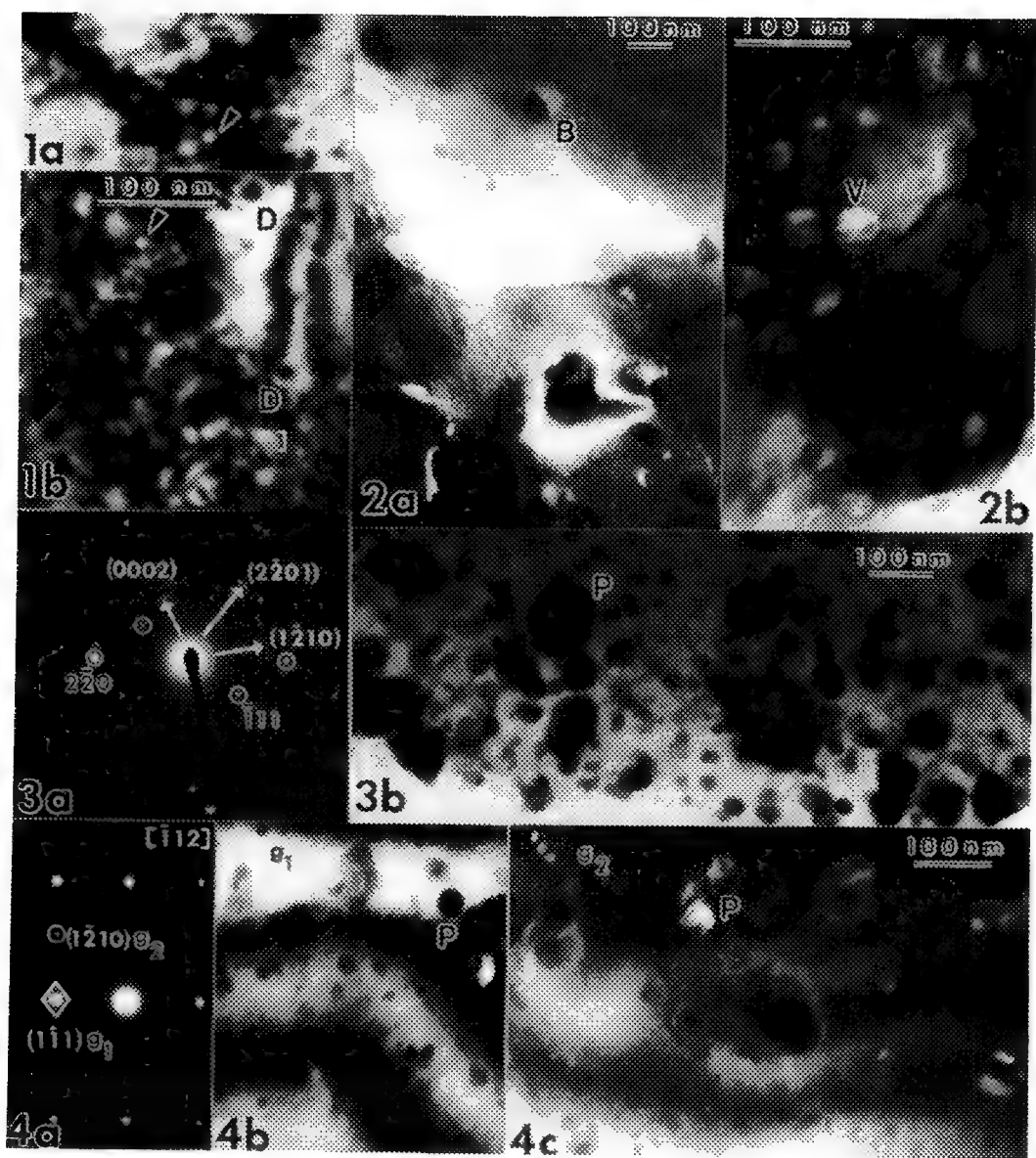
Fig.1 Plan-view dark-field images of Si (a) as-implanted with $10^{17}H/cm^2$ (b) after laser desorption. Defect clusters (▲), clusters with complex configuration ( ]) and dislocation loops (D).

Fig.2 Plan-view images showing (a) gas bubbles (B) in implanted area (dark-field) (b) voids (V) in laser desorbed area (bright-field).

Fig.3 Cross-section TEM of precipitates (P) after laser desorption.

Fig.4 (a) Cross-section diffraction from laser desorbed area showing spots for both Si $[\bar{1}12]$ and precipitates. Dark-field images obtained (b) with the g_1 Si spot (c) with the g_2 SiO$_2$ spot.

HREM STUDY OF CRYSTAL-AMORPHOUS TRANSFORMATION OF Cu-Ti MULTILAYERS BY COLD-ROLLING

W. A. Chiou, C. S. Lin, and M. Meshii

Department of Materials Science and Engineering
Northwestern University, Evanston, IL 60208

Amorphous alloys have been of scientific interest for more than three decades because of their improved properties (physical, mechanical, magnetic, corrosion, etc.) as compared with those of the same alloys in the crystalline states. Recently, solid-state reactions have been shown to be a potential technology for synthesis of amorphous metallic alloys[1,2,3]. While different mechanisms of amorphization have been proposed, the real process is still in debate. To study the amorphization process in more detail, information of structural transformation from crystalline to amorphous states during the processing (e.g., mechanical alloying) is essential. This paper presents an interfacial study of Cu and Ti foils by cold-rolling.

To study the microstructure of the multilayer interface and the physical extent of reaction, cross-sectional TEM is the most powerful and direct technique. The sample used in this study was prepared from 25 micron thick high purity elemental foils. Cu and Ti foils were cut to 5 cm (w) by 10 cm (l) and the surface cleaned by acetone. A total of twenty alternatively stacked Cu and Ti foils was cold-rolled. After each rolling pass, the composite mutlilayers were cleaned with acetone, cut to half and stacked together, and then rolled again until the average thickness of each individual layer (total thickness/total number of layers) was less than 50 nm. Specimen of composite layers was embedded with conductive epoxy in 3 mm tubing. Cross-sectional specimens were prepared for TEM observation by mechanical grinding, dimpling, and ion-beam milling.

A typical cross-sectional view of Cu and Ti multilayers after repeated rollings of 15 times is shown in Fig.1. Ti (thin white areas) thins down faster than Cu (dark areas). Fig.1 also shows that most of the layers which are less than 5 nm are amorphous. Close-up views of the HREM image show the structures of the interfacial boundaries between the Cu and Ti layers (Figs.2 and 3), indicating the interdifussion between the elemental layers. In addition, many nanocrystalline grains with diameters ranging from 2 to 25 nm are also observed. These nanocrystals appear being suspended in the amorphous matrix which are the same as those observed in the plane-view micrographs[4]. There are also areas where the amorphous phase coexists with well-defined crystalline phases (Fig.4).

The present observation indicates that the formation of nanograins precedes amorphization. The interdiffusion between Cu and Ti apparently takes place and may facilitated by the formation of nanograins. The relation between nanograin formation and amorphization and the rate of the local concentration gradient will be discussed in the report.

References:
1. X.L. Yeh, K.Samwer, and W.L. Johnson, Appl. Phys. Lett. (1983) 42:242
2. R.B. Schwarz and W.L. Johnson, Phys. Rev. Lett. (1983) 51:415
3. R.B. Schwarz and W.L. Johnson, eds. Solid State Amorphizing Transformations (1988) Elsevier Sequoia S.A.,Lausanne.
4. W.A. Chiou et al.. Proc. 12th Intl. Cong. Elec. Micro.(1990) 146
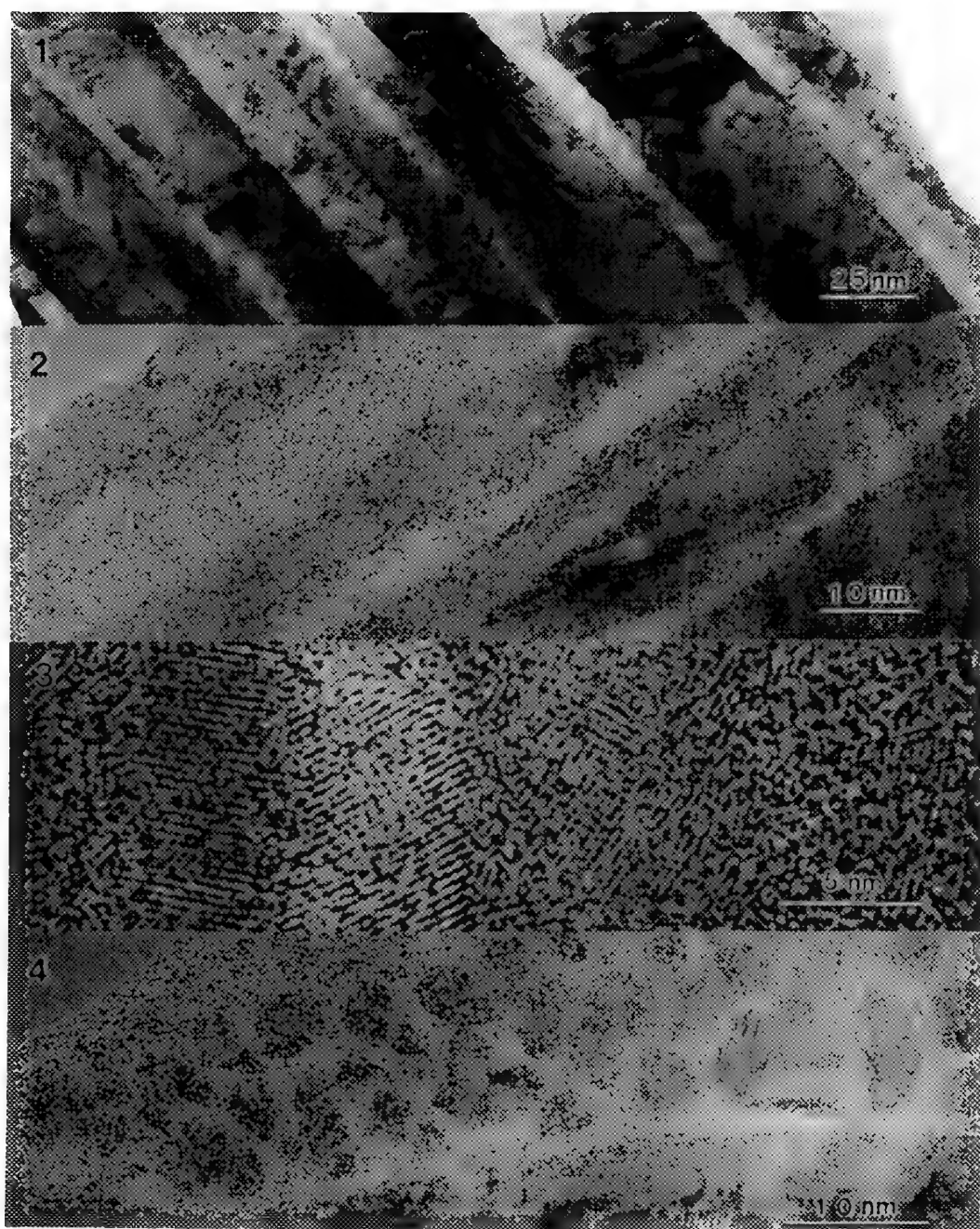
Fig. 1 TEM Cross-sectional view of Cu and Ti multilayers
Fig. 2 HREM micrograph showing amorphous image in thin layer and interface areas.
Fig. 3 HREM image revealing few sharp interfacial boundaries.
Fig. 4 HREM image showing amorphous, nanocrystals and large crystalline phases.

HREM OBSERVATIONS OF INTERMETALLIC ALLOY FORMATION IN Pt-Sn THIN FILMS

D.C. Dufner

Electron Microscopy Center, Texas A&M University, College Station, Texas 77843

The general goal of this research is to clarify mechanisms of solid state reactions at the atomic level as a step in the rationalization of macroscopic reaction behavior in solids. A study of intermetallic alloy formation resulting from interdiffusion of metals in thin films can be made by HREM. In this work, reactions between Pt and Sn in thin films are studied to elucidate mechanisms for structural and compositional changes during the interdiffusion process.

Thin films of Pt and Sn used in this study were prepared by the two-film method introduced by Shiojiri.[1] Few hundred angstroms of Pt were vacuum-deposited onto holey carbon films mounted on TEM grids. Sn films with an average thickness of 200Å were created by evaporation at rates of 15-30 Å/sec onto air-cleaved KBr substrates.[2] The Sn films were wet-stripped and collected on the holey Pt grids. Figure 1 shows a cross-section schematic of a Pt-Sn couple. While this two-film arrangement did not allow observations of the actual reaction interface, microtomy was used to produce cross-sections.[3]

HREM observations were carried out on a JEOL 2010 200kV TEM equipped with an analytical polepiece having a resolution of 2.3 Å. Observations were enhanced by a Gatan model 622 Mark II TV camera system. Microanalysis was carried out on an Oxford Instruments eXL system equipped with EDS quantitation and electron diffraction analysis packages. Because of the extensive coverage by the Sn films on the grid, regions of interest were found by translating the grid in the diffraction mode until certain patterns were obtained. A videocassette recorder was used to record TV images and diffraction patterns.

Since an intervening carbonaceous layer was present between the metal films, heating of the grids at 200°C in vacuo was carried out to induce the chemical reactions.[2] Figure 2 shows a typical image of several grains of Pt-Sn alloys observed after heating.

Observations of the initial reactions after heating revealed two different orientations of $PtSn_4$: [100] and [110]. The [110] orientation, shown in the images in Figure 3 and 4, was more prevalent. In Figure 3, a region of $PtSn_4$ (a) was bordered by a region (b) consisting of Sn as indicated by the presence of the (200) fringes having a spacing of 2.9 Å. The parallel orientation of the (200) fringes of Sn and the (002) fringes of $PtSn_4$ in this image suggested a possible conversion of Sn into $PtSn_4$ by doubling the a-axis of Sn (5.83 Å) to form the c-axis of $PtSn_4$ (11.32 Å). Because of this doubling, a slight mismatch of the c-values of $PtSn_4$ would occur and result in the formation of stacking faults as shown in Figure 4. Since $PtSn_4$ has a layered structure, such faults would be formed by shifts in the Pt and Sn layers. Image simulation calculations by MacTempas are currently underway to clarify these structural mechanisms.[4]

References

1. M. Shiojiri, et al., J. Crystal Growth 52(1981)883.
2. D.C. Dufner and L. Eyring, J. Solid State Chem. 62(1986)112.

3. D.C. Dufner, Proc. Ann. EMSA Meeting 49(1991)1114.
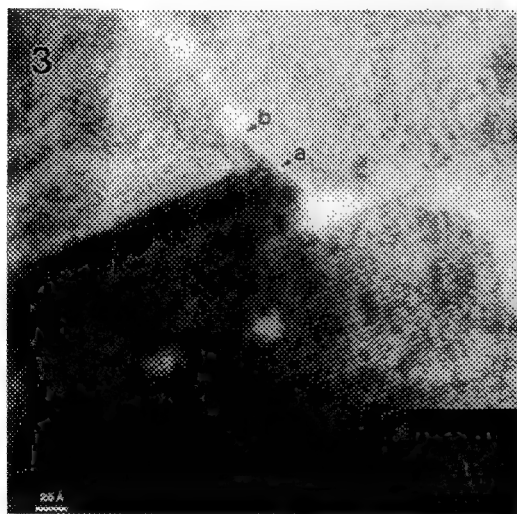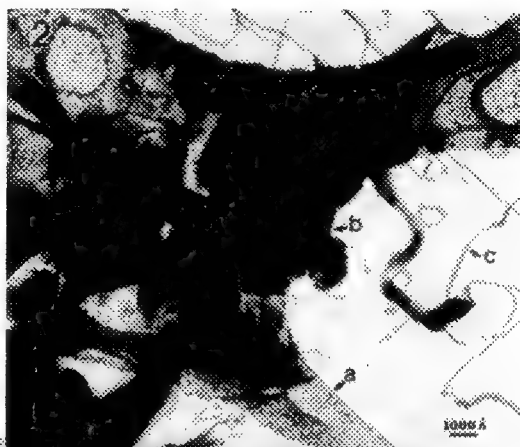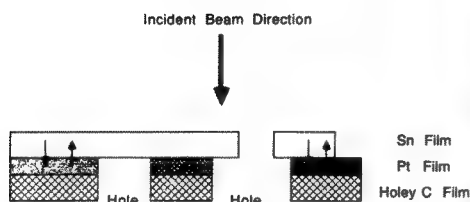
FIG. 1. -- Cross-section schematic of the thin-film couple.
FIG. 2. -- Typical image of Pt-Sn alloy films after heating. (a) Pt islands on
            holey carbon film, (b) grains of Pt-Sn alloy, (c) remnant of
            carbonaceous layer caused by recession of Sn film during heating.
FIG. 3. -- HREM image of [110] $PtSn_4$ (indicated by (a)) bordered by a region
            of Sn (b).
FIG. 4. -- HREM image of [110] $PtSn_4$ showing (002) stacking faults (indicated
            by arrows).

STUDY OF Ni/Ni₃Al DIFFUSION-COUPLE INTERFACE BY ANALYTICAL ELECTRON MICROSCOPY AND HIGH
RESOLUTION ELECTRON MICROSCOPY

M. Watanabe, Z. Horita, David J. Smith*, M. R. McCartney*, T. Sano and M. Nemoto

Department of Materials Science and Engineering, Faculty of Engineering 36, Kyushu
University, Hakozaki, Fukuoka 812 JAPAN
* Center for Solid State Science, Arizona State University, Tempe, AZ 85287

The interface between the Ni-rich solid solution phase (γ phase) and the intermetallic
phase (γ'phase) with the L1₂-ordered Ni₃Al structure plays an important role in the
strengthening of Ni-based two-phase alloys such as superalloys. In this study, we have
examined microstructure and diffusional phenomena across the γ / γ' interface by
analytical electron microscopy (AEM) and high resolution electron microscopy (HREM).

Fully annealed high-purity Ni (99.9%) was coupled with Ni-25mol%Al and subjected to
diffusion anneal at temperatures of 1073 and 1173K. Thin specimens were prepared from
these diffusion couples by careful cutting, grinding, electro-polishing and ion-milling,
details of which are described elsewhere[1]. We used three different types of electron
microscopes: (a) JEM-2000FX (at 200kV) for measurements of the overall concentration
gradient with a probe size of ∼20nm, microstructure observations and selected area
diffraction analyses, (b) EM400T-FEG (at 100kV) for high spatial resolution micro-
chemical analysis with a probe size of ∼3nm, and (c) JEM-4000EX (at 400kV) for
observations of lattice images at the interface. Characteristic x-ray lines of Ni Kα,
Al Kα, and Ni Lα were measured by energy dispersive x-ray spectrometers with a Be-type
window which were attached on both JEM-2000FX and EM400T-FEG. Ni Kα and Al Kα lines
were used for the determination of compositions, and Ni Kα and Ni Lα lines were for the
determination of local thicknesses. X-ray absorption corrections were made by the
differential x-ray absorption (DXA) method[2] when determining concentration gradients
and by the extrapolation method[3] when determining k-factors[4].

Figure 1 plots variations of the Al concentration (C_{Al}) and the thickness across the
couple interface annealed at 1173K for 3hrs. X-ray absorption correction is shown to be
important from a comparison between corrected (●) and uncorrected (○) results. The
abrupt change in C_{Al} corresponds to the γ / γ' phase boundary. Microstructure
observations showed that the γ phase in contact with the γ' phase consisted of
subgrains and extended over certain distance from the original interface. From selected
area electron diffraction analysis, this γ phase was found to lie in almost the same
orientation as the γ' phase. Figure 2 is an HREM micrograph of the γ / γ' phase
boundary taken in the <110> zone axis orientation. Superlattice fringes due to {100}
reflections are seen in the γ' region. Although the boundary is not clearly defined,
there is coherency between the two phases. Interdiffusivities were measured from the
overall concentration gradient by applying the Boltzmann-Matano technique. The values
obtained at the γ and γ' regions are plotted in Figure 3 together with those from
the specimen annealed at 1073K for 25hrs. For comparison, Figure 3 includes also values
obtained at higher temperatures by electron probe microanalysis (EPMA) and those from
the literature[5-9,10].

References

1. M. Watanabe, Z. Horita, D. J. Smith, M. R. McCartney, T. Sano and M. Nemoto, International
Conference on Diffusion in Materials (DIAMAT-92, Kyoto, Japan), 1992, to be presented.
2. Z. Horita, K. Ichitani, T. Sano and M. Nemoto, Phil. Mag. A (1989) 59, 939.
3. Z. Horita, T. Sano and M. Nemoto, Ultramicroscopy (1987) 21, 271.
4. G. Cliff and G. W. Lorimer, J. Microsc. (1975) 103, 203.

5. M.M.P.Janssen, Metall.Trans. (1973)4, 1623.
6. T.C.Chou and Y.T.Chou, Mat. Res. Soc. Symp. Proc. (1985)39, 461.
7. H.Bakker, Phys. Stat. Sol. (1968)28, 569.
8. K.Maier, H.Mehrer, E.Lessmann and W.Schüle, Phys. Stat. Sol.(b) (1976)78, 689.
9. K.Hoshino, S.J.Rothman and R.S.Averback, Acta Metall. (1988)36, 1271.
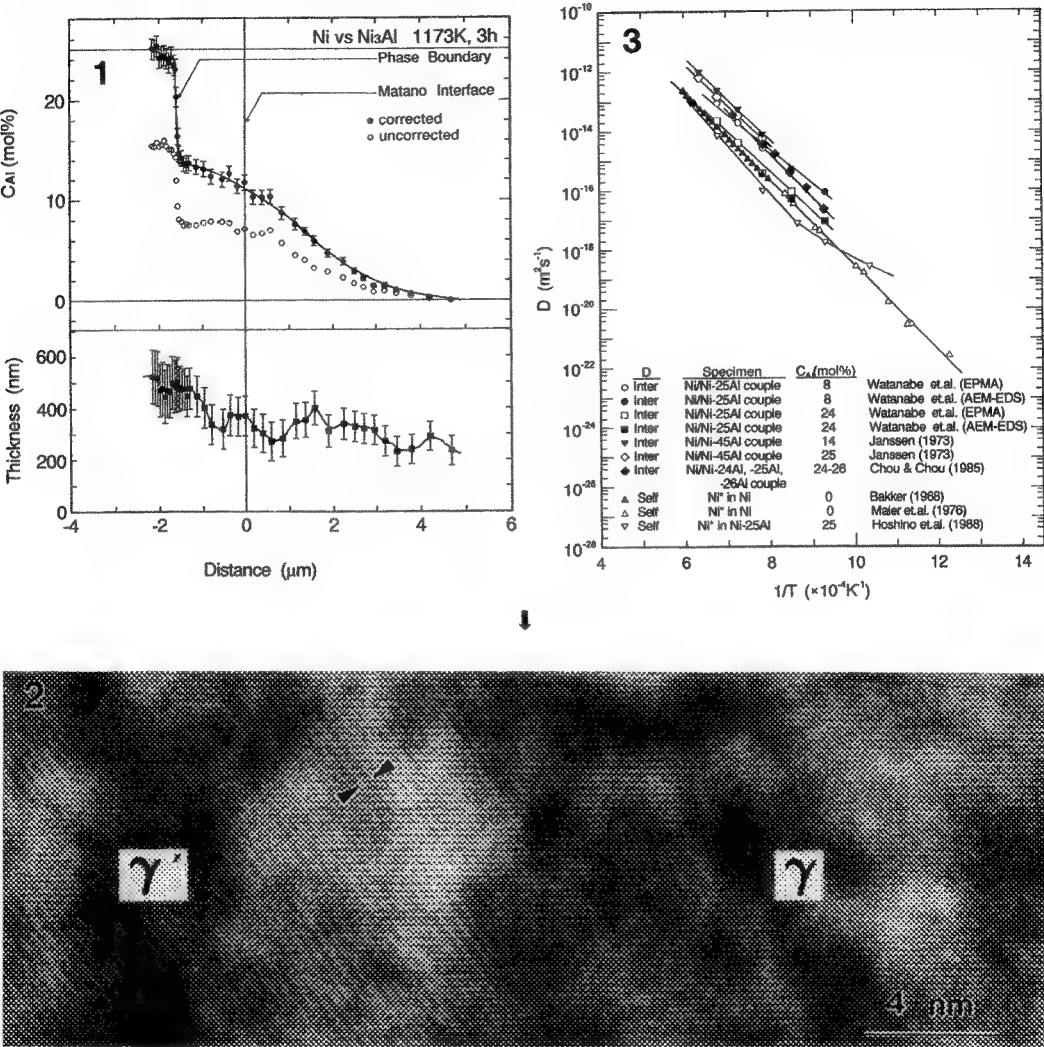
↑ phase boundary

FIG.1.--Variations of Al concentration (upper) and thickness (lower) across diffusion-couple interface.
FIG.2.--HREM micrograph of γ/γ' phase boundary taken from <110> zone axis. Arrows in micrograph indicate distance between {100} planes(~0.357nm).
FIG.3 --Diffusivity plotted against reciprocal temperature.

PHASE TRANSFORMATIONS IN RAPIDLY SOLIDIFIED $Nd_{33}Fe_7$ ALLOY

A.Zaluska, L.X.Liao, X.Chen, Z.Altounian, J.O. Ström-Olsen

Physics Department, Centre for the Physics of Materials,
McGill University,3600 University St., Montreal, Quebec, H3A 2T8, Canada

Nd-Fe alloys are important for high performance permanent magnets (usually in combination with B, C or N) and a knowledge of the metastable and stable phases of the system is necessary for the development of these new materials. An effective way to investigate such phases is by crystallizing an amorphous precursor.

Amorphous ribbons of the binary alloy $Nd_{33}Fe_{77}$ were produced by melt-spinning. The phase transformations induced by heat treatment of the as-quenched ribbons is complex involving first the production of metastable phases followed by subsequent transformation into stable phases and finally eutectic melting.

Crystallization of the amorphous phase starts with primary precipitation of a Nd-rich phase with a f.c.c. structure and lattice parameter a = 0.51 nm (Fe content is less than 5 at.%). At higher temperatures (above 880 K) the remaining amorphous matrix crystallizes into a second metastable phase and a stable phase Nd_2Fe_{17} (with a hexagonal structure and lattice parameters a = 0.85 nm and c = 1.24 nm).

Subsequent annealing of the ribbons leads to the formation of Nd_5Fe_{17} with a very complex hexagonal structure and lattice parameters a = 2.02 nm and c = 1.23 nm . Nucleation of this phase occurs at the Nd-rich grains and it appears that oxygen (which accumulates in Nd-rich phase) may be necessary to nucleate of the Nd_5Fe_{17}. Crystals of Nd_5Fe_{17} show either a rod-like morphology, or a faceted hexagonal or square shape. At 935 K melting of Nd_2Fe_{17} and Nd occurs.

Fig.1. Nd-rich phase crystallized from amorphous matrix.
Fig.2. Mixture of two phases after complete crystallization: Nd-rich phase and Nd_2Fe_{17}.
Fig.3. HREM image of defects in Nd_2Fe_{17} crystal.
Fig.4. Faceted hexagonal Nd_5Fe_{17} crystal.
Fig.5. Rod-like Nd_5Fe_{17} crystal nucleated at Nd-rich phase.
Fig.6. Triple junction of three phases: Nd_5Fe_{17} and Nd_2Fe_{17} and Nd-rich. There is a thin Nd-rich layer between Nd_5Fe_{17} and Nd_2Fe_{17} grains.

56
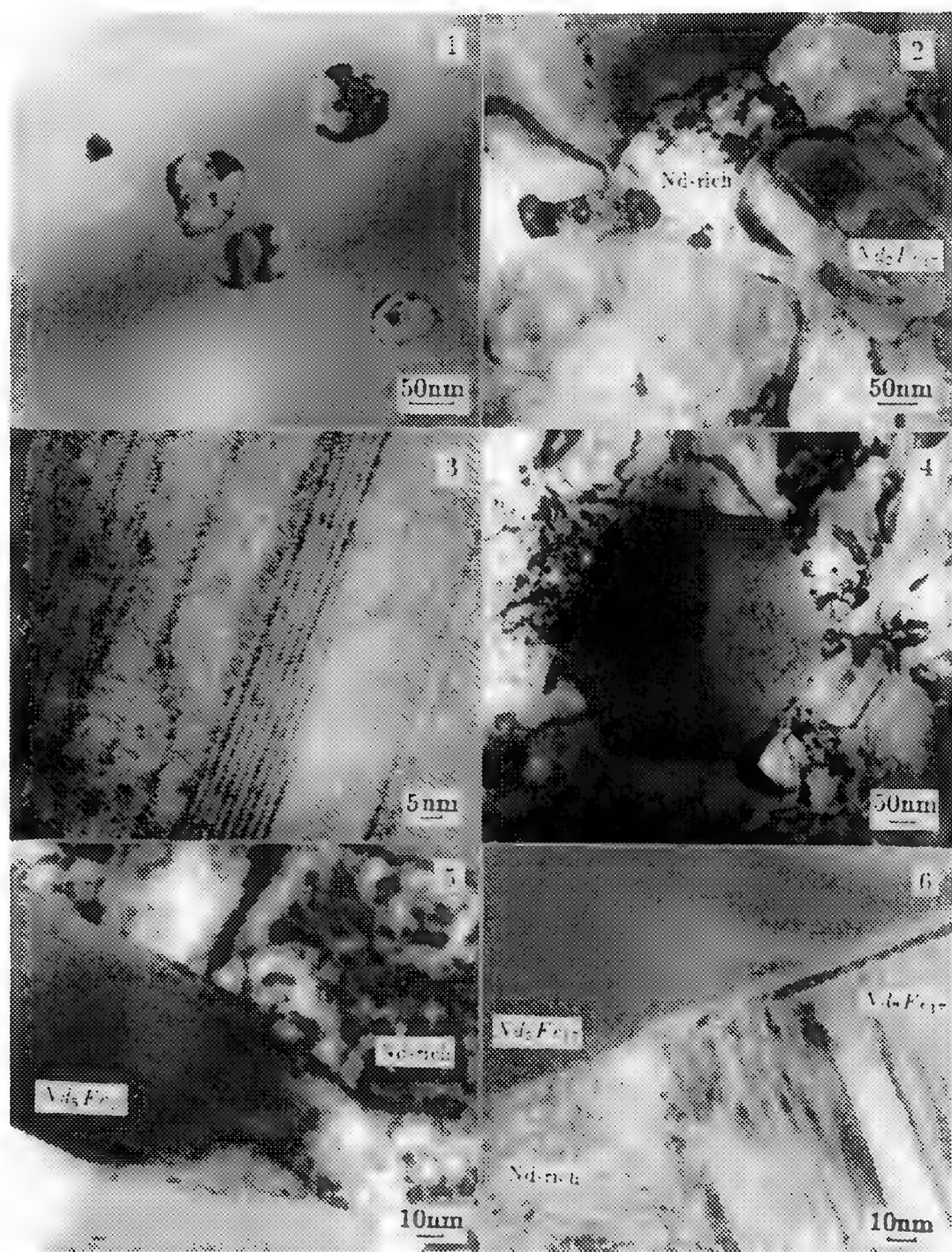
INCOMMENSURATE MODULATED PHASES OF THE $Nb_xTa_{1-x}Te_4$ CHARGE DENSITY WAVE SYSTEM

S. Ritchie[†], J. C. Bennett[†], A. Prodan [‡], F.W. Boswell[†] and J.M. Corbett[†]

† Guelph-Waterloo Program for Graduate Work in Physics, University of Waterloo, Waterloo, Ontario, Canada N2L 3G1
‡ J. Stefan Institute, Jamova 39, 61000 Ljubljana, Slovenia

A continuous sequence of compounds having composition $Nb_xTa_{1-x}Te_4$; $0 \leq x \leq 1$ have been studied by electron diffraction and microscopy. Previous studies have shown that the end members of the series, $TaTe_4$ and $NbTe_4$ possess a quasi-one-dimensional character and exhibit charge density wave (CDW) distortions. In these compounds, the subcell structure is tetragonal with axes $(a \times a \times c)$ and consists of the metal atoms (Nb or Ta) centered within an extended antiprismatic cage of Te atoms. At room temperature, $TaTe_4$ has a commensurate modulation structure with a $2a \times 2a \times 3c$ unit cell [1]. In $NbTe_4$, an incommensurate modulation with $\sqrt{2}\,a \times \sqrt{2}\,a \times \sim 16c$ axes is observed [1]. Preliminary studies of the mixed compounds $Nb_xTa_{1-x}Te_4$ showed a discontinuous jump of the modulation wave vector $\vec{q}$ from commensurate to incommensurate when the Nb dopant concentration x, exceeded $x \simeq 0.3$ [2]. In this paper, the nature of the compositional dependence of $\vec{q}$ is studied in greater detail and evidence is presented for a stepwise variation of $\vec{q}$. This constitutes the first direct evidence for a Devil's staircase in CDW materials.

The modulation vector may be directly determined from measurement of satellite positions in the electron diffraction patterns. The compositions of the corresponding crystallites were determined by EDX. In the [100] z.a. pattern, two types of satellite rows parallel to the c-axis may be distinguished: main rows which contain the subcell reflections, and superlattice rows which lie half way between the subcell rows (Fig. 1 (a)). As the Nb dopant concentration was further increased above $x \simeq 0.3$, the amount of incommensurability was observed to increase discontinuously. Even though the changes are small, this variation may be observed from the shift of the main row satellites from the commensurate positions in the [100] z.a. pattern (Fig. 1 (a) and (c)) and from the increased separation between of the doublets in the [130] z.a. pattern (Fig. 1 (b) and (d)). The values of the c-component of the modulation wavevector $\vec{q}$ measured from the position of the satellite reflections are plotted against x in Fig. 2. Step like features are clearly defined from the plot: plateaus corresponding to $TaTe_4$ and $NbTe_4$ as well as the clustering of the data points at several intermediate values. A least-squares fitting method was used to model the $\vec{q}$ vs. x dependence. In this analysis, the standard deviation for a step function type of variation was found to be considerably lower than that for a linear model. In addition, the estimated q_{1c} values corresponding to these steps agree with those predicted from a model in which the mixed crystals are described as a series of long period commensurate phases [3]. The details of this model will be presented.

Two new phase transitions between CDW modulated structures have been observed in the mixed crystals on heating above room temperature. For crystals with $x < 0.3$, a commensurate to incommensurate transition occurs at around $T = 350K$. In the satellite dark-field (SDF) images formed using a main row reflection (Fig. 3), a fringe pattern, characteristic of the incommensurate phases, appears above the transition in originally commensurate regions. Upon further heating above $T \simeq 450K$, the satellite row reflections vanished indicating a transition from a $2a \times 2a$ unit cell base to a new phase with $\sqrt{2}\,a \times \sqrt{2}\,a$ base. In SDF images using a superlattice row reflection (Fig. 4), a dense network of antiphase boundaries (APB), similar to those observed in the RT incommensurate mixed crystals, form above 350K covering the formerly commensurate regions. At $T \simeq 450K$, the APBs gradually broadened to convert the entire crystal to dark contrast (i.e. to a $\sqrt{2}\,a \times \sqrt{2}\,a$ incommensurate phase).

1. Boswell, F.W., Prodan, A. and Brandon, J.K. (1983) *J. Phys. C*, **16**, 1067–1076.
2. Kucharczyk, D., Budkowski, A., Boswell, F.W., Prodan, A., and Marinkovic, V. (1990) *Acta Cryst.*, B **46**, 153.
3. Prodan, A., Boswell, F.W., Bennett, J.C.,Corbett, J.M., Vidmar, T., Marinkovic, V. and Budkowski A (1990) *Acta Cryst.* B **46**, 587.
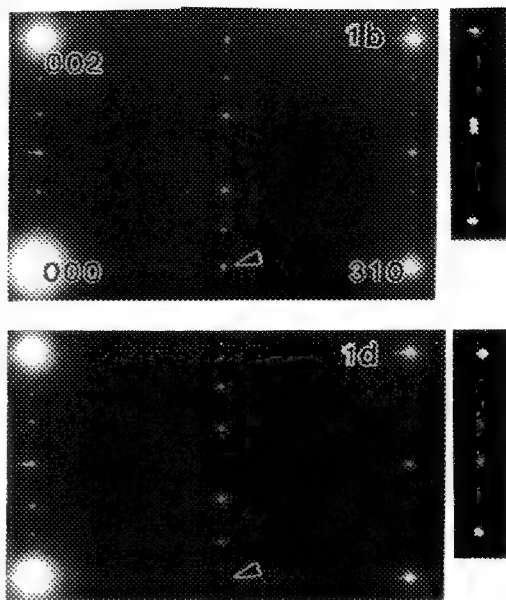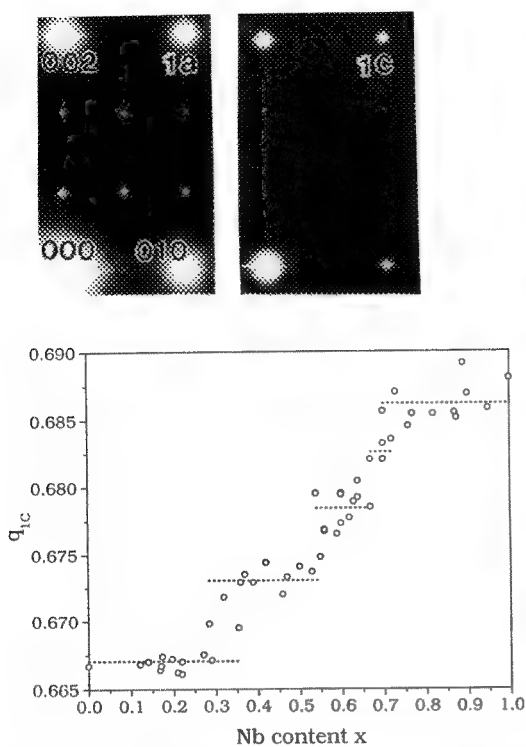
Fig. 1: Electron diffraction pattern for $Nb_xTa_{1-x}Te_4$. (a)[100] z.a. and (b)[130] z.a. patterns for $x \simeq 0.3$; (c)[100] z.a. and (d)[130] z.a. patterns for $x \simeq 0.7$. The doublets in (b) and (d) are shown enlarged.

Fig. 2: Variation of the modulation vector $\vec{q}$ with Nb content in $Nb_xTa_{1-x}Te_4$. Open circle represent the experimental data. The dotted lines are the best fit from the stepwise analysis.
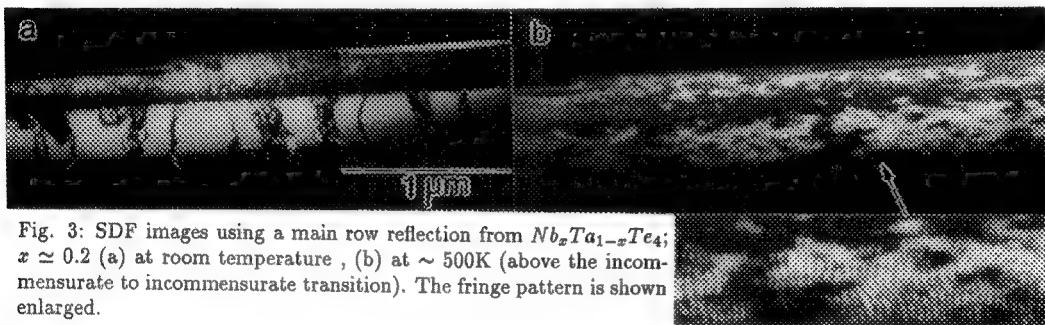
Fig. 3: SDF images using a main row reflection from $Nb_xTa_{1-x}Te_4$; $x \simeq 0.2$ (a) at room temperature , (b) at $\sim 500K$ (above the incommensurate to incommensurate transition). The fringe pattern is shown enlarged.
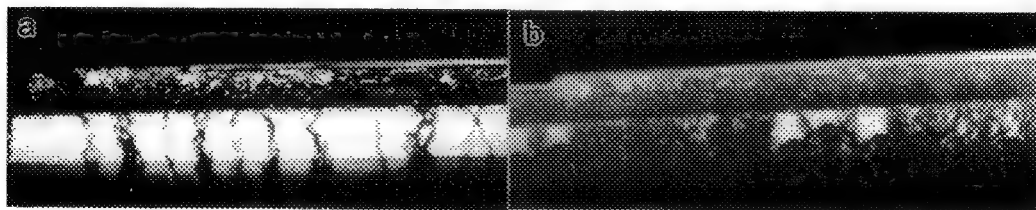
Fig. 4: SDF images using a superlattice row reflection from $Nb_xTa_{1-x}Te_4$; $x \simeq 0.2$ (a) at room temperature, (b) at $\sim 400K$.

59

PRECIPITATION AT α/γ INTERFACES IN DUPLEX STAINLESS STEEL

M.G. Burke and E.A. Kenik*

Westinghouse Science and Technology Center, Pittsburgh, PA 15235
*Metals and Ceramics Division, Oak Ridge National Laboratory, Oak Ridge, TN 37831

Duplex (austenite/ferrite) stainless steels are used in a variety of applications in the nuclear industry, particularly for coolant pipes, valves and pumps. These materials may become embrittled after prolonged ageing in the temperature range ~350 - 550°C due to precipitation of G-phase, an FCC-based Ni silicide, and the formation of a Cr-rich α' phase in the ferrite.[1-3] In addition to the intragranular G-phase precipitates, preferential precipitation of other phases is often observed at grain boundaries, particularly α/γ interfaces. In this examination, the precipitates formed in a Nb-containing duplex stainless steel have been identified using analytical electron microscopy.

The composition of the alloy is listed in Table 1. Both thin foil and carbon extraction replica specimens were prepared in order to study the precipitates. The specimens were examined in a Philips CM12 analytical electron microscope equipped with a Link Analytical energy dispersive x-ray spectrometer (EDS) system, and in a Philips EM400T/FEG interfaced with an EDAX 9100 EDS system and a Gatan 666 parallel electron energy loss spectrometer (PEELS).

TEM examination of the thin foil specimens revealed the presence of numerous Nb(CN) precipitates in both the ferrite and austenite phases. The precipitates primarily exhibited a square plate-like morphology with evidence of internal faulting, Fig. 1, although some fine cuboidal Nb(CN) were also observed. Significant grain boundary migration associated with thin plate-like Nb-rich precipitates was also evident, Fig. 2. A small amount of $M_{23}C_6$ was observed along the grain boundaries. Carbon extraction replica samples provided a much clearer indication of the extent of intergranular precipitation in this material; an extensive network of precipitates that had formed along the α/γ boundaries was readily visible in the replica specimens. Intergranular $M_{23}C_6$ and the intragranular Nb(CN) cuboidal and square plate-like precipitates were present. Furthermore, an array of discrete globular precipitates, approximately 0.1 - 0.3 μm in size, and irregular plate-like features (~0.5 - 3 μm in length) were observed, as shown in Fig. 3. Although initial TEM analysis indicated that the globular features were discrete, comparing transmission (TE) and secondary electron (SE) images of these precipitates showed that they were agglomerated, Fig. 4. Electron diffraction patterns obtained from these precipitates could be interpreted as a complex icosohedral structure, similar to that reported in an austenite/ferrite steel by Auger et al.[3] Detailed diffraction analysis of the coarse and fine precipitates, coupled with EDS and PEELS microanalysis, confirmed that the coarse plate-like precipitates were NbC, whereas the fine globular precipitates were an $(FeCr)_2(MoSiNb)$ Laves phase, in contrast to the results of Auger et al.[4]

References
1. H.M Chung and T.R. Leax, Mat. Sci. and Technology 6(1990)249.
2. M.K. Miller and J. Bentley, Mat. Sci. and Technology 6(1990)285.
3. P. Auger et al., Mat. Sci. and Technology 6(1990)301.
4. This research was sponsored in part by the Division of Materials Sciences, U.S. Department of Energy, under contract DE-AC05-84OR21400 with Martin Marietta Energy Systems, Inc. and through the SHaRE program under contract DE-AC05-76ORO0033. The authors wish to thank Dr. J. Bentley for valuable technical discussions, and J.J. Haugh for his assistance.

C	Mn	Cr	Ni	Mo	Nb	Si	S	P	Fe
0.045	0.76	20.70	10.07	2.59	0.20	1.16	0.001	0.022	bal
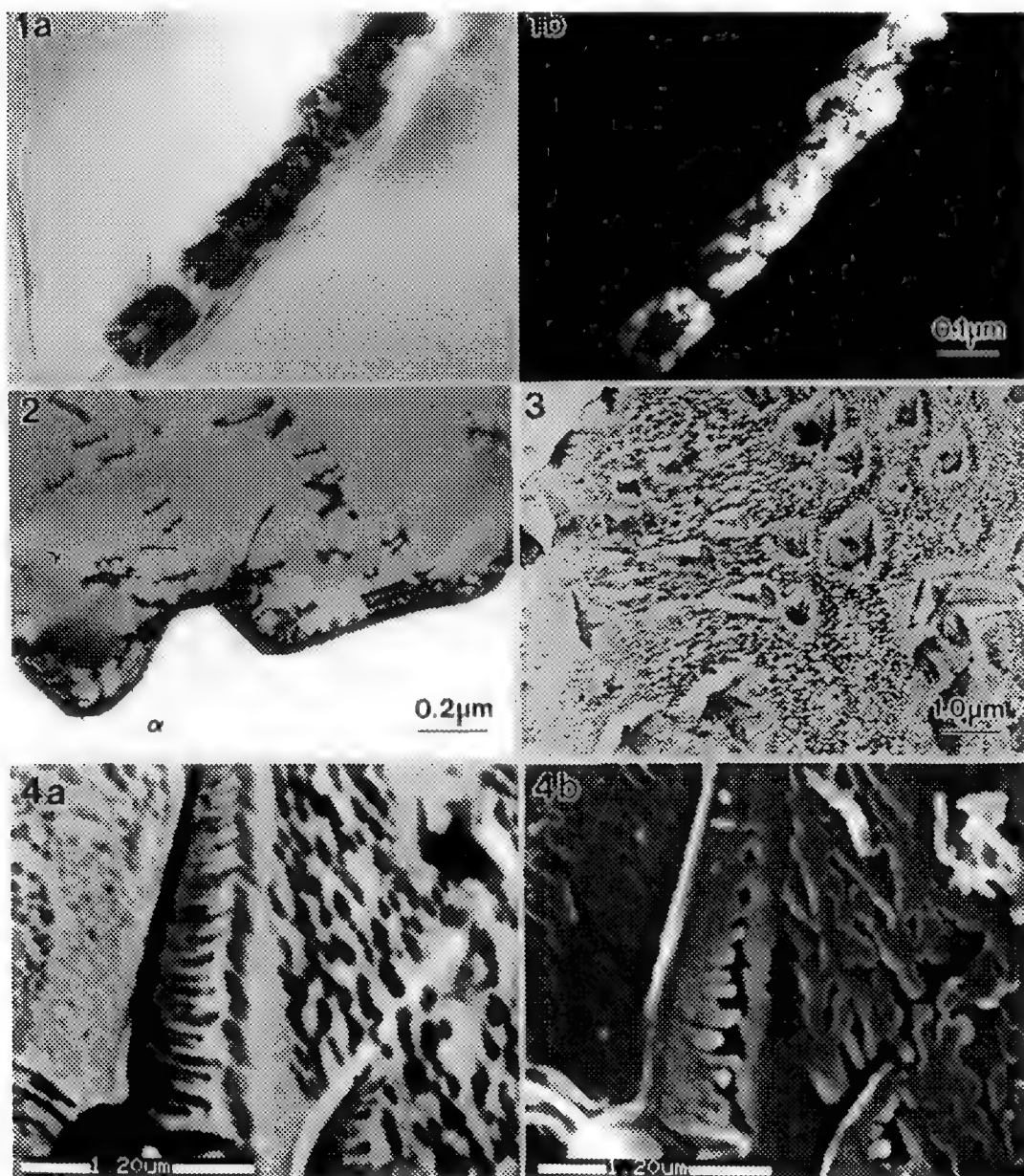
Fig. 1-- Nb(CN) in α. a) Bright and b) dark field TEM micrographs. Fig. 2-- Grain boundary bowing associated with Nb-rich precipitates. Fig. 3-- Precipitates observed at α/γ interfaces; replica sample. Fig. 4-- Complementary a) TE and b) SE images of extracted NbC and Laves phase precipitates.

61

EFFECT OF PROCESSING TEMPERATURE ON INTERFACIAL LAYER FORMATION IN SiC FIBER-REINFORCED GLASS-CERAMIC COMPOSITES

Hyun-Ho Shin, Yolande Berta, and Robert F. Speyer

New York State College of Ceramics, Alfred University, Alfred, NY 14802

The high fracture toughness and non-catastrophic fracture behavior of fiber-reinforced ceramic matrix composites are due to the weak interfacial shear strength between fiber and matrix, permitting fiber-matrix sliding during failure. In SiC fiber-reinforced glass or glass-ceramic composites, such low interfacial shear strength is obtained by the presence of a carbon-rich interfacial layer.[1] This provides a path for crack propagation, fiber pull-out, and fiber delamination during fracture.[2] Hence, these composites have demonstrated very high fracture toughness (critical stress intensity factor of ~ 17 MPam$^{1/2}$) and high fracture strength (3 to 4 times larger than that of monolithic glass or glass-ceramics).[3] The carbon-rich interfacial layer in these glass or glass-ceramic composites is formed by oxidation of the SiC fiber by the oxide matrix during hot pressing.[4,5,6] Its thickness is governed by hot pressing time, temperature, and pressure. In our results on Nicalon SiC fiber-reinforced lithium aluminosilicate glass-ceramic composites, hot pressing temperature governed not only the thickness of the interfacial layer, but also the phases residing within it. In this paper, the effect of hot pressing temperature on the phases formed in the interfacial area is described.

Fabrication of the composite included: glass melting and quenching, crushing and grinding by ball milling to less than $10\mu m$, slurry preparation (PVA/water solution and glass powder), slurry infiltration into Nicalon SiC fiber (yarn), binder burn-out, and hot pressing. Two selected compositions for matrix materials were $Li_2O \cdot Al_2O_3 \cdot 4SiO_2$ (LAS-A) and $1.1Li_2O \cdot 2.1Al_2O_3 \cdot 6SiO_2$ (LAS-B). Hot pressing temperatures and times for LAS-A and LAS-B were, 1400°C for 60 min and 850°C for 60 min, respectively (both at 10 MPa). TEM samples were cut to 3 mm diameter discs, thinned to 140 μm, dimpled to 40 μm, and Ar ion milled to electron transparency using a liquid nitrogen cold stage.

The matrices of the LAS-A and LAS-B composites were both devitrified to β-spodumene solid solution during heating of green bodies for hot pressing. Fig. 1 shows the TEM microstructure of the LAS-A composite hot pressed at 1400°C. The interfacial area of this composite was single-phased with a uniform (~ 270 nm) C-rich layer between the fiber and matrix, which is consistent with published results.[1,6] However, when the composite was hot-pressed at 850°C (LAS-B), there were two interphase regions as shown in Fig. 2. The comparatively dark interfacial region (marked "s") in Fig. 2 was silica-rich as shown in the EDS spectrum (Fig. 3). The bright area (marked "c") in Fig. 2 contained relatively more carbon as shown in the EDS pattern (Fig. 4). The silica rich interfacial region has not been reported in composites fabricated over 1300°C. Therefore, the previously proposed[6,7] carbon-rich interphase formation mechanism, i.e., $SiC(s) + O_2(g) = C(s) + SiO_2(s)$ or $SiC(s) + 2CO(g) = 3C(s) + SiO_2(s)$ is only valid for our LAS-B composite, or in general, composites fabricated at relatively low temperatures (less than about 1000°C[4]). An appropriate interfacial layer formation mechanism which explains the presence of

a C-rich phase as well as the absence of a by-product silica layer for composites processed at high temperature is given elsewhere[4].

References

1. J.J. Brennan, *Proc. Conf. on Tailoring Multiphase and Composite Ceramics*, pp. 549, Eds., R.E. Tressler *et al.*, Penn. State Univ., Plenum Press, New York, 1986.
2. D.B. Marshall and A.G. Evans, *J. Am. Ceram. Soc.*, (1985)**68**[5] 225.
3. J.J. Brennan and K.M. Prewo, *J. Mater. Sci.*, (1982)**17** 2371.
4. H.H. Shin *et al.*, in preparation.
5. J. Homeny *et al.*, *J. Am. Ceram. Soc.*, (1990)**73**[7] 2054.
6. R.F. Cooper and K. Chyung, *J. Mater. Sci.*, (1989)22 3148.
7. P.M. Benson *et al. Ceram. Eng. Sci. Proc.*, (1988)**9**[7-8] 663.
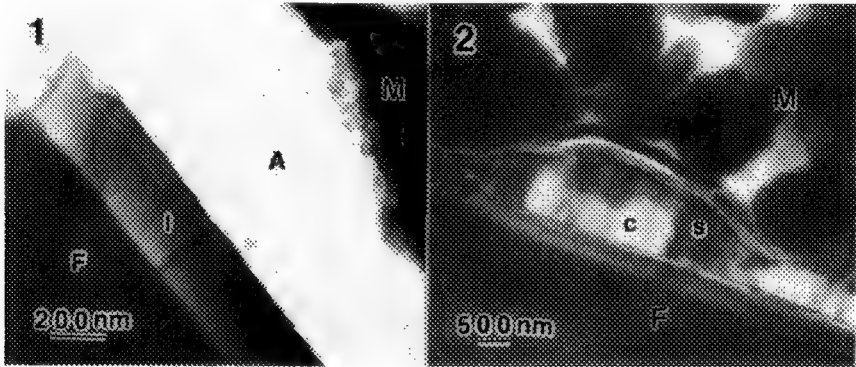
FIG. 1. TEM microstructure of interfacial area in the LAS-A composite (F: fiber, I: C-rich interphase, A: air gap caused by sample preparation, M: matrix).

FIG. 2. TEM microstructure of interfacial area in the LAS-B composite (s: silica-rich region, c: carbon-silica region, F: fiber, M: matrix).
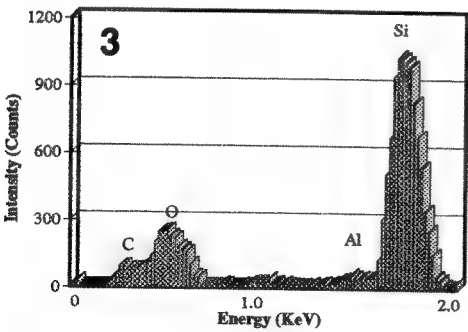
FIG. 3. EDS spectrum at s-region in Fig. 2.
FIG. 4. EDS spectrum of c-region in Fig. 2.
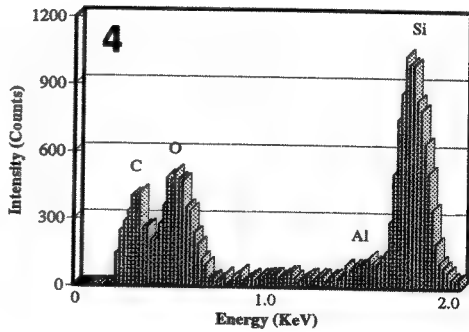
ANALYSIS OF CERAMIC-METAL BRAZE ALLOY SYSTEMS BY EPMA

J. Hefter, G. Werber, and S. Kang

GTE Laboratories Incorporated, 40 Sylvan Road, Waltham, MA

The development of advanced material systems for brazing silicon nitride-based ceramics to various metallic substrates (e.g. Incoloy 909 Fe-based superalloy) depends strongly upon the structural and chemical nature of a number of interfaces (ceramic-braze and braze-metal) as well as on the braze microstructure.[1] Such systems are being considered for joining ceramic rotors to metal shafts in automotive applications. Coatings may be deposited on the ceramic surface prior to brazing to promote braze adhesion and wetting.[2] These materials further complicate the resulting microstructure of the system.

Electron probe microanalysis can play a substantial role in the elucidation of the resulting braze microstructures since both phase morphology, distribution, and chemistry may be obtained. Here, a PY-6 silicon nitride ceramic was brazed to Incoloy 909 by using a Mo interlayer brazed between the two materials, Figure 1. The braze is a Au-5Ni-2Pd solid solution system and was used as a 50 µm thick foil. Brazing was accomplished by holding the specimen at 1080 °C for 10 min in a vacuum furnace. A cross-section for EPMA analysis was obtained by normal metallographic methods. All EPMA data were collected using a JEOL JXA-840 coupled with a Noran 5402 EDS system. Digital, background-subtracted maps (256x256, 0.1 s/point) were collected using "IPP" software.

The microstructure clearly shows that the inner and outer braze thicknesses are different (183 vs. 422 µm) for the inner and outer braze region, respectively. Additional braze alloy was added to the outer braze to accommodate the differences in thermal expansion between the Mo and the Incoloy during brazing. A higher magnification view of the outer braze region is provided in Figure 2. It is clear that the braze alloy solid solution separated into multiple phases. EDS point counting in both areas indicated the following relative compositions: light-contrast phase= 94Au-2Ni-2Pd-2Mo and dark-contrast phase= 66Au-4Ni-4Pd-2Fe-5Co-19Mo. These data show that a new Mo-rich phase was formed as the braze system cooled. Further, the Mo has preferentially diffused into the Ni-rich portion of the braze solid solution. Digital X-ray maps for Au and Ni, Figures 3 and 4, clearly indicate the extent of the overall phase separation.

In most cases, the brazing of silicon nitride to Incoloy 909 failed without the presence of the Mo interlayer, resulting in premature cracking of the joint. This was attributed to the development of high residual stress at the ceramic-metal interface. Ductile Au-Pd-Ni braze could not accommodate the difference in thermal expansion between the two materials alone.

The introduction of the Mo interlayer enabled the joints to withstand 225 in-lb torque at room temperature (185 in-lb is the maximum torque required for an automotive engine application). The braze alloy showed an intrinsic weakness in high temperature applications, resulting in no joint strength over 650 °C. The interdiffusion of Mo or other elements into Incoloy 909 was not found to provide a sufficient resistance to high temperature creep. Thus, other braze alloys and interlayer materials are under study to improve this performance.

References

1. R.E. Loehman and A.P. Tomsia, Amer. Ceram. Soc. Bull. 67[2], 375-380 (1989).
2. S. Kang, E. Dunn, J.H. Selverian, and H. Kim, Amer. Ceram. Soc. Bull. 68[9], 1608-1617 (1989).

100 μm   100 μm
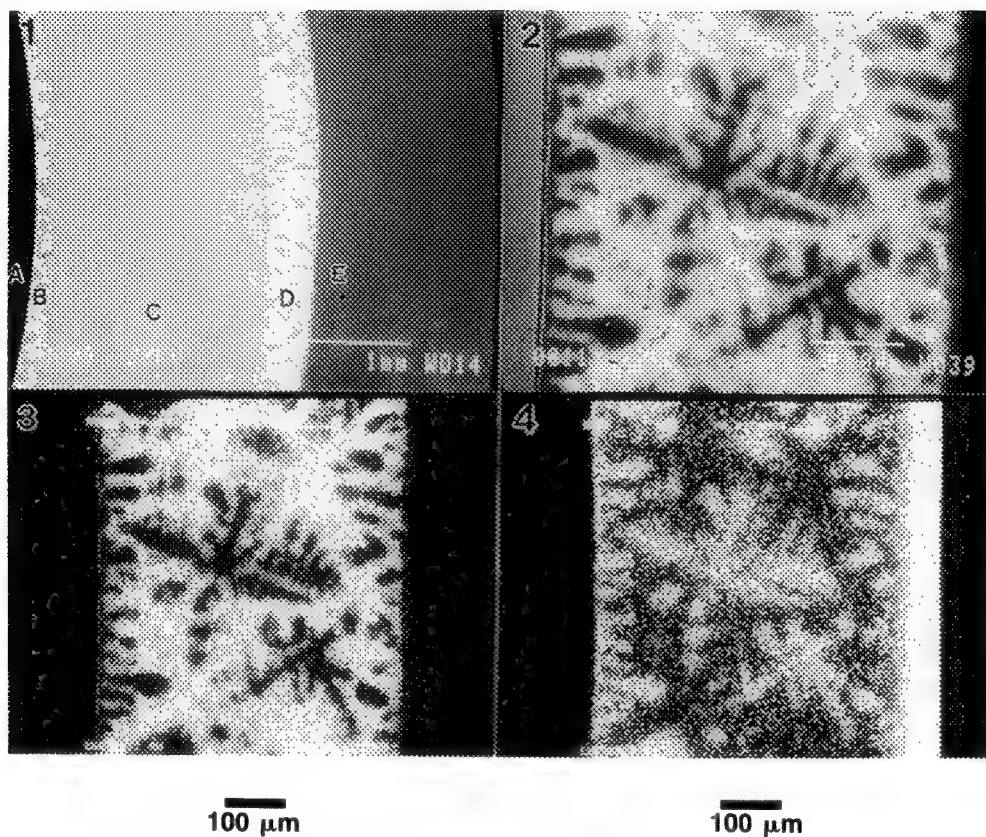
Fig. 1. Low magnification backscattered electron contrast image of a section of the specimen in cross-section showing the overall sample structure (A=PY-6, B=inner braze layer, C=Mo interlayer, D=outer braze layer, E=Incoloy 909 superalloy).

Fig. 2. Higher magnification BSE image of the outer braze located between the Mo interlayer and the Inconel 909.

Fig. 3. Digital Au map for a portion of the outer braze layer.

Fig. 4. Digital Ni map for a portion of the outer braze layer.

EM STUDY OF PHASE TRANSFORMATION IN ZINC COATINGS

C. A. Drewien

Materials Science and Engineering Department, Lehigh University, Bethlehem, PA   18015

Electrodeposited iron-zinc alloy (EZA) coatings, used for barrier and galvanic corrosion protection of steel by the automotive industry, are deposited under conditions, which give rise to small grain sizes and non-equilibrium phases. Subsequent processing of automotive body panels requires a paint bake cycle of 175 °C for 30 minutes. The as-deposited microstructure has not been investigated by TEM due to difficulty of sample preparation, and information on the effect of heat treatment upon EZA coatings is lacking. In this study, the as-deposited microstructure of a 6 w/o Fe EZA coating is investigated with electron microscopy, and in-situ heating in the TEM is used to observe the thermal stability of the microstructure.

A 6 w/o bulk iron content EZA coating was electrodeposited from a chloride bath onto a steel surface. The 7 µm thick coating was removed from the substrate, and three mm disks, punched from the material, were electropolished at 30-40 V in a room temperature, aqueous chromic-acetic acid mix. Samples were imaged with a JEOL 6300 FEG-SEM operated with an accelerating voltage of 1 keV and with a Philips 430 EM under an operating voltage of 250 keV.

The as-deposited microstructure, as examined in the SEM, exhibited a porous surface distribution of 0.3 µm wide by 1.5 µm long crystals. Figure 1 shows thirty nm wide growth steps on the crystals' surfaces. Planar section TEM micrographs (Figure 2) demonstrated the same 0.3 µm wide crystals (x in Figure 2) sectioned by 30 nm growth steps (y in Figure 2). Selected area diffraction pattern (inset) revealed spots from the hexagonal closed-pack eta phase and fine rings from a second phase that was body centered-cubic in structure.

After in-situ heating to a temperature of 175 °C, the linear growth steps divided into many smaller regions. The new phase, referred to as G phase, nucleated along boundaries and grew across the growth step and along the length of the growth step. With continued heating, growth of the new grains resulted (Figure 3), and the growth steps could no longer be detected. The microstructure contained small amounts of a hcp phase, but mainly contained equiaxed grains of a body centered cubic G phase. Selected area diffraction pattern (inset) shows rings from the G phase. The G phase was a metastable precursor to more equilibrium phases, such as zeta and delta phases in the known binary iron-zinc equilibrium diagram, that formed after continued heating at longer times or higher temperatures.

In-situ heating allowed the thermal stability of a 6 w/o Fe EZA coating to be studied and revealed that the non-equilibrium microstructure undergoes a phase transformation from eta to G phase in the temperature range near 175 °C. The same phase transformation will result during the paint bake cycle of EZA coated steel sheet[1].

References
1. The author would like to acknowledge the technical support of thesis advisors, Dr. A. R. Marder and Dr. J. I. Goldstein, and the financial support provided by International Lead and Zinc Research Organization.
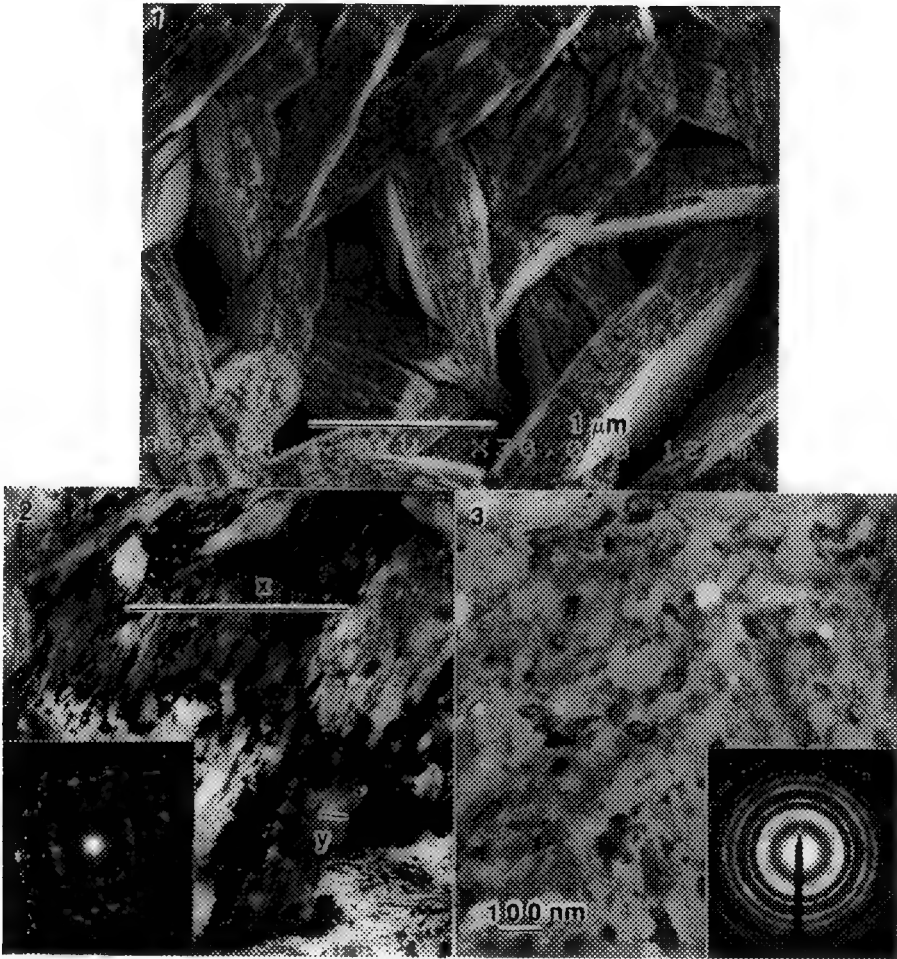
FIGURE 1.--Scanning electron micrograph of the surface of 6 w/o Fe EZA coating, imaged with an accelerating voltage of 1 keV (bar represents 1 μm).

FIGURE 2.--Transmission electron micrograph of planar section of 6 w/o Fe EZA coating shows same features observed on the surface of coating. The x indicates the crystal width observed in SEM image, and the y indicates growth steps of 30 nm width (bar represents 30 nm), which parallel the crystal lengthwise. The inset SADP shows two phases exist--spots from a hcp phase, eta, and rings from a bcc phase, G.

FIGURE 3.--In-situ heating of sample at 175 °C for 5 minutes allowed the formation and growth of grains of G phase (bar represents 0.1 μm). The inset SADP shows rings from G phase only.

ELECTRON HOLOGRAPHY OBSERVATION OF FLUX-LINE DYNAMICS

Takaho Yoshida, Tsuyoshi Matsuda, and Akira Tonomura

Advanced Research Laboratory,Hitachi Ltd.,Hatoyama,Saitama 350-03,JAPAN

With the sufficient spatial resolution and magnetic sensitivity, Electron holography [1] has opened a new way to directly observe the flux lines in superconductors. It has successfully shown the detailed magnetic field distribution of individual flux lines penetrating Pb thin films [2]. This technique also excels at observing flux line dynamics. By taking the holograms with a TV camera and recording them on a video tape, it became possible to observe the flux motion microscopically and continuously. Using this technique, the present study will demonstrate the thermally excited and the electrical current induced flux line dynamics.

(1) Thermally excited flux dynamics [3]
    First, we observed the behavior of thermally excited flux lines. The Pb thin film (1μm in thickness deposited on a W wire) was prepared for the sample.
    When the temperature rose to around Tc, the trapped flux lines were thermally released from the pinning and began to move about. Fig.**1a** - **c** shows the continuous motion of the flux lines, which were reconstructed into the magnetic lines of the force from video-recorded holograms. A couple of the anti-parallel paired flux lines are seen indicated by the contour loops. One pair on the right collided with each other to annihilate at last moment, **b** - **c** .

(2) Current induced flux line dynamics and flux pinning [4]
    When a transport current is applied to the superconductor, the flux lines move driven by the Lorentz force. In this case, especially, the flux pinning plays a crucial role. Electron holography directly demonstrated the flux pinning at a specific pinning center in the presence of the transport current for the first time.
    In contrast to (1), it is not the reconstructed image but the electron interference fringe was utilized to detect very rapid flux motions. This fringe instantly indicates the flux location and polarity in the manner explained in Fig.**2a** - **c**.
    Figure **3a** - **d** shows flux line behavior around a pinning center while the current gradually increased. Fig.**3b** indicates a flux line trapped at the pinning center. Thermal excitation released such trapped flux lines after brief pinning. As the current increased, this flux pinning and depinning became frequent (Fig.**3c**). Subsequently the pinning center turned to inactive because of the intensive Lorentz force (Fig.**3d**). Finally, the superconductivity was broken down due to such violent flux motions.
    Based on this direct observation, it became possible to directly estimate the elementary pinning force at specific pinning centers.

References
1)   A. Tonomura, Phys. Today (1990) 43, 22
2)   S. Hasegawa et al., Phys.Rev.B (1991), 43, 7631
3)   T. Matsuda et al., Phys.Rev.Lett. (1991), 66, 457
4)   T. Yoshida et al., to be submitted.
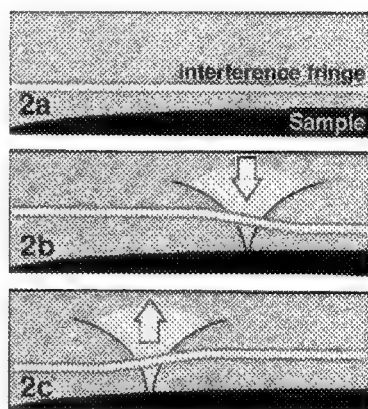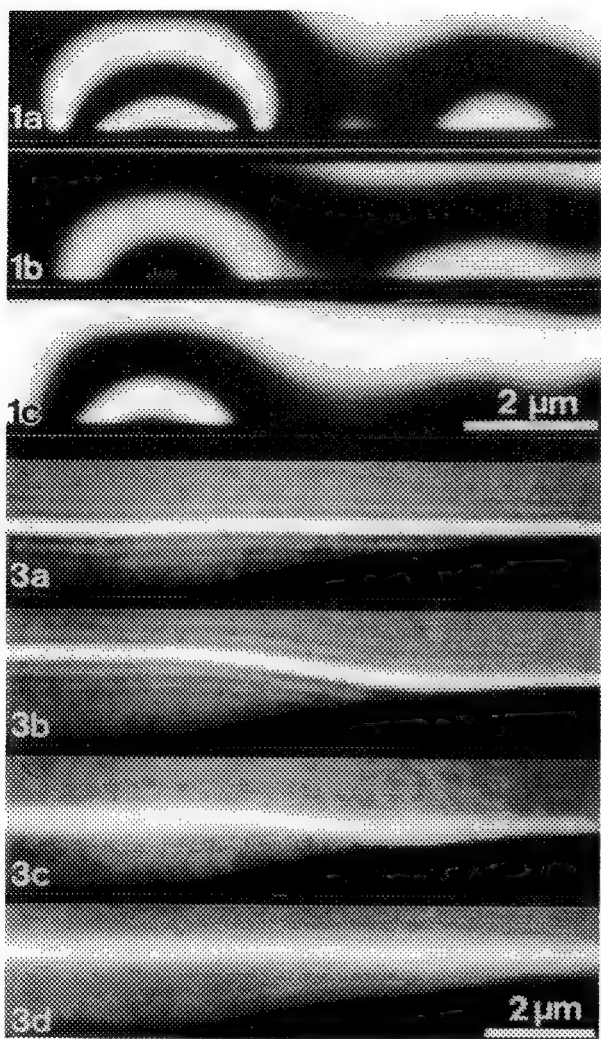
Fig.1 Thermally excited flux line motion in superconducting Pb film 1 μm in thickness at about 7 K. Contour lines springing out from the bottom sample surface show magnetic lines of force of individual flux lines; one contour line represents one flux quantum $\Phi_0 = h/2e$. **1a** at t=0.0 sec. **1b** at t=2.0 sec. **1c** at t=2.2 sec.

Fig.2 Interpretation of electron interference fringe response to flux line. Fringe deformation reflects the electron wave phase shift due to the Aharonov-Bohm effect of the flux line. **2a** Fringe remained straight without flux line. **2b,2c** When a flux line come to be pinned, the fringe was displaced at its location according to flux polarity.

Fig.3 Current-induced flux line motion and flux pinning in Pb film 1 μm in thickness. Temperature was fixed at 7 K, while the current was gradually increased. **3a** j= 600 A/mm^2. **3b** j= 650 A/mm^2, fringe displacement indicated a flux line with a value of $2\Phi_0$ and downwards polarity came to be trapped at the pinning center. **3c** j= 700 A/mm^2, flux pinning succeeded so frequently that the fringe oscillated between the straight and displaced form. **3d** j= 720 A/mm^2, intensive Lorentz force made the pinning center inactive. Consequently, the fringe began to oscillate uniformly.

69

DIRECT OBSERVATION OF THE FLUX LINE LATTICE IN Al-DOPED $YBa_2Cu_3O_{7-\delta}$

I.V. Grigorieva, P.A. Midgley, K.E. Bagnall, K. Sasaki and J.W. Steeds

H.H. Wills Physics Laboratory, University of Bristol, Tyndall Avenue, Bristol, U.K.

There has been much interest in the effect of partial substitution of Cu atoms in $YBa_2Cu_3O_{7-\delta}$ (YBCO) by dopant atoms such as Fe, Al and Co. It has been found that an increase in the doping level alters the structure of YBCO - the twin domain size drops to 30-100Å for x>0.025 and the domains form the so-called 'tweed' structure.[1] HREM has confirmed that within the domains the structure remains orthorhombic but on a macroscopic scale is quasi-tetragonal. This, in turn, leads to a change in superconducting properties: a rapid decrease in the transition temperature T_c, critical current, etc.[2]

In the present contribution the first results are reported on the direct observation of the magnetic flux structure in $YBa_2(Cu_{1-x}Al_x)_3O_{7-\delta}$ single crystals (x=0.04) which was also expected to be influenced by Al doping. The flux line (vortex) distribution was observed using the high resolution Bitter pattern technique which involves evaporation of fine ferromagnetic particles (both Fe and Co were used in our experiments) to 'decorate' vortices at the surface of a superconductor.

Two main features were found to be characteristic of the flux line lattice (FLL) in Al-doped YBCO that contrasted with those from undoped crystals. Firstly, we have not found the FLL to be dominated by bulk structural defects (compare the adjustment of the FLL to the twin distribution in undoped YBCO): vortices are arranged homogeneously and the extent of their ordering rapidly increases with an increase of the external magnetic field so that they form a regular lattice in a field as small as 20G (see Fig. 1). Twin boundaries do not have any pronounced effect on the vortex distribution, evidently, because their scale (~30Å) is much smaller than all scales in the FLL. In addition, the vortex lattice (for fields of 15G and 20G), where it was regular, was found to consist of misoriented domains with a regular hexagonal FLL inside correlation regions (see Figs 1,2) whose size increased sharply with the magnetic field. Such behaviour is known to be characteristic for collective pinning from weak pinning sites.[3] This enabled us to estimate the volume pinning force from the observed correlation dimensions R_c: $F_p \approx (\sqrt{8\pi C_{66} r_p})/R_c^2$, where the pinning range, $r_p \approx a$, the average vortex spacing and C_{66} is the shear modulus of the FLL.[4] We found $F_p \approx 2\times10^5 dyn/cm^3$ which corresponds to a critical current density, $j_c \approx 1\times10^3 A/cm^2$, which is two orders of magnitude smaller than $j_c(B=0, 4.2K) \approx 10^5 A/cm^2$ typical for undoped YBCO crystals.

An interaction of vortices has also been studied with different elements of surface relief such as growth steps or small-scale natural modulation of the sample thickness ('ripple'). Vortices were found to be strongly pinned by these surface defects as seen in Fig. 3.

References

1. Y. Xu et al. (1989) *Phys Rev B* **39** 6667.
2. R. Wordenweber et al. (1989) *J. Appl. Phys.* **65** 1648.
3. I.V. Grigorieva, (1989) [Russian] *JETP* **69** 194.
4. A.I. Larkin and Yu. N. Ovchinnikov (1979) *J. Low Temp. Phys.* **34** 409.
5. P.A.M. would like to acknowledge financial assistance from The Royal Commission for the Exhibition of 1851.
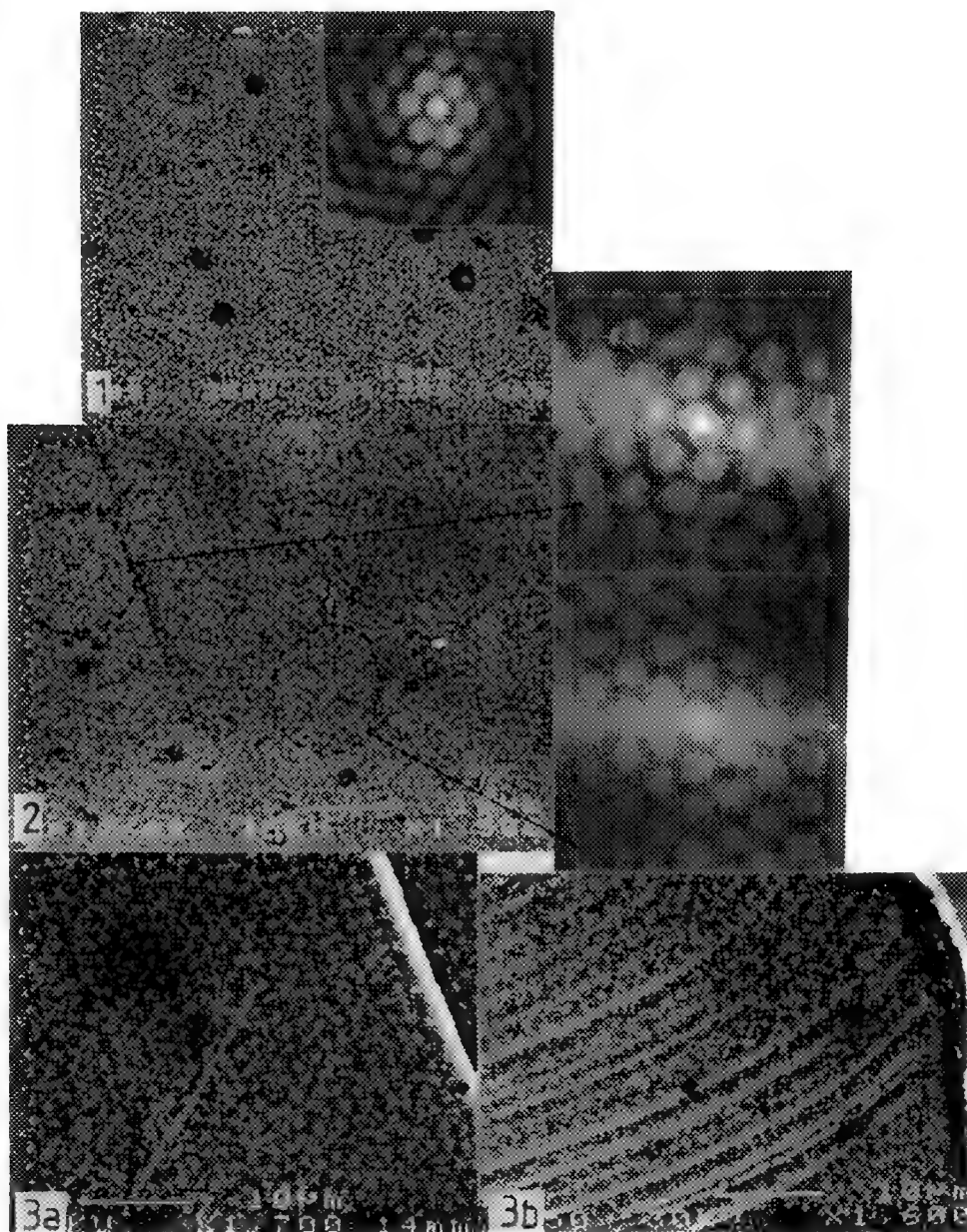
Fig. 1 FLL of Al-doped $YBa_2Cu_3O_{7-\delta}$ at 20G and the corresponding ACF.
Fig. 2 FLL of Al-doped $YBa_2Cu_3O_{7-\delta}$ at 15G and two ACFs from the outlined regions.
Fig. 3 (a) Alignment of the FLL with growth steps and (b) vortex pinning at surface ripple.

INTERFACE MICROSTRUCTURES IN MELT-TEXTURED $YBa_2Cu_3O_{7-\delta}$ ON Ag-Pd AND FLUX PINNING CENTERS INTRODUCED BY Y_2BaCuO_5 PARTICLES

Z. L. Wang*, A. Goyal and D. M. Kroeger

Metals and Ceramics Division, Oak Ridge National Laboratory, P.O. Box 2008, Oak Ridge, TN 37831-6376; * also at Department of Materials Science and Engineering, The University of Tennessee, Knoxville, TN 37996-2200

Transmission electron microscopy (TEM) and energy dispersion X-ray spectroscopy (EDS) were used to study the microstructure of the melt-textured $YBa_2Cu_3O_{7-\delta}$ (123) thick films on Ag-Pd substrate. The samples used for this study were melt-textured thick films of 123 on a Ag10%Pd alloy substrate. The film was prepared using a paint-on technique and was processed according to a schedule described elsewhere [1]. Domains of 123, as large as 5-6 mm, are formed in the film. Analytical electron microscopy (AEM) studies of this material were made using a Philips EM400 TEM/STEM (100 kV) with a field emission gun (FEG). A small electron probe of diameter approximately 2 nm was generated, and used in determining the compositional change across grain boundaries.

123/Ag-Pd interface: The interface between the Ag-Pd substrate and the 123 film is found to be very sharp as indicated in Fig. 1 with negligible inter-diffusion of chemical species. This indicates that Ag-Pd is a suitable substrate for melt-processed 123. No preferred orientation relationship between 123 grains and the substrate was found. EDS analysis has shown there is no diffusion of Pd or Ag into the boundaries between 123 grains near the substrate. Increasing the Pd content however does result in the formation of Ba-Cu-Pd-O phases. These phases are found at the substrate interface for a 30% Pd substrate. The 211 phase forms as a layer on top of the Ba-Cu-Pd-O phases.

211/123 interface: A melt-processed 123 grain usually contains many Y_2BaCuO_5 (211) particles. A significant increase in the stacking fault density in 123 near the 211/123 interface has been found (Fig. 2). The non-uniform distribution of stacking faults around the 211 particle is an important indication of strain inhomogeneity. To confirm the above observations, the 211 particles were also examined along the [001] zone axis. In this orientation, small precipitate-like defects ranging in size from ~ 5 - 40 nm were observed (Fig. 3). These defects tend to cluster around the 211 particles and are probably small dislocation loops around the stacking faults in the basal plane.

Their dimensions suggest that the numerous stacking faults observed around 211 particles may be effective flux-pinning sites for a magnetic field oriented parallel as well as perpendicular to the c-axis. A conservative estimate of the stacking faults density is $\sim 10^{15}/cm^3$. The stacking faults around the 211 particles can be viewed as discs of non-superconducting material. For **H//c**, these stacking faults may act as "point" pins, and for **H//ab** plane, as extended or planar pins. It is also found that there exists a significant compositional disorder in the 123 matrix near the 211 particles. EDS compositional analysis of stacking fault-free 123 near 211 particles indicates a significant Y-excess and Ba-deficiency, suggesting a high density of cation-disorder related point defects. The observed compositional variation is also consistent with that expected during dissolution of 211 leading to the formation of 123 at the solid/liquid interface [2]. These defects may also be effective flux-pinning sites. Thus, two microstructural features have been observed which may explain the increase in flux-pinning with 211 surface area which has been found in melt-processed 123 [3,4].

1. A. Goyal et al., Manuscript in preparation (1992).
2. K.B. Alexander, A. Goyal, D.M. Kroeger, V. Selvamanickam, and K. Salama, Phys. Rev. B (1992).
3. Z.L. Wang, A. Goyal and D.M. Kroeger, to be submitted to Phys. Rev. B (1992).
4. M. Murakami et al., Cryogenics, 30 (1990) 390.
5. Research sponsored by the U.S. Department of Energy, Assistant Secretary for Conservation and Renewable Energy, Office of Utility Technologies, Office of Energy Management/Advanced Utility Concepts - Superconducting Technology Program for Electric Energy Systems under contract DE-AC05-84OR21400 with Martin Marietta Energy Systems, Inc.
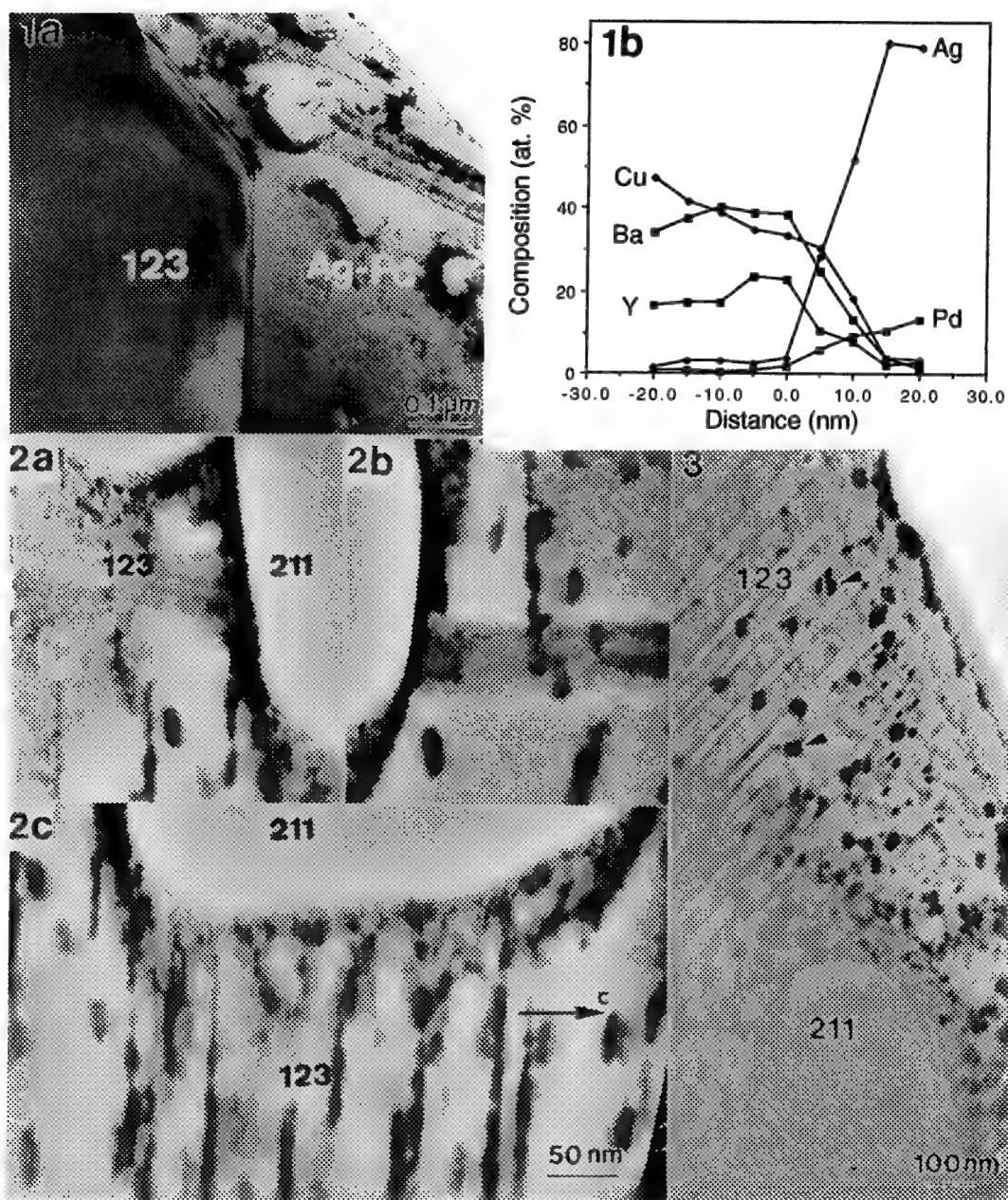
FIG. 1.-- (a) Cross-section TEM image of 123/Ag-Pd interface. (b) Composition profile determined by EDS across interface region as indicated in (a).
FIG. 2.-- TEM images of 211 particle in 123 matrix viewed along [100] or [010] showing high density distribution of stacking faults around 211 particle. (a), (b) and (c) are from same particle.
FIG. 3.-- TEM image of 211/123 interface viewed along [001] showing small dislocation loops.

73

Atomic Resolution Analytical Electron Microscopy (ARAEM) of Oxide Superconductors

Vinayak P. Dravid, H. Zhang, L.D. Marks and J.P. Zhang
Department of Materials Science & Engineering, and
Science and Technology Center for Superconductivity
Northwestern University, Evanston, IL 60208

A 200 kV cold field emission gun atomic resolution analytical electron microscope (ARAEM, Hitachi HF-2000) has been recently installed at Northwestern. The ARAEM offers an unprecedented combination of atomic structure imaging of better than 0.20 nm nominal point-to-point resolution and about 0.10 nm line resolution, alongwith nanoscale analytical capabilities and electron holography in one single instrument. The ARAEM has been fully functional/operational and this paper presents some illustrative examples of application of ARAEM techniques to oxide superconductors. Additional results will be presented at the meeting.

Identity of Planar Defects in Quench-Melt-Grown YBCO[1]: Quench-melt-grown (QMG) YBCO has well-aligned grain structure with planar lattice defects dispersed in the matrix grains. Such planar defects have been the focus of a number of investigation since such fine scale defects are anticipated to play a significant role in flux pinning in YBCO[2,3]. It has been suggested that the planar defects are stacking faults with extra Cu-O layers inserted in the regular YBCO crystal lattice[2,3]. Using a combination of HRTEM imaging, x-ray microanalysis and EELS, we have been able to confirm the identity of these defects[1]. Figure 1A is an HRTEM image of QMG YBCO exhibiting a typical two-layer planar defects. X-ray microanalysis employing planar channeling conditions indicate copper enrichment at the defect core (Figure 1C). EELS Cu L_{23} fine structure associated with the planar defect (with < 1 nm beam) is remarkably similar to that of CuO (Figure 1 D). These collective results confirm that the planar defects such as in Figure 1A are in fact insertion of pure Cu-O layers in otherwise regular YBCO crystal unit cell.

Hole Formation and Charge Transfer in $Y_{1-x}Ca_xSr_2Cu_2GaO_7$[4]: Occurrence of superconductivity is recently reported in $Y_{1-x}Ca_xSr_2Cu_2GaO_7$ system, but only after high pressure oxygenation. Interesting characteristics of this superconductor are the replacement of Cu-O chains with Ga-O tetrahedra and that copper is the only cation with variable oxidation state. EELS fine structure of O-K edge reveals an appearance of a pre-edge peak (~ 528.4 eV) with Ca-doping, indicating formation of holes on oxygen sites. These holes, however, are clearly not associated with superconductivity since these specimens did not undergo high pressure oxygenation treatment, thus are not superconducting. After high pressure oxygenation treatment, the O-K edge of Ca-doped specimens exhibits a secondary pre-edge feature at about 527.2 eV. This O-K secondary feature correlates well with a high energy shoulder on the Cu L_3 edge of the same specimen. Thus, only those specimens which undergo high pressure oxygenation treatment exhibit the secondary O-K pre-edge feature and high energy shoulder on the Cu L_3 edge. We interpret these results in terms of two types of holes in this system. The first ones are induced by Ca-doping alone and are associated with oxygen sites other than the crucial CuO_2 planes. The second types of holes, most probably associated with CuO_2 planes, manifest themselves in the form of secondary O-K pre-edge feature (527.4 eV). The high energy shoulder on the Cu L_3 edge can be interpreted in terms of charge transfer between oxygen and copper in CuO_2 planes, implying oxidation of CuO_2 planes brough about by high pressure oxygenation treatment[6].

REFERENCES
1. V.P. Dravid, H. Zhang, L.D. Marks and J.P. Zhang, Physica(C) to be published, March 1992.
2. H. Zendbergen et al., Nature (1988), Vol. 331, p. 596.
3. L.D. Marks et al., J. Electron Micro. Tech. (1988), Vol. 8, p. 297.
4. V.P. Dravid and H. Zhang, Submitted to Phys. Rev. Lett., Feb. 1992.
5. J.T. Vaughey et al., Chemitsry of Materials (1991), Vol. 3, No. 5, p. 935;
6. This research is supported by the NSF-DMR through the Science and Technology Center for Superconductivity (STcS, NSF-DMR-8809854).
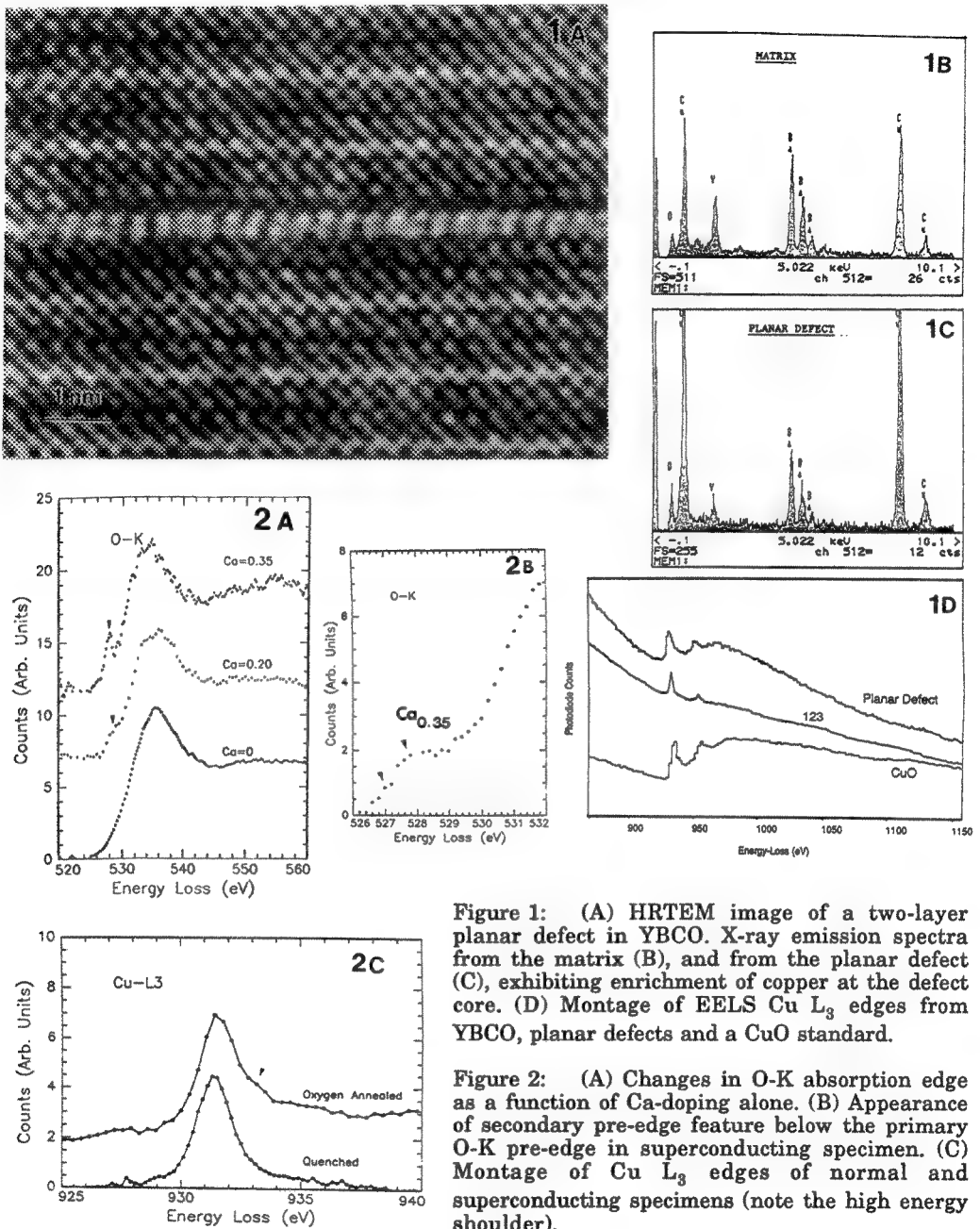
Figure 1: (A) HRTEM image of a two-layer planar defect in YBCO. X-ray emission spectra from the matrix (B), and from the planar defect (C), exhibiting enrichment of copper at the defect core. (D) Montage of EELS Cu L_3 edges from YBCO, planar defects and a CuO standard.

Figure 2: (A) Changes in O-K absorption edge as a function of Ca-doping alone. (B) Appearance of secondary pre-edge feature below the primary O-K pre-edge in superconducting specimen. (C) Montage of Cu L_3 edges of normal and superconducting specimens (note the high energy shoulder).

OBSERVATIONS ON THE GROWTH OF BARIUM BISMUTH OXIDE THIN FILMS

M. G. Norton,[*] E.S. Hellman,[**] E.H. Hartford Jr.,[**] and C.B. Carter [***]

[*] Department of Mechanical and Materials Engineering, Washington State University, Pullman, Washington 99164
[**] AT&T Bell Laboratories, 600 Mountain Avenue, Murray Hill, New Jersey 07974
[***] Department of Chemical Engineering and Materials Science, University of Minnesota, Minneapolis, Minnesota 55455

The bismuthates (for example, $Ba_{1-x}K_xBiO_3$) represent a class of high transition temperature superconductors. The lack of anisotropy and the long coherence length of the bismuthates makes them technologically interesting for superconductor device applications[1]. To obtain (100) oriented $Ba_{1-x}K_xBiO_3$ films on (100) oriented MgO, a two-stage deposition process is utilized. In the first stage the films are nucleated at higher substrate temperatures, without the potassium. This process appears to facilitate the formation of the perovskite (100) orientation on (100) MgO. This nucleation layer is typically between 10 and 50 nm thick[1]. In the second stage, the substrate temperature is reduced and the $Ba_{1-x}K_xBiO_3$ is grown. Continued growth of (100) oriented material is possible at the lower substrate temperature.

The objectives of this study were to examine the early stages of growth of the undoped barium bismuth oxide layer. The films were grown by molecular beam epitaxy—the experimental method has been reported in detail elsewhere[2]. Film growth was studied by transmission electron microscopy (TEM), reflection high-energy electron diffraction (RHEED), and Rutherford backscattering spectroscopy (RBS). Observation of the very thin films by TEM is possible by utilizing a novel specimen preparation technique. The films are deposited onto specially prepared electron-transparent thin-foil substrates[3]. Following deposition these substrates can be transferred directly to the electron microscope without the need for any further specimen preparation. Thereby eliminating artifacts due to specimen preparation which can complicate the interpretation of the micrographs. Previous studies in this materials system[4] showed that the phase that formed during the early stages of growth (film thickness ~ 6 nm) had the composition $BaBi_2O_y$. The RHEED studies indicated that the deposited material did not agglomerate into islands at the start, nor was the growth initially coherent, as in Stranski-Krastanow systems. Instead, islands appear after one or more unit cells of atoms have been deposited in a disordered film.

In this present study, the growth of the undoped barium bismuth oxide layer was studied as a function of time, from 45 seconds up to 10 minutes. RBS results recorded from the films are summarized in Table I. The thinnest films appear to be barium rich. A possible reason for this is that the bismuth may not stick until there is a monolayer of barium—the amount of barium in the thinnest films is almost exactly a monolayer. Figures 1(a) to 1(d) show a series of bright-field electron micrographs which illustrate the stages of film growth for the different times indicated in Table I. Fig. 1(a) shows the extent of film growth after 45 seconds. Regions of the film can be identified by the presence of moiré fringes in the image. In dark-field images, formed using a (110) reflection arising from the film, these areas appear bright, whilst the surrounding areas are dark. By examination of the moiré fringe patterns in all the images shown in figure 1 it is clear that there are regions of small misorientation. The thickness of the islands during the early stages of growth can be determined by measuring the area of the substrate covered by islands which show moiré fringes and by considering the initial layer thickness. For the thickest films (~ 27 nm) the films consist of individual grains of ~ 40 nm in diameter. Selected-area electron diffraction patterns recorded from these films show that the grains are highly oriented with respect to the substrate. This study has demonstrated the importance of using a variety of techniques, which provide complimentary information, in understanding film growth.

References

1. E.S. Hellman, E.H. Hartford, and E.M. Gyorgy, Appl. Phys. Lett. 58, 1335 (1991).
2. E.S. Hellman, E.H. Hartford, and R.M. Fleming, Appl. Phys. Lett. 55, 2120 (1989).
3. M.G. Norton, S.R. Summerfelt, and C.B. Carter, Appl. Phys. Lett. 56, 2246 (1990).
4. M.G. Norton *et al.*, J. Cryst. Growth, 113, 716 (1991).
5. This research was supported, in part, by the Consortium for Superconducting Electronics (MDA 972-90C-0021) and by the National Science Foundation through the use of the facilities of the Materials Science Center at Cornell.

Table I. RBS Data for Barium Bismuth Oxide Films as a Function of Deposition Time.

Deposition Time	Metal Ratio	Thickness
45 secs	Ba 0.427: Bi 0.359	1.1 nm
1.5 mins	Ba 0.427: Bi 0.573	3.2 nm
4 mins	Ba 0.307: Bi 0.639	9.6 nm
10 mins	Ba 0.385: Bi 0.615	27.3 nm
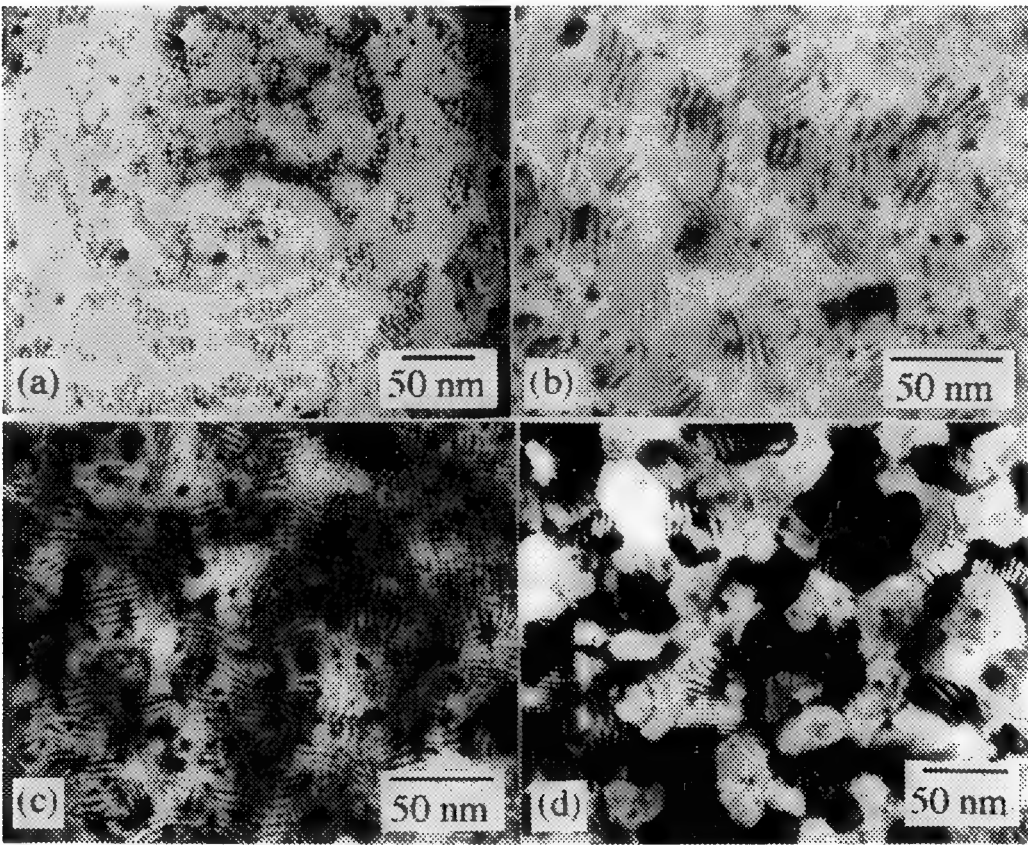
Figure 1. Bright-field electron micrographs recorded from barium bismuth oxide films deposited by molecular beam epitaxy for (a) 45 seconds, (b) 1.5 minutes, (c) 4 minutes, (d) 10 minutes.

MICROSTRUCTURE OF BSCCO-AG COMPOSITES MADE BY FLOATING-ZONE METHOD

Y.Ikuhara, T.Suzuki, Y.H.Ikuhara, K. Michishita, K.Takahashi*
and Y.Kubo

Functional Ceramics Division, Japan Fine Ceramics Center,
Nagoya 456 JAPAN, * Super-GM

To develop applications of oxide superconductors,in addition to
the enhancement of the critical current density (Jc), improving
their mechanical properties is also important. The Bi-oxide
superconductors are intrinsically brittle because of clevage
in the basal plane. We have found that doping by Ag is very
effective in improving the mechanical properties of Bi-oxide
superconductor without decreasing its Jc. In this study,the
microstructure of BSCCO-Ag was observed by transmission electron
microscopy (TEM) in order to clarify the relationship of
microstructure to mechanical properties.

BSCCO-Ag composites were fabricated by floating zone (FZ)
method[1]. The critical temperature(Tc) and Jc were 89K and
$3000A/cm^2$, respectively. The mechanical properties were measured
by three-point bend test and indentation fracture measurements.
A JEOL 4000FX (400kV) was used to analyze the microstructure.

The average bend strength of BSCCO without Ag was 126MPa,
while that of Ag-doped BSCCO was 171Mpa. Moreover the addition
of Ag decreased the data scatter of bend strength,i.e., the
Weibull modulus increased from 3.8 to 9.8. Fracture toughness
also improved by about three times. Thus, Ag doping is certainly
effective in improving the mechanical properties of BSCCO
superconductors.
Fig.1 is a back scattered electron image of the BSCCO-Ag
composite. Three phases are present; $Bi_2Sr_2CaCu_2O_x$ (2212 phase),
$Bi_2Sr_2Cu_1O_x$(2201 phase), and Ag phase. Ag is located both within
the grains and also at grain boundaries, as shown in the figure.
Fig.2 shows the periodically-located Ag particles in the 2212
phase, which suggests the occurrence of an eutectic-like reaction
between Ag and BSCCO. Fig.3 is a magnified photograph of an Ag
particle, in which strain contrast due to coherent particles can
been seen. According to the results of Energy Dispersive
Spectroscopy (EDS), these particles include Cu. This means that
Ag is strengthened by the coherent Cu particles. At the interface
between Ag and BSCCO, a Bi single layer was frequently in contact
with the Ag phase(Fig.4). The clevage in BSCCO is thought to arise
from the weak Bi-Bi bond. Ag is likely to cut this bond to form a
Bi-Ag bond.At the interface,the following orientation relationship
was obtained:(001)Ag//(001)BSCCO, <100>Ag//<100>BSCCO. A micro-
faceted interface was observed when the basal plane of BSCCO was
not parallel to the interface.

1. Y.Kubo et. al., Jap.J.Appl.Phys., (1989) 28, L1936
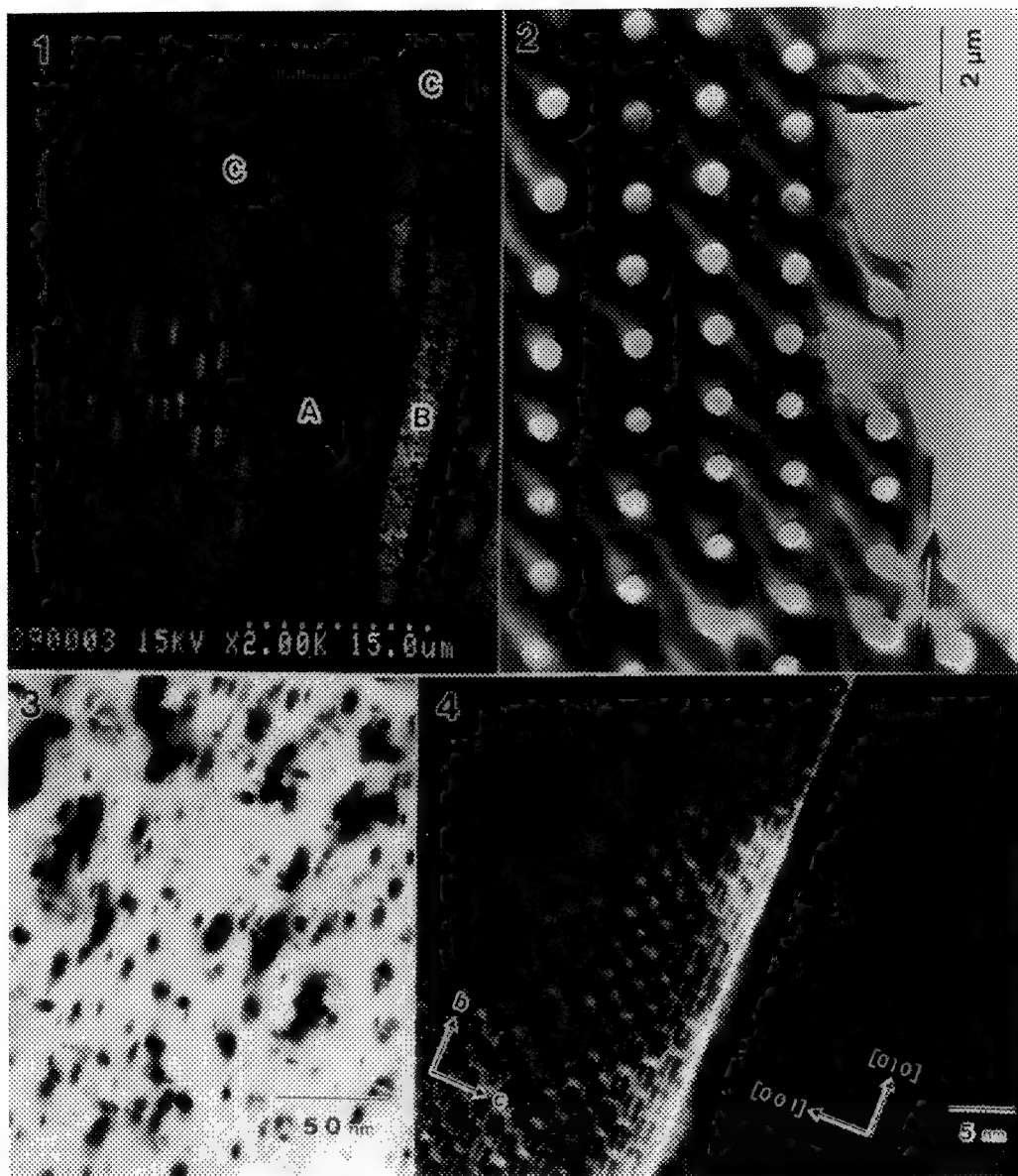
FIG.1. Back-scattered electron image of the BSCCO-Ag composite, which is composed of (A) 2212 phase, (B) 2201 phase and (C) Ag phase.
FIG.2. TEM micrograph of Ag precipitates which are located periodically in the 2212 phase.
FIG.3. TEM micrograph of the coherent Cu-rich particles in the Ag phase.
FIG.4. HREM micrograph of the interface between the 2212 phase and the Ag phase. Note that a single layer of Bi is adjacent to the Ag phase.

ON THE OPTIMUM HOLE CONCENTRATION, NANOSTRUCTURE AND SUPERCONDUCTIVITY IN Bi-CUPRATE CERAMICS

M. A. Subramanian and P. L. Gai

Central Research and Development Department, E.I. Du Pont de Nemours, Wilmington, DE 19880-0356

Many outstanding questions about *optimum* hole concentrations, hole doping mechanisms and complex structural issues in Bi-Sr-Ca-Cu-O high temperature superconductor system[1,2] could be addressed by their study in the undoped system, and by cationic substitution able to modify the anion stoichiometry of the system, in various reducing and oxidizing environments. Such critical studies in different environments are very limited. A number of studies exist in the system, in which the role and concentrations of charge carriers in oxide superconductivity are discussed by correlating T_c with in-plane Cu-O bond lengths, or with substitutional contents. However, most of the work relates to samples treated in air or oxygen where overdoping of holes in the CuO_2 sheet can occur due to excess oxygen. Here we report experimental measurements of hole concentrations and T_c in "$Bi_2Sr_2Ca_{1-x}Y_xCu_2O_{8+d}$" with x= 0 to 1,(abbreviated to 2212 for x= 0) in reducing N_2, Ar and oxidizing environments. We have studied their effects on the structural modulation and composition using electron diffraction and chemical iodometric titration analyses on the same samples.

We prepared the undoped and Y-doped $Bi_2Sr_2Ca_{1-x}Y_xCu_2O_8$ (with x=0 to 1) samples using stoichiometric proportions of Bi_2O_3, CaO, CuO ,SrO (and Y_2O_3) in sealed gold tubes at both 860 °C and 870 °C in air. Two of the samples were then reduced (annealed) in N_2 at 400 °C for 12 hours and two were annealed in oxygen at 400 °C for 12 h. A further sample was prepared *entirely* in nitrogen. Y-doped samples were prepared in a similar way with x varying between 0.2 and 1.0. Superconductivity was checked by magnetic susceptibility and electrical resistivity. Magnetic flux exclusion data for the undoped and Y = 0.2 doped samples annealed in N_2 and O_2 are shown in Figs 1 a and b, respectively, and show the effect of the environments on T_c. Chemical composition (which showed ~16% strontium deficiency),and electron diffraction were recorded simultaneously from the same crystals using a Philips CM 30ST analytical EM. In N_2, (001) electron diffraction showed commensurate modulations with a periodicity of 5 (Fig.2a), and in O_2, incommensurate modulations with a periodicity of ~4.6 (Fig.2b). The (010) atomic structure images showed a decrease in the modulation amplitude in N_2 (Fig.2c) relative to that in O_2 (Fig.2d). The former may contribute to the observed decrease in the c-axis but the exact dependence is unclear at present. These data show that interstitial oxygen merely causes incommensurability and is not the origin of the modulations. For $Y_{0.2}$ -2212, the x-ray diffraction profiles and electron diffraction data (with an incommensurate superstructure of periodicity of 4.45 ± 0.05), were identical in N_2 and O_2 except for intensity variations and peak-broadening. We believe that the substitution of smaller Y cation in 2212 simply alters the modulation periodicity.

We determined hole concentrations by titrimetry[3]. The accuracy was checked by determining n_h values in standard samples and the values agreed within ±0.04. Experimentally determined formal copper valence states (hole concentrations) and T_c in different environments are summarized in Table 1.

Based on the results we suggest that contrary to presupposition optimum hole concentration is obrtained essentially at the ideal anion stoichiometry in *reduced* 2212 containing the cation point defects but is dominated by the atomic substitution in the doped systems and that the structural modulation is intrinsic.

References:
1. H. Maeda *et al,Jpn. J. Appl. Phys.*, (1988) **27**, L209, 2 .
2. P.L. Gai and J.M. Thomas, *Superconductivity Review* (1992) **1**, 1-47. (ed: C.P. Poole), Gordon & Breach Science Publ., London, New York.
3. M.W. Shafer *et al*, *Phys.Rev.B*, (1987), **36**, 4047.

Table 1

Transition temperature T_c (K) in different environments and experimental formal valence states of Cu (Cu^{V+}) by chemical analysis in $Bi_2Sr_{1.67}Ca_{1-x}Y_xCu_2O_{8+\delta}$

x	N₂ or Ar T_c		Cu^{V+}	δ	O₂ T_c	Cu^{V+}	δ	air T_c	Cu^{V+}	Cu-nominal (δ =0,Sr=2)
0.0	90	92	2.35	0	71	2.51	0.18	79	2.48	2.0
0.2	93	92	2.31		90	2.39		88	2.32	1.9
0.4	75	73	2.18		80	2.26		80	2.23	1.8
1.0	No	No	< 2.0		No	< 2.0		No	< 2.0	1.5
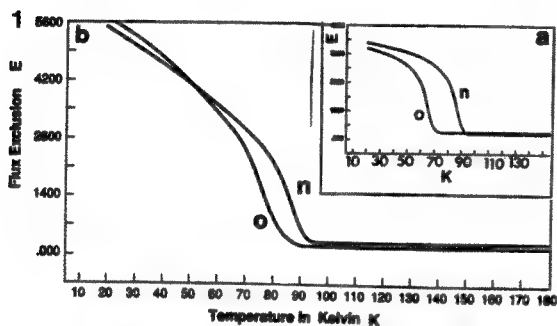
Fig 1. Flux exclusion in N_2 (n) and O_2 (o), for (a) undoped-2212 (b) $Y_{0.2}$- doped 2212.

Fig 2. Electron diffraction and atomic images; undoped-2212 in N_2 and O_2:(a) commensurate modulations in (001)in N_2;(b) incommensurate modulations in O_2;Bragg reflections are indexed with the primary cell :a=5.39,b=5.41,c=30.9Å; (c) (010) atomic image in N_2;(d) (010) atomic image in O_2.Modulation amplitude decreases in N_2 (e.g. shown by the dotted line).
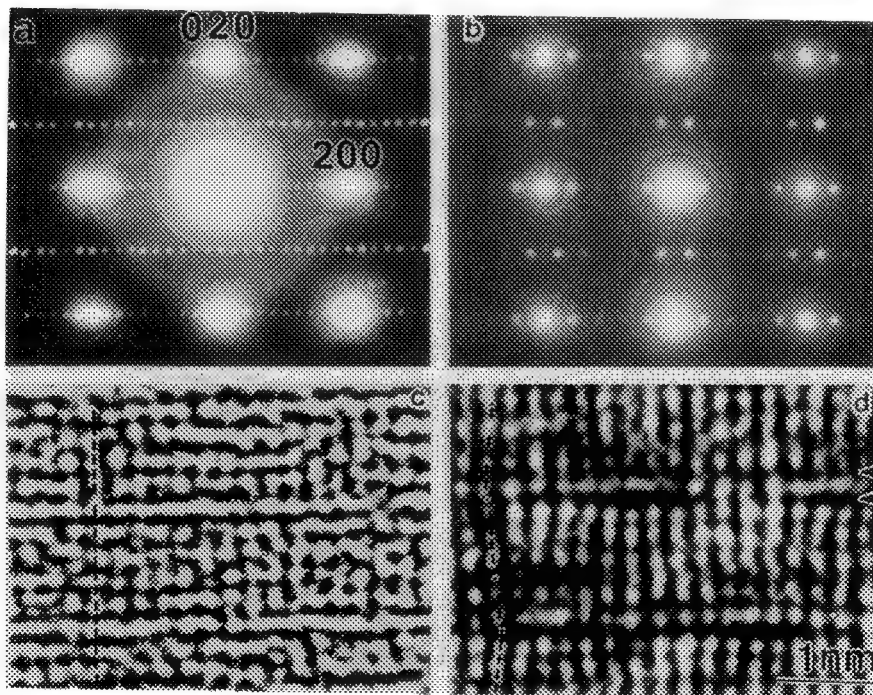
CHEMICAL-SHIFT ANALYSIS OF O Kα BY EPMA COLOR-MAPPING METHOD FOR BiSrCaCuO SUPERCONDUCTIVE SPECIMEN

H. Takahashi*, T. Okumura*, Y. Seo*, A. Kabaya,* C. Nielsen**

*JEOL Ltd.,1-2 Musashino 3-chome, Akishima, Tokyo 196, Japan
**JEOL (U.S.A.) Inc. 11 Dearborn Road, Peabody, Mass. 01960

The chemical shifts of x-ray spectra are now frequently observed with EPMA (Electron Probe Microanalysis). The conventional method of chemical-shift analysis with EPMA is to compare the peak shapes and peak positions of standard spectra with those of unknown spectra. We reported that O-Kα peak shapes detected by using a TAP (Thallium acid phthalate) crystal reflect their crystal structures.[1] Fig. 1 shows these O-Kα spectral peaks. In the present study, concerning the BiSrCaCuO superconductor made by the sintering method, it was observed that the O-Kα spectra of several kinds of phases reflected their crystal structures. Moreover, it is now possible to observe these chemical shifts of spectra by using the color mapping method in EPMA.

The JEOL JXA-8621, a WD/ED combined with EPMA, was used to analyze chemical shifts. The JXA-8621 is capable of using a TAP crystal to analyze chemical shifts of O-Kα $[2\theta=25°$ to $136°$, (O-Kα)=132°]. The TAP crystal has a better resolution than a Pb-STE (Stearate) crystal. In a BiSrCaCuO superconductive specimen, four phases was observed in the backscattered electron image shown in Photo 1. These phases were analyzed quantitatively with EPMA in the electron beam spot mode. The results are shown in Table 1. In each phase, the O-Kα peak was measured by using the TAP crystal. The results are shown in Fig. 2. The two-dimensional distribution of the crystalline phases in the BiSrCaCuO superconductive specimen was obtained by chemical shifts. At first, two color maps were collected at the peak positions A and B shown in Fig. 2. At the position B, each peak shape is significantly different. In each map, the intensities at 250 x 200 points were measured, and at each point, the ratio of x-ray intensity at the position A to that at B was calculated. The result of the ratio mapping, which indicates the chemical-shift distribution, is shown in Fig. 3.

From the results of quantitative analyses, it was found that the dark-gray phase b in Photo 1 corresponded to the 243 phase [$Bi_2(Sr,Ca)_4Cu_3O_x$; Tc=110K], the matrix a to the 232 phase (Tc=80K), the white phase c to the 221 phase (Tc=8~20K), and the black phase d to an incomplete reaction phase. Moreover, it was observed that the O-Kα peak shapes of the three superconductive phases, that is, the 243, 232, and 221 phases matched with the perovskite-type shape in Fig. 1. The O-Kα spectrum of the incomplete reaction phase is similar to that of the CuO in Fig. 1, except the right side of the peak being a little lower than that of the trapezoidal shape of CuO. From the result of the quantitative analyses, it is seen that this incomplete reaction phase includes a small amount of Bi, Sr, and Ca besides pure CuO, one of the initial materials before sintering. From these quantitative and chemical-shift analyses, it is assumed that this incomplete reaction phase is an intermediate phase between the initial CuO material and the last perovskite-type superconductor. Meanwhile, the ratio of the x-ray intensity at the position A to that at B of perovskite-type structures are close to 1.9, that of the incomplete reaction phase to 1.5, and that of the CuO phase to 1.0. Corresponding to these phases, therefore, the color levels of white, gray, and black were set. Fig. 3 shows the result. From this, small particles of the CuO phase was found to remain in the incomplete reaction phase of this specimen. Thus, from the ratio map obtained by EPMA color-mapping method, a two-dimensional distribution of chemical shifts reflecting the crystal structures could be obtained.

In addition to the above results, an atomic ratio map could be obtained by dividing a Bi map divided by a Ca map as shown in Fig. 4. The 243 (near 2223), 232 (near 2212), 221 (near 2201) and incomplete reaction phases have ratios close to "1", close to "2", "a large number", and close to "0". These phases correspond to the dark-gray, light-gray, white and black portions, respectively.)

1) H. Takahashi, Y. Kondo, T. Okumura, Y. Seo :JEOL NEWS, Vol. 27E, No.2, 2-7(1989)
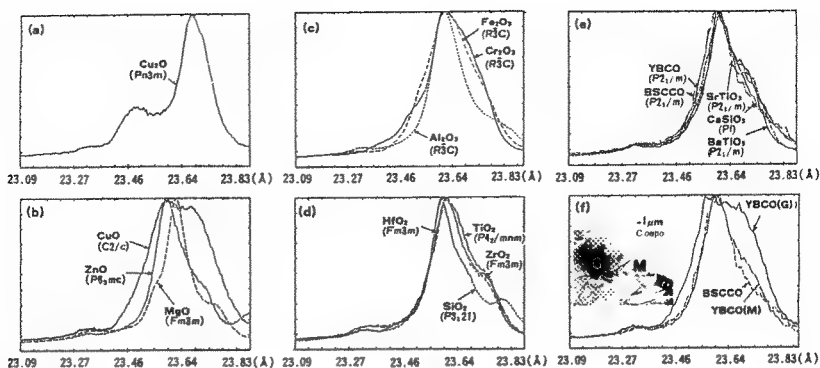
Fig. 1
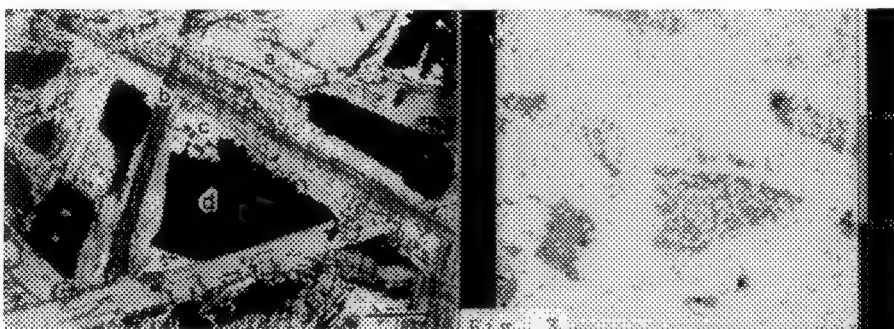
Table 1

	a-phase (232)	b-phase (243)	c-phase (221)	d-phase
Bi	2	2	2	0.04
Sr	1.62	1.76	0.85	0.47
Ca	1.01	1.59	0.67	0.67
Cu	2.07	2.72	1.10	2
O	7.36	9.04	5.09	3.36
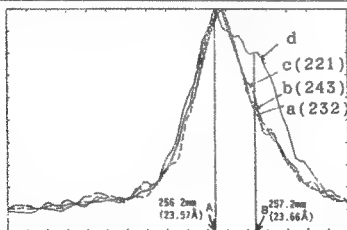
Fig. 2

Fig. 1. O-Kα spectra of (a) A_2O type, (b) AO type, (c) A_2O_3 type, (d) AO_2 type, (e) ABO_3 type, and (f) superconductive specimen. In (f), "G" is a gray non-superconductive phase, and "M" is a light gray superconductive matrix phase. A and B : cation.
Photo 1. Composition image of BiSrCaCuO superconductor. Bar = 10μm
Table 1. Quantitative analysis of BiSrCaCuO specimen.
Fig. 2. O-Kα spectra of four phases in BiSrCaCuO specimen.
Fig. 3. Chemical-shift distribution of O-Kα obtained from the ratio map made by dividing the A map by the B map.
Fig. 4. Atomic ratio map made by dividing the Bi map by the Ca

83
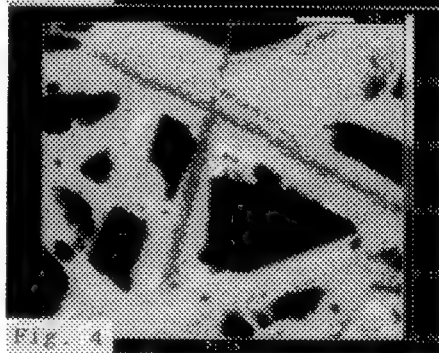
STRUCTURAL EFFECT OF THE SC-AF TRANSITION IN BSCYCO SYSTEM

Shulin WEN, Chenyu SONG and J.A.Eades*

Shanghai Institute of Ceramics, Chinese Academy of Sciences, 1295 Dingxi Rd. Shanghai 200050, CHINA
* Materials Research Lab, University of Illinois at Urbana, 104 S. Goodwin Ave. Illinois 61801

The transition between the SC (superconductor) and the AF (antiferromagnetic semiconductor) has been investigated in the BSCYCO ($Bi_2Sr_2Ca_{1-x}Y_xCu_2O_{8+y}$) system. During the investigation a tetragonal(T)-orthorhombic(O) structural transformation accompanied by a sharp drop in Tc around at Xc=0.4 has been observed.

Some of previous studies on BSCYCO [1,2] revealed the transition from the SC to the AF around at x=0.5, and interpreted it as a result of a decreasing hole concentration [2-4]. We have also studied the SC-AF transition of BSCYCO with analytical data combination from not only Tc measurements, but also X-ray diffraction, electron diffraction and energy dispersive spectroscopy (EDS) results. We found that a structural transformation from the tetragonal(T) to the orthorhombic(O) system would be mainly responsible for the SC-AF transition.

The samples of $Bi_2Sr_2Ca_{1-x}Y_xCu_2O_{8+y}$ for x=0, x=0.1, x=0.2, x=0.3, x=0.4, x=0.5, x=0.65, x=0.85 and x=1.0 were prepared by solid state reaction from the mixed powders of Bi_2O_3, $SrCO_3$, $CaCO_3$, Y_2O_3 and CuO with above ratio. The mixed powders were heated at 800°C for 24 h in air, then thoroughly reground and pressed into pellets and finally refired in air at 840-860°C for 48 h.

The results of X-ray diffraction indicated basically a single phase for our BSCYCO samples with the lattice parameters shown in the Fig.1. It can be seen from the fig. that with substitution of Ca^{2+} for Y^{3+}, the c-axis decreases while both the a-axis and b-axis increase. A T-O structural transition, accompanied by an obvious drop of the c-axis, occurred around x=0.4. In the Bi-2212 ($Bi_2Sr_2CaCu_2O_8$) structure, the coordination number of the Ca-site is eight. So the coordination may be stabilized only when the ionic radii of the atoms in Ca-sites satisfy the following relationship:

$$\frac{r_{Ca}}{r_O} = \frac{1.12(A)}{1.40(A)} < 0.732 \quad , \quad \frac{r_Y}{r_O} = \frac{1.01(A)}{1.40(A)} > 0.732$$

Here r_{Ca}, r_Y and r_O represent the radii of Ca^{2+}, Y^{3+}, and O^{2-} respectively. A drop of c-axis indicates a shorter distance of CuO_2-Ca(Y)-CuO_2 sandwich sheets with Ca^{2+} substituted by the smaller Y^{3+}. However, when such a substitution reaches a certain extent (at Xc=0.4), the CuO_2 sheets expand along the a-axis and b-axis (especially along the b-direction) and give a stable structure with minimum volume of unit-cell at that transition point.

The structure modulation is one of most important microstructural features in BSCYCO system. The results from above methods showed that the modulation length drops from 4.79 to 4.0 gradually with the substitution of Y^{3+} for Ca^{2+}, as shown in Fig.2. The lattice constants and modulation lengths of different grains in a same sample (x=0.4) are listed in Table 1.

Table 1 Structural parameters in different grains of the sample at x=0.4.

No. of grains	a(A)*	b(A)*	ML(b)*	Y/(Ca+Y)**	Symmetry
1	5.42	5.42	4.69	0.18	tetra.
2	5.43	5.43	4.46	0.45	tetra.
3	5.42	5.46	4.33	0.64	orth.

* The data were calculated from electron diffraction results.
** The data were calculated from EDS results.

As for the structural effect on Tc, with the substitution of Y^{3+} for Ca^{2+}, two effects can be estimated: (1) The hole concentration would be changed because of the different valence of ca^{2+} and Y^{3+}.(2) the atomic structure would be changed because of the different ionic radii of Ca^{2+} and Y^{3+}. The hole concentration of BSCYCO decreases smoothly with increasing Y-content, and no obvious variation was observed around Xc=0.4 [2]. Therefore, the hole concentration theory can not interpret the abrupt drop of Tc although it may play an important role for the Tc enhancement at x < 0.2. On the other hand, it is noteworthy that the transition point of Tc matches very well with the transition point of structure at Xc=0.4 as shown in the Fig.1. So we conclude that the SC-AF transition of BSCYCO is not controlled by hole concentration, and is indeed very sensitive to a T-O structure transformation.

Although with the substitution of Y^{3+} for Ca^{2+} in BSCYCO, both hole concentration and atomic structure influence critical temperature Tc, the T-O structure transition has a dominant effect on Tc, which caused an abrupt transition from superconductor to nonsuperconductor.The superconductivity in BSCYCO is strongly structure sensitive, only the tetragonal structure of BSCYCO makes it highly superconducting. However,the structure modulation in the BSCYCO is not structure sensitive, as the modulation length decreased gradually from 4.79 to 4.00 with the content of substitution, x , from 0.0 to 1.0

References

1. N. Fukushima, H. Niu and K. Ando, Jpn J. Appl. Phys. 27 (1988) L1432.
2. T. Tamegai, K. Koga, K. Suzuki et al., Jpn. J. Phys. 28 (1989) L112.
3. W. A. Groen, D. M. de leeuw and L. F. Feiner, Physica C 165 (1990) 55.
4. W. A. Groen, D. M. de leeuw and G. P. J. Geelen, Physica C 165 (1990) 305.
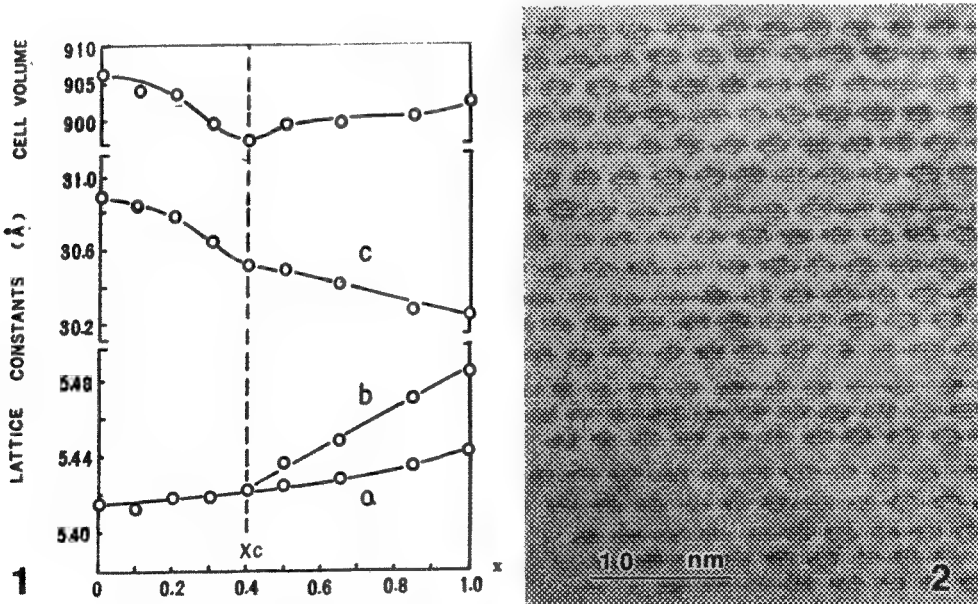
FIG.1-- Substitutional dependence of lattice parameters in $Bi_2Sr_2Ca_{1-x}Y_xCu_2O_8$, showing the relationship between the parameters (a, b, c, and the unit-cell volume) and the x (substitutional content).
FIG.2--Lattice image of BSCYCO, showing structure modulation.

STEM BSE Imaging and Monte Carlo Simulation of α–β Microstructures in NbTi Superconductors

T. J. Headley,* J. R. Michael,* F. A. Greulich,* M. J. Carr,* and J. M. Seuntjens**

*Materials and Process Sciences, Sandia National Laboratories, Albuquerque, NM 87185
**Magnet Division, Superconducting Super Collider Laboratory, Dallas, TX 75237

High current density NbTi multifilamentary superconductors have α–β microstructures tailored by thermo-mechanical processing involving interspersed cold drawing and heat treatment.[1,2] A final heat treatment in the two-phase α–β field controls the volume fraction of α-Ti precipitates and subsequent cold drawing refines the scale of the microstructure to a level that optimizes flux pinning properties which affect critical current density (J_c). The volume fraction, particle size, shape and spacing of α-Ti precipitates present after the final heat treatment are important parameters of interest, and should be measurable by image analysis techniques if suitable images were available.

Fig. 1 is a BF TEM image of the α–β microstructure in transverse section of a NbTi filament after final heat treatment. The lower density α-Ti precipitates generally appear light against the denser β-matrix, but deliniation of the entire set of α-Ti precipitates for image analysis is greatly complicated by diffraction contrast effects in both α and β phases. In addition, the α and β diffraction rings are too closely spaced to·image the phases separately by DF techniques.[3] Such difficulties have motivated a search for other imaging techniques that would delineate the α–β structure sufficiently for image analysis.[4]

The submicrometer-sized α-Ti precipitates are too small to be adequately resolved by backscattered electron (BSE) imaging in an SEM. We have found that STEM BSE imaging of thin foils of NbTi in the final heat treatment condition provides ample resolution and contrast between α and β phases for subsequent image analysis with high accuracy. Fig. 2 is a 300 kV BSE image of the region in Fig. 1 obtained in a Philips CM30 STEM equipped with an annular BSE detector. The α-Ti precipitates appear in dark contrast to the β-matrix. The digitized image was captured on an Oxford Instruments, Link Analytical eXL analyzer and is reproduced here prior to image processing. Image processing and analysis were performed on a MacIntosh IIfx Computer using Adobe Photoshop and Automatix Image Analyst software. The variation in background gray level across the image in Fig. 2 arises from varying BSE yield due to changing foil thickness, and is removed by a Gaussian blur technique. Subsequent processing routines then provide a high quality binary image for image analysis, as shown in Fig. 3. From such images, the volume fraction of α-phase in this microstructure was measured at 22% in good agreement with data on laboratory NbTi monofilament with similar final drawing strain and J_c.[5]

Monte Carlo simulations via massively parallel computing[6] of the BSE process in thin NbTi have confirmed the α–β contrast observed experimentally, and elucidated the effects of foil thickness and beam energy on image contrast. For example, a simulation of 10^7 electron trajectories at 300 kV in a foil 100 nm thick gave BS coefficients (yield) of 6.07×10^{-5} and 1.10×10^{-4} for the α and β phases, respectively. This contrast difference of approximately 40% is in good agreement with contrast observed experimentally in thin foils at 300 kV. Fig. 4 shows the calculated BS coefficients of the α and β phases in foils ranging from 25 to 200 nm thick at both 100 and 300 kV. The BS coefficients increase linearly with foil thickness, with 100 kV producing more BSE than 300 kV. The difference in absolute BS coefficients for α and β phases increases with increasing foil thickness and is larger at 100 kV than at 300 kV. However, contrast is the relative difference in coefficients and this is found to remain approximately constant at about 40% over the range of foil thickness and beam energy investigated. Selecting an appropriate foil thickness for imaging then becomes a tradeoff between poor signal-to-noise ratio in thinner regions and decreasing resolution in thicker regions.[7]

1. A.W. West and D.C. Larbalestier, Met. Trans. A (1984)15A, 843.
2. A.W. West, Proc. Ann. EMSA Meeting 43(1985)190.
3. P.J. Lee and D.C. Larbalestier, Proc. Ann. EMSA Meeting 43(1985)186.
4. P.J. Lee, Proc. Ann. EMSA Meeting 45(1987)358.
5. P.J. Lee, SSC Laboratory/Industry Technical Transfer Meeting, June 17, 1991.
6. A.D. Romig, Jr. et al., MAS-1990, 275.
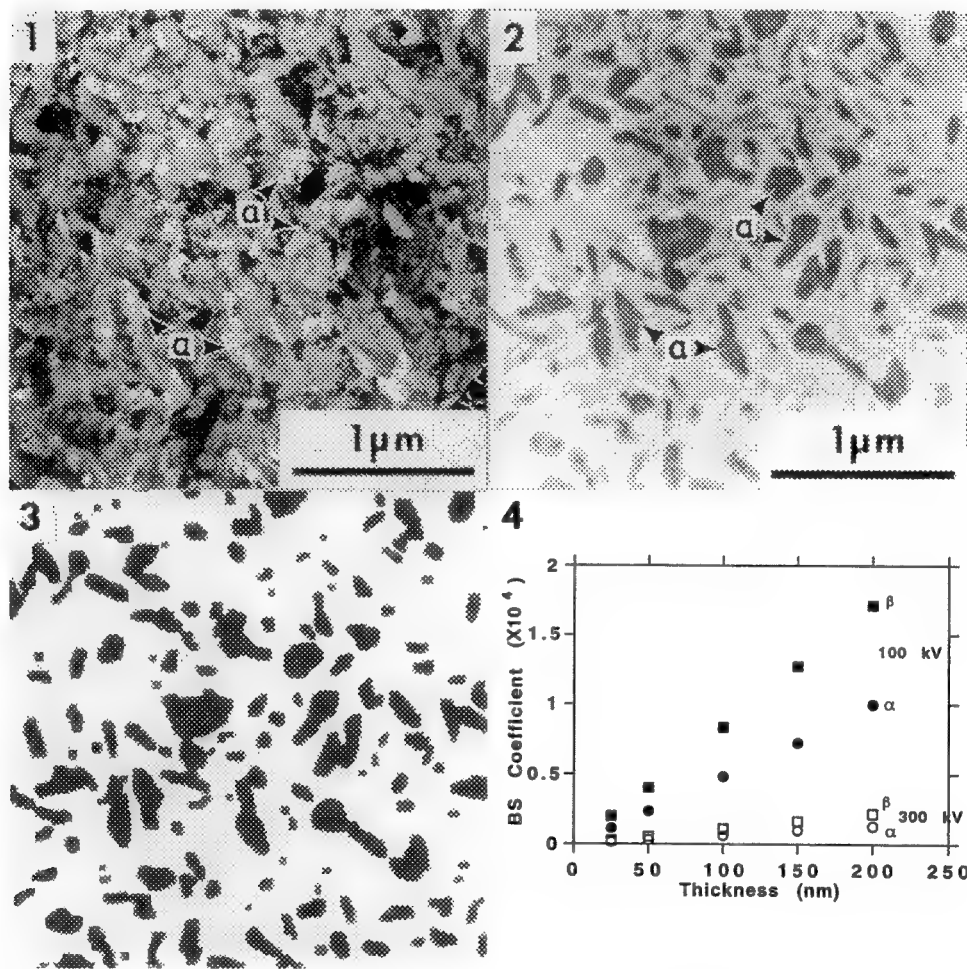
FIG. 1.--BF TEM image of α–β microstructure in Nb 47wt.% Ti filament.
FIG. 2.--Digitized STEM BSE image of the same region obtained at 300 kV.
FIG. 3.--Processed binary image.
FIG. 4.--Monte Carlo calculations of effects of foil thickness and beam energy on BS coefficient (yield) for α and β phases in Nb 47wt.% Ti.

LOW–TEMPERATURE ANNEALING OF $YBa_2Cu_3O_{7-x}$

R.L. Sabatini, Yimei Zhu, Masaki Suenaga, and A.R. Moodenbaugh

Materials Science Division, Brookhaven National Laboratory, Upton, N.Y. 11973

Low temperature annealing ($< 400°C$) of $YBa_2Cu_3O_{7-x}$ in a ozone containing oxygen atmosphere is sometimes carried out to oxygenate oxygen deficient thin films. Also, this technique can be used to fully oxygenate thinned TEM specimens when oxygen depletion in thin regions is suspected. However, the effects on the microstructure nor the extent of oxygenation of specimens has not been documented for specimens exposed to an ozone atmosphere. A particular concern is the fact that the ozone gas is so reactive and the oxygen diffusion rate at these temperatures is so slow that it may damage the specimen by an over-reaction. Thus we report here the results of an investigation on the microstructural effects of exposing a thinned $YBa_2Cu_3O_{7-x}$ specimen in an ozone atmosphere using transmission electron microscopy and energy loss spectroscopy techniques.

Samples of bulk $YBa_2Cu_3O_{7-x}$ which were quenched from $675°C$ into liquid nitrogen and were determined to have a nominal oxygen content of $O_{6.6}$ were used as the starting material for the experiment. The ozone annealing consists of placing a thinned TEM specimen in a porcelain boat. The boat is then placed inside a tube furnace which is connected to an ozone generator. Several as prepared and ozone annealed samples were analyzed using a Gatan PEELS system to monitor the oxygen pre-peak at approximately 528 eV. This feature is a signature for the content and ordering of the oxygen in the high T_c $YBa_2Cu_3O_{7-x}$ material. Temperatures of 100, 200, and 300°C were investigated.

Fig. 1 shows spectra comparing a quenched (A) (oxygen deficient sample), fully oxidized sample (B) after ion milling, and an ozone treated sample (C) after being heat treated at 200°C for 2.5 hr. The pre-peak in the ozone treated sample is sharp (indicating that O_2 was absorbed at this low temperature), compared to the other two samples. This sharp peak is similar to what one finds in a crushed powder sample of a fully oxygenated $YBa_2Cu_3O_{7-x}$ sample.

The effect of the ozone treatment on the microstructure shows one must take care in the heat treatment using ozone of the $YBa_2Cu_3O_{7-x}$ sample or damage will occur. Fig. 2 shows the effect of O_2 uptake in a sample annealed an ozone atmosphere at 200°C for 2.5 hr. as evidenced by the growth of fine twins perpendicular to the original twinning direction, indicating that O_2 was absorbed at this low temperature. Fig. 3 shows the effect of too much exposure to ozone, as evidenced by the formation of many defects in the regions undergoing O_2 uptake. These defects remain even after further annealing in O_2. Fig. 4 shows a sample which was annealed originally at 200°C for 2.5 hr. and then analyzed in the TEM for two days and subsequently heat treated in ozone at 300°C for 2.5 hr., it has undergone a transition or decomposition to a more stable oxide form due to an over-exposure to ozone. The optimum temperature and duration for our specimens is 200°C for 2.5 hr.
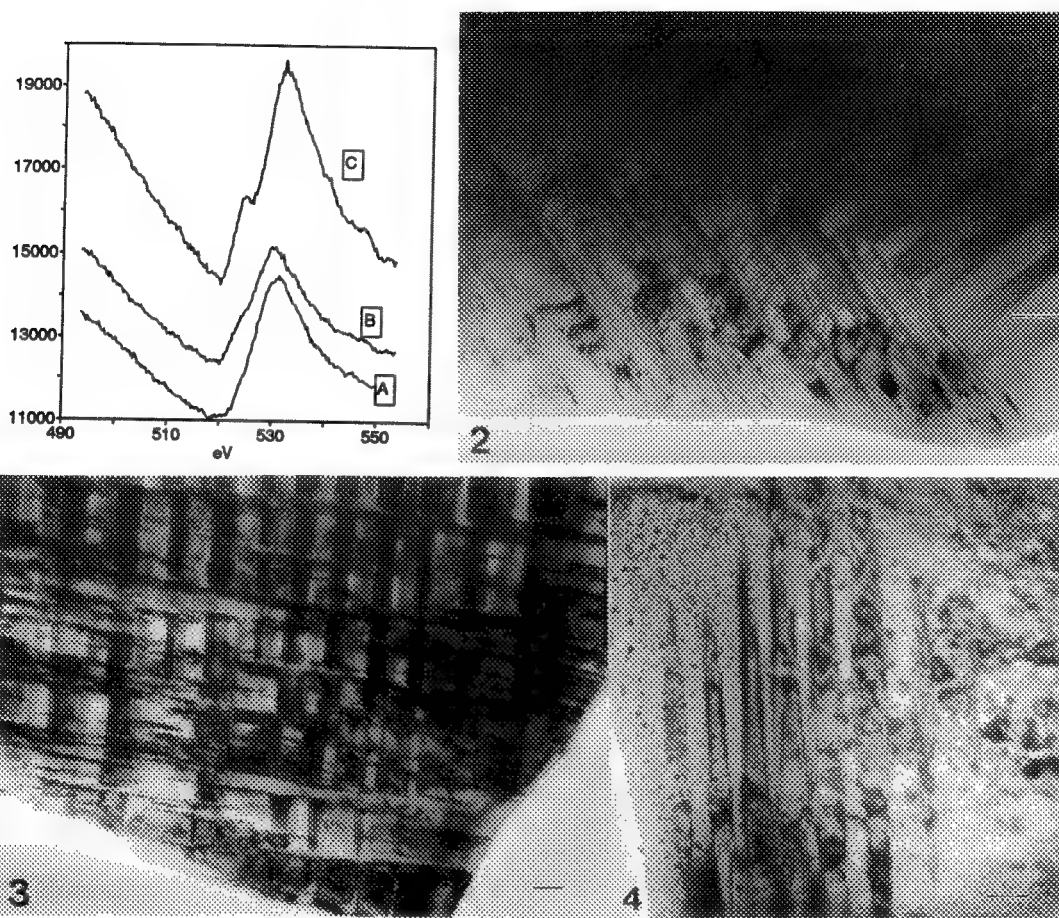
FIG. 1. Shows EELS spectra of the oxygen k-edge comparing (A) quenched (oxygen deficient) sample, (B) fully oxidized sample after ion-milling, and (C) an ozone treated sample after 200°C for 2.5 hr.. The pre-peak of the ozone treated sample is sharp compared to the other two samples indicating O_2 uptake .

FIG. 2. Shows the effect of O_2 uptake in a sample annealed in ozone at 200°C for 2.5 hr. as evidenced by the presence of fine twins perpendicular to the original twinning direction. Bar = 100nm.

FIG. 3. Shows the effect of too much exposure to ozone as evidenced by the formation of many planar defects in the region undergoing O_2 uptake. Bar = 200nm.

FIG. 4. Shows a sample which was ozone annealed originally at 200°C for 2.5 hr. and then analyzed in a TEM for two days and subsequently heat treated with ozone at 300°C for 2.5 hr., it has undergone a transition or decomposition to a more stable oxide form due to an over-exposure to ozone. Bar = 200nm.

SIMULATION AND INTERPRETATIONOF IMAGE CONTRAST AND DIFFUSE SCATTERING OF TWEED STRUCTURE

Yimei Zhu, Z.X. Cai, M.Suenaga and D.O.Welch

Materials Science Division, Brookhaven National Laboratory, Upton NY 11973

The so-called tweed structure exhibits a roughly periodic lenticular-domain image (Fig.1) associated with the streaking of diffuse scattering around the fundamental reflections in an electron diffraction pattern (Fig.2(c)). Tweed was observed in high T_c oxides $YBa_2(Cu_{1-x}M_x)_3O_{7-\delta}$ (M=Fe, Co, Al, x≥0.03; M=Cu, δ~0.6-0.8), as well as in some binary alloys, which usually show statistical fluctuation in their composition or in an order parameter.

Although tweed has long been studied, crystallographic aspects of tweed modulation is not well understood. To shed light on the details of the structure, we performed simulations both on the tweed image and diffuse scattering, based on our TEM observations of $YBa_2(Cu_{1-x}M_x)_3O_{7-\delta}$.

Fig.2 compares the calculated and observed electron diffuse scattering patterns. TEM observations show that diffuse scattering from a particular Bragg spot exhibit characteristic extinctions. In the zone axis diffraction pattern, this effect is not apparent because of double diffraction.[1] Around (h00) (Fig.2(g)), the diffuse patterns are streaked along two equivalent (110) directions, while for (hh0) (Fig.2(h)), one set of the (110) streaks (the radial streaks) vanishes. Around (hk0) (Fig.2(i)), h≠k≠0, the intensity and the length of the streaks depend on their distance from the origin. These features suggest that the diffuse scattering arises from <110>/{-110} shear displacement in the crystal. Based on an approach involving the lattice displacement wave / oxygen concentration wave, we performed Monte Carlo simulations of an anisotropic lattice gas model, which represents well the interactions between oxygen-oxygen and oxygen-impurity atoms. Fig.2(a)-(c) shows the calculated results considering only lattice distortion (Huang scattering). The results reproduced the major features of the diffuse patterns, but was unsatisfactory in representing the symmetry of the Bragg spot. Because the diffuse scattering was observed at room temperature, then thermal diffuse scattering is not negligible. Fig.2(d)-(f) shows the calculated total intensity of the diffuse scattering due to both Huang scattering and thermal diffuse scattering. The intensity profiles of (040), (240) and (220) agree very well with the experimental data.

The simulation of tweed contrast was accomplished by a kinematical calculation, which give the same result as a two-beam dynamical calculation when the deviation from the Bragg position, s, is sufficiently large. We envision domains with shear displacive modulation stacked on top of each other in a TEM sample, because the broadening of the reflection in electron diffraction suggests that the coherence length of these domains is 10-30 nm along the c-axis. This approach is similar to the calculation of the stacking fault. However, for the stacking fault, the displacement **R** is a constant, while for the tweed, **R** varies with the position. Fig.3 is the calculated intensity profiles of two-beam dark-field images from a domain interface (with sinusoidal displacement **R**) running from the top to the bottom of the specimen. Our simulated tweed image shows that the intensity of tweed contrast decreases with the wave length of modulation. The width of the tweed contrast depends on the wave period, but is independent of s. The length of the tweed contrast is limited by the depth oscillation (determined by the effective extinction distance ξ_g) or the domain size in a-b plane (when ξ_g is large). All these results are consistent with our TEM observations.[2]

Reference

1. Y. Zhu, M.Suenaga and J.Tafto, Philo. Mag. Lett., **64** (1991) 29.
2. This research was supported by U.S. Department of Energy, Division of Materials Science, Office of Basic Energy Science under Contrast No.DE-AC02-76CH00016.
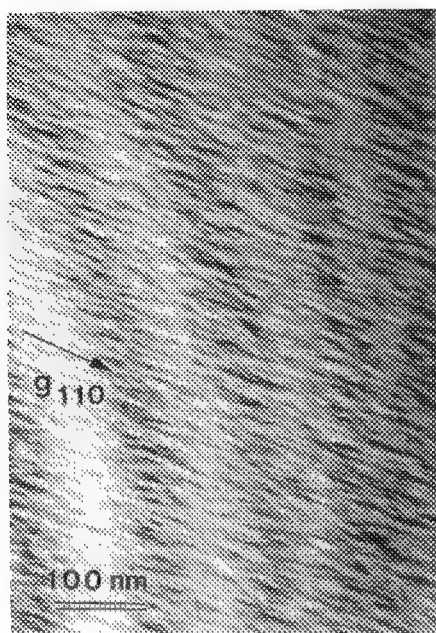
Fig.1 (above)
Tweed contrast under two-beam condition (**g**=200).
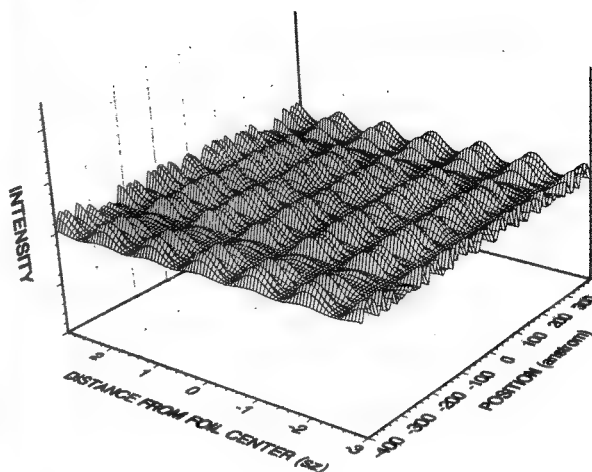
Fig.3 Simulated two-beam image from an interface of tweed domains with a displacive modulation.
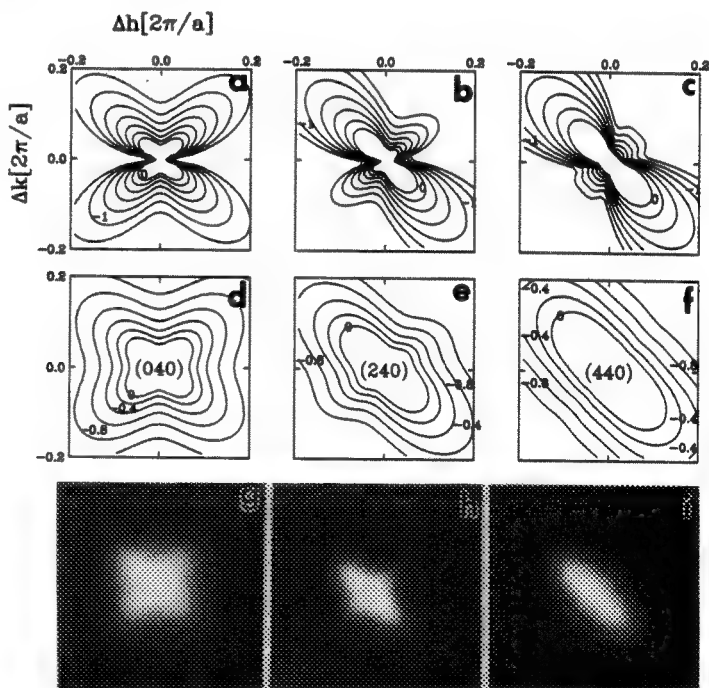
Fig.2 (right)
Intensity of diffuse scattering around (040), (240) and (440) Bragg spots. (a)-(c): due to the Huang scattering
(lattice displacement); (d)-(f): the combined Huangscattering and thermal diffuse scattering; (g)-(i): the TEM observations.

91

CURRENT AND FUTURE PROSPECTS IN INSTRUMENTATION OF HIGH-RESOLUTION ELECTRON MICROSCOPY

K.-H. Herrmann

Institute of Applied Physics, University of Tuebingen, Auf der Morgenstelle 12, D-7400 Tuebingen, FRG

In material research the goal of the electron optical system is the optimum recovery of the object information carried by the beam aiming at the retrieval of both structural and chemical information down to atomic dimensions. Instrumentation has reached a high level of maturity in approaching physical limits set by both electron wavelength and aberrations of axially symmetrical lenses in CTEM and STEM. Present trends are seen in further perfections of the optical components to attain an interpretable transfer limit above 10 nm^{-1}, in increasing the spatial resolution and overcoming the present limits of detection in microanalysis, in the uncompromising combination of several techniques in one instrument (e.g. HREM, CBED, STEM and EELS), in the progressing use of computers for EM control, conversion and storage of data, in on-line processing for immediate interpretation of images and feed-back to the EM as well as in some rather "non-conventional" ways for restoring the object wave function under elimination of aberrations, for which holography may be a particularly promising example.

The gun/condenser system shall be optimized for intense illumination with highest spatial and temporal coherence approaching the plane monochromatic wave to extend the contrast transfer limit and, alternatively, to be adjustable to small beam probe operation for analytical and CBED purposes. While formerly the tungsten filament was replaced by the LaB$_6$ cathode, the increased brightness and life time of which was purchased with an increased vacuum requirement of 10^{-8} mbar, recently the field emission gun, offering almost infinite life time but requiring UHV, has been developed to high stability and reliability. Profiting from their still higher brightness and small source diameter requires very careful condenser design, indeed, but by using a single field condenser objective both mentioned modes of operation should be optimally realizable in one instrument, allowing highly resolving CTEM, STEM and CBED on the same specimen area. Future improvements may be a gun monochromator[1], a gun microlens with STM tip adjustment[2], possibly using a monoatomic tip[3] for still more increased coherence. Presently, the simultaneous attainment of both high lateral and longitudinal coherence is a problem still waiting for a perfect solution.

Due to careful numerical analysis and improved materials, the imaging system has again made progress with respect to the aberration coefficents, adjustment stability and versatility. Although, however, the correction of third order spherical and first order chromatic aberrations has proven to be feasible in principle[4], the application in a well-designed instrument performing the pretentious engineering prerequisites for sub-Å resolution is still to be expected. Perhaps the inconvenient limitation of object space in low aberration medium energy instruments, occasionally an argument for MeV microscopes, may be overcome by a corrector. A stimulating new development of an old idea is the imaging energy filter with medium energy capability using purely magnetic sector fields and sextupole elements for the correction of second order aberrations[5]. Using an energy selecting slit the energy loss window contributing to the image can arbitrarily be chosen independently of the respective mode of operation. Thus, not only analytical maps or elastically filtered HREM images and diffraction patterns can be displayed, but also EELS spectra of selected areas or reflection angles can be recorded in parallel. Another way[6] of solving the same problem consists in adding an optical system to the exit of the sector field spectrometer underneath the column in combination with the parallel EELS capability. The advantage of this "add-on" solution, however, may potentially lead to smaller pixel numbers and more difficult optical adjustment, besides the spatial interference with the subsequently described devices.

Electronic image read-out using advanced slow-scan CCD sensors is replacing the photoplate not only with respect to speed but even to the storable information due to their extremely high dynamic range ($> 10^4$), pixel numbers above 1k $\times$ 1k and an almost ideal DQE of optimized systems[7]. Due to both negligible distortion and strictly quantitative output a high level numerical on-line processing is feasible with the appropriate computer equipment. Immediate feed-back to the computer-controlled EM for all adjustment requirements becomes applicable using both real or reciprocal space procedures being developed[8].

A peculiar question is the optimum choice of electron energy with respect to the transfer limit, radiation damage and economic effort. Atomically resolving MeV instruments approaching the Scherzer transfer limit of 10 nm^{-1} are available. Due to the growing displacement damage, however, their use may be partially limited, particularly in semiconductor research. Thus some rather unconventional but very promising attempts to overcome the transfer limitations with medium energy microscopes are of actual interest.

Electron holography is the only method to record simultaneously phase and amplitude of the image wave by superposing a coherent reference wave using a Möllenstedt biprism[9]. Recently, the off-axis image plane holography has attained atomic resolution[10]. Using advanced numerical image processing a number of benefits was demonstrated: the complex object wave can be reconstructed eliminating the (non-chromatic) aberrations (even adjustment imperfections if some a-priori information on the specimen is available), thus surpassing the Scherzer limit and avoiding the gaps of the transfer function (including that at zero spatial frequency); inelastic background does not influence the fringe contrast. This almost ideal response is made available even on-line by advanced read-out and processing technology[11]. However, the chromatic aberration due to the energy spread of the primary beam cannot be eliminated. Thus, for extension of the ultimate transfer limit at lower energies either a gun monochromator or chromatic correction may be required and feasible.

In conclusion, a future rather visionary HR instrument for material research may have the following features: 200-300 keV electron energy, FE gun (optionally monochromatized) with condensor system allowing both coherent wave and small scanning spot illumination (STEM), large gap objective with C_s and C_c corrector, biprism (optionally), integrated energy filter for image, diffraction pattern and spectrum display, multi-purpose CCD converter for slow- and fast scan mode with flexible control for read-out of images, diffraction patterns and parallel EELS as well as configurable STEM detector[12], subsequent computerized processing and long-term mass storage equipment. Although some features of this conception are presently unsolved, it may be feasible in future and may allow remarkable advances in the reseach of microstructures in atomic dimensions.

References:

1. E.Plies und W.Hoppe, Optik 46 (1976) 75–92
2. T.H.P.Chang et al., J.Vac.Sci.Technol. B 7 (1989) 1855–1861
3. H.-W.Fink, Phys.Scr.38 (1989) 260
4. H.Rose, Optik 85 (1990) 19–24
5. S.Lanio, H.Rose and D.Krahl, Optik 73 (1986) 56
6. O.L. Krivanek et al., Microsc.Microanal.Microstruct. 2 (1991)
7. I.Daberkow, K.-H.Herrmann, Liu Libin and W.D.Rau, Ultramicr.38 (1991),215–223
8. A.J.Koster and A.F.de Jong, Ultramicr.38 (1991) 235–240
9. G.Möllenstedt and H.Düker, Z.f.Physik 145 (1956) 377
10. H.Lichte, Adv.Opt.El.Micr 12 (1991),25–91
11. W.D.Rau et al., J.Comp.Ass.Micr. 3 (1991), 51–63
12. I.Daberkow and K.-H.Herrmann, Proc.EUREM 88, 125–126

MIRROR–HEXAPOLE CORRECTOR WITH COMPACT BEAM SPLITTER FOR ELIMINATING THE CHROMATIC AND SPHERICAL ABERRATION OF LOW–VOLTAGE ELECTRON MICROSOPES

H. Rose

Institute of Applied Physics, Technische Hochschule Darmstadt, D-6100 Darmstadt,
Germany

To significantly improve the performance of electron microscopes it is necessary to enlarge the usable aperture. At low voltages this requirement can only be met if the chromatic and the spherical aberration are corrected simultaneously. For imaging surfaces with reflected electrons (LEEM) a magnetic deflection system separating the illuminating beam from the image–forming beam must be incorporated in the region above the objective lens[1]. Since the use of an electrostatic mirror for the correction of the chromatic aberration also necessitates such a system[2], it would be extremely helpful if the beam splitter can be designed in such a way that it also separates the parts of the image–forming beam heading toward and away from the mirror.

An optimum separator should (a) consist of very few elements, (b) be free of first–order astigmatism and distortion and (c) not introduce any resolution–limiting second–order aberrations at the final image. A compact separator which fulfills all these requirements is shown in Fig. 1. The field of this beam splitter consists of an inner homogeneous region of quadratic shape surrounded by an outer field whose strength B_2 is about three times stronger than B_1. The separator deflects the beam by an angle of 90° and acts like a stigmatically imaging round lens. The courses of the x and y components of the fundamental rays differ only slightly within the deflecting field. Focusing in the direction perpendicular to the plane containing the curved optic z–axis is obtained by the inhomogeneous field within the gap between the pole faces of the inner and outer magnets where the direction of the optic axis is different from that of the normal to the pole faces.

The compact beam splitter is optimally suited as the central element of a corrected LEEM. The arrangement is depicted in Fig. 2. The source, the retarding objective lens and a mirror–hexapole corrector are arranged about the separator such that the paraxial path of rays is highly symmetric within the region of the deflection field. The symmetric course is obtained by placing the mirror at an intermediate image of the diffraction plane and by the symmetry of the separator. Owing to these symmetries and the reversal of the direction of flight by the mirror all geometric second–order aberrations produced along the way from the object to the mirror cancel out along the way back to the image.

Although the chromatic and the spherical aberration of the mirror are both negative, they can in general not simultaneously compensate for the corresponding aberrations of the objective lens. Therefore a magnetic hexapole is centered at another image of the diffraction plane located in front of the mirror. These images are formed by the electric immersion lenses L_3 and L_4. The hexapole allows one to eliminate the spherical aberration independently from the preceding correction of the chromatic aberration obtained by properly adjusting the mirror voltage and the focal length of the lens L_4. To guarantee that the corrector does not produce a second–degree dispersion at the image nullifying the chromatic correction, the

diffraction plane must also be imaged ($x_\gamma = y_\delta = 0$) into the diagonal plane of the separator as depicted in Fig. 1.

The separator-corrector system can also be used for a low-voltage scanning microscope. In this case the reflected and the secondary electrons emanating from the object are guided by the separator toward the detector.

References
1. W. Telieps and E. Bauer, Ultramicroscopy 17 (1985) 57.
2. G. F. Rempfer, J. Appl. Phys. 67 (1990) 6027.
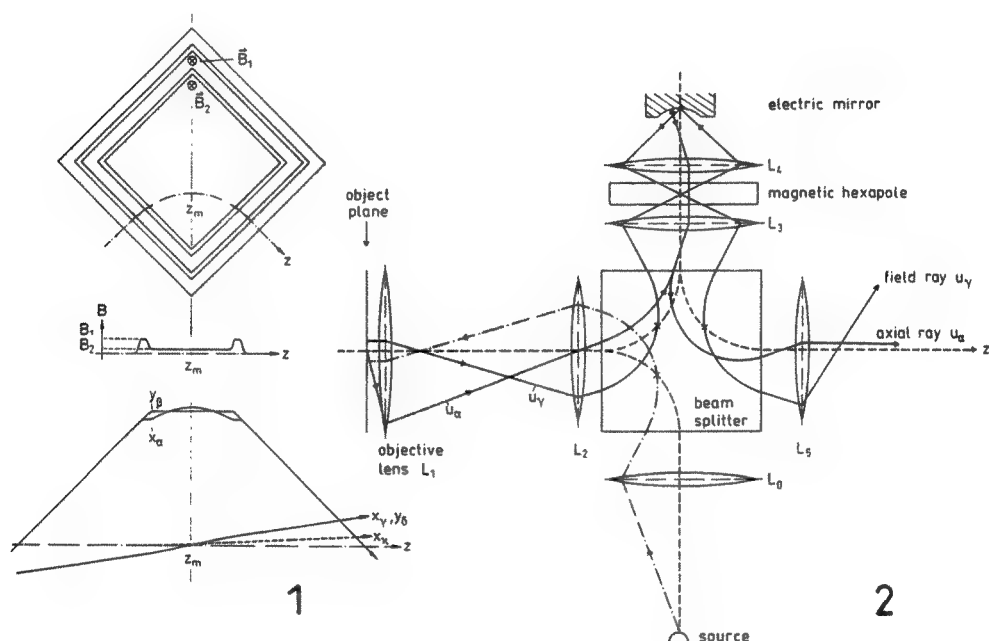
Fig. 1 Scheme of a stigmatically imaging magnetic 90° beam splitter and the course of the magnetic induction B and of the fundamental rays x_α, y_β, x_γ, y_δ, x_κ along the straightened optic axis. Outside the separator the components of both the axial rays and the field rays coincide: $x_\alpha = y_\beta = u_\alpha$, $x_\gamma = y_\delta = u_\gamma$.

Fig. 2 Schematic arrangement of an aplanatic LEEM corrected for chromatic and third–order spherical aberration and coma. Owing to the high symmetry of the separator and the paraxial rays, the dispersion of first and second degree and all second–order aberrations vanish at the final image too.

COMPLETE HREM AUTOTUNING USING AUTOMATED DIFFRACTOGRAM ANALYSIS

O.L. Krivanek and G.Y. Fan

Gatan Research and Development, 6678 Owens Drive, Pleasanton, CA 94588

Complete autotuning of a high resolution electron microscope (HREM) aligns the electron illumination along the true axis of the objective lens (autoalignment), corrects the astigmatism (autostigmation) and sets the focus to a user-selected value (autofocusing). We have developed a new method which performs complete autotuning with just 3 images, and is faster and more accurate than the best human operators.

Our method uses diffractograms of images of amorphous materials recorded with a slow-scan CCD camera[1] (SSC) at magnifications of 200-800 kx. Diffractograms computed from SSC images have better quality than diffractograms formed in an optical bench from a micrograph recorded on film, and are the perfect starting point for the autotuning procedure. The diffractograms are analyzed by an automatic routine described previously[2]. The analysis yields the defocus, astigmatism, and astigmatism direction, and the computer then applies the needed corrections to the microscope. A single image recorded in typically 0.5 - 1.0 secs plus about 8 secs of processing time on a Macintosh Quadra are therefore sufficient for complete autostigmation and autofocusing. This time is likely to decrease in the future simply because of the increasing power of new generations of computers.

Because a single diffractogram typically carries no information about the misalignment of the incident illumination with respect to the true axis of the objective lens, autoalignment is more complicated. In our method, 3 images are recorded with 0, +t and -t intentional tilt. The intentional tilt causes a change in the "apparent" defocus and astigmatism as determined by diffractogram analysis[3]. The changes are symmetric about the true lens axis, and this is used qualitatively in standard coma-free alignment procedures[4]. Our method analyzes the tilt-induced astigmatism (TIA) quantitatively[5], and is able to locate the true lens axis starting from any reasonable initial condition in about 28 seconds total.

Practical implementations of the autotuning means that the computer which acquires and analyses the SSC images needs to control the microscope. This is best accomplished over a digital interface (high speed serial or parallel). The key parameters are the objective lens defocus and astigmatism (x and y), and the tilt of the incident beam (x and y). Calibration of the computer control is done simply by changing each parameter by a set amount, and analyzing the resultant effect with the automatic diffractogram analysis routine. The only other information needed by the autotuning routine is microscope kV and magnification, and the spherical aberration coefficient of the objective lens.

Figs 1-3 illustrate the autotuning with practical results obtained on a Philips CM12ST TEM at 120 kV. Alignment is independent of the focus and the astigmatism, and is therefore typically carried out first. Fig. 1 illustrates the TIA autoalignment routine with diffractogram tableaus[3,4] recorded before the autoalignment, and after one and two passes of the procedure. The initial misalignment of about 4 mrad was reduced to 0.4 mrad by the first pass of the procedure. The second pass resulted in a further correction of 0.3 mrad. Further passes produced no additional correction, showing that the true axis had been reached to within the smallest computer-controllable tilt step on the CM12 (about 0.1 mrad). Practical experience with the procedure on the CM12 and on a JEOL 2010 shows that the typical imprecision is about 10 % of the initial misalignment or 0.1 mrad, whichever is larger.

Fig. 2 illustrates the autostigmation correction with 3 diffractograms corresponding to the initial condition, and two passes of the procedure. The initial astigmatism was 53 nm. The first pass corrected it to within 3 nm, which is about the best precision that human operators attain. The second pass found and corrected the remaining 3 nm. Further passes produced less than 1 nm correction. Fig. 3 shows a diffractogram produced by the autotuned microscope when the user clicked on the "Scherzer defocus" button of the "Set Defocus" dialog box in the DigitalMicrograph software running on the Macintosh.

In conclusion, HREM tuning can now be done faster, more accurately, and with less specimen irradiation by a personal computer coupled to an SSC camera than by even the most skilled human operators. Together with the tilt-induced displacement (TID) autotuning method[6], which works on most specimens and is especially well suited for low and medium magnification imaging, TIA autotuning should lead HREM into an era of unprecedented accuracy and ease of operation.

We are grateful to M.L. Leber and C.E. Meyer of Gatan R&D for help with DigitalMicrograph software. Environmental note: no silver halide and no associated chemicals were used in the preparation of this abstract.

References:

1. P.M. Mooney *et al.*, Proc. 12th Int. EM Congr. (Seattle) **1**, 164 (1990).
2. G.Y. Fan and O.L. Krivanek, Proc. 12th Int. EM Congr. (Seattle) **1**, 332 (1990).
3. O.L. Krivanek, Proc. 9th Int. EM Congr. (Toronto) **1**, 168 (1978).
4. E. Zemlin *et al.*, Ultramicroscopy **3**, 49 (1978).
5. O.L. Krivanek and G.Y. Fan, proceedings 10th Pfefferkorn conference, to be published.
6. A.J. Koster and W.J. DeRuijter, Ultramicroscopy, to be published (1992).

Fig. 1. Diffractogram tableaus recorded before the first pass of the autoalignment procedure (a), and after one (b) and two passes (c) of the procedure. Philips CM12ST, 120 kV. Tableau tilt increments of 6 mrad are indicated next to the diffractograms. Mistilt of about 4 mrad in (a) was reduced to 0.4 mrad in (b) and to < 0.1 mrad in (c). Each pass of the procedure took 28 seconds.
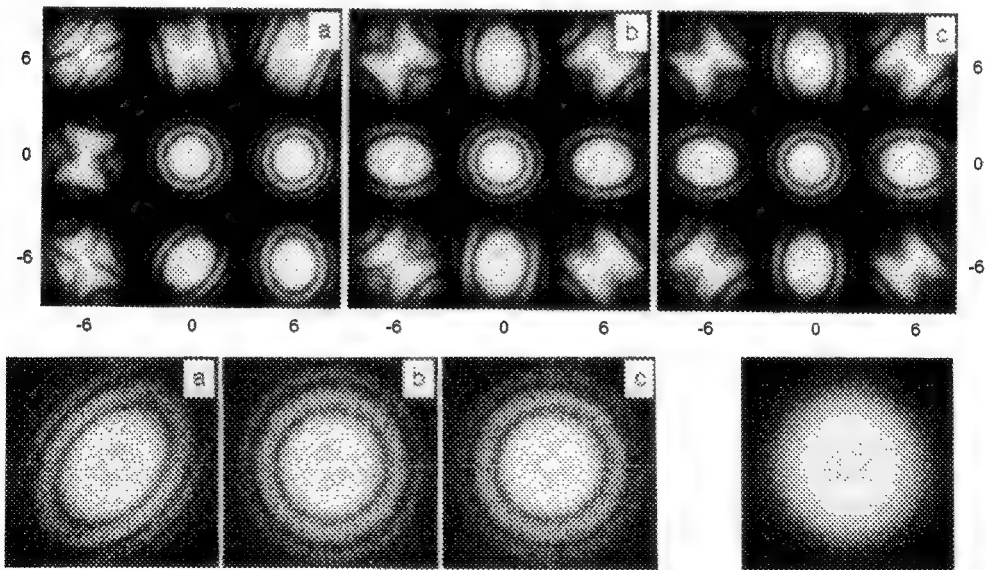
Fig. 2. Diffractograms illustrating the autostigmation procedure. (a) initial condition (A = 53 nm), b) after one pass (A = 3 nm), c) after the second pass (A < 1 nm). Each pass of the procedure took 8 seconds.

Fig. 3. Diffractogram of an image recorded after asking the computer to set the TEM to Scherzer defocus.

CONTROLLED HOT–STAGE EXPERIMENTS IN THE HREM WITH ACTIVE DRIFT COMPENSATION AND 2Å LATTICE RESOLUTION

E D Boyes, L Hanna and P L Gai

Du Pont Company, CR&D, PO Box 80356-383, Wilmington, DE 19880-0356

An electronic system has been developed to compensate electronically, with <2Å lattice resolution, for the image shift due to specimen and/or stage drift in the HREM. A simple system has been highly effective in compensating for the drift which has long limited many scientifically important but technically demanding applications of TEM in both the physical (1,2,3) and biological sciences (4). It has facilitated controlled hot stage experiments with full HREM resolution.

Over an extended period of time (>15s) which is fully adequate to record a high resolution image photographically or electronically, most drift of either the stage or the specimen can be approximated to a constant and relatively slow rate along a straight line path segment. With the new system the drift characteristic is video analyzed and an inverse correction ramp derived from a 12-bit DAC or external analog function generator is applied to existing post-specimen electrical image shift coils to stabilize the image position at the TEM camera. Image stabilization is also necessary for high quality data recording by digital processing of multiple (e.g. 256 or more) TV frames for an equivalent exposure time of several (8.5) seconds. This is the main data recording method for the dynamic experiments and with it low dose techniques can be used to minimize the beam damage effects which otherwise can be a serious problem in many HREM applications.

The (AC) drift compensation controls are adjusted interactively, on the basis of the digitally processed signal from the TV camera, to achieve accurate cancellation of any drift, and thereby to stabilize the image for recording. The new controls are similar in function and layout to those conventionally used for correcting residual astigmatism in the microscope image. A smooth predictive system over a period of a few seconds is used to avoid the potential for oscillations and over-compensation which can create instability in a realtime active system. Additional (DC) controls are used for precise and convenient image positioning; and also reducing the need for many small but potentially destabilizing mechanical movements of the microscope stage controls. The new drift compensation systems have been very effective in both general HREM operations and in opening up better control of more specialized TEM applications with hot and cold stages, and with AEM and STEM stages more generally. They facilitate the use for HREM imaging of regular side entry goniometer stages with which it is also possible to combine EDX chemical analysis and an extended range of STEM diffraction techniques. The compensation systems are relatively simple in concept, construction and operation. Universal application is expected. A major limitation on the productivity of the TEM since the invention of the instrument has finally been overcome. Controlled TEM hot stage experiments on the mobility and structural stability of small particle systems which form the basis of many heterogeneous catalysts technology and studies of the initial stages of the nucleation and growth of many types of thin films can now be productive.

References

1. R Sinclair et al, Nature 290 (1981) 386
2. E D Boyes, Proc EMSA 1989, San Francisco Press, (1989) 626
3. E D Boyes, Proc EMAG 91, Inst of Physics, (1991) 539
4. D Cattermole and R Henderson, Ultramicroscopy, 35 (1991) 55
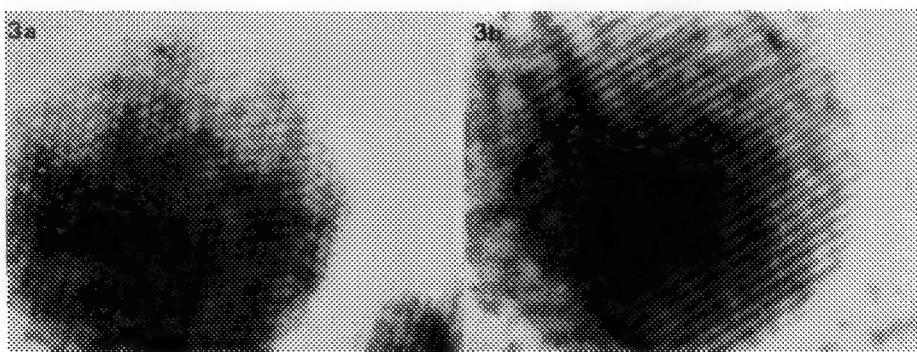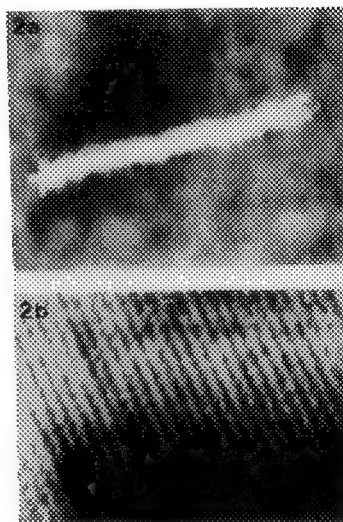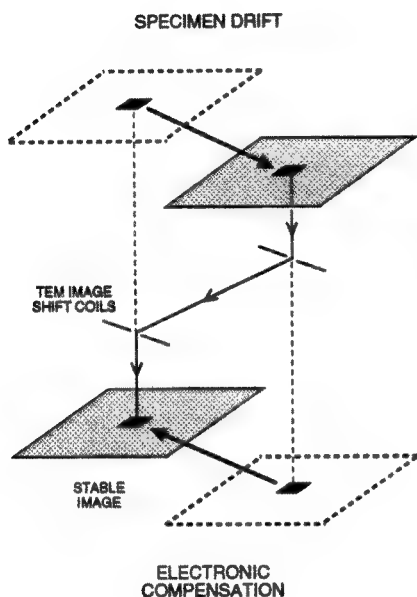
Fig. 1 Image position stabilization system for Philips CM30ST HREM with STEM unit.
Fig. 2 (a) Drift analysis and (b) Compensation with graphite sample (3.4Å) at 500°C
Fig. 3 Gold particle video lattice images (2.3 and 2Å have been recorded) in the hot
stage at 500°C and digitally integrated for 16 TV frames (~0.5 sec exposure).

FEG - TEM : the route to HREM

W. Coene[1], A.F. de Jong[1], H. Lichte[2], M. Op de Beeck[3], H. Tietz[4], D. Van Dyck[3]

[1] Philips Research Laboratories, PO Box 80.000, 5600 JA Eindhoven, The Netherlands
[2] Inst. für Angew. Physik, University of Tübingen, Germany
[3] RUCA, University of Antwerp, Belgium
[4] Tietz Video and Image Processing Systems GmbH, Gauting, Germany

Several technological improvements in TEM have nowadays been realized which offer possibilities for ultra-high resolution electron microscopy at intermediate voltages. These improvements include new objective lens polepieces, field emission gun (FEG) TEMs and slow-scan CCD camera's. A project has been initiated for the period 1990-1994, for the development of ultra-HREM, which combines know-how both from industry (Philips, Tietz) and university (Antwerp, Tübingen, Delft, Arizona). The project is partly sponsored by the European Community (Brite-Euram program nr. 3322). The goal of the project is to achieve 0.1 nm structural resolution by using the information limit rather than the point resolution of the instrument. The information limit is extended towards the 0.1 nm range (at 300 kV) by the much better spatial and temporal coherence of the FEG as compared with LaB6 sources.

Obtaining direct benefit from the extra HREM information extending up to the information limit of the FEG, is difficult since the image interpretation is hampered by the oscillating behaviour of the contrast transfer function (CTF), leading to contrast reversals and delocalisation effects. For the interpretation of the ultra-HREM information yielded by the FEG, phase retrieval or image reconstruction methods are needed, which compensate for the CTF of the microscope. Since these reconstruction methods require dedicated image processing techniques, the step towards quantitative digital microscopy is inevitable in order to reach reliable ultra-HREM information. Direct digital image acquisition is enabled by means of CCD cameras.

The present state-of-the-art of phase retrieval in HREM with a FEG distinguishes focus variation methods and electron holography as two workable routes towards ultra-high resolution. In the first method, a focal series of images is recorded and digitally processed in two distinct ways, i.e. by the 'paraboloid method' (PM) or by the 'maximum-likelihood method' (MAL). The PM [1] aims at selecting directly the linear imaging contributions in the focal series, with a correction for non-linear imaging effects by iteration. The MAL is a modified Kirkland procedure [2,3] which uses both linear and non-linear image information in a recursive reconstruction algorithm. The PM is less demanding with respect to computational efforts, but the accuracy of the MAL is higher, especially around the information limit. In the second phase retrieval method, electron holography [4], an electron biprism is used to realize interference of a reference wave with the object wave. Deconvolution of the CTF in the sidebands of the Fourier transform of the hologram enables retrieval of the phase information and to compensate for the microscope aberrations.

For the refinement from point to information resolution, it becomes increasingly important to know accurately the microscope parameters during the recording of the focal image series or hologram; i.e. C_s, focus, residual astigmatism and beam misalignment. For accurate

parameter measurement, a method has been devised [5] which uses beam tilt induced image displacements for a series of beam tilts along two perpendicular directions.

Image reconstruction experiments are presently being carried out on CM20 and CM30 FEGs. Fig. 1 shows images recorded with a slow scan CCD camera on a CM20 FEG (point resolution 0.24 nm), for a $YBa_2Cu_4O_8$ sample (cfr. [6]). Comparison of the PM reconstruction with the structure model shows that (apart from O-Y-O) all atom positions are revealed.
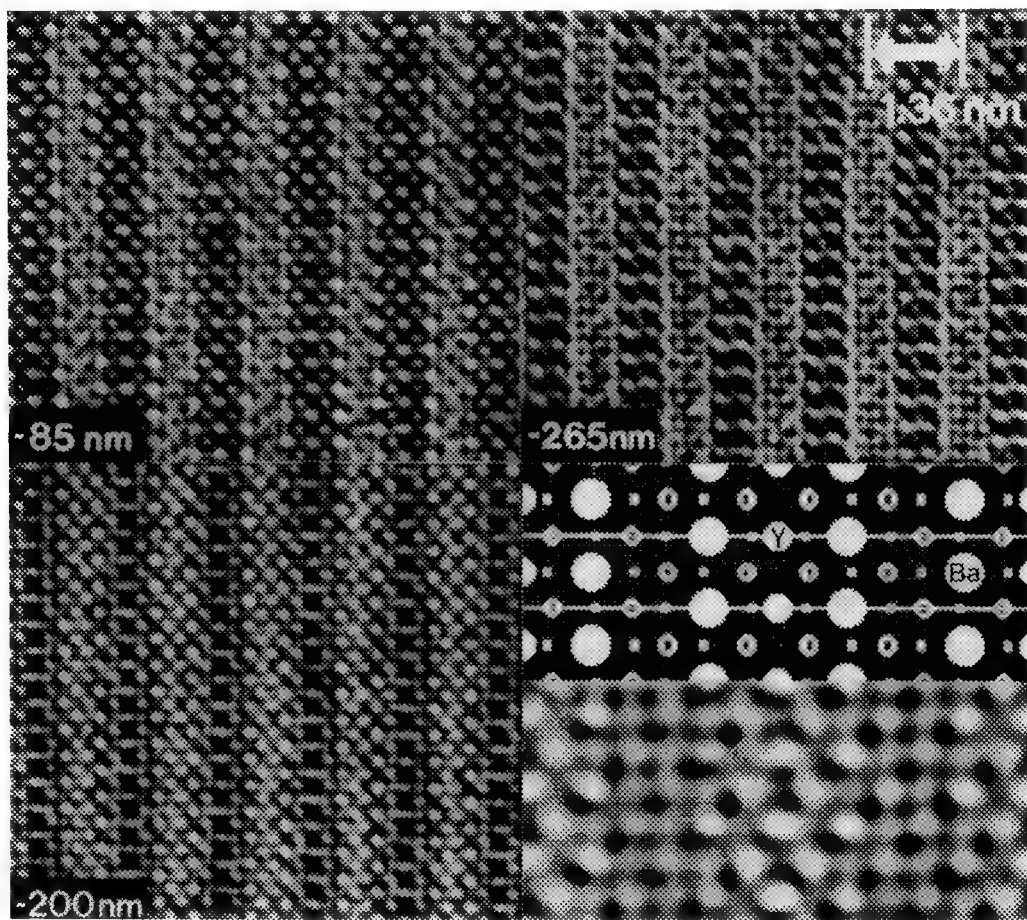
Fig. 1. HREM images of $YBa_2Cu_4O_8$ in [100] orientation (CCD camera on CM20 FEG - SuperTWIN). PM reconstruction and structure model are displayed in enlarged format. Specimen courtesy Dr. T. Krekels, RUCA.

References
1. D. Van Dyck and M. Op de Beeck, Proc. XIIth ICEM Seattle (1990), Vol. 1, 26-27.
2. E.J. Kirkland, Ultramicroscopy 15 (1984), 151-172.
3. W. Coene (1992), this conference.
4. H. Lichte, Adv. Opt. El. Microsc. 12 (1991), 25-91.
5. A.F. de Jong and A.J. Koster, Proc. Pfefferkorn Conf., Scan. Micr. (1992), in press.
6. T. Krekels, G. Van Tendeloo, S. Amelinckx, D.M. de Leeuw, M. de Kraan, Physica C 169 (1990), 457-463.

NEW DETECTION SYSTEM FOR HAADF AND HOLOGRAPHY IN STEM

Marian Mankos, Shi Yao Wang, J.K. Weiss and J.M. Cowley

Department of Physics and Astronomy, Arizona State University, Tempe, AZ 85287

A novel detection system has been designed and realized experimentally on the HB5 STEM instrument. Shadow images, diffraction patterns as well as high-angle annular dark field and bright field images are observed simultaneously with high efficiency using CCD and TV cameras. The microscope can be operated in a wide range of instrument modes which includes the implementation of new techniques for high resolution imaging.

As shown in Fig. 1, the detection system has three triple choice stages. Diffracted beams can be collected by three P47 fast phosphor annular detectors inclined at 45 degree to the axis and having different inner and outer acceptance angles, which can be adjusted by the postspecimen lenses. The detector is observed through a window by a photomultiplier. The annular detectors have been used also for a new bright field STEM technique which utilizes the inner rim of the detectors to collect only the outermost annular part of the central beam and promises an improvement in resolution by a factor of about 1.6. Initial results show some promise (Fig. 2). The transmitted beam is then converted into a light signal in YAG and P47 detectors; optionally the central part of the beam can be detected in the EELS spectrometer. The generated light signal is reflected through a system of mirrors, exits the vacuum chamber and is collected with high efficiency by high aperture optical lenses.

The outcoming signal is further processed in two separate imaging systems. In the first system, the intermediate image is transmitted into a photomultiplier or focused on the TV camera, hence allowing an easy switching between the STEM and shadow image modes. The intermediate image can be focused in the plane of a mask. Various masks can be inserted for imaging of selected diffraction beams. In addition, a configured detector can be used in the mask plane to implement the form of holography proposed by Veneklasen [1]. The configured detector reconstructs the hologram formed by diffracted beams in real time which is observed at usual STEM frame speeds and requires no further reconstruction. In the second system, the image is observed on a TV or CCD camera (Fig. 3). The CCD camera is the key improvement in image quality compared to the previous TV and VCR system. A Photometrics CH 200 slow scan CCD camera records the images on a 512x512 pixel CCD array to 14-bit precision. The CCD camera has a much lower noise and higher linearity than the TV camera but the readout rate, which is limited by the digitization to 200 kHz, is much slower than that of the TV camera. The frame rate is then limited to about one frame per second as opposed to the 60 frames per second recorded by the TV camera on the VCR, but the image quality in the individual frames recorded by the CCD camera is much better. CCD images are stored in the computer and can be directly used for holography reconstruction for the in-line STEM holography scheme of Gabor [2], the dark-field holography scheme of Konnert et al. [3] or the off-axis STEM holography proposed by Cowley [4].

References
1. L.H. Veneklasen, Optik 44 (1975) 447.
2. D. Gabor, Nature 161 (1948) 777.
3. J. Konnert et al.,Ultramicroscopy 34 (1989) 371.
4. J.M. Cowley, Ultramicroscopy 34 (1990) 293.
5. This study is supported under NSF grant DMR-9014975 and made use of the ASU Facility for HREM supported by NSF grant DMR-8913384. Financial support for J.K. Weiss was provided by the Industrial Associates Program at Arizona State University.
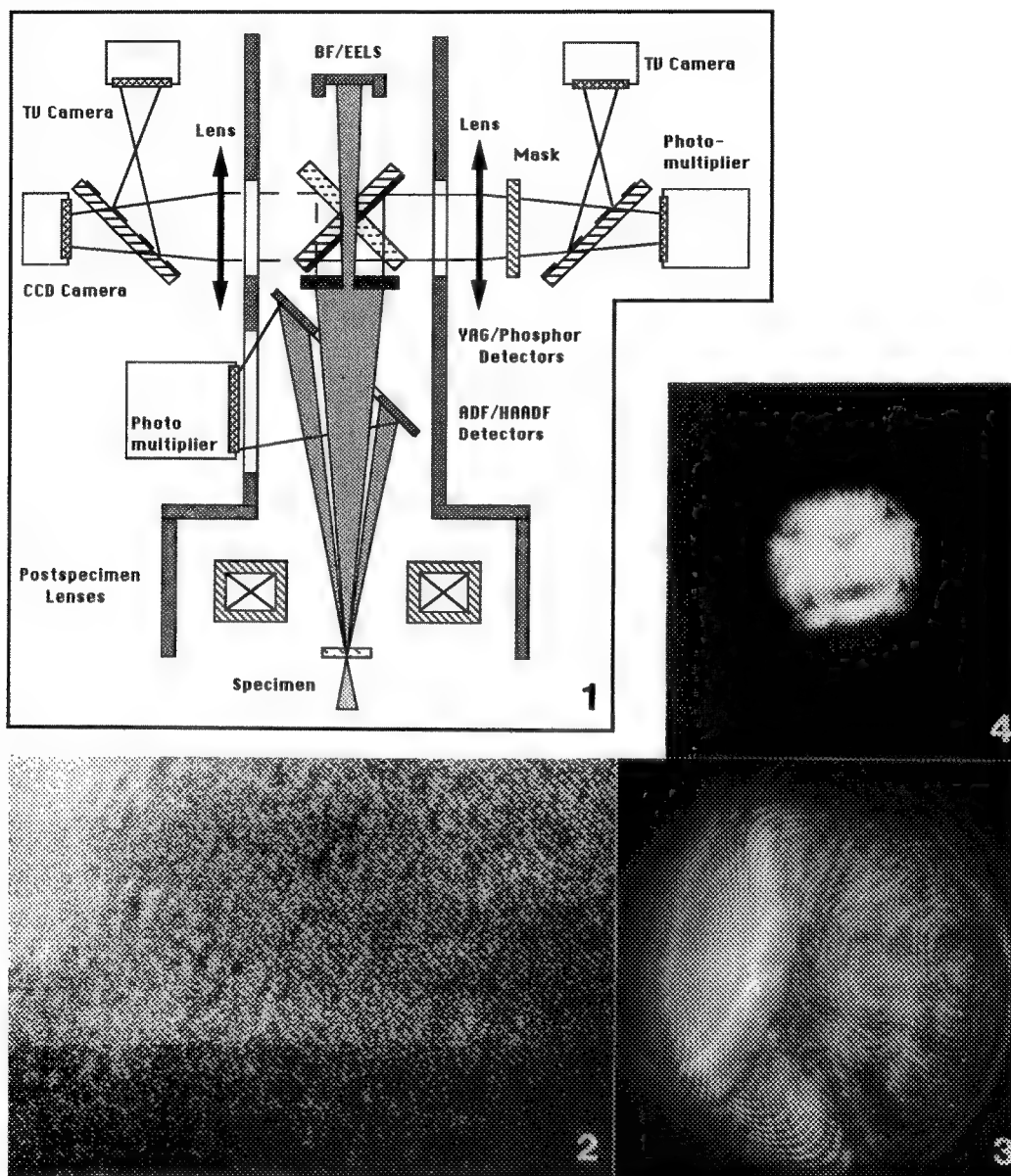
Figure 1. Schematic diagram illustrating the geometry of the new detection system.
Figure 2. High resolution STEM image, utilizing the outermost annular ring of the central beam, reveals 1.9Å resolution for periodic structures and 2-3Å nonperiodic details.
Figure 3. Shadow image of a silicon sample observed by the CCD camera.
Figure 4. Convergent Nanodiffraction pattern from Si [110].

HREM in Solid-State Chemistry and Crystallography

Lars Kihlborg, Margareta Sundberg and Gunnar Svensson

Department of Inorganic Chemistry, Stockholm University, S-10691 Stockholm, Sweden

High-resolution electron microscopy has had a great impact on solid state chemistry. The possibility it offers of directly imaging the structure of solids has made it an invaluable complement to conventional diffraction methods. Disorder and extended defects have become accessible to observation, superstructures, structural modulations and microphases can be identified and particles down to nanometer size can be studied. Combined with electron diffraction and x-ray microanalysis it is a powerful tool for phase analysis, giving guidance to synthesis of new compounds. Under certain conditions even chemical reactions can be studied *in situ* at atomic resolution. Numerous examples can be found in the fields of high-temperature superconductors, zeolites, ferroelectrics and solid state ionics.

HREM has contributed enormously to our knowledge of *intergrowth*, which has proved to be a common proliferating mechanism in structural chemistry. The variety of intergrowth between perovskite-, rock salt- and fluorite-type elements in the oxide superconductor systems provide recent examples in this context. Here, particularly two cases of intergrowth phases will be discusssed; selected from the U-Mo-O and Ba-Nb-O systems, respectively.

In the U-(Mo,W)-O system a number of phases can be prepared.[1] Some of these can be considered as intergrowth of ReO_3-type and hexagonal tungsten bronze (HTB)-type slabs with -U-O-U-O- (partly) occupying the hexagonal tunnels, thus being closely related to the intergrowth tungsten bronzes and bronzoids (ITB) *(Fig. 1)*. Other phases in the same system have similar structures but with pentagonal tunnels *(Fig. 2)* fully occupied by -U-O-U-O- chains to form pentagonal bipyramids. Although the two structures give distinctly different ED patterns they may nevertheless be rather difficult to distinguish in the HREM images. Image processing may be a resource in such cases. In both systems, several homologues have been prepared and disorder and defects are rather common.

In the *A*-Nb-O system (*A*= K,Sr,Ba) intergrowth of NbO (defect sodium chloride type) and $ANbO_3$ (perovskite) type has been found, 1-dimensional as well as 2-dimensional.[2] In the 2-dimensional case a rich variety of microphases have been observed in quasi-ordered phasoid regions. Some of these have been possible to synthesize as single phases [3]. *Fig. 3* shows an example of a crystal with an ordered structure (composition $Ba_4Nb_{14}O_{23}$) while *Fig 4* shows a typical disordered crystal from the same system.

The combination of results obtained by HREM, microanalysis and x-ray diffraction has been essential in these studies.

References

1. M. Sundberg and V. Tabachenko, *Microsc. Microanal. Microstruct.* **1** (1990) 373.

2. G. Svensson, *Microsc. Microanal. Microstruct.* **1** (1990) 343.

3. G. Svensson, J. Köhler and A. Simon, *J. Alloys and Compounds* **176** (1991) 123.
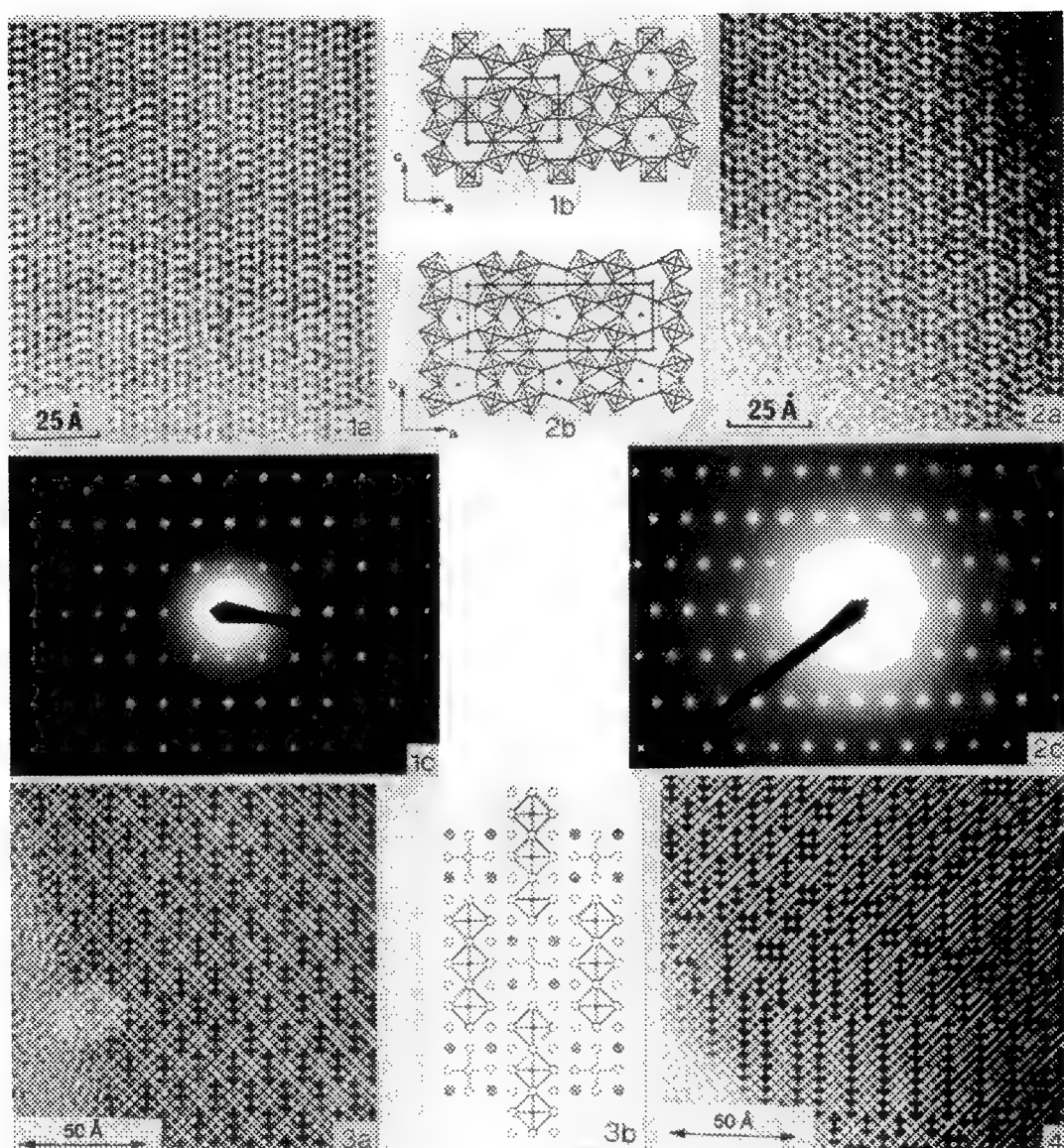
Fig. 1 $U_{1-x}Mo_5O_{16}$ **a.** Image along [010]. **b.** Structure model depicted as corner-linked MoO_6 octahedra. -U-O-U-O- strings (partly) fill the hexagonal tunnels. **c.** Corresponding ED pattern.

Fig. 2 β-UMo_2O_8 **a.** Image along [001]. **b.** Structure model. The -U-O-U-O- strings fill the pentagonal tunnels.

Fig. 3 $Ba_4Nb_{14}O_{23}$ **a.** Image. **b.** Structure model. The Nb_6 octahedra forming NbO-type clusters are indicated by heavy lines and correspond to the strings of dark crosses in the image. The Ba atoms are indicated by large shaded circles.

Fig. 4 Image of a quasi-ordered intergrowth of NbO (dark) and $BaNbO_3$.

SURFACE RECONSTRUCTIONS OF (001) CLEAVED $GdBa_2Cu_3O_{7-\partial}$

H.W. Zandbergen[1] and M.R. McCartney[2]

1. National Center for HREM, Delft University of Technology, 2628 AL Delft, The Netherlands
2. Center for Solid State Science, Arizona State University, Tempe AZ 85087-1704

Very few electron microscopy papers have been published on the atomic structure of the copper oxide based superconductor surfaces. Zandbergen et al. [1] have reported that the surface of $YBa_2Cu_3O_{7-\partial}$ was such that the terminating layer sequence is bulk-Y-CuO_2-BaO-CuO-BaO, whereas the interruption at the grain boundaries is bulk-Y-CuO_2-BaO-CuO. [2] Bursill et al. [3] reported that HREM images of the termination at the surface are in good agreement with calculated images with the same layer sequence as observed by Zandbergen et al. but with some oxygen deficiency in the two surface layers. In both studies only one [3] or a few [1] surfaces were studied.

Detailed HREM studies of the surface of (001) cleaved $YBa_2Cu_3O_{7-\partial}$ can help to understand unexpected results in photoemission spectroscopy measurements [4]. These XPS studies on (001) cleaved $YBa_2Cu_3O_{7-\partial}$ do not show the presence of a superconducting gap. This absence could be explained by a change in the surface due to the exposure of the cleaved material to the atmosphere of the XPS system which is typically 10^{-6}Torr or better vacuum. Another possible reason is the occurrence of a surface reconstruction or surface relaxation, due to an interruption of the structure, leading to a non-superconducting slice at the surface. In order to check this last possibility, HREM was performed on cleaved specimens of $GdBa_2Cu_3O_{7-\partial}$. In this investigation a surface relaxation was observed for all interruptions. Only in the case of an interruption with the CuO_2 plane at the surface a $\sqrt{2}x\sqrt{2}$ surface reconstruction occurs.

HREM was performed with a Philips CM30ST electron microscope and a JEM4000EX electron microscope. HREM images were recorded as a through focus series and as single images recorded at a defocus slightly less than Scherzer focus, at which all cations are imaged as black dots. In the HREM observations of clean and flat (001) surfaces, a number of different layers are observed as the terminating layer at the surface. The most dominant one (about 65%) is the CuO_2 layer whereby the first missing layer is the BaO layer (bulk-Gd-CuO_2). In addition to this termination a termination bulk-BaO-$CuO_{1-\partial}$-BaO is found to occur relatively frequently. Figure 1 shows a micrograph in which both terminations are present.

Detailed analysis of [100] and [110] HREM images, using image processing and through focus series, showed that a relaxation of the atoms in the two surface layers had occurred for both types of terminations as can be seen from Fig 1. [110] images of clean (001) surfaces which terminate at the CuO_2 layer show a $\sqrt{2}x\sqrt{2}$ surface reconstruction involving changes in both Gd and CuO_2 layers. This reconstruction leads to a doubling of the d_{110} period as can be seen in Figure 2. This $2d_{110}$ period was found to be mostly short range ordered.

Image calculations with the model for the $\sqrt{2}x\sqrt{2}$ surface reconstruction given in Figure 3 give good agreement between calculated and experimental images. The model for the surface reconstruction is based on compensating arrangements of the negative and positive ions. In bulk material the negative charge of the CuO_2 layer is compensated by the Gd-vacancy layer. At a surface, however, a negatively charged CuO_2 layer is energetically unfavorable. By shifting some of the oxygen ions from the CuO_2 layer to the Gd-vacancy layer an almost neutral surface layer can be obtained.

In conclusion, the most dominant surface layer obtain by cleavage is the CuO_2 layer, which is modified to a CuO_{1+x} layer by a shift of some of the oxygen ions to the Gd-vacancy layer. This surface reconstruction leads to a $\sqrt{2}x\sqrt{2}$ repetition period. The changes in the atom positions at the surface are expected to influence strongly the properties of the surface layers, which is in agreement with the absence of a superconducting energy gap in XPS measurements [5]

References
1. H.W. Zandbergen, R. Gronsky and G. Thomas, phys. stat. sol (a) (1988) 105, 207.
2. H.W. Zandbergen and G. van Tendeloo, Materials Reseach Society Proc. (1990) 183, 337.
3. L.A. Bursill and X.D. Fang, phys. sta. sol. (a) (1988) 107, 505.
4. R. Cleassen, et al., Phys. Rev, (1989) B39, 7316.
5. Some of this work was performed at Arizona State University at the National Facility for HREM supported by NSF grant DMR89-13384.
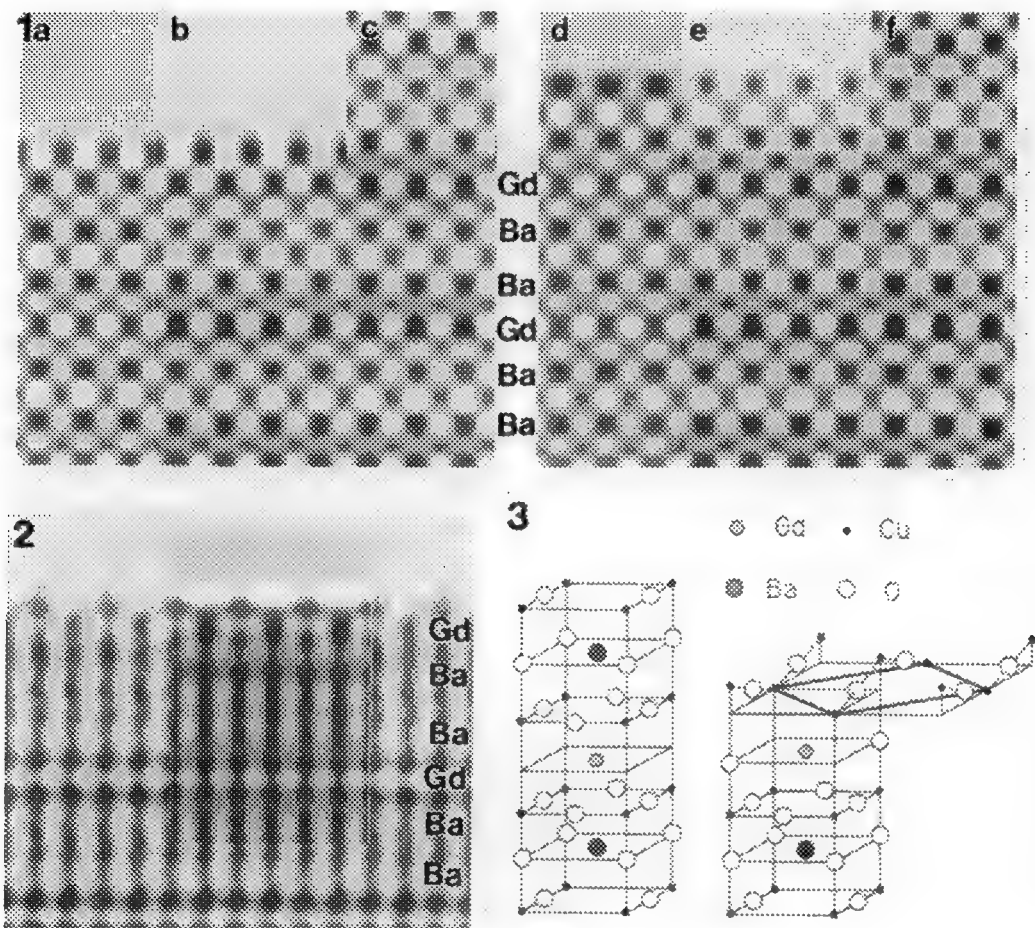
FIG 1. [100] micrograph of (001) surface, showing two types of terminations A) bulk-Gd-CuO_2 and B) bulk-$CuO_{1-\partial}$-BaO. Averaged images (over 8 unit cells + mirror imaging) of these interruptions are shown in b) and e), respectively. a) and d) give calculated images for thickness of 4 nm and defocus of -45 nm. c) and f) give the same images as b) and e) but shifted one unit cell upwards. The surface relaxation, visible as a jump in (001) planes across images b)-c) and e)-f), can best be seen by looking along the surface at a glancing angle.

FIG 2. Averaged [110] image (over 5 unit cells). Calculated image using model given in Figure 3 for thickness of 4 nm and defocus of -40 nm is given as an inset. Gd and BaO planes are indicated.

FIG 3. Schematic representation of the surface reconstruction used as a model in calculations. Cu-O chains at the surface are given by dashed lines. The $\sqrt{2}$x$\sqrt{2}$ enlarged basal plane is indicated with thick full line. Gd atoms were shifted 0.05 nm from the bulk. For comparison, the unit cell of $GdBa_2Cu_3O_{7-\partial}$ is given at left.

HIGH-RESOLUTION TRANSMISSION ELECTRON MICROSCOPY OF C_{60} THIN FILMS

W. KRAKOW, N.M. RIVERA, R.A. ROY and J.J. CUOMO

IBM Research Division, T. J. Watson Research Center, P. O. Box 218, Yorktown Heights, NY 10598

The ability to fabricate buckminsterfullerenes, C_{60} molecules[1], in reasonably large quantities[2,3] has made possible studies of the structural properties of this form of carbon when it is in a crystalline state. At room temperature, x-ray diffraction from three-dimensional bulk C_{60} crystals shows that the molecules are centered on sites of a face-centered-cubic Bravais lattice[4], $A_o = 14.2$Å. Somewhat earlier in time, a study of C_{60}/C_{70} bulk material using electron diffraction and high resolution electron microscopy has revealed a hexagonal phase.[5] It is now believed that this phase is a simple cubic structure rather than a hexagonal structure. Since it is reasonable to expect that highly ordered C_{60} thin films will have superior properties to bulk material, several studies have been undertaken to understand the early stages of C_{60} thin film growth. Monolayer growth on GaAs has been studied by scanning tunneling microscopy.[6], and on mica at room temperature using helium scattering.[7] Along similar lines we have grown thin films of C_{60} molecules on mica and NaCl and characterized the crystallinity and local structural arrangements. Here we present some of our results of the electron microscope examination of these materials.

Films of C_{60} were prepared by depositing pristine material by resistance evaporation. Both rate and thickness were controlled while the substrate temperature was varied from room temperature up to 250°C. Thin films were then removed by lift off and viewed with a 400kV incident beam energy in the microscope. An example of a 150Å thin film grown on (100) NaCl at 200°C is shown in Fig. 1. Randomly oriented f.c.c. grains are observed as evidenced by the diffraction pattern insert. Above 150°C films exhibited a polycrystalline behavior while at lower temperatures an amorphous structure was indicated (not shown).

An example of a 150Å thin film grown on mica is shown in Fig. 2 along with a diffraction pattern insert from a similar area. The three sets of crossed lattice spacing observed in the image correspond to {220} planar spacings of ~5Å indicating a (111) oriented thin film. Faint lattice spacings of ~8.7Å are also present due to different surface termination layers. These monolayer periodicities produce forbidden reflections in the diffraction pattern located at the 1/3{422} positions. These appear as faint spots near the origin. The best results appeared at 200°C with the results being somewhat poorer at other temperatures. At 100°C or less an amorphous film was observed. Films as thin as 24Å were observed in the TEM with the hope of seeing the cage structures of the individual molecules.

1. H.W. Kroto, J.R. Heath, S.C. O'Brien, R.F. Curl and R.E. Smalley, Nature (London) (1985), **318**, 162.

2. W. Krätschmer, K. Fostiropoulos, D.R. Huffman, Chem. Phys. Lett., (1990), **170**, 167.

3. W. Krätschmer, L.B. Lamb, K. Fostiropoulos and D.R. Huffman, Nature(London) (1990), **347**, 354.

4. P.A. Heiney, J.E. Fischer, A.R. McGhie, W.J. Romanow, A.M. Denenstein, J.P. McCauley Jr. and A.B. Smith III, Phys. Rev. Lett., (1991), **66**, 2911.

5. G. VanTendeloo, M. Op DeBeeck, S. Amelinckx, J. Bohr and W. Krätschmer, Europhysics Let., (1991), **15**, 295.

6.   Y.Z. Li, J.C. Patrin, M. Chander, J.H. Weaver, L.P.F. Chibante and R.E. Smalley, Science, (1991), **252**, 547 and **253**, 429.

7.   D. Schmicker, S. Schmidt, J.G. Skofronick, J.P. Toennies and R. Vollmer, Submitted to Phys. Rev. B, Aug. 8, 1991.
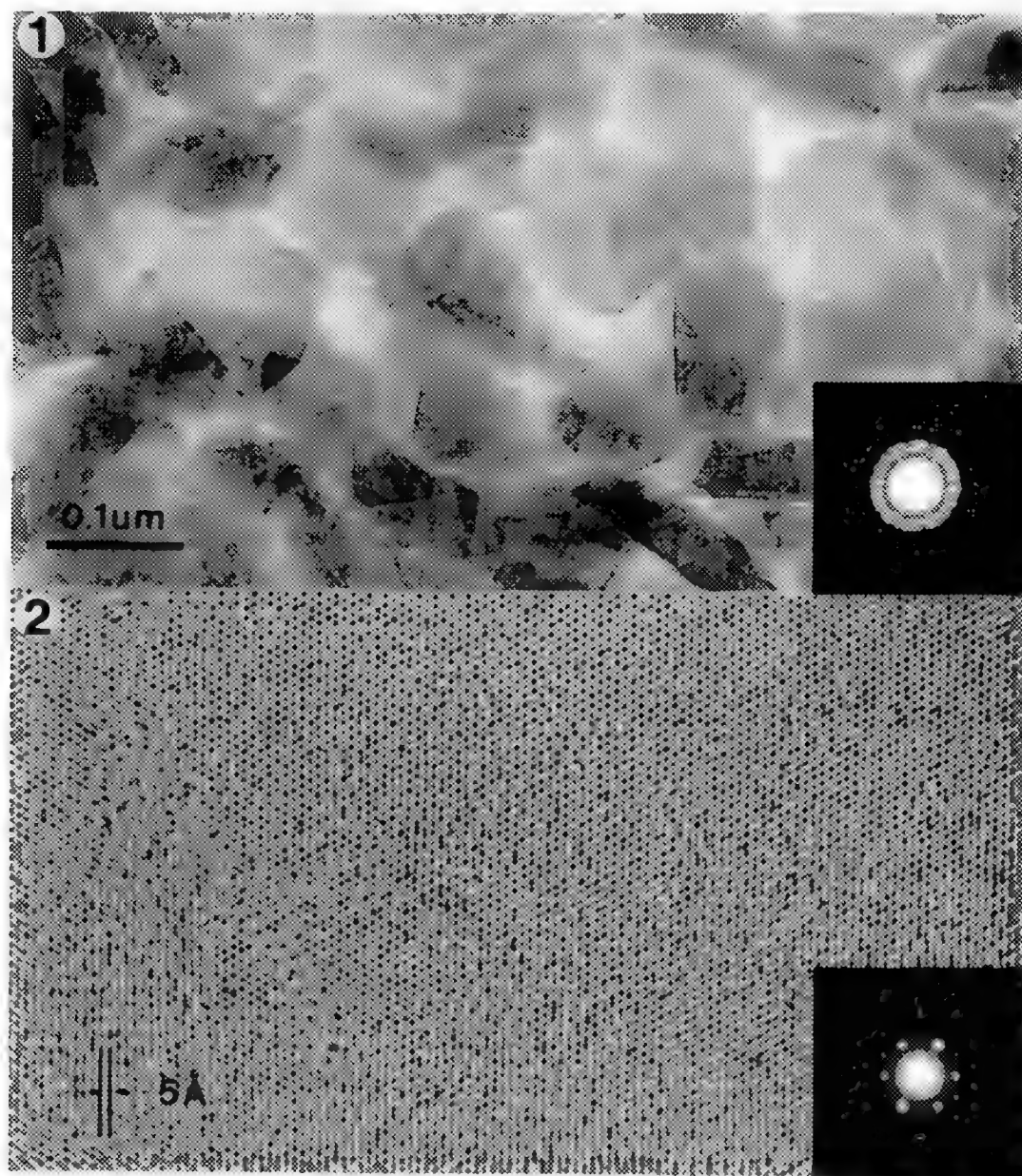
Fig. 1. 150Å C_{60} film deposited on (100) NaCl at 200°C.

Fig. 2. 150Å C_{60} deposited on mica at 200°C.

OBSERVATIONS OF COEXISTENCE OF FCC AND HCP PHASES IN C_{60} BY HREM

Z. G. Li and Paul J. Fagan

Du Pont Research and Development, Experimental Station, P. O. Box 80356
Wilmington, DE 19880-0356

Since the discovery of a large scale synthesis of fullerenes there has been intense interest in the structure of these materials[1]. The first diffraction data suggested that crystalline C_{60} had a hexagonal close-packed (hcp) structure with a nearest neighbor distance of 10.04 Å. The possibility of a disordered stacking of C_{60} molecules was first noted in this study. Since then, there has been some confusion regarding the exact crystalline structure of C_{60} as determined by electron and X-ray diffraction. In particular, a diffraction feature corresponding to a spacing of 8.7 Å has been noted in several studies[2][3]. Recently there had been a growing consensus that fcc is the correct structure for sublimed C60. Although the internal carbon atom arrangement of the C_{60} molecules cannot be determined, the actual packing and defects in C_{60} crystals over small and relatively large regions are readily seen by HRTEM. We have found by direct imaging a relatively large region of defect-free hcp packing of C_{60} spheres sublimed onto a relatively cool microscopy grid.

The sublimed C_{60} sample was prepared by suspending a holey amorphous carbon grid on indentations in a glass pyrex tube (see ref. 4). Although the sublimed C_{60} sample contained fewer defects than the benzene grown sample, typical fcc twinning defects and stacking faults were observed [4][5]. As shown in figure A, two types of crystallites of fcc and hcp symmetry were found bound together in the sample. A region of disorder joins the two crystallites. Two of the fcc {111} lattice images with a spacing of 8.2 Å (a = 14.2 Å) are shown (left side figure a). On the right is shown one section of a large region of hcp structure in [001] projection with a and b axes of 10.0 Å (c = 16.3 Å). One of these planes with a spacing of 8.7 Å, (100), is indicated. This spacing is exactly the value determined for the unexplained diffraction peaks in previous X-ray powder and electron diffraction studies [1][2][3]. As a check, high resolution images, shown in figure b, and diffraction patterns were obtained for fcc crystals in the [111] projection. These are much different than the hcp phase, with fcc {220} spacing of 5.0 Å.

In conclusion, the coexistence of fcc and hcp phases helps to explain some anomalous features observed in previous X-ray and electron diffraction studies of both solution and sublimed samples. The direct images in our study provide compelling evidence for the existence of a relatively large scale defect-free hcp phase in sublimed C_{60}. The coexistence of two phases in C_{60} can be explained by the relatively weak   Van der Waals attraction among the balls.

References

1. W.Kratschmer, L.D.Lamb, K.Fostiropoulos, D.R.Huffman, Nature 347 (1990) 354
2. J.Q.Li, Z.X.Zhao, D.B.Zhu, Z.Z.Gan, D.L.Yin, Appl. Phys. Lett. 59 (1991) 3108
3. D.E. Luzzi, J.E.Fisher, X.Q.Wang, D.A.Ricketts-foot, A.R.McGhie, W.J.Romanow, J. Mater. Res. (1992) in press
4. Z.G.Li, P.J.Fagan, Chem. Phys. Lett., (1992), submitted
5.M.M.Disko, S.K.Behal, R.D.Sherwood, F.Cosandey, P.Lu, K.M.Creegan, P.Tindell, D.M.Cox, Proc. 49th Ann. Meet. Electr. Microsc. Soc., (1991) 1024
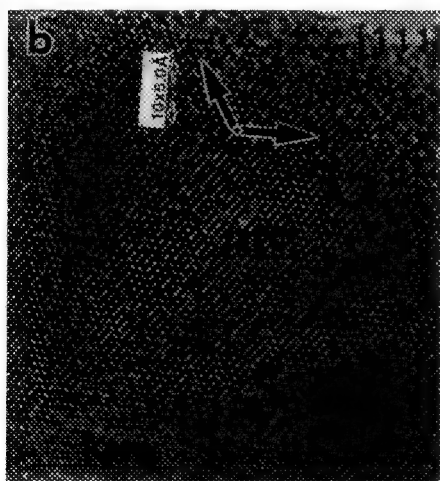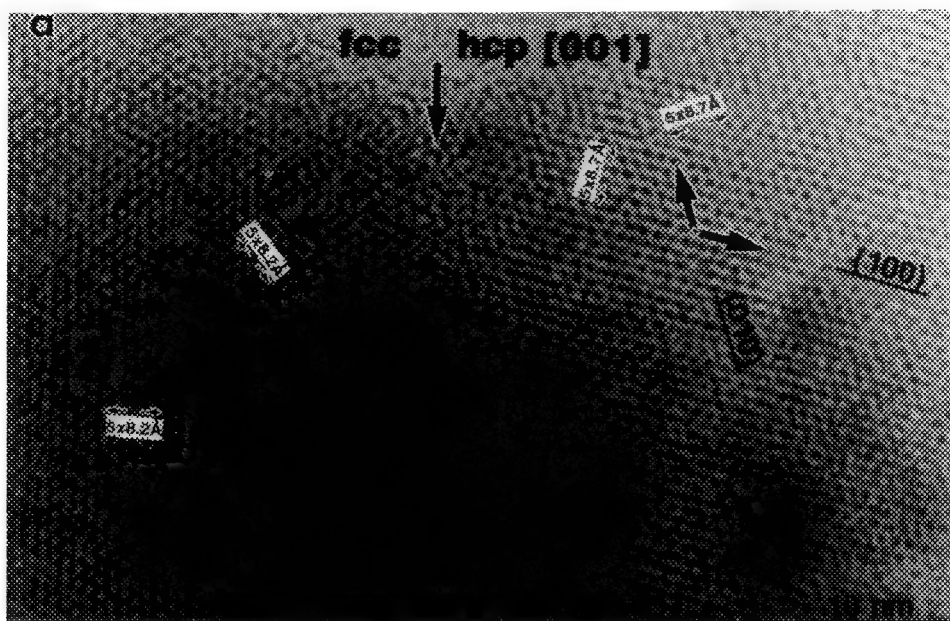
Fig. a. two types of crystallites of fcc and hcp symmetry were found bound together in the sublimed C_{60} sample. A region of disorder joins the two crystallites, as indicated by an arrow.

Fig. b. a C_{60} crystal in [111] projection with {220} spacing of 5.0Å.

HIGH-RESOLUTION IMAGING OF CERAMICS

C. Barry Carter and Stuart McKernan

Department of Chemical Engineering & Materials Science, Amundson Hall, 421 Washington Avenue, SE, University of Minnesota, Minneapolis, MN 55455

Ceramic materials have now been studied for many years using high-resolution transmission electron microscopy (HRTEM). The technique has had a major impact on our understanding of both the solid-sate chemistry of the materials themselves and the interfaces and defects present in the materials. The development of both aspects of the field have progressed in parallel as summarized in Figure 1. It is the purpose of this paper to review the current status and assess the needs for future studies.

HRTEM is uniquely suited for examining the chemistry and structure of ceramic materials on the local scale. Although it does not directly give information on the chemical composition of these materials, it does provide information on the local crystal structure which can, in turn, be used to infer the local crystal chemistry. A particularly clear illustration of such an application is shown in Figure 2 where a small particle with the spinel structure has grown inside a matrix of olivine as a result of internal oxidation of the matrix. The selected-area diffraction pattern confirmed the FCC nature of the particle although due to its small size, the diffraction spots were all considerably elongated [1].

The HRTEM image in Figure 2 also illustrates the second application to ceramics, namely locating, identifying and characterizing defects and interfaces. The structural interface between the two phases is clearly very sharp although the image gives no direct information about the chemistry. More information concerning the chemistry can be extracted by careful and systematic use of image simulation programs; this information should, of course, be supplemented where possible by z-contrast imaging or high-resolution analytical electron microscopy (HRAEM). However, the distances which are often of importance in ceramic materials, as in many other systems, are frequently too small for either of these techniques as is illustrated in Figure 3 for the spinel/NiO interface; here the pseudo-close-packed oxygen planes are only 2Å apart [2,3]. This interface is shown schematically in the <110> projection and emphasizes another difficulty: even in this "open" projection, some of the atomic sites, for example the occupied tetrahedral sites, will essentially be overlapping when viewed by HRTEM. It is essentially the occupancy of these sites which defines the position of the interface.

The situation for grain boundaries and surfaces viewed in profile is similar. In these cases, as for the others discussed above, the situation is complicated further by the methods used to thin the sample for observation in the electron microscope [4]. When a defect is present in a ceramic, it can induce a local change in the density of the material which will influence the HRTEM image through the Fresnel contrast from the defect region. This effect is directly related to the local change in inner potential seen by the electron beam. Unfortunately, the "density", and thus the contrast, can also be affected by preferential thinning at the defect or segregation of lighter/heavier atoms to the defect region [5]. Examples of both experimental and theoretical results will be presented [6].

References

1. McKernan, S., Carter, C.B., Ricoult, D. and Cullis, A.G., MRS. Symp. Proc. (1990) **159**, 407.
2. Summerfelt, S.R. and Carter, C.B., Acta Metall. Mater. (1992) in press.
3. Summerfelt, S.R. and Carter, C.B., Phil. Mag. (1992) in press.
4. Kouh, Y.M., Carter, C.B., Morrissey, K.J., Angelini, P., and Bentley, J., J. Mat. Sci. (1986) **21**, 2689.
5. Rasmussen, D.R. and Carter, C.B., Ultramicroscopy (1990) **32**, 337-348,
6. The author would like to acknowledge many valued discussions former students and postdocs at Cornell University. This research is supported by the DoE under grant No DE-FG02-89ER45381 and NSF under grant No. DMR-8901218
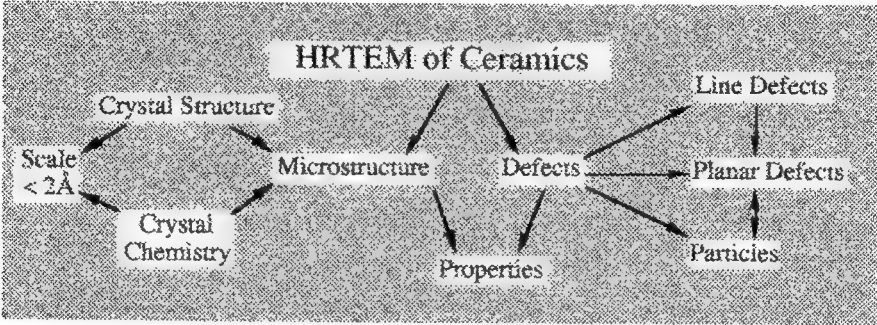
Figure 1 The impact of HRTEM on the understanding of ceramic materials. This simplified schematic emphasizes the relationship between different defects and the structure of the material.
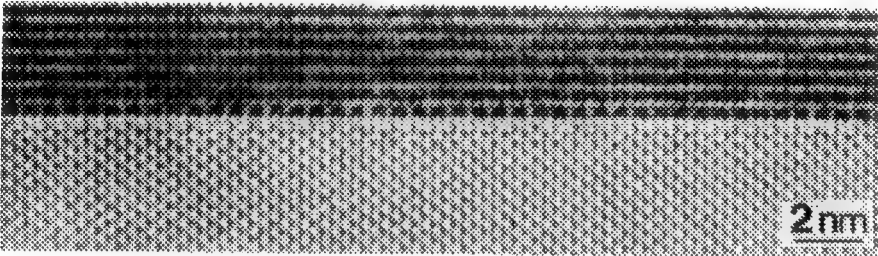
Figure 2 The interface between olivine and spinel viewed by HRTEM (the spinel appears darker).
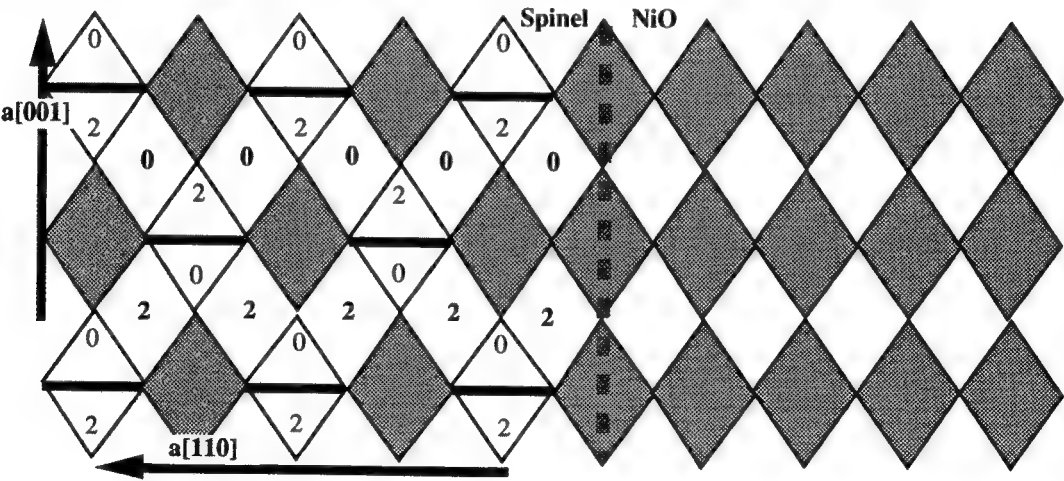
Figure 3 A schematic diagram illustrating the geometry of the spinel/NiO interface; the vertical dashed line indicates the position of the interface. Cations are present at 4 levels (0,1,2,3); dark rhombi represent octahedra occupied on levels 1 and 3; open rhombi represent octahedra occupied on levels 0 and 2. Lattice vectors shown in the spinel are 0.8nm and 1.1nm long. Bars identify the positions of occupied tetrahedra.

113

APPLICATIONS OF HREM TO THE STRUCTURAL ANALYSIS OF CRYSTALLINE INTERFACES

U. Dahmen, N. Thangaraj and P. Lours

National Center for Electron Microscopy, University of California, LBL, Berkeley, CA 94720

The investigation of the atomic structure of crystalline interfaces by HREM has recently become more prominent because of greatly improved resolution of modern electron microscopes, better means of sample preparation and wider availability of more generally applicable atomistic simulation procedures. As a result, a number of recent investigations have reported new and interesting features of crystalline interfaces and compared them with models based on atomistic, crystallographic or elastic theories. Examples of such features are stand-off dislocations in metal-ceramic[1] and ceramic-ceramic[2] interfaces, structural multiplicity of grain boundaries[3], solute segregation to selected facets[4], grain boundary microfaceting[5] and dissociation[6] and elastic distortion fields around interfacial ledges[7].

This paper will present an overview of some of these recent advances due to high resolution electron microscopy with an emphasis on the quantitative information that has been obtained from these studies.

In addition, detailed examples of ongoing HREM work on the atomic structure of grain boundaries in mazed bicrystal films of Al will be given. These films have a unique microstructure which may be described as a polycrystalline layer with only two allowed grain orientations. As a result of their special crystallography, this microstructure displays only 90° <110> tilt boundaries. Because all boundaries are free to migrate to their optimum orientations (inclinations), a well-annealed mazed bicrystal film gives a good indication of the preferred boundary orientations. These special boundaries can then be studied in detail by HREM. Two boundary inclinations are found to be preferred, the symmetrical (557)|(55$\bar{7}$) boundary and the asymmetrical (001)|(110) boundary (see Fig. 1). The symmetrical boundary lies along (100) or (110) mean boundary plane and is periodic with a relatively short repeat period. Its structural unit was found to agree with that predicted by atomistic simulations[8]. By comparison, the asymmetrical boundary lies on a (11$\sqrt{2}$) mean boundary plane and is not periodic even though along the interface two low-index planes are parallel. Since the periodicities of planes perpendicular to the boundary are in the ratio of $1/\sqrt{2}$, this boundary will be quasiperiodic, i.e. although it displays local relaxations, the spacing of the relaxed structural units can never be periodic. It is difficult to model such non-periodic structures theoretically, and structural analysis must begin with models based on experimentally obtained images. The important feature to be obtained from a high resolution analysis of the boundary structure is the type of local relaxation into structural units rather than spacing between centers of atomic relaxation.

A similarly non-periodic heterophase interface is commonly observed in Al-Ge alloys aged to form plate-shaped precipitates on (111) planes. Fig. 2 shows a high resolution micrograph of such an interface viewed along a common <110> zone axis. The precipitate is seen to obey the cube-twin orientation relationship typical for many of these plates. As in the case of the quasiperiodic grain boundary, the feature of interest is the fact that along the interface the periodicity of the two lattices is not commensurate. However, unlike the grain boundary, here no localized relaxation could be detected and the interface could be adequately described by a simple geometrical model[9].

114

References

1. e.g. W. Mader, Z. Metallk. **80**, 139 (1989)
2. A. Heuer, private communication
3. e.g.,V. Vitek et al. Scr. Met. **17**, 183 (1983), M. Mills, M.S. Daw, MRS Proc. **183**, 15 (1990)
4. e.g., D.E. Luzzi et al., Phys Rev. Lett. **67**, 1894, 1991
5. e.g., M.D. Vaudin et al., Acta Met. **31**, 1109 (1983), K. Merkle and D. Wolf, MRS Proc. **229**, 185 (1991)
6. e.g., A. Garg and W.A.T. Clark, MRS Proc. **122**, 75 (1988)
7. R. Bonnet and M. Loubradou, MRS Proc. **238**, (1992), in press
8. U. Dahmen, C.J.D. Hetherington, M.A. O'Keefe, K.H. Westmacott, M.J. Mills, M.S. Daw and V. Vitek, Phil Mag. Lett., **62**, 327 (1990)
9. This work is supported by the Director, Office of Energy Research, Office of Basic Energy Sciences, Materials Sciences Division of the U.S. Department of Energy under Contract No. DE-ACO3-76SFOOO98.

Fig. 1.-- HREM image of non-periodic asymmetrical 90° <110> tilt grain boundary in Al showing localized atomic relaxations (ARM at 800keV and Scherzer defocus).
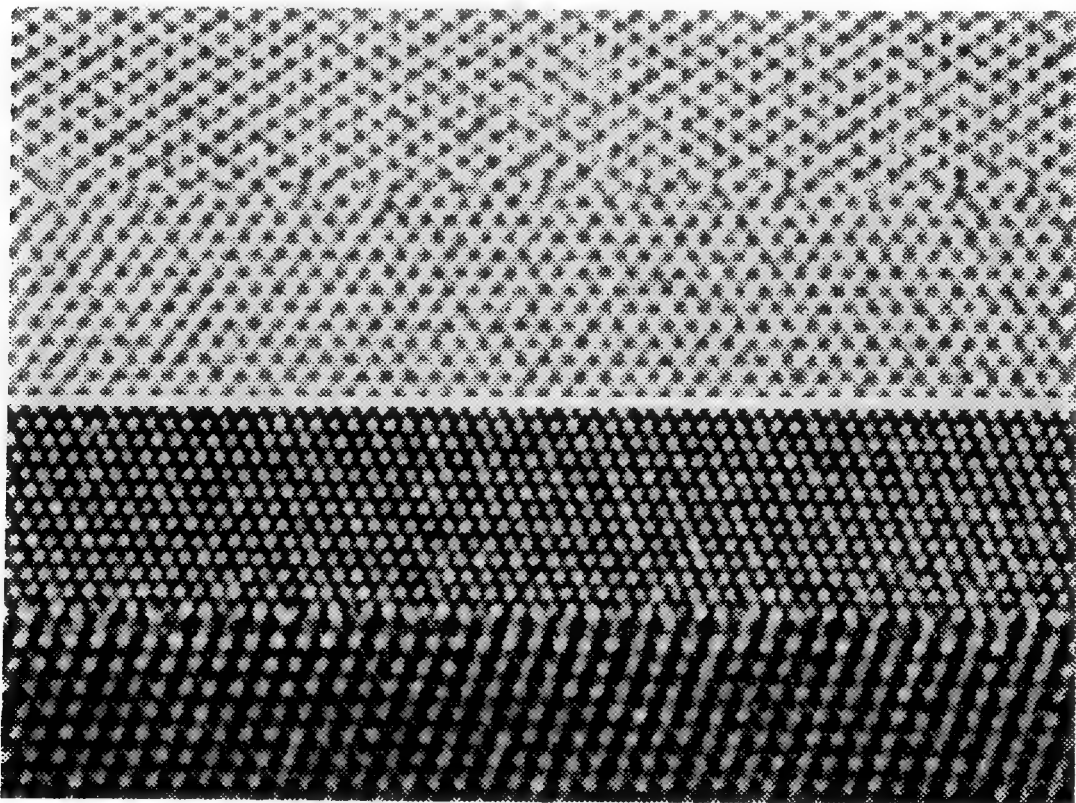
Fig. 2.--High resolution image of non-periodic Al-Ge precipitate/matrix interface displaying no apparent atomic relaxation (ARM at 800keV and approximately -800Å defocus).

EXTENSION OF THE "THIN-CRYSTAL" CONDITION BY SMALL CRYSTAL TILTS: WHY HREM IMAGES OF SiC POLYTYPES ALWAYS LOOK TILTED

Michael A. O'Keefe and Velimir Radmilovic⬦

National Center for Electron Microscopy, University of California and LBL, Berkeley, CA 94720
⬦Permanent address: University of Belgrade, Dept. of Physical Metallurgy, Belgrade, Yugoslavia

Both experimental and simulated high-resolution electron microscope images of silicon carbide polytypes commonly exhibit symmetry changes in thicker crystal regions compared to the perfect (projected) space group symmetry of images from thin crystals. However, the changes predicted by simulation, and those found experimentally, are quite different.

High-resolution transmission electron microscope images of silicon carbide polytypes were obtained with the JEOL ARM-1000 high-resolution electron microscope in the course of an investigation into a series of metal matrix composites.[1] Like all HRTEM images of silicon carbide, these images failed to show the correct symmetry in the thicker parts of the specimen. Changes in image symmetry as crystal thickness is increased also occur when images of silicon carbide are simulated; for example, Smith and O'Keefe[2] simulated images of polytypes of silicon carbide for crystals oriented so that the electron beam was precisely along the $<1\bar{2}10>$ direction, and found marked departure from thin-crystal symmetry at thicknesses of the order of 150Å for an electron energy of 500keV. However, the lack of symmetry in their simulated images appears to be due to the presence of many second-order terms[3,4] contributing to the intensity spectra of the thick-crystal images, whereas the symmetry changes in experimental images from thicker crystals are usually of the form that preserves the thin-crystal-like contrast for one set of "twin" spots, yet smears out the contrast of the other. A typical example of this latter effect can be seen in the image of the 6H variant of SiC shown in figure 1.

Following the procedures given by Wang et al[5], we analyzed the diffractogram of the image from which figure 1 was extracted (the area was approximately twenty times that shown in figure 1 and the image character did not vary appreciably), and found that this area of crystal was tilted about 2⁰ so that the Laue circle center was close to h,k =25,10. Simulations using the NCEMSS[6] programs confirmed that the best match occurred for a tilt of 2.33⁰ (fig.1 insert). This result is in agreement with the findings of Smith et al[7] that, although the image from thicker areas is "smeared", this degree of specimen tilt can still produce a good structure image from areas of thin crystal.

Subsequent examination of many other examples of images of silicon carbide polytypes showed that experimental images were invariably obtained from tilted specimens. To shed light on why HRTEM operators appear to choose tilted conditions for SiC imaging, we computed maps of SiC-6H images as a function of crystal thickness and tilt. An example of such a map (fig.2), shows that "on-axis" images (col.1) appear as "good" structure images to a thickness of only 100Å, whereas images tilted by 6mrad (col.2) show "thin crystal" character up to almost 200Å. Images tilted by greater amounts (cols.3&4) show the familiar "smeared" character of figure 1. Obviously, an operator faced with a good image showing thin-crystal character up to almost 200Å would not willingly tilt into a condition in which thin-crystal character vanishes at 100Å -- i.e. to column 1 from column 2 (or even from column 3 or 4).

Of course, the tilted images show extended thin-crystal character because columns of atoms no longer stack exactly along the electron beam direction; thus the projection of the tilted columns produces much lower amplitudes in the projected potential, a condition that allows the weak-phase-object approximation to be satisfied[8] to much greater specimen thicknesses, and reduces the contribution of the "second-order" terms[3] which dominate[2] simulated thick-crystal on-axis images.[9]

1. V. Radmilovic, M.A. O'Keefe & G. Thomas, *Proc. 10th Euro. Congr. on Electron Microscopy,* Granada, Spain, (1992).
2. David. J. Smith & M.A. O'Keefe, *Acta Cryst.* A**39** (1983) 322-324.
3. M.A. O'Keefe, *37th Ann. Proc. EMSA,* San Antonio, Texas (1979) 556-557.
4. M.A. O'Keefe and W.O. Saxton in *41st Ann. Proc. EMSA,* Phoenix, Arizona (1983) 288-289.
5. D.N. Wang, S. Hovmöller, L. Kihlborg and M.Sundberg, *Ultramicroscopy* **25** (1988) 303-316.
6. R. Kilaas, Proc. *45th Ann. Meeting EMSA, Baltimore* (1987) 66 - 69.
7. D.J. Smith, W.O. Saxton, M.A. O'Keefe, G.J. Wood & W.M. Stobbs, *Ultramicro.* **11** (1983) 263.
8. M.A. O'Keefe, *Proc. 3rd Pfefferkorn Conf. on Electron Optical Systems,* (1984) 209-220.
9. The assistance of J.H. Turner with image processing is gratefully acknowledged. This work was supported by the Director, Office of Energy Research, Office of Basic Energy Sciences, Chemical Sciences Division of the U.S. Department of Energy, under contract No. DE-AC03-76SF00098.
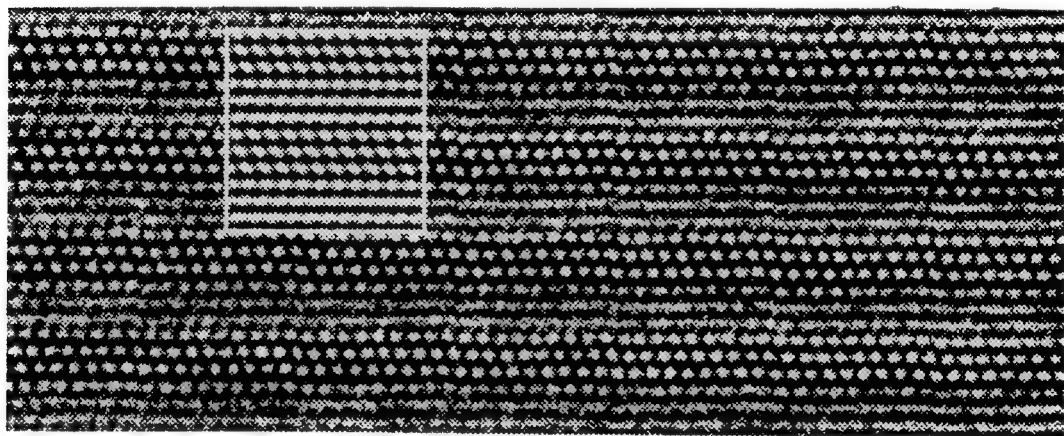
Fig.1. An experimental image of polytypical SiC obtained with the JEOL ARM-1000 at 800keV for Scherzer focus. The insert shows a simulated image[6] of 6H SiC of 115Å thickness with Laue circle center at h,k = 25,10. C_S = 2mm, defocus value of -600Å, convergence semi-angle of 0.8mrad, spread of focus of 140Å halfwidth.
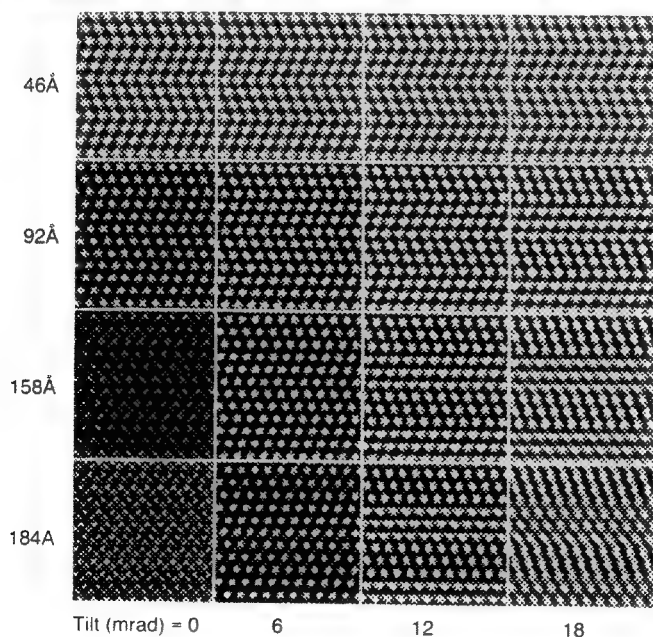
Fig.2. Map of crystal tilt (across) out to 1°, with crystal thickness (down) to 184Å for 6H SiC under ARM conditions.

HIGH – RESOLUTION TRANSMISSION ELECTRON MICROSCOPY OF Al-Cu-Fe QUASICRYSTALS

WILLIAM KRAKOW[1], DAVID P. DiVINCENZO[1], PETER A. BANCEL[1], ERIC COCKAYNE[2] and VEIT ELSER[2]

[1]IBM Research Division, T. J. Watson Research Center, P. O. Box 218, Yorktown Heights, NY 10598, USA; [2]Dept. of Physics, Cornell University, Ithaca, NY 14853

High resolution electron microscopy and electron diffraction have always been key tools for the study of quasicrystals.[1] The unique features of quasicrystals are their long range orientational order despite the absence of periodic translational order, and their non-crystallographic symmetry. The early work in electron microscopy and diffraction assessed the degree of perfection of these materials; microdomains with slightly different orientations, phason strains and dislocations were found which masked the fundamental atomic structure. A defect free material was sought to deduce the atomic arrangement of these materials and this was found in Al-Cu-Fe. Preliminary examinations of these materials using 20 at.% Cu and 15 at.% Fe indicated they are almost entirely free of phason strains when viewed in a 200kV microscope.[2-4] At the time of these investigations the microscopes employed were limited in resolution and thus provide limited information about the atomic arrangements of these quasicrystals. Recently, studies were made using a more powerful microscope operating at 400kV where the point resolution is improved to 1.7Å.[5,6] In that case, a Al-Mn-Si specimen was viewed along the five-fold axis under apparent optimum imaging conditions. These prior studies have interpreted various image features as being due to dynamical scattering processes and therefore little about the atomic arrangement of the quasicrystal is obtained. Our interpretation of the image feature is different and is due to modification of the phase contrast transfer function. Here clarification is given of the information contained in high resolution micrographs of quasicrystals.

The Al-Cu-Fe quasicrystals were prepared from elemental constituents by high temperature annealing for several days. Samples were then prepared by dispersing shards onto holey carbon films and looking at the edges where the specimens are thinnest. Fig. 1 shows two enhanced micrographs taken at a 400kV incident beam energy with the five-fold axis parallel to the incident beam direction. For image (a) the objective lens was adjusted to be near Scherzer focus. Although it is not shown in this small field of view, further from the specimen edge dynamical and inelastic scattering events dominate; image features become washed out and atomic features are difficult to discern. Image (b) is from a different area which has a defocus value about 300Å further under focus than (a). Here a different type of ten-fold spoke pattern is observed.

In order to interpret the lattice images, models of Al-Cu-Fe were developed for image simulations by: 1) choosing an appropriate atomic cluster motif, 2) joining clusters to form tiles, 3) constructing space-filling tiling with long range quasiperiodic order. A large quasicrystallite is obtained for image simulations containing 59,567 atoms and is 80Å thick along the five-fold axis. Fig. 2 shows image simulations at defocus values of: (a) 250, (b) 450 and (c) 750Å underfocus. Image (d) is the projected model structure. Below each image is its corresponding optical transform. The correspondence between the atom positions in the model and the image can be seen from the pentagon superimposed on each image. (a) and (c) show white atom positions; (b) has black atom positions. The most important result of our study is, at least locally, we have determined the microscope conditions which lead to the most faithful images of the projected atomic structure.

1. D. Shechtman, I. Blech, D. Gratias and J.W. Cahn, Phys. Rev. Lett., **53**, No. 20, (1984) 1951-1953.

2. A.-P. Tsai. A. Inoue and T. Matsumoto, Japanese J. of Appl. Phys., **26**, No. 9, (1987) L1505-1507.

3. K. Hiraga, B.-P. Zhang, M. Hirabayashi, A. Inoue and T. Matsumoto, Japanese J. of Appl. Phys., **27**, No. 6, (1988) L951-953.

4. T. Ishimasa, Y. Fukano and M. Tsuchimori, Phil. Mag. Lett., **58**, No. 3, (1988) 157-165.

5. K. Hiraga and D. Shindo, Mater. Trans., JIM, **31**, No. 7, (1990) 567-572.

6. K. Hiraga, in *Quasicrystals: The State of the Art*, eds. D. P. DiVincenzo and P. J. Steinhardt, (World Scientific, Singapore, 1991) 95-110.
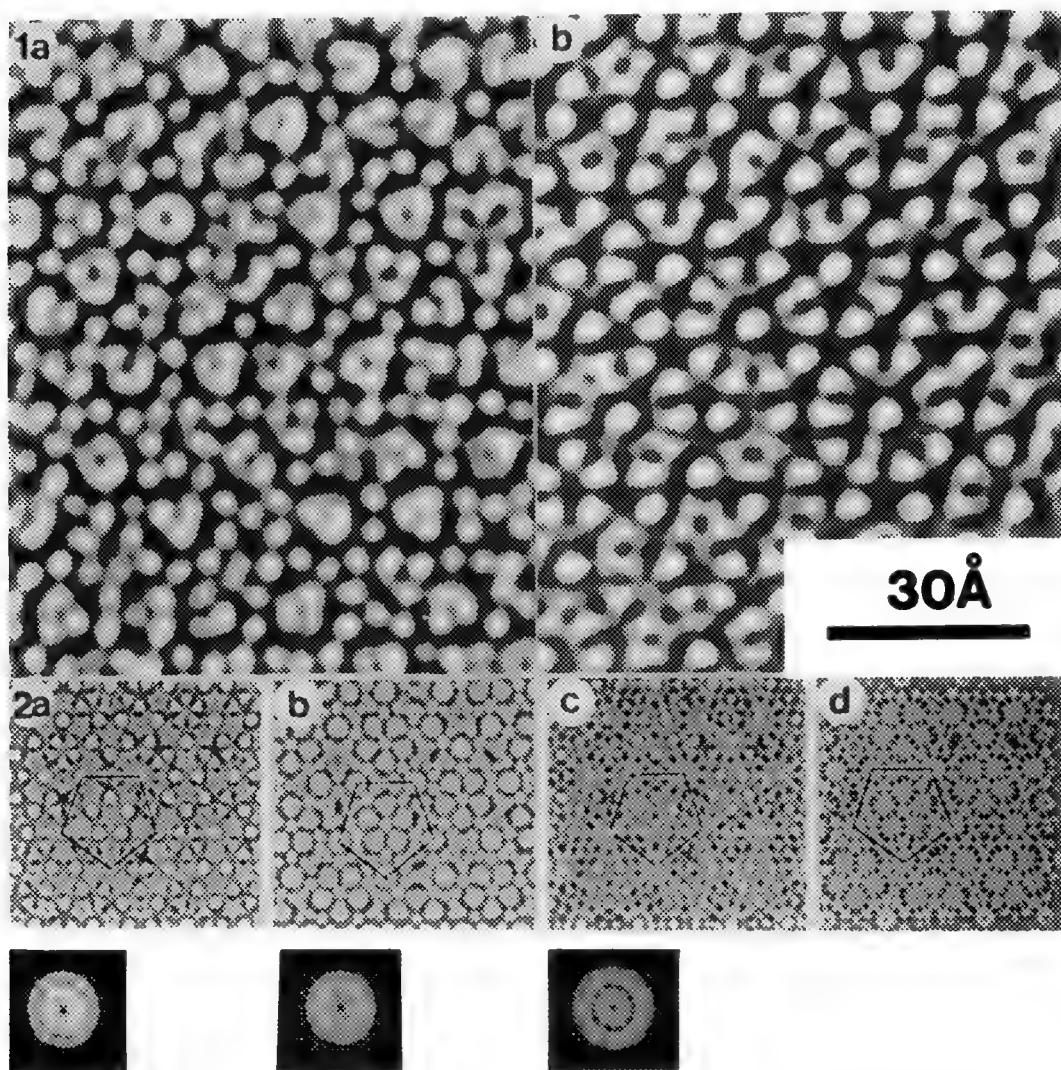
Fig. 1. Bright-field images of Al-Cu-Fe along the five-fold axis at 400kV. (a) Scherzer focus, (b) 300Å further underfocus.

Fig. 2. Computer simulated bright-field images with axial illumination at 400kV. Defocus values: (a) 250, (b) 450, (c) 750Å. (d) is the projected model.

CHARACTERIZATION OF STRUCTURAL UNITS IN TILT GRAIN BOUNDARIES

Stuart McKernan and C. Barry Carter

Department of Chemical Engineering and Materials Science, Amundson Hall, University of Minnesota, Minneapolis, MN 55455

General tilt grain boundaries can be viewed in terms of small structural units of varying complexity. High-resolution electron microscope (HREM) images of these boundaries in many materials show this repetitive similarity of the atomic structure at the boundary plane. The structure of particular grain boundaries has been examined for several special cases and commonly observed configurations include symmetric tilt grain boundaries and asymmetric tilt grain boundaries with one grain having a prominent, low-index facet. Several different configurations of the boundary structure may possibly occur, even in the same grain boundary. There are thus many possible ways to assemble the basic structural units to form a grain boundary. These structural units and their distribution have traditionally been examined by high-resolution electron microscopy. The images of the projection of the atomic columns (or the tunnels between atomic columns) providing a template for constructing "ball-and-stick" models of the interface.

There are several potential pitfalls in the interpretation of HREM images of boundaries. The contrast of images obtained in this way is extremely insensitive to the presence of dislocations lying in the plane of the grain boundary [1]. The images are also affected by steps or ledges in the boundary plane, which occur within the thickness of the foil. Also since the bonding at the grain boundary is different from that in bulk material, it may be expected to erode at a different rate to bulk material during the specimen preparation process, leading to preferential grooving along the grain boundary, or even amorphization of substantial amounts of the grain boundary region. The assignment of atom positions at the interface on the basis of image contrast in the HREM images must therefore be carried out with considerable care. This is particularly true if a more detailed analysis is required than, for example, a identification of the presence of 5-fold and 7-fold coordinated rings in <110> tilt grain boundaries of semiconductors. For accurate determinations of the morphology of these structural units careful image simulation and matching procedures are required.

The interface in a Σ=27 <110> tilt grain boundary segment in Ge [2] is shown in the HREM images in Figures 1. These images form part of a through-focus series, and show the extreme sensitivity of the contrast at the grain boundary to the precise imaging conditions. The contrast of the bulk material in both grains is relatively unaffected by the change in focus, whereas the contrast generated by the structural units varies from very weak in the upper image to very strong in the lowest one. Through-focus, through-thickness series such as these can be used to determine the thickness and misorientation of the bulk crystals. By combining the information from all the micrographs in the series, the requirements for any particular structural model to match the image contrast become more stringent. A degree of sensitivity to structure along the electron beam direction is also acquired. By varying the defocus over a larger range than in bulk material, additional information about the grain boundary structure may be obtained. At relatively large defocus values, the presence of end-on dislocations parallel to the beam direction may be revealed because of the change in inner potential at the dislocation cores. At even larger defocus values Fresnel fringes are obtained which have previously been used to investigate various average grain boundary properties [3]. By combining these different techniques it should be possible to obtain a more detailed image of the structural units. The characterization of these structural units and the relationship between the structure of the boundary and the contrast of the different HREM images will be reported, using both experimental and simulated images [4].

References

1. D. R. Rasmussen and C.B. Carter; Phil. Mag. (1990) **A63**(3), 503.
2. Z. Elgat, and C.B. Carter; Ultramicroscopy (1985) **18**, 313.
3. D. R. Rasmussen and C.B. Carter; Ultramicroscopy (1990) **32**, 337.
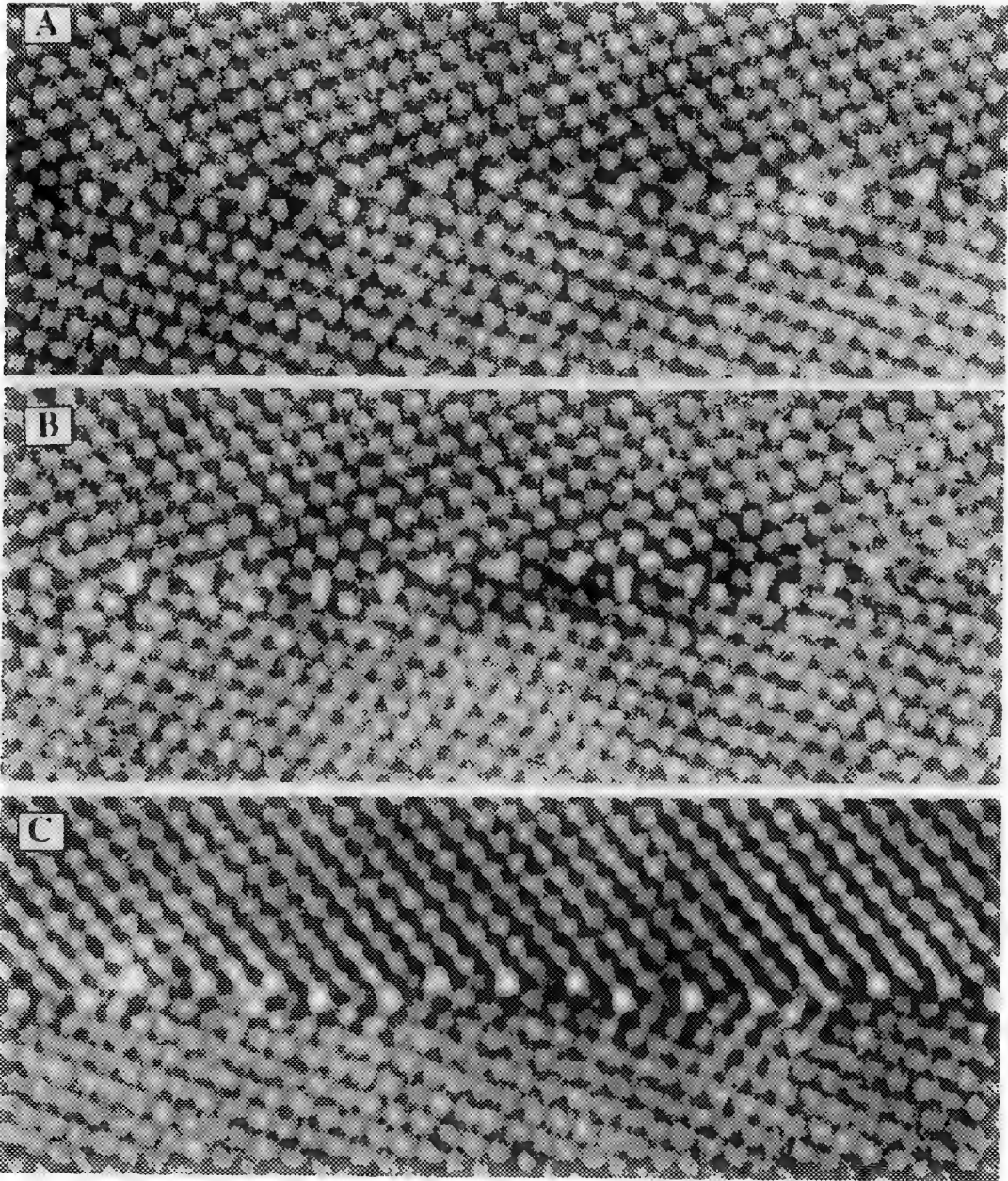
Figure 1 Three high-resolution electron micrograph of a near $\Sigma=27$ tilt grain boundary in Ge, viewed along the [110] tilt axis at different defocus values. The atomic columns appear dark. Note that the contrast of the boundary region is close to that of the grain interior in the top image, slightly enhanced in the middle image, and greatly enhanced in the bottom image.

CHARACTERIZATION OF Rh/Si MULTILAYER STRUCTURE BY HREM AND HAADF

Y. Cheng, J. Liu*, M.B. Stearns and D.G. Stearns**

Physics Department, Arizona State University, Tempe, AZ 85287
*Also at Center for Solid State Science, Arizona State University, Tempe, AZ 85287
**University of California, Lawrence Livermore National Laboratory, Livermore, CA 94550

The Rh/Si multilayer (ML) thin films are promising optical elements for soft x-rays since they have a calculated normal incidence reflectivity of ~60% at a x-ray wavelength of ~13 nm. However, a reflectivity of only 28% has been attained to date for ML fabricated by dc magnetron sputtering.[1] In order to determine the cause of this degraded reflectivity the microstructure of this ML was examined on cross-sectional specimens with two high-resolution electron microscopy (HREM and HAADF) techniques .

Cross-sectional specimens were made from an as-prepared ML sample and from the same ML annealed at 298 °C for 1 and 100 hours. The specimens were imaged using a JEM-4000EX TEM operating at 400 kV with a point-to-point resolution of better than 0.17 nm. The specimens were viewed along Si [110] projection of the substrate, with the (001) Si surface plane parallel to the beam direction.

All these specimens were also viewed using the newly developed high angle annular-dark-field (HAADF) microscopy which provides an image having contrast proportional to the square of the atomic number. Thus HAADF is found to be very useful for characterization of the compositional variation of ML thin films. The HAADF images were obtained on a HB-5 STEM operated at 100 kV which has an incident beam probe size of 0.3 nm and an inner detection angle of 100 mrad. This detection angle has been found to be sufficiently large to eliminate most of the diffraction and phase contrast presented in bright field TEM and thus insures high atomic number sensitivity.[2]

Figure 1 shows the HREM image and HAADF intensity line scan of the as-prepared ML sample. The HREM image (1a) shows that the ML has a very regular and well defined layer structure. This was also confirmed by small angle x-ray scattering and selected area electron diffraction of the same sample. The bilayer thickness was found to be 7.00 nm with 5.21 nm and 1.86 nm Rh-rich and Si-rich regions, respectively. The Rh and Si layers appear to be amorphous with no discernable Rh crystallites. The HAADF intensity line scan (1b) shows the compositional modulation of the layer structure with a intensity contrast of ~1.6. The HAADF intensity contrast of an ideal Rh/Si ML is expected to be $(Z_{Rh}/Z_{Si})^2$, which is 10.3. The small intensity contrast of the Rh/Si sample indicates that the ML was highly interdiffused during deposition. Since the degree of roughness at the interfaces is seen to be very small from the HREM image, the low reflectivity of the Rh/Si ML is apparently caused by the interdiffusion of the Rh and Si atoms. Fig. 2a shows the HREM image of the ML annealed at 298 °C for 1 hour. The bilayer thickness was observed to be 6.81 nm, which is smaller than the as prepared sample due to ML contraction after annealing. The Rh and Si layers were seen to be further diffused with the Rh-rich region increased to ~6.05 nm and a corresponding decrease of Si-rich region to ~0.79 nm. The HAADF intensity line scan, as seen in Fig. 2b, shows an decrease of image contrast from ~1.6 to ~1.3 due to increased interdiffusion. After the ML was annealed for 100 hours at 298 °C, the layered structure almost disappeared, as shown in Fig. 3 of the HREM image and the HAADF intensity line scan. In conclusion, the as prepared Rh/Si ML was found composed of amorphous Ru-rich and Si-rich layers. The Rh and Si atoms were seen to be highly diffused causing a significant decrease in normal reflectivity. The Rh/Si ML structure was found less thermally stable than other x-ray ML samples, such as Mo/Si ML. No Rh silicide crystallites were seen to be formed in the annealing process.[3]

References

1. D.G. Stearns, SPIE Proc., 1547(1992)2.
2. J. Liu and J.M. Cowley, Ultramicrosc., 34(1990)119; Ultramicrosc., 37(1991)50.
3. This work was supported by LLNL through the DOE contract No. W-7405-Eng-48, and by Shell Development Company, and made use of the ASU Facility for HREM, supported by NSF via grant DMR-8913384. The authors wish to thank D. Wright of Materials Preparation Laboratory of ASU for his help in preparing annealed ML samples.
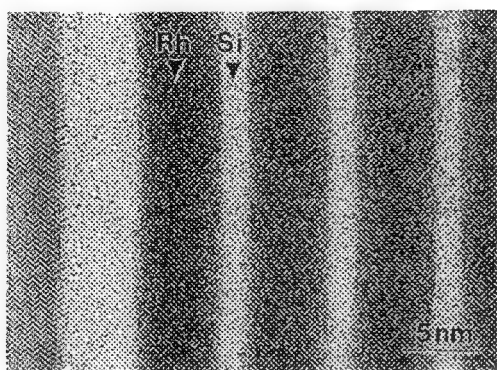
Figure 1a
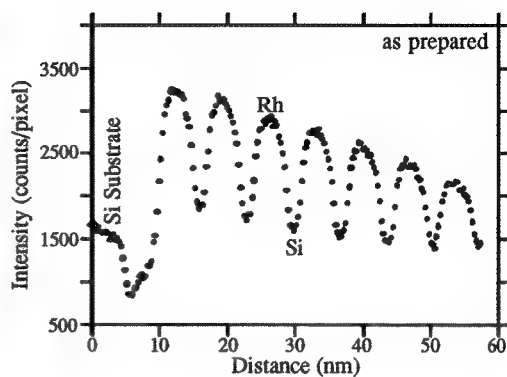
Figure 1b
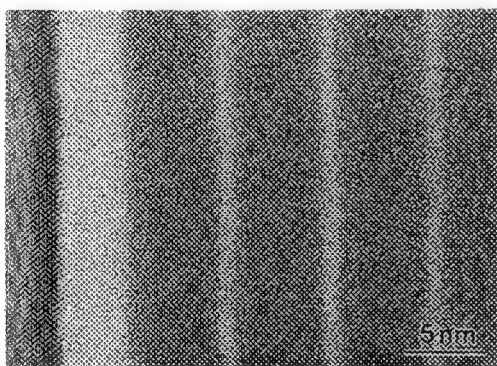
Figure 2a
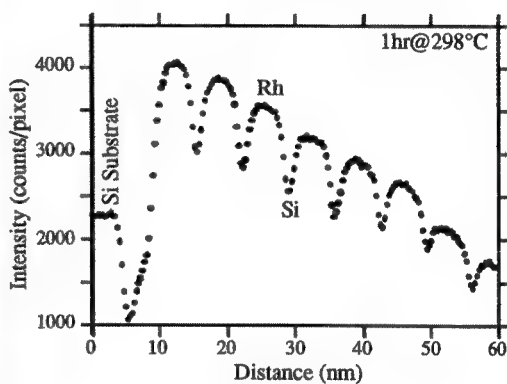
Figure 2b
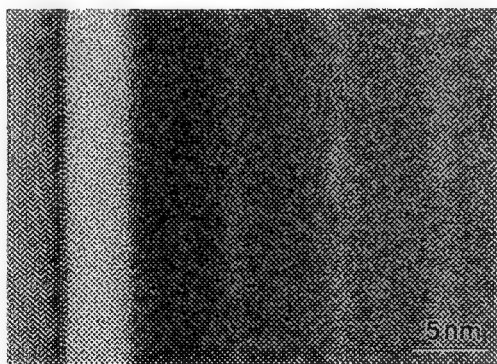
Figure 3a
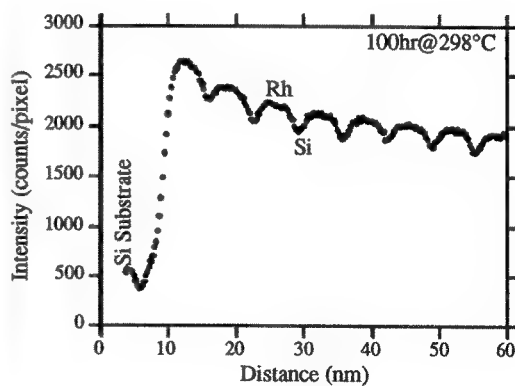
Figure 3b

FIG.1.--HREM image (a) and HAADF intensity line scan (b) of the as prepared Rh/Si ML.
FIG.2.--HREM image (a) and HAADF intensity line scan (b) of the Rh/Si ML annealed at 298°C for 1 hour.
FIG.3.--HREM image (a) and HAADF intensity line scan (b) of the Rh/Si ML annealed at 298°C for 100 hours.

STRUCTURES AND DEFECTS IDENTIFIED BY DARK-FIELD HREM

J.P.Zhang

Science and Technology Center for Superconductivity and Materials Research Center, Department of
Materials Science & Engineering, Northwestern University, Evanston, IL 60208

The tilted illumination dark field high resolution imaging technique was applied to structures and defects of semiconductors and superconductors. We used a Hitachi-H9000 top entry microscope with a high resolution pole-piece of Cs=0.9 mm, operated at 300 Kv. Proper apertures, tilting angle and imaging conditions were chosen to minimize the phase shift due to aberrations. Since the transmitted beam was moved outside the aperture, the noise ratio was greatly reduced[1], which resulted in a significant enhancement of image contrast and apparent resolution. Images are not difficult to interpret if they have a clear correspondence to structure - information from image simulations in bright field mode can be used to assist in dark field image interpretation.

An example in a semiconductor, $GaAs/Ga_{0.49}In_{0.51}P^2$ superlattice imaged along [110] direction is shown in Figure 1. In this dark field image the GaAs and GaInP layers can be easily distinguished by their different contrast, and the difference in quality between both sides of interfaces is clear. An enlarged image in Figure 1 shows the defective area on the rough side of interface. Since this image shows the same pattern as the [110] projection of an fcc structure, the major structural information about {111}, {200}, {220} planes can be obtained from this zone. Note that in bright field mode, [110] is not a good zone for imaging such multilayers[3].

In the new superconducting material, Ca-doped $YSr_2Cu_2GaO_7$,[4], dark field imaging was used to detect trace dopant atoms. Image simulation in bright field mode showed that hexagons in SrO-GaO-SrO sandwich layers, the major feature of this structure, appears as a 'flower' pattern in the image. We, therefore, can interpret the 'flower chain' in [021] dark field image, see Figure 2, as an indication of the location of the SrO-GaO-SrO layer, and the dotted lines between chains as the projected yttrium planes which are difficult to detect in a bright field image[5].

REFERENCES
1. J. C. H. Spence, "Experimental High_Resolution Electron Microscopy", Oxford Univ. Press, p216, 1988.
2. M. Razeghi, et al, J. Appl. Phys. **63** 4511 (1988).
3. H. Cerva and H. Oppolzer, Crystal Growth and Charact., **20** 231 (1990).
4. J. T. Vaughey, et al, Chem. Mater., **3** 935 (1991).
5. This work was supported by the Science and Technology Center for Superconducting on grand number NSF/DMR-8809854.

Figure 1. $GaAs/Ga_{0.49}In_{0.51}P$ superlattice viewed along [110] showing high contrast and good apparent resolution in a dark field image. Inset is an enlarged image of an interface area.
Figure 2. Dark field high resolution image from a [021] crystal of Ca-doped $YSr_2Cu_2GaO_7$ superconductor.

GaAs

GaInP

10 nm

2 nm

125
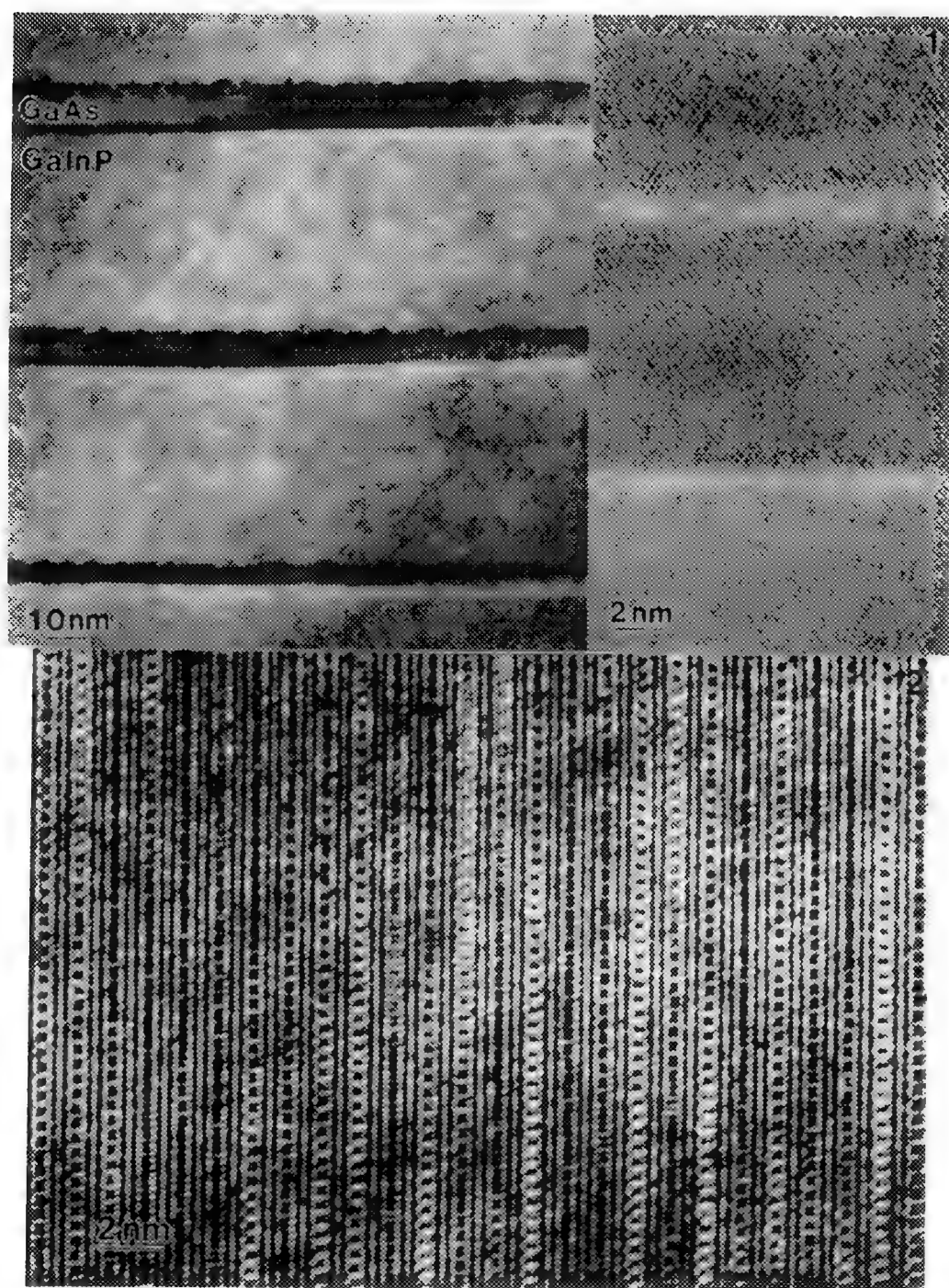
INTERPRETING HVEM OF MUSCLE CELL IMPULSE NETWORKS

Paul DeCosta, Kyugon Cho, Stephen Shemlon, Heesung Jun and **Stanley M. Dunn**

Department of Electrical and Computer Engineering, and Department of Biomedical Engineering,
Rutgers University, Piscataway, NJ 08855

Introduction: The analysis and interpretation of electron micrographs of cells and tissues, often requires the accurate extraction of structural networks, which either provide immediate $2D$ or $3D$ information, or from which the desired information can be inferred. The images of these structures contain lines and/or curves whose orientation, lengths, and intersections characterize the overall network.

Some examples exist of studies that have been done in the analysis of networks of natural structures. In [1], Sebok and Roemer determine the complexity of nerve structures in an EM formed slide. Here the number of nodes that exist in the image describes how dense nerve fibers are in a particular region of the skin. Hildith [2] proposes a network structural analysis algorithm for the automatic classification of chromosome spreads (type, relative size and orientation).

The major inconvenience with the above methods is their inability to guarantee accurate extraction of network arcs and nodes and the low reliability of the algorithms when the images are noisy. In this paper we are proposing a network analysis algorithm that can permit near accurate extraction of network arcs and intersections. Our algorithms are applied to HVEM stereo pair images of muscle fiber impulse networks.

We start by first producing a global segmentation of the network in each image of the stereo pair. The extracted networks in these primary segmentations are too thick to guarantee accurate detection of the vertices. The segmented images have to be *thinned* to provide a skeleton (one pixel thick) of the network before intersection detection algorithms can be applied. Next, the concept of forks and their neighbors is used for detecting nodes.

Image segmentation: A global segmentation of the stereo pair image can be obtained by using simple thresholding techniques. Thresholding is efficient if the peaks in the image histogram are resolved. This is not often the case especially in noisy images. Image quality can greatly be improved using filtering. Shemlon examines filtering and thresholding for images of natural structure in [3]. In the work we are reporting, simple thresholds for segmentation can either be operator specified or automatically chosen from an examination of the image histogram [3]. Figure 2 shows a segmentation of a single image of a stereo pair (Figure 1) of a muscle fiber network.

Network extraction: To insure accurate detection of network nodes, the segmented images produced above must be skeletonized. The skeletonization can be done using either regular thinning algorithms or binary morphological operations. Regular thinning operations iteratively delete boundary pixels whose removal would not violate the connectivity of a homogeneous region. Chen and Hsu's modified version [4] of Zhang and Suen's [5] fast parallel thinning algorithm is implemented for the experiments we are reporting.

A skeleton of the segmented image can also be obtained using the following morphological operation
$$S(X) = \bigcup_n s_n(X) \text{ where } s_n(X) = (X \ominus nB)/(X \ominus nB)_B, X/Y \text{ denotes set difference, } X \ominus B \text{ is the erosion of X by}$$
a structuring element B, nB is a structuring element obtained by dilating B by itself n times, and X_B is the closing of X by B. See J. Serra in [6] for details.

Unlike regular thinning, morphological skeletonization has the advantage of accurately reproducing network intersection points. Morphological operations however suffer from the inconvenience of possible violation of region connectivity constraints that are respected in classical thinning algorithms.

Figure 3 shows the thinned network extracted from the segmentation in Figure 2.

Intersection detection: In developing the method for node detection, characteristics of thinned intersects must be exploited. As shown in [7] all nodes are thinned into combinations of 3 and 4 *forks* using 4–connectivity constraints. A pixel with more than 2 neighbor sets, constitutes a fork. A neighbor set is made up of pixels with 4-neighbors, none of which belong to other sets. Thus, by merely searching the thinned image for these fork pixels, locations of nodes can be determined and pixel neighbor sets of each of the forks can then be used to find linked nodes. This

126

nodal information can be used to match stereo pairs and create a $3D$ representation of the network.

Figure 4 shows the nodes detected in the extracted network in Figure 3.

Conclusions: This new robust network processing procedure is capable of accurately extracting and efficiently representing structures of networks in the images we have processed. Our procedure has been shown to be effective in representing structure and locating nodes in muscle fiber images. However, its usage is not at all limited to this study. Because of its versatility, it can be used on any image containing a network whose node location and links are of interest.

In future we hope to incorporate robust image processing routines to handle noisy images and some intelligent histogram analysis routines to handle cases of unresolved histogram modes. We are also working on algorithms for stereo pair matching and extraction of $3D$ information for the construction of $3D$ structures of the networks being analyzed.

References

[1] T. J. Sebok and L. E. Roemer, "An algorithm for line intersection identification," *Pattern Recognition*, vol. 13, no. 2, pp. 15-166, 1981.

[2] C. J. Hildith, "Linear skeletons from square cupboards,". *Machine Intelligence*, vol. 4, pp. 403-420, 1969.

[3] S. Shemlon, Image Segmentation with Models of Expected Structure, Masters thesis, Rutgers University, Piscataway, NJ 08855, May 1990.

[4] Y.–S. Chen and W.–H. Hsu, " A modified fast parallel algorithm for thinning digital patterns," *Pattern Recognition Letters*, vol. 7, pp. 99–106, February 1988.

[5] T. Y. Zhang and C. Y. Suen, "A fast parallel algorithm for thinning digital patterns" *Communications of the ACM*, vol. 27, number 3, pp. 236–239, March 1984.

[6] J. Serra, *Image Analysis and Mathematical Morphology*, Academic Press Limited, London, 1982.

[7] C. Liao and J. S. Huang, "Stroke segmentation by Bernstein-Bezier curve fitting," *Pattern Recognition* 23(5):475-484, 1990. vol. 23, number 5, pp. 475–484, 1990.
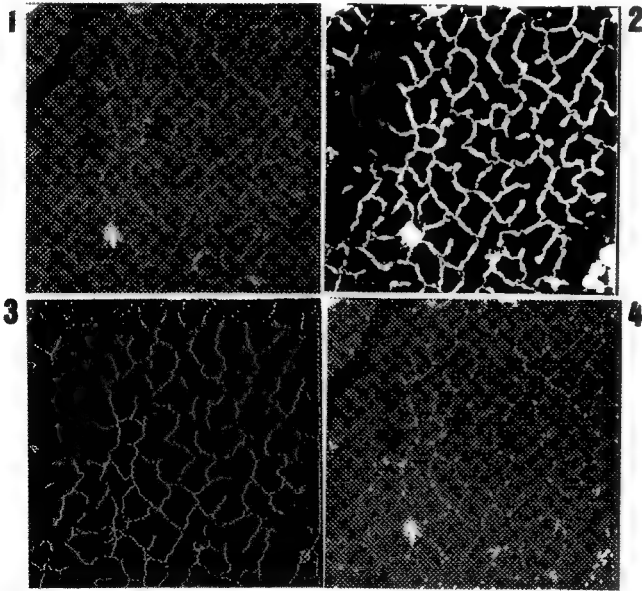
Figure 1: Gray level image.
Figure 2: Segmented image.
Figure 3: Extracted network.
Figure 4: Nodes detected.

TEST OF A METHOD FOR PHASE RETRIEVAL IN HREM

M.J. Beeching and A.E.C. Spargo

School of Physics, University of Melbourne, Parkville, Victoria 3052, Australia

1. Introduction

Several methods of phase retrieval from HRTEM image intensity distributions have been proposed but no standard method has emerged. We report on the results achieved using a technique based on a development of the "focus variation method" (1). The dependence of the retrieved wavefunction on various experimental parameters is investigated and the method tested using computer simulated images. The method is shown to be useful in finding the complex wavefield at the exit surface of the specimen, but the relationship of this to the specimen structure is left as a seperate problem.

2. The Retrieval Method

The wavefunction at defocus z is related to that at defocus 0 by

$$\psi(\bar{x}) = \psi_o(\bar{x}) * exp(-i\pi x^2/\lambda z)$$
$$= c + \int_{\bar{u} \neq 0} exp(-2\pi i \bar{u}.\bar{x})\psi_o(\bar{u})exp(i\pi \lambda z u^2)d\bar{u}$$

where the second equality follows by inverse fourier transform, with the $\bar{u} = 0$ term seperated out. Fourier transforming the image intensity, $\psi\psi^*$, and keeping terms to first order yields

$$\mathcal{F}\{I_z\} \simeq |c|^2\delta(\bar{u}) + c^*\psi_o(\bar{u})exp(i\pi \lambda z u^2) + c\psi_o^*(-\bar{u})exp(-i\pi \lambda z u^2).$$

If we have a stepped through focal series of images at defocus values $z_n = z_o + n\Delta$, each can be fourier transformed and then added together, with appropriate defocus-dependent phase multipliers, to yield the series

$$S(N, z_n, \Delta) = \sum_{n=0}^{N-1} \mathcal{F}\{I_{z_n}\}e^{-i\pi\lambda z_n u^2}$$
$$= A\delta(\bar{u}) + B\psi_o(\bar{u}) + C\psi_o^*(-\bar{u}) + \mathcal{O}(u^4)$$

where A and B are constants and

$$C = c\, exp(-i\pi\lambda u^2[2z_o + (N-1)\Delta])\, sin(N\pi\lambda\Delta u^2)/sin(\pi\lambda\Delta u^2).$$

In this series the first term contributes only at the origin, the second gives the required $\psi_o(\bar{u})$ and the third represents an unwanted contribution whose value determines the fidelity of the retrieved $\psi_o(\bar{u})$. The magnitude of the unwanted term is determined by the intereference function $I_N = sin(N\pi\lambda\Delta u^2)/sin(\pi\lambda\Delta u^2)$, the first major sideband peaks of which occur at $u_1 = 1/\sqrt{\lambda\Delta}$. For good wavefunction retrieval, u_1 should be outside the required resolution and the dependence of u_1 on Δ for various λ is shown in fig 1. For a given Δ and λ the fidelity depends on the strength of the unwanted term at $\bar{u} > 0$ and this can be assessed by the value of the halfwidth of I_N which is as shown in fig 2 as a function of N. These curves suggest that $N = 20 - 30$ should achieve faithful retrieval. The exit surface wavefunction can then be found, trivially, if the transfer function is known.

3. Test Results

The procedure has been tested using computer simulation techniques to generate a through focus series of images for the crystal structure of $Ti_2Nb_{10}O_{29}$. The series of images with focal step size of $30\mathring{A}$ were calculated for an accelerating voltage of $400kV$, $C_s = 0.94mm$, chromatic spread $80\mathring{A}$ and no divergence; as appropriate for a JEM 4000EX HRTEM. The recovered exit surface phase functions using N = 2 to 30 have been generated and a selection of these is shown in fig 3, together with the calculated phase function. Evidently the retrieved phase improves as N increases and for N = 30 the standard deviation of the difference is about 3°. The effects of some problems that inevitably arise when using 'real' experimental data rather than 'ideal' simulated test data are being investigated, including the experimental accuracy required in the determination of the defocus and defocus step values. The limitation imposed by noise is also being examined but this is not expected to be severe because the inherent resolution limitation imposed by the technique effectively applies a low pass filter to the noise.

(1) D. Van Dyck and W. Coene, Optik **77**, 3, 125 (1987).
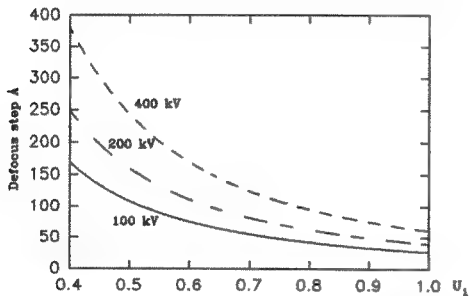
Fig 1. U_1 vs defocus step for various wavelengths.

Fig 2. Half width of I_N vs N.

Exact phase   N = 2   N = 3

N = 5   N = 10   N = 15

N = 20   N = 25   N = 30
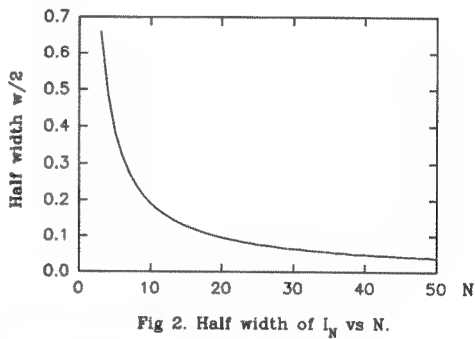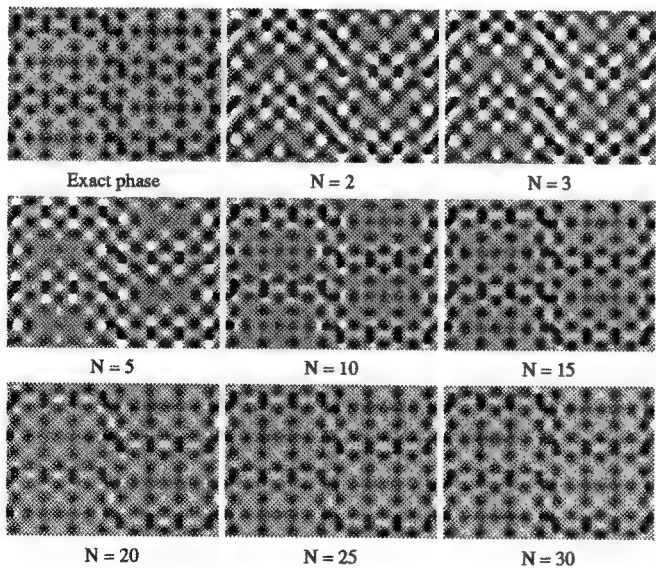
Fig 3.

Calculated wavefunction phase at exit surface of $Ti_2Nb_{10}O_{29}$ crystal and retrieved phase for values of N indicated.

DEFOCUS RAMP CORRECTION IN SPOT-SCAN IMAGING

Kenneth H. Downing

Lawrence Berkeley Laboratory, Berkeley CA, 94720

Three-dimensional structures of a number of samples have been determined by electron crystallography. The procedures used in this work include recording images of fairly large areas of a specimen at high tilt angles. There is then a large defocus ramp across the image, and parts of the image are far out of focus. In the regions where the defocus is large, the contrast transfer function (CTF) varies rapidly across the image, especially at high resolution. Not only is the CTF then difficult to determine with sufficient accuracy to correct properly, but the image contrast is reduced by envelope functions which tend toward a low value at high defocus.

We have combined computer control of the electron microscope with spot-scan imaging in order to eliminate most of the defocus ramp and its effects in the images of tilted specimens. In recording the spot-scan image, the beam is scanned along rows that are parallel to the tilt axis, so that along each row of spots the focus is constant. Between scan rows, the objective lens current is changed to correct for the difference in specimen height from one scan to the next.

The direction of the tilt axis, tilt angle, and required focus change are calculated from focus current values around the area of interest. The image is focused successively at four points as indicated in fig. 1, and the lens currents are read and used by the control computer to calculate the scan parameters. This procedure, at low resolution, keeps the entire image in proper focus. At higher resolution, some image defects are still present, although their effect is far less than in a conventional image. A beam diameter of around 1000Å is often used in our spot-scan images. With a tilt angle of 60°, the change in focus across a single illumination spot is then close to 2000Å, well beyond the depth of field at high resolution. Thus there is still some variation in the CTF within the small spots, which must be corrected during the image processing.

The variation of CTF within the image can be corrected by, in effect, squaring the CTF for each spatial frequency (1). The procedure involves extracting a small region of the Fourier transform around each reciprocal lattice point and transforming this region to real space. The CTF calculated for this spatial frequency, as a function in real space, is then multiplied by the small transform, and then transformed back to reciprocal space. This procedure has been used in processing conventional images (2) and has now been extended to images with dynamic focus correction, the only modification being that the calculated CTF in real space takes into account the focus correction applied between scan lines.

In an ideal case, each diffraction peak in the transform of the image is confined to a single pixel of the transform (or, in general, four adjacent pixels, when the diffraction peak falls between pixels). In the case of spot-scan images, each peak has satellite peaks, spaced away from the main peak by as many pixels as there are scan rows in the image. In addition, oscillation of the CTF across the image causes the main peak to be split into two peaks at a distance from the center point equal to the number of oscillations of the CTF across the image. At the boundary between scan rows, there will in general be a discontinuity in the CTF, resulting in further spreading of the diffraction peak.

Figure 2 illustrates one case of CTF variation in the image, the resulting splitting of the spots, and correction by the image processing. Figure 2a shows the CTF at one particular resolution calculated for an image consisting of four rows of spots. Within each spot the CTF goes through about four oscillations, and there is a jump in CTF between the rows. Figure 2b shows the central region of the Fourier transform of the CTF variation; a diffraction spot from an image of a crystal would be split as shown. Every fourth element in the transform is non-zero, owing to the sampling inherent in the spot-scan image. The oscillation of the CTF causes the main peak to be split into two peaks away from the central point. The transform of the square of the CTF is shown in fig. 2c. After this correction, the peak power is restored to the actual reciprocal lattice point.

1. R. Henderson, J. R. Baldwin, K. H. Downing, J. Lepault, F. Zemlin Ultramicroscopy 19, 147-178 (1986)
2. R. Henderson, J. M. Baldwin, T. Ceska, F. Zemlin, E. Beckmann and K. H. Downing   J. Mol. Biol. 213, 899-929 (1990)

Fig.1. Schematic diagram of setup for spot-scan image. Image is focused at four points, F1...F4, which are typically twice as far from the center as the corners of the area to be recorded. Objective lens currents at these points are then used to define direction of tilt axis and correct focus at each point in image. Image is recorded by stepping beam along tilt axis direction, with focus correction between rows.
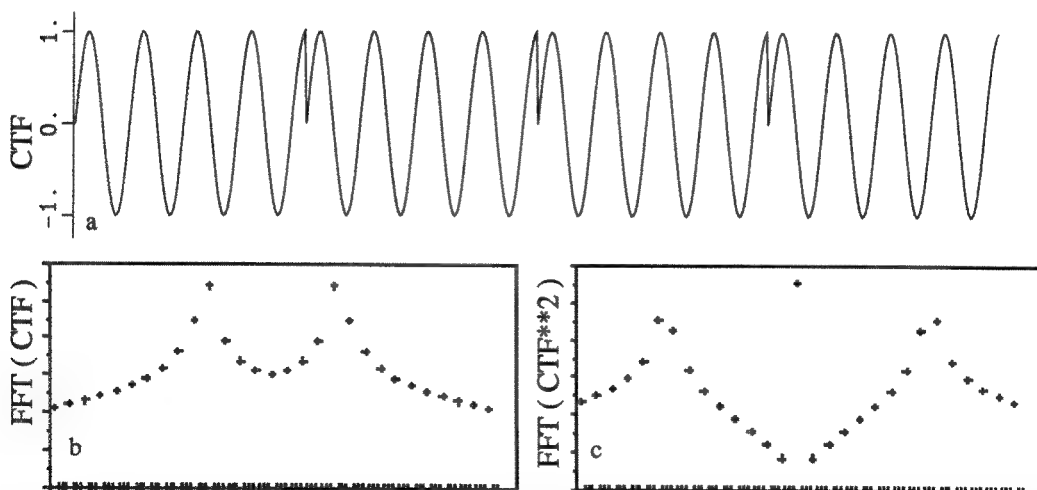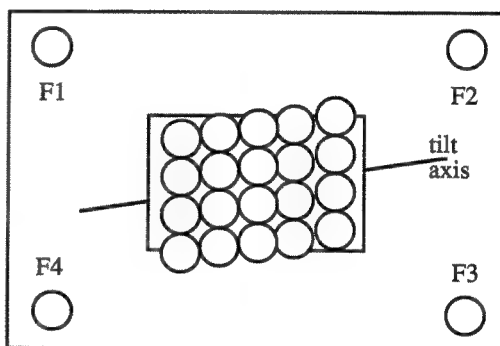
Fig. 2a Contrast transfer function along line perpendicular to tilt axis, in a spot-scan image consisting of four rows of spots. This curve is calculated for resolution of 4Å at 100kV with a defocus range of 2000Å within each spot. b. Central region of Fourier transform of CTF in a, corresponding to shape of peak in Fourier transform of crystal image. c. same region of transform of square of CTF in a, as obtained after processing image to compensate for CTF variation.

SPECTRA: A PROGRAM FOR PROCESSING ELECTRON IMAGES OF CRYSTALS

M. F. Schmid, R. Dargahi and M. W. Tam

Verna and Marrs McLean Department of Biochemistry and W.M. Keck Center for Computational Biology, Baylor College of Medicine, Houston, TX 77030

Electron crystallography is an emerging field for structure determination as evidenced by a number of membrane proteins that have been solved to near-atomic resolution. [1,2,3] Advances in specimen preparation and in data acquisition with a 400kV microscope [4] by computer controlled spot scanning [5] mean that our ability to record electron image data will outstrip our capacity to analyze it. The computed fourier transform of these images must be processed in order to provide a direct measurement of amplitudes and phases needed for 3-D reconstruction.

In anticipation of this processing bottleneck, we have written a program that incorporates a menu- and mouse-driven procedure for auto-indexing and refining the reciprocal lattice parameters in the computed transform from an image of a crystal. It is linked to subsequent steps of image processing by a system of data bases and spawned child processes; data transfer between different program modules no longer requires manual data entry. The progress of the reciprocal lattice refinement is monitored visually and quantitatively. If desired, the processing is carried through the lattice distortion correction (unbending) [6] steps automatically.

Images are now processed in 1/10 the time formerly required, with less operator error. Up to 100 images, each containing up to 6000 reflections in its fourier transform, must be processed to produce a high resolution actin bundle 3-D data set. Analyzing this much data will not be practical without a program like this. SPECTRA is written in a portable, modular style for standard X-window display devices and MOTIF, and will be useful for any protein electron crystallographic image analysis.

Figure 1 shows a snapshot of the main screen at one stage of the process. It illustrates the division of the screen into two halves, the transform viewport on the left and the peak list on the right. At the bottom right are four pairs of buttons that control the program.

The first pair deals with the viewport, including the magnification, low and high cutoffs, grid display, resolution scale, etc. and conveys information about the amplitudes at specified points in the transform. The user can pan across a transform that is too big to fit all at once inside the transform viewport.

The second pair controls the generation of a highest-peak list by neighbor-excluding histogram methods. The list can also be sorted in various ways, including by resolution and IQ [6] (after "mmbox" generation of the amplitudes and phases). The list can be accessed for indexing by mouse selection in the transform or in the list itself.

The third pair launches the reciprocal lattice refinement, either based only on the selected (highlighted) reflections or by a method which takes the rough reciprocal lattice based on these highlighted reflections and tries all possible indices to see if any unindexed member of the peak list lies close to a predicted position. If so, it is given that index and included in the next round of reciprocal lattice refinement until no new reflections are predicted. All reflections in the peak list in Figure 1 except the two highlighted (reversed contrast) ones were indexed and included in the refinement in this way. The remaining unindexed peaks represent transform noise peaks off the reciprocal lattice.

132

The last pair of buttons controls several possible output flows from the program. A simple list of amplitudes and phases can be generated internally to SPECTRA for further reciprocal lattice refinement or they may be output to a file. Alternatively, SPECTRA can automatically generate a command file to perform the unbending operation, using the data generated in the program such as reciprocal lattice parameters, the center of crystallinity, and the strong spots for mask-averaging that is performed before the cross corrrelation [6], in addition to other parameters that can be generated by user input or by default. The submission of the job for the lattice distortion correction procedure can be done off-line.

This program carries out the major manipulations on an image area, once it has been fourier transformed. The output amplitudes and phases, either with or without lattice distortion correction, are ready for CTF correction and the three-dimensional merging program. The modular nature of the package means that special programs needed for the analysis of images, such as those for analysis of images from tilted specimens, can easily be incorporated, usually without recompilation of SPECTRA.[7]

1. R. Henderson *et al.*, *J. Mol. Biol. 213(1990)899*.
2. B. Jap *et al.*, *Nature 350(1991)167*.
3. W. Kuhlbrandt and D.N. Wang, *Nature 350(1991)130*.
4. J. Brink and W. Chiu, *J. Microscopy 161(1991)279*.
5. K. Downing, *Science 251(1991)53*.
6. R. Henderson *et al.*, *Ultramicroscopy 19(1986)147*.
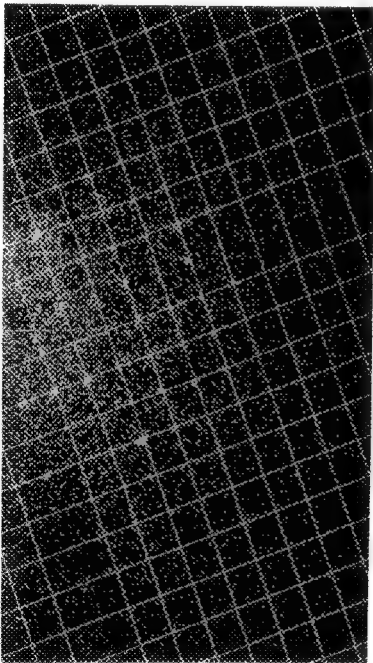
H	K	Observed X	Observed Y	Calculated X	Calculated Y	INTENSITY	RESOLUTION	IQ
2	0	50.00	22.00	50.20	22.15	6095 43	88 52	
1	2	52.00	56.00	52.05	56.03	2719 76	65 36	
1	2	6.00	78.00	6.19	78.24	2602 46	63 85	-
0	-2	23.00	-67.00	22.95	-67.17	2399 50	70 51	-
2	-2	81.00	-45.00	81.23	-45.01	2070 70	53 91	-
2	2	35.00	89.00	35.33	89.32	1992 39	52 23	-
4	0	117.00	44.00	116.57	44.31	1245 51	39 96	
6	0	175.00	67.00	174.85	66.46	1185 88	26 66	-
2	-1	70.00	-12.00	69.76	-11.43	1133 44	70 33	-
2	1	47.00	56.00	46.81	55.74	1118 95	68 32	-
0	-4	46.00	-134.00	45.90	-134.33	1038 75	35 26	-
3	1	76.00	67.00	75.95	66.82	971 30	49 30	-
4	-1	128.00	10.00	128.04	10.73	929 44	38 90	-
4	1	105.00	78.00	105.09	77.89	872 31	38 19	-
6	2	152.00	134.00	151.90	133.63	869 59	24 65	-
3	-1	99.00	-1.88	98.90	-0.35	785 39	50 45	-
2	-4	133.00	-101.00	133.32	-101.10	775 36	29 91	-
4	3	82.00	145.00	82.14	145.86	756 54	29 99	-
4	-3	151.00	-56.00	150.99	-56.44	727 94	31 02	-
3	4	42.00	168.00	41.53	167.56	718 58	28 84	-
---	---	109.00	-34.90	--------	--------	716 01	43 75	-
5	1	134.00	89.00	134.23	88.97	658 11	31.05	-
6	1	163.00	100.00	163.37	100.05	644 81	26 12	-
1	-3	63.00	-90.00	63.57	-89.67	626 00	45 47	-
3	2	64.00	100.00	64.48	100.40	624 51	42 07	-
5	-2	169.00	-12.00	168.66	-11.78	604 96	29 48	-
6	-1	187.00	33.00	186.32	32.88	564 62	26.30	-
---	---	199.00	-1.00	--------	--------	557 62	25 10	-
5	3	111.00	156.00	111.28	156.14	554 54	26 09	-
5	-1	157.00	22.00	157.18	21.80	513 60	31 51	-

Transform Info	Get Peaks	Refine	Get Reflections
Transform Vars.	Sort List	Setup	Setup

Figure 1. View taken from the X-window display during the running of SPECTRA. The results of reciprocal lattice refinement and auto-indexing have just appeared, and the transform shows a grid superimposed on it based on this lattice. Reflections indexed by hand are highlighted by reverse contrast, all others were auto-indexed, and remaining unindexed peaks have blank indices.

133

ACCURATE MEASUREMENTS OF MEAN INNER POTENTIAL OF CRYSTAL WEDGES USING ELECTRON HOLOGRAPHY

M. Gajdardziska-Josifovska, M. R. McCartney and J. K. Weiss
Center for Solid State Science, Arizona State University, Tempe, AZ 85287

The phase of an electron wave which has interacted with a material is measured in electron holography experiments with respect to a coherent reference wave which has travelled through vacuum. In non-magnetic electron-transparent materials, and under kinematical diffracting conditions, the phase change ($\Delta\varphi$) of the transmitted electron wave depends only on the thickness (t) and the mean inner potential (U_i) of the material: $\Delta\varphi = c |U_i| t$; c being an energy-dependent constant.[1] This phase change measured from electron holograms has been used previously to determine the mean inner potential of amorphous and polycrystalline films of known thicknesses.[2] Refraction effects in RHEED patterns have also been used to determine the mean inner potential of several crystals with flat surfaces.[3] The reported accuracies in these studies have ranged from 2.5% to 9.5%, although uncertainties in specimen thickness and the unknown effects of surface contamination and/or reconstruction are very likely sources of systematic errors. This paper shows that numerical reconstruction of digital holograms, combined with use of cleaved crystal wedges, enables measurement of the mean inner potential of crystals with enhanced accuracy.[4]

A Philips EM400ST-FEG transmission electron microscope equipped with an electron biprism was used to create the holograms which were recorded with a Gatan 679 slow-scan CCD camera equipped with a 1024x1024-pixel detector. Three different systems were studied: i) GaAs 90° wedge with cleavage along {110} crystal planes; ii) MgO 90° wedge with cleavage along {100} crystal planes; and iii) Si 70.5° and 109.5° wedges with cleavage along {111} crystal planes.

Figure 1 shows a typical hologram from the Si 109.5° wedge which has been tilted deliberately away from a zone axis to avoid dynamical diffraction effects. The Fresnel fringes from the biprism are visible at the corners of the hologram and the holographic fringes can be seen in the enlarged upper inset. The lower inset shows the sideband which was used to reconstruct the phase image in Fig. 2. Superimposed on the phase image are contours of constant phase showing the flatness of the phase in vacuum in the lower part of the figure and the linearly increasing phase in the crystal wedge. A box is marked to show the area which was averaged along the direction parallel to the crystal edge to give the phase profile in Fig. 3a. Figures 3b and 3c show similar phase regions and profiles for MgO and GaAs, respectively. With accurate knowlege of the change of the projected thickness and an accurate magnification calibration, the value of the mean inner potential can be calculated from the slope of the phase profiles. Table 1 summarizes the results of these experiments. The uncertainty in our method is dominated by the limited statistical accuracy of the phase measurement, and by uncertainty in the hologram magnification.[4] Only in the case of Si have imperfections of the cleaviage contributed to the uncertainty.

In summary, the advent of digital image recording capabilities and the use of crystal wedge samples allows the quantification of mean inner potential to accuracies of about 1%. Diffraction effects have been minimized by tilting the wedges away from a zone axis. We have also studied the case of zone axis orientations and the influence of dynamical diffraction on the phase images. Knowledge of both mean inner potential and diffraction effects will be crucial for the futher applications of quantitative electron holography to materials studies.

References
1   L. Reimer, in *Transmission Electron Microscopy*, Springer-Verlag, (1989)p57.
2   R. Buhl, *Z. Phys.* (1959)**155**, 395 ; M. Keller, *Z. Phys.* (1961)**64**, 274; C. Jönsson, H. Hoffmann and G. Möllenstedt, *Phys. Kondens. Mater.* (1965)**3**, 193; H. Hoffmann and C. Jönsson, *Z. Phys.* (1965)**182**, 360.
3   K. H. Gaukler and R. Schwarzer, *Optik* (1971)**33**, 215; N. Yamamoto and J. C. H. Spence, *Thin Solid Films* 1983)**104**, 43.
4   M. Gajdardziska-Josifovska, M. R. McCartney, J. K. Weiss, W. J. de Ruijter and D. J. Smith, *Phys. Rev. Lett.*, submitted.
5   This work was performed at the National Facility for HREM at ASU supported by NSF grant DMR-8913384. Support for one of the authors (J. K. Weiss) was provided by the Industrial Associates Program at ASU.
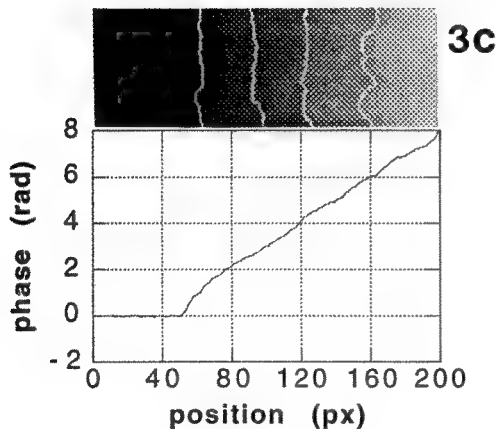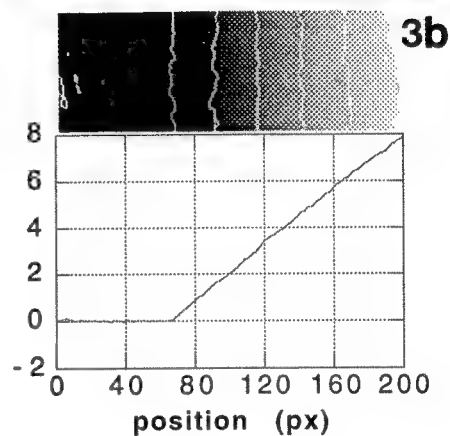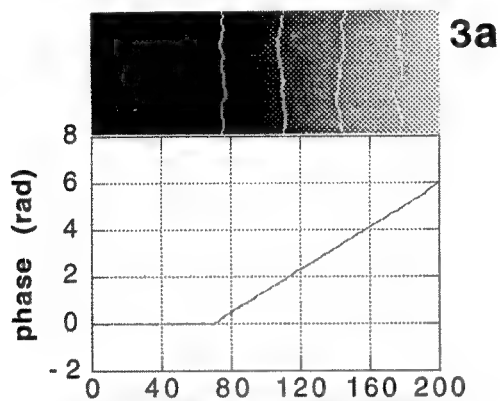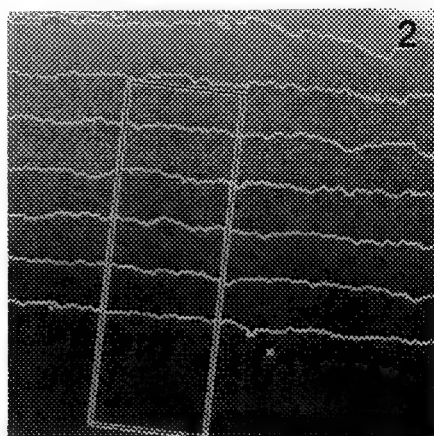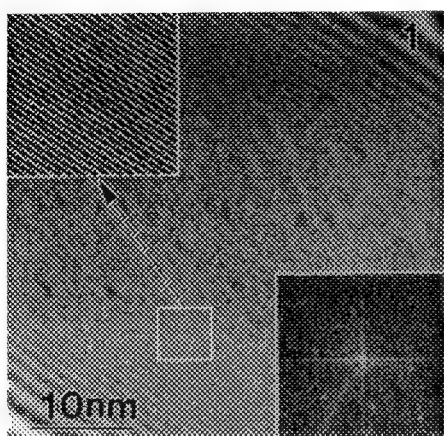
Table 1. Mean inner potential for three studied crystals

crystal	U_i (V)
Si	9.01±0.12
MgO	12.75±0.08
GaAs	14.21±0.16

FIG. 1 Hologram from Si wedge with fringes seen in enlarged inset and sideband used for reconstruction.

FIG. 2 Reconstructed phase image from hologram in Fig. 1 with superimposed equiphase lines. Box marks region which is extracted to generate phase profile as shown in Fig. 3.

FIG. 3 Part of phase images with equiphase lines at $\pi/2$ intervals and phase profiles obtained by averaging over 70 pixels parallel to the wedge edge for: (a) Si 109.5° wedge; (b) MgO 90° wedge; (c) GaAs 90° wedge.

MEASUREMENT OF PCTF PARAMETERS WITH HIGH ACCURACY

A.F. de Jong[1], W.M.J. Coene[1] and A.J. Koster[2]

[1]Philips Research Laboratories, P.O. Box 80000, 5600 JA Eindhoven, The Netherlands
[2]University of California (San Francisco), School of Medicine, Dept. of Biochemistry and Biophysics

Measurement of electron-optical parameters in TEM is important for two reasons: a) for automatic correction of focus, astigmatism and beam-tilt misalignment (autotuning) and b) for the accurate determination of the phase-contrast transfer function (PCTF) which is needed for a correct interpretation of high-resolution electron microscopy (HREM) images. This paper addresses specifically methods adapted to reach the second goal, stressing accuracy rather than speed and robustness.

For correct HREM image interpretation, high accuracies in the PCTF parameters are required if it is intended to extract information beyond the point-resolution of the microscope, as is the case with image reconstruction procedures via focal series or holography. It has been derived[1] that in order to restore the phase of the wavefunction with an accuracy below $\pi/3$ at the maximal spatial frequency G_{max}, the coefficient for spherical aberration C_s must be known with an accuracy of $\Delta C_s/C_s = 0.056 \, (\rho_i/\rho_s)^4$. Here $\rho_i = G_{max}^{-1}$ is the information limit and ρ_s is the point resolution of the microscope. The accuracy needed thus depends on the ratio ρ_i/ρ_s and when this ratio approaches 0.5, the required accuracy in C_s drops below 0.5%, which is very difficult to achieve. Similar equations and constraints can be derived for parameters like focus, beam-tilt misalignment and magnification calibration.[1]

Two methods seem promising candidates to perform very accurate measurements on the PCTF: beam-tilt induced image shifts and beam-tilt induced astigmatism. In the weak phase-object approximation, and neglecting higher spatial frequencies, the effect of an induced beam tilt may be described by a simple shift of the image. This principle has also been proposed as a method for autotuning.[2] When residual beam tilt misalignment m and astigmatism $Aa=A\cos(2\varphi_a)$is taken into account, the displacement d as the result of an induced beam tilt t follows a trajectory according to:

$$d = C_s\lambda^3 \{ (t + m)^3 - m^3 \} + \lambda(f - A/2) t + \lambda A/2 \, (t \cdot a)a,$$

where λ is the electron wavelength and f the defocus. Note that the displacement is not always parallel to the induced tilt because of the vector character of the misalignment and the astigmatism. Image displacements may be measured very accurately using cross-correlations and are not very sensitive to the nature of the contrast. By measuring a series of 10 to 20 displacements and fitting these to a third-order curve, all the parameters of the PCTF may be found. A critical step, especially for the measurement of the C_s, is the independent calibration of the beam tilt increment.

We have performed various measurements on several Philips CM-microscopes, which were controlled by a Tietz computer. Both a standard TV camera with image intensifier as well as a slow-scan CCD camera were used for the image pickup. As an example, the displacement curve of a sample of gold particles on a carbon foil, recorded in the CM20-UltraTWIN microscope at a magnification of about 250,000 is shown in fig. 1. The parameters found from two (perpendicular) tilt series are shown in Table 1, together with the standard deviations found from the fit. The measured value of C_s (0.509 ± 0.004 mm) is in excellent agreement with the predicted[3] value (0.5 mm). The deviation from a straight line parallel to the tilt-axis is caused by a beam-tilt misalignment in the y-direction.

The image shift method has been used on various specimens, both at low magnification and in HREM. The inclusion of a crystalline part of the specimen into the field-of-view does not degrade the method too much, but a certain amount of amorphous material (or background) has to be present. At high magnifications, for weak contrasts, the use of a slow-scan CCD camera is a clear advantage. The largest disadvantage of the method is its sensitivity to sample drift. This may be partly compensated by a suitable procedure, but ultimately sample drift limits the accuracy.

136

Measuring PCTF parameters by beam-tilt induced astigmatism was originally proposed by Zemlin et al.[4] For several induced beam tilts, a diffractogram is calculated from an amorphous part of the sample. The effective astigmatism and defocus may be extracted from the diffractogram, and by combining several diffractograms all PCTF parameters may be measured.[5] This method is not sensitive to drift, but needs an (almost) totally amorphous image. The potential accuracy makes this method a promising candidate for fine-tuning of the parameters, but the conditions under which well-defined rings are produced make the method somewhat restrictive. The C_s may also be measured from the diffractogram, but then a series of images at several defocus values is needed. Recently we have developed new procedures for the fitting of the zeros of the diffractogram which enable us to achieve a much better statistical precision.[6] From measurements performed on the CM20-UltraTWIN microscope, using an amorphous germanium foil, we found a C_s of 0.494 mm ± 0.004 mm. In this case, the magnification calibration is a critical step.

1. A.F. de Jong and A.J. Koster, Proc. 10th Pfefferkorn Conference (Cambridge, 1991), Scanning Microscopy, 1992 in press.
2. A.J. Koster and W.J. de Ruyter, Ultramicroscopy (1992) in press.
3. J.G. Bakker and P.E.S. Asselbergs, Proc. XIIth ICEM (Seattle, USA) 1 (1990) 132.
4. F. Zemlin et al., Ultramicroscopy 3 (1978) 49.
5. O.L. Krivanek and G.Y. Fan, Proc. 10th Pfefferkorn Conference (Cambridge, 1991), Scanning Microscopy, 1992 in press.
6. W.M.J. Coene and T.J.J. Denteneer, Ultramicroscopy 38 (1991) 225.
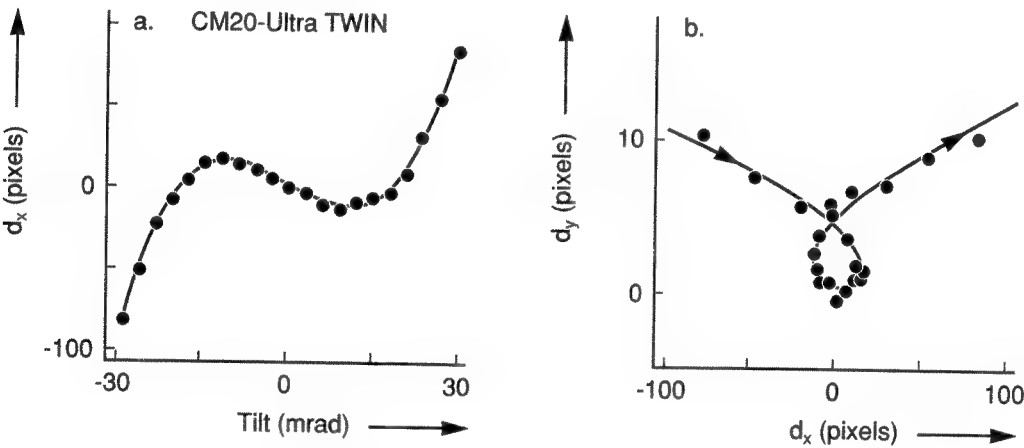
FIG. 1.--Image displacement as a function of induced beam tilt as measured on the CM20- UltraTWIN microscope, using the x tilt-coils. The dots indicate the measured points, the drawn lines are simulated displacements using the fitted parameters (Table 1). a. Parallel displacement as a function of beam tilt. b. Trajectory of the image shift parallel (d_x) and perpendicular (d_y) to the induced tilt. Note the difference in scale along the vertical and horizontal axes.

TABLE 1.--Measured values of the beam tilt, defocus and astigmatism for a typical experiment on the CM20-UltraTWIN microscope, with their standard deviations.

$C_s =$ 0.509	± 0.004 mm	f	= -177	± 3 nm
$m_x =$ 0.14	± 0.03 mrad	A =	12	± 6 nm
$m_y =$ -1.06	± 0.04 mrad	$\varphi_a =$	10	± 10 deg. (from pos. x-axis)

137

PRINCIPLE AND PRACTICE OF HIGH-RESOLUTION IMAGING WITH A FIELD-EMISSION TEM

Max T. Otten[1] and Wim M.J. Coene[2]

[1] Philips Electron Optics, Applications Laboratory, Bldg. AAE, 5600 MD Eindhoven, The Netherlands
[2] Philips Research Laboratories, Bldg. WY-2, P.O.Box 80.000, 5600 JA Eindhoven, The Netherlands

High-resolution imaging with a LaB_6 instrument is limited by the spatial and temporal coherence, with little contrast remaining beyond the point resolution. A Field Emission Gun (FEG) reduces the incidence angle by a factor 5 to 10 and the energy spread by 2 to 3. Since the incidence angle is the dominant limitation for LaB_6, the FEG provides a major improvement in contrast transfer, reducing the information limit to roughly one half of the point resolution. The strong improvement, predicted from high-resolution theory, can be seen readily in diffractograms (Fig. 1) and high-resolution images (Fig. 2). Even if the information in the image is limited deliberately to the point resolution by using an objective aperture, the improved contrast transfer close to the point resolution (Fig. 1) is already worthwhile.

A practical consequence of the high coherence is a difficulty in performing stigmation, focussing and coma-free alignment. Because images of amorphous material on a FEG instrument nearly always show a wide range of spatial frequencies over a large range in focus, differences in focus become indistinct. On-line diffractometry provides a good solution here, while it is also possible to reduce the coherence during setup by focussing the beam. With the beam almost focussed, the image is quite similar to the image from a LaB_6 microscope. After setup, the beam is spread and the full coherence of the FEG is used.

Other consequences are the re-occurrence of the same type of image (Fourier images) over a large range of focus conditions and the occurrence of delocalisation effects (displacement of information from the correct position, depending on the oscillation speed of the contrast transfer function for the spatial frequency involved).

In contrast with a LaB_6 source, the information arising from frequency regimes where the contrast transfer function is oscillating rapidly, does survive in the image from the FEG due to the small effective source size. As a consequence, high-resolution images with fine image detail (Fig. 3) are observed over a much larger focus range (more than 1μm) with the FEG than with LaB_6. The sensitivity of image contrast to the rapid oscillations of the contrast transfer function may make comparison of experimental and simulated images difficult and time-consuming. Direct image retrieval methods, based on holography or through-focus series reconstruction, are therefore probably the most effective way of extracting all the information available in the high-resolution images from a FEG instrument.

The various types of FEGs have different practical consequences for high-resolution imaging. One important parameter is the size of the isoplanatic patch[1], which is the area where coma (a beam-tilt induced aberration) is insignificant. For a cold (or thermally assisted cold) FEG the isoplanatic patch covers only a small fraction of the total exposure, with strong image distortions towards the edge of the exposed area[1], while a Schottky FEG shows no discernible effects, making the latter much more suitable for high-resolution imaging.

Reference
1) K.J. Hanszen, R. Lauer, G. Ade (1985) Ultramicroscopy 16, 47-57.
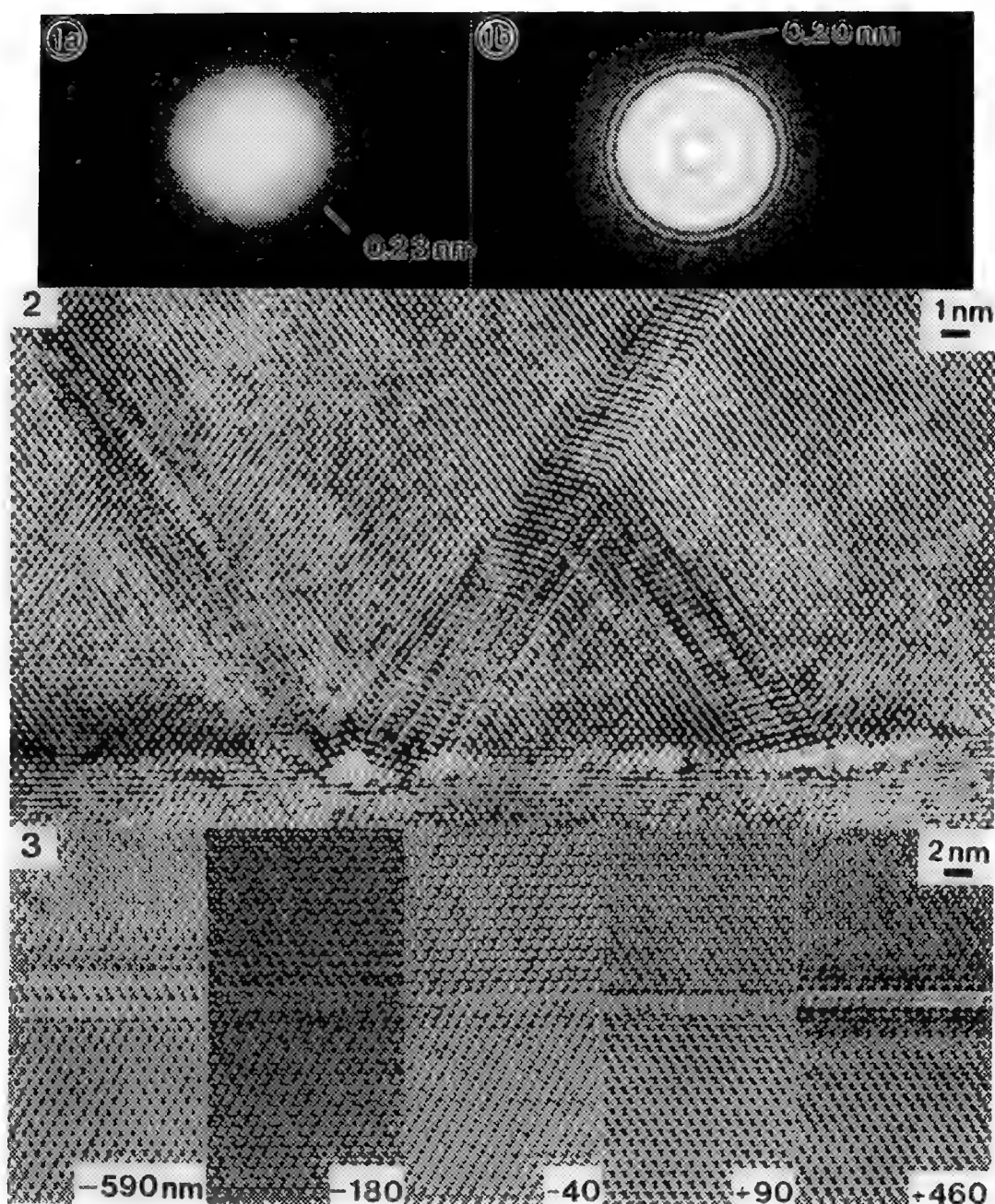
Fig. 1. Comparison of optical diffractograms from an amorphous film for the CM20-TWIN with (a) LaB$_6$ and (b) FEG. The contrast transfer for the FEG is clearly superior.

Fig. 2. High-resolution image of defects at the interface between Si and GaAs, showing many high spatial frequencies. Specimen courtesy of Dr. B. Kabius, KFA Jülich, Germany.

Fig. 3. High-resolution images from a through-focus series of Si$_3$N$_4$ show fine detail over a wide range of focus. Specimen courtesy of Dr. J. Marti, Allied Signal, Morristown, NJ, USA.

139

HREM APPLICATIONS TO INDUSTRIAL PRODUCTS : OBSERVATION OF THICK-FILM RESISTORS WITH VERY LARGE ELECTRON TRANSPARENT AREA

Z.G. Li, P.F. Carcia, P. Donohue

Du Pont Research & Development, Experimental Station,
P.O.Box 80356, Wilmington, DE 19880-0356

HRTEM is a very powerful tool for structural characterization of materials. However, its role in industry is still very limited and electron microscopy is generally considered as a secondary support technique, although it can uniquely provide microstructural information leading to understanding and improvement of product quality, especially for those materials in the form of films. An example in the semiconductor industry is recently described by Anderson[1]. He points out that the main concerns of imaging using a conventional cross-section sample preparation method[2] are too small imaged areas, not representative of the product, and artifacts that may be introduced during the ion-milling process. Here we apply HREM to thick film resistors and attempt to overcome these obstacles.

Thick film resistors are a common component in hybrid microcircuit technology. They consist of finely-divided powders of a glass and an electrically conducting phase, LaB_6 in the resistors we studied, mixed with an organic vehicle. Their properties can be very different, depending, for example, on the surface area of these small particles. We used a new technique developed by the IBM group[3] to prepare our samples. Consequently, we were able to produce very large electron transparent areas in thick film resistors (close to a mm) and either avoided or used only very short ion-milling times[4]. We "scanned" the resistor parallel to the substrate surface by moving the sample at low magnification (5000x), and we observed a number of different features over this large area. At high magnification and with selected area electron diffraction, we further analyzed and identified these features. Fig. 1 is a low magnification electron micrograph of a resistor with lower surface area intemediates. The electron transparent area of the thick film resistor was much larger than the non-uniform region revealed in the images. The entire resistor thickness (~ 20 μm) and a part of the alumina substrate were visible. This resistor consisted of elongated paticles of $CaTa_4O_{11}$, branch-like particles of TaB_2 and an amorphous phase, as indicated in Fig. 1. Conducting phase TaB_2 was finely-divided, 6-8 nm, and formed a branch-like network in the resistor (shown in the corner of the figure). We found no evidence for LaB_6 by HREM and X-ray diffraction, which we assume had decomposed or fully reacted with the glass.

From examination of microstructure, we found that resistors made with higher surface area intermediates almost fully suppressed formation of crystallizable phases from the glass, such as $CaTa_4O_{11}$, and consisted predominantly of finely-divided crystalline TaB_2 and an amorphous phase. Resistors made with higher surface area intermediates also had better voltage properties. Although the presence of $CaTa_4O_{11}$ crystals in resistors made with lower surface area intermediates may not itself have caused poor voltage properties, it may indicate the more sluggish development of the TaB_2 conducting network, which was then more susceptible to change under voltage stress.

In conclusion, a series of LaB_6-base thick film resistors with very large electron transparent area were characterized by high resolution electron microscopy. The structural information helped us to understand the influence of particle size of intermediates on the properties of LaB_6-base thick film resistors [5].

References

1. R.M. Anderson, Proc. 49th Ann. Meet. of the Electr. Microsc. Soc. of Ame., (1991), 828
2. J.Bravman, R. Sinclair, J. Electr. Microsc. Techno., 1, 53 (1984)

3. S.J.Klepeis, J. P. Benedict, and R. M. Anderson, MRS Symposium Proceedings **115**, 179 (1989)
4. Z.G.Li, P.F.Carcia, P.Donohue, J. Mater. Res. (submitted)
5. We thank to S.J.Klepeis and R.M.Anderson for very useful discussions on their sample preparation method.
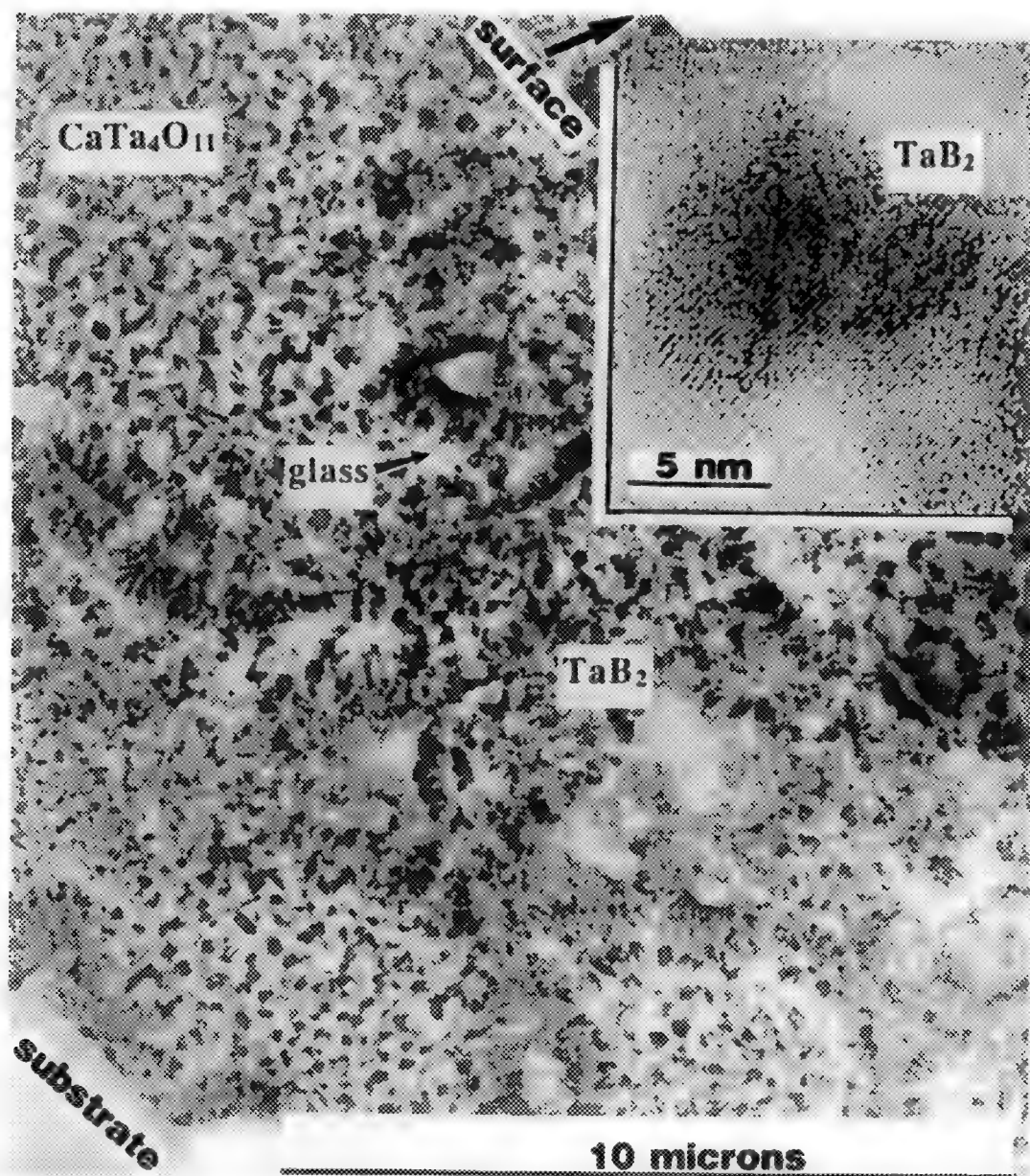
FIG. 1. TEM micrography of thick film resistor with very large electron transparent area. HREM image of TaB2 is shown in upper-right corner.

SHADOW IMAGES FOR IN-LINE HOLOGRAPHY IN STEM

Shi-Yao Wang, J. K. Weiss* and J. M. Cowley

Dept. of Physics and Astronomy, Arizona State University, Tempe, AZ 85287-1504
*Center for Solid State Science, Arizona State University, Tempe, AZ 85287

Shadow images are obtained on the detector plane when the specimen in a STEM instrument is illuminated by a stationary beam formed with a very large or no objective aperture. It has been recognized [1,2] for some time that the shadow image formed after a thin crystal specimen in the diffraction plane of a STEM instrument with a field emission gun can be treated as an in-line hologram. Since the transmitted and diffracted beams are added to give interference effects, all the information on the relative phase of the scattered beams is recorded in the shadow image. In fact, this is basically equivalent to the original scheme envisioned by Gabor [3], where he proposed that a reconstruction could be made from a hologram so that the imperfection due to spherical aberration of the objective lens could be corrected and improved resolution could be achieved.

The STEM instrument used in this work is the HB5 from VG microscopes Ltd, but the means for the observation and recording of shadow image are still under development. In the previous arrangement, a P20 phosphor screen is used to transfer the electron signal to light which is viewed using an intensified TV camera. Recently a new detection system has been installed [4]. A YAG scintillator is used to convert electrons into photons which are then transferred to a CCD camera. The CCD camera is a Photometrics CH200 slow-scan camera fitted with a Tektronics 512x512-pixel CCD array digitized to 14 bits. This camera allows for the recording of shadow images with a much better signal-to-noise ratio and linearity and a higher number of pixels than the intensified TV camera. In addition, the direct storage of digitized images makes possible on-line or off-line numerical reconstruction without the need for later digitization of an analog image. Fig 1 shows shadow images of the edge of a silicon sample far out of focus and at near focus. It shows that the magnification of the shadow image is strongly defocus dependent. Close to focus, the image is heavily distorted because of the effect of the objective lens aberration but far from focus the distortion becomes less serious and good quality, relatively low magnification image is produced.

The main obstacle with in-line holography is that the reconstruction gives two superimposed images, one the required real image of the object and the other a defocused, aberrated conjugate image. The reconstructed image is always degraded by the presence of the conjugate image. Under large defocus characterized by $\Delta \gg 2D^2/\lambda$, where D is the size of an object, the disturbance vanishes because the conjugate image could be made so far out of focus by the reconstruction process that it only forms a weakly-modulated background. Fig 2b is the digital reconstruction of Fig 2a, which was extracted from Fig 1a. The fringe spacing in Fig 2a corresponds to 3.1 Å. In Fig 2b there is a complicated remnant of the periodic part of the image due to an inexact matching of parameters but it is noted that there is a considerable improvement in resolution of non-periodic background detail.

For the near-focus shadow image (hologram), theory and simulation [5,6] show that a possible way to get rid of the conjugate image is to use the probe-shift method. When the incident probe scans across the specimen, the required image moves in one direction, while the conjugate image moves in the opposite direction. Thus we can shift the probe laterally and get a hologram for each probe position. If we do the reconstruction for each of these holograms and then overlay them by back shifting, the conjugate image will be smeared out and the real image significantly improved. This method requires both the consecutive recording of holograms with photometric precision and the exact measurement of the relevant experimental parameters. Further efforts are under way towards this direction.

References

1. J. M. Cowley and D. J. Walker, Ultramicroscopy 6(1981) 71
2. J. M. Cowley, Ultramicroscopy, in press.
3. D. Gabor, Proc. Royv Soc. (London) A197 (1949) 454

4. M. Mankos et al, in this proceeding.
5. J. A. Lin and J. M. Cowley, Ultramicroscopy 19 (1986) 179
6. Shi-Yao Wang and J.M. Cowley, Proc. Ann EMSA (1991) 682
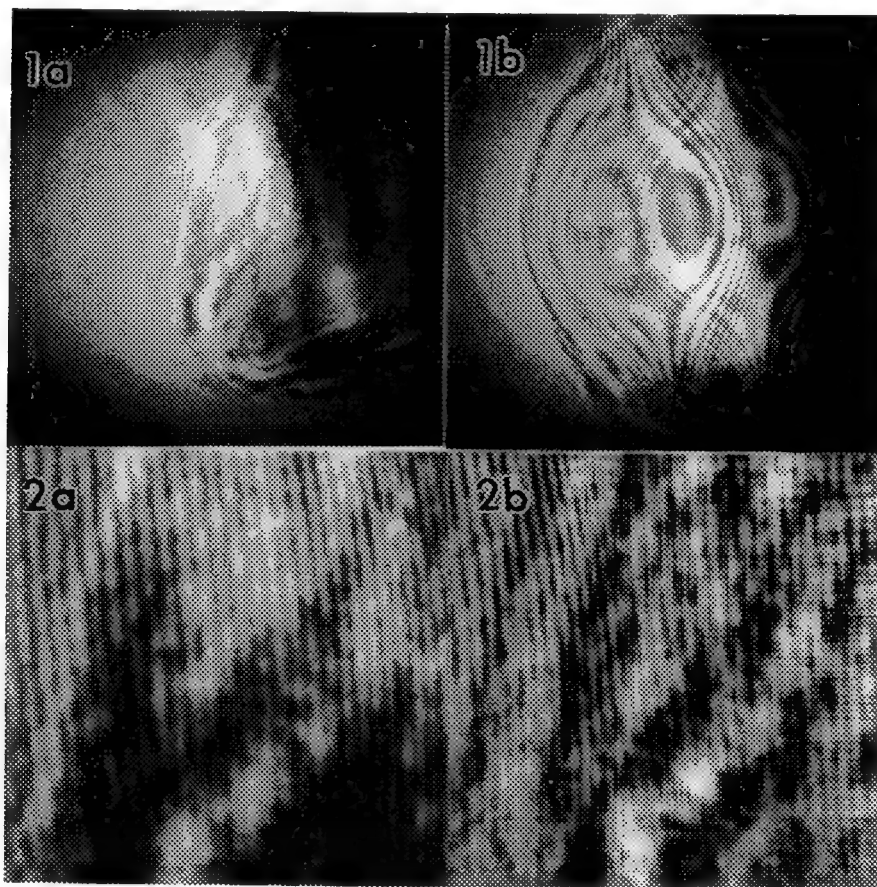
Fig 1   Shadow images of Si specimen. (a) Far out of focus (overfocus). (b) near focus.
Fig 2   (a) Hologram extracted from Fig 1a. (b) reconstruction of Fig 2a.

DETERMINATION OF THE STRAIN FIELD FROM AN HREM IMAGE OF A Si LOMER DISLOCATION

K.-H. Tsai, A. F. Schwartzman, R. Gallego, M. Ortiz, M. A. O'Keefe* and K.-S. Kim

Division of Engineering, Brown University, Providence, RI 02912
* National Center for Electron Microscopy, Lawrence Berkeley Laboratory, University of California, Berkeley, CA 94720

A novel approach to quantitative deformation characterization of high-resolution electron microscopy (HREM) defect images has been developed. The essential principle of this technique, called Computational Fourier Transform Deformation (CFTD) analysis, is to extract an accurate displacement field about a defect from its HREM image using Fourier transformation procedures. The methodology's unique feature is to digitize the defect image and compute the Moire pattern, from which the displacement field is obtained, without the need for an external reference lattice image, normally associated with the interference phenomena. Details of the image processing steps are described elsewhere.[1] The motivation is that from this data, the displacement gradient can be calculated which yields much information on the experimental deformation mechanics of some solid undergoing a specific growth process or mechanical testing. One question that has arisen is whether different imaging conditions of the same defect affects the results of the CFTD analysis. We have studied this problem by analyzing the strain components of simulated images of a Lomer dislocation in Si and present our findings here.

The calculation of atom positions about a Lomer dislocation in Si is based on the minimization of the energy of the atomic lattice, employing the Stillinger-Weber interatomic potential.[2] The reason for using this potential is that by careful numerical simulations, Stillinger and Weber demonstrated the ability of their potential to accurately replicate a wide range of physical properties of perfect Si. Image simulations were performed at the National Center for Electron Microscopy at Lawrence Berkeley Laboratory using the NCEMSS computer program. The image simulations are for an 80 Å thick crystal in a JEOL JEM-2010 electron microscope operated at 200 kV and equipped with the ARP pole pieces (a C_s of 1.0 mm, a Gaussian spread of focus of 70 Å, a convergence semi-angle of 0.85 mrad and an objective aperture radius corresponding to 0.6 Å^{-1}). The results are shown in Figure 1 for a black atom simulation at Scherzer defocus of -600 Å and a white atom picture at a defocus of -900 Å.

Figure 2 depicts the results of the strain components analysis of the simulated images by the CFTD method, along with theoretically calculated images based on anisotropic linear elasticity theory. The dynamic range is ±7%. In previous work, the image processing steps produced a noisy background. This artefact has been suppressed by filtering the whole domain that lies two Burgers vectors away from the core, using a smoothing function that satisfies the equilibrium and compatibility condition for anisotropic linear elasticity. Within the core region, another nonlinear filter is used to remove random noise. We can see excellent agreement for all the strain components, except e_{yy} inside the core region, between the black and white atom image simulations. Thus, the CFTD analysis is insensitive to the imaging conditions of the electron microscope, except for a field of large strain-gradient such as the dislocation core region. For a large strain-gradient field, the HREM image does not represent the lattice configuration accurately. Moreover, the analysis of the simulated images compares well with the theoretical results. In conclusion, the CFTD analysis continues to be a viable procedure for extracting continuum mechanics information from discrete atomic-resolution images of defects in solids.[3]

References

1. H. C. Choi, A. F. Schwartzman and K.-S. Kim, *Thin Films: Stress and Mechanical Properties*, Materials Research Society Proceedings, in press (1991).
2. F. H. Stillinger and T. A. Weber, Phys. Rev. B **31**, 5262 (1985).
3. This work was supported by ONR (N00014-90-J-1295) and the Materials Research Group on Micro-Mechanics of Failure-Resistant Materials at Brown University (NSF grant DMR-9002994).
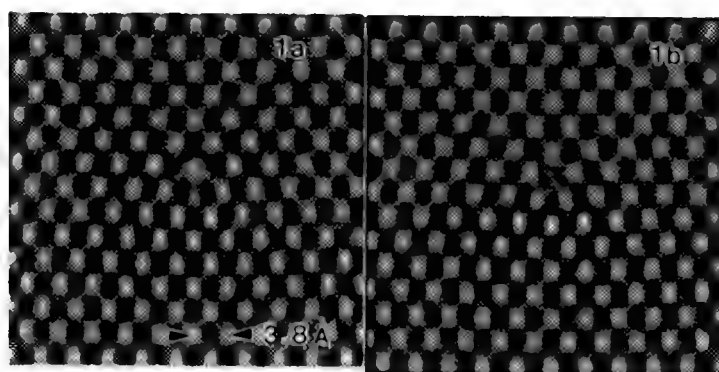
Fig. 1.--(a) Black and (b) white atom image simulations of Lomer dislocation in Si.

Fig. 2.--Strain components analyzed by CFTD method for (a) black and (b) white atom simulations. (c) Theoretical calculations using linear elasticity theory.

145
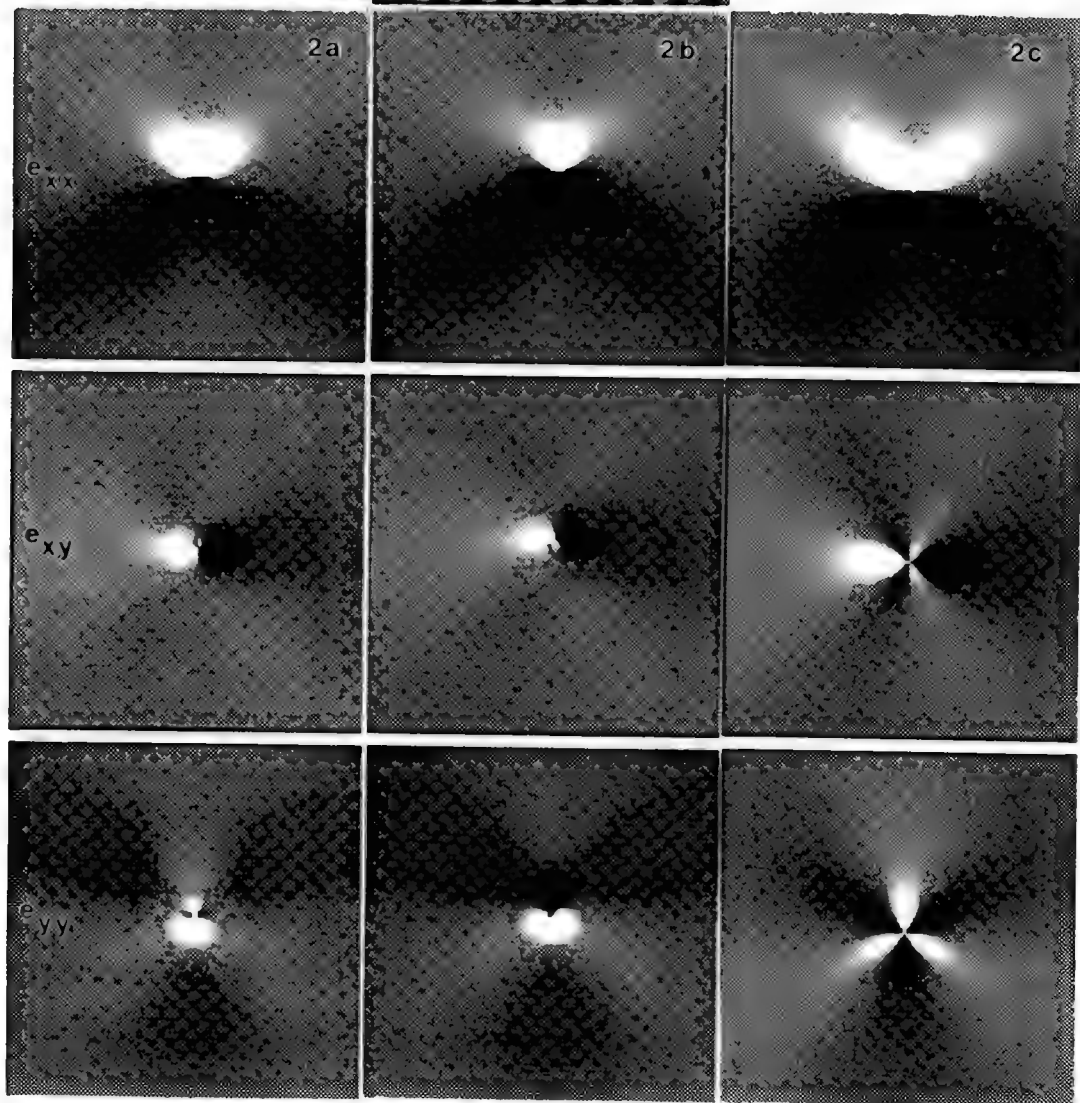
A HIGH-RESOLUTION ELECTRON MICROSCOPY STUDY OF V/Al$_2$O$_3$ INTERFACE

Y. Ikuhara, P. Pirouz, A. H. Heuer, S. Yadavalli*, and C. P. Flynn*

Department of Materials Science and Engineering, Case Western Reserve University, Cleveland, OH 44106, *Department of Physics and Materials Research Laboratory, University of Illinois, Urbana, IL 61801

The interface structure between vanadium and the R-plane of sapphire (α-Al$_2$O$_3$) was studied by conventional and cross-sectional high resolution electron microscopy (HREM) to clarify the atomic structure of the interface.

A 57 nm thick vanadium film was deposited on the $(1\bar{1}02)$ (R) plane of sapphire by molecular beam epitaxy (MBE) at a substrate temperature of 920 K in a vacuum of 10^{-10} torr. The HREM observations of the interface were done from three directions: two cross-sectional views (parallel to $[0\bar{2}2\bar{1}]_{Al2O3}$ and $[\bar{1}\bar{1}20]_{Al2O3}$) and a plan view (parallel to $[\bar{2}201]_{Al2O3}$) by a top-entry JEOL 4000EX electron microscope (400 kV).

Fig. 1 shows the plan view HREM of the interface along the $[\bar{2}201]_{Al2O3}$ direction. The measured Moire spacings along the $[\bar{1}\bar{1}20]_{Al2O3}$ and $[5\bar{5}0\bar{4}]_{Al2O3}$ directions are 1.55 nm and 1.03 nm, respectively, which indicates that there is about 4% residual compressive strain at the vanadium side of the interface. Fig. 2 is a cross-sectional HREM micrograph of the same interface. The interface plane is almost parallel to $(001)_V$ and $(1\bar{1}02)_{Al2O3}$ and the incident beam is parallel to $[110]_V//[\bar{1}\bar{1}20]_{Al2O3}$. The $(001)_V$ is tilted with respect to the $(1\bar{1}02)_{Al2O3}$ plane by 2.1°; the misfit parameter between these planes is 17.9%. There are misfit dislocations (arrowed) at the interface with a $\frac{a}{2}<110>$ Burgers vector. These are spaced periodically with one dislocation at every six $(110)_V$ planes (i.e. a separation of ~1.28 nm). Fig. 3 is a cross-sectional HREM micrograph along the $[0\bar{2}2\bar{1}]_{Al2O3}//[100]_V$ direction. The (001) plane of vanadium is tilted by 3° with respect to the $(1\bar{1}02)_{Al2O3}$ plane. This tilt, which results in the continuity of $(\bar{1}01)_V$ and $(\bar{1}\bar{1}20)_{Al2O3}$ planes, is thought to occur by an array of misfit dislocations periodically spaced by 3.0 nm. The misfit parameter between these planes is 8.4%, and the misfit dislocation Burgers vector is $\frac{a}{2}<111>_V$. The mechanism whereby the lattice tilts is thought to involve the motion of dislocations on the vanadium side from the film surface to the interface.
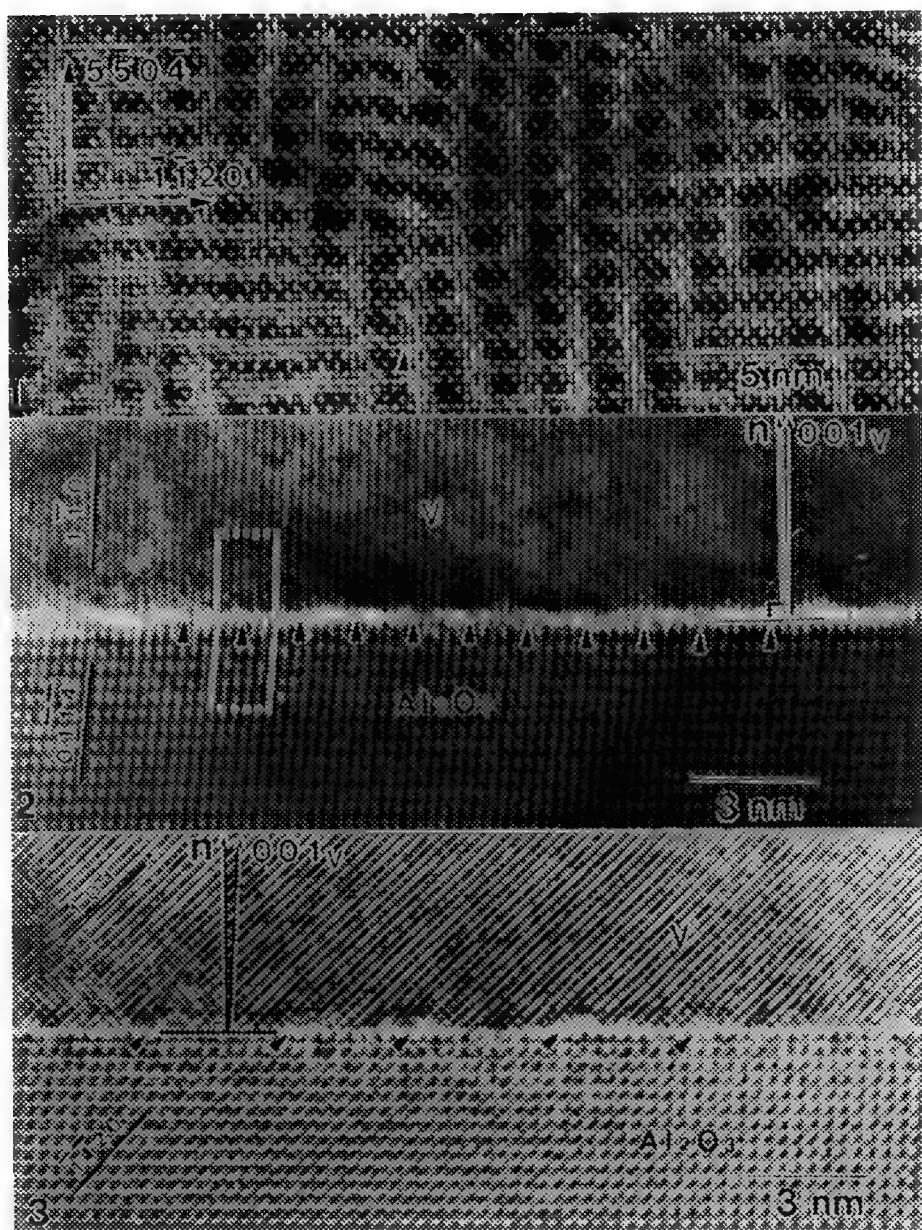
FIG. 1. Plan-view HREM micrograph of the interface along the $[\bar{2}201]_{Al2O3}$ direction. Note the Moire pattern consisting of an orthogonal set of fringes.

FIG. 2. Cross-sectional HREM micrograph of the interface along the $[\bar{1}\bar{1}20]_{Al2O3}$ direction.

FIG. 3. Cross-sectional HREM micrograph of the interface along the $[0\bar{2}2\bar{1}]_{Al2O3}$ direction.

THE VALUE OF MICROSCOPY IN RESEARCH IN CERAMIC AND METALLIC MATERIALS

M H Loretto

IRC in Materials for High Performance Applications, The University of Birmingham, Edgbaston B15 2TT, UK

This somewhat provocative symposium is scheduled to look at the (real) role of (transmission) electron microscopy in engineering materials. The very fact that the organisers have framed the title in this way, implies that there is a school of thought that questions the value of transmission electron microscopy (TEM) in areas other than in academic research - and perhaps even its value in academic research! Hence the aim of this paper is to assess whether TEM has made a contribution to the understanding, and thus to the successful application, of engineering materials or whether, as with so much physical metallurgy, it has simply confirmed what was already known to the practitioner for many years.

In order to make an assessment of the value of TEM in the field of engineering materials, it is necessary firstly, to appreciate the information that is available from (analytical) TEM and secondly, to appreciate what knowledge is of value to the materials engineer for the successful application of engineering materials. One of the problems with TEM is that many of the papers written by active practitioners are not written with the aim of emphasising its relevance to real materials; rather they are written for those specialists interested in TEM for its own sake, for crystallographers and for those interested in crystal defects. It will be shown in this paper that it is the relatively simple applications that have now found their way into contributing to everyday, real engineering materials. Nevertheless these applications are based upon the information published in these relatively esoteric papers.

Conventional analytical TEM allows crystallographic information, compositional information and information concerning the nature of crystal defects, to be obtained at resolutions between about 1 and 10nm. For some specific applications, high resolution TEM allows information to be obtained at somewhat better resolution than this. The questions that need addressing in the context of the world of engineering materials are therefore (i) What value is crystallographic information? (ii) What value is compositional information and phase distribution? (iii) What value is defect information? The information which is of value to materials engineers, in making use of engineering materials is the information that allows the development of new materials, information that allows economical application of materials and information that allows the safe use of materials.

In the field of new materials there is no question that TEM is playing a significant role as can be illustrated with a few examples. Thus, the ability to determine the crystallographic and compositional information to characterise phases, plays an important part in the determination of phase diagrams. Where there is uncertainty concerning the precise position of a phase boundary it is commonplace to make up an alloy of appropriate overall composition and then to determine, using analytical TEM the phases present. This is particularly significant in new alloys based on intermetallics, where it is important to establish phase fields of ternary and quaternary alloys. Whilst these can be calculated, the calculations rely on the accuracy of experimental information and TEM is essential to fill in regions of phase diagrams where there is some uncertainty. Similarly, when new alloys are being investigated, it is essential to understand their response to thermal treatments and the determination of TTT curves of the complex alloys currently available requires TEM rather than optical microscopy. The development of superplastic Li-containing alloys such as 8090, provides another nice example of the role of TEM in the development of new alloys. The role of continuous nucleation of new grains and the ability to characterise subgrains and precipitates was an essential part in the development of these alloys and it is not easy to see how this work could have yielded such useful alloys were it not for the application of TEM.

148

The new materials which have been developed recently, or are still under development, include composites with both ceramic and metallic matrices, and intermetallic-based materials. The nature of the interface, between the matrix and the reinforcement, is one of the most important parameters in determining the properties and analytical TEM allows assessment of this interface. In this specific example diffraction and compositional information is needed. The diffraction data required is commonly as simple as the crystal system and the lattice parameters, rather than space group information. Similarly qualitative compositional analysis is commonly adequate to recognise the nature of phases and analysis corrected for absorption and/or fluorescence is not required.

In the case of intermetallic alloys the problem of the limited plasticity, which underlies the brittleness of this class of materials, can be understood in some cases using TEM. As these alloys continue to be developed, there is an important role in this area for TEM using defect analysis.

There are examples from earlier work where TEM has made valuable contributions; for example in the case of HSLA steels the nature of the precipitate phases, which are important in imparting strength, and in controlling grain growth, can be determined and the alloying addition adjusted to produce the precipitates required. In this case the identification of the composition and structure of small particles is required from diffraction and microanalytical data - again basic information is usually adequate. In the case of the development of Ti-Cu alloys, the heat treatment required to optimise the properties was developed using TEM to assess the effect of a range of heat treatments. In this way the best duplex aging treatment was developed which could generate the properties required, and which made sense commercially, so that heat treatment schedules could conveniently fit into shift times. Similar work on Al alloys has shown that the particular properties can be developed by a wide range of heat treatments, but it is only by using TEM to assess the details of the underlying mechanisms is it possible to predict the influence of complex aging procedures and thus save a great deal of development time. The development of high Al-content Ti alloys, for high temperature applications, led to embrittlement and it was mainly through the use of TEM that this was related to the formation of Ti_3Al in these alloys.

TEM can contribute to the production and processing of materials by short cutting the development of processing routes, by developing a better understanding. This is true for alloys which rely on the precipitation of phases that can be seen only with TEM, as already mentioned for TTT curves and superplastic alloys. This approach also plays a role in processing of Al and Ti-based alloys.

The obvious areas of maintenance, where TEM could be considered to have a role, are in prediction of creep and fatigue response ie in lifing, and in the assessment of the resistance to stress corrosion cracking and corrosion. The contributions of TEM in all of these areas are again more fundamental than of immediate value. TEM has uncovered some of the factors, which are important in creep and fatigue and in defining some of the principles that are important, but these observations do not allow prediction or a sufficient understanding to argue that they have made a valuable engineering contribution. In this area the emphasis of TEM has been in defect analysis and it must be admitted that this is the area where the role of TEM is the least significant from the engineering viewpoint.

The safe use of materials involves TEM in two ways. Firstly, if TEM has played a role in developing new materials, then their safe application in service will be partly measured by the confidence which TEM has generated in the relation between structure and properties. Secondly, TEM is used as a quality control and as a totally reliable way to ensure that heat treatments have been accurately carried out. Conversely, if there is some doubt about the properties of a batch of material, it is easy to see if this is associated with incorrect heat treatment by using TEM. This approach is used for example in the routine monitoring of Ti alloys and with Ni superalloys, where the size of gamma prime can be assessed using TEM.

On the basis of the brief consideration of the role of TEM in engineering materials, it appears that there are some areas where TEM has played and is playing, an important role, but it is hardly the most important tool available to the engineer. Its role will, however, increase as materials become more complex and as the approach based on nano technology increases in importance.

THE ROLE OF ELECTRON MICROSCOPY STUDIES ON THE DEVELOPMENT OF CERAMIC COMPOSITES

K. B. Alexander, H. T. Lin and P. F. Becher

Metals and Ceramics Division, Oak Ridge National Laboratory, P.O. Box 2008, Oak Ridge, TN 37831-6068

Advances in the development of ceramics and ceramic composites rely on an understanding of the mechanisms which contribute to the formation of desired microstructural features or control the mechanical response of the material. For example, in silicon nitride, careful control of the liquid phase composition and growth conditions permits the development of elongated grains which provide *in-situ* reinforcement of the material. Electron microscopy studies have aided in understanding the solution-reprecipitation process which controls the growth of silicon nitride as well as the role of the liquid phase on this process.[1] The composition and thickness of the residual glass phase at the grain boundaries and triple points are important for both the toughening and creep response of the material and can only be realistically analyzed by high resolution analytical and electron imaging techniques.

The use of ceramics is often limited by their inherent lack of resistance to crack growth. The intended applications of many ceramic components require long-term exposure to stress at high temperatures, thus creep resistance is also an important consideration.   Confirmation of the proposed toughening and creep mechanisms has relied heavily on electron microscopic observations. In transformation-toughened ceramics and composites, the transformation behavior and the role of microcracking have been clarified by transmission electron microscopy (TEM) studies.[2,3] Ceramics reinforced with non-ductile reinforcements are toughened as the result of a combination of crack bridging, crack deflection, and reinforcement pullout. Examples of some of these phenomena are shown in Fig. 1. In order for these mechanisms to be operative, the interface must be strong enough to transfer the load to the reinforcement but weak enough to debond and permit crack deflection and/or pullout.   The nature of the reinforcement/ceramic interface is therefore crucial to the toughening response and studies have emphasized the role of interface modification on the mechanical response.[4] Electron microscopy has been a critical component in these studies as the chemical and physical nature of the interface may be altered during the processing and fabrication of the composite. For example, the application of carbon films to fibers in fiber-reinforced ceramic composites fabricated by chemical vapor deposition methods has yielded substantial improvements in the toughening response.[4] Carbon coatings on silicon carbide whiskers used to reinforce alumina, however, have yielded inconsistent toughening results. The images in Fig. 2a and 2b show that the carbon film is no longer uniformly at the interface after composite fabrication, despite being present on the whiskers prior to fabrication, Fig. 2c. Recent results have shown that most of the carbon is abrasively removed from the whisker surface under certain powder/whisker mixing procedures and is present as pockets within the composite.[5]

Confirmation of the controlling creep mechanisms has often relied on electron microscopic observation of creep cavitation, grain boundary sliding, and reinforcement pullout. Often the scale of the creep damage is beyond the resolution of other techniques, and electron microscopy allows the presence and role of microstructural features such as grain-boundary films and amorphous triple-point pockets to be unambiguously determined. TEM observations of creep-induced reinforcement pullout and creep cavitation are shown in Figs. 3a and 3b, respectively.

Although electron microscopy can certainly yield impressive high resolution micrographs of ceramic crystal structures, its application to studying the mechanisms controlling microstructural development and toughening/creep response has resulted in the most useful information. These results have contributed to an increased understanding of the role of microstructure on the mechanical response and, thus, permit a basis for the design of advanced ceramic composites to be established.[6]

1. G. Petzow and M. J. Hoffmann, to published in S. Somiya, Ed., Advanced Structural Ceramics - V, Barkington, United Kingdom: Elsevier Applied Science Publishers (1992).

2. M. Ruhle et al., J. Am. Ceram. Soc., 69 (1986)195.
3. M. Ruhle et al., in N. Claussen et al., Ed., Advances in Ceramics, Vol. 12, Columbus, OH: The American Ceramic Society , Inc. (1983)256.
4. R. A. Lowden and K. L. More, in C. G. Pantano and E. J. H. Chen, Eds., Interfaces in Composites, MRS Symposium Proceedings 170, Pittsburgh, PA: Materials Research Society (1990) 273.
5. K. B. Alexander and P. F. Becher, Proc. Ann. EMSA Meeting 49(1991)920.
6. Research sponsored by the Division of Materials Sciences, Office of Basic Energy Sciences, U.S. Department of Energy under contract DE-AC05-84OR21400 with Martin Marietta Energy Systems, Inc. Part of the research was conducted utilizing the High Temperature Materials Laboratory User Program Facilities at Oak Ridge National Laboratory.
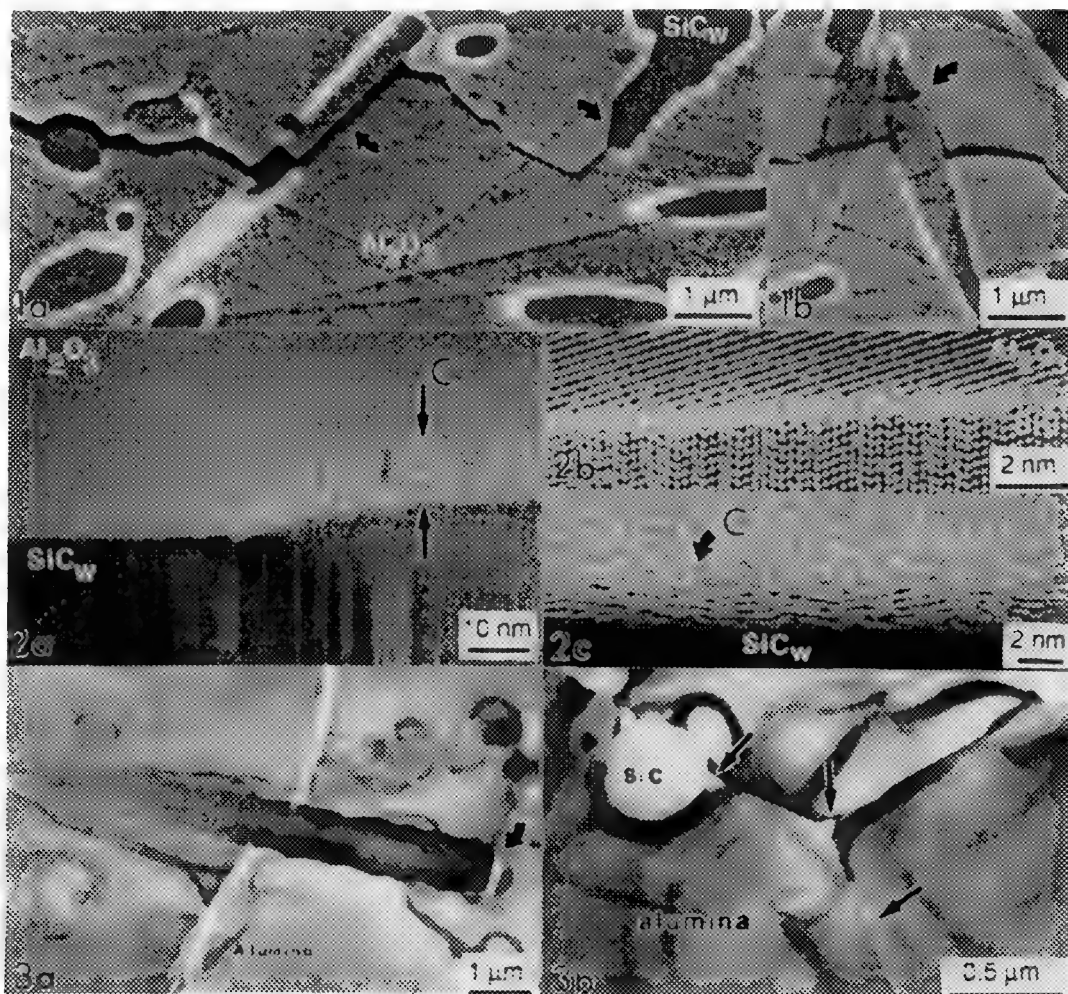
FIG. 1.--SEM images of crack interactions with silicon carbide whiskers (SiC_w) in reinforced alumina showing (a) crack deflection and debonding and (b) whisker pullout.

FIG. 2.--(a) Partial fragment of carbon film retained at the interface in alumina composite reinforced with carbon-coated SiC_w. (b) HREM image of interface representative of most of the interfaces. (c) Carbon-coating on whisker surface prior to composite fabrication.

FIG. 3.--(a) Whisker-pullout in SiC_w/alumina composite occurring during creep deformation. (b) Creep cavitation in SiC_w/alumina occurring during creep deformation.

PHASE IDENTIFICATION IN SiC WHISKER REINFORCED Al_2O_3-R_2O_3-BASED COMPOSITES

C.M. Sung, K.J. Ostreicher, M.L. Huckabee, and S.T. Buljan

GTE Laboratories Incorporated, 40 Sylvan Road, Waltham, MA 02254

A series of binary oxides and SiC whisker reinforced composites both having a matrix composed of an α-$(Al, R)_2O_3$ solid solution (R: rare earth) have been studied by analytical electron microscopy (AEM). The mechanical properties of the composites as well as crystal structure, composition, and defects of both second phases and the matrix were investigated. The formation of various second phases, e.g. garnet, β-Alumina, or perovskite structures in the binary Al_2O_3-R_2O_3 and the ternary Al_2O_3-R_2O_3-SiC(w) systems are discussed.

Sections of the materials having thicknesses of 100 μm - 300 μm were first diamond core drilled. The discs were then polished and dimpled. The final step was ion milling with Ar^+ until breakthrough occurred. Samples prepared in this manner were then analyzed using the Philips EM400T AEM. The low-Z energy dispersive X-ray spectroscopy (EDXS) data were obtained and correlated with convergent beam electron diffraction (CBED) patterns to identify phase compositions and structures. The following EDXS parameters were maintained in the analyzed areas: accelerating voltage of 120 keV, sample tilt of 12° and 20% dead time.

A bright field micrograph of the binary Al_2O_3-Er_2O_3 system revealed the lighter matrix grains (1~2 μm in diameter) and the darker contrast second phase grains, Figure 1. The darker grains contained Al, Er, and O. Overlapping of Al K_α and Er M_α peaks in the low energy region made the quantitative ratio of Al/Er difficult to obtain. Three phases have previously been reported for the binary Al_2O_3-Er_2O_3 system[1]. The identification of this phase was performed by means of crystal symmetry determination of CBED patterns. Initially, the relative orientations of three CBED patterns of low-index high symmetry were obtained. The symmetries exhibited by these patterns from which the possible diffraction groups were deduced are 4mm or $4mm1_R$ for the case of the [001] zone axis and 2mm or $2mm1_R$ for the [110] zone axis, Figure 2. The patterns of the [111] zone axis revealed a diffraction group of 6_Rmm_R. The point group corresponding to these diffraction groups was deduced as m3m. The space group was determined as Ia3d since no discrepancies between the allowed and observed reflections were found in terms of the indexing scheme and the presence of a (010) glide plane. Therefore, this phase was identified as $Er_3Al_5O_{12}$ (Erbium Aluminum Garnet: EAG) phase with a lattice parameter, a=1.1994 nm. The same EAG phase and SiC whiskers were found along with alumina matrix in the Al_2O_3-Er_2O_3-SiC system. Grains of this garnet phase were observed as a fan-shape pattern with grains likely having grown out from the core. Defects such as dislocations were not found in the EAG grains. However, a relatively higher density of dislocations were observed within the alumina grains adjacent to the agglomerated EAG grains.

Samples of Al_2O_3-Nd_2O_3-SiC revealed three phases: 1) alumina-rich matrix, 2) SiC whiskers, and 3) a second phase (darker in contrast). There was no evidence for any reaction between SiC whiskers and neodymium oxides. The second phase grains were located adjacent to SiC grains and showed a high density of twins which contained a small amount of Nd as well as Al and O, Figure 3. A CBED pattern taken from the second phase, Figure 4, was indexed properly as the $[2\bar{1}\bar{1}0]$ axis according to space group P6₃/mmc (a=0.563, c=2.201 nm). By tilting the crystal around the c-axis to avoid the forbidden reflections due to multiple diffraction, the extinction rule of this phase was obtained. The crystal was hexagonal and the systematic absent reflections were $l=2n+1$ for $00l$ and hhl. It was apparent that the characteristic diffraction spots of P6₃/mmc were present with changes in intensities according to the presence of Nd^{+3} introduced in the lattice of the $NdAl_{11}O_{18}$ structure[2,3]. The collection of zone axis

pattern (ZAP) maps will be continued and reported in future work to clarify crystal symmetry and structure of the $NdAl_{11}O_{18}$ phase.

In summary, an identification of unknown second phases present in the Al_2O_3-R_2O_3 and Al_2O_3-R_2O_3-SiC systems was performed by CBED and EDXS analysis. Such phase and microstructural information can be utilized to understand structure-property relationships in these systems.

References
1 J.J. Kingsley, K. Suresh, and K.C. Patil, J. of Solid State Chemistry, (1990)87, 435.
2. J.P. Coutures, J. Am. Ceram. Soc., (1985)68, 105.
3. D.J. Simkin, J. Phys. Chem. Solids, (1991)52, 175.
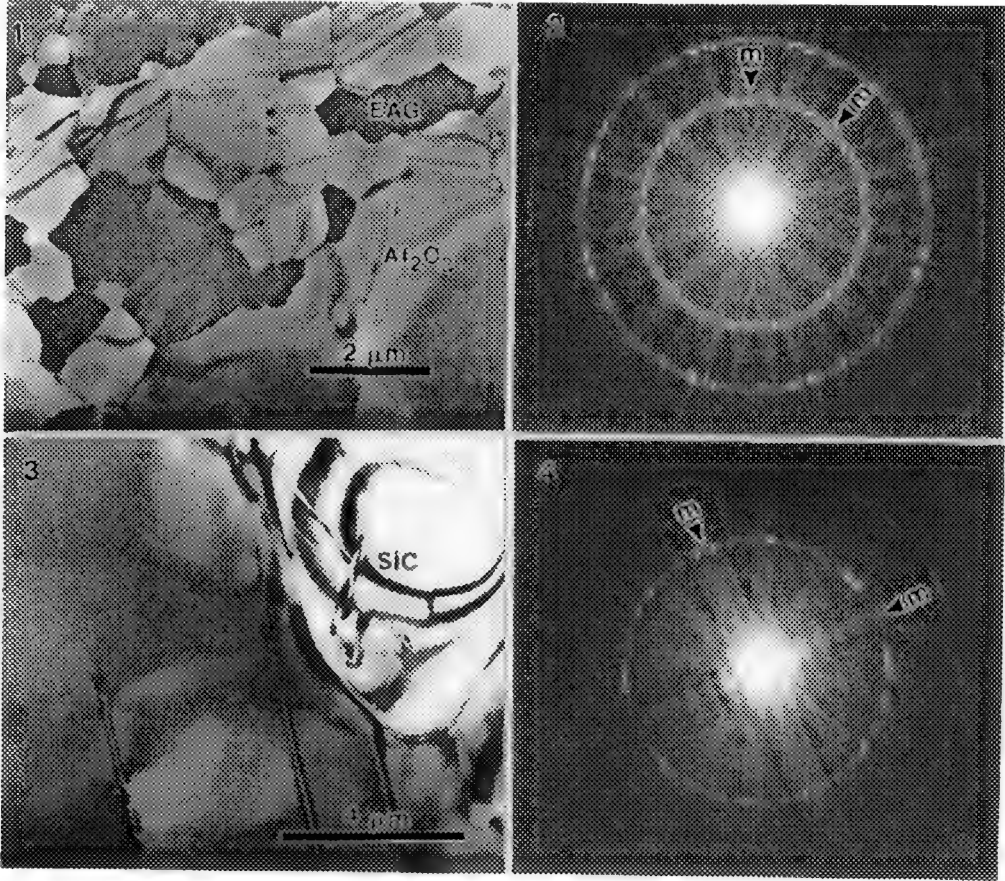
FIG. 1. Bright field image of the Al_2O_3-Er_2O_3 sample showing two phases.
FIG. 2. Whole pattern of CBED from a second phase; [001] zone axis, 4mm symmetry.
FIG. 3. Second phase grains adjacent to SiC showing twins in Al_2O_3-Nd_2O_3-SiC sample.
FIG. 4. CBED pattern from Al-Nd-O phase showing 2mm symmetry.

MEASUREMENT OF RESIDUAL STRESSES IN B4C-Al CERMETS BY CBED

G. H. Kim, M. Sarikaya, and I. A. Aksay

Department of Materials Science and Engineering, Advanced Materials Technology Center, Washington
Technology Center, University of Washington, Seattle, WA 98195

Ceramic-metal composites (cermets) are designed for improved toughness and strength over monolithic ceramic or metal components alone. They are used for structural applications where either metal or ceramic component cannot be employed separately, such as in impact- or wear- resistant structures which require high hardness and toughness. A well-known example is the WC-Co system (density 14.00 g/cc). We have been successful in developing a low-density (2.65 g/cc) B_4C-Al cermet system having fully dense cermet structures that are both tough, K_{IC} up to 16 MPa-m$^{1/2}$ in 3-pt SENB tests, and strong, 700 MPa in 4-pt bending tests, for ambient temperature applications (impact resistant).[1] In these cermets, B_4C (with a composition range from 60-85 v/o) and Al form a three-dimensional network as depicted in the BF/DF pair in Fig. 1.

Although the toughening mechanisms have been extensively studied in cermet systems, the strengthening mechanisms have not been well explained since strength depends on microstructural parameters such as the volume fraction and mean free path of metal phase, contiguity and grain size of ceramic phase. The strength of the cermet increases as the amount of metal is increased, reaches a maximum, and then decreases (Fig. 2). This strengthening behavior cannot be explained by simple composite rules, such as the rule-of-mixture shown as a straight line in Fig. 1. One possible strengthening mechanism may be the residual stresses that are created from the differential contraction in the metal and ceramic phase during cooling after the high-temperature infiltration (1200°C) of Al into the B_4C skeleton.

In order to test this hypothesis, we used convergent beam electron diffraction (CBED) patterns to determine quantitatively the amount and also the local variations of residual stresses in both B_4C and Al phases. In this procedure, the shifts in the positions of the higher order Laue zone, HOLZ, lines are determined in the central beam in various zone axis orientations. CBED patterns from the cermet were recorded along the 3-fold rotational symmetry axes that displayed clear HOLZ line shifts, and these were cross-checked against both the calculated patterns and those obtained from B_4C and Al standards, as shown in Fig. 3 (a - d). (All the experiments were conducted at 100 kV in a Philips 430T TEM/STEM using a probe diameter of about 200 Å and with a liquid-nitrogen-cooled double tilt holder.)

The results of the measurements indicate that the residual stresses in the Al phase range from 24 to 340 MPa and, similarly, residual compressive stresses from -137 to -314 MPa exist in B_4C phase which is consistent with the differences in coefficients of thermal expansion. The measured residual tensile stress in the Al region exceeds normal yield strength of Al by almost 300%, and since the B_4C phase is under compression, the failure strength is expected to increase.[2] The unique interpenetrating microstructure is believed to be responsible for constraining the deformation of the Al phase, allowing high tensile residual stresses to develop. The variations in the magnitude of residual stresses in both B_4C and Al phases reveal that the microstructural parameters such as mean free path and contiguity dictate localized stress profile and consequently the strength of the cermet. The amount of residual stress as a function of Al content in B_4C-Al cermets is consistent with the variation of strength of cermet (Fig. 2). The significance of these results is that residual stresses may play an important role in strengthening the B_4C-Al cermet, and it is likely that this mechanism may also operate in other cermet systems.[3]

1. A. J. Pyzik, I. A. Aksay, and M. Sarikaya, Ceramic Microstructures'86, (Plenum, New York,1987), pp. 45 - 54.
2. G.H. Kim, Ph.D. Thesis, University of Washington (1992).
3. Supported by the Air Force Office of Scientific Research under Contract No.AFOSR-91-0040.
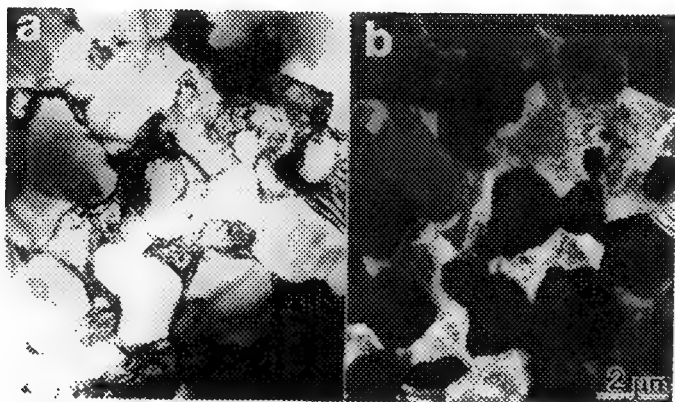
FIG. 1 TEM images of B$_4$C - Al cermet microstructure (a) BF and (b) DF image revealing three dimensional interpenetrating structure.
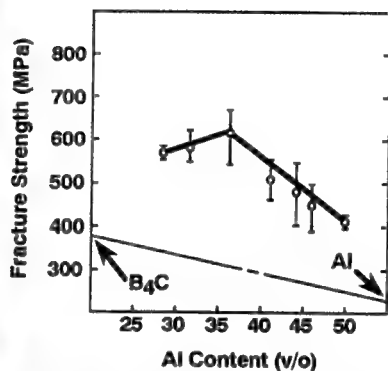
FIG. 2 Strength of B$_4$C - Al cermet as function of Al content.
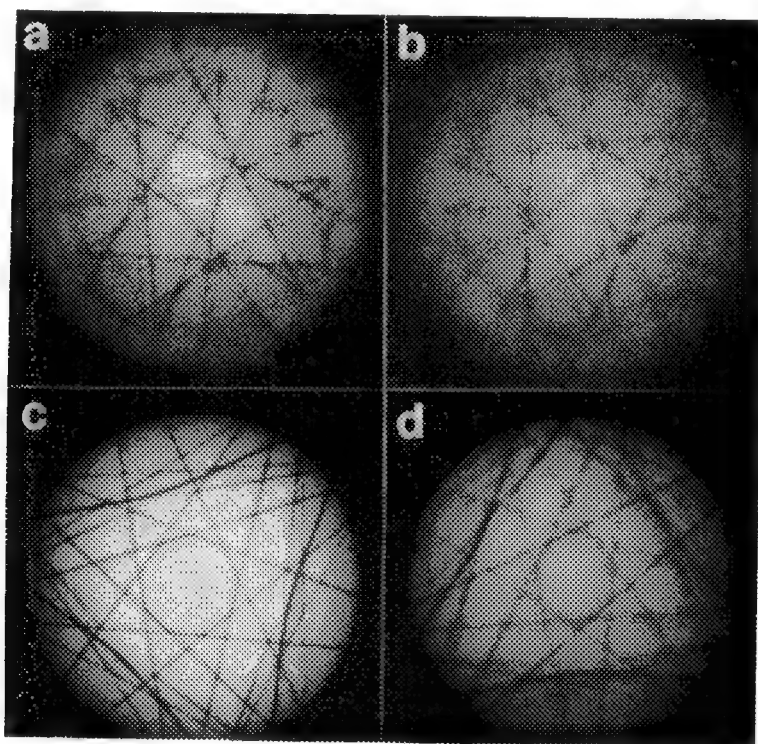
$$-\frac{\Delta a}{a} = \frac{2}{3} \cdot \left(\frac{q_{std}}{p_{std}} - \frac{q_i}{p_i}\right) \cdot \left(\frac{8}{131}\right)^{1/2}$$

Fig. 3 TEM CBED patterns taken from (a) B$_4$C powder as standard, (b) B$_4$C grain in B$_4$C-Al cermet, (c) Al standard, and (d) Al phase in B$_4$C-Al cermet (p_i = r$_{220}$; q_i = height of triangle).

155

EFFECT OF MATRIX CRYSTALLINITY ON THE CHARACTERISTICS OF THE INTERFACIAL LAYER IN SiC FIBER-REINFORCED Si-Al-O-N COMPOSITES

Hyun-Ho Shin, Yolande Berta, Chan Park, and Robert F. Speyer

New York State College of Ceramics, Alfred University, Alfred, NY 14802

Glass or glass-ceramics have been used as matrix materials for fiber reinforcing by the slurry infiltration process, followed by hot pressing. These matrices have been used for two major reasons: (i) They oxidize the SiC fiber to form a C-rich interfacial layer between the fiber and matrix during hot pressing $(2SiC(s) + O_2(g) = 2C(s) + 2SiO(g))$.[1] Such carbon-rich layers cause low fiber-matrix interfacial shear strength resulting in high composite fracture toughness. (ii) A low viscosity matrix is required to minimize fiber damage during hot pressing.[3] In the present study, the Si_2N_2O - Al_2O_3 system was used as a new host material for Nicalon SiC fiber: it has a more refractory nature and is able to provide a liquid phase (with the presence of a sintering agent, e.g., Al_2O_3, CaO, etc.) to avoid fiber damage during densification. This matrix system can also provide oxygen to form a C-rich interphase. In this paper, the effect of matrix crystallinity on the interfacial characteristics is described.

Composite fabrication required matrix powder mixing by ball milling for 12 h, slurry preparation (PVA/water solution and matrix powder), slurry infiltration into Nicalon SiC fiber (yarn), binder burn-out, and hot pressing at 1600°C for 30 min (15MPa). The two selected compositions for matrix materials were 50 wt% Si_2N_2O - 50 wt% Al_2O_3 (SA) and 60 wt% Si_2N_2O - 30 wt% Al_2O_3 - 10 wt% CaO (SAC). TEM samples were cut into 3 mm discs, thinned mechanically to 120 μm, dimpled to 40μm, and then Ar ion milled to electron transparency using a liquid nitrogen cold stage.

The x-ray diffraction (XRD) pattern (Fig. 1) of the SAC matrix showed only Si_2N_2O, but at a reduced relative intensity (one-fourth) as compared to the pattern for pure Si_2N_2O (not shown). In the TEM microstructure of the SAC composite (Fig. 2), the Si_2N_2O phase and a large volume of amorphous phase (G) are observed, the glassy phase having been the cause of reduced XRD intensity for Si_2N_2O. The TEM SAD pattern (Fig. 3) at G in Fig. 2 confirms the amorphous nature of that area. Figs. 4 and 5 show the bright and dark field images, respectively, of the SA composite. As shown in the figures, the SA matrix contained no apparent glassy phase. From XRD (Fig. 1), the SA matrix showed a reduced intensity of Si_2N_2O, as well as the new sialon phase. The absence of calcia and the higher alumina content in SA as compared to SAC tended to form the new sialon phase in favor of glassy phase. As shown in Figs. 2 and 4, the C-rich interphase was relatively thick ($\sim$ 100 nm) and uniform when the matrix contained glassy phase (SAC sample), and was thin ($\sim$ 35 nm) and irregular when the matrix contained no apparent glassy phase (SA sample). The carbon-rich interphase was formed via the oxidation of SiC fiber by the oxide matrix.[1,3] The thickness of the carbon-rich interphase can be correlated to the amount of fluid phase in the matrix during hot pressing, observed in the TEM microstructures as glassy phase. The oxygen in this liquid phase (within the SAC matrix) is expected to be less tightly bound and hence more easily donated for interphase formation, than would the oxygen in the crystalline phases in the SA matrix. It is thus concluded that carbon-rich interphase formation is strongly governed by the degree of matrix crystallinity.

References

1. H.H. Shin *et al.*, in preparation.
2. K.M. Prewo, *Am. Ceram. Soc. Bull.*, (1988)**68**[2] 387.

3. R.F. Cooper and K. Chyung, *J. Mater. Sci.*, (1989)**22** 3148.
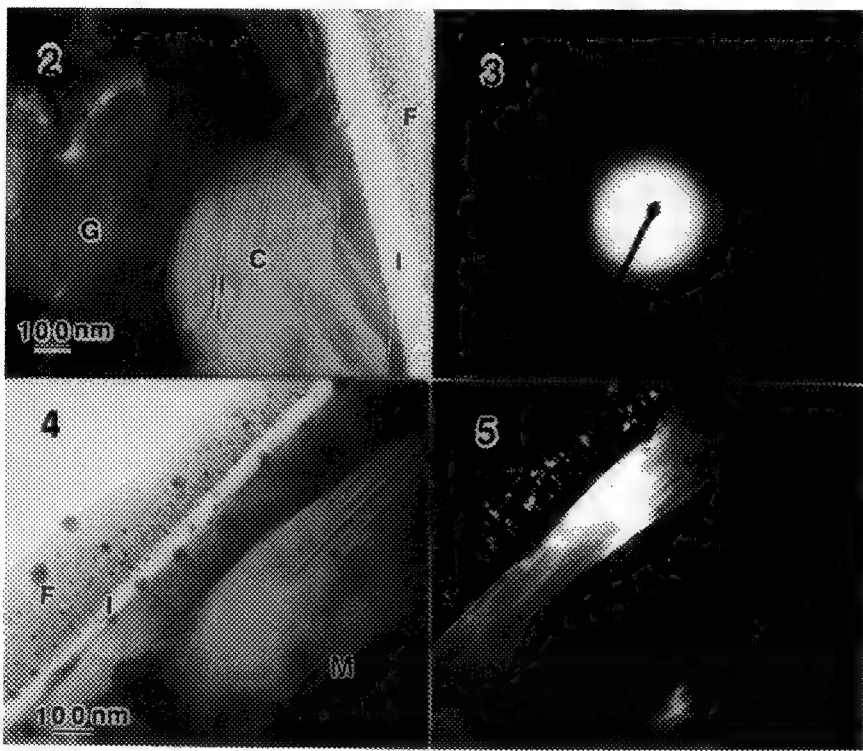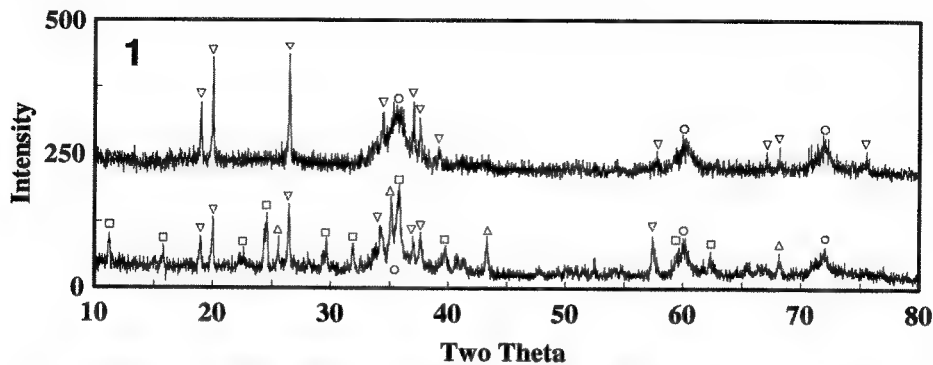
FIG. 1. XRD patterns of SAC (upper) and SA (lower) composites (circle: SiC fiber, reverse triangle: Si_2N_2O, square: sialon x (JCPDS: 31-32), triangle: residual alumina).
FIG. 2. TEM microstructure of the SAC composite (G: glassy phase, C: crystalline phase, I: interphase, F: fiber).
FIG. 3. SAD pattern of area G in Fig. 2.
FIG. 4. TEM microstructure of the SA composite (F: fiber, I: interphase, M: matrix).
FIG. 5. Dark field image of Fig. 4.

DEFORMATION AT INTERFACES OF Ti-6Al-4V/SiC FIBER COMPOSITES

Warren J. Moberly*, Daniel B. Miracle** & S. Krishnamurthy**

*Department of Materials Science & Engineering, Stevens Institute of Technology, Hoboken, NJ 07030
**Air Force Materials Laboratory, WRDC/MLLM, Wright-Patterson AFB, OH 45433-6533

Titanium-aluminum alloy metal matrix composites (MMC) and Ti-Al intermetallic matrix composites (IMC), reinforced with continuous SCS6 SiC fibers are leading candidates for high temperature aerospace applications such as the National Aerospace Plane (NASP). The nature of deformation at fiber / matrix interfaces is characterized in this ongoing research [1]. One major concern is the mismatch in coefficient of thermal expansion (CTE) between the Ti-based matrix and the SiC fiber. This can lead to thermal stresses upon cooling down from the temperature incurred during hot isostatic pressing (HIP), which are sufficient to cause yielding in the matrix, and/or lead to fatigue from the thermal cycling that will be incurred during application [2, 3]. A second concern is the load transfer, from fiber to matrix, that is required if/when fiber fracture occurs. In both cases the stresses in the matrix are most severe at the interface.

The deformation in the matrix near the interface, especially between fibers of close proximity, is "constrained" such that initial deformation is expected to occur displaced from the interface. This constrained deformation [4] occurs in two modes in this composite system. Firstly, when two fibers are closely spaced, a region of the more ductile matrix is "surrounded" by brittle material. When pulled in tension, the ductile material between fibers is constrained such that necking is hindered. Secondly, when a fiber fractures, the load that was carried by the fiber must be transferred to the surrounding matrix. Again the matrix region surrounding a fractured fiber exhibits a constrained stress state. In both cases the Von Mises stress is lowered near to the interface, and deformation is predicted to first occur in the matrix at some distance from the interface.

In this study composites have been prepared from Ti - 6 wt% Al - 4 wt% V and three Textron SCS6 SiC fibers of ~140 μm diameter. The continuous fibers have been placed between foils of the matrix and subsequently HIPed at 1200°C. The microstructure of tensile specimens which have undergone 1/2% and 19% tensile deformation are compared to the as-HIPed microstructure. Cross-section TEM samples have been prepared and analyzed by TEM and HVEM. (The sample preparation methodology for MMC and IMC composites is discussed in a separate paper presented at this EMSA conference.) With only three fibers in the composites, the overall volume fraction of fibers is <1%. However, the close proximity of fibers results in the "localized" volume fraction between fibers to be as high as 40 - 60%. Finite Element Method (FEM) models of this high volume fraction indicates that deformation is expected due to stress resulting from CTE mismatch in the as-processed composites. Such localized deformation is observed by TEM. Matrix grains not situated between fibers exhibit no dislocations. Some matrix grains between fibers of <50 μm spacing exhibit a row of dislocations displaced from the interface (FIG.1a). FIG.1b depicts dislocation pile-ups perpendicular to the interface in matrix grains that are between fibers of <20 μm spacing. Such pile-ups differ from other composite systems comprised of reinforcing fibers (or particulates) which are substantially smaller than the matrix grains, where dislocation emission from the fiber / matrix interface has been observed [5].

After 1/2% tensile deformation, a higher dislocation density is observed in α Ti matrix grains near the fiber / matrix interfaces, as compared to α grains far from the interface. Although HVEM allowed for the analysis of dislocations in thicker grains, no significant difference in dislocation density has been measured by HVEM vs. traditional TEM analysis, as has been reported for Al-based composites [6]. The majority of the dislocations have $b = <2\bar{1}10>$. Planar slip (see FIG.2a) is more commonly observed in α grains near the fiber interface. Such planar slip in Ti alloys has been attributed to oxygen (or other interstitial) contaminants [7], which in this case may be associated with interdiffusion between fiber and matrix during processing. Dislocations that are in rows which are perpendicular to the fiber / matrix interface exhibit pile-ups at grain boundaries (FIG.2b), whereas dislocations in rows which are parallel to the composite interface do not exhibit pile-ups (FIG.2c).

References
1. W. J. Moberly, AFOSR-SFRP report published by Research Development Corporation, 1991.
2. G. S. Daehn & G. Gonzalez-Doncel, Metall. Trans., 1989, 20A, p.235.
3. R. P. Nimmer, R. J. Bankert, E. S. Russell & G. A. Smith, *Proceedings ASM,* Indianapolis, 1989.
4. M. F. Ashby, F. J. Blunt & M. Bannister, Acta Metall., 1989, 37, p.1847-1857.
5. R. J. Arsenault & N. Shi, Matls. Sci. Eng., 1986, 81, p.175.
6. M. Vogelsang, R. J. Arsenault & R. M. Fisher, Metall. Trans., 1986, 17A, p.379.
7. J. C. Williams & G. Luetjering, *Proceedings 4th IC on Titanium,* Kyoto, Japan, 1980, p. 671.
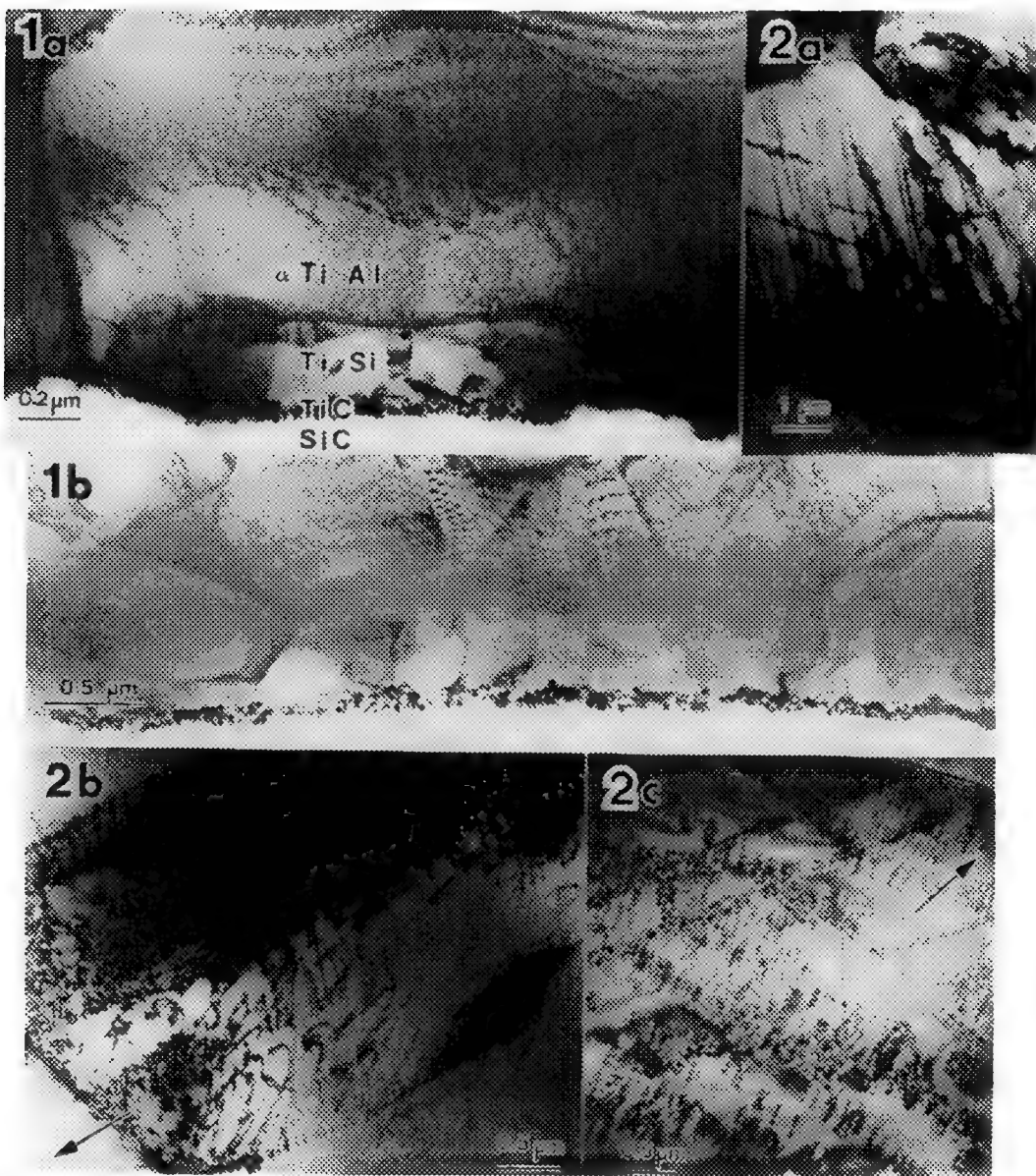
FIG.1a.--TEM micrograph of interface region of Ti-6Al-4V / SiC fiber-reinforced composite, as-Hot-Isostatic-Pressed at 1200°C. Rows of dislocations in α Ti grains, displaced from the interface phases, are observed in α grains nearest the interface, when the inter-fiber-spacing is <50 microns. FIG.1b.--TEM micrograph of dislocation pile-up in α Ti grains at interface of as-HIPed composite, where inter-fiber-spacing is <20 microns. FIG.2a.--High Voltage (1500 KeV) TEM micrograph of planar slip in α Ti grains close to the interface, after 1/2% tensile deformation. FIG.2b.--HVEM micrograph of dislocation pile-up after 1/2% tensile deformation. FIG.2c.--TEM micrograph of α Ti grain, where no dislocation pile-up at grain boundaries is observed in rows of dislocations parallel to nearby composite interface. Arrows in FIG.2b and 2c point toward composite interface. BF TEM images are acquired with a 2-beam condition of $g = <1\bar{1}01>$ (except FIG.2c where $g = <1\bar{1}00>$), and dislocations have $b = <2\bar{1}\bar{1}0>$.

159

USE OF EDS MAPPING TO CHARACTERIZE THERMOCHEMICAL STABILITY OF FIBERS IN INTERMETALLIC MATRIX COMPOSITES

John R. Porter

Rockwell International Science Center, Thousand Oaks, CA 91360

New ceramic fibers, currently in various stages of commercial development, have been consolidated in intermetallic matrices such as γ-TiAl and FeAl. Fiber types include SiC, TiB_2 and polycrystalline and single crystal Al_2O_3. This work required the development of techniques to characterize the thermochemical stability of these fibers in different matrices.

SEM/EDS elemental mapping was used for this work. To obtain qualitative compositional/spatial information, the best realistically achievable counting statistics were required. We established that 128 x 128 maps, acquired with a 20 KeV accelerating voltage, 3 sec. live time per pixel (total mapping time, 18 h) and with beam current adjusted to give 30% dead time, provided adequate image quality at a magnification of 800X. The maps were acquired, with backgrounds subtracted, using a Noran TN 5500 EDS system. The images and maps were transferred to a Macintosh and converted into TIFF files using either TIFF Maker [1], or TNtoIMAGE, a Microsoft QuickBASIC program developed at the Science Center. From TIFF files, images and maps were opened in either NIH Image [1] or Adobe Photoshop for processing and analysis and printed from Microsoft Powerpoint on a Kodak XL7700 dye transfer image printer.

From the elemental maps, two approaches were used to produce phase maps. If only three elements were to be combined into a phase map, then the maps were opened in Adobe Photoshop as grayscale images, contrast enhanced with the aid of the histogram outputs to expand the image intensity to the full 255 gray levels and the Adobe Photoshop "despeckle" noise reduction filter applied. The three elemental maps were then used as the red, green or blue channels of full color RGB images allowing the different associations of elements to be clearly identified and portrayed. For example, the combination Ti (red), Al (green) and Mo (blue) clearly showed γ-TiAl as a yellow phase. For phase maps with more than three contributing elements, maps were converted to binary images, with thresholds selected by examination of map histograms. Phase maps were then prepared by using each binary map to turn on one bit in each byte of the phase map. The resulting phase maps were then opened in NIH Image and pseudocolored to reveal each phase. The limitation of this technique in practice is the number of distinct colors that can be created on a screen and on a print, making a 4 element phase map the practical limit.

As an example, figure 1 depicts a sapphire fiber in a γ-TiAl matrix that was fabricated with a thin layer of Ag as a consolidation aid at the interface. The fiber was degraded by the matrix and the reaction product at the interface of oxygen stabilized Ti_3Al was confirmed using TEM of fiber interface cross sections. Elemental mapping, using the long acquisition times, was able to detect the migration of Ag back into the γ-TiAl matrix, although it was not apparent in the Ti_3Al phase.

Reference.
1.   Electron Microscopy and Microanalysis Public Domain Library, 1-800-627-EMSA, (1991).
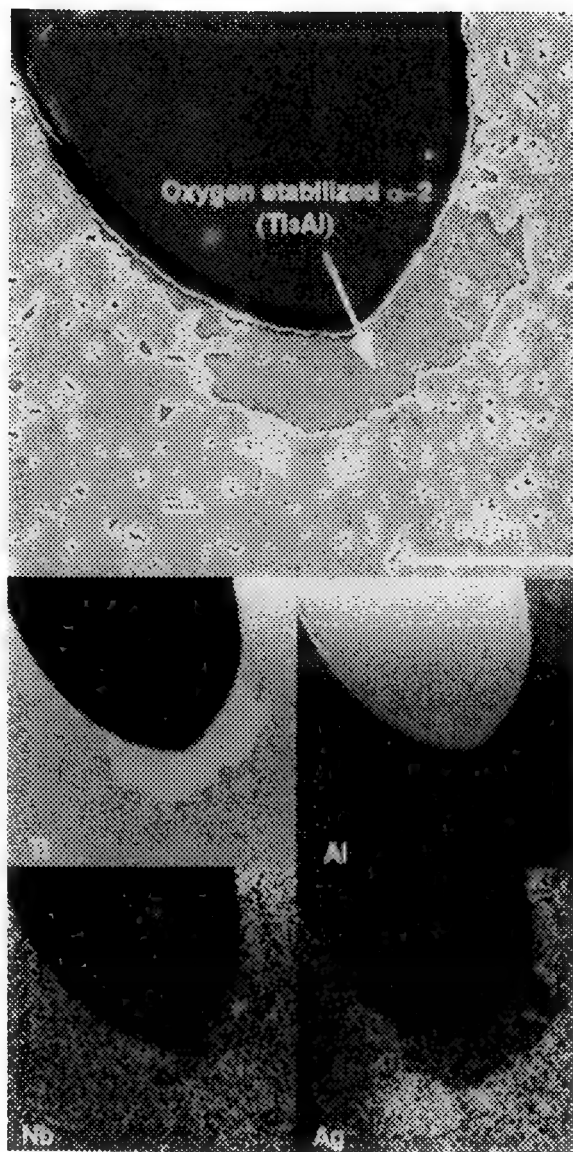
FIG. 1. Saphikon Al_2O_3 fiber in γ-TiAl. Fabrication by transient liquid consolidation using Ag in Ti, 48% Al, 2.5% Nb, 0.3% Ta matrix (Sample courtesy C. C. Bampton).

THE ROLE OF MICROSCOPY IN THE DEVELOPMENT OF METAL MATRIX COMPOSITES

Gilles L'Espérance and David J. Lloyd*

Centre for Characterization and Microscopy of Materials, $(CM)^2$, Department of Metallurgy and Materials Engineering, École Polytechnique de Montréal, Montréal, Canada, H3C 3A7
* Alcan International Ltd, Kingston Research and Development Centre, P.O. Box 8400, Kingston, Ontario, Canada, K7L 5L9

From the very beginning of the development of metal matrix composites, (MMC's), electron microscopy has played a major role in their development. Thus, analytical transmission electron microscopy, (ATEM), has been used to characterize and study: (1) the reinforcements in MMC's, (2) interfacial reactions and products that can occur at the interface between the matrix and the reinforcement and (3) the detailed matrix microstructure, particularly the dislocation and grain structure and the precipitation/constituent phases. In this presentation, we will review and discuss the contribution of ATEM to each of these points and describe how it provided necessary information in the design and use of these materials. The presentation will mainly discuss Al-based composites although work from Ti and Mg-based composites will also be presented.

Figure 1 shows a dark field TEM micrograph of a SiC whisker. The whisker is heavily twinned with the {111} twins normal to the longitudinal <111> growth axis as reported previously for VLS grown whiskers [1]. Perturbations in the growth, however, induced thicker areas for which the macroscopic [200] growth direction is the bisector of the angle between two microscopic [$\bar{1}11$] and [$\bar{1}1\bar{1}$] growth directions defined by two series of twinning planes (Figure 2). The effect of faulting of the reinforcements on the final properties of the material is not clear but it is unlikely that it can be avoided as it is clearly a feature of the growth process itself.

Interfacial reactions between the matrix and the reinforcement are generally considered deleterious to the properties of the material because they degrade the reinforcement. Thus, figure 3 shows a scanning electron micrograph of spinel ($MgAl_2O_4$) crystals formed at the interface between Al_2O_3 reinforcing particles and an Al matrix containing Mg. Interfacial reactions can also significantly modify the chemistry of the matrix and therefore the subsequent properties of the composite. For example, the interface can serve as a preferential site for precipitation of potentially matrix hardening phases and spinel crystals formed at the interface will deplete the matrix in Mg and sometimes totally suppress age hardening of the material [2]. This information allows adjustment of the composite composition to account for the depletion in Mg and thus control age hardening.

During processing, it is often critical to control the size and morphology of grains of the matrix as well as the structure and chemistry of the matrix/reinforcement interface to achieve the behaviour desired. Figure 4 shows that Mg, Cu and O is segregated at the $Si_3N_4w/2124$ interface during fabrication of the composite by powder metallurgy. The local melting point of the matrix at the interface will be lower than that in the bulk of the matrix due to the higher Mg content at the interface so that it is thought to be in a semi-liquid state during deformation at high temperature. The semi-liquid interface and the very small grain size of the matrix are considered to largely account for the superplastic behaviour of this material and the accommodation processes that must occur at the $Si_3N_4(w)/2124$ interface during deformation to yield the very large tensile elongations observed (> 300%) at relatively large strain rates (0.2 s^{-1}). These examples have served to show that the ability to characterize in detail the microstructure of MMC's by ATEM enables one to determine and understand the roles of both material and process parameters and thus contribute to a better control of the final properties of these new materials.

References

1. W. Braw, R.W. Carpenter and D.J. Smith, 46th EMSA Proceedings, (1988), p. 734.
2. D.J. Lloyd, H.P. Lagacé and A.D. McLeod, Proc. ICCI-III, "Controlled Interphases in Composites Materials" ed. H. Ishida, Elsevier, (1990), p. 359.

162
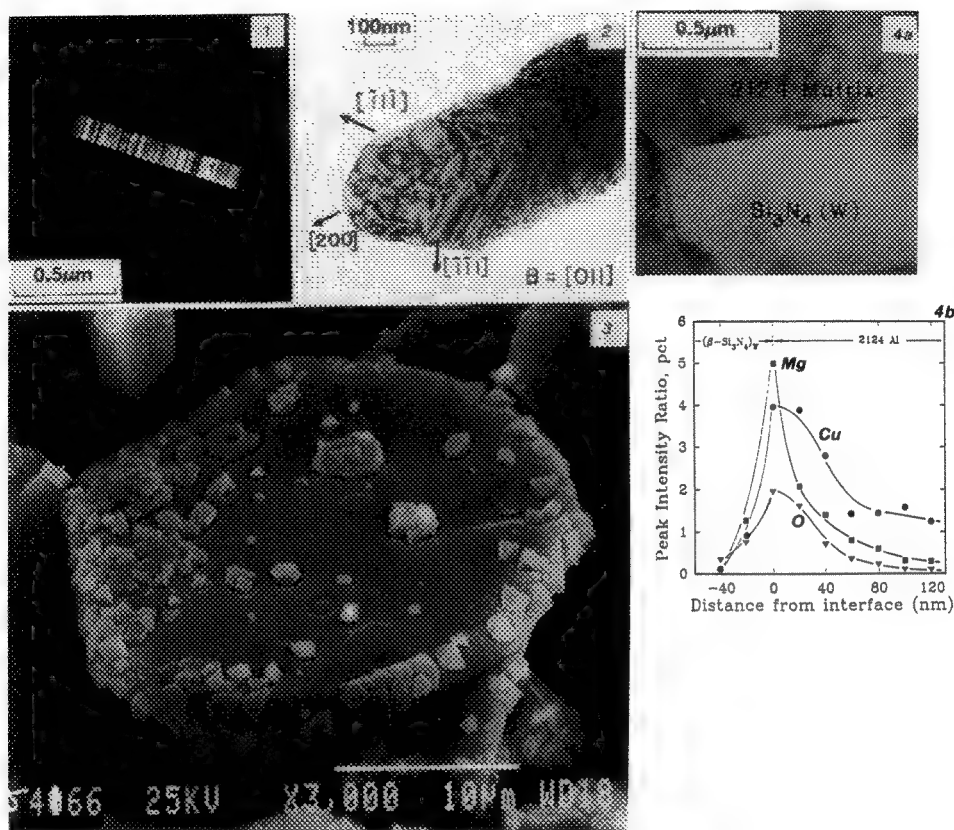
Figure 1:   Dark field TEM micrograph of a SiC whisker. The longitudinal growth direction of the whisker is <111>, normal to the {111} twins.

Figure 2:   TEM micrograph of a thicker area of a SiC whisker. The macroscopic [200] growth direction is the bisector of two microscopic <111> growth directions.

Figure 3:   SEM micrograph of spinel crystals formed at the interface between Al_2O_3 particulates and a Mg-containing Al matrix. The matrix was preferentially dissolved prior to observation of the particles.

Figure 4a): TEM micrograph of a Si_3N_4(w)/2124 interface in a composite deformed at 525°C and 0.17 s^{-1}.

4b):   EDS profile across the Si_3N_4(w)/2124 interface. The intensities of Mg, O and Cu are expressed as a ratio with respect to Al.

163

THE ROLE OF MICROSCOPY IN THE DEVELOPMENT OF Ti-BASED INTERMETALLIC ALLOYS

Ernest L. Hall

GE Corporate Research and Development, PO Box 8, Schenectady, NY 12301

For the past two decades there has been interest in the development of Ti-based intermetallic alloys for aircraft structural and engine applications, culminating in intense activity over the past five years. The primary driver for this interest is the increase of the strength/weight ratio for aircraft materials, and the low density, high modulus, and high melting temperature of some Ti alloys make them promising candidates. Most of the work has centered on the Ti-Al system, particularly Ti_3Al (ordered DO_{19} structure, space group P6$_3$/mmc), TiAl (ordered $L1_0$, space group P4/mmm), and, more recently, an new ordered orthorhombic alloy (O-phase) based on Ti_2AlNb (space group Cmcm). The primary limitation of these alloys is low ductility at room temperature, although improvements in ductility, strength, and creep resistance at low and elevated temperatures are also continuing goals. Transmission electron microscopy has played a key role in the understanding of the behavior of these alloys and has defined possible pathways for property improvement. Microscopy studies have focused on many issues, including: deformation mechanisms at low and elevated temperatures, and their relation to ductility, strength, creep, and fracture; the role of interstital elements; the role of ternary and quaternary additions; phase equilibria and stability; and the microstructure of alloys containing dispersoids or reinforcing fibers. Some highlights of these studies will be discussed briefly below.

In the TiAl alloy system, pioneering work by Shechtman et al.[1] showed that TiAl had very low ductility at room temperature, and that the ductility increased dramatically above 700°C. Their microscopy studies showed that the room temperature deformation structure was characterized by pinned faulted partial dislocation dipoles trailing from superdislocations, and that these dipoles disappeared at or near 700°C. Nearly 15 years later, two new microscopy results stimulated the growth in interest in this alloy system. In the first, Hug et al.[2] described in detail the nature of the superdislocation in TiAl alloys deformed at room temperature, the mechanism of formation of the faulted dipoles, and the effect of temperature on the deformation mechanisms. In the second, Hall and Huang[3] showed that TiAl alloys containing a small amount of Ti_3Al as a second phase ("duplex" alloys) had higher strength and ductility than single-phase TiAl alloys (Fig. 1). They also showed a marked difference in the deformation mode of these duplex alloys at room temperature, with twins and unit dislocations predominating in the duplex alloys (Fig. 2). Subsequent work by them showed that ductile behavior in TiAl was always associated with unit dislocations and twins as the microstructural features. More recent work has centered on defining the key factors responsible for the difference between the behavior of duplex and single-phase alloys, and on improving the ductility of duplex alloys. Interstital elements such as O and N have been shown to be important, with the Ti_3Al phase in the duplex alloys acting as a getter for these elements. Hug and Veyssiere[4] have described a dislocation mechanism for the transition from superdislocations to unit dislocations and twins, and suggested the importance of stacking fault energy. Ternary and quaternary additions have been shown to improve ductility primarily by increasing the amount of second phase and by their effect on stacking fault energy. There has also been much speculation on the role of covalent bonding on dislocation mobility.[5] A yield-stress anomaly has been noted in TiAl single crystals, and a dislocation mechanism proposed to explain this phenomenon.[6] A much more complete review of the role of microscopy in the understanding of mechanical behavior in TiAl has been published by Hall and Huang.[7] Finally, some very recent work has concentrated on the role of boron in improving the castability, strength, and ductility of TiAl alloys, and has shown that ribbons of TiB_2 act to refine the grain size in castings.

A similar body of work exists concerning microstructure/property relations in Ti_3Al alloys. For binary alloys, limited ductility at room temperature has been shown by microscopy to be the result of a single dominant slip system and limited mobility of screw segments in this system[8]; this limited mobility may also be related to covalency effects. The effect of increasing temperature on deformation is primarily to increase the mobility of these dislocations and to activate climb. Small amounts of Nb (4%) have been shown to increase the number of slip systems active at room and elevated temperatures. For several years, the use of stable dispersoids (usually Er_2O_3) to strengthen Ti_3Al was an area of active microscopy investigation. More recently, the strengthening of Ti_3Al matrices with fibers (usually SiC) has been explored, and microscopy has shown in detail the nature of the

reaction between the fibers and the matrix. This has led to a better understanding of the role of fiber coatings and of the overall mechanical behavior of these composites.

A final group of Ti-based intermetallic alloys in which microscopy has played a key role is the orthorhombic, or O-phase, alloys based on Ti_2AlNb. This phase occurs in Ti_3Al alloys containing 15-30% Nb. This phase was first identified, and the crystal structure determined, by Banerjee et al.[9] using convergent-beam electron diffraction. They showed that the O-phase is based on Ti_3Al with a slight distortion of the unit cell and a change in ordering to produce orthorhombic symmetry. O-phase alloys exhibit superior strength and toughness compared to Ti_3Al, and Banerjee has also recently conducted TEM dislocation studies which show the relationship between Ti_3Al and O-phase deformation modes.[10]

1. D. Shechtman et al., Metall. Trans. 5(1974)1373.
2. G. Hug et al., Phil. Mag. A 54(1986)47.
3. E. L. Hall and S. C. Huang, J. Mater. Res. 4(1989)595.
4. G. Hug and P. Veyssiere, Proc. Int. Symp. on EM in Plasticity and Fracture Res. of Materials, Dresden, 1989.
5. S. A. Court et al., Phil. Mag. A 61(1990)141.
6. G. Hug et al., Phil. Mag. A 57(1988)499.
7. E. L. Hall and S. C. Huang, in Y.-W. Kim and R. R. Boyer, eds., Microstructure/Property Relationships in Ti Aluminides and Alloys, Warrendale, PA:TMS (1991) 47.
8. S. A. Court et al., Phil. Mag. A 61(1990)109.
9. D. Banerjee et al., Acta Metall. 36(1988)871.
10. D. Banerjee et al., Materials Research Society Symp. Proc., 213(1991)285.
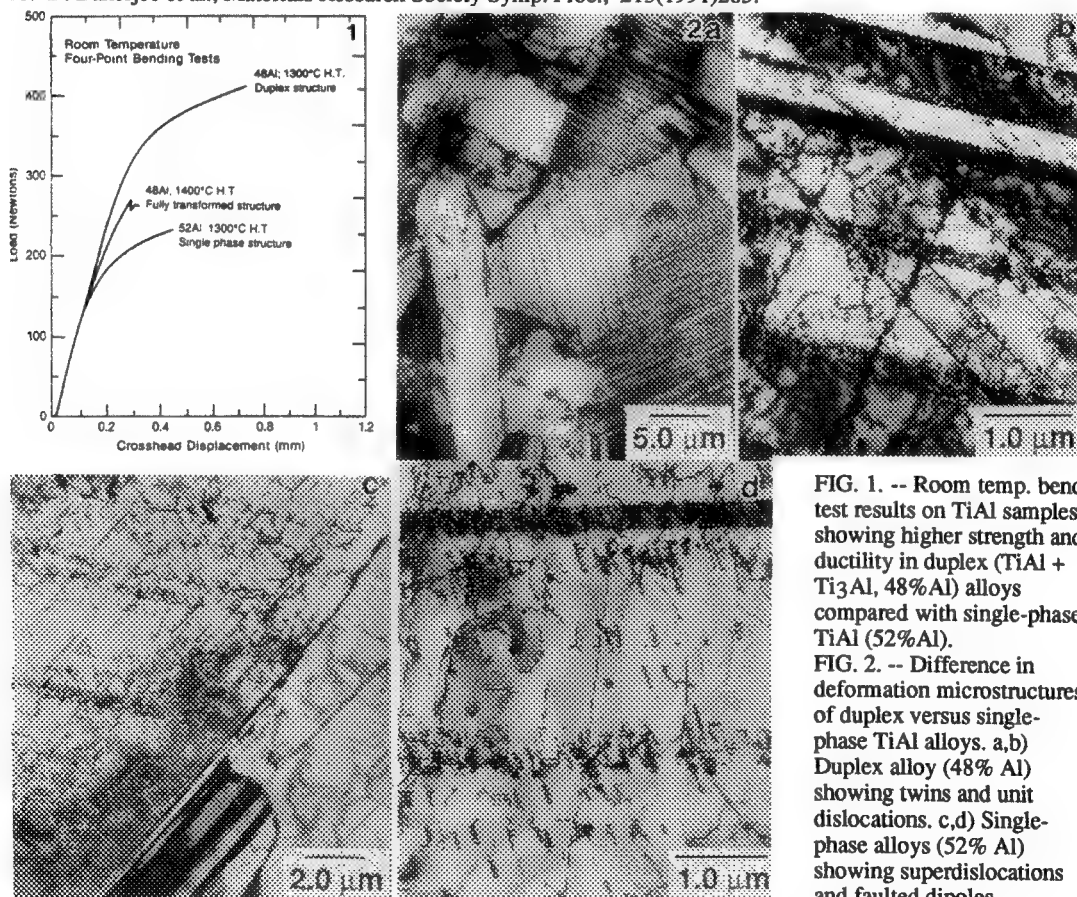
FIG. 1. -- Room temp. bend test results on TiAl samples, showing higher strength and ductility in duplex (TiAl + Ti_3Al, 48%Al) alloys compared with single-phase TiAl (52%Al).

FIG. 2. -- Difference in deformation microstructures of duplex versus single-phase TiAl alloys. a,b) Duplex alloy (48% Al) showing twins and unit dislocations. c,d) Single-phase alloys (52% Al) showing superdislocations and faulted dipoles.

THE MICROSTRUCTURE OF AN OXIDIZED γ-TiAl+Cr ALLOY

J.A. Sutliff, S.C. Huang, and D.W. McKee

GE Corporate Research and Development, 1 River Road, Schenectady, NY 12309

Alloys based on the intermetallic phase γ-TiAl are considered good candidates for some high temperature aircraft engine applications. While a tremendous effort has been made to understand the mechanical properties of γ-TiAl, relatively little effort has been made to understand its oxidation behavior. Two of the authors have studied oxidation of several γ-TiAl alloys containing ternary and quaternary additions including Cr, Mn, Nb, Ta, and W.[1] In this paper, we present some of the microstructural observations on an oxidized γ-TiAl alloy.

An oxidized γ-TiAl alloy with a nominal composition of 50 at% Al and 2 at% Cr was examined using analytical electron microscopy. Oxidation of polished pieces occurred in air at 850°C for 6 hours. The pieces were ground from the unpolished side to a thickness of ~75 μm and 3 mm disks were punched. The disks were electropolished in a perchloric/methanol solution. Electropolishing was done from the metal side only until "perforation" of the metal substrate. This resulted in a sample with an oxide 'window'. The samples were further thinned by ion beam milling (5kV/500μA Ar⁺) from the oxide surface toward the oxide/metal interface. The sample was examined in a Philips EM430 TEM operated at 300 kV and x-ray spectra collected with an EDAX energy dispersive x-ray spectrometer having a windowless Si(Li) detector.

The oxide layer contained two phases, α-alumina (Al_2O_3) and rutile (TiO_2), as determined by electron diffraction and qualitative x-ray analysis. Figure 1 shows the structure of the mixed oxide. The rutile occurred primarily as an extremely fine grain, filler amongst coarser blocky or lath-like alumina grains. Coarser needles of rutile were also found in very thick oxide regions. Neither oxide phase contained Cr. No nitride phases were detected in the oxide layer.

The microstructure of the zone near the metal/oxide interface was complex. Figure 2 is a micrograph of Cr containing phases in the zone. Electron diffraction identified the pseudo-cubic gamma phase as expected, but two other phases were also identified. The first phase produced diffraction patterns consistent with a Ti-Cr-Al phase described in Pearson's Handbook[2] (HP structure a=0.4956 nm, c=0.8090 nm) and was found to have a relatively high Cr concentration. The second phase was not a known Ti-Al-Cr phase. The x-ray spectrum from this phase, shown in Figure 3, contains about twice the Cr signal and half the Al signal of that from an adjacent gamma grain, shown in Figure 4. This chemistry is more like an alpha- or beta-Ti phase. Diffraction patterns were obtained from the new phase and these showed cubic 4-fold, 3-fold, and 2-fold axes with all primitive reflections present for a cubic lattice having a lattice parameter of 0.69 nm, Figure 5.

In summary, the oxidation in 850°C air of a γ-TiAl alloy containing 2% Cr produces a complex Cr-enriched zone and a mixed oxide layer of α-alumina and rutile. No nitrides were detected in the oxide layer. Neither the alumina nor rutile incorporate the ternary addition of Cr. Enrichment of the base alloy in Cr leads to the formation of new phases (other than gamma), one of which appears to be a beta-like phase of Ti, Al, and Cr having a primitive cubic structure and a lattice parameter, a_o, of approximately 0.69 nm.

References

1. D.W. McKee and S-C. Huang, submitted for publication.
2. P. Villars and L.D. Calvert, Eds., Pearson's Handbook of Crystallographic Data for Intermetallic Phases, Metals Park: ASM (1985)
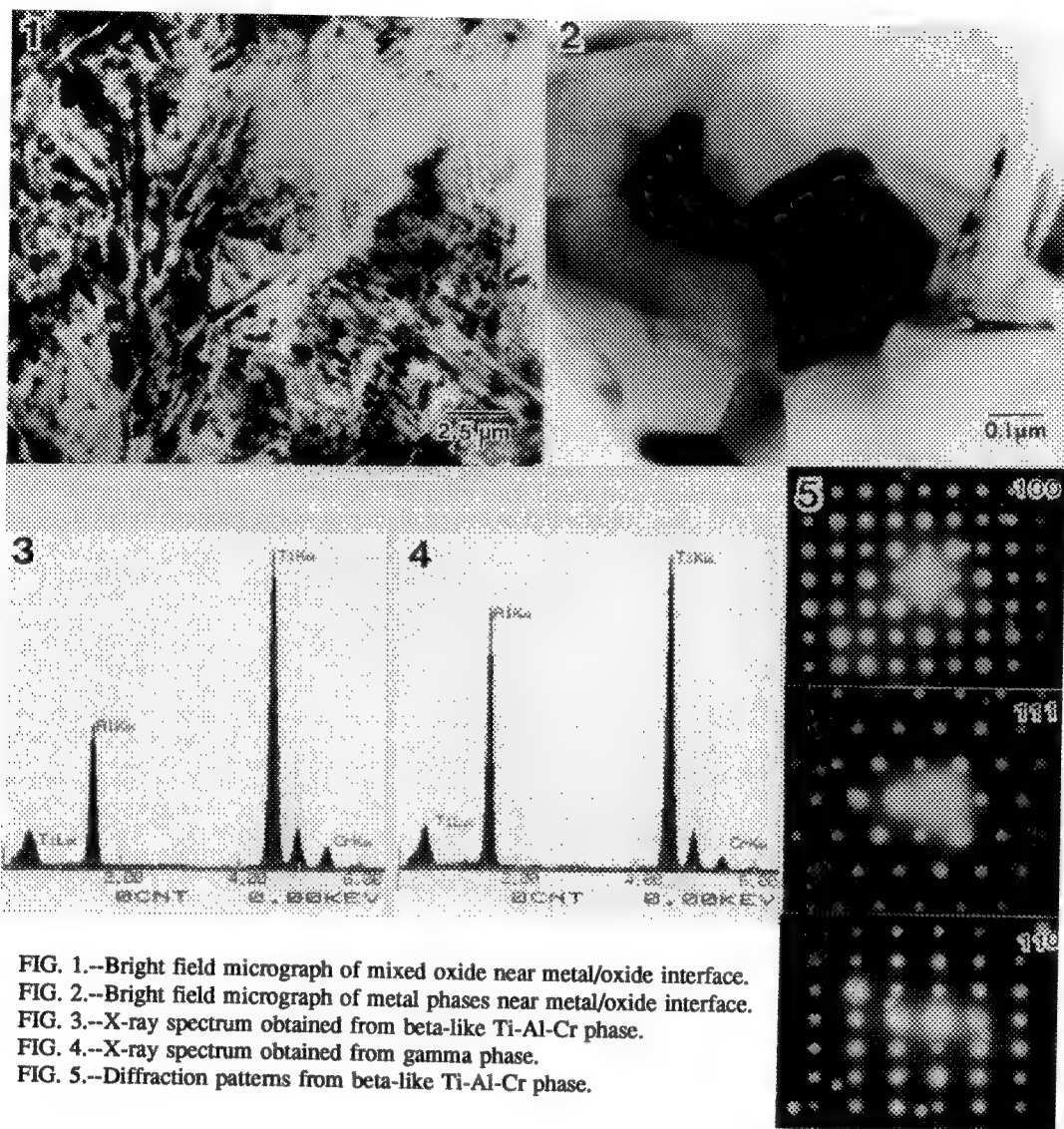
FIG. 1.--Bright field micrograph of mixed oxide near metal/oxide interface.
FIG. 2.--Bright field micrograph of metal phases near metal/oxide interface.
FIG. 3.--X-ray spectrum obtained from beta-like Ti-Al-Cr phase.
FIG. 4.--X-ray spectrum obtained from gamma phase.
FIG. 5.--Diffraction patterns from beta-like Ti-Al-Cr phase.

THE ROLE OF MICROSCOPY IN THE ALLOY DESIGN OF Ni- AND Fe-BASED ALUMINIDES

J.A. Horton

Metals and Ceramics Division, Oak Ridge National Laboratory, P.O. Box 2008, Oak Ridge, TN 37831-6115

During the last 10 years, there has been a resurgence of interest in ordered alloys for structural uses due to the discovery of the dramatic ductilizing effect of boron on grain boundaries in Ni_3Al.[1,2] With this discovery, it was hoped that the property of an increase in strength as the temperature is increased could be utilized as well as the excellent oxidation resistance. Now, alloys based on Ni_3Al are in use in specialized industrial applications, such as high temperature forging dies and being tested for use as turbocharger rotors. Due to the successful control of the grain boundary strength in Ni_3Al, other systems were reexamined. For example, Fe_3Al was also thought to have inherently brittle grain boundaries, however it was found that with purer alloys the material failed by cleavage.[3,4] Subsequently, development of practical, inexpensive, oxidation resistant alloys has proceeded. Fe_3Al alloys are currently being tested for automobile exhaust applications.

The role of electron microscopy in the development of ordered alloys has mostly been one of increasing our fundamental understanding of these unusual materials. This increased understanding has aided the overall direction of the alloy design programs. For example, the dramatic boron effect was initially assumed to be the result of a fairly obvious microstructural change in or near the grain boundaries. Since no borides, other second phases, or any nickel or aluminum enrichment were found by TEM on the grain boundaries, it pointed to a more subtle effect.[5] Boron solubility limits were determined by TEM. Boron enrichments at grain boundaries were found by Auger electron spectroscopy and by atom probe microscopy. While boron does segregate to grain boundaries and does increase the strength, we now know that several dynamic environmental effects take place at crack tips and control the overall ductility. These include a high temperature dynamic oxygen embrittlement that is solved by addition of about 8 at.% chromium. Initially, it was thought that the chromium formed a protective surface film, however TEM examination after only a few seconds of oxidation at the embrittling temperature showed that a continuous protective film was not there and therefore some dynamic-rate controlled and quicker crack tip process was indicated.[6] At room temperature, we now know that moisture contained in normal laboratory air reacts with aluminum at the crack tips, produces hydrogen and embrittles the alloys. Ni_3Al without boron, tested in dry oxygen shows several percent ductility. Boron segregation to the boundaries is thought to tie up the hydrogen penetration.[7] The historic mindset concerning ordered aluminides was that the grain boundaries were inherently weak. We know now that the fundamental problems in intermetallics are cleavage failure in systems with low crystal symmetries and crack tip environmental processes in high crystal symmetry structures which manifest themselves either as grain boundary or cleavage failures.

TEM has played a fundamental role in understanding and describing the various dislocation configurations that occur as a function of test temperature. Weak beam microscopy which routinely yields dislocation image widths of less than 1 nm has shown how the leading superlattice dislocation can locally cross slip at higher temperatures, produce locks and thereby increase the flow stress. Extensive fundamental work has been done in this area to explain the yield stress anomaly and other related mechanical properties, but this has not been critical to the development of practical alloys and so will not be further discussed.

An alloy development program typically involves a number of elemental additions. In Ni_3Al, for example, Hf or Zr improve the oxide adherence, Zr improves the castability and Cr solves the high temperature dynamic embrittlement. TEM has been very useful in identifying, measuring the compositions, and showing the morphology of a number of precipitates that can form, including Cr carbides, Ni-Zr tau phase, Ni_5Zr precipitates, and various configurations of a disordered chromium-enriched γ phase. Precipitation of these phases is usually a function of the base alloy aluminum-nickel ratio.

Chromium was found to dramatically improve the ductility in Fe_3Al.[8] Pure Fe_3Al fails by cleavage with 5% ductility. In the absence of moisture this value increases to about 10%, while chromium additions increase ductility to about 15%. TEM and by surface slip trace analysis showed that chromium additions resulted in wavy slip and less likelihood for cleavage. TEM showed that chromium additions resulted in a greater separation of the superlattice dislocations, Fig. 1, sometimes enough for uncoupling and more cross slip. However, while chromium effects on the dislocation structure aids ductility, the major chromium effect was found to be environmental and related to surface and crack tip processes.

Several ternary modifications, Fe and V, can be made to Al_3Ti to produce the $L1_2$ structure. The resulting

alloys (including Al$_3$Sc with the L1$_2$ structure) have a rather low yield stress, but they exhibit no tensile ductility. Initial assumptions to explain this lack of ductility center around an APB energy too high to permit the relatively easy emission of superpartial dislocations from crack tips. However, it was found by weak beam that the superlattice dislocations have a spacing of about 3.5 nm (Fig. 2). While this is about half that of Ni$_3$Al , a high APB energy is apparently not the fundamental cause for cleavage failure in these alloys. In this example TEM has provided critical information concerning the APB energy and the dislocation characteristics thereby pointing out that the cleavage failure is a result of a low cleavage strength.

In situ deformation experiments have been performed on a number of ordered alloys, including brittle stoichiometric Ni$_3$Al without boron, FeAl, and NiAl. The initial impetus was to ascertain the ease of slip accommodation at grain boundaries in Ni$_3$Al, which indeed was found to occur. In general, the observed slip characteristics are surprisingly ductile in appearance and compare very well with disordered alloys. Note that the good vacuum in a TEM may eliminate the real causes of brittle behavior in these materials. In NiAl the dislocations cross slip readily and are able to form a cell structure. These TEM results again indicate that deformation processes are not the fundamental limitation in these aluminides.

Since the phase relationships in the Ni and Fe aluminides are rather simple, TEM has not led the way in the development of these alloys. However, TEM has aided the alloy design effort and has significantly aided our basic understanding of these systems.

References
1. K. Aoki and O. Izumi, *Nippon Kinzoku Gakkaishi* **43**(1979)1190.
2. C.T. Liu, C.L. White, and J.A. Horton, *Acta Metall.* **33**(1985)213.
3. J.A. Horton,, C.T. Liu, and C.C. Koch, *Proc. of High Temp. Alloys: Theory and Design*, ed. by J.O. Stiegler (TMS-AIME, 1984), pp. 309-321.
4. W.R. Kerr, *Metall. Trans. A*, **17A**(1986).
5. J.A. Horton and C.T. Liu, *Scripta Metall.* **24**(1990)1251.
6. J.A. Horton, J.V. Cathcart, and C.T. Liu, *Oxid. of Metals*, **29**(1988)347.
7. C.T. Liu, to be published
8. C.G. McKamey, J.A. Horton, and C.T. Liu, *J. Mater. Res.* **4**(1989)1156.
9. Summary of research sponsored by the (1) Division of Materials Sciences, (2) the AR&TD Fossil Energy Materials Program, and (3) the Conservation Advanced Industrial Materials program, U.S. Dept. of Energy under contract DE-AC05-84OR21400 with Martin Marietta Energy Systems, Inc.
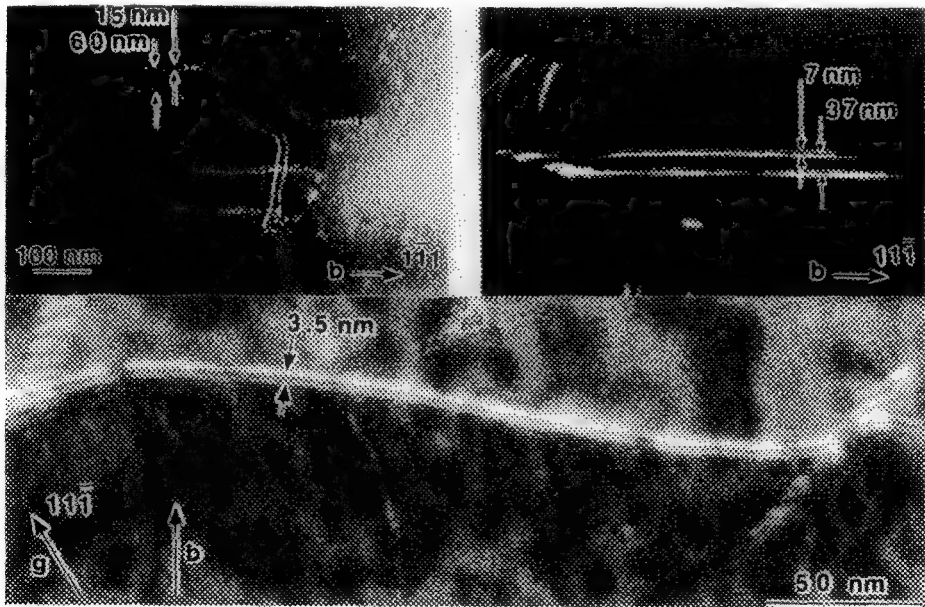
Fig. 1.--TEM of Fe$_3$Al with (a) and without (b) Cr showing superlattice separations.
Fig. 2.--TEM of Al$_3$Sc showing a 3.5 nm superlattice separation

169

DEFECTS IN MOLYBDENUM DISILICIDE

T. E. Mitchell, S. R. Srinivasan and R. B. Schwarz

Center for Materials Science, Los Alamos National Lab., Los Alamos, NM 87545

INTRODUCTION. Molybdenum disilicide($MoSi_2$) is used mainly as an electrical conductor in integrated circuits and as a heating element in furnaces. It is now being studied as a potential high temperature structural material because of its good strength and oxidation resistance. $MoSi_2$ has the tetragonal $C11_b$ crystal structure, space group I4/mmm, with a=3.202Å and c=7.851Å. At temperatures >1900°C, $MoSi_2$ has the hexagonal C40 structure where the basal planes have ABC stacking. This compares with the AB stacking of the pseudo-hexagonal {110} planes of the tetragonal structure. In the present paper we will describe and discuss TEM observations of defects in $MoSi_2$ prepared variously by hot pressing, plasma spraying and mechanical alloying.

EXPERIMENTAL. Hot-pressing of 99.9% pure commercial $MoSi_2$ powder was performed at 1700°C under 30 MPa pressure in grafoil-lined dies, giving 98% dense material. Plasma-sprayed material, 97% dense, was prepared using a SG-100 Plasmadyne spray torch in a low pressure atmosphere.[1] Mechanical alloying(MA) of elemental powder was used to synthesize $MoSi_2$ powder which, because of its fine size(10-15nm), could then be consolidated at 1500°C under 12MPa pressure to 97% density.[2] Thin foil specimens of all these materials were prepared by standard techniques and examined in a Philips CM30 microscope operated at 300kV.

RESULTS AND DISCUSSION. The $MoSi_2$ which was hot-pressed at 1700°C had a grain size of 2 to 3 μm and contained pockets of SiO_2 both at the grain boundaries and within the grains. An example of this microstructure is shown in Figure 1. This particular sample had been deformed at 1500°C and the occasional grain, such as that shown in Figure 1, contains a high density of dislocations. Standard g.b analysis shows that these dislocations have Burgers vectors of <100>, <110> and 1/2<111>, which are the shortest lattice vectors in the structure. The much longer 1/2<331> Burgers vectors reported by others[3] are not observed. Node reactions of the type [100]+[010]=[110] and 1/2[111]+[111]=[100] occur in the networks seen in Figure 1. The plasma-sprayed material has a heterogeneous microstructure due to the variable solidification rates of the splats. Fine-grained mixtures of $MoSi_2$ and Mo_5Si_3 are found in some areas; the Mo_5Si_3 presumably forms due to Si loss by vaporization in the hot plasma. Large-grained regions have a high density of twins lying on the {110} planes, as shown in Figure 2. Diffraction pattern analysis shows that the twin system is {112}<111>; these twins are thought to be variants resulting from rapid cooling through the hexagonal-to-tetragonal transformation at high temperatures.[4] The {110} twin boundaries arise because the change in stacking occurs on these planes. Figure 2 also shows the presence of small(~10nm) particles of Mo_5Si_3: the Moire fringe contrast indicates that there is an orientation relationship between the particles and the matrix. The microstructure of the $MoSi_2$ prepared by MA and then hot-pressed at 1500°C is illustrated in Figure 3. The grain size is uniform and small(3-5μm) but the most prominent feature in Figure 3 is the wide dispersion of SiO_2 particles. These particles range up to a few hundred nanometers in diameter and occur at the grain boundaries, at triple points, and occasionally within the $MoSi_2$ grains. The SiO_2 originates from oxide on the surface of the powder. The question of whether the SiO_2 is continuous along the grain boundaries was checked by high resolution electron microscopy; the boundaries were found to be clean, as illustrated in Figure 4 for the $MoSi_2$ hot-pressed at 1700°C. It appears that SiO_2 does not wet the grain boundaries and so the grain boundaries in the $MoSi_2$ prepared by MA are probably also free of a silica film. However, the presence of SiO_2 particles is likely to be deleterious to the mechanical properties at high temperatures and processing techniques are being developed to minimize their occurrence. For example, the use of a high-purity argon atmosphere while loading the $MoSi_2$ powder prepared by MA into the hot-pressing dies results in a factor of four reduction in oxygen content.[2,5]

REFERENCES
1. R. G. Castro, R. W. Smith, A. D. Rollett and P. W. Stanek, Scripta Metall. Mater.26(1992)207.
2. R. B. Schwarz, S. R. Srinivasan, J. J. Petrovic and C. J. Maggiore, Mater. Sci. Eng., in press(1992).
3. Y. Umakoshi, T. Sagami, T. Hirano and T. Yamane, Acta Metall. Mater.38(1990)909.
4. T. E. Mitchell, R. G. Castro and M. M. Chadwick, Phil. Mag., in press(1992).
5. This research was supported by the US DOE-OBES.
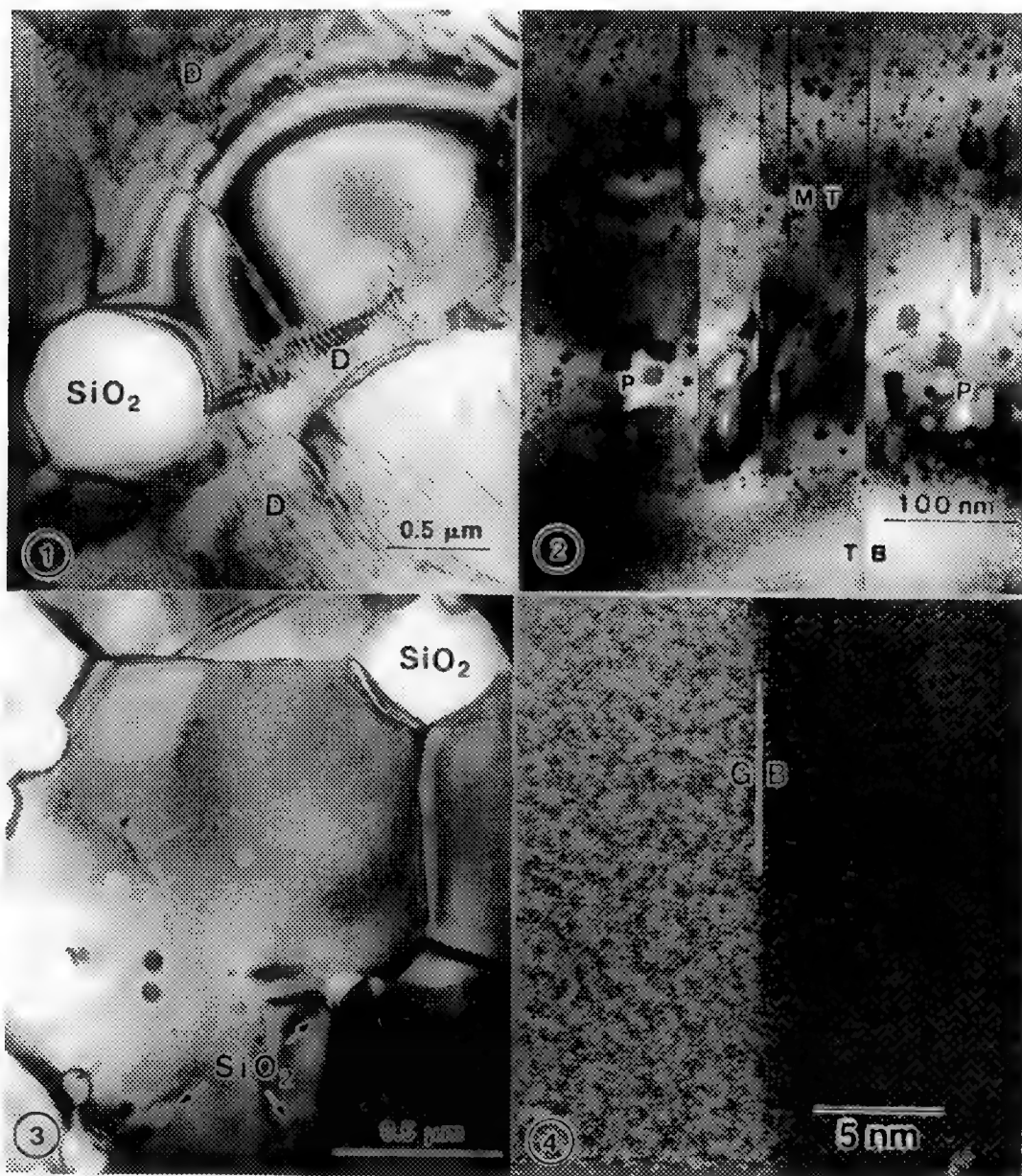
FIG. 1.--TEM BF image of MoSi$_2$ hot-pressed at 1700°C and deformed at 1500°C. Note the holes due to preferential thinning of SiO$_2$ and the dislocation networks(D).

FIG. 2.--TEM BF image of plasma-sprayed MoSi$_2$. Note the twin boundaries(TB), microtwins(MT) and Mo$_5$Si$_3$ particles(P).

FIG. 3.--TEM BF image of MoSi$_2$ prepared by mechanical alloying and hot-pressing at 1500°C.

FIG. 4.--HREM image of MoSi$_2$ hot-pressed at 1700°C, showing a clean grain boundary. The right-hand grain is oriented exactly along [111].

INTERACTION OF DISLOCATIONS WITH GRAIN BOUNDARIES IN Ni$_3$Ge

J. Fang and E. M. Schulson

Thayer School of Engineering, Dartmouth College, Hanover, NH 03755

An important aspect of deformation in L1$_2$ intermetallic compounds at low temperature is the interaction of gliding dislocations with grain boundaries [1]. *In-situ* straining in Ni$_3$Al revealed one mode of interaction: dislocations piling up at grain boundaries and emitting into the adjoining grain [2]. The present paper shows another mode of dislocation-grain boundary interaction in Ni$_3$Ge: dislocations piling up against grain boundaries and being ejected back into the original grain. In the present case, this phenomenon is broadly termed "dislocation reflection". However, in both of these modes, the outcoming dislocations are not necessarily the same as the incoming ones.

Miniature tensile samples, with a grain size of about 15 μm, were made from Ni-23.5at.%Ge with 0.06 at.% B. Geometry of the samples was designed to ensure that deformation and fracture occur in the thin area of the specimens [2]. The tensile deformation was performed *in-situ* in a JEOL 2000FX operated at an accelerating voltage of 200 kV.

Fig. 1 shows the dynamic interaction of a dislocation pile-up with a grain boundary. Fig. 1 (a) shows a dislocation pile-up, in front of a propagating crack, encountering a grain boundary. The first three leading dislocations reorient their line and partially enter the boundary. With increasing straining, more dislocations intersect the grain boundary, as indicated by the slip band in Fig. 1(b), but no dislocation activity is observed in the neighboring grain. From the grain boundary region away from the point where the dislocation pile-up impinges on the boundary, two dislocations (A and B) are reflected back into the original grain, Fig. 1(c). While one reflected dislocation A is visible on the micrograph, the other (B) could not be seen because it has rapidly moved away from the boundary, but its movement is traced by the slip band. One dislocation loop segment (arrowed) protrudes from the boundary and into the original grain. However, in this case, the reflection process only lasts a short time at the beginning of the interaction before dislocation emission into the adjoining grain starts to operate, Fig. 1(d). Fig. 2 shows another case, where the dislocation reflection lasts much longer. In Fig. 2 (a), dislocations A in grain 1 are piling up against the grain boundary, dislocations B and C reflecting back into grain 1, and dislocations D emitting into grain 2. The incoming dislocations A are antiphase boundary (APB)-coupled dislocation partials with a scalloped appearance, as in Ni$_3$Al [3]. The reflected dislocations C move through grain 1 and form pile-up E at the grain boundary on the other side of the grain. On further straining, more dislocations reflect to join the pile-up E and eventually, dislocations are ejected into grain 3, as seen in Fig. 2 (b).

Dislocation reflection has been observed in type 304 stainless steel [4] and in Al [5], but not reported in intermetallic compounds hitherto in the literature. The mechanism for the reflection is not well understood. One possibility is that pile-up dislocations dissociate into grain boundary dislocations, which, if glissile in the boundary plane, can spread the strain energy of the trapped dislocation over a region of the boundary. Eventually, the accumulated strain will exceed a critical value, and activate grain boundary dislocation sources, from which the reflected dislocations could be generated. This mechanism seems to be supported by the fact that the grain boundary region where dislocation reflection occurs does not have to be coincident with the impinging point of the pile-up [6].

References
[1]. E.M.Schulson, T.P.Weihs, I.Baker, H.J.Frost, J.A.Horton, Acta Metall. 34, 1395 (1986).
[2]. I. Baker, E. M. Schulson and J. A. Horton, Acta Metall. 35, 1533 (1987).
[3]. I. Baker, J. A. Horton and E. M. Schulson, Phil. Mag. Lett. 55, 3 (1987).
[4]. Z. Shen, R. H. Wagoner and W. A. T. Clark, Acta Metall. 36, 3242 (1988).
[5]. T. C. Lee, I. M. Robertson and H. K. Birnbaum, Metall. Trans. 21A, 2437 (1990).
[6]. Research sponsored by the U. S. Department of Energy, contract No: DE-FG02-86ER45260.
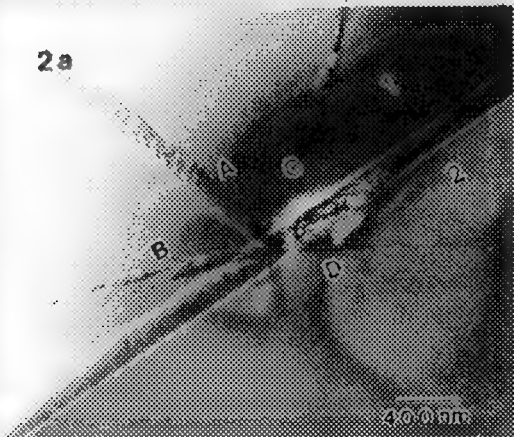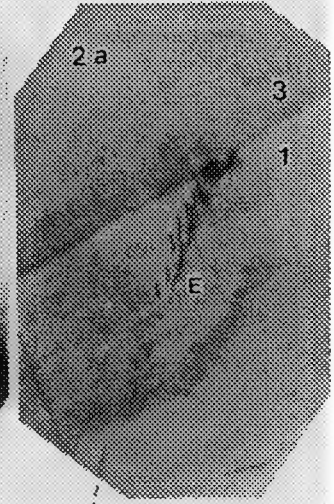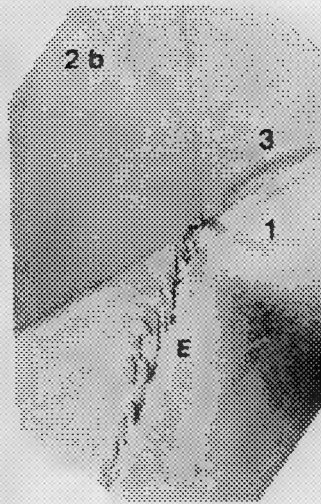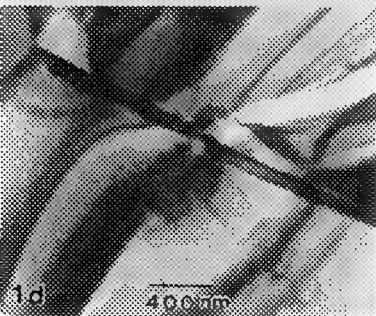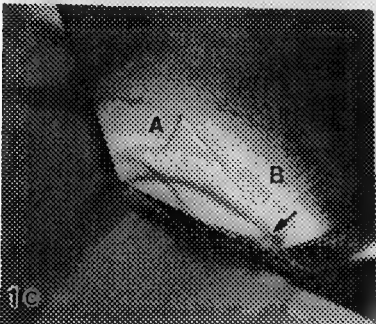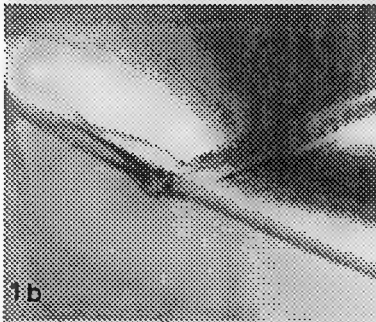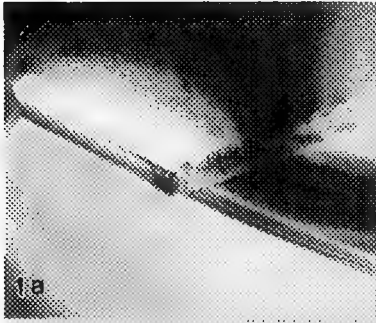
Fig. 1a Dislocations piling up and entering grain boundary.
Fig. 1b More dislocations joining pile-up.
Fig. 1c Dislocations being ejected back into original grain.
Fig. 1d Massive dislocation emission into adjoining grain.

Fig. 2a Two sets of dislocations being reflected into original
grain and one of them piling up at another grain boundary.
Fig. 2b Reflected dislocations initiates slip in ajoining grain.

173

A COMBINED AEM/APFIM CHARACTERIZATION OF ALLOY X-750

M.G. Burke and M.K. Miller*

Westinghouse Science and Technology Center, Pittsburgh, PA   15235
*Metals and Ceramics Division, Oak Ridge National Laboratory, Oak Ridge, TN 37831-6376

In the development of advanced alloys for power system applications, the primary emphasis is placed on attaining specific mechanical properties with resistance to environmental attack. An important part of alloy development is the detailed characterization of the microstructure, because it is the composition, size and morphology of the microstructural features that define the mechanical properties of the material. The good mechanical properties of Ni-base superalloys are a result of the formation of fine coherent precipitates. In addition, other coarser phases may form which can degrade the properties of the alloys. Analytical electron microscopy (AEM) provides important information concerning the type and distribution of the phases in the alloys, but quantitative microchemical analysis of the ultra-fine precipitates is not readily obtainable with conventional AEM techniques. The high spatial resolution of the atom probe field-ion microscope (APFIM) makes this technique ideally suited to the analysis of the ultra-fine precipitates and surrounding matrix. The analysis of the matrix is particularly important in predicting the subsequent ageing response of the alloy, as previously shown in a detailed AEM/APFIM examination of Alloy 718.[1] In this paper, a combined AEM/APFIM study of precipitation in Alloy X-750 is presented.

The composition of the Alloy X-750 used in this investigation is listed in Table 1. Specimens were annealed for 1 h at 1093°C, followed by either an air-cool or water-quench to ~25°C. Samples of the air-cooled and water-quenched materials were then given a standard ageing treatment at 718°C for 24 h and air-cooled to 25°C. Samples were examined in a Philips EM400T analytical electron microscope equipped with a Link Analytical energy dispersive x-ray spectrometer (EDS) analysis system. APFIM analyses were performed in the ORNL energy-compensated atom probe with a specimen temperature of 50K.

The microstructure of the air-cooled material consisted of spheroidal ultra-fine $L1_2$-ordered γ' precipitates throughout the γ matrix (Fig. 1), and fine (~10 to 50 nm) $M_{23}C_6$ along most high angle grain boundaries. The size of the γ' in this material was determined by transmission electron microscopy (TEM) to vary from 5 to 10 nm, in good agreement with the average size of 6 nm measured from FIM micrographs. Atom probe analysis revealed that Ti and Al partitioned to the brightly-imaging γ', whereas Cr and Fe partitioned to the γ. In contrast to the air-cooled material, neither technique showed any evidence of γ' or carbide precipitation in the water-quenched samples. The γ matrix contained numerous dislocations related to quenching stresses. In addition, atom probe statistical analysis of the distribution of Ti and Al atoms in the matrix failed to detect any indication of clustering or precipitation. In both the air-cooled and water-quenched materials that had been aged for 24 h at 718°C, coarser 10 to 30 nm diameter γ' precipitates were observed, as shown in Fig. 2. A comparison of the atom probe results from the air-cooled and air-cooled + aged materials revealed that the concentrations of Ti and Al in the γ matrix and the Cr in the γ' precipitates all decreased upon ageing at 718°C. This behavior suggests that the air-cooled material had not reached an equilibrium condition. Although there was considerable variation from one γ' precipitate to another, the average Ti/Al ratio was found to be approximately 2 in all materials examined. AEM analysis revealed notable differences in the morphology of the intergranular Cr-enriched $M_{23}C_6$ (discrete globular versus discontinuous) found in the air-cooled and water-quenched samples, and corresponding differences in the extent of the Cr-depleted zones associated with these microstructures.[2,3]

References
1. M.G. Burke and M.K. Miller, Superalloys 718 and 625, Warrendale:TMS (1991) 337.
2. M.G. Burke et al., in E. Simonen,Ed, 5th Int'l. Symp. Environmental Degradation of Materials in Nuclear Power Systems—Water Reactors, La Grange Park, Il.:ANS, in press.

TABLE 1. COMPOSITION OF ALLOY X-750 (wt.%)

Ni	Cr	Fe	Ti	Nb	Al	Si	Mn	S	B	C
73.4	15.2	6.81	2.54	0.93	0.80	0.14	0.08	0.001	0.001	0.04
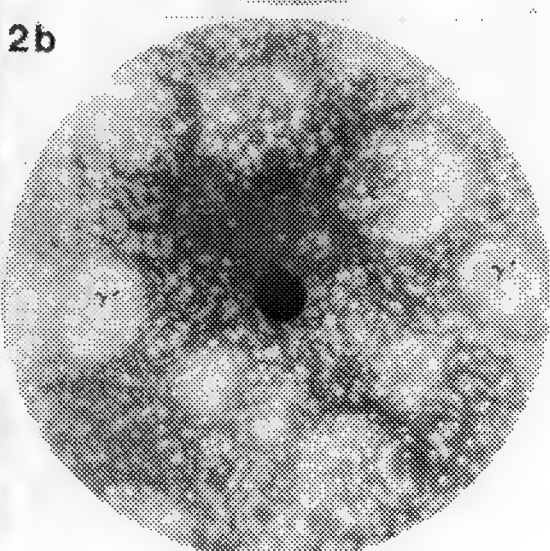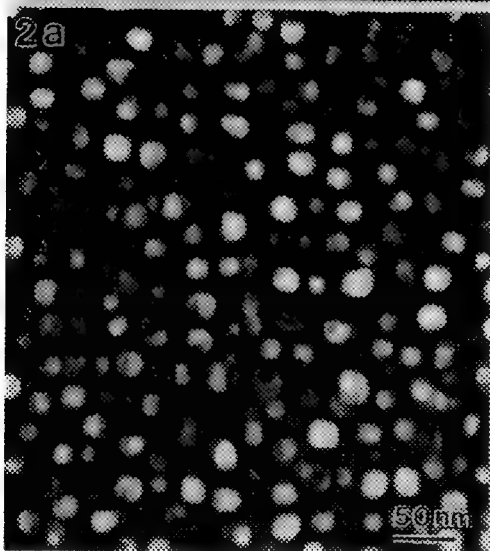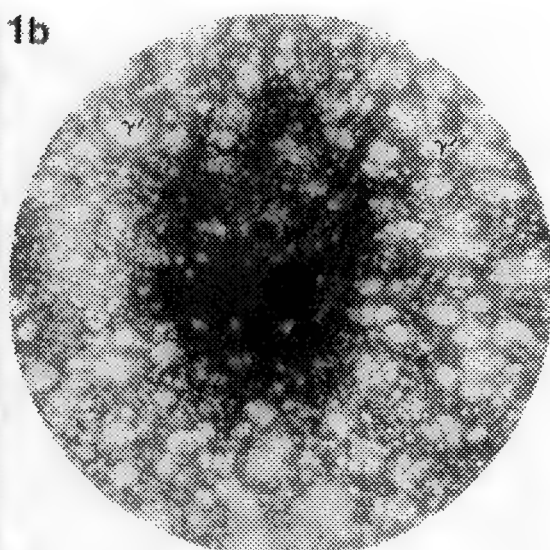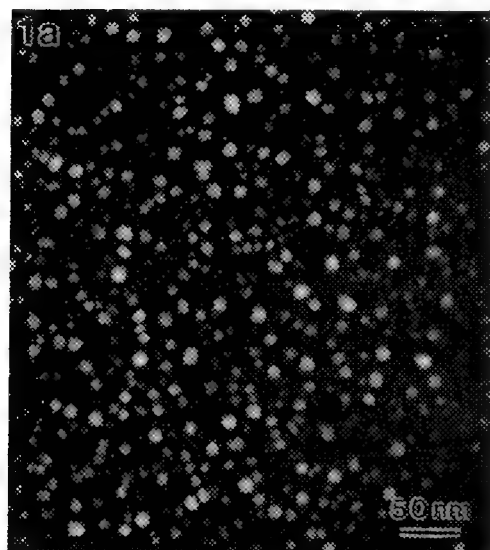
Fig. 1-- γ' in air-cooled Alloy X-750; a) Dark-field TEM and b) FIM micrographs.
Fig. 2-- γ' in air-cooled + aged Alloy X-750; a) Dark-field TEM and b) FIM micrographs.

175

AN ATOM-PROBE FIELD ION-MICROSCOPE INVESTIGATION OF γ-γ' INTERFACES IN A MODEL NICKEL-BASED SUPERALLOY

Raman Jayaram and M.K. Miller

Metals and Ceramics Division, Oak Ridge National Laboratory, Oak Ridge, TN 37831-6376

Nickel-based superalloys are of great technological interest because of their attractive mechanical properties at high temperatures. Their ability to maintain high strength under extreme conditions of thermal cycling makes them highly suitable for applications such as turbine blade material for aircraft engines. Single crystal nickel-based superalloys containing refractory elements such as Mo, Ta and Re have received considerable attention on account of their high creep strength at elevated temperatures.[1] In these materials, the $L1_2$-ordered γ' phase is initially present as discrete cuboids in the disordered γ matrix. During high temperature creep, with the stress applied along the <100> direction, these cuboids directionally coarsen to form continuous γ' lamellae perpendicular to the applied-stress axis.[2] The improvement in creep strength that occurs as a result of this change in the γ' morphology has been attributed to a number of different possible mechanisms.[3] One mechanism suggested is the segregation of molybdenum to the γ-γ' interface which could impede dislocations producing increased creep strength.

Atom Probe Field Ion Microscopy (APFIM) has been used to characterize the γ-γ' interface since this powerful technique can measure compositional changes across interfaces with near-atomic resolution. The alloys used in this study had a nominal bulk composition of Ni-x at. %Mo-2.0 at. %Ta-13.7 at. %Al with x ranging from 8.7 to 9.2 at. %. The details of alloy fabrication and high temperature (982°C) creep tests are described elsewhere.[3] APFIM specimens were prepared from crept tensile specimens using standard techniques and analyzed in the ORNL energy-compensated atom probe. The compositions of the different phases as measured by atom probe analyses are shown in Table 1. These results indicate that molybdenum partitions to the γ and DO_{22}-ordered phases and tantalum and aluminum partition to the γ' phase. A composition profile across a pair of γ-γ' interfaces in Fig. 1 shows no evidence of molybdenum segregation to the interfaces and thereby eliminates solute segregation as a possible mechanism for enhancing creep resistance. Atom probe and transmission electron microscope results confirm the existence of a distinct, DO_{22}-ordered phase.[4] Dark-field electron micrographs of the DO_{22}-ordered phase in the uncrept and crept materials are shown in Figs. 2 and 3, respectively. The DO_{22}-ordered phase is present in the form of thin platelets on the {100} faces of the γ' cuboids in the uncrept alloy, whereas it is dispersed in the γ matrix in the crept material. This change in the microstructural feature of the crept material is reflected in the Mo content of the matrix which ranges between the γ and DO_{22} values. However, it has been suggested that the DO_{22}-ordered phase is unlikely to play a beneficial role in creep resistance at 982°C since it is stable only below 800°C.[1,5]

References

1. D.D. Pearson et al., in B. Wilshire and D.R.J. Owen, Eds., Creep and Fracture of Engineering Materials and Structures, Swansea: Pineridge (1981) 213.
2. D.D. Pearson et al., Proc. 4th Int. Symp. on Superalloys (1980) 513.
3. R.A. MacKay et al., Metall. Trans. 21 A (1990), 381.
4. R. Jayaram and M.K. Miller, Surf. Sci., (1992), in press.
5. This research was sponsored by the Division of Materials Sciences, U.S. Department of Energy, under contract DE-AC05-84OR21400 with Martin Marietta Energy Systems, Inc. and through the Postgraduate Research Program administered by Oak Ridge Associated Universities. The authors would like to thank Dr. D.D. Pearson of United Technology Research Center and Dr. R.A. MacKay of NASA Lewis Research Center for supplying the alloys used in this investigation.

Table 1. Composition of various phases in crept alloy containing 8.7 at. % Mo. Balance of these analyses is nickel (at. %).

	Mo(at. %)	Ta(at. %)	Al(at. %)
Nominal bulk	8.7	2.1	13.6
γ/DO$_{22}$	21.2±0.3 - 25.7±0.5	0.9±0.1	2.6±0.2
γ'	6.5±0.1	3.0±0.3	19.0±0.8
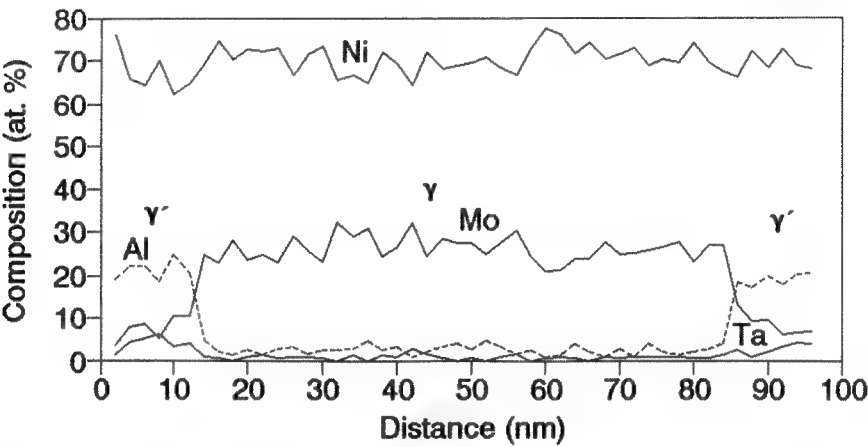
Fig. 1. Atom probe composition profile through γ-γ' interfaces in crept material. No evidence of segregation to interface is observed. Distance probed is approximately 95 nm.
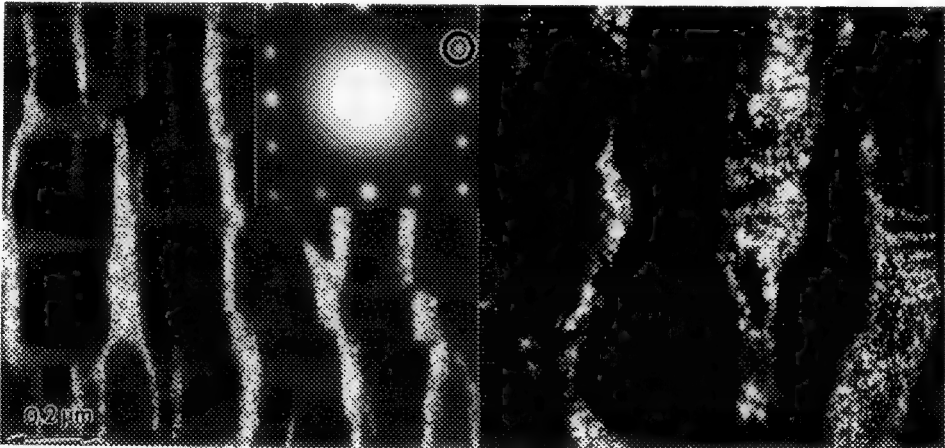
Fig. 2. Dark-field electron micrograph of DO$_{22}$-ordered phase platelets in uncrept material. [001] diffraction pattern is shown in inset. Stress axis is parallel to [001].

Fig. 3. Dark-field electron micrograph of DO$_{22}$-ordered phase dispersed in γ matrix in crept material.

177

A TEM CHARACTERIZATION OF PRECIPITATES EVOLUTION AND THEIR EFFECT ON THE GRAIN-GROWTH BEHAVIOR OF GAS ATOMIZED SUPERALLOY A-286

Keesam Shin

Department of Materials Science and Engineering, University of Wisconsin, Madison WI 53706

It is generally accepted that the refined grain size and stable grain boundaries observed in rapid-solidification-processed (RSP) materials are due to the fine precipitates produced during and after the processing[1-3]. This is based on the observation of the materials after consolidation of the powders. Though there is little doubt that the as-atomized powder structure is crucial for the understanding of the consolidated sample, there are few studies of the powder. This is mainly because of the difficulty in preparation of thin electron-transparent samples.

The most common method of powder sample preparation uses two or three different embedding materials whose polishing conditions are usually not identical. In this study, a monolayer of powder was gold coated, electroplated with nickel, and then electropolished. Electropolishing provided a nice and smooth surface without any surface artifact. In this study, as-atomized and heat treated powders were studied by TEM (JEOL JEM 200CX) and STEM (VG HB501). Because of the fineness of the defects involved, TEM observation is crucial.

The microstructures of the RSP samples show sharp contrast with conventionally processed counterpart (Fig. 1). Fig. 2 shows the morphology of as-atomized powder and evidence of segregation at the dendrite boundaries. STEM analysis showed that the segregation is mostly titanium with traces of carbon and oxygen. The segregation appears as elongated regions at the dendrite walls (Fig. 3). When the as-solidified powders were annealed for 1 hour at 900°C, the elongated regions evolved into aligned spheroidal precipitates of TiC (Fig. 4). Though there are some contrast differences among the dendrite arms, they have almost the same orientation as demonstrated by selected area electron diffraction. These cells appear to agglomerate and form a single grain when annealed. The aligned precipitates are mostly inside grains and appear not to be involved in pinning the grain boundary. The precipitates on the grain boundary did not show an aligned nature until after a significant annealing time (Fig. 5). Thus the precipitates which pin the grain boundary appear to be those which were formed or happen to be on the grain boundary (Fig. 6). However, in the 100-hour annealed powder and the consolidated and heat treated ones, the aligned precipitates were found on the grain boundary in high frequency (Fig.5, 6). This indicates that they are retarding the grain growth at this later stage when the grain boundaries are released from the boundary precipitates. The grain boundary only crosses these precipitates in high angle, which shows the effectiveness of the aligned precipitates in pinning the grain boundary (Fig. 6). In addition to the large (100-300 nm in diameter) precipitates formed from the primary segregation which were mostly aligned, there were fine precipitates (less than 50 nm) whose density increased until a certain temperature (1100-1200°C) was reached. Both the large and the fine precipitates were found to have the same composition which is TiC.

From the observation, it can be concluded that:

1. Precipitates formed on the grain boundary pins the grain boundary at early stage of grain growth.

2. The aligned precipitates due to solute segregation on the solidification cell wall are very powerful for retarding the grain growth but they only act at the later stage of the grain growth.

3. The fine precipitates which form after atomization do not appear to exert a great force in this case.

References

1. M. Suga, et al., Rapid solidification Processing; Principles and Technologies, P. 364, (R. Mehrabian, B.H. Kear, M. Cohen, eds.), Claitor's Publishing Division, Baton Rouge, Louisiana (1980).

2. J.E. Flinn et al. Rapidly Solidified Materials, P. 153, (P.W. Lee and J.H. Moll ,eds.), ASM, (1988).

3. C.Y. Hsu, Ph.D. Thesis in Materials Science and Engineering at M.I.T. (1984).

4. The author thanks Professor Thomas F. Kelly and Dr. John E. Flinn at INEL.

5. This work is supported by DOE grant #C87-101251.
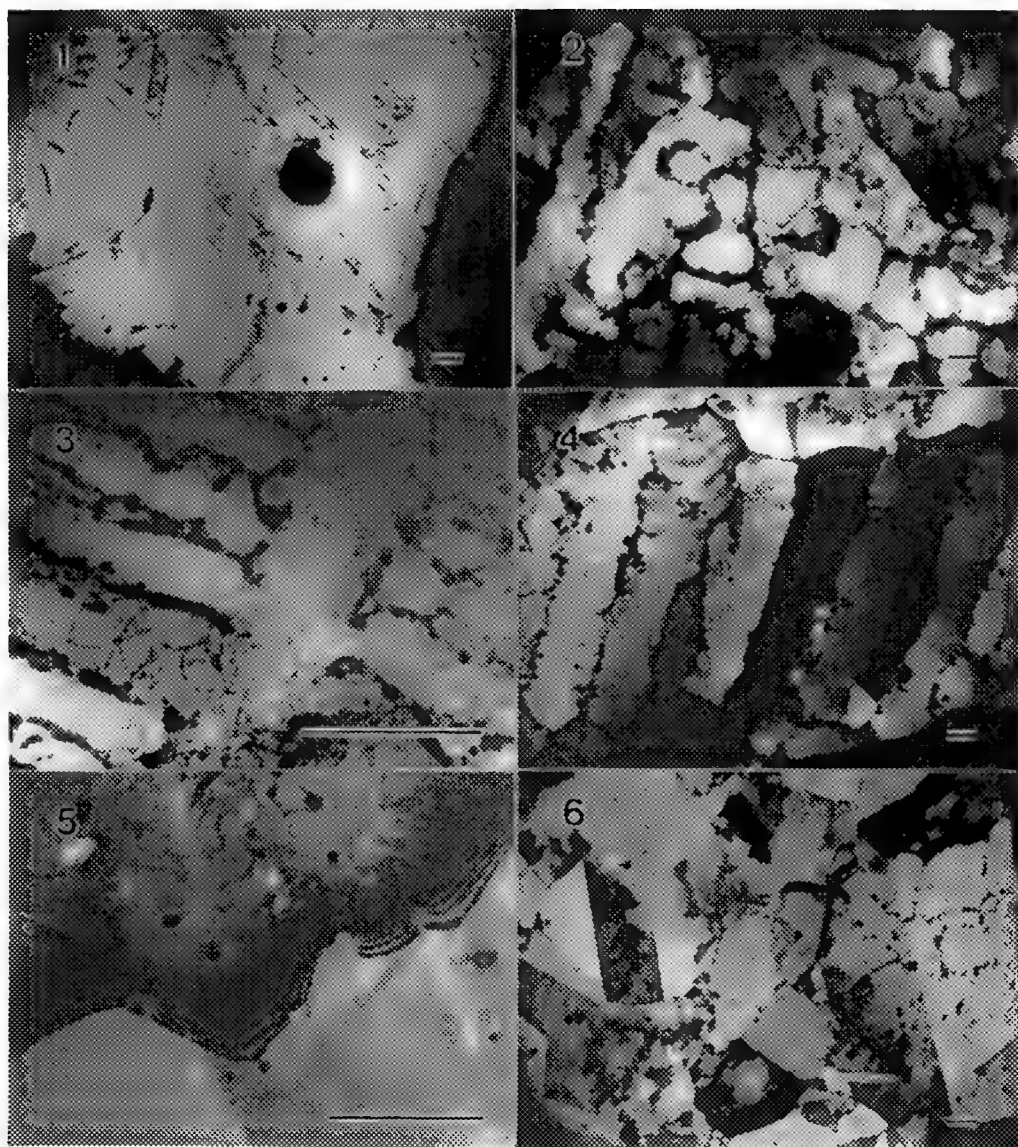
bar = 1 μm

Fig. 1. Conventionally processed sample (900°C/1 hour, water quenched).
Fig. 2. As-atomized powder.
Fig. 3. As-atomized powder.
Fig. 4. Annealed powder (900°C/10 hour, water quenched).
Fig. 5. Annealed powder (900°C/100 hour, water quenched).
Fig. 6. Hot extruded and annealed powder (900°C/1 hour, water quenched).
*All TEM micrographs

179

ROOM TEMPERATURE DEFORMATION AND STRESS-INDUCED PHASE TRANSFORMATION IN LAVES PHASE Fe_2Zr

Yaping Liu, Samuel M. Allen and James D. Livingston

Massachussetts Institute of Technology
Department of Materials Science and Engineering
77 Massachusetts Avenue, Cambridge, MA 02139, USA

Laves phases have three structures: Cubic C15 ($MgCu_2$), hexagonal C14 ($MgZn_2$) and dihexagonal C36 ($MgNi_2$). Their high-temperature deformability has been studied by many investigators. But the study of their room-temperature deformation is very limited. By such studies, it may be possible to enhance the room-temperature deformability of Laves phases.

In the present study, arc-melted samples of Fe-10 at% Zr, containing α-Fe and Fe_2Zr Laves phase, were annealed at 1190°C for 48 hr and then compressed at 0.001 inch/min to strains of 46~48% at room temperature. The 0.2% offset yield stress is about 75 kg/mm^2. Micrographs revealed dislocation structures in α-Fe and cracks in proeutectic Fe_2Zr after deformation. X-ray diffraction patterns show that the crystal structure of Fe_2Zr is mainly C36 before deformation. After compression, the C15 peaks, which overlap other peaks in the pattern, increase in intensity, as seen in Fig. 1. This demonstrates that a phase transformation occurred as a result of deformation. The detail and mechanism of the transformation were studied by TEM. A characteristic banded structure which was rarely found in undeformed sample was frequently observed in the compressed Fe_2Zr particles, as shown in Fig. 2. Electron diffraction patterns and high-resolution TEM showed that these bands have a C15 structure with a {111} plane parallel to the basal plane of C36 structure in the adjacent parts of a particle. Fig. 3 is a high-resolution TEM picture showing the stacking sequence of the close-packed planes of the particle containing the C15 band in Fig. 2. It has a ABCABC stacking sequence in the central part (C15) and ABAC on the two sides (C36). Inside the C15 band there are many stacking faults on {111} planes. A twinned region ($C15_T$) is also seen to the right of the C15 region.

The phase transformation between C36 and C15 can be accomplished by shear on the close-packed planes, through the glide of Shockley partial dislocations having b = (a/6)<211>. Every four planes there are two partials gliding on two neighboring close-packed planes causing the stacking sequence to change between ABAC↔ABCA. This transformation seems to proceed by the motion of an interface with microscopic ledges composed of a series of Shockley partial dislocations between C36 and C15. An example is shown in Fig. 4. The shear strain resulting from the transformation is 0.3535. A shear stress of opposite direction on C36 structure can cause a transformation to a C15 structure with another orientation ($C15_T$) : ACAB↔ACBA. The transformation of C36 is "two-way", in which shear stresses of opposite directions can cause transformation to C15 and $C15_T$. But for C15 or $C15_T$ the transformation is "one-way", only a specific direction of the stress can cause the transformation to C36.

In some particles, a complex mixture of C36, C15 and $C15_T$ was found, where C15 and $C15_T$ were separated by C36, also seen in Fig. 4. By analyzing the stress and the orientation of the Laves particles, a mechanism called "double transformation" can be used to explain the deformation: C15→C36→$C15_T$. The strain resulting from this transformation is 0.7070, the same as twinning. The transformation should be a easier way to achieve the strain than direct twinning due to the similarity in energy in C36 and C15 in this alloy.

180
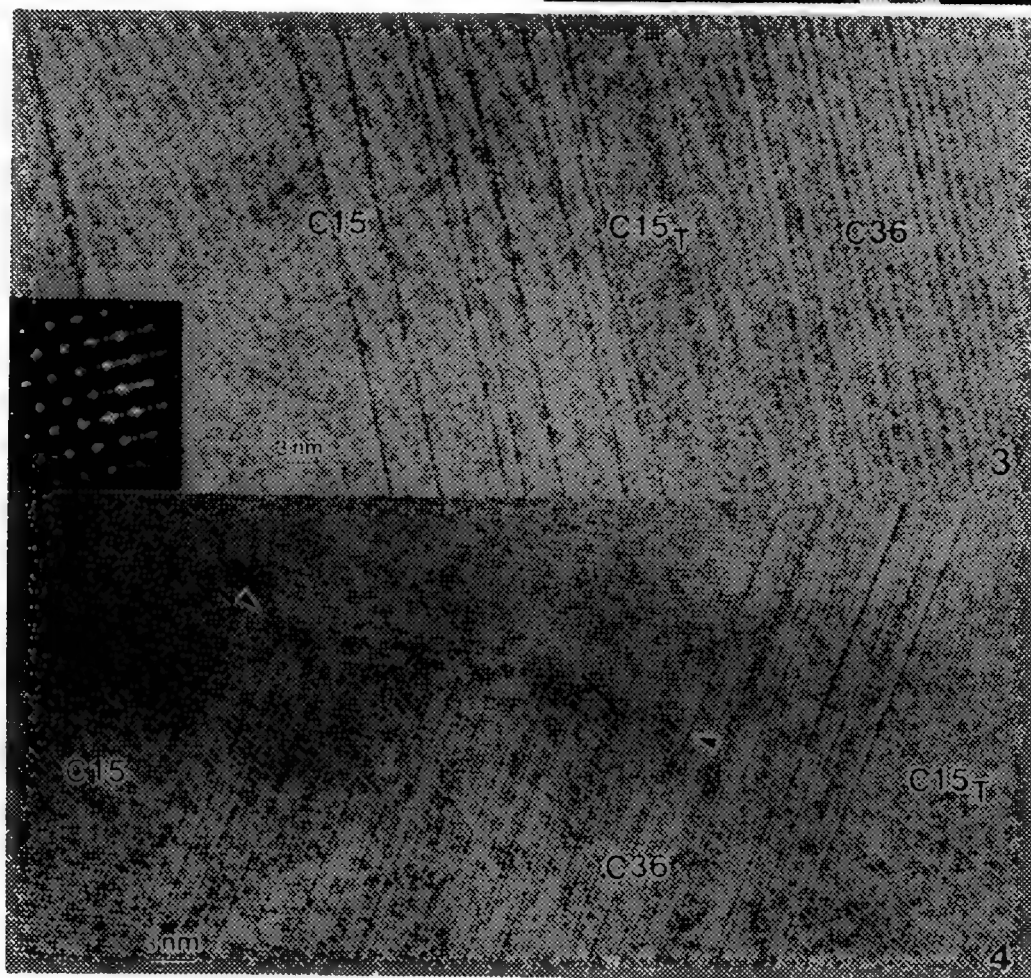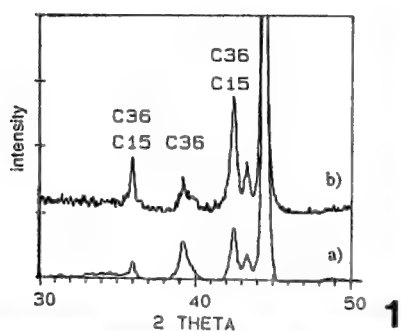
Fig. 1 X-ray diffraction patterns of (a) undeformed and (b) deformed alloy.
Fig. 2 C15 band on C36 partical (B = $[011]_{C15}/[2\bar{1}\bar{1}0]_{C36}$ for all TEM pictures).
Fig. 3 SAD pattern and high resolution image of C15 band (the area indicated by arrow in Fig. 2).
Fig. 4 Mixture of C36, C15 and $C15_T$ and ledge interface (indicated by arrows).

ALUMINUM-LITHIUM ALLOYS: A SOLUTION LOOKING FOR A PROBLEM?

D. B. Williams

Department of Materials Science and Engineering, Lehigh University, Bethlehem, PA 19015-3195

For over a decade, Al-Li base alloys have been described as "the next generation of aerospace alloys", although to date not much metal is actually flying. The addition of up to 3 wt. % (11 at.%) Li to Al results in decreased density (for obvious reasons) and increased modulus (for unknown reasons). This combination of decreased density and increased stiffness translates into millions of dollars saved in aircraft operation (whether military or civilian) and as a result the aerospace and aluminum industries have invested tens of millions of dollars in an attempt to produce commercial Al-Li based alloys. Electron microscopy and microanalysis have played a major role in the understanding of the physical metallurgy of these alloys, which have yet to see significant service. Their future is uncertain, although there is some limited use for alloys of Al-Li-Cu-Mg-Zr.

The attraction of the alloys lies in the behavior of the ordered, metastable Al_3Li phase. Like other A_3B ordered phases, Al_3Li has the potential for highly efficient precipitation hardening, with the opportunity to tailor the matrix/precipitate interface mismatch to control dislocation cut through or by-passing. In an attempt to achieve this control, the precipitation behavior of Al_3Li has been thoroughly documented and the phase diagram determined, almost exclusively through electron microscopy. It is now well known that Al_3Li exhibits classical homogeneous nucleation unaffected by lattice defects such as grain boundaries (Figure 1), but it can be constrained to nucleate heterogeneously on dislocations (Figure 2) at low undercoolings. At high undercoolings Al_3Li undergoes spinodal decomposition. Its miniscule interfacial energy and almost zero misfit have been measured through electron microscopy techniques (critical nucleus measurements from images such as Figure 1 and Ashby-Brown strain contrast (Figure 3)). Growth is controlled through classical $r^2 \alpha t$ diffusion control (r = particle radius and t = time) and coarsening through classical Lifshitz-Wagner $r^3 \alpha t$ diffusion control or through a discontinuous grain boundary process ($r \alpha t$) (Figure 4). As a result of these electron microscopy studies, Al_3Li is one of the best understood phases in terms of its properties and precipitation processes. Al_3Li exhibits classical behavior at all stages of its life, making it an ideal phase to test the validity of phase transformation theories. In addition, the metastable phase boundaries have been defined through TEM imaging studies of phase dissolution or directly through EELS core-loss microanalysis (Figure 5).

One reason for the lack of success of Al-Li alloys is that Al_3Li is too perfect in its behavior and dislocations cannot easily cross slip, giving slip localization and reduced ductility. So Cu is added to form thin semi-coherent T1 (Al_2CuLi) precipitates that induce cross slip. The Al_3Li is metastable and the thermodynamically stable AlLi phase is highly reactive and therefore undesirable, so Mg is added to produce inert ternary intermetallics. Finally Zr is added for grain refinement. At all stages of the alloy development, the phases such as $Al_3Zr(Li)$ responsible for the improved behavior have been characterized by TEM, CBED and microanalysis. Much interest has centered on the T2 intermetallic (Al_6Li_3Cu) which exhibits external five-fold (icosahedral) symmetry (Figure 6). T2 was the first stable icosahedral phase that could be cast into bulk ingots, although it has yet to show any exciting properties, given its strange symmetry. Processing problems, mainly impurity-containing intermetallics give rise to poor short transverse strength of the commercial alloys, which remains the main hurdle to be overcome before aerospace manufacturers will consider major use of the alloys. If such use does not occur, then these alloys are indeed a solution looking for a problem. Possible answers include "the next generation of Al alloy automobiles" and high performance bicycles. Limited military use in spy satellites will of course continue, depending on the rate of mutual reconciliation in the political arena.[1]

Reference
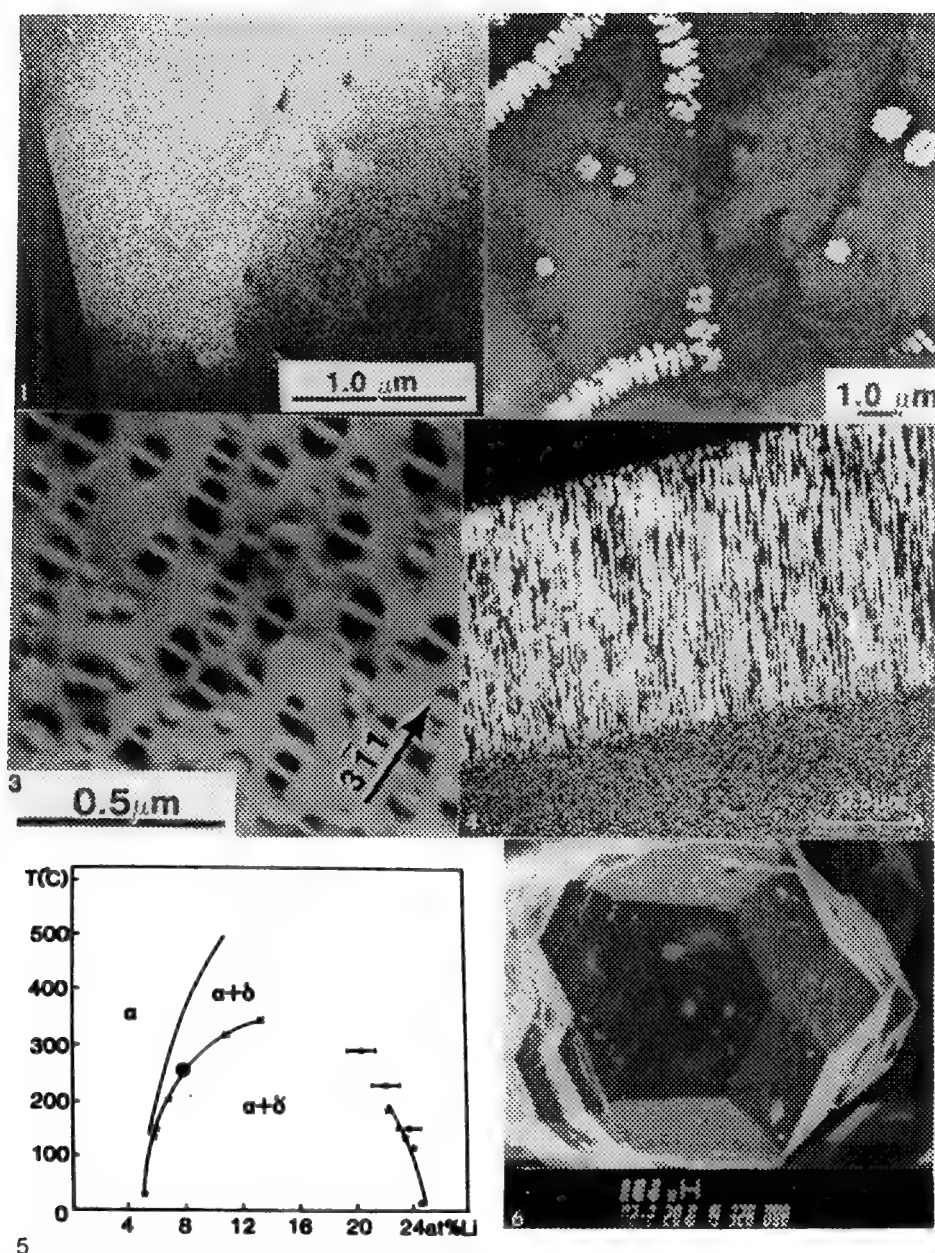
FIG. 1.— Superlattice CDF of homogeneously nucleated Al₃Li formed during quenching.
FIG. 2.— Superlattice CDF of dendritic Al₃Li heterogeneously nucleated on dislocations.
FIG. 3.— Superlattice CDF of discontinuous grain boundary coarsening of Al₃Li.
FIG. 4.— High order BF image showing Ashby-Brown strain contrast around spherical Al₃Li.
FIG. 5.— The metastable (alpha solid solution + Al₃Li) phase field determined by TEM and EELS.
FIG. 6.— SEM image showing the external five-fold symmetry of a large area of a casting of T2.

MICROSTRUCTURE AND PROPERTIES OF Al-Cu-Li-Ag-Mg-Zr ALLOY

M.J. Kim,* C.S. Lee,* M. Catalano** and K.S. Shin***

*Center for Solid State Science, Arizona State University, Tempe, AZ 85287-1704
**Dipartimento Scienza dei Materiali, Universitá di Lecce, Via Arnesano, Lecce 73100, Italia
***Department of Metallurgical Engineering, Seoul National University, Seoul, Korea

Weldalite™ 049 is an ultrahigh strength weldable Al-Cu-Li based alloy containing minor amounts of Ag, Mg and Zr, developed at Martin Marietta.[1] Additions of Ag and Mg seem to stimulate precipitation in this alloy, but the exact role of these elements in promoting the precipitation of strengthening phases is as yet unclear. In this paper, we report the characteristic microstructure of the Weldalite™ 049 alloy in the near peak aged T8 temper condition and its effect on the measured tensile properties of this alloy.

The alloy used in this study was prepared by the Reynolds Metals Company. Measured alloy composition was Al-4.36 Cu-1.25 Li-0.39 Mg-0.35 Ag-0.14 Zr (wt.%). Tensile tests were performed at both room and cryogenic temperatures. The samples for TEM observations were cut from the mechanical testing specimens and then thinned to electron transparency by polishing and ion milling. Liquid nitrogen cooled specimen holder was used for ion milling to avoid local specimen heating. Diffraction contrast and tilting experiments were performed at 200kV in a JEM-2000FX. HREM was done in an ISI-002B at 200kV, with an interpretable resolution limit of 0.18 nm.

Fig. 1(a) is a TEM BF image showing a typical microstructure of the alloy in the near peak aged condition. A corresponding SAD pattern close to a $[112]_{Al}$ zone axis is shown in Fig. 1(b). An array of fine plate-like precipitates on $\{111\}_{Al}$ plane, giving rise to streaking along the $<111>$ direction in the electron diffraction pattern, is readily seen in Fig. 1(a). They were the most prominent precipitates observed in this alloy. This precipitate was T_1 (Al_2CuLi) phase, which is known to be the major strengthening precipitate in the Al-Cu-Li alloy system.[2,3] A high resolution image of this T_1 precipitate at this orientation is shown in Fig. 2. The precipitate appears to be one T_1 unit cell thick (c=0.935 nm ≈ four $\{111\}_{Al}$ planes) and has $(0001)_{T1}//\{111\}_{Al}$ orientation relationship, as reported by others.[3,4] The SAD pattern shown in Fig. 1(b) also exhibits weak streaking along the $<210>_{Al}$ direction. Thin precipitates lying on $\{210\}_{Al}$ planes are visible in the BF image shown in Fig. 1(a). These precipitates were S'-type phase, which had lath-like morphology with a $\{210\}_{Al}$ habit plane. HREM images of this S'-type precipitate viewed along $<210>_{Al}$ and $<001>_{Al}$ directions are shown in Figs. 3(a) and 3(b), respectively. A minor volume fraction of plate-type θ' (Al_2Cu) precipitates with a $\{100\}_{Al}$ habit plane was also observed. Fig. 4(a) is a BF image with a $<001>_{Al}$ zone axis orientation, showing thin precipitates lying on two sets of $\{100\}_{Al}$ planes. A HREM image of the θ' precipitate is shown in Fig. 4(b). The present Weldalite™ 049 T8 alloy also has small amounts of other precipitates distributed heterogeneously. Their morphology and structure will be reported.

The yield strength and ultimate tensile strength of this alloy, measured along the rolling direction at room temperature, are 611 and 630 MPa, respectively. The strength of the alloy was higher at cryogenic temperature. The strength of this alloy is significantly higher than that of conventional 2XXX Al alloys and 7XXX Al alloys. The improved properties observed in the present alloy can be attributed to the presence well-developed fine T_1 precipitates as a major strengthener, as reported by others.[1] The role of other precipitates observed and structural evolution upon plastic deformation will also be discussed. Chemical analysis by nanospectroscopy is in progress, and the results will be reported.[5]

References

1. J.R. Pickens et al., Proc. 5th Int. Aluminum-Lithium Conference (1989) 1397.
2. W.T. Tack et al., Scripta Metall. 24 (1989) 1685.
3. J.C. Huang and A.J. Ardell, Proc. 4th Int. Aluminum-Lithium Conference (1987) 373.
4. W.A. Cassada et al., Metall. Trans. A, 22A (1991) 287.
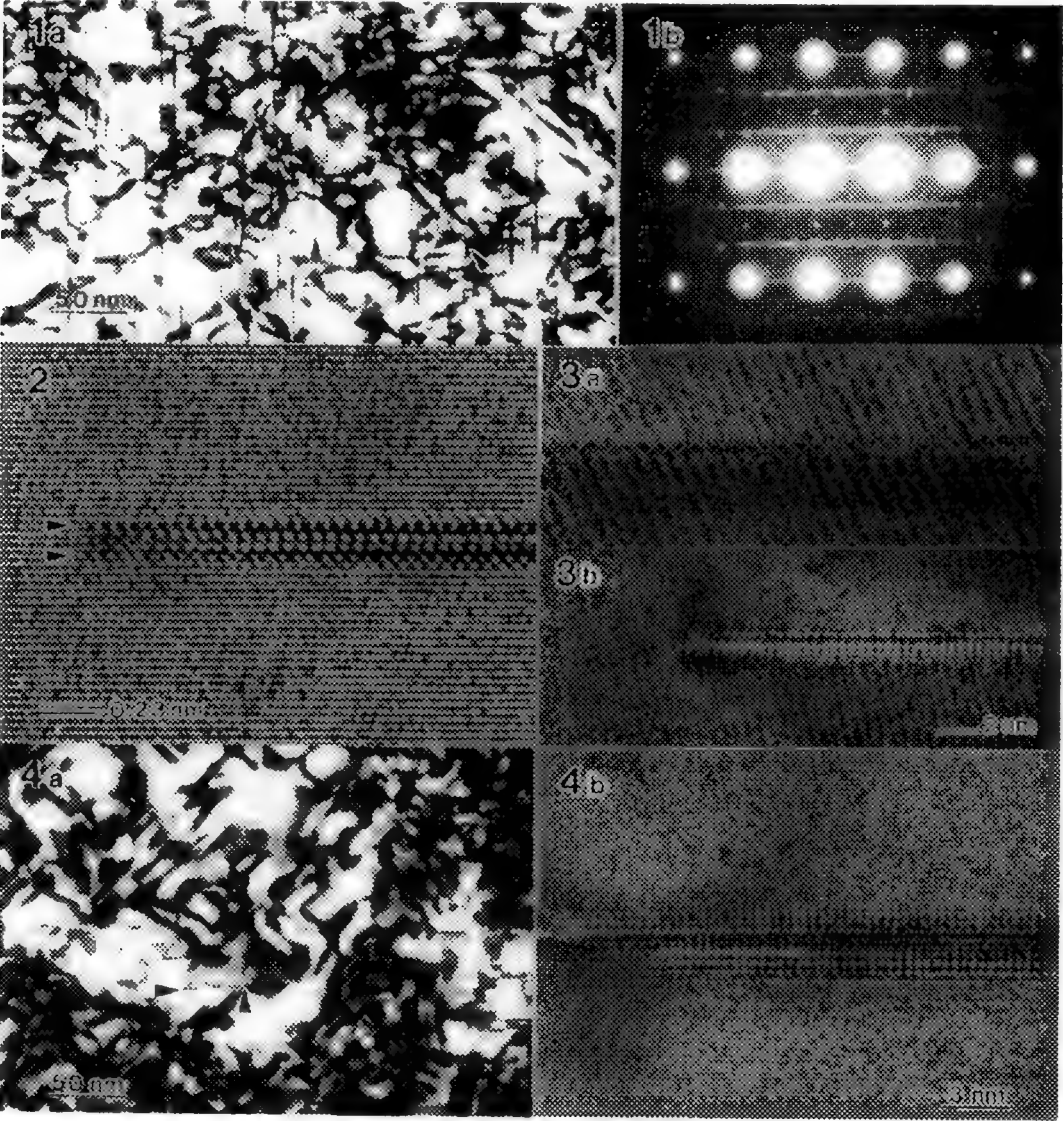
FIG. 1.--(a) TEM image of the Weldalite™ 049 T8 alloy, showing an array of plate-like precipitates, and (b) SAD pattern from a $<112>_{Al}$ zone axis. Note streaking along the $<111>_{Al}$ direction, due to the precipitation on $\{111\}_{Al}$ planes. Also note weak streaking along the $<210>_{Al}$ direction.

FIG. 2.--HREM image of the T_1 precipitate on $\{111\}_{Al}$. Z.A.= $<112>_{Al}$.

FIG. 3.--HREM images of the S'-type precipitate on $\{210\}_{Al}$ planes, viewed along (a) $<112>_{Al}$ and (b) $<001>_{Al}$ directions.

FIG. 4.--(a) BF image showing thin precipitates lying on two sets of $\{100\}_{Al}$ planes, and (b) HREM image of the θ' precipitate shown in (a). Z.A. = $<001>_{Al}$.

185

PRECIPITATION IN Al-Li-Zr ALLOYS

D.M. Vanderwalker

U.S. Army Materials Technology Laboratory,Watertown, Massachusetts 02172

Aluminum-lithium alloys have a low density and high strength to weight ratio.
They are being developed for the aerospace industry.The high strength of
Al-Li can be attributed to precipitation hardening. Unfortunately when aged,
Al-Li aquires a low ductility and fracture toughness. The precipitate in
Al-Li is part of a sequence SSSS → Al₃Li → AlLi[1]. A description of the phases
may be found in reference 1 . This paper is primarily concerned with the
Al₃Li phase. The addition of Zr to Al-Li is being explored to find the optimum
in properties. Zirconium[2,3] improves fracture toughness and inhibits
recrystallization. This study is a comparision between two Al-Li-Zr alloys
differing in Zr concentration.

Al-2.99Li-0.17Zr(alloy A) and Al-2.99Li-0.67Zr (alloy B) were solutionized
for one hour at 500ºC followed by a water quench. The specimens were then
aged at 150°C for 16 or 40 hours. The foils were punched into 3mm discs.
The specimens were electropolished with a 1/3 nitric acid 2/3 methanol solution.
The transmission electron microscopy was conducted on the JEM 200CX microscope.

Two Al-Li-Zr alloys were examined to compare structures. The mechanical
properties of both alloys have been measured by Wang and Wells[4] who found
the alloy of higher Zr content to have higher hardness and strength. Al-2.99Li-
0.17Zr and Al-2.99Li-0.67Zr both have Al₃Li homogeneously nucleated throughout
the structure. (FIG.1) Al₃Li was verified by electron diffraction in alloy
A. Alloy B is more abundant with precipitation especially Al₃Zr. Al₃Li and
Al₃Zr are both transition phases with identical crystal structures. There
are also large precipitates on grain boundaries. The presence of Al₃Zr was
shown by finding Zr peaks in X-ray spectra from microanalysis. (FIG.2)
FIG. 3 shows the structure of alloy B. In addition to Al₃Li and Al₃Zr there
are composite precipitates Al₃(Li,Zr). The cluster of large precipitates
in the matrix region appear to be associated with Fe impurities. (FIG.4)
The Fe peak was found from STEM X-ray data. Mo was detected in some cases.
Discontinuous precipitate reactions were observed in the form of a fan.
Precipitate free zones[5] are found in the overaged alloys. (FIG.5) The zones
are 400A wide on each side of the boundary.

References

1. L.F. Mondolfo Aluminum Alloys: Structure and Properties, London:Butterworth
(1976).
2. P.L. Makin and B.Ralph, J. Mater. Sci(1984)19,3835.
3. F.W. Gayle and J.B. Vander Sande, Acta. Metall.(1989)37,1033.
4. W.Wang and M.G.H. Wells, Light Weight Alloys for Aerospace Applications
II, E.W. Lee and N.J. Kim (Eds.) Warrendale: AIME (1991)189.
5. A. Kelly and N.B. Nicholson, Prog.Mat.Sci. (1963)10,151.
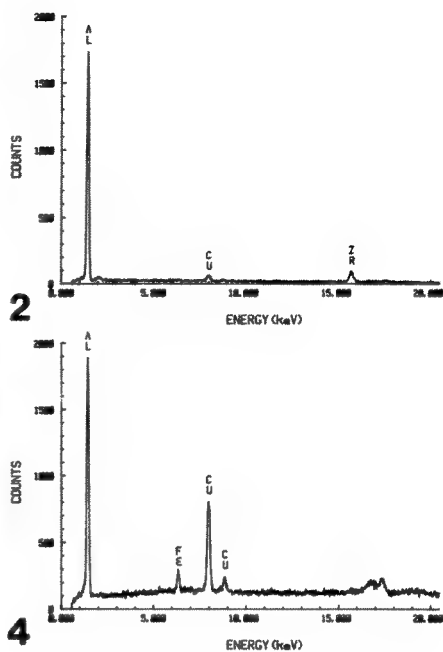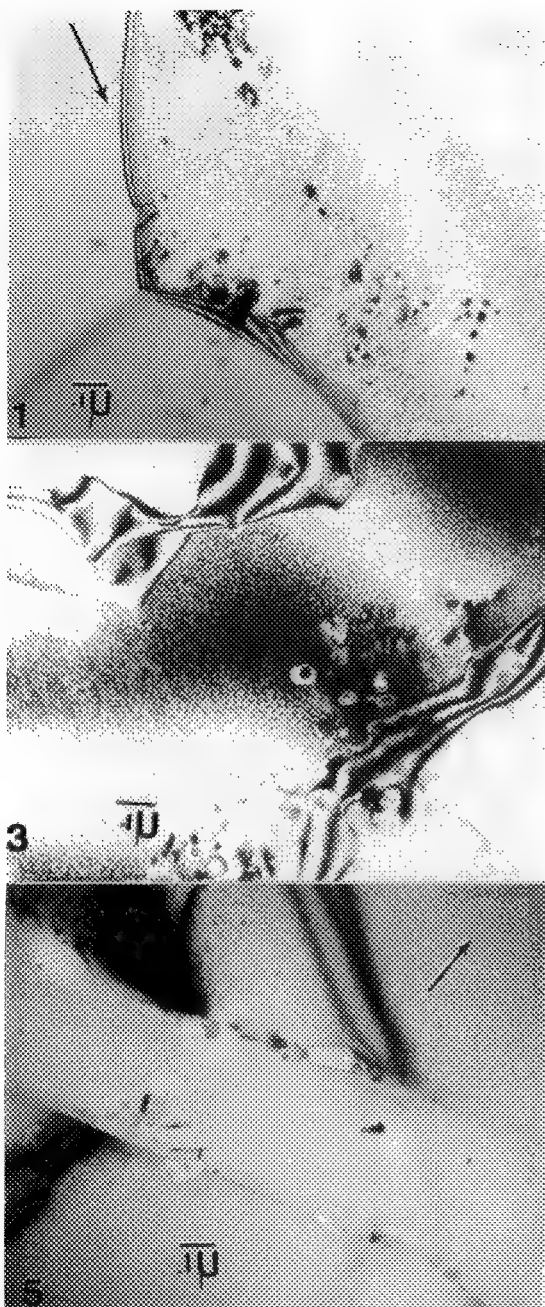
FIG. 1.--Al$_3$Li is visible in background. Note large grain boundary phases in alloy A.
FIG. 2.--Al$_3$Zr was found by Zr peak in x-ray data.
FIG. 3.--Micrograph from alloy B where Al$_3$Li, Al$_3$Zr, and Al$_3$(Li, Zr) are present.
FIG. 4.--Fe in spectrum shows there are impurities at sites where nucleation has occured.
FIG. 5.--Precipitate-free zones in overaged alloy.

IDENTIFICATION OF T1 PHASE IN Al-Li-Cu ALLOY (2090)

J. S. Kim, S. S. Baek, G. H. Kim, and C. H. Chun

Materials R&D Center, Agency for Defense Development, 305-600, Taejeon, Youseong P.O.Box 35, Korea

In Al-Li-Cu alloy(2090) the extra spots in the Selected Area Diffraction Pattern (SADP) of $[112]_\alpha$ zone axis have been argued. Huang and Ardell described that the extra spots were originated from T1 variants tilted to electron beam.[1,2] Rioja and Ludwiczak , however, presented that the precursor of T1 termed T1' was present in alloy(2090) and generated the extra spots.[3] Rioja and Ludwiczak explained the existence of extra spots as making the simulated SADP diagrams and analyzing x ray diffraction lines of T1'. The existence of T1' has been inconsistent with the other papers.[4,5,6] Huang and Ardell's model has been well recognized in present. The investigations on the extra spots had mainly been restricted in $[112]_\alpha$ SADP. In the present paper, the extra spots from $[110]_\alpha$ and $[100]_\alpha$ zone axes were investigated using High Resolution Electron Microscope (HREM) and optical laser diffractometer.

The Al-Li-Cu alloy(2090) was heat-treated for 3min. at the T1 peak temperature analyzed by differential scanning calorimetry results and quenched so that the extra spots were present in SADP. Transmission Electron Microscope(TEM) specimens were prepared using a 70% methanol+30% nitric acid solution at 12~15V, -30~-40° C. HREM images were observed using a JEOL 4000FX. Optical Diffractograms (O.D.) were obtained from the HREM images of about 50Å diameter. X-ray diffractometer was used to obtain x ray data.

The HREM images show T1 precipitates (ppts) on $\{111\}_\alpha$ parallel to electron beam in $[112]_\alpha$ and $[110]_\alpha$ zone axes, respectively (Fig. 1.& Fig. 2.). The other HREM images show T1 ppts on $\{111\}_\alpha$ inclined to electron beam in $[110]_\alpha$ and $[100]_\alpha$ zone axes, respectively (Fig. 3.& Fig. 4.).

T1 and T1' ppts have $\{111\}_\alpha$ habit planes[7,2] The interplanar spacings d of T1 and T1' ppts parallel to $\{111\}_\alpha$ are $d(0001)_{T1} \approx 9.35$Å and $d(031)_{T1'} \& (101)_{T1'} \approx 2.34$Å, respectively. The HREM images of edge-on ppts on $\{111\}_\alpha$ in $[112]_\alpha$ and $[110]_\alpha$ zone axes show the periodic spacings of 9.4Å identical with $d(0001)_{T1}$. The O.D.s of edge-on ppts in $[112]_\alpha$ and $[110]_\alpha$ zone axes reveal [T2T0] and [01T0] zone axes of T1, respectively. There is no evidence for the existence of T1' phase in edge-on ppts. The other HREM images of inclined ppts on $\{111\}_\alpha$ in $[110]_\alpha$ and $[100]_\alpha$ zone axes show the extra spots of $[1\bar{2}13]_{T1}$ and$[\bar{2}\bar{2}\bar{1}]_{T1}$ zone axes of T1, respectively. The distinguishable d-spacings of T1', including 3.67Å & 2.72Å similar to those of the extra spots were not resolved in our own x ray results. Through the results of HREM images and O.D.s we concluded that the Huang and Ardell's model is well consistent with our results.

References

1. J. C. HUANG and A. J. ARDELL, Aluminium-Lithium Alloys III, London: The Institute of Metals, (1986),455.
2. J. C. HUANG and A .J. ARDELL, Mat. Sci. and Tech., (1987), 3, 176.
3. R. J. RIOJA and E. A. LUDWICZAK, Aluminium-Lithium Alloys III, London: The Institute of Metals, (1986),471.
4. M. TAKEDA et al., Scripta Metall., (1991), 25, 89.
5. V. RADMILOVIC and G. THOMAS, J. de Physique, (1988), 48, supp.C3(9), 385
6. W. A. CASSADA et al., Scripta Metall., (1987), 21, 387.
7. B. NOBLE and G. E. THOMPSONS, Met. Sci. J., (1972), 6, 167.
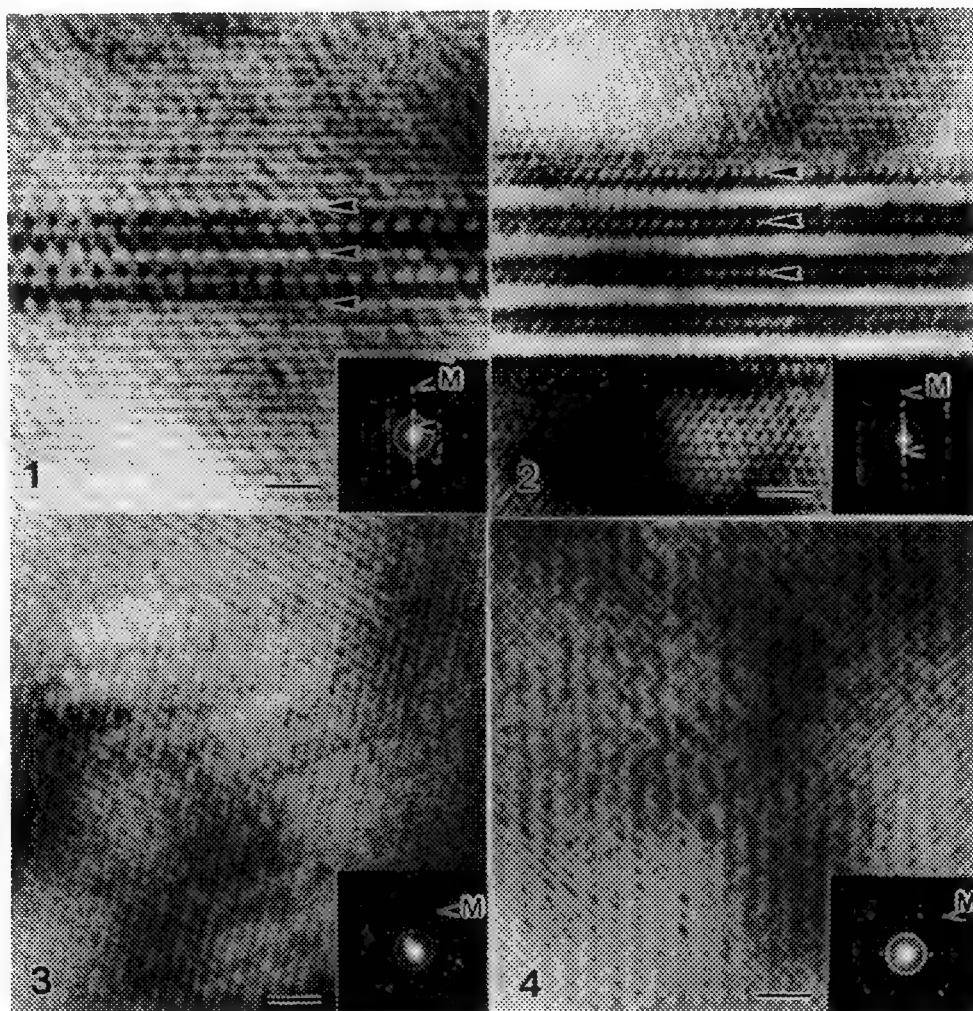
FIG. 1.--HREM image and O.D. of edge-on T1 phase in $[112]_\alpha$ zone axis.   Note 9.4Å spacings of $(0001)_{T1}$ planes (arrows), $(\overline{1}\overline{1}1)_\alpha$ matrix spot (M), and O.D. of T1 in $[\overline{1}2\overline{1}0]_{T1}$ zone axis.   Bar=10Å

FIG. 2.--HREM image and O.D. of edge-on T1 phase in $[110]_\alpha$ zone axis.   Note 9.4Å spacings of $(0001)_{T1}$ planes (arrows), $(1\overline{1}1)_\alpha$ matrix spot (M), and O.D. of T1 in $[01\overline{1}0]_{T1}$ zone axis.   Bar=10Å

FIG. 3.--HREM image and O.D. of inclined T1 phase in $[110]_\alpha$ zone axis.   Note superimposed HREM image of T1, $(1\overline{1}\overline{1})_\alpha$ matrix spot (M), and O.D. of extra spots of T1 in $[1\overline{2}13]_{T1}$ zone axis.   Bar=10Å

FIG. 4.--HREM image and O.D. of inclined T1 phase in $[100]_\alpha$ zone axis.   Note superimposed HREM image of T1, $(020)_\alpha$ matrix spot (M), and O.D. of extra spots of T1 in $[\overline{1}2\overline{1}1]_{T1}$ zone axis.   Bar=10Å

189

INVESTIGATION OF THE VISIBILITY OF EARLY-STAGE Ω PRECIPITATES IN AN Al-Cu-Mg-Ag ALLOY

Y. C. Chang

Department of Materials Science and Engineering, University of Virginia, Charlottesville, VA 22903

Nucleation is the process through which the smallest stable particle of a new phase of critical size r^* is formed. During precipitation, growth of such a particle takes place solely by statistical diffusional fluctuations. Typical examples of this occur in the Al-Cu system, where precipitation involves the nucleation and growth of several metastable phases according to the sequence: Al (solid solution) → G.P. zones → θ' → θ (Al_2Cu). In the case of Al-Cu-Mg-Ag alloys, nucleation of the Ω phase on the {111} Al planes is thought to be fundamentally different from nucleation of the other θ', θ or S' phases [1,2]. In order to understand this difference, the nucleation behavior of Ω phase in an Al-3.9Cu-0.5Mg-0.5Ag (wt. pct.) alloy was examined by high-resolution transmission electron microscopy (HRTEM). The visibility of small precipitates embedded in a matrix is an important question that arises in such an investigation and that is the subject of this paper.

Figure 1(a) shows a HRTEM image of an edge-on Ω precipitate in a $[110]_{Al}$ orientation taken just before it dissolved in the Al matrix during an *in situ* hot-stage (160°C) TEM experiment. In this image the particle has a radius of 1.3 nm. Another small Ω precipitate in the same orientation is shown in Fig. 1(b) and this particle, which was formed by a conventional aging treatment, has a slightly larger radius of 1.9 nm. These small precipitates could represent critical nuclei of size r^* although they may also be larger particles that appear to have these sizes as a result of limited visibility due to superimposed matrix.

HRTEM image simulations were performed to investigate the visibility of Ω precipitates in the Al matrix using the TEMPAS multislice program [3]. Two supercell models were constructed for edge-on Ω precipitates in $<110>_{Al}$ and $<112>_{Al}$ zone axes as shown in Figs. 2(a) and (b), respectively. A layered structure of Ω precipitate embedded in the foil was formed by stacking slices of the edge-on Ω precipitates in Figs. 2(a) and (b) between similar slices of pure Al along the electron beam direction. Fig. 3 shows a representative series of simulated images with pure Al on the left, one unit-cell of edge-on Ω through the foil thickness on the right and 10% increments of Ω precipitate in between these extremes for a foil thickness of 8.6 nm in a $<110>_{Al}$ zone axis. The Ω precipitate can be resolved when it occupies between 20 to 30% of the foil thickness, i.e., HRTEM does not reveal the precipitate when its diameter is less than 20% of the foil thickness. This ratio did not change appreciably with the foil thickness and a value of 25% of the foil thickness was visible for most conditions. Similar experiments for a $<112>_{Al}$ zone-axis showed that the precipitates were visible when they occupied at least 15% of the foil thickness. Therefore, a $<112>_{Al}$ zone axis is a better orientation to observe small Ω precipitates in order to determine r^*. It is also possible that the objective lense defocus value (Δf) will affect the visibility of an Ω precipitate. Figs. 4(a) and (b) show simulated images as a function of defocus for a 17.1 nm thick crystal with a minimum diameter of Ω phase in $<110>_{Al}$ and $<112>_{Al}$ zone axes, respectively. The precipitate visibility appears to increase for defocus values far from Scherzer defocus (Δf_{Sch} = -48.6 nm), although the thickness and diameter of the precipitate in these images are distorted.

In general, a precipitate diameter measured from a HRTEM image is smaller than the actual diameter due to limited visibility along the precipitate edge. From the visibility ratio obtained above, the actual radii for the particles shown in Fig. 1 can be calculated as 2.0 and 2.3 nm, when the foil thicknesses are assumed to be 15 and 10 nm for Figs. 1(a) and (b), respectively. Therefore, it is possible to measure the critical nucleus r^* for the Ω phase when r^* is greater than about 7.5% of the foil thickness.

References

1. I. J. Polmear: *Materials Science Forum*, (1987)**13/14**, 195.
2. B. C. Muddle and I. J. Polmear: *Acta Metall. Mater.*, (1989)**37**, 777.
3. R. Kilaas: *Proc. 45th Ann. EMSA Meeting*, San Francisco Press, San Francisco, (1987), 66.
4. This research was supported by the National Science Foundation under grant DMR-9107550 and CSIST (Taiwan).

Δf=-10 nm   -20 nm   -30 nm   -40 nm   -50 nm   -60 nm   -70 nm   -80 nm

Fig. 1   (a) *In situ* HRTEM image for an Ω precipitate (arrowed) before complete dissolution into the matrix. The foil was heated to 160°C for 43 minutes. (b) An early-stage Ω precipitate in a specimen aged for 8 hours at 130°C.

Fig. 2.   Supercell models for layered HRTEM image simulations: (a) for $[010]_\Omega$ and $[10\bar{1}]_{Al}$, and (b) $[100]_\Omega$ and $[1\bar{2}1]_{Al}$.

Fig. 3.   A representative series of simulated images for the layered structures with pure Al on the left, pure edge-on Ω (one unit-cell of Ω between Al) on the right, and 10% increments of Ω precipitate in a $[110]_{Al}$ zone-axis (400 keV, thickness = 8.6 nm, Δf = -65 nm).

Fig. 4.   Simulated images as a function of defocus for the minimum visible precipitates: (a) 25% Ω along $[010]_\Omega$ // $[10\bar{1}]_{Al}$ and (b) 15% Ω along $[100]_\Omega$/$[1\bar{2}1]_{Al}$ (thickness = 17.1 nm).

191

CHARACTERIZATIONS OF LaNi$_{5-y}$Al$_y$ ALLOYS

W. C. Mosley

Westinghouse Savannah River Company, Savannah River Laboratory, P. O. Box 616, Aiken, SC, 29802

LaNi$_{5-y}$Al$_y$ alloys which reversibly form hydrides are used to store, pump, and separate hydrogen isotopes during processing of tritium at the Department of Energy's Savannah River Site (SRS).[1] Over forty alloys with nominal bulk aluminum contents (Y) from 0 to 1.16, including several made with intentional excesses and deficiencies of lanthanum, were characterized by scanning electron microscopy (SEM), energy dispersive x-ray (EDX) analysis and x-ray diffractometry (XRD) to determine distributions and compositions of constituent phases. Objectives were to (1) produce primary LaNi$_{5-y}$Al$_y$ phases with desired absorption and desorption pressures for hydrogen isotopes and (2) minimize secondary phases with undesirable absorption/desorption behaviors. Electron probe microanalysis (EPMA) was used to determine aluminum contents (y) of primary LaNi$_{5-y}$Al$_y$ phases. A relationship between y and hexagonal unit cell parameters was established. Pressure-composition- temperature (PCT) measurements allowed development of equations for predicting hydrogen desorption plateau pressures from XRD or EPMA data.

LaNi$_{5-y}$Al$_y$ alloys were procured as Hy-stor® Metal Hydrides from Ergenics, Inc. Elements were melted and cast into ingots which were homogenized by heating at 1050-1260°C in argon. SEM/EDX analyses were performed on an International Scientific Instruments, Inc., DS-130 SEM with a Tracor Northern TN-5500 EDX system. EPMA was performed with an Applied Research Laboratories Scanning Electron Microprobe Quantometer modified with a Tracor Northern TN-5500 EDX system. A Philips automated scanning diffractometer was used for XRD.

Secondary phases were detected in all alloys. Ni, cubic and tetragonal Ni$_3$Al, NiAl, La$_2$Ni$_7$, LaNi and La(OH)$_3$ were detected by XRD. Figure 1 is a composite ternary diagram constructed from EPMA. Phases which can form stable hydrides are La$_2$Ni$_{7-z}$, LaNi, La$_2$Ni$_3$Al, LaNi$_2$Al and small inclusions of nearly pure lanthanum. To avoid these undesirable phases, Ergenics prepares alloys used for processing tritium with slight deficiencies of lanthanum. Secondary phases in lanthanum deficient alloys include Ni, Ni$_3$Al and NiAl, which are inert in hydrogen, and small inclusions of nearly pure lanthanum. Lanthanum-rich inclusions are thought to be unreacted impurities from elemental lanthanum and are limited to < 1 volume % by specifications.

EPMA of seven alloys with Y = 0-1.16 showed primary La$_x$Ni$_{5-y}$Al$_y$ phases to be stoichiometric with respect to lanthanum content (x=1.00 ±0.03). Linear variation in the LaNi$_{5-y}$Al$_y$ hexagonal unit cell volume (V) with y occurs for y=0.1 to1.0 and is given by V(Å^3) = 86.78+3.28y (Figure 2).[2] Deviation from linearity at y>1.0 is attributed to limited solid solubility of aluminum in the primary phase.

Desorption pressures (P) and temperatures (T) are related by the Van't Hoff equation: lnP=A+(B/T) where A=ΔS^o/R and B=-ΔH^o/R and ΔS^o, ΔH^o and R are the transition entropy and enthalpy and gas constant, respectively. PCT and XRD measurements for sixteen alloys showed A=13.5±0.7 and B=43406-543V for P in atmospheres and T in °K. Thus, hydrogen desorption pressures for a LaNi$_{5-y}$Al$_y$ alloy may be predicted (within about 20%) from XRD by modified Van't Hoff equations: lnP=13.5+[(43406-543V)/T] or lnP=13.5-[3716+1781y)/T].[3]

References

1. M. S. Ortman et al., J. Vac. Sci. Tech. A (1990)8, 2881
2. H. Diaz et al., Int. J. Hydrogen Energy (1979)4, 445
3. This work was supported by the U. S. Department of Energy under Contract No. DE--AC09--89SR18035. The author thanks P. K. Smith, R. E. Howell, W. H. Miller, Jr., R. M. Everson, F. E. Odom, C. B. Johnson, R. T. Walters, and E. L. Huston for their technical assistance.
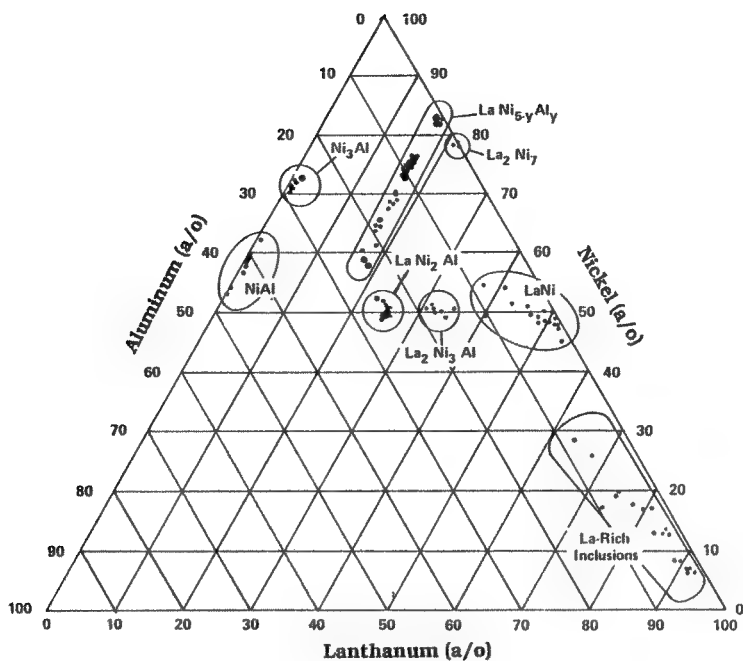
FIG. 1.--Composite ternary phase diagram for LaNi5-yAly alloys determined by EPMA/EDX,

Figure 1 labels: Aluminum (a/o), Nickel (a/o), Lanthanum (a/o), La Ni5-yAly, La2 Ni7, Ni3 Al, NiAl, La Ni2 Al, LaNi, La2 Ni3 Al, La-Rich Inclusions

Figure 2:

V (Å³)

89174

87656

1253

1288

Vol = 86.78 + 3.28 y
(y = 0.0 - 1.0)

Diaz et al.

82099
Alloy Batch

87075
SEMQ.EDX.ZAF
Mean ± σ

87659
Dwight (ASTM PDF # 17-126)

y
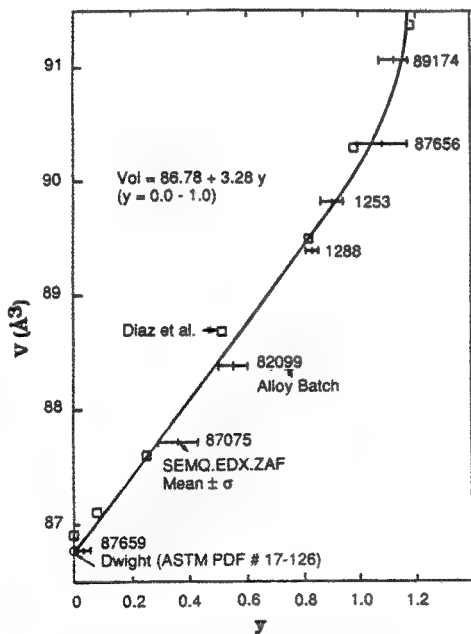
FIG. 2.--Variation of **V** determined by XRD
with **y** measured by EPMA/EDX.

Figure 3:

P (atmospheres)

Nominal Bulk
Al Content

Symbol	Y
■	0.0
□	0.3
●	0.5
×	0.75
○	0.85
+	1.0

115° C

200° C

25° C

80° C

150° C

60° C

Modified Van't Hoff Equation

$$\ln P \text{ (atm)} = \frac{(43406.543 V)}{T \text{ (°K)}} + 13.5$$

V (Å³)
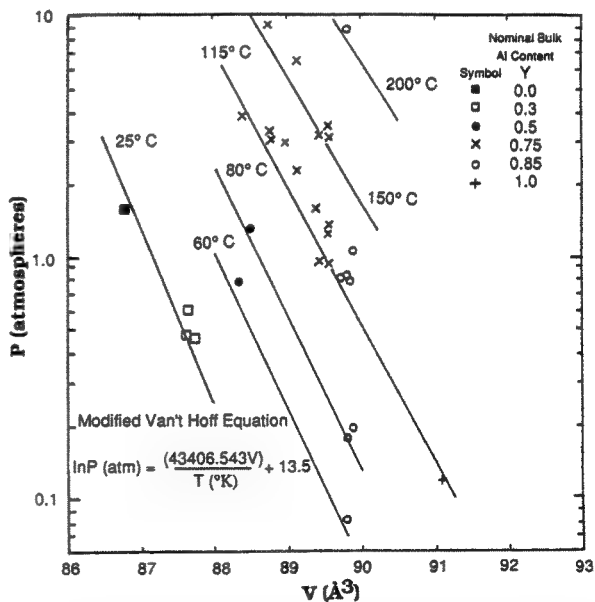
FIG. 3.--Comparisons of hydrogen desorption
plateau pressures (P) determined by PCT with
values calculated with modified Van't Hoff
equation based on **V** determined by XRD.

THE ROLE OF TEM IN A GOVERNMENT LABORATORY SERVING INDUSTRIAL CLIENTS

Tom Malis

Metals Technology Laboratories (MTL), CANMET, 568 Booth St., Ottawa, Canada K1A 0G1

The challenge of meeting demands for enhanced performance while maintaining a competitive price has become the norm for industries producing engineering materials. A government laboratory intending to assist such industries in a formal manner must adapt its policies, structure and capabilities as the needs of its clients change. TEM would come under close scrutiny in this process because of the relatively high financial and intellectual investment required to produce good results. The following project examples illustrate secondary, but quite important aspects of the prime goal of solving the client's problem(s). They include judicious facility/methodolgy upgrading (including in-house development and external networking), fruitful interactions with project scientists (including accurate prediction of resource usage) internal and external marketing, and dealing creatively with personnel shortages, all while producing what is hopefully the 'good science' needed for institutional and individual recognition!

Fig 1 shows typical precipitates in a pipeline steel for which the distribution and composition vis-a-vis various microalloying elements were crucial to the mechanical behavior of the product (via austenite grain size control). Before acquisition of a suitable in-house TEM, university work was funded which demonstrated the complex nature of coprecipitation in these steels, a fact not then appreciated by the steel industry. Subsequent in-house work built upon these findings to the point where characterization of such precipitates has become a most useful component of formalized collaborations with steel companies in that both resource usage and delivery of useful information have become quite predictable.

Unfortunately, theoretical predictability is often derailed by the pragmatic reality of 'the TEM process'. Fig 2 illustrates what should have represented the successful conclusion to a study seeking to ascertain the presence and degree of Li segregation to grain boundaries in Al-Li aerospace alloys, segregation suspected of producing embrittlement. However, the significant segregation of Fig 2 was not duplicated in an exhaustive number of later attempts despite such measures as using ultrathin microtomed sections for energy loss quantification, carbon coating to 'trap' the mobile Li within the sections and a variety of EELS collection procedures. Li mobility/loss under electron irradiation apparently was (and remains) too great for reliable analysis. For the electropolished thin foil in Fig 2, it appears that only the chance coincidence of analysing a boundary segment between two closely-spaced boundary precipitates (X) combined with the presence of surface contamination films enabled at least some portion of the boundary Li concentration to be analyzed. (It is noteworthy that other techniques, such as Auger and SIMS have not had any greater success in detecting such Li segregation). Despite this setback, the project provided invaluable experience regarding energy loss spectroscopy[1] and established ultramicotomy as a fast and effective means of providing reliable TEM specimens from a large variety of other industrial materials.[2]

Development of metal matrix composites is assisted greatly by a detailed knowledge of the structure and chemistry of the metal-ceramic interface. In general, it is desireable to have rather weak interfacial bonding, but Fig 3, from a prototype Al-SiC industrial alloy, illustrates a signigicant (and unexpected) shallow penetration of Al into the ceramic reinforcement during processing which would produce overly strong bonding.[3] A secondary but equally important aspect of the work, namely marketing the laboratory's range of capabilities, was the fact that numerous other characterization techniques (image analysis, SEM, SIMS, microprobe) were involved in a complimentary fashion which elicited much more information than TEM alone could supply. A later study of an Al-coated graphite fiber system involved only TEM, but of a particularly detailed and arduous nature, ie in the chemical and crystallographic identification of a large number of reaction phases.[4] The intensive effort was well worth the time consumed in the sense that the quality of the data convinced otherwise skeptical project scientists to redesign their proposals which had been based on much more limited and simplified reactions.

Occasionally scientific quality may not seem so relevant. The SiC composite reinforcing fibers shown in Fig 4 were subject to an intensive study using diffraction to study the orientation relationships between regions of high and low microtwin (or fault) density, and to combine this with EEL data showing a small but significant chemical variation between the segments in order to make some reasonable hypotheses

concerning a fiber growth model.[5] While the fibers performed adequately for the client's customers so as not to require any immediate process modification, the model will provide a basis for adjustment should property requirements change. In addition, a scientist seconded from the company conducted much of the microscopy, a useful means of coping with an increasing workload in the TEM facility.

References

1.T.F. Malis and J.M.Titchmarsh, Proc. Inst. Phys. Conf. Series 78 (1985) 181.
2.T.F. Malis and D. Steele, Spec. Prep. for TEM of Materials II, Mat. Res. Soc. Symp. 199 (1990) 3.
3.L.M. Dignard-Bailey et al, Proc. Int. Symp. on Adv. Str. Materials, London:Pergammon (1989).
4.G.J.C. Carpenter and S.H. Lo, J. Mat. Sci., in press.
5.G. McMahon, G.J.C. Carpenter and T.F. Malis, J. Mat. Sci. (1991) 26, 5655.
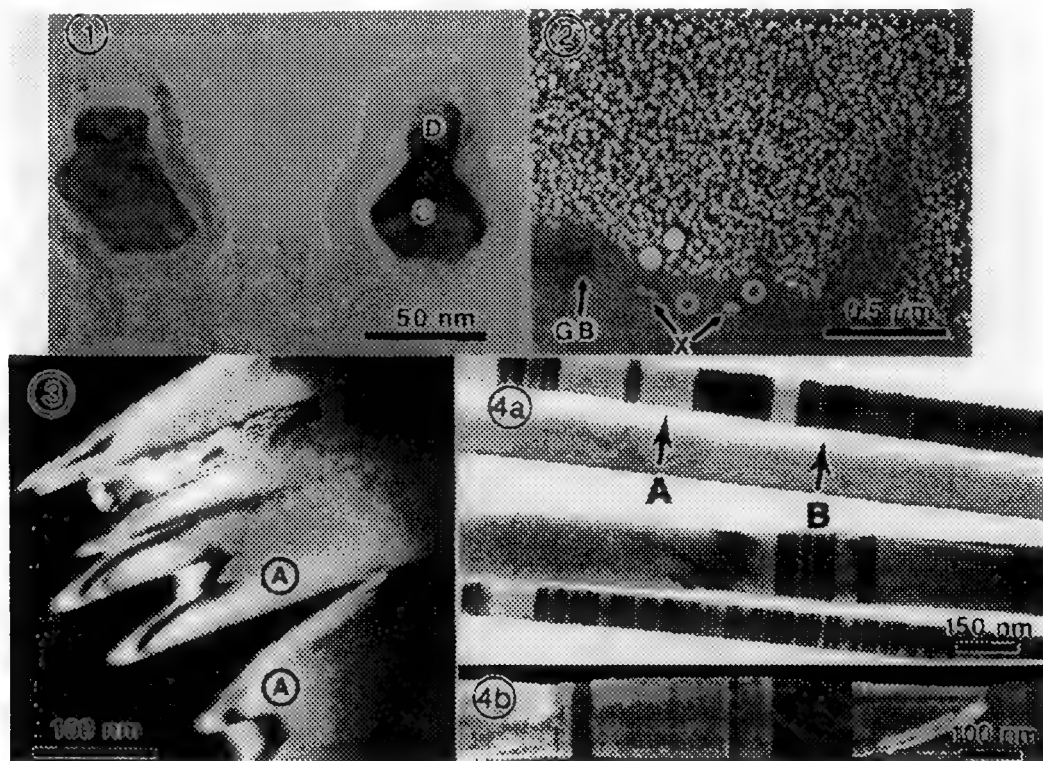
Fig 1 Microalloy steel precipitates extracted via SiO_x film. EELS showed carbonitride nature, EDX showed 'cores' (C) to have Nb/Ti/V/Mo as 80/10/8/2 (wt%), whereas 'caps' (D) had Ti/Mo as 50/50.
Fig 2 DF of Al_3Li precipitates in overaged commercial Al-Li alloy showing clear denuded grain boundary zone. With a 30nm beam, EELS at circled locations (k-factor based on Al_3Li stoichiometry) showed 12 at% Li in matrix (11.2 nominal), no detectable Li in denuded zone, and 16.5% at boundary.
Fig 3 Al-SiC (particulate) composite, SiC DF showing diffuse nature of metal-ceramic interface at certain serrated segments. EELS showed 10-20 at% Al at regions such as A, whereas EDX showed Al Al extending nearly 1 micron into SiC, likely due to secondary fluorescence of Al by Si-K x rays.
Fig 4 a) SiC reinforcing fibers showing regions of varying defect density and diameter, eg A & B. EELS showed higher Si/C ratio in low defect density regions, a chemical change which may be linked to the structure change. b) [111] DF illustrating erratic twin relationships amongst segments.

195

The Structure and Chemistry of Polymer Metal Interfaces: A Combined EM and XPS Investigation

D. B. Leong, M. A. Helfand, R. L. McConville, F. W. Mercer

Raychem Corporation, Menlo Park, CA 94025

Polymer to metal relationships for applications from coating finishes to electronic devices require interfacial synergy. Polymer application requirements range in temperature, thermal stability, thermal expansion, moisture absorption, oxidative stability, etc. and choice of metal and deposition technique must take into account these characteristics. While the ability to deposit metal in a controllable fashion is well established the present study focuses on what takes place at the polymer metal interface. Polymer/metal interactions on polyimide systems have been studied in detail for the past decade by a variety of analytical techniques (1). For the first time this is being investigated in the FPAE polymers combining EM study for structural analysis and XPS for chemical analysis. Fluorinated poly (arly ethers) FPAE, are a newly developed class of polymeric dielectric materials for electronic packaging. These new materials exhibit excellent oxidative stability, low moisture absorption and low dielectric constant (2). While these parameters are critical for electronic device performance and longevity, device performance is also highly dependent on metallization of the polymer.

Figure 1 shows a bright field cross sectional image of the Cr/polymer interface tilted so that the plane of the interface was vertical. Because of the limited image contrast of the polymer the well resolved metal deposition layer was used to optimize the tilt. The Cr layer has a well defined highly micro-crystillized region approximately 20 nm thick above the interface region. Figure 2 shows a high resolution dark field planer view of the microcrystallites in the Cr layer. Crystallite size varies from 2 to 5 nm. In figure 3 the C 1s spectra from the FPAE surface (approximate probing depth ~75A) prior to metalization is shown. The spectra has been fit by the non-linear least squares curve fitting to include the three carbon species present in the the polymer, aromatic C (~285ev), C-O bonding (~287ev), and C-F bonding (294ev) . Following metallization XPS observes strong chemical interactions between the F component of the polymer and the metal. The parameters important in controlling the structure and morphology of the crystalline region as well as the interface region will be discussed and further characterized using the capabilities of XPS and Electron Microscopy.

References
(1) P.S.H. , P.O. Hahn, J.W. Bartha, G.W. Rubloff, F.K. LeGoves, B.D. Silverman
J. Vac. Sci. Technol. A3(3) p739 (1995)
(2) (a) F.W. Mercer and T.D. Goodman, Polymer Preprints,32 (2) , 189 (1991).
(b) F.W. Mercer, D. Duff, J Wojtowicz, and T. Goodman, Poly. Mater. Sci. Eng., 66, 0000 (1992)
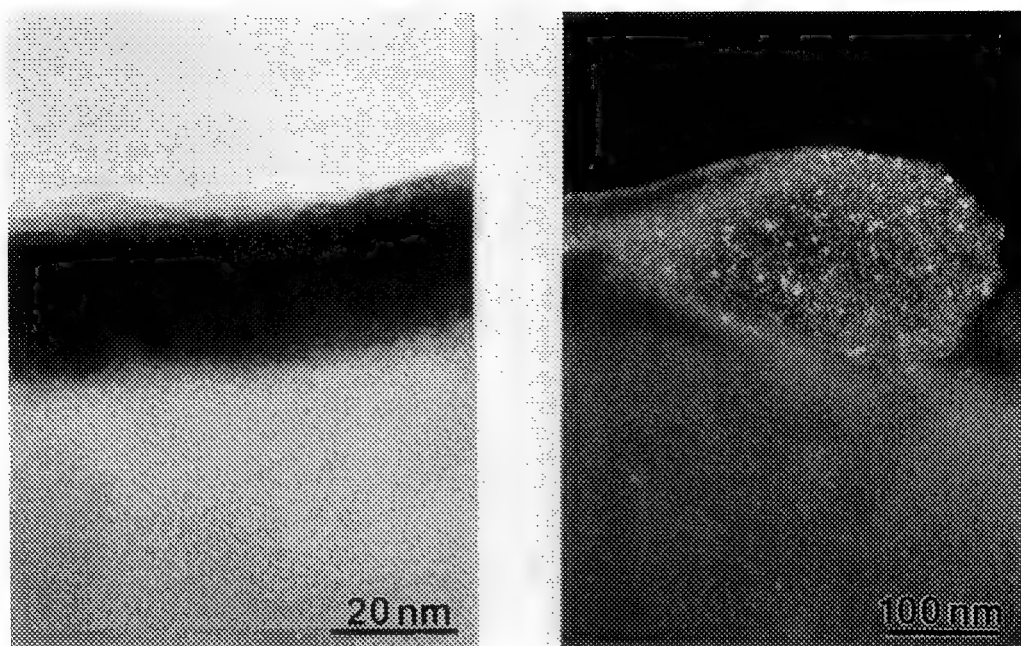
Figure 1. Bright field cross-sectional image of the Cr/polymer interface.
Figure 2. High resolution dark field planar view of the Cr layer.
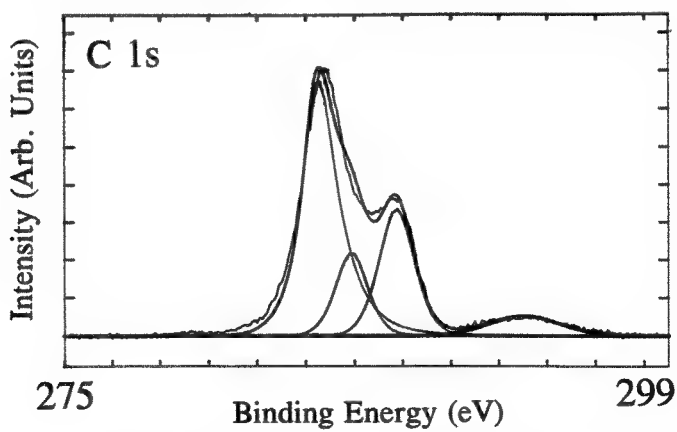
Figure 3. Carbon 1s photoelectron spectra obtained from the surface of as-cast FPAE.

ELECTRON MICROSCOPY OF RAPIDLY SOLIDIFIED PERMANENT MAGNETS

Raja K. Mishra

Physics Department, G. M. Research and Environmental Staff, Warren, MI 48090

The discovery of a new class of permanent magnets based on $Nd_2Fe_{14}B$ phase in the last decade has led to intense research and development[1] efforts aimed at commercial exploitation of the new alloy. The material can be prepared either by rapid solidification or by powder metallurgy techniques and the resulting microstructures are very different. This paper details the microstructure of Nd-Fe-B magnets produced by melt-spinning.

In melt spinning, quench rate can be varied easily by changing the rate of rotation of the quench wheel. There is an optimum quench rate when the material shows maximum magnetic hardening. For faster or slower quench rates, both coercivity and maximum energy product of the material fall off. These results can be directly related to the changes in the microstructure of the melt-spun ribbon as a function of quench rate. Figure 1 shows the microstructure of (a) an overquenched and (b) an optimally quenched ribbon. In Fig. 1(a), the material is nearly amorphous, with small nuclei of $Nd_2Fe_{14}B$ grains visible and in Fig. 1(b) the microstructure consists of equiaxed $Nd_2Fe_{14}B$ grains surrounded by a thin noncrystalline Nd-rich phase. Fig. 1(c) shows an annular dark field image[2] of the intergranular phase. Nd enrichment in this phase is shown in the EDX spectra in Fig. 2.

The overquenched ribbons can be hot-pressed to form fully dense magnets. At the hot pressing temperature, the amorphous ribbons crystallize and form a microstructure similar to that shown in Fig. 1(b). The grains in Fig. 1(b) are isotropically oriented and the magnets with this microstructure are isotropic. Fresnel image in Fig. 3 taken from a hot-pressed material shows magnetic domain walls which reside near the grain boundaries. Combining these results with magnetization measurements leads to the conclusion that magnetic hardening occurs by domain wall pinning mechanism[3].

Besides the isotropic magnets, it is also possible to produce anisotropic magnets from the melt-spun alloys. This is done by hot deforming the material when both the grain sizes and grain orientations change. The microstructure of a hot deformed (die-upset) magnet prepared from melt-spun material is shown in Figure 4. The material is sectioned parallel to the press axis and shows flat platelet shaped grains stacked on top of each other, all oriented with their c-axes parallel to the press direction. A Fresnel Lorentz image from the same material is shown in Fig. 5. The straight domain wall ww passing from grain to grain deviates from a straight line near the grain-edge marked by the arrow. As in the ribbon materials, there is an intergranular phase in these materials as well and domain wall pinning by the intergranular phase controls magnetization-demagnetization characteristics of this material.[4]

References

1. J. Herbst, Rev. Mod. Phys. <u>63</u>, (1991), 819.
2. R. Mishra, J. Magn. Magn. Mater. <u>54-57</u>, (1986), 450.
3. F. E. Pinkerton, J. Appl. Phys. <u>63</u>, (1988) 5427.
4. R. Mishra, Mater. Sci. Engin. <u>B7</u>, (1991) 297.
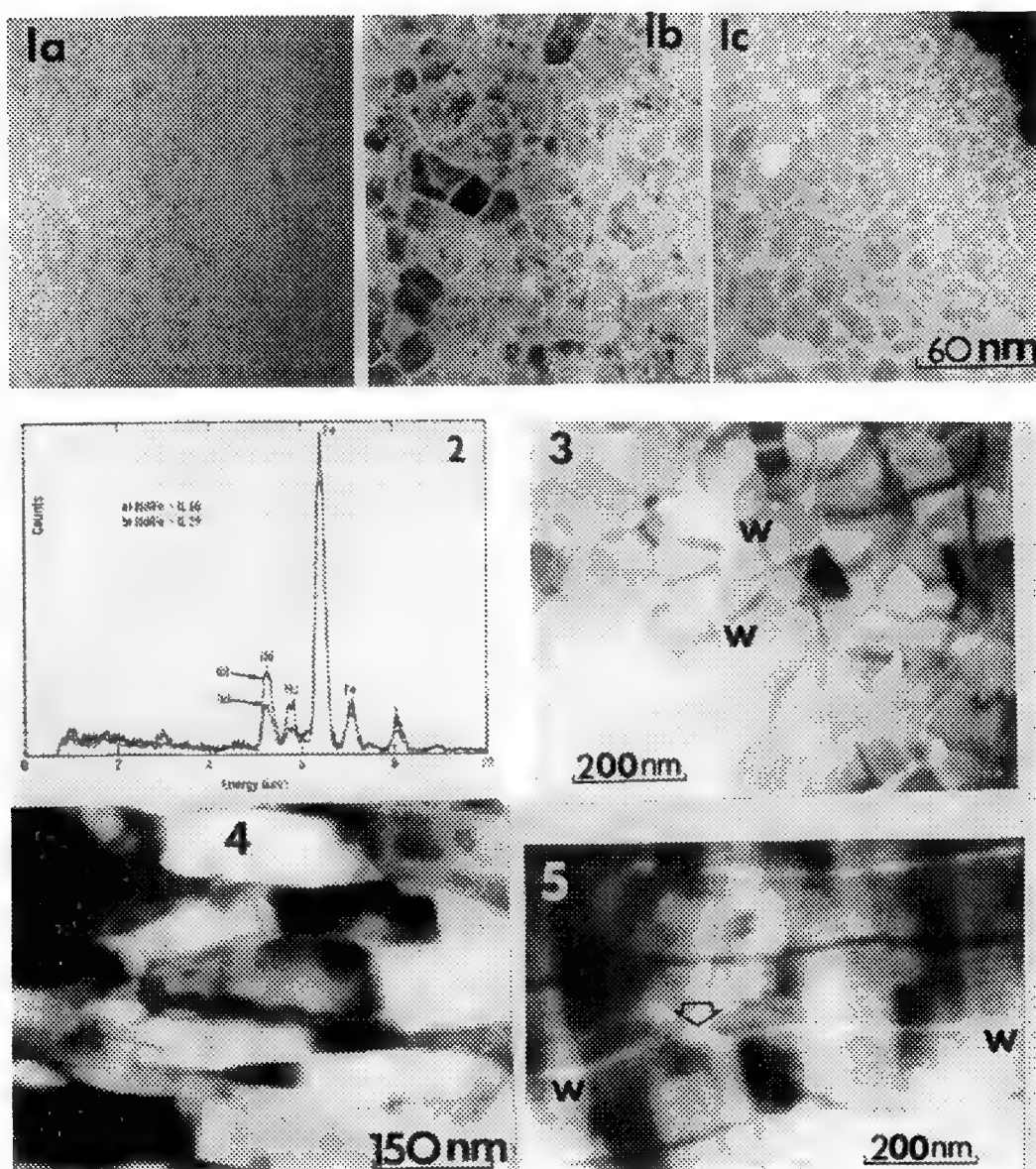
Fig. 1. BF image of (a) overquenched Nd-Fe-B alloy, note the nuclei of $Nd_2Fe_{14}B$,
(b) optimally quenched Nd-Fe-B alloy, (c) DF image of optimally quenched alloy.
Fig. 2. EDX spectra from (a) $Nd_2Fe_{14}B$ grain and (b) intergranular phase.

Fig. 3. Lorentz image from a hot pressed Nd-Fe-B magnet, domain wall marked ww.
Fig. 4. BF image of an aligned Nd-Fe-B magnet showing platelet shaped grains.
Fig. 5. Lorentz image from an aligned magnet, note kinks in the domain wall ww.

HIGH-RESOLUTION TEM OF Cr-Gd AND Co-Gd MULTILAYERS

Gerardo A. Bertero

Department of Materials Science and Engineering, Stanford University, Stanford, CA 94305

Thin film multilayered structures have assumed significant technological importance. In particular, several have proven adequate for magneto-optic recording applications in which vertical magnetization, large coercivities and a large Kerr rotation effect are needed[1]. In this regard, Co-Gd and Cr-Gd, among others, are candidate systems and specifically Gd-Co has already been used with some success.

In the present work, HRTEM was performed on sputter-deposited Cr-Gd and Co-Gd multilayers. These two systems are expected to show contrasting behavior which may affect the long term magneto-optic performance of the multilayer. Cr and Gd are almost totally immiscible, suggesting a large positive heat of mixing. Conversely, Co and Gd form a large number of intermetallic phases and show a deep eutectic at 60 at.% Gd indicating a negative, and possibly large, heat of mixing. Thus, a tendency for intermixing and solid state amorphization is expected for the Co-Gd system and not so for Cr-Gd. These considerations may be of importance since thermal stability is required for magneto-optical applications where the magnetic media is subjected to local thermal cycling during the magnetic writing process[1].

Figures 1 and 2 show cross-section TEM micrographs of a Cr-Gd multilayer with 100 Å bilayer period, produced by alternately sputtering each element at room temperature. It is seen that both Cr and Gd are crystalline (bcc and hcp respectively) with no evidence of an amorphous structure and no noticeable intermixing in good agreement with the expected behavior for this system. Roughness at the interfaces is minimal and non conformal as shown clearly in figure 1. In the figures, traces of {110} Cr and {10$\bar{1}$0} Gd planes are the most visible.

Figure 3 shows a HRTEM micrograph of a 100 Å bilayer period Co-Gd multilayer where extensive intermixing and amorphization is evident. A small fraction of the Co is crystalline. However, there is no evidence of crystalline Gd so it is presumably consumed into the amorphous phase. The figure also shows that the last layer of Gd, onto which a protective layer of 100 Å of Cr has been deposited, is mostly crystalline. Similarly, figure 4 shows a 50 Å bilayer period structure where amorphization is complete, except at some localized regions of the Gd layer in contact with the capping layer of Cr. These results show that Gd deposits in crystalline form, as illustrated by the last layer in contact with the Cr (since Cr does not react with Gd), and that Co amorphizes the Gd upon deposition in good agreement with the x-ray study of Hufnagel et al[2]. It is also seen that for the 50 Å layer case, some Co is crystalline but in the 25 Å thickness case, all the Co is in the amorphous state. This suggests also a critical thickness above which Co can form as a crystalline phase when deposited onto Gd.

In summary, a solid state amorphization reaction takes place in Co-Gd during deposition when Co is deposited onto Gd. This reaction is not found in the Cr-Gd system where abrupt interfaces, even to the atomic level, and crystalline phases are observed. These results are important in understanding the long-term stability of such multilayer structures.[3]

REFERENCES:

[1] B.N. Engel and C. M. Falco, MRS Bulletin, pp. 34-37, Sept. 1990
[2] T.C. Hufnagel, S. Brennan, A.P. Payne, and B.M. Clemens, "Observation of a Rapid Amorphization Reaction", submitted for publication.
[3] The author wishes to thank Prof. R. Sinclair for advice and guidance, Kobe Steel USA for financial support, and T.C. Hufnagel and Prof B.M. Clemens for providing the sample material and helpful discussions.
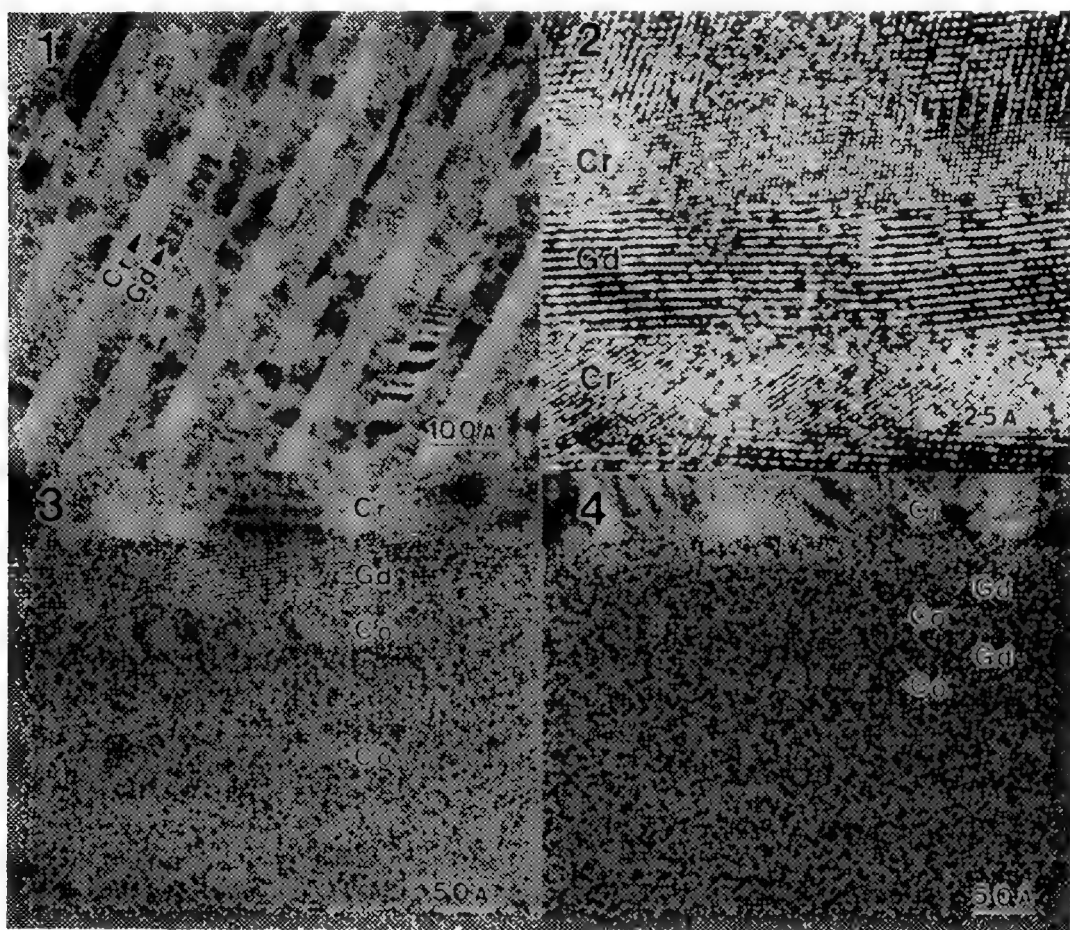
Fig. 1: High Resolution TEM micrograph of a Cr-Gd multilayer structure of 100 Å bilayer period.

Fig. 2: Cr-Gd multilayer as in Fig. 1 at a higher magnification.

Fig. 3: High Resolution TEM micrograph of a Co-Gd multilayer structure of 100 Å bilayer period.

Fig. 4: High Resolution TEM micrograph of a Co-Gd multilayer structure of 50 Å bilayer period.

EVOLUTION OF INTRINSIC COERCIVITY IN Pt-Co-B ALLOYS

N. Qiu

Department of Materials Science and Engineering
Vanderbilt University, Nashville, TN 37235

New permanent magnets based on Pt-Co-B ternary alloys have been developed by rapidly solidification with subsequent heat treatments.[1,2] The coercivity achieved in the Pt-Co-B ternary alloys is more than double the highest coercivity observed in the Pt-Co binary system. Good thermal stability of the coercivity produced by annealing provides a basis for consolidation processes such as hot isotropic pressing to produce bulk magnets from the rapidly solidified Pt-Co-B materials. Increased coercivity coupled with special properties such as high Curie temperature, corrosion resistance and ductility may expand the potential applications for these alloys. The evolution of microstructure and its effect on coercivity from annealing the as-quenched materials are investigated to understand the magnetic hardening mechanism and optimize the magnetic properties.

Rapidly solidified samples of $Pt_{53}Co_{47}$ (at.%) (Pt-Co) and of $Pt_{42}Co_{45}B_{13}$ (at.%) (Pt-Co-B) were prepared by melt-spinning. After systematic annealing of the melt-spun ribbons, the coercivity was measured for each condition. The microstructures were characterized using X-ray diffraction, scanning electron microscopy and analytical electron microscopy (AEM) including convergent beam electron diffraction, energy dispersive X-ray spectroscopy and electron energy loss spectroscopy. Samples for AEM analysis were dimpled and ion milled with cryogenic cooling to electron transparency. These samples were analyzed using a Philips CM20T TEM/STEM operated at 200 kV. The magnetic domain structure was studied by Lorentz phase contrast imaging. Lorentz conditions were achieved by operating the CM20 in the LM mode where the objective lens is turned off and by defocusing the diffraction lens to improve the Fresnel contrast. An image intensified Gatan 622 video camera was used to increase the magnification.

The dark field image in figure 1 from the binary Pt-Co alloy annealed at 700°C for 30 minutes shows the finely dispersed $L1_0$ lamellae in a disordered face centered cubic matrix. This microstructure produced the highest coercivity of 4.3 kOe for the Pt-Co binary alloys. Annealing of the ternary Pt-Co-B initiated the disorder-order phase transformation and Co-boride precipitation, and resulted in significantly greater coercivities as shown in figure 2. Different conditions in annealing of the Pt-Co-B brought about changes in the kinetics of the matrix disorder-order transformation, the precipitate morphology, and the precipitate nucleation and growth process, which lead to the variation in coercivity development of the Pt-Co-B alloys. The highest coercivity of 11.2 kOe was obtained in the Pt-Co-B annealed for 2400 minutes at 650°C. The addition of boron increases the $L1_0$ ordering transformation as shown by the completely ordered matrix from the Pt-Co-B alloy annealed at 650°C for 30 minutes in figure 3. A dark field image formed by the (001) $L1_0$ superlattice diffraction vector in (a) and a bright field image in (b) show an ordered $L1_0$ structure with anti-phase boundaries with Co-boride precipitates within the matrix as well as on the grain boundaries. This microstructure resulted in the optimum coercivity of the Pt-Co-B alloys. Electron diffraction identified the precipitates as orthorhombic Co_3B (a = 0.409 nm , b = 0.532 nm, c = 0.627 nm). Lorentz imaging reveals the magnetic domain structure and shows that each $L1_0$ matrix grain contains several magnetic domains of different shapes and sizes. However, most Co_3B precipitates are magnetic single-domains.

Pt-Co systems derive their coercivity primarily from the magnetic anisotropy of the ordered $L1_0$ PtCo matrix.[3] Substantial annealing is needed for the binary Pt-Co alloys to obtain the completely ordered phase, which causes coarsening of the matrix, the production of numerous low magnetic anisotropy sites such as twins and anti-phase boundaries, and the degeneration of coercivity. In the binary Pt-Co, the maximum coercivity results from magnetic domain wall pinning by the formation of finely dispersed ordered lamellae in the disordered matrix. In the ternary Pt-Co-B, the refined magnetic anisotropy PtCo

matrix with small Co3B precipitates which has substantial magnetic anisotropy limits the reverse magnetic domain nucleation and contributes to the significant increases in coercivity. Extended annealing of the Pt-Co-B increases the matrix ordering and enhances the crystallographic alignment, which effectively increases the magnetic anisotropy and yields the additional increase in the coercivity. [4]

References

1. J. A. Teubert et al., Mater. Sci. Forum Trans. Tech. Pub., vol. 50(1989)197.
2. N. Qiu et al., J. Appl. Phys., 70(1991)6137.
3. G. Hadjipanayis and P. Gaunt, J. Appl. Phys., 50(1979)2358.
4. This work is supported by the NASA Office of Commercial Programs. The author wishes to thank the Engelhard Corporation for providing the Pt-Co-B materials and the Francis Bitter National Magnet Laboratory at MIT for technical support for magnetic measurements.
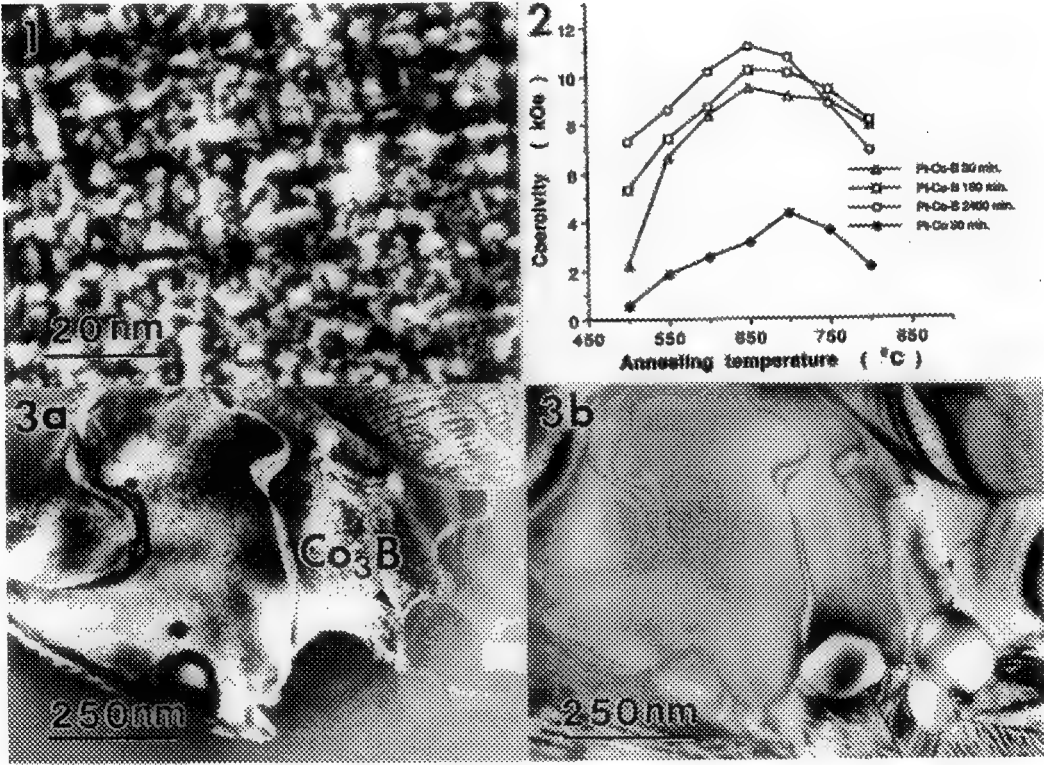
Figure 1 A dark field image produced by the (001) $L1_0$ superlattice diffraction vector from the binary Pt-Co alloy annealed at 700°C for 30 minutes shows the finely dispersed $L1_0$ lamellae in a disordered face centered cubic matrix.
Figure 2 Coercivity development from annealing the binary Pt-Co and the ternary Pt-Co-B as-quenched melt-spun ribbons.
Figure 3 A dark field image formed by the (001) $L1_0$ superlattice diffraction vector in (a) and a bright field image in (b) from the Pt-Co-B alloy annealed 30 minutes at 650°C show an ordered $L1_0$ structure with anti-phase boundaries.

ANALYSIS OF SOLUTE AND PRECIPITATE EFFECTS IN MICROALLOYED MEDIUM CARBON STEELS BY TEM

M.A. McCormick and J.D. Boyd

Dept. of Materials and Metallurgical Engineering, Queen's University, Kingston, K7L 3N6, CANADA

Modern microalloyed steels most often utilize the austenite grain refining and precipitation strengthening effects of microalloy precipitates.[1] In addition, effects of these elements as solutes have also been noted, although it is often difficult to determine whether solute or precipitate processes are dominant from mechanical or microstructural data. Extensive work has been done to quantify the mechanisms of grain coarsening, recrystallization, and precipitation for austenite in low carbon, flat rolled products.[2] Presently, work is underway to develop this knowledge for medium carbon, round products with the goal of tailoring the final microstructure by thermomechanical processing.[3]

To study austenite grain coarsening, three steels based on SAE 5160 (5160, 5160 + 0.18V, 5160 + 0.18Nb) were given a 30 minute soak at temperatures between 900°C and 1200°C then water quenched. Figure 1 shows that the austenite grain growth behaviour of all three steels was continuous throughout the temperature range. 5160+V showed the greatest grain refinement followed by 5160+Nb and the base 5160. These results were somewhat surprising as it was believed that the precipitates would dissolve within this temperature range, resulting in discontinuous grain growth.[4] However, TEM of carbon extraction replicas showed that although there was considerable dissolution of precipitates as the temperature increased, Al-rich precipitates remained at even the highest temperature studied (Figure 2). Although solute effects may be present, the kinetics of precipitate dissolution was found to control grain growth.

The effects of microalloying upon austenite decomposition behaviour have been studied in three different microalloyed SAE 1043 steels (1043 + 0.02Al, 1043 + 0.08V, and 1043 + 0.02Nb) using a quench-deformation dilatometer. Samples were induction heated to 1200°C and held for 10 minutes, quenched, reheated to 1050°C for 10 minutes, and then deformed 40% at either 1000°C or 800°C and cooled at 1°C/s to room temperature. Some samples were also quenched prior to deformation and prior to transformation to determine the austenite condition. The results in Table 1 show very different effects of the microalloying additions. The precipitates visible in the 1043 + Al steel (Figure 3) are either Ti or Al-rich and their size and number remain relatively unchanged by deformation. The V steel shows some precipitation prior to deformation, this amount increasing with deformation. The greatest number of precipitates are observed in the sample deformed at 800°C (Figure 4), this being attributed to the strain-induced precipitation of V(C,N) which acts to retard recrystallization and increase the transformation start temperature.[5] The 1043 + Nb steel reacted much differently as no precipitates were evident in any of the quenched samples. The austenite was observed to be recrystallized for both deformation temperatures, but little grain growth occurred and the transformation start temperature was reduced. Here, the solute Nb atoms can segregate to austenite grain boundaries and impede transformation.[6,7]

References

1.   Fundamentals of Microalloyed Forging Steels, ed G. Krauss and S.K. Banerji, TMS (1987).
2.   Mathematical Modelling of the Hot Rolling of Steel, Ed. S. Yue, CIM (1990).
3.   G. Nadkarni, M.A. McCormick, and J.D. Boyd, Processing, Microstructure, and Properties of Microalloyed and Other HSLA Steels, AIME/ISS (1991).
4.   L.J. Cuddy and J.C. Raley, Met. Trans 14A (1983), 1989.
5.   J.J. Jonas, THERMEC '88 (1988), 9.
6.   B. Garbarz and F.B. Pickering, Mat. Sci. and Tech. 4 (1988), 867.
7.   This work has been funded by a grant from the Ontario Centre for Materials Research (OCMR)

Table 1. Results of Dilatometer Experiments on 1043 Steels. Grain Size (GS) in μm, Transformation Start Temperature (T_s) in °C.

Steel	GS @ 1050°C	T_s (no deformation)	GS, 1000°C deform	T_s (deform @ 1000°C)	GS, 800°C deform	T_s (deform @ 800°C
1043+A1	32.1	675	41	668	32.1	675
1043+Nb	100	609	31	642	12.4	652
1043+V	41	-	18.6	664	10.5	695
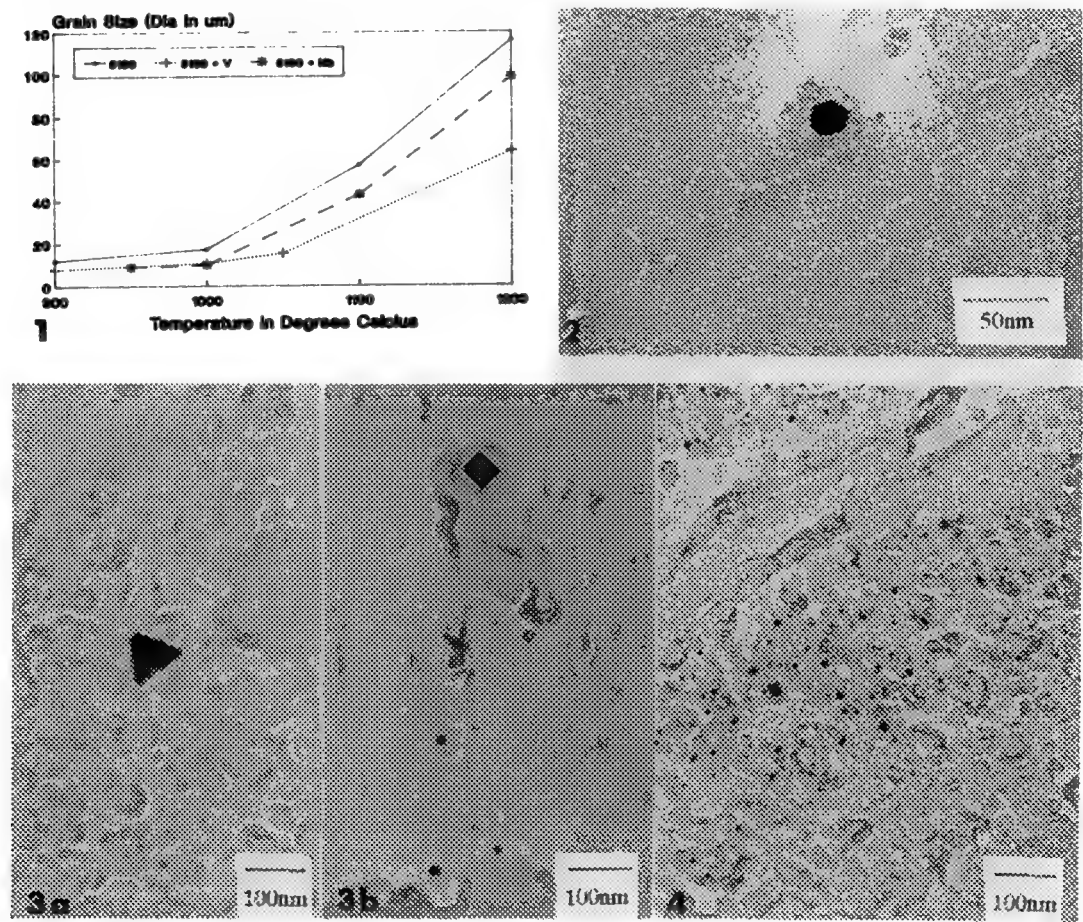
FIG. 1. Austenite Grain Coarsening Data for Microalloyed 5160 Steels.
FIG. 2. TEM of extraction replica. 5160 + V, 1200°C. Precipitate is found to be Al-rich.
FIG. 3. TEM of extraction replica. 1043 + Al; deformed at 800°C, quenched at 700°C. a) Al rich precipitates. b) Ti rich precipitates.
FIG. 4. TEM of extraction replica. 1043 + V deformed at 800°C, quenched at 700°C. Precipitates are found to be V rich; some show Ti.

205

ROLE OF ANALYTICAL TRANSMISSION ELECTRON MICROSCOPY IN THE STUDY OF Zr PRESSURE-TUBE ALLOYS

G.G. Weatherly[*], A. Perovic[*], V. Perovic[**] and G.R. Purdy[*]

[*] Department of Materials Science and Engineering, McMaster University, Hamilton, Canada, L8S 4M1
[**] Ontario Hydro Research Laboratories, 800 Kipling Avenue, Toronto, Canada, M8Z 5S4

Zirconium alloys are widely used in the Candu nuclear power generating system because of their unique combination of creep and corrosion resistance properties coupled with a low neutron cross section. The Zr–2.5 wt%Nb alloy has been extensively studied because it is the key component in pressure tubes. Pressure tubes are fabricated by extrusion in the two phase $(\alpha + \beta)$ field in the binary phase diagram, followed by cold work and stress relief heat treatments. As a result of this treatment, the alloy has a complex microstructure consisting of a duplex $\alpha + \beta_{zr}$ or $\alpha + \beta_{Nb}$ structure (depending on the particular heat treatment), superimposed on which is a dislocation structure associated with the working operation[1,2]. Typical microstructures are shown in Figs.1 and 2. If the alloy is quenched from the β phase field (1000°C), a Widmanstätten α–β_{zr} microstructure is produced (Fig.1a). In the extruded state (Fig.1b), the β_{zr} phase is now elongated and linked by a substructure which contains both <a> and <c> dislocations[2]. Cold working followed a stress relief heat treatment at 400°C for 24 hrs introduces predominantly <a> dislocations, while the β_{zr} phase (which is metastable) has decomposed to form discrete arrays of β_{Nb} (Fig.1c). Examples of the dislocation substructure are shown in Fig.2. Boundaries containing both <a> and <c> dislocations are observed[2]. The misorientation at the boundaries is typically a few degrees. They are often stepped or faceted. In Fig.2 the steps correspond to a <c> dislocation which has dissociated to form two <c>/2 dislocations.

A Vacuum Generator HB5 dedicated STEM instrument, equipped with a windowless EDX detector, has been used to follow the distribution of Nb and Fe at different stages in the processing of the alloy. Fe is present as an important impurity in the alloy (600–1100 ppm), known to enhance the apparent rate of self diffusion in Zr by several orders of magnitude at these impurity levels. For the analysis, a probe size of 1 nm and counting times of 100 s. were used. The results are summarized in Table I. Significant segregation of Fe to α–α sub–grain boundaries was detected. Stepped x–ray profiles taken across sub boundaries lead to a maximum Fe concentration of about 7wt% Fe concentrated in a 1 nm wide region after beam broadening effects were accounted for. The values quoted for the Fe and Nb levels are not absolute values, and have to be corrected for foil thickness effects, since the β_{Nb} phase is present as discrete particles smaller than the foil thickness.[3] The decomposition of β_{zr} to β_{Nb} is seen to lead to substantial enrichment of Fe and Nb in the β_{Nb} phase. Our current research program is studying the influence of in–reactor deformation and irradiation on the redistribution of Fe and Nb and the role of the dislocation substructure.

References

1. V. Perovic, G.C. Weatherly and R.G. Fleck, Can. Met. Qu. (1985)24, 253.
2. V. Perovic, G.C. Weatherly and R.G. Fleck, J. of Nucl. Mat. (1990)171, 327.
3. G.W. Lorimer, G. Cliff, P.E. Champness, C. Dickinson, F. Hasa and P. Kenway in "Analytical Electron Microscopy" (1984)153, San Francisco Press.

Table 1. – X–ray analysis of Nb and Fe in Zr–2.5 wt%Nb pressure tube alloy

Treatment	α–matrix		α–α grain boundary		β_{zr} or β_{Nb}	
	wt % Fe	wt % Nb	wt % Fe	wt % Nb	wt % Fe	wt % Nb
β quench	< 0.1	0.67±0.12	–	–	0.44±0.07	11.00±0.38
Extruded	< 0.1	0.62±0.11	0.28±0.06*	0.93±0.17	0.46±0.07	16.30±0.57
Standard tube	< 0.1	0.60±0.10	0.29±0.06*	0.84±0.15	0.32±0.05	46.72±1.63

*Approx. 30% of boundaries contained no detectable Fe(< 0.1 wt%)
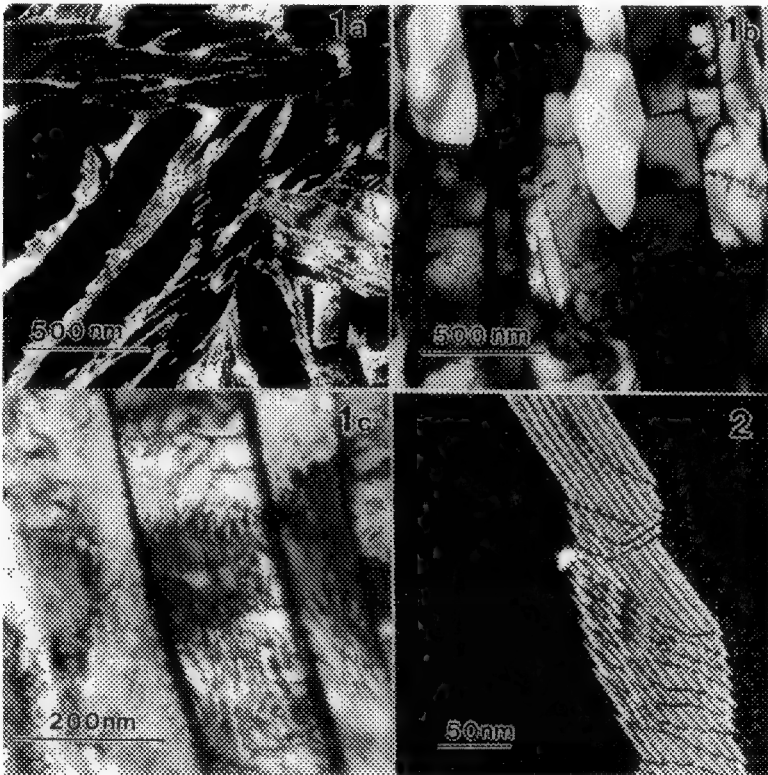
Figure 1. Typical microstructures of Zr–Nb pressure tube alloys (a) β quenched (b) As–extruded (c) Standard treatment.

Figure 2. Sub–boundary showing steps and dissociated <c> dislocations.

ROLE OF ELECTRON MICROSCOPY IN INTERFACE SCIENCE AND ENGINEERING

Gareth Thomas

Professor, Materials Science, U. C. Berkeley; Scientific Director, NCEM, Lawrence Berkeley
Laboratory; University of California, Berkeley, Department of Materials Science and Engineering,
Berkeley, CA 94720

The world of materials is a world of interfaces. Indeed many technologically significant materials have properties both physical and mechanical which are determined by the structure, composition, and bonding of the interfaces within these materials. Thus, electron microscopy and microanalysis, with its high resolution and specificity of information, is one of the key methods needed for characterization. Imaging can be done by amplitude contrast but is limited by the factor $g \cdot R$ (where R is a displacement vector), or resolution in phase contrast, and in today's modern instruments atomic arrangements can be imaged directly, both in plan and cross-sectional views. Beautiful examples are now being published. However so far, few developments to utilize this information for materials design have been forthcoming. On the other hand, interface or intergranular phases are very important in many metallurgical and ceramic systems. In fact many materials are composites of one kind or another and composites involving intergranular phases are an important group of such materials.

Direct in-situ studies of precipitate growth and dissolution such as the role of partial dislocations in the γ'- Al-Ag system is another example where the TEM can provide quantitative information to analyze structural dislocations, ledges, and steps. The establishment of HREM since the 1980's allowed more attention to be paid to the interfaces themselves, especially in semiconductor systems. In magnetic materials serious limits are imposed for HREM analysis due to the problem of objective lens fields which saturate the specimens. A special type of TEM is needed for this as has been proposed at Berkeley (1) and elsewhere. Overall what is needed is a much closer "attack" on interface analyses by theory and experiment simultaneously, including interpretation of images and high resolution spectroscopy. Nanometer electron probes of sufficient intensity are needed for improved compositional analysis but the compromise between resolution and radiation damage must always be a concern.

Some examples of current problems in materials engineering include: (a) ceramics, generic problems; intergranular phases resulting from processing can cause mechanical and electrical property deterioration as illustrated in the schematic (fig. 1). In addition, polytypoids of varying cation/anion ratios affect superconducting properties (e.g., fig. 2), since the polytypoid has lower Tc with lower CuO content; (b) heterogenetics at grain boundaries in alloys, e. g., PFZs (undesirable) but interlath austenite in martensitic steels benefits toughness (desirable); c) Magnetic materials, e.g., the coupling of oxide layers to permalloy (magnetoresistance); problems of roughness (fig. 3).

In the analyses of such problems the crystallography is often complicated and interfaces can be irrational. Interphase interfaces (e.g., in metal-ceramic bonding) involve changes of bonding and composition – instrumentation is needed to resolve these details; specimen preparation of uniformly clean undamaged thin foils is critical. Resolution of glassy phases and glass/crystal interfaces requires HREM with accurate alignment of crystal and beam. Definitions of the glass-crystal interfaces must differ from the standard crystal-crystal interfaces. In magnetic materials, chemical and magnetic structures to be resolved at 1-10 nm require special new instrumentation. Interface roughness affects properties; (e.g., fig. 3) these relations need quantification. In the final analysis quantitative correlation of the desired properties with the structure and composition of the relevant interfaces is essential if we are to optimize material performance.

Ref. 1.   Characterization of Crystalline Interfaces by Advanced Electron Microscopy, Ed. U. Dahmen, Report of Workshop at NCEM, Berkeley LBL report 30365, 1991.
Ref. 2.   This work was supported by the Director, Office of Energy Research, Office of Basic Energy Sciences, Materials Science Division, United States Department of Energy under Contract No. DE-AC0376SF00098.

Grain boundaries/ Interfaces	Examples	Properties limited
Amorphous films	Si₃N₄	Creep
Partly crystalline films	Some Sialons	Creep
	Ferrites	Magnetic: permeability
	Varistors	Voltage drop required
Additives / impurities	ß Na alumina	Na⁺ conduction
	ZrO₂ / mullite composites	Varied (creep, etc.)
Lattice defects Faulting Transformation defects Polytypoids	Superconductors (high Tc): YBa₂Cu₃O₇₋ₓ (RE) (Pb)Bi-Sr-Ca-Cu-O Tl compounds	Defects limited; poor g.b. conduction Polytypoids of variable Tc; poor g.b. conduction
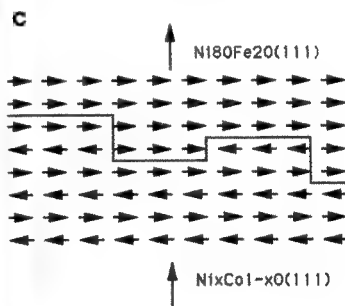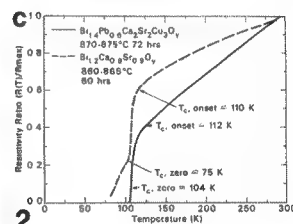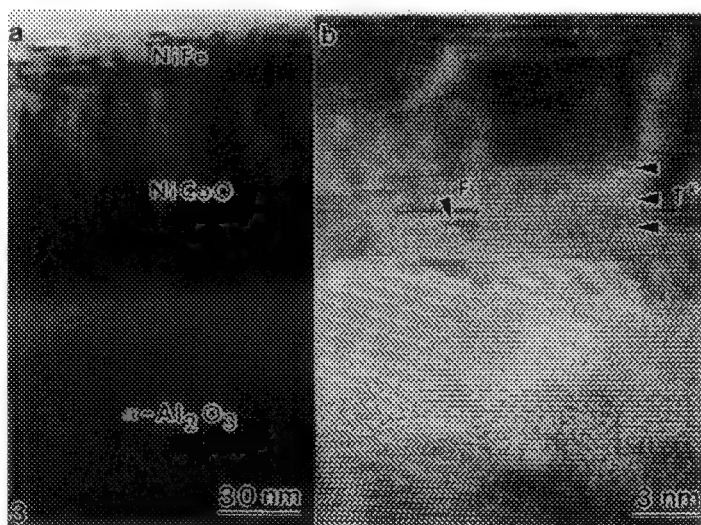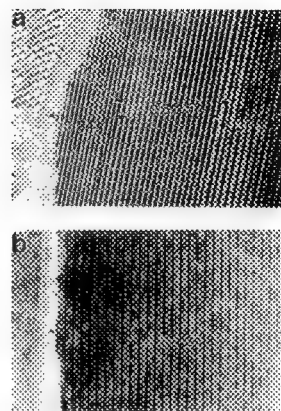
Fig. 1 Some generic microstructures of ceramics.
Fig. 2 (a) High resolution micrograph of unleaded sample showing decrease in c-parameter close to grain boundary: for 24Å spacing polytypoid, Tc=20K; for 30.5Å polytypoid, Tc=75K; for 38.2Å polytypoid, Tc=110K; (b) lattice image from leaded sample showing uniform c-parameter of 38.2Å up to grain boundary; (c) plot for leaded (—) and unleaded (---) Bi-containing superconducting materials; note step in resistivity plot for unleaded sample, resulting in lower Tc.
Fig. 3 (a) Cross-sectional TEM image of Ni₈₀Fe₂₀/Ni.₅₀Co.₅₀O) epitaxial films on α–Al₂O₃ substrate (0001); (b) HREM image of Ni₈₀Fe₂₀/Ni.₅₀Co.₅₀O interface; (c) schematic diagram of ferro- and anti-ferromagnetic exchange coupling at interface; arrows represent the electron spin.

209

TEM STUDY OF GRAIN BOUNDARY PHASE TRANSFORMATIONS IN Cu-12 at PPM Bi POLYCRYSTALS

E. C. Urdaneta, C. J. McMahon, Jr. and D. E. Luzzi

Department of Materials Science and Engineering
University of Pennsylvania
Philadelphia, PA 19104

Grain boundary segregation-induced faceting is being studied in Cu-12 at ppm Bi polycrystals as a model two-component alloy for grain boundary transformations. It has been demonstrated that Bi segregation is responsible for grain boundary faceting in copper and that this transformation is reversible[1]. Previous Auger electron spectroscopy fracture surface analysis in Bi-doped Cu have shown that grain boundary faceting only occurs after the segregated Bi reaches a saturation concentration of about 1 monolayer[2,3].

In the present work, conventional electron microscopy has been used to characterize the crystallography of faceted boundaries in specimens aged at 600°C. Figure 1 shows an example of a faceted boundary. Selected area diffraction analysis of the grains neighboring the faceted boundaries showed that boundaries between grain pairs with misorientation $\Sigma=3$ (coincidence site lattice formalism) exhibit a strong tendency to facet. In specimens aged for 6h, all of the completely faceted boundaries were found to be between $\Sigma=3$ grain pairs. In specimens aged for 24h the population of completely faceted boundaries had increased and at least 67% of them were between $\Sigma=3$ grain pairs. At the longer aging time, grain boundary dissociation transformations were also observed. Grain boundaries between $\Sigma=9$ grain pairs were dissociated into two new $\Sigma=3$ boundaries. One of the new boundaries was parallel to the old boundary and the other was faceted (Fig. 2). This observation supports the apparent preference for $\Sigma=3$ boundary faceting.

Since boundaries between $\Sigma=3$ grain pairs seem to have a strong tendency to facet, the investigation was therefore focussed into the study of the crystallography of the individual facet planes of $\Sigma=3$ boundaries. This study involves two distinct aspects: a) the determination of the orientation of the facet planes and b) the determination of the atomic structure of the facet planes. Figure 3 contains the results of the facet-plane orientation analysis for $\Sigma=3$ boundaries. Although many different facet orientations were found, the majority of facets were found to lie parallel to the $\{111\}_1/\{111\}_2$ crystal planes. About two thirds of the total $\Sigma=3$ faceted length had facet planes of this type in specimens aged for 6h, and this did not increase for specimens aged for 24h. This marked preference for facet planes of orientation $\{111\}_1/\{111\}_2$ is also supported by the dissociation transformation, were the majority of the new boundary length was found to be oriented parallel to planes of the type $\{111\}_1/\{111\}_2$. High-resolution electron microscope imaging coupled with image calculations is being used to determine the atomic structure of the facet planes in $\Sigma=3$ boundaries. Knowledge of the atomic structure of these facets will be necessary if the high stability of the $\{111\}_1/\{111\}_2$ facet is to be explained. (Supported by the NSF-DMR program under grant # 91-11775)

[1] T.G. Ference and R.W. Balluffi, Scripta Metall. 22, 1929 (1989)

[2] M. Menyhard, B. Blum, C. j. McMahon, Jr, S. Chikwembani and J. Weertman, J. Physique 49, C5, 457 (1988)

[3] M. Menyhard, B. Blum and C.J. McMahon, Jr, Acta Metall. 37, 549 (1989)
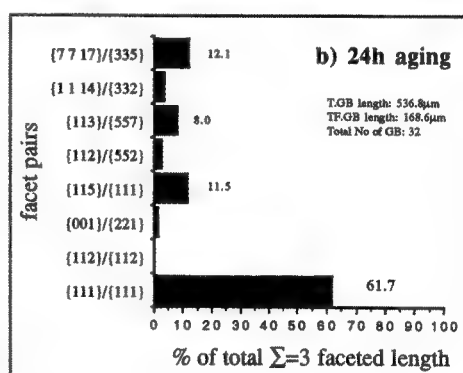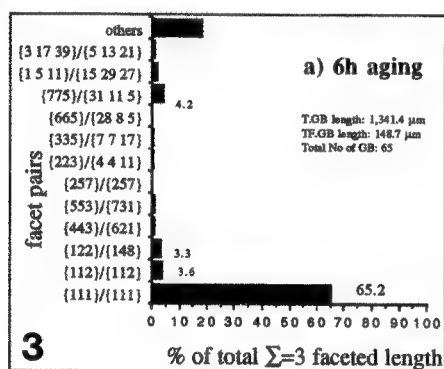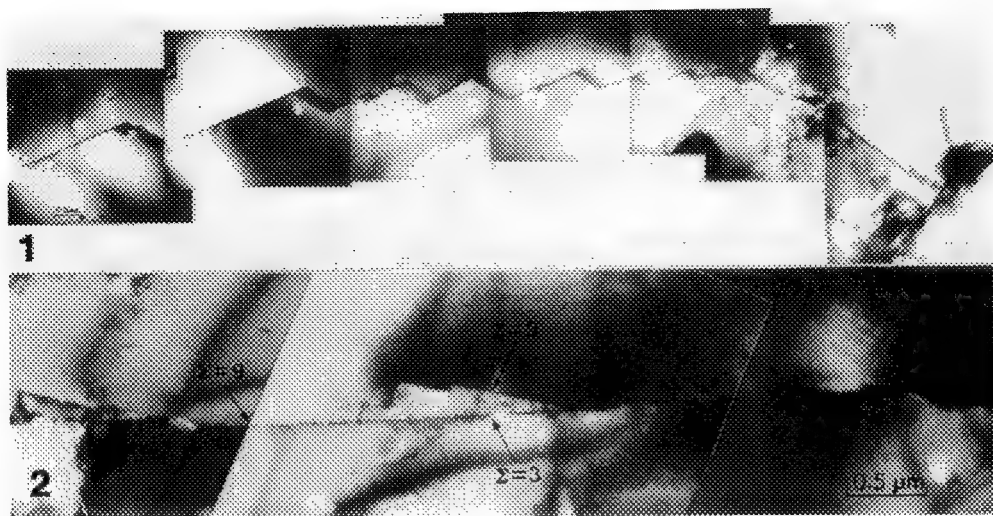
Fig. 1. Bright field image (BFI) of a completely faceted grain boundary in a specimen aged at 600°C for 6h

Fig. 2. BFI of a dissociated grain boundary in a sprecimen aged at 600°C for 24h. The misorientations across the old and the new boundaries are indicated.

Fig. 3. Orientation analysis of the facet planes of boundaries between $\Sigma=3$ grain pairs in specimens aged at 600°C for a) 6h and b) 24h.

QUANTUM MOLECULAR DYNAMICS SIMULATION OF Σ13 GRAIN BOUNDARY IN SI

M.J. Kim,* H. Ma,* R.W. Carpenter,* S.H. Lin* and O.F. Sankey**

*Center for Solid State Science, Arizona State University, Tempe, AZ 85287-1704
**Department of Physics, Arizona State University, Tempe, AZ 85287

Grain boundary (GB) structure determination at an atomic level by HREM had received increasing attention in recent years. However, models of grain boundary structure deduced from the experiment results are usually not unique, and they do not necessarily represent the equilibrium structure. A newly developed quantum-molecular-dynamics (QMD) method,[1] which does not depend on any empirical potentials, can be used to test these models and find the equilibrium atomic structure through simulated quenching. The method employs an electronic structure tight-binding model based on density functional theory within the local density approximation and the nonlocal pseudopotential scheme, and is used to compute the total energy and atomic forces for a variety of covalent materials. In the present study, this QMD method, coupled with image simulation, was used to predict the relaxed atomic configuration for the Σ=13 (510), [001] tilt grain boundary in Si.

The Si bicrystal with a Σ=13 (510), [001] tilt grain boundary was grown by the Czochralski method. Specimens for TEM observations were made from wafers with <001> surface normal parallel to the [001] bicrystal growth direction. HREM was performed at 200 kV in an ISI-002B and at 400 kV in a JEM-4000EX.[2] Images were recorded close to the optimum defocus, under axial illumination conditions. The experimental image, shown in Fig. 1, was used for comparison with the simulated images. Image simulations were done for relaxed boundary structures predicted by QMD using the EMS multislice program[3] on a Silicon Graphics IRIS workstation.

Σ=13 (510), [001] tilt grain boundary structure in a diamond cubic lattice can be constructed with a misorientation angle θ of 22.6° or 67.4°. Supercells with 96 Si atoms each were constructed for both cases. The supercell dimensions in the x, y and z directions are 1.384, 3.000 and 0.543 nm, respectively. The grain boundary is perpendicular to the y axis. The simulated quenching was performed, with a time step of 0.5 fs, in order to find the minimum energy configuration. On each time step the forces on the atoms were calculated and the equations of motion were solved to compute updated positions of the atoms. The first GB structure considered was the boundary with θ = 22.6°, which is similar to the IH+ structure proposed for Ge.[4] The equilibrium structure for this geometry was obtained after 144 steps. The largest relaxation was about 0.138 nm. Fig. 2 shows the relaxed atomic structure compared with the initial unrelaxed one, projected along [001] and [150]. A simulated image based on the relaxed structure is shown in Fig. 3. A supercell with θ = 22.6° and also rigid body translations was considered. A local-minimum energy structure, with a slight increase in total energy, was obtained after 320 steps when the translation was included. There was a minimal difference in the predicted structures with and without the translation. The third configuration considered was the boundary structure with θ = 67.4° and translations. A relaxed structure for this configuration was obtained, but the tetrahedral coordination along the boundary was distorted more in this case than the previous two cases. The total energy was also higher than the previous ones. A simulated image based on the relaxed structure of the configuration with θ = 67.4° and translations is shown in Fig. 4.

Close similarity of the intensity distributions in the edge on boundary planes is apparent between the experimental and the simulated images based on the predicted structures, but a few contrast details observed in the experimental image were not reproduced in the simulations. The energy differences per atom among the 96 Si atom supercells were only between 0.1 and 0.25 of the fusion energy per atom for elemental crystalline silicon. These small differences are not regarded as physically significant. Within the limits of experimental uncertainty the QMD method appears capable of predicting the structure of Σ=13 (510), [001] grain boundaries in Si. The above results and further discussion will be reported in detail.[5]

212

References

1. O.F. Sankey and D.J. Niklewski, Phys. Rev. B 40 (1989) 3979.
2. M.J. Kim et al., Ultramicroscopy (1992) in press.
3. P. Stadelmann, Ultramicroscopy 21 (1987) 131.
4. A. Bourret and J.L. Rouviere, in Polycrystalline Semiconductors, Berlin: Springer (1989) 8.
5. This research was supported by grant DE-FG02-87ER42305, Basic Energy Sciences, Materials Science, Department of Energy, and performed at ASU/NSF HREM Facility.
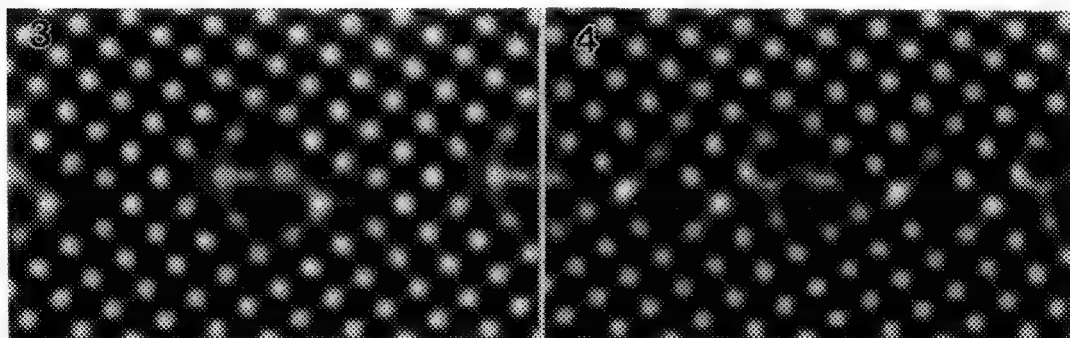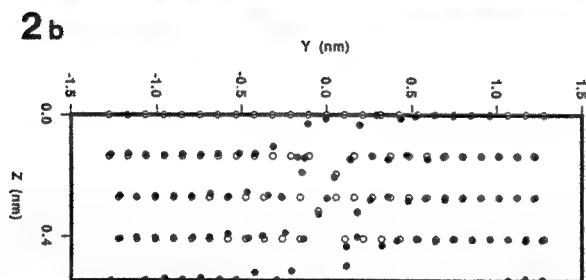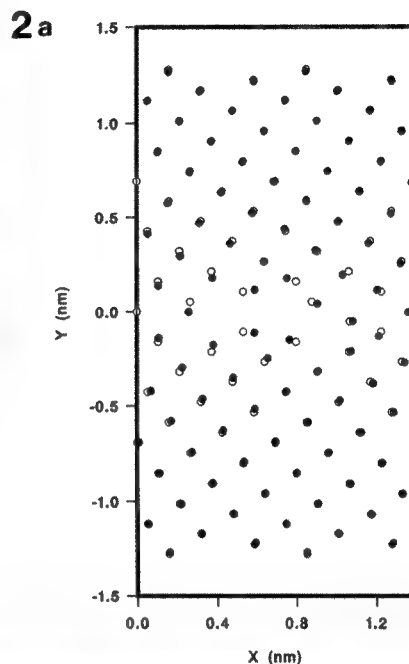
FIG. 1.--Experimental HREM image of $\Sigma=13$ (510), [001] tilt grain boundary in Si.[2] Atomic columns appear as black dots.
FIG. 2.--Relaxed atomic structure of $\Sigma=13$ (510), $\theta=22.6°$, [001] tilt boundary in Si as predicted by QMD (closed circles) compared with the initial unrelaxed one (open circles), projected along [001] and [$\bar{1}$50].
FIG. 3.--Simulated image based on the relaxed structure shown in Fig. 2 ([001] Z.A., Scherzer defocus).
FIG. 4.--Simulated image based on the relaxed structure of $\Sigma=13$ (510), $\theta = 67.4°$, [001] tilt boundary (with translations) in Si.

213

THE STRUCTURE OF A NEAR Σ=27 <110> TILT GRAIN BOUNDARY IN Ge

Stuart McKernan and C. Barry Carter

Department of Chemical Engineering and Materials Science, Amundson Hall, University of Minnesota, Minneapolis, MN 55455

The modeling of tilt grain boundaries in terms of repeating structural units of varying separation is now a well established concept. High-resolution electron microscope (HREM) images of different tilt grain boundaries in many materials display a qualitative similarity of atomic configurations of the grain boundary structure. These boundaries are frequently described in terms of characteristic structural units, which may be separated from each other by regions of 'perfect' crystal (as, for example, in low-angle grain boundaries), or may be contiguous, forming ordered arrays of the structural units along the boundary. In general there will be a different arrangement of the structural units or an arrangement of different structural units, according to the precise geometry of the particular grain boundary. The structure of some special grain boundaries has been examined and these are found to exist in several different configurations, depending on the orientation of the grain boundary plane among other parameters. Symmetry-related symmetric tilt grain boundaries and asymmetric tilt grain boundaries with one grain having a prominent, low-index facet, are commonly observed, low-energy configurations. Structural multiplicity of these configurations along the same grain boundary has been observed in some systems. Defects in the perfect ordering of the structural units may be caused by deviations of the grain boundary plane away from the perfect tilt orientation. Deviations of grain boundary structure away from the exact orientation will also produce defects in the repeating structural unit configuration. These deviations may have a regular and well-defined structure, producing a more complex structural unit.

The interface structure of a particular Σ=27 <110> tilt grain boundary segment in Ge has been examined [1-3]. Germanium bicrystals were grown from oriented seeds using a modified Czochralski technique to produce an incoherent Σ=3 boundary [5]. The bicrystal boundary plane was found to have dissociated into several different boundaries very soon after the start of growth. One of the most prominent boundaries is the Σ=27, third order twin boundary. TEM samples were prepared from this boundary by cutting 3mm-diameter discs from the transverse slices of bicrystal with the boundary lying along a diameter of the disc. The discs were mechanically polished and ion-milled to perforation.

An example of this tilt boundary viewed edge-on is shown in Figure 1. The average boundary plane is very close to the symmetrical orientation, although the boundary itself appears to be very asymmetric. Short {111} facets are clearly evident in an alternating arrangement along each side of the boundary, giving the appearance of a saw-tooth boundary plane. The separation of these {111} facets (which corresponds to the repeat period of the boundary structure) is generally four {111} planes, although some variability is observed. This spacing corresponds very closely to the spacing of five {110} planes in the adjacent grain. These two sets of planes are misoriented by only ~7° across the boundary, and the misfit between them is reduced to only ~1% as a result of this slight misorientation. The interface plane for this repeat facet is a {13 13 5} (i.e., {26 26 10}) plane in both crystals, which is very close to the {5 5 2} (i.e., {25 25 10}) plane for the symmetric, exact Σ=27 configuration. An idealized model for the projected structure of the grain boundary segment is shown schematically in Figure 2. The structural units consisting of 5-, 6-, and 7-membered rings can be identified along the boundary. The repeat unit of this particular grain boundary segment is denoted by AA. The repeating structural units are clearly denoted; every third 7-, 5-membered ring combination being interrupted by a "twin" structural unit labeled T. The occurrence of rather complex, periodic structural units in tilt grain boundaries close to coincidence orientations will be demonstrated. The factors affecting the choice of the low energy configurations for the grain boundary in these circumstances will be discussed. And the applicability of these observations to more general grain boundaries will be examined [4].

214

References

1. Z. Elgat; PhD Thesis, Cornell University, (1985).
2. Z. Elgat, and C.B. Carter; Ultramicroscopy (1985) **18**, 313.
3. D.A. Smith, Z. Elgat, W. Krakow, A.A. Levi and C.B. Carter; Ultramicroscopy (1989) **30**, 8.
4. The electron microscopy was performed at the ASU Center for HREM. This research has been supported by the DoE under contract No. DE-FG02-89ER45381
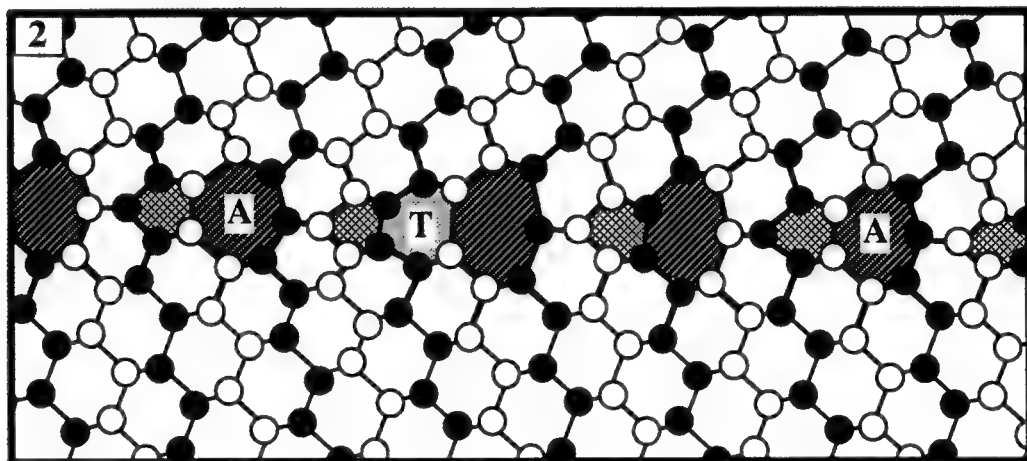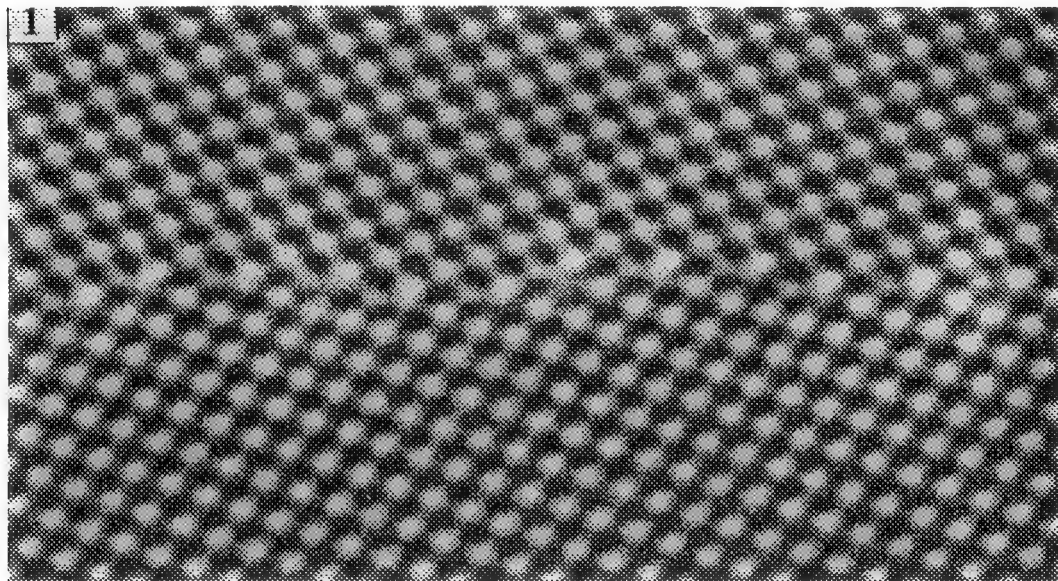
Figure 1 High-resolution electron micrograph of a near Σ=27 tilt grain boundary in Ge, viewed along the [110] tilt axis.

Figure 2 Model structure of part of the grain boundary segment shown in Figure 1. 7-fold rings are shaded dark, 5-fold rings are shown cross-hatched, and the 6-fold "twin" structural unit is marked T.

THE MENSURATION OF INTERFACES

W. M. Stobbs

Department of Materials Science and Metallurgy, Pembroke St, Cambridge CB2 3QZ, UK

I do not have access to the abstracts of the first meeting of EMSA but at this, the 50th Anniversary meeting of the Electron Microscopy Society of America, I have an excuse to consider the historical origins of the approaches we take to the use of electron microscopy for the characterisation of materials. I have myself been actively involved in the use of TEM for the characterisation of heterogeneities for little more than half of that period. My own view is that it was between the 3rd International Meeting at London, and the 1956 Stockholm meeting, the first of the European series , that the foundations of the approaches we now take to the characterisation of a material using the TEM were laid down. (This was 10 years before I took dynamical theory to be etched in stone.) It was at the 1956 meeting that Menter showed lattice resolution images of sodium faujasite[1] and Hirsch, Horne and Whelan showed images of dislocations[2] in the XIVth session on "metallography and other industrial applications". I have always incidentally been delighted by the way the latter authors misinterpreted astonishingly clear thickness fringes in a beaten (!) foil of Al as being contrast due to "large strains", an error which they corrected with admirable rapidity as the theory developed. At the London meeting the research described covered a broad range of approaches, including many that are only now being rediscovered as worth further effort: however such is the power of "the image" to persuade that the above two papers set trends which influence, perhaps too strongly, the approaches we take now. Menter was clear that the way the planes in his image tended to be curved was associated with the imaging conditions rather than with lattice strains, and yet it now seems to be common practice to assume that the dots in an "atomic resolution image" can faithfully represent the variations in atomic spacing at a localised defect. Even when the more reasonable approach is taken of matching the image details with a computed simulation for an assumed model, the non-uniqueness of the interpreted fit seems to be rather rarely appreciated. Hirsch et al., on the other hand, made a point of using their images to get numerical data on characteristics of the specimen they examined, such as its dislocation density, which would not be expected to be influenced by uncertainties in the contrast. Nonetheless the trends were set with microscope manufacturers producing higher and higher resolution microscopes, while the blind faith of the users in the image produced as being a near directly interpretable representation of reality seems to have increased rather than been generally questioned. But if we want to test structural models we need numbers and it is the analogue to digital conversion of the information in the image which is required.

Arguably the relationships between the image and the structure of the object examined have not been examined as much as they should have been simply because there really are too many unknowns to make the full relationship properly accessible. The problem here is in the main associated with the effects to be expected due to the contributions to the atomic resolution detail which will arise from electrons which have suffered energy losses[3,4,5], though uncertainties about the quantification of "absorption" are also non trivial. The unstated agreement of the users thus seems to have been that only the pattern of contrast, rather than its numerical evaluation, should be used in the assessment of structure. This perhaps explains why it is still the normal practice for a local composition change to be measured using a probe approach and EDX or PEELS rather than by the quantitative assessment of the elastic scattering. Yet inelastic cross sections are no more straightforwardly related to the nature of the atoms present than are the elastic scattering factors. Furthermore, if a composition could be assessed from the elastic image at its potentially high inherent resolution all the difficulties in using small probes to refine the resolution of a chemical analysis could be forgotten, as could worries about the way the high

216

current densities in the probes required can tend to alter the specimen examined. Frustratingly however there remain difficulties in taking the approach implied to its natural conclusion and measuring both the local structure changes and the local inhomogeneities in composition at an interface from the TEM image. These problems centre around the same uncertainties which make the full characterisation of a structural inhomogeneity problematic, and relate to the difficulty in knowing how to add the atomic detail image associated with electrons which have lost energy to the fully elastic image. An incoherent addition seems natural, but there are arguments which suggest that the addition should be coherent[6]. It is for this reason that current work on the development of image filters is so important. Once high resolution versions become available it should be as easy to measure a local composition change to a spatial resolution at the atomic level as to quantify more accurately than is now possible a local displacement.

While we await these developments in instrumentation we must go on using the methods currently available to us, while recognising their limitations. It is for example rare that a weak beam image of the defects at an interface is any less quantifiable than a high resolution interference image. At the same time there are features of an interference image which can be used to allow the measurement of some characteristics of a boundary to an accuracy far exceeding the resolution The rigid body displacement is a case in point, and values below 0.01nm are readily accessible in the right circumstances without image calculation.

More interestingly there are now two methods for the evaluation of the composition profile at an interface which use the assessment of the elastic scattering in the measurement. While, in this way, the two techniques are similar, they otherwise differ in the principles used to evade the fundamental problems discussed above. The more straight forward approach, at first sight, simply involves the direct quantification of the high resolution image of the interface: a rather neat vector approach to the characterisation of the contrast is used to compare the area to be analysed at the interface with "templates" drawn from representative areas of the image of the bulk material[e.g.7]. The method has been argued to have the spatial resolution of the template used and it is by using a comparative approach that the method apparently evades some of the potential difficulties in the full characterisation of the intensities. At the resolution noted it seems that the Fresnel effects at the interface do not cause major problems when the imaging conditions are chosen appropriately. The Fresnel Method[e.g.8,9], on the other hand, uses the quantitative assessment of the Fresnel effects themselves for the quantification and is thus related to holography. In this approach one dimensional profiling of a composition change can be achieved to spatial accuracies of about 0.2nm using images of much poorer resolution. In this case the effects of inelastic contributions are much less worrying than in the more conventional approach, because the defoci applied are so large. The method can be applied at interfaces where there are gross structure changes and has been used for the evaluation of the boundary changes in a wide range of materials problems. Currently it is being applied to the measurement of grain boundary rigid body displacements as well as segregation. FEGTEMS will make the technique more accurate and easier to use.

References

1. J. W. Menter, Ist EUREM (Stockholm) (1956) eds: F.S.Sjostrand and J.Rhodin. p.88.
2. P. B. Hirsch et al., Ist EUREM (Stockholm) (1956) eds: F.S.Sjostrand and J.Rhodin. p.312.
3. W. M. Stobbs and W. O. Saxton, J.Microsc, (1988) 151,171.
4. C. B. Boothroyd and W. M. Stobbs, Ultramocrosc.(1988) 26,361.
5. C. B. Boothroyd and W. M. Stobbs, Ultramocrosc.(1989) 31, 259.
6. A. Howie, Proc. Roy. Soc. A. (1963) 271, 268.
7. A. Ourmazd, D. W. Taylor, J. Cunningham and C. W. Tu, Phys. Rev. Lett. (1989) 62,933
8. J. N. Ness, W. M. Stobbs and T. F. Page, Phil.Mag. (1986) A54, 679.
9. F. M. Ross and W. M. Stobbs, Phil.Mag. (1991) A63, 1.

IN SITU HOT-STAGE TEM STUDY OF A DIFFUSION-BONDED Al/SiC INTERFACE

P. L. Ratnaparkhi

Department of Metallurgical Engineering and Materials Science, Carnegie Mellon University, Pittsburgh, PA 15213-3890

Metal/ceramic interfaces have been of great scientific and technological interest for the past two decades. Most studies have been performed on commercially important ceramic-fibre and particulate-reinforced metal-matrix composites. In this investigation, the interfacial structure and chemistry at a diffusion bonded Al/SiC interface was examined at the atomic level in order to understand the fundamental principles that govern bond formation in the solid state between a low temperature non-reactive metal and a high-temperature covalently bonded ceramic.

A 0.5 mm thick pure Al foil was diffusion bonded between two blocks of SiC for two minutes at 600°C under a pressure of 50 MPa. The SiC/Al/SiC couple was heated from room temperature to 600°C at 25°C/minute under a pressure of 15 MPa. After bonding, the sample was rapidly cooled. The interface was studied in cross section by conventional and high-resolution transmission electron microscopy (HRTEM). A 10 nm thick amorphous phase (labelled A) was observed at the Al/SiC interface (Fig. 1a). The amorphous character of this phase was confirmed by diffuse dark-field, defocus Fresnel-fringe imaging and HRTEM. Voids (indicated by an arrow in Fig. 1a) linked by a Fresnel fringe were also observed near the center of the amorphous phase. The presence of a Fresnel fringe indicates that there is a abrupt change in composition, suggesting that the amorphous phase actually consists of two distinct glassy phases. It is proposed that the initial amorphous phase undergoes phase separation on reaching a critical thickness. Auger spectroscopy of the interfacial region indicated that the amorphous phase consists of Al, C, Si and O. Having characterized the interfacial structure and chemistry, an effort was made to determine the factors that govern the formation of the amorphous phase. Two possible routes leading to amorphisation are: (1) solid state amorphisation (SSA) and (2) formation of an amorphous phase by freezing of a eutectic liquid. There are no reported studies on SSA in metal/ceramic couples but this phenomenon has been widely observed in metal/metal and metal/metalloid couples.[1] The second mechanism has been reported in the Pd/SiO_2, Pt/SiO_2 and Cu/Al_2O_3 systems.[2,3]

In order to distinguish between the two methods of amorphisation, a TEM sample was heated in a Philips EM 400T microscope in a Philips hot stage and *in situ* observations of the interface were recorded on film. A continuous increase in void concentration occurred with increasing temperature leading to virtual separation of the two glassy phases by about 617°C (Fig. 1). This separation occurred along the Fresnel fringe observed in the amorphous phase at room temperature. At 600°C, the amorphous phases are mechanically stable suggesting that amorphisation had taken place by solid state reaction rather than by freezing of a eutectic liquid. If the amorphous phase were an Al-Si-C-O eutectic liquid at the bonding temperature, considerable mechanical instability should have been observed. It is likely that the liquid would flow irregularly and display characteristic surface tension profiles. Finally in order to determine the thermodynamic stability of the glassy phase, the sample was heated above 600°C at approximately 0.5°C/min. At 617°C, nucleation and growth of a crystalline phase (indicated by an arrow in Fig. 1e) at the amorphous solid/Al interface was observed. Selected area diffraction pattern (SAD) analysis identified this crystal as Al_4C_3. Figure 2c shows a dark-field image of the Al_4C_3 crystal using a spot indexed as $(1\bar{1}08)$. Dark field imaging of this crystal using extra spots which corresponded to Al_4C_3 d-spacings was performed in four different zone axes to confirm the identity of the crystal.[4]

References

1. K. Samwer, Physics Reports (1988)161, 1.
2. S.Mellul and J. Chevalier, Phil, Mag. A (1991)64, 561.
3. A. F. Moodie and C. F. Warble, Phil. Mag. A (1977)64, 201.
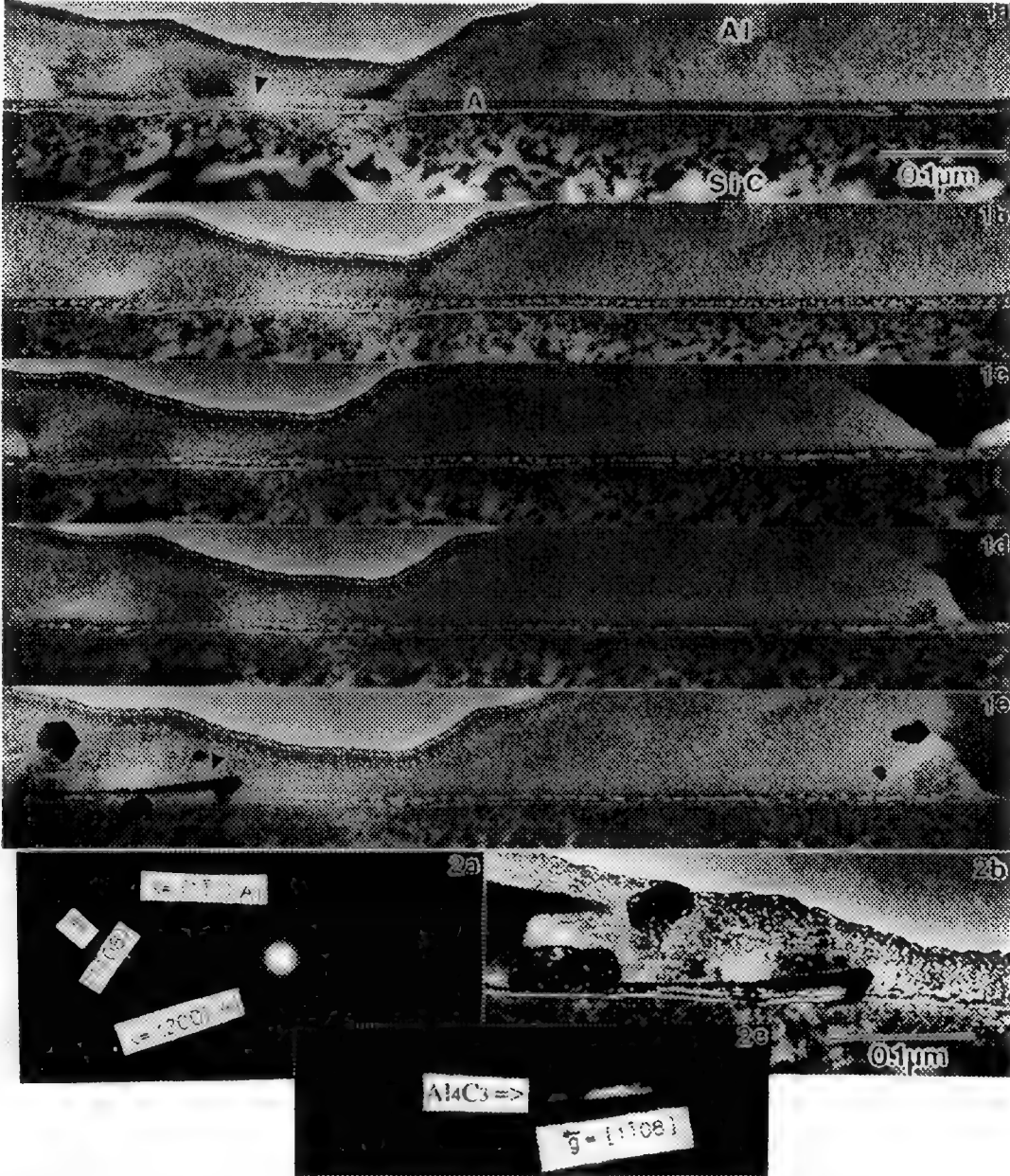
Figure 1.--Conventional transmission electron micrographs of the Al/SiC interface imaged edge-on at various temperatures: (a) room temperature, (b) 350°C, (c) 544°C, (d) 600°C, and (e) 617°C.
Figure 2.--Micrographs identifying the crystal at the amorphous-solid/Al interface as Al_4C_3: (a) SAD pattern, (b) bright-field image, and (c) dark-field image using the Al_4C_3 reflection in (a).

TWIN BOUNDARY STRUCTURE IN L1₀ ALLOYS

Abha Singh and A.H. King

Department of Materials Science & Engineering, State University of New York at Stony Brook,
Stony Brook NY 11794-2275

Ordered alloys have been of great interest in the last decades for their potential use as high temperature structural materials. The most commonly studied ordered alloys are Ni_3Al, with $L1_2$ structure, and $L1_0$ TiAl. Grain boundary fragility, however, is a major problem in the practical application of many ordered alloys, although it can be ameliorated in Ni_3Al by boron doping. The problem calls for improved understanding of grain boundary structure in ordered alloys. Most studies so far have been done on alloys based on $L1_2$ and B_2 structure. An investigation of twin boundary structure in $L1_0$ CuAu(I) has been carried out in the present work, by means of CTEM and computer image matching techniques.

The twins in the present study are order twins; i.e. they are formed upon ordering, when a cubic to tetragonal phase transformation occurs. The lattice strains associated with the cubic-tetragonal transformation are accommodated by a repeated twinning structure which consists of alternating twins on parallel {101} planes, as observed by Pashley and Presland[1].

CuAu specimens were made by melting high purity copper and gold in vacuum. The alloy was rolled to a thickness of about 80μm. Discs of 3mm diameter were punched from the resulting sheet and were recrystallized at 700°C for about 10 hours to obtain large grain sizes and annealed at 300°C for 148 hours to obtain ordered CuAu. TEM specimens were made by jet polishing, using an electrolyte containing 17% perchloric and 83% acetic acid at a temperature of 17°C. These specimens were further annealed in vacuum for about 48 hours to avoid any disordering that may have occurred during punching or jet thinning. The specimens were then examined in a Philips CM12T electron microscope operating at 120kV, using a double-tilt side-entry holder.

The crystallographic details such as misorientation, dislocation line direction and boundary plane normal were determined with accuracies as good as 0.1° by comparing experimentally obtained Kikuchi patterns and the computer generated ones. The twin boundary misorientation was found to be 84.6° about the [100] axis, the dislocation line direction and the boundary plane normal were [211] and [01$\bar{1}$] respectively. It is to be noted that all the analysis was done using the face-centered tetragonal description of the unit cell (which is directly comparable with the disordered fcc structure) rather than the body-centered tetragonal description, which is the correct Bravais lattice.

The Burgers vectors of the twin boundary dislocations were determined by using **g.b** and **g.b×U** techniques and further confirmed by image matching. An image simulation program originally written for grain boundary dislocations in cubic crystals[2] was modified for tetragonal crystals[3]. The direction of the Burgers vectors was found to be [211], parallel to the line directions of the dislocations, and they did not cause antiphase shifts of the boundary structure. Fig 1a and 1b are examples of experimental and simulated images. The shortest lattice vector parallel to [211] in the $L1_0$ structure is a[211], which is therefore deduced to be the Burgers vector of these dislocations.

Dissociation of these dislocations into $2 \times \frac{1}{2}[211]$ is energetically favored over dissociation into $2 \times a[100]$ and $a[011]$, at least on the basis of elastic strain energy. The $\frac{1}{2}[211]$ Burgers vector, however, is a superpartial, so the two dissociation products are bound together by an antiphase domain within the twin boundary. The superpartials were unresolvable, and on the basis of image simulations, as shown in Fig.2. we deduce that their maximum separation could be no more than approximately 7nm. This would correspond to a minimum antiphase domain energy of 240 mJ/m².

1.   D.W. Pashley and A.E.B. Presland, J. Inst. Met. (1959) , **87**, 419.
2.   A.K. Head, P. Humble, L.M. Clarebrough, A.J. Morton and C.T. Forwood, *Computed Electron Micrographs and Defect Identification*, Amsterdam, North Holland (1973).
3.   Abha Singh and A.H. King, this volume.
4.   This work is supported by the National Science Foundation, under grant number DMR-8901994.
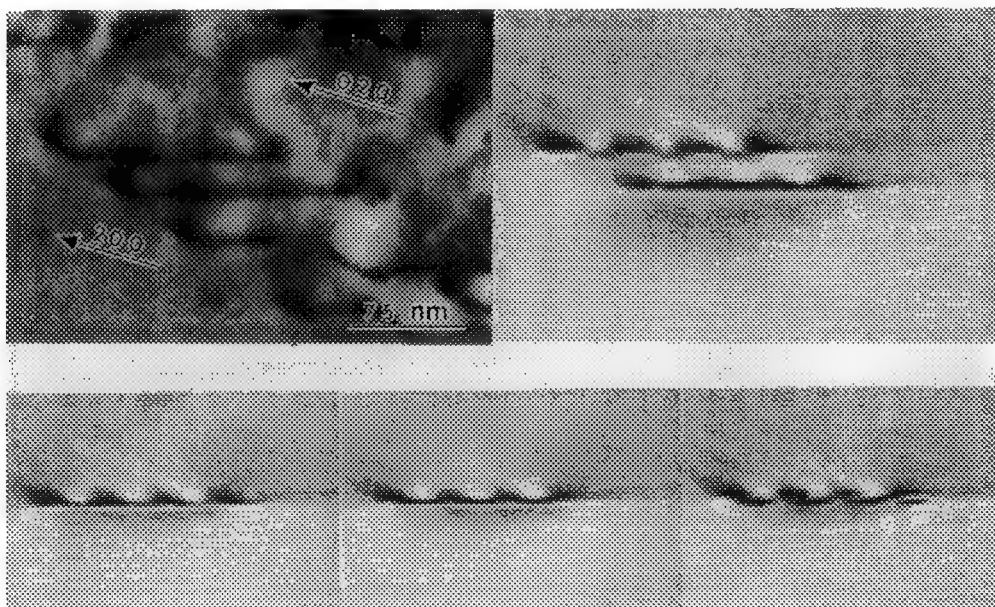
Fig. 1. (Top) Comparison showing experimental (left) and simulated images of dislocations (right) with $\mathbf{b}=2\times[211]$, $\mathbf{g_1}=(020)$, $\mathbf{g_2}=(200)$, $\omega_1=0.60, \omega_2=0.62$, dislocation line direction = [211], Foil Normal = [001], beam direction = $[10\,\overline{4}]$, boundary plane normal = $[01\overline{1}]$, foil thickness = $3.00\,\xi_{020}$ and the separation between the two dislocations = $1.5\,\xi_{020}$.

Fig 2.   (Bottom) Computer simulated images of $2 \times \frac{1}{2}[211]$ dislocations for a separation between the two dislocations = $0.0\,\xi_{020}$ (left), $0.2\xi_{020}$ (middle) and $0.3\,\xi_{020}$, (right), ξ_{020} being the extinction distance for the (020) diffraction, 25.9nm. The other parameters are the same as in Fig.1. This indicates that it is possible to distinguish the two dislocations when they are separated by approximately 7.5nm.

HIGH RESOLUTION STUDY OF THE Σ=5 [0 0 1] TWIST GRAIN BOUNDARY IN NiO

J. L. Lee and S. L. Sass

Department of Materials Science and Engineering, Cornell University, Ithaca, NY 14853

The existence of grain boundaries (GBs) in many advanced ceramics can significantly alter their performance, rendering the study of GB structure an essential part of understanding ceramic properties on a fundamental level. Furthermore, the debate regarding the stability of [0 0 1] twist GBs in rocksalt-structured oxides[1,2] provides the impetus for comparing experimental observations of the Σ=5 [0 0 1] twist GB structure in NiO with the stable GB structure calculated by Tasker and Duffy[3] (Fig. 1). The Tasker and Duffy structure was obtained by introducing a Schottky defect in each of the GB unit cells, resulting in a 20% decrease in atomic density at the GB. High resolution TEM (HRTEM) employing Fresnel fringe[4,5] and lattice imaging techniques (Fig. 2) supplemented with image simulations of six possible configurations for the NiO Σ=5 [0 0 1] twist GB structure using the TEMPAS program[6] (Fig. 3) were the primary experimental methods used in an attempt to detect this reduced atomic density in NiO Σ=5 [0 0 1] twist GBs manufactured by a modified Schober-Balluffi method.[7] Since the Fresnel fringe technique consists of a change in Fresnel fringe contrast with defocus due to a change in mean inner potential at the GB, it becomes necessary to consider the contribution of the various causes of a change in mean inner potential to the resulting contrast. These causes include: (i) a change in atomic density or a change in atomic structure at the GB, (ii) the existence of a space charge at the GB, (iii) the existence of a thin amorphous film at the GB, (iv) the presence of impurities at the GB or a change in composition across the GB, and (v) GB grooving. The contribution of a GB space charge to the change in mean inner potential at the GB is assumed to be small, given that the space charge associated with with a GB in an ionic crystal is on the order of a few tenths of a volt, whereas the mean inner potential at the GB is on the order of 15 - 20 V.[8] An attempt to address the impurity and grooving issues was made by performing EDS and EELS across the GB in an ultra-high vacuum, high resolution STEM.

Diffraction pattern and Kikuchi line analysis showed the misorientation angle of the manufactured specimen to deviate from the "perfect" Σ=5 misorientation angle of 36.87° (Fig. 1) by +3.1°. Lattice images of the GB in an edge-on configuration do not show strong evidence of any GB structural periodicity associated with either the "perfect" Σ=5 GB structure or the Tasker and Duffy GB structure (Fig. 2b). However, this periodicity may be obscured by the deviation of the specimen from the "perfect" Σ=5 misorientation angle and the faceting which appears to occur at the GB. It is also evident from the lattice images that no amorphous film is present at the GB. Results of the Fresnel fringe imaging technique show a change in fringe contrast with defocus (Fig. 2) which correlates to a decrease in mean inner potential at the GB. This is consistent with the fact that the experimental micrographs agree best (as determined by comparing line scans taken across the GB on both the micrographs and the simulated images) with the simulated structure consisting of a 72Å thick foil possessing the Tasker and Duffy GB structure with a shallow GB groove located at both top and bottom surfaces of the foil (Fig. 4) Since EDS data indicate that only Mg and C are present in the vicinity of the GB in concentrations of less than about 5 at. %, the contribution of impurities to the change in mean inner potential at the GB is small. Hence, it is presumed that a reduction in atomic density at the GB and GB grooving are primarily responsible for the observed Fresnel fringe contrast change with defocus at the GB. Current efforts are under way to verify the existence of GB grooving in the specimen and to estimate its contribution to the change in image contrast. If this can be done, then it will be possible to determine the change in mean inner potential due to the boundary structure itself.[9]

References

1 D. Wolf and R. Benedek, Advances in Ceramics 1 (1981) 107.
2. C. P. Sun and R. W. Balluffi, Phil. Mag. A 46 (1982) 49.
3. P. W. Tasker and D. M. Duffy, Phil. Mag. A 47 (1983) L45.
4. J. N. Ness et al., Phil. Mag. A 54 (1986) 679.
5. D. R. Rasmussen et al., Ultramicroscopy 30 (1989) 52.
6. R. Kilaas, Proc. Ann. EMSA Meeting 45 (1987) 66.
7. T. Schober and R. W. Balluffi, Phil. Mag. 20 (1969) 511.
8. W. D. Kingery, J. Am. Ceram. Soc. 57 (1974) 1.
9. This work was supported by the U. S. Department of Energy. JLL received additional support from the U. S. Department of Education fellowships in the Areas of National Need. Thanks are due to Dr. R. Keyse, Dr. E. Kirkland, and Prof. J. Silcox of Cornell University for helpful discussions.
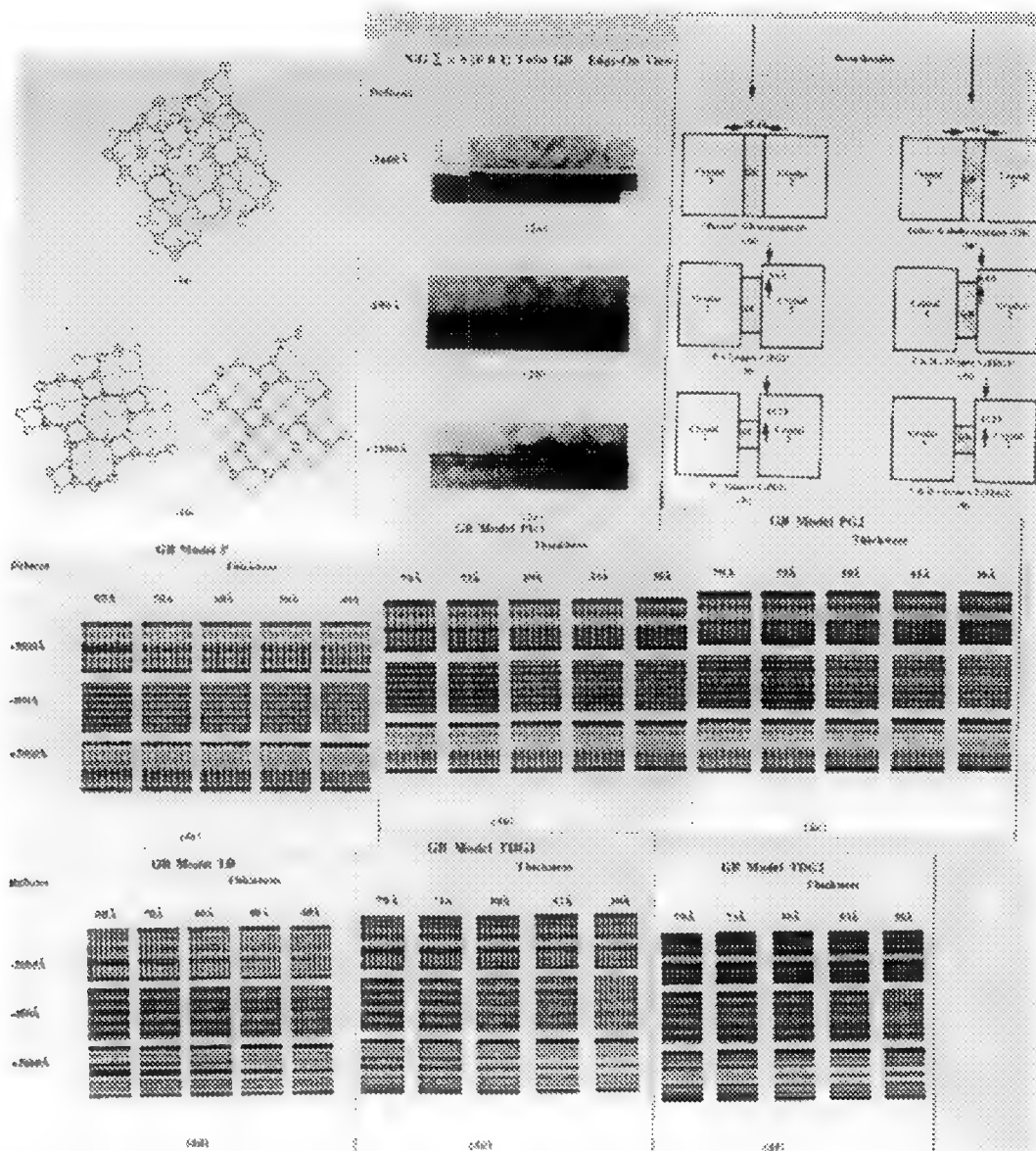
Fig. 1a) "Perfect" Σ=5 [0 0 1] twist GB structure in rocksalt-structured crystal, as vieweed along [0 0 1] direction. Misorientation betwen top and bottom grain is 36.87°. (1b) Structure of NiO Σ=5 [0 0 1] twist GB calculated by Tasker and Duffy. Diagram on left shows view of lower grain (dotted lines) and GB plane (solid line) along [0 0 1] direction; diagram on right shows similar view of upper grain (dotted lines) and GB plane (solid lines). Three-plane sequence through GB introduces 36.87° misorientation of upper grain with respect to lower grain. Note that GB plane consists of array of squares and octagons.

Fig. 2a-c) Through-focus series of NiO GB in edge-on orientation, showing change in Fresnel fringe contrast from bright to dark with underfocus to overfocus imaging.

Fig. 3) Side view illustration of six different GB structures simulated using TEMPAS image simulation program.

Fig. 4a-f) Results of image simulation using TEMPAS for each of six GB structures from Fig 3. GB is horizontal, running across center of each simulated image.

223

INTERFACES AND PRECIPITATION

G.C. Weatherly, Department Materials Science and Engineering, McMaster University, Hamilton, Canada, L8S 4M1

An important class of alloy transformation involves the precipitation of a body–centred cubic phase in a close packed cubic or hexagonal matrix (or vice–versa). In the past ten years, numerous investigations have demonstrated that the precipitate grows as a lath or needle–shaped particle, with the growth direction of the axis of the particle parallel to an invariant line of the phase transformation.[1-4] Although there are an infinite number of potential invariant lines in such a transformation, commonly one observes that the growth direction is close to the common close–packed directions e.g. $<1\bar{1}0>_f$ and $<1\bar{1}1>_b$, with a rational or near–rational orientation relationship between the two phases. These observations can be rationalized by invoking the geometric principles embodied in Bollmann's O–lattice theory[5] or by appealing to the minimization of strain energy principle associated with the set(s) of misfit dislocations lying parallel to the invariant line.[6] Figure 1 shows an example of this characteristic morphology of a lath of γ (face–centred) precipitated in a matrix of α (body–centred) in a two–phase stainless steel.[7] The lath is bounded by well–developed facet planes (see Fig. 1) with a growth direction about 5° from the common close packed $[11\bar{1}]_\alpha$, $[\bar{1}01]_\gamma$ directions. Sets of misfit dislocations and steps are visible at the $(416)_\alpha$ and $(\bar{2}75)_\alpha$ facet planes.

As the misfit dislocations and steps lie parallel to the invariant line,[4] direct lattice resolution studies of the interface are complicated because both the invariant line and the facet planes are irrational (Fig. 1). Our knowledge of the ledge structure at this class of interface has to date been limited to conventional diffraction studies. Figure 2 illustrates the ledge structure observed at the $(121)_f$ facet planes in a Ni–Cr alloy.[4] A series of ledges with well–defined kinks are visible. Overall the ledges lie parallel to the invariant line of the phase transformation, as expected. They are about 1 nm high and where they terminate, matrix dislocations are observed. The origin of the diffraction contrast from these steps is poorly understood. They appear to have an effective displacement vector lying perpendicular to the habit plane with sharp strain field contrast[4] (Fig.2). Although the crystallography and facet plane development can be rationalized by O–lattice theory, such a displacement vector cannot be explained by the O–lattice approach. It appears that the concept of a Somigliani dislocation, first introduced by Bonnet et al[8], might be the correct approach to describe the strain field of the ledges in this system.

References

1. U. Dahmen, Acta Metall. (1982)30, 63.
2. U. Dahmen, P. Ferguson and K.H. Westmacott, Acta Metall. (1984)32, 803.
3. C.P. Luo and G.C. Weatherly, Acta Metall. (1987)35, 1963.
4. C.P. Luo and G.C. Weatherly, Phil. Mag. (1988)58, 445.
5. W. Bollmann, "Crystal Defects and Crystal Interfaces", Springer, Berlin (1970).
6. Wen–Zhen Zhang and G.R. Purdy, to be published (1992).
7. K. Ameyama, G.C. Weatherly and K.T. Aust, Acta Metall. (1992) in press.
8. R. Bonnet, G. Marcon and A. Ati, Phil. Mag. (1985)51, 429.

224
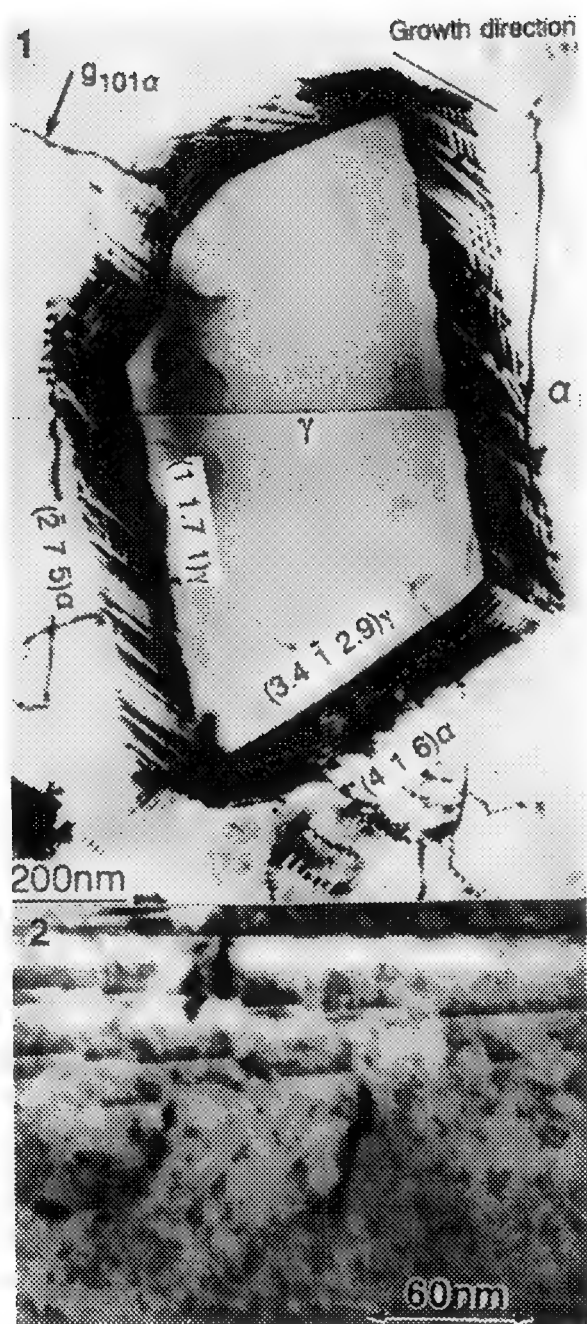
Figure 1. Cross section of γ-lath in a two phase α-γ stainless steel.[7]

Figure 2. Ledges terminating at dislocations at the $(121)_f$ facet plane of a Cr rich lath in a Ni–Cr alloy.[4]

225

CRYSTALLOGRAPHY AND STRUCTURE OF (0001)α-Al₂O₃//(110)Pd INTERFACE

F. Cosandey and P. Lu

Materials Science and Engineering, Rutgers University, Piscataway NJ 08855-0909

A fundamental understanding of the behavior of metal/oxide composites requires a detailed knowledge of interface properties and HREM studies have provided important information on interfacial structure and composition.[1,2] The aim of the present investigation was to study the equilibrium shape, orientation relationship and atomic structure of low energy plane orientations in the Pd/α-Al₂O₃ system. Metal/Oxide interfaces were produced by first preparation of Pd-3wt%Al alloys followed by oxidation in air at 1000 °C for 48 hours leading to the formation of Al₃O₃ particles. For the TEM observations we used an ISI-002B high resolution microscope with a resolution limit of ~0.18 nm at 200 KeV.

After oxidation various metastable transition phases have been observed which include δ , η and Θ, in addition to the stable α-Al₂O₃ phase. A low magnification picture taken along the Pd <110> zone axis is shown in Fig. 1a. All alumina particles have their <1100> axis parallel to the <110> direction of Pd. The largest α-Al₂O₃ particles are faceted with their primary facets parallel to (0001) plane. The particle orientations are such that the (0001) Al₂O₃ plane is rotated with respect to (110) Pd by a small angle ranging from 0° to 10°, which can be seen in the selected area diffraction pattern depicted in Fig.1b. The diffraction pattern of a single particle in an exact parallel orientation is shown in Fig.1c. corresponding to the perfect orientation relationship: $[1\bar{1}00]$Al₂O₃//$[1\bar{1}0]$Pd and (0001)Al₂O₃//(110)Pd. For this plane orientation the lattice misfit is about 18% along the [001] Pd direction and 0.7% along the $[1\bar{1}0]$ Pd direction. This observed low energy orientation corresponds to the line invariant strain criteria[3], for which, perfect lattice fit is observed along one direction.

Two high resolution images of the α-(0001)Al₂O₃//(110)Pd interface, taken along the <110> Pd direction and at Scherzer defocus (~38 nm) or with an additional defocus of -25 nm are shown in Figs. 2a and 2b respectively. Image simulations have been performed using the multislice formalism with EMS programs (Figs. 2c, 2d). The correspondence between simulated and high resolution images for the two defocus values, indicates that the alumina structure formed during internal oxidation corresponds to the stable α-Al₂O₃ phase. The image contrast is broad and not uniform along the interface. In addition the interface appears to be incoherent. The (0001) interface of Al₂O₃ is polar and can be terminated by either Al or O. The observed contrast variations can be attributed to small steps associated with local variations in plane termination having a step height of 0.11 nm. Larger steps have been observed as well, with height corresponding to ⅓ c-axis (0.43 nm).[5]

1. T. Muschik and M. Rühle, Phil. Mag. (1992) In press
2. P. Lu and F. Cosandey, Acta Metall. Mater. (1992) (to be published)
3. U. Dahmen, Acta Metall. 30(1982)63
4. P. Stadelmann, Ultramicroscopy, 21(1987)131
5. This work is supported by the Materials Research Group Program of NSF under Grant # NSF-DMR-89-07553
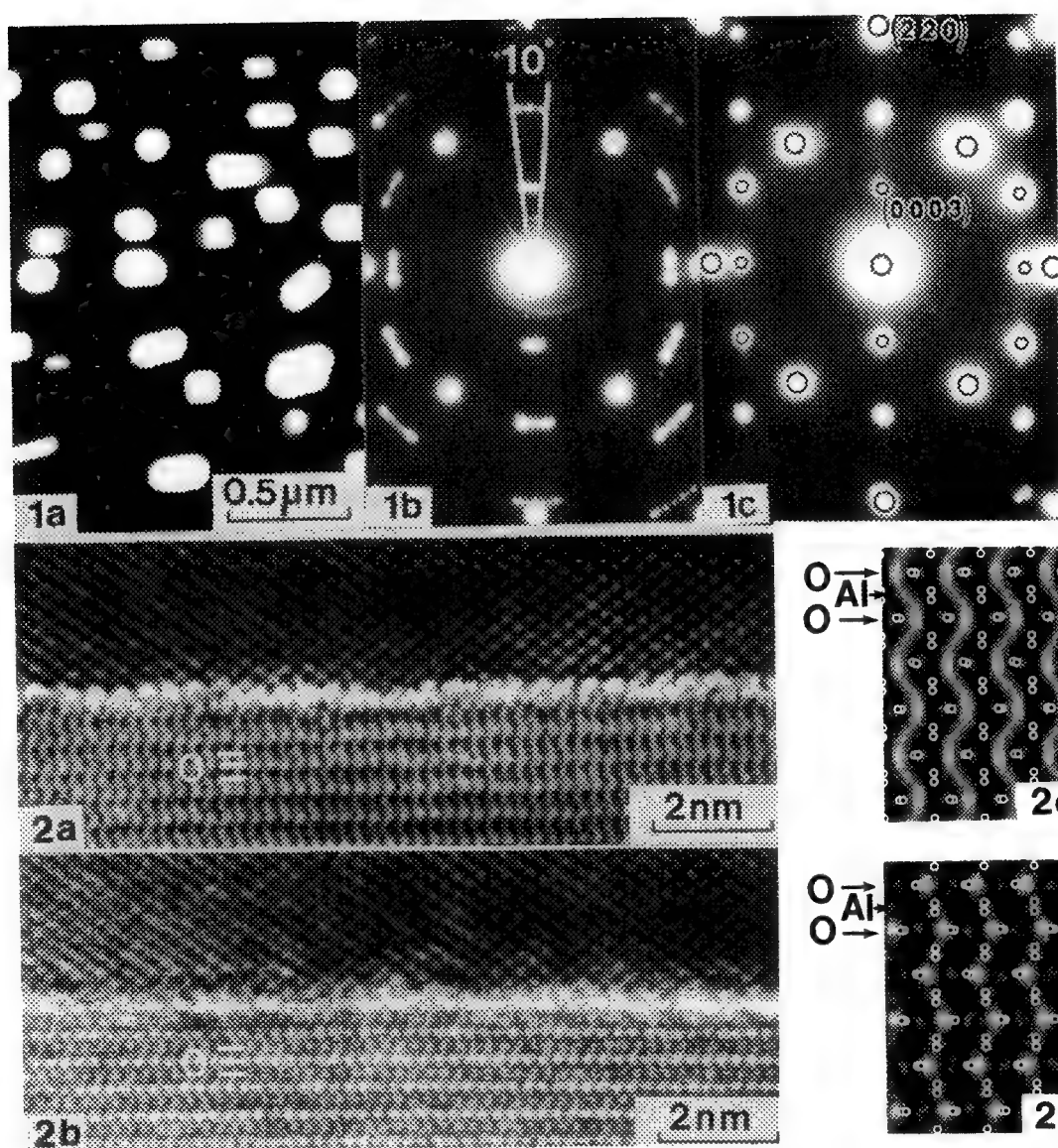
Fig.1a TEM micrograph of α-Al₂O₃ precipitate in Pd matrix with (1b) selected diffraction pattern including many precipitates and (1c) diffraction pattern from a single particle in perfect orientation relationship.

Fig.2 HREM micrograph of (0001) α-Al₂O₃//(110) Pd interface taken at Scherzer defocus (~38 nm) and (2b) at ~65 nm defocus with simulated images of alumina calculated for a thickness of 7.5 nm and defocus values of (2c) -39 nm and (2d) -63 nm.

A HREM STUDY OF THE INTERFACES BETWEEN TIO$_2$ PRECIPITATES AND THE AL$_2$O$_3$ MATRIX IN STAR SAPPHIRE

S. Q. Xiao, A. H. Heuer and P. Pirouz
Department of Materials Science and Engineering,
Case western Reserve University, Cleveland, Ohio 44106

The asterism, or star effect, present in star sapphire (Ti-doped Al$_2$O$_3$) single crystals is known to arise from the needle-like rutile(r) (TiO$_2$) precipitates in the sapphire(s) matrix. The specific orientation relationship between the precipitates and the matrix is $\{100\}_r//\{0003\}_s$ and $<011>_r//<1010>_s$. In this work we report a HREM study of the rutile/sapphire interface.

The cross-section perpendicular to the needle axis of a very small precipitate, which is coherent, or has just one misfit dislocation at its interface, is a rhombus; the precipitate/matrix interface (habit plane) is $\{111\}_r//\{1123\}_s$. As the coherency break down and misfit dislocations are introduced into the interface, the shape of the cross-section becomes nearly square; the two orthogonal interfaces are $\{100\}_r//\{0003\}_s$ and $\{011\}_r//\{1120\}_s$. Larger precipitates show rectangular interfaces elongated along the $\{100\}_r//\{0003\}_s$ interface (Fig.1). A regular array of misfit dislocations with Burger vector $\mathbf{b} = 1/3<0001>_s$ are present at the $\{011\}_r//\{1120\}_s$ interface, the mean distance between every two adjacent $1/3<0001>_s$ misfit dislocations being 8.7 nm which compensates exactly the 5.9% lattice mismatch estimated from the lattice constants of these two structures. Similarly, a regular array of misfit dislocations with Burgers vector $\mathbf{b} = 1/3<1010>_s$ at the $\{100\}_r//\{0003\}_s$ interface compensates the 4.5% lattice mismatch at that interface.

Over 40 precipitates have been studied; every one is twinned on the $\{011\}_r$ plane and some of them are multiply twinned. The twinning in rutile is probably produced at the nucleation stage. Since the shear vector of the twin is $1/2<011>_r$, which is parallel to the needle axis, the twin is not revealed in the edge-on precipitates studied by HREM. In addition, crystallographic shear(CS) planar defects were found on $\{211\}_r$ of rutile (Fig.1); they are always associated with the misfit dislocations and can not penetrate the twin boundaries.

Based on the HREM observations, an atomic scale model for the coherent to semi-coherent transition of the interface is proposed.

Fig.1: An edge-on rutile precipitate in sapphire showing misfit dislocations at the interface and a crystallographic shear(CS) planar defect related to one misfit dislocation.

DIFFRACTION FROM INTERFACES

D.J. Eaglesham

AT&T Bell Laboratories,
600 Mountain Avenue,
Murray Hill,
NJ 07974

A wide variety of approaches have been used to study diffraction from interfaces and thereby gain information on the structure or chemistry at the interface. In this paper the various techniques will be reviewed and a few examples will be used to illustrate the methods.

Techniques for studying interfaces can be broadly divided into cross-section and plan-view approaches, and further classified according to whether the information to be extracted lies on the coincident site lattice or at some intermediate position (i.e. whether diffraction will determine a rigid body shift or a full reconstructed interface structure).   While cross-section diffraction studies have been shown to be extremely powerful in elucidating a number of problems, we will concentrate here on plan-view methods. The reasoning for this is that cross-section diffraction retains many of the drawbacks to cross-sectional HREM (small field of view, indeterminate averaging and above all increased specimen preparation damage) and has substantially reduced signal, whereas plan-view diffraction can give us access to unique information on both local and long-range variations in the interface.

In cross-section, the presence of additional spots in the pattern may be used to look for either interfacial reconstructions or new phases at the interface. In the presence of a periodic array of interfaces (superlattice) diffraction due to the interfaces themselves becomes very strong and is highly sensitive to features such as the interface abruptness. Plan-view diffraction has been used in a wide range of ways to study interfaces. Convergent beam studies can give information on the symmetry of a bicrystal, on the relative phases of Bloch states in the two crystals (and from either of these a rigid shift), or on the effective shape transform of an interface or superlattice (and hence abruptness). Selected area diffraction provides additional sensitivity to interfacial spots, and the kinematical interpretation of these spots has been successful in solving surface structure (Si 7x7) and interfacial reconstructions such as $CoSi2/Si(100)$. We have used SAED to observe buried surface reconstructions preserved in crystal material, such as the buried Boron 2x1 in Si (Fig. 1). SAED has also been applied to studying the growth of Si in MBE; Si deposition at low T on the Si 7x7 reconstructed (111) surface leaves a buried 7x7 at the amorphous-crystal interface. With increasing T this interface becomes more disordered as some epitaxial deposition occurs before the amorphous-crystal interface forms; we thus can monitor the initial stages of crystal growth by the changes in the buried 7x7 (Fig.2).

230

10°C
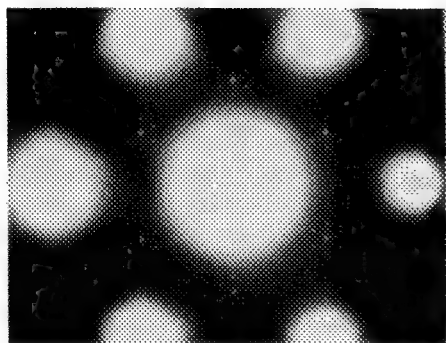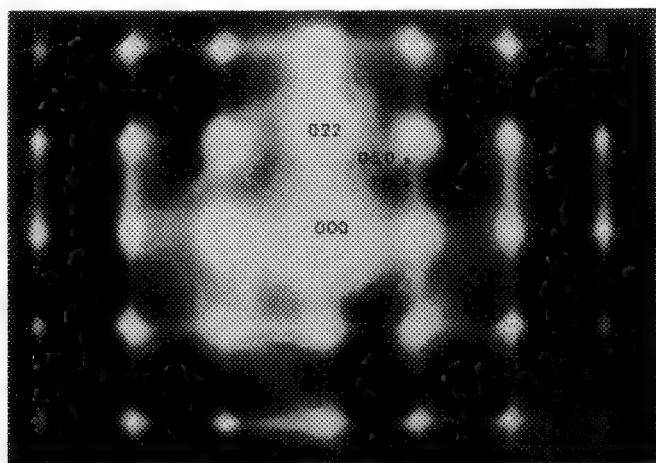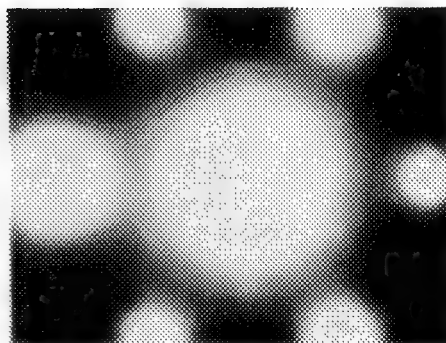
200°C

APPLICATION OF CONVERGENT-BEAM ILLUMINATION METHODS TO THE STUDY OF LATTICE DISTORTION ACROSS THE INTERFACE

Zuzanna LILIENTAL-WEBER*, T. KANEYAMA, M. TERAUCHI and M. TANAKA

Institute for Scientific Measurements, Tohoku University, Sendai, 980 Japan

* permanent address: Materials Science Division, Lawrence Berkeley Laboratory, 1 Cyclotron Rd., Berkeley, CA 94720

A high accuracy measurement of the lattice parameter can be obtained by x-ray diffraction. However, these methods have low spatial resolution and are limited by sample thickness. Therefore, for heterolayers much better information about local distortions near the interface can be obtained by electron microscopy using convergent-beam illumination. Large-angle convergent-beam electron diffraction (LACBED) patterns and convergent-beam imaging (CBIM) were applied to study of the lattice distortion across the interface of the GaAs epilayer grown on [001] GaAs substrate and the GaAs layer grown at 200°C (called the low-temperature (LT) layer). These LT GaAs layers are grown by molecular beam epitaxy from As oversaturation and are known to be As rich [1]. Particle-induced x-ray studies reveal up to 1.5 % extra As. This excess As leads to the expansion of the lattice parameter up to 0.15% when measured by x-ray diffraction along the (004) reflection. From this study, it was expected that a cubic expansion of the lattice parameter would be equal in all three directions [1]. However, TEM studies do not reveal the formation of dislocations at the interface, which would be expected taking into account the difference in the lattice parameter across the interface [2]. Convergence beam illumination methods were applied to study in detail the strain, lattice parameter variation, and crystallographic distortion across the interface, since these methods have spatial resolution several orders of magnitude higher than x-ray diffraction. A CBED pattern taken in the substrate and in the layer with an incidence close to the [530] direction (exact orientation [0.869 0.495 0]) reveals the lattice parameter change, since the position of the cross of the $\overline{1}1\overline{1}3$ and $\overline{1}113$ lines changes when an electron beam is placed in the substrate and the layer, respectively (Fig. 1a,b). This change in the cross position can be interpreted either by a cubic lattice expansion (a = 0.5662 nm, changing from the bulk GaAs value of a_s=0.5653 nm) or a tetragonal lattice expansion ($a=b=a_s$= 0.5653 nm and c =0.5658 nm). However, it is most likely an expansion in the c axis, since the cross is formed by the planes inclined at near right angle to this axis. An LACBED pattern taken at the [221] incidence reveals that 220 types of HOLZ lines do not shift their positions across the interface (Fig.1c), while other lines, such as $\overline{5}7\overline{5}$, $\overline{8}10\overline{6}$, $\overline{5}17$, $6\overline{2}\overline{8}$, and $\overline{2}68$, are all shifted in the same direction. This implies that both (100) and (010) planes do not change their positions in the substrate and in the layer, and the change in lattice parameter is mainly due to the change in the c axis along the [001] direction. The expansion in the c axis would explain the lack of dislocations at the interface with the LT-GaAs layer, as was shown earlier [2]. A CBIM pattern taken at the same incidence would confirm this suggestion, since $2\overline{2}0$ Kikuchi lines perpendicular to the interface do not change their position while the $5\overline{7}3$ and $5\overline{1}9$ lines shift across the interface. Both these experiments would be consistent with a tetragonal distortion with $a=b=a_s$, and with the c axis much larger than a_s (much longer than the one expected from x-ray studies). In order to confirm this prediction, two different CBIM patterns were obtained in the same interfacial area, with incidence directions of [510] and [150]. Very large bending of all HOLZ lines was observed across the interface. In addition, the shift of these lines on the layer was observed in opposite direction, when a particular line is considered, such as $\overline{2}12\overline{2}$ in the [510] projection (Fig. 1d) and an equivalent $122\overline{2}$ line in the [150] projection (Fig. 1e). Such a large shift cannot be expected from the slight lattice parameter change as was detected by x-ray studies. In order to explain the line bending, it is necessary to take into account the z-component contribution (parallel to the incident electron beam) of the $\Delta g = g_l - g_s$ between the layer and the substrate. The simple tetragonal distortion expected from LACBED and [221] CBIM would give Δg_z =0 and would not give bending of the Kikuchi lines. Therefore, the bending of the planes along the [110] direction (parallel to the electron beam) is expected since the thin foil is prepared in this direction. The lattice parameter far from the interface is different for the substrate and the layer, as was shown by Figs. 1a,b. However, in the interfacial

area the lattice parameter of the substrate and the layer are probably equal. When thin foil is prepared, the surface relaxation described earlier [3] needs to be considered. Different surface relaxation can be expected on both sides of the interface. This difference will lead to bending of the planes in the interfacial area, as observed by Humphreys et al [3], and to the curvature of HOLZ lines. Fig.1f shows the reciprocal space of the interface with the [001] incidence axis, where the reciprocal lattice points of the substrate and the layer are superimposed. The shift of the reciprocal lattice points of the layer after surface relaxation are marked as well. Note that no shift of $2\bar{2}0$ lines is expected when observed along the [221] direction. This surface relaxation will lead to monoclinic distortion which can be as well described in orthorombic coordinates. This distortion can explain both CBIM patterns obtained in the [510] and [150] incidence directions, and it would explain the absence of shifting of the $2\bar{2}0$ lines in the [221] projection.

1. M. Kaminska, E.R. Weber, Z. Liliental-Weber, R. Leon, and Z. Rek, J. Vac. Sci. Technol., **B7**, 710 (1989).
2. Z. Liliental-Weber, W. Swider, K.M. Yu, J.B. Kortright, F. W. Smith, and A.R. Calawa, Appl. Phys. Lett., **19**, 2153 (1991).
3. C.J. Humphreys, M. Maher, H.L. Fraser, and D.J. Eaglesham, Phil. Mag. **A58**, 787 (1988)
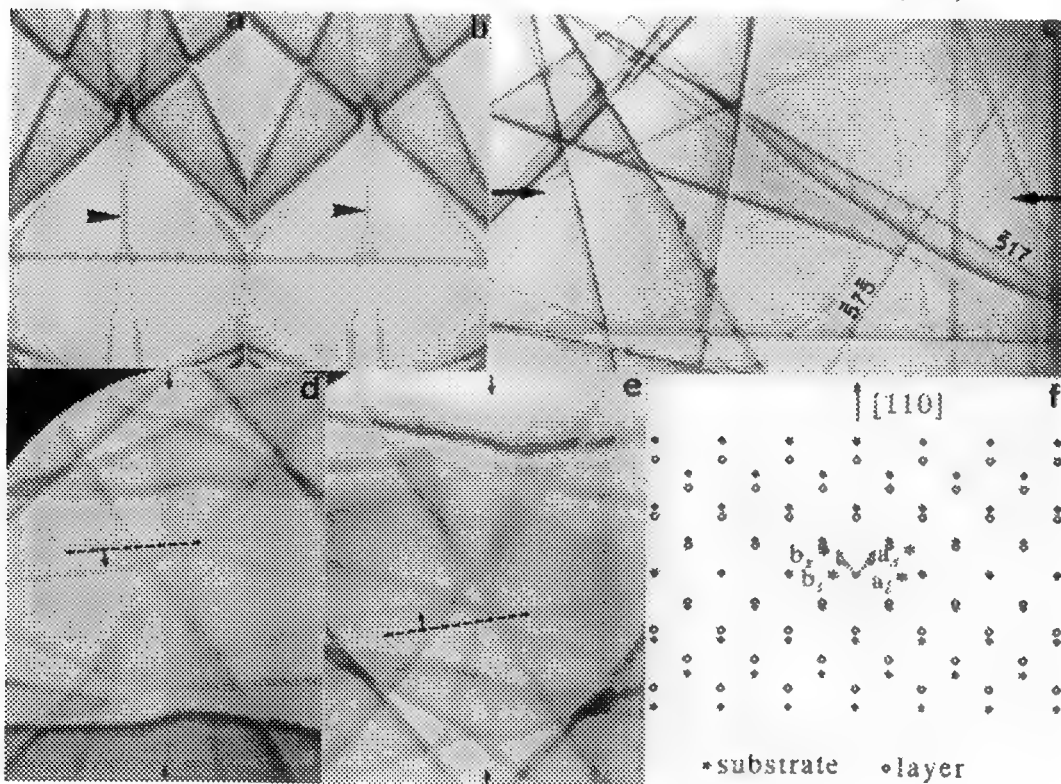
Fig.1 CBED pattern taken near the [530] incidence direction: a) on the substrate and b) on the layer showing the lattice parameter change; c) LACBED taken at the interface with the [221] incidence direction showing shift of HOLZ lines except the $2\bar{2}0$ lines; the CBIM patterns taken with d) the [510] incidence direction and e) the [150] incidence direction, showing the shift of Kikuchi lines in opposite direction in these two equivalent projections; f) a model showing reciprocal lattice points for the substrate (filled circles) and the layer after surface relaxation (open circles) resulting in the monoclinic (orthorombic) distortion.

INTERFACES IN HIGH-TEMPERATURE SUPERCONDUCTORS

K. L. Merkle and Y. Gao

Materials Science Division, Argonne National Laboratory, Argonne, IL 60439

After the discovery of high-temperature superconductors (HTS) five years ago, it soon became apparent that their interfacial characteristics would play an extremely important role in any foreseeable applications of these materials. In recent commercial devices, the weak-link characteristics of grain boundaries (GBs) have in fact been exploited to manufacture Josephson junction SQUIDS.[1] On the other hand, the low critical current density of HTS is a considerable limitation for practical applications of the zero-resistance property, particularly in bulk materials.[2] The weak-link behavior of GBs is largely responsible for this, but other types of interfaces such as those formed by metallic contacts or the interfaces between the substrate and a HTS thin film are also critical to the application of these materials. We shall review here some of the important interface issues that have been addressed by TEM techniques, but shall focus largely on the connection between the critical current (J_c) that can be transported across a grain boundary and its atomic-scale structure and composition.

Historically EM techniques have been involved in the identification of the types of boundaries by their macroscopic and microscopic geometry. It is found that special geometries are often preferred in the high-angle regime; not unusual are GBs involving one or two low-index planes.[3] One typically finds preferred orientations and well developed planar facets which are mostly due to the strong anisotropy of the HTS materials. Small angle GBs exist in a variety of preparations and geometries and their study has revealed a number of interesting structures.[4] The production of samples with phase-pure, well-structured high-angle GBs remains a challenge for most materials, but at least for the $YBa_2Cu_3O_{7-x}$ system consistently "clean" GBs can presently be prepared by a number of processing routes. For samples sintered in O_2 atmospheres containing small amounts of CO_2, it has been shown that minute quantities of impurities can drastically change intergranular current transport.[5] The local stoichiometry of the main constituents at a GB can also strongly influence transport properties. Small enrichments of Cu have been indicated for some high-angle GBs, whereas others show no significant compositional variation by x-ray spectroscopy in field emission STEM.[6,7]

Measurements of J_c in <001> bicrystal films by Dimos et al.[8] as a function of misorientation found a sharp drop in the GB J_c, by almost 2 orders of magnitude, as the tilt angle is increased beyond ~10°. MOCVD grown films of the same geometry have been analyzed by HREM, and it was found that the edge dislocations, which constitute a low-angle tilt GB, have extended cores (diam.~2nm). HREM image simulations indicated that the Y, Ba atomic columns are replaced by Cu within the core (see Fig. 1).[9] Since such nonsuperconducting cores would start to overlap at ~ 10°, the precipitous drop of J_c in this range can be understood. While initial experiments appeared to indicate weak-link characteristics for all high-angle GBs,[8] it has been found that bicrystals of $YBa_2Cu_3O_{7-x}$ show quite diverse electrical characteristics, including close-to-bulk behavior.[10] Rather unimpeded current transport across special high-angle GBs may be possible, such as for the 90°, <100> tilt GB shown in Fig. 2 , which shows an uninterrupted continuation of the CuO planes across the GB within its (013) symmetric facets.[11] Electric-transport measurements and HREM on the same bicrystals have shown that on a qualitative level the superconducting properties are consistent with the observed microstructural differences that have been observed among the GBs.[12] From these investigations it has become clear, however, that fine atomic-scale details are important in regard to the electrical characteristics of HTS GBs. Several efforts are underway to establish correlations between electric-transport properties of GBs and their atomic-scale microstructure, including investigations by analytical techniques that can give information on the local chemical composition and electronic structure.

References
1. K. Char, M. S. Colclough, L. P. Lee, and G. Zaharchuk, Appl. Phys. Lett. **59** (1991) 733, ibid. 2177 .
2. D. C. Larbalestier, Physics Today (June 1991) 74 .
3. L. A. Tietz and C. B. Carter, Physica C **182** (1991) 241; D. A. Smith, M. F. Chisholm, and J. Clabes, Appl. Phys. Lett. **53** (1988) 2344; O. Eibl, Physica C **168** (1990) 239 .

5. Y. Gao, Y. Li, K. L. Merkle, J. N. Mundy, C. Zhang, U. Balachandran, and R. B. Poeppel, Materials Letters **9** (1990) 347; U. Balachandran, R. B. Poeppel, S. E. Dorris, C. Z. Zhang, D. Xu, K. L. Merkle, Y. Gao, Y. Li, J. J. Picciolo, and J. T. Dusek, Ceramic Transactions **18** (1991) 341 .
4. M. F. Chisholm and D. A. Smith, Phil. Mag. A **59** (1989) 181; Y. Gao, K. L. Merkle, G. Bai, H. L. M. Chang, and D. J. Lam, Ultramicroscopy **37** (1991) 326 .
6. S. E. Babcock and D. C. Larbalestier, Appl. Phys. Lett. **55** (1989) 393 .
7. D. H. Shin, J. Silcox, S. E. Russek, D. K. Lathrop, B. Moeckly, and R. A. Buhrman, Appl. Phys. Lett. **57** (1990) 508 .
8. D. Dimos, P. Chaudhari, J. Mannhart, and F. K. LeGoues, Phys. Rev. Lett. **61** (1988) 219; D. Dimos, P. Chaudhari, and J. Mannhart, Phys. Rev. B **41** (1990) 4038 .
9. Y. Gao, K. L. Merkle, G. Bai, H. L. M. Chang, and D. J. Lam, Physica C **174** (1991) 1 .1.
10. S. E. Babcock, X. Y. Cai, D. L. Kaiser, and D. C. Larbalestier, Nature **347** (1990) 167 .
11. Y. Gao, G. Bai, D. J. Lam, and K. L. Merkle, Physica C **173** (1991) 487 .
12. D. C. Larbalestier, S. E. Babcock, X. Y. Cai, M. B. Field, Y. Gao, N. F. Heinig, D. L. Kaiser, K. L. Merkle, L. K. Williams, and N. Zhang, Physica C **185-189** (1991) 315 .
13. This work was supported by the U.S. Department of Energy, Basic Energy Sciences- Materials Science, under contract W-31-109-Eng-38 and by the National Science Foundation (DMR88-09854) through the Science and Technology Center for Superconductivity.
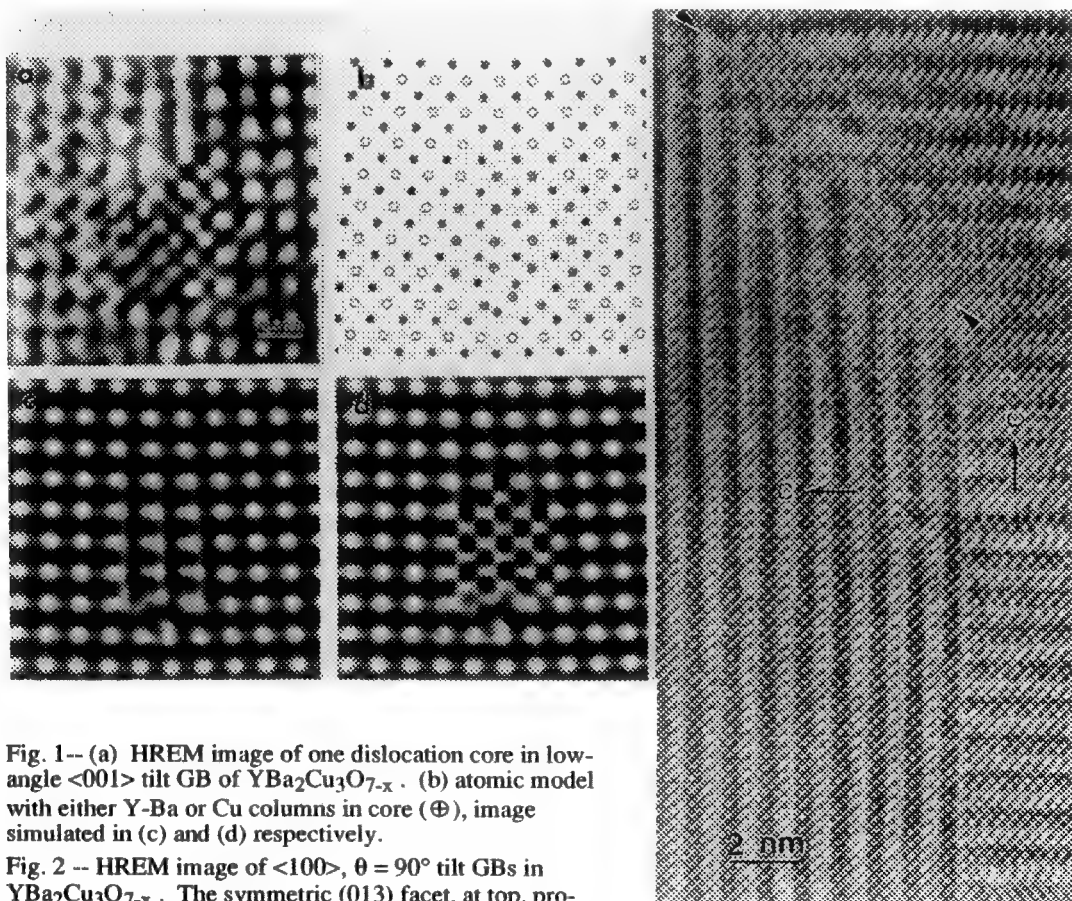
Fig. 1-- (a) HREM image of one dislocation core in low-angle <001> tilt GB of $YBa_2Cu_3O_{7-x}$. (b) atomic model with either Y-Ba or Cu columns in core ($\oplus$), image simulated in (c) and (d) respectively.

Fig. 2 -- HREM image of <100>, $\theta = 90°$ tilt GBs in $YBa_2Cu_3O_{7-x}$. The symmetric (013) facet, at top, provides a direct continuation of CuO planes across the GB.

235

ANALYSIS OF MOIRÉ PATTERNS IN IMAGES OF THIN YBa$_2$Cu$_3$O$_{7-\delta}$ FILMS ON MgO

M. Grant Norton* and C. Barry Carter**

* Dept. of Mechanical and Materials Engineering, Washington State University, Pullman WA 99164.
** Dept. of Chemical Engineering and Materials Science, University of Minnesota, Minneapolis MN 55455

Moiré fringes arise from the interference between diffracted beams from two overlapping crystals (double diffraction) and in the bright-field case the forward scattered beam. The fringe patterns act as magnifiers of lattice imperfections and small deviations from perfect crystallographic orientation and symmetry. Moiré patterns have been used previously to study, for example, the growth of metal films on substrates such as molybdenum disulfide—which can easily be prepared to electron transparency[1]. Moiré patterns can be used to identify microstructural defects in epitactic deposits. For example, the presence of rotationally misaligned grains, the presence of dislocations, and residual interfacial strain will be revealed in the fringe pattern.

In this study, the formation and analysis of moiré fringe patterns produced by the deposition of very thin films of YBa$_2$Cu$_3$O$_{7-\delta}$ onto specially prepared electron-transparent thin foils of (001) oriented MgO[2,3] will be discussed. Following film deposition these specimens can be transferred directly to the electron microscope without the need for further specimen preparation. Thereby eliminating artifacts due to specimen preparation which can complicate the interpretation of electron micrographs.

Figure 1 shows a typical bright-field image of a YBa$_2$Cu$_3$O$_{7-\delta}$ thin film (~ 20 nm) on MgO. The presence of moiré fringes implies that either there is a discommensuration at the heterojunction or an array of misfit dislocations at the interface. The fringe spacing is consistent with the predicted value of the {200} fringe spacing in the absence of any rotation[3]. The spacings of the [200] and [020] moiré fringes are half those of the corresponding misfit dislocations. Thus, in an epitactically aligned c-axis oriented grain, the misfit will be accommodated by [100] and [010] misfit dislocations. If a threading edge dislocation is present in the layer it will be visible as one or more terminating fringes, depending on the magnitude of the Burgers vector. Areas where terminating fringes are visible have been indicated in figure 1 by arrows. Figure 2 is a montage of enlarged images of these areas. For example, at a threading [100] dislocation, two [200] moiré fringes will terminate, illustrated in figure 2(e)—this appears to be the most common situation. However, single terminating fringes are also found, which may indicate the presence of partial dislocations, for example in figure 2(a) and 2(c). Possible mechanisms for introducing dislocations during growth are; the accommodation of rotational displacements between agglomerating islands that are close to the exact epitactic orientation, and the accommodation of displacement misfits. As the film thickens pinholes remain, illustrated in figure 2(d) and 2(e). So-called incipient dislocations are often observed to be associated with such pinholes[4]. When two moiré fringes terminate on one side of the pinhole it implies that one dislocation would have to be formed if the pinhole were to be eliminated and this may be energetically unfavorable. In some cases more than two moiré fringes may terminate on the pinhole, for example in figure 2(f). Other microstructural features have been observed through analysis of moiré fringe patterns (e.g., refs 3,4) and these will be discussed in addition to the features already mentioned[5].

References

1. D.W. Pashley, in, *Thin Films*, American Society for Metals, Metal Park, OH (1964) p. 59.
2. M.G. Norton, S.R. Summerfelt, and C.B. Carter, Appl. Phys. Lett. <u>56</u>, 2246 (1990).
3. M.G. Norton, *et al.*, Appl. Phys. Lett. <u>55</u>, 2348 (1989).
4. M.G. Norton and C.B. Carter, J. Cryst. Growth, <u>110</u>, 641 (1991).
5. Support from the Consortium for Superconducting Electronics and the National Science Foundation, through the Materials Science Center at Cornell, is gratefully acknowledged.
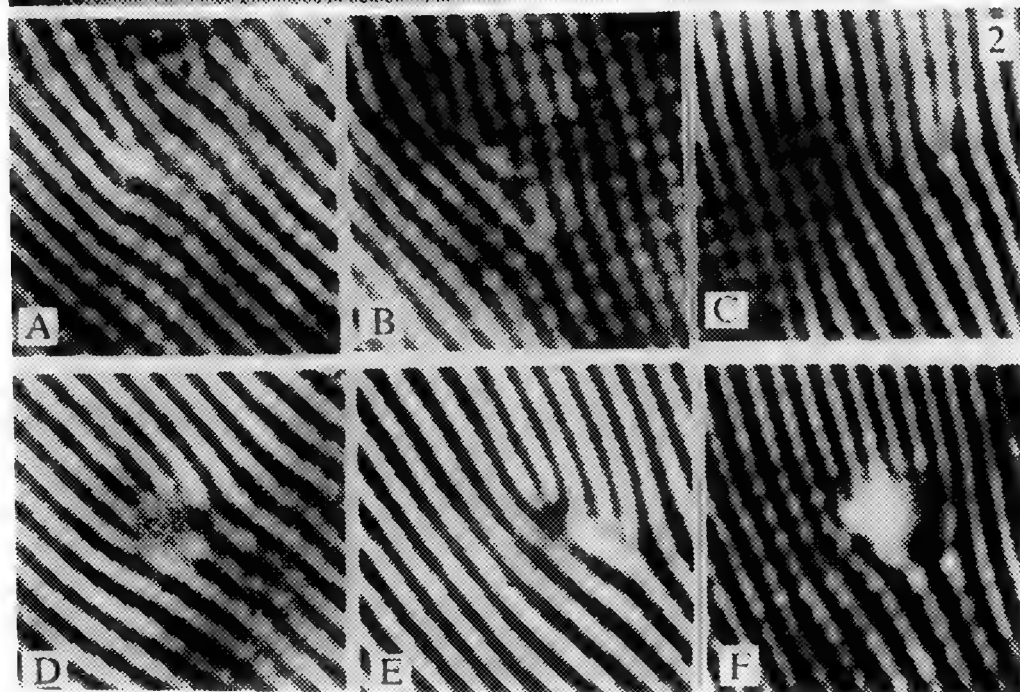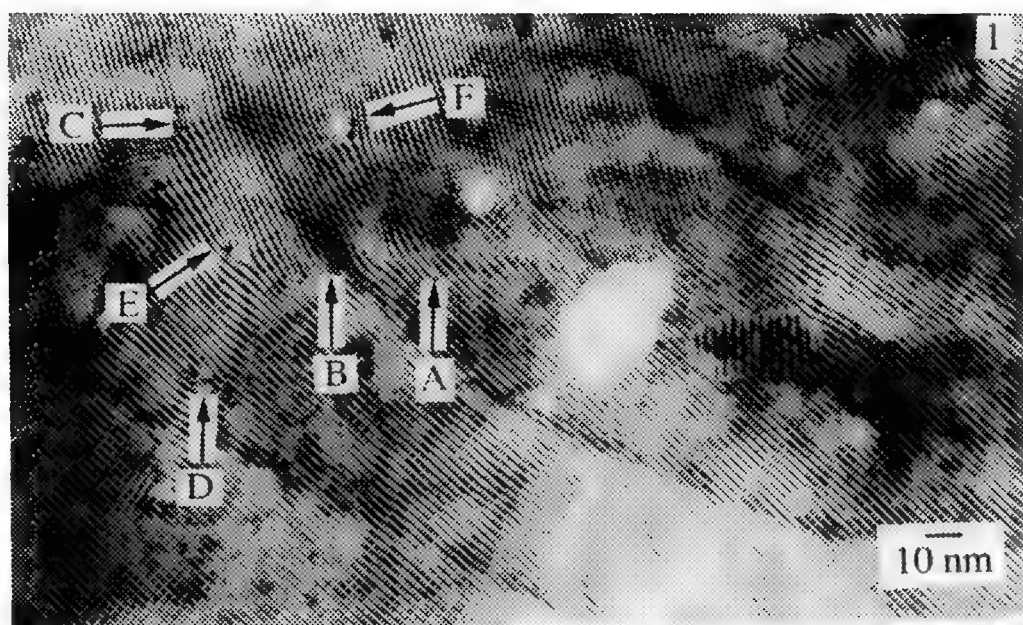
Fig. 1. Bright field micrographs showing moiré patterns in images of $YBa_2Cu_3O_{7-\delta}$ islands on MgO.
Fig. 2 (a-f). Bright field micrographs showing enlarged regions of figure 1.

237

TWINNING DISLOCATIONS AND STRUCTURAL TRANSITION
OF TWIN BOUNDARY IN YBa$_2$Cu$_3$O$_{7-\delta}$

Yimei Zhu and M. Suenaga
Materials Science Division, Brookhaven National Laboratory, Upton, NY 11973

HREM studies suggest that there are two types of twin boundaries in YBa$_2$Cu$_3$O$_{7-\delta}$: one with a lattice translation ($\sim$d$_{110}$) along the boundary for fully oxygenated samples, and the other without a lattice translation for oxygen-deficient ones. Originally, the displacement was attributed to observational phenomena caused by misalignment of the crystal. However, diffraction analysis[1] and twin boundary fringe contrast analysis[2,3] showed that the lattice translation at the boundary is an intrinsic property of the twin boundary in fully oxygenated YBa$_2$(Cu$_{0.98}$M$_{0.02}$)$_3$O$_{7-\delta}$ (M=Cu, Zn, and Ni, and $\delta \approx 0.0$). To further understand the kinetics of twin boundary formation, we present additional observations on twinning dislocation and structural transition of the twin boundaries.

Fig.1 is an example of a twin boundary in YBa$_2$Cu$_3$O$_7$ showing a lattice shift along the boundary. The boundary also contains a twinning step (marked by a circle), where the center of the twin boundary leaves one (110) lattice plane and moves to a neighboring (110) lattice plane. Such step is associated with a twinning dislocation. When the step propagates, atoms near the step rearrange themselves in the manner of a dislocation motion. The twinning dislocation can be defined rigorously using the so-called Frank circuit (Fig.2). The closure failure is the Burgers vector of the dislocation:

$$\mathbf{B} = \oint_1 (\partial u/\partial l) \, dl = [5b(1)-5a(2)]+[6a(1)-6b(2)] = a(1)-b(2) = |a-b|[-110].$$

Fig.3 shows another type of twinning dislocation, observed during an in-situ experiment. The twin boundary is a mixture of the two types: one with a lattice shift at the right, and the other without a lattice shift at the left (see the white lines as a reference). An extra (110) plane can be found in the region where the two types of boundary merge. The proposed atomic configuration is shown in Fig.4. The twin boundary with a lattice shift is centered at chain-oxygen plane, and that without a lattice shift is centered at cation plane. The change of the boundary center produces a 1/4·2d$_{110}$ twinning step (h=1.35 Å, not visible because of the resolution). The corresponding perfect edge-dislocation was determined to be $\mathbf{B}$=1/2[-110]+1/2|a-b|[-110].

The motion of the twinning dislocation was observed under electron beam irradiation.[4] Our results suggest that the early stage of evolution of a twin boundary in YBa$_2$Cu$_3$O$_{7-\delta}$ ($\delta \approx 0.0$) is associated with the switching from a twin boundary centered on oxygen atoms to one centered on cation atoms. The kinetics of such a transition may be explained by the motion of twin boundary dislocations. Under irradiation, the strain energy may be reduced by the loss and/or disordering of chain oxygen. The dislocations, associated with twinning steps moving through the (110) twin boundary plane, would eliminate the cation lattice-shift and create a cation-centered twin boundary (Fig.4), resulting in a lower boundary energy. Because the twin boundary plane is the dislocation glide plane containing both the dislocation line and its Burgers vector, the dislocation is "glissile", and can move very fast, even under the action of small internal shear stress without atomic diffusion.

Geometrical analyses of the twin boundary using Coincidence-Site-Lattice (defined as a Σ64 interface), and the twinning dislocation using Displacement-Shift-Complete-Lattice also will be presented.[5]

References

1. Y. Zhu, M. Suenaga and Y. Xu, J. Mater. Res., 5 (1990) 1380.
2. Y. Zhu, M. Suenaga, J. Tafto and D. O. Welch, Phys. Rev. B. 44 (1991) 2871.
3. S. C. Cheng, S. S. Sheinin, J. Jung, M. K. Yu and J. P. Frank, Physica C, 184 (1991) 385.
4. Y. Zhu and M. Suenaga, *Philo. Mag. A*, (1992) in press.
5. This research was supported by the U.S. Department of Energy, Division of Materials Science, Office of Basic Energy Science under Contract No. DE-AC02-76CH00016.
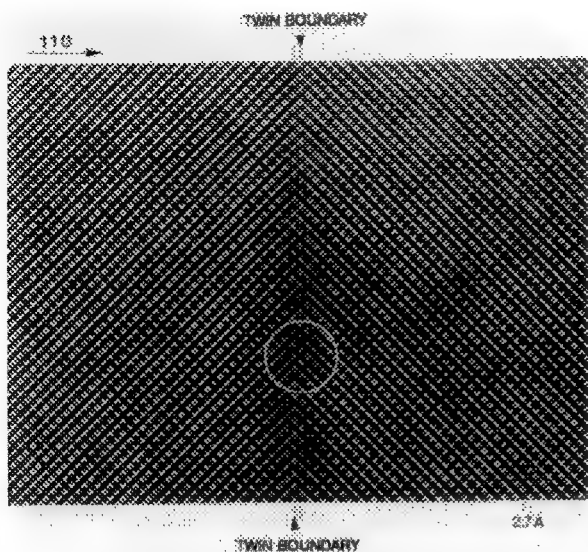
Fig.1 HREM image of a twin boundary containing a twinning step.

Fig.4 A proposed model for Fig.3.

Fig.2 A model of a twinning step associated with a twinning dislocation. The open circles represent chain-oxygen atoms, and the copper atoms are located at the corners.
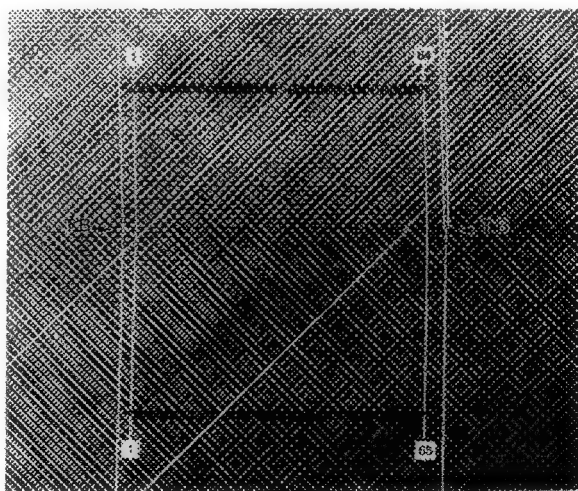
Fig.3 A mixture of two types of twin boundary (see text).

239

MICROSTRUCTURAL ISSUES IN c-PARALLEL YBa$_2$Cu$_3$O$_{7-\delta}$ THIN FILMS

S.K. Streiffer, B.M. Lairson, E.M. Zielinski, T. Umezawa[§,†], T.H. Geballe[†], and J.C. Bravman

Department of Materials Science and Engineering, Stanford University, Stanford, CA   94305
[§]on leave from Yokogawa Electric Corporation, Japan
[†]Department of Applied Physics, Stanford University, Stanford, CA   94305

Considerable effort has been directed at understanding the microstructures present in YBa$_2$Cu$_3$O$_{7-\delta}$ films with the c-axis perpendicular to the plane of the substrate. This work has largely been driven by the high critical currents achieved in this particular film orientation. Although the critical currents are in general lower, the demonstration of high crystal quality, extremely smooth, dense films with their c-axis parallel to the plane of the substrate has opened the possibility of exploiting the highly anisotropic nature of YBa$_2$Cu$_3$O$_{7-\delta}$.[1] To fully utilize such films, a thorough investigation of microstructural issues is as necessary for this film orientation as for the c-perpendicular case. We have used transmission electron microscopy and scanning force microscopy to examine c-parallel films grown on SrTiO$_3$ and LaAlO$_3$ substrates by single-target, off-axis magnetron sputtering. Films were deposited at block temperatures ranging from 600°C to 640°C, in atmospheres ranging from 30 millitorr oxygen and 40 millitorr argon to 60 millitorr oxygen and 90 millitorr argon. In an effort to improve superconducting properties while maintaining as smooth a surface as possible, films were also grown by a template method in which an initial nucleation layer was deposited at 625°C and the remainder of the film deposited at 700°C.

Figures 1 and 2 are representative micrographs of the near-interface regions of two films, deposited on SrTiO$_3$ in 30 millitorr oxygen and 40 millitorr argon at 610°C, and on LaAlO$_3$ in 60 millitorr oxygen and 90 millitorr argon at 640°C, respectively. Figure 1 is taken along the (110) zone axis of the substrate, while Figure 2 is along the (100) zone axis of the substrate. Both films contain small volume fractions of c-perpendicular material as determined by x-ray diffraction (0.5% and 2% respectively), but dramatic differences are obvious in the distribution of this "impurity" orientation. In the film on SrTiO$_3$, a continuous c-perpendicular layer of thickness 2 to 15 nm is present everywhere at the film-substrate interface, while in the film on LaAlO$_3$ this interfacial layer is absent and c-perpendicular material is confined to well-separated, discrete grains that in some cases encompass the entire film thickness. While others have made similar observations on the variable distribution of c-perpendicular components in c-parallel films laser-deposited at 700°C onto SrTiO$_3$ in oxygen partial pressures ranging from 20 millitorr to 100 millitorr, it should be emphasized that the films examined in this study demonstrate qualitatively different trends and are grown in a very different portion of temperature-pressure phase space.[2] Work is under way to better understand the systematics of such behavior.

Two other microstructural features with a strong dependence on the deposition conditions are grain size and surface roughness. In many cases the surface features of c-parallel films are too fine to be observed by scanning electron microscopy, so we have used scanning force microscopy to quantify the surfaces of a series of films grown at different temperatures on SrTiO$_3$ substrates. Both grain size and roughness are found to decrease with decreasing substrate temperature, as would be expected, and a transition is seen from an essentially equiaxed structure for films grown at 600°C, Figure 3, to the precursor of the bar-like morphology observed in early c-parallel films, for films grown at 640°C, Figure 4. The details of our results on film surfaces will be discussed, as will the effect of the template method on surface and bulk film structure.[3]

References

1. C.B. Eom, et al., Science (1991)251, 780.
2. Hiromi Takahashi, et al., Physica C (1991)179, 291.
3. We wish to thank EPRI for support under contract # RP8009-11.
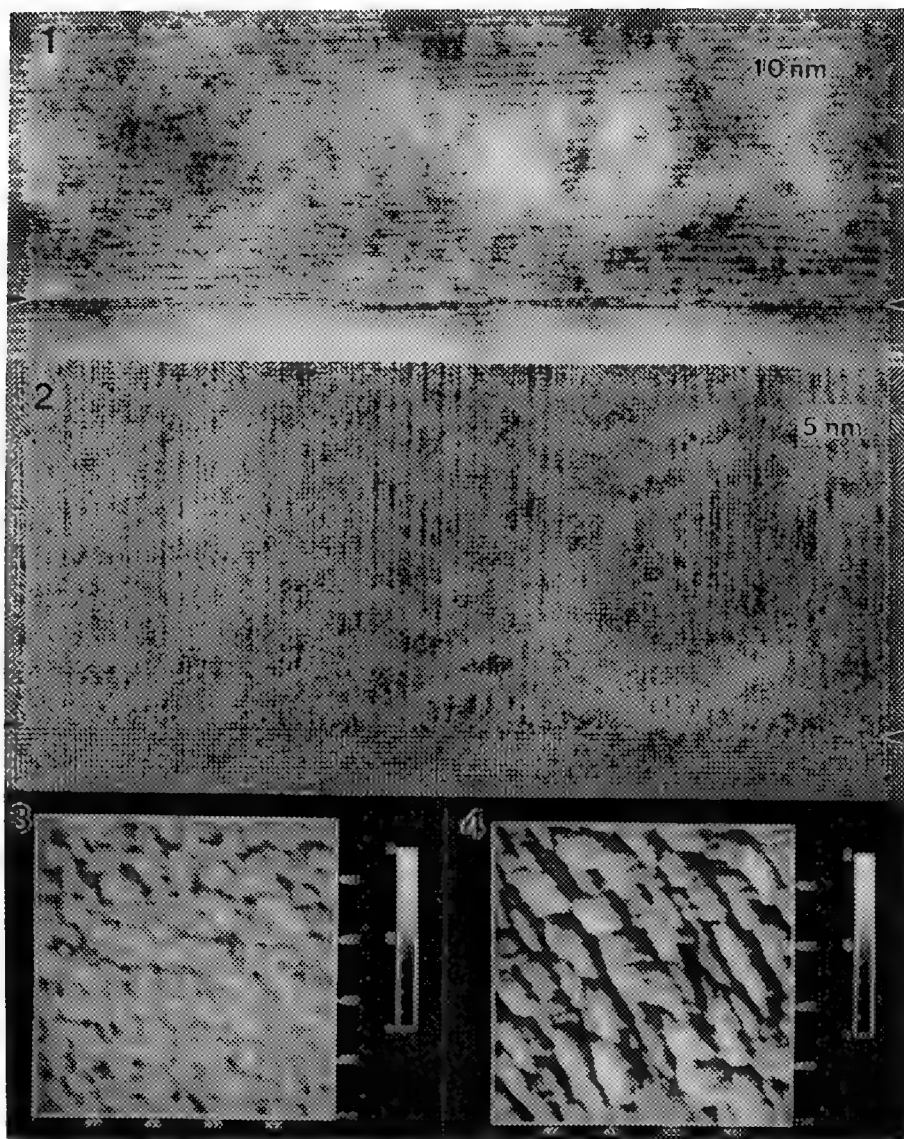
FIG. 1. - (110) Z.A. high-resolution image of near-interface region of c-parallel film on SrTiO3. Film-substrate interface is marked by arrows. Note variable thickness c-perpendicular layer.
FIG. 2. - (100) Z.A. high-resolution image of near-interface region of c-parallel film on LaAlO3. Film-substrate interface is marked by arrows. Note absence of c-perpendicular layer.
FIG. 3. - Scanning force microscope image of c-parallel film on SrTiO3 grown at 600°C. Roughness is 14 nm peak-to-peak, 2 nm standard deviation. Z-height full scale is 50 nm.
FIG. 4. - Scanning force microscope image of c-parallel film on SrTiO3 grown at 640°C. Roughness is 36 nm peak-to-peak, 4.5 nm standard deviation. Z-height full scale is 50 nm.

MORPHOLOGY AND ORIENTATION OF ULTRAFINE Y_2O_3 PRECIPITATES IN $YBa_2Cu_3O_{7-x}$ THIN FILMS

P. Lu, J.Zhao*, C.S.Chern,Y.Q.Li**, B.Gallois**, P.Norris*, B.Kear and F.Cosandey

Dept.of Mechanics &Materials Sci., Rutgers University, Piscataway, NJ 08855-0909.
*EMCORE Corporation, 35 Elizabeth Ave., Somerset, NJ 08854
**Dept. of Materials Science &Engineering, Stevens Institute of Technology, Hoboken, NJ 07030

Yttrium-rich $YBa_2Cu_3O_{7-x}$ (YBCO) thin films grown by plasma-enhanced metalorganic chemical vapor deposition (PE-MOCVD), have been reported to have high critical current densities (Jc) of $> 1x10^6$ A/cm^2 at 77K. [1] Electron microscopy has been used to understand how excess Y is incorporated into thin film microstructures without affecting their superconducting properties. [2,3] In this work, we report identification of small Y_2O_3 precipitates, their morphologies and orientation relationships in YBCO thin films.

Details of thin film growth process have been reported elsewhere. [3] The films were examined both in planar and in cross-sectional view by electron microscopy. TEM samples were prepared by conventional mechanical polishing and ion milling techniques. An ISI-002B high resolution electron microscope with a resolution limit of ~0.18 nm at 200keV was used for observations.

A dense distribution of Y_2O_3 precipitates with a cubic structure (a=1.06 nm) was identified in the Y-rich films. Fig.1a is a planar view of YBCO thin film along the [001] direction, showing small Y_2O_3 precipitates with an average size of about 5 nm. A density as high as $10^{24}/m^3$ has been observed for a film with a Ba/Y ratio of about 1.4.[2] In the planar view, the precipitates exhibit three types of morphologies as indicated by A, B_1 or B_2, corresponding to the following three orientation relationships with YBCO matrix: (A) $[001]_p//[001]_m$, $(110)_p//(010)_m$; $(B_1)[1\bar{1}0]_p//[001]_m$, $(001)_p//(100)_m$; and $(B_2)[110]_p//[001]_m$, $(00\bar{1})_p//(010)_m$. A HREM image of the precipitate in orientation A is shown in Fig.1b. Electron diffraction patterns from precipitates with A and B_1 morphologies along with their schematic representations are shown in Fig.2a and 2b, respectively. For orientation A, lattice misfit between precipitate and matrix is about 3% in ab plane of YBCO, and about 9% along the c-axis. The misfit in large precipitates(>5nm) is accommodated by misfit dislocations as shown in Fig.1b. The precipitates in orientation B_1 and B_2 are rotated with respect to the precipitates in A orientation by 90° about their [110] and $[1\bar{1}0]$ axes, respectively. The planes with the smallest misfit of ~3% for orientation B_1 and B_2 are parallel to bc and ac planes of YBCO, respectively. The precipitates are not readily visible in cross-section due to (001) lattice of YBCO matrix which dominates the contrast. [3] Figs.3a and 3b show the precipitates in three orientations viewed along [100] direction of YBCO. The precipitate in A orientation exhibits an elongated shape and shows weak Moire fringes due to overlapping of the precipitate with the matrix. The precipitates in B_1 orientation have a disk shape as shown in Fig.3b.

Combining the planar and cross-sectional observations, we conclude that Y_2O_3 precipitates have a plate-like morphology with the flat surface parallel to plane of the smallest misfit, as shown in Fig.4. Their width to thickness ratio has an average value of about 2.0. The precipitate shape is a result of strain energy associated with misfit. The formation of high density and small Y_2O_3 is very likely due to the in-plane lattice match with YBCO phase, and will have a significant effect on critical current densities.

1. J. Zhao *et al*. Appl. Phys. Lett. <u>58</u>, 2839 (1991).
2. P.Lu *et al*. Appl. Phys. Lett. <u>60,</u> (1992) in press.
3. P.Lu *et al*. J. Mater. Res. submitted.
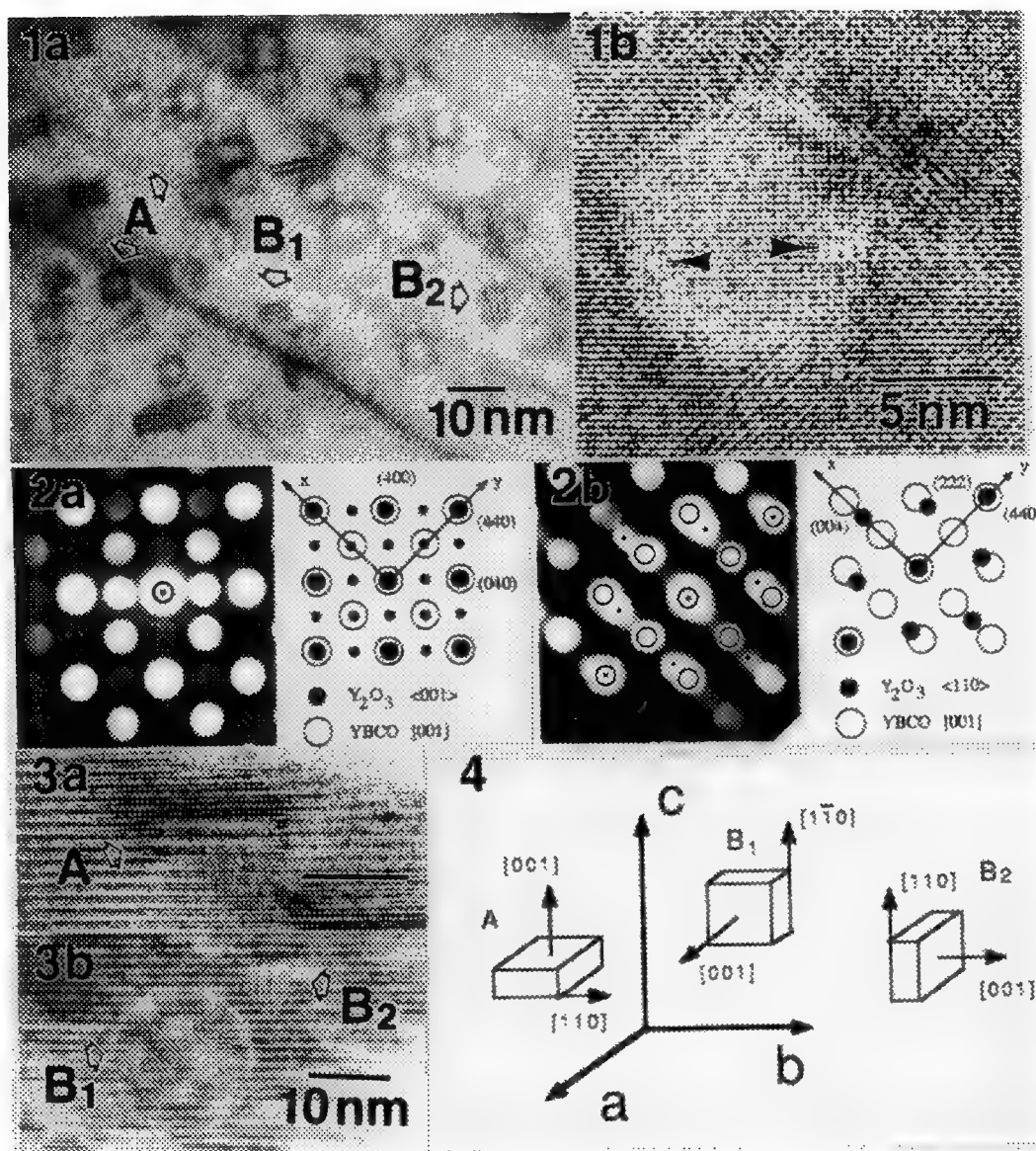
Fig.1. (a) planar view TEM micrograph of the Y-rich thin film in [001] direction; (b) HREM micrograph of a Y2O3 precipitate with type A morphology in [001] direction.

Fig.2. Electron diffraction patterns of small Y_2O_3 precipitates along with their schematic representations. (a) type A; (b) type B_1. The (h,k,l) indices are for Y_2O_3; x and y axes are parallel to the a and b axes of YBCO matrix, respectively.

Fig.3. Cross-section micrographs taken in [100] direction of YBCO, showing precipitates in A orientation(a) and in B_1 and B_2 orientations(b).

Fig.4. Morphology and orientation of Y_2O_3 precipitates with respect to YBCO matrix.

243

OFF-AXIS ELECTRON HOLOGRAPHY APPLIED TO THE STUDY OF INTERFACES

J. K. Weiss, M. Gajdardziska-Josifovska, M. R. McCartney & David J. Smith*

Center for Solid State Science, Arizona State University, Tempe, AZ 85287-1704
*also at Dept. of Physics, Arizona State University, Tempe, AZ 85287-1504

Interfacial structure is a controlling parameter in the behavior of many materials. Electron microscopy methods are widely used for characterizing such features as interface abruptness and chemical segregation at interfaces. The problem for high resolution microscopy is to establish optimum imaging conditions for extracting this information. We have found that off-axis electron holography can provide useful information for the study of interfaces that is not easily obtained by other techniques.[1]

Electron holography permits the recovery of both the amplitude and the phase of the image wave. Recent studies have applied the information obtained from electron holograms to characterizing magnetic and electric fields in materials and also to atomic-scale resolution enhancement.[2] The phase of an electron wave passing through a specimen is shifted by an amount which is proportional to the product of the specimen thickness and the projected electrostatic potential (ignoring magnetic fields and diffraction effects). If atomic-scale variations are ignored, the potential in the specimen is described by the mean inner potential, a bulk property sensitive to both composition and structure. For the study of interfaces, the specimen thickness is assumed to be approximately constant across the interface, so that the phase of the image wave will give a picture of mean inner potential across the interface.

Our electron holograms have been recorded using off-axis TEM holography on a Philips EM400ST equipped with a field emission gun operating at 100 kV and an electron biprism mounted in one of the selected area aperture positions. The electron interference patterns were recorded on a Gatan 679 slow-scan CCD camera fitted with a 1024x1024-pixel CCD array. The complex image wave was reconstructed off-line on a VAXStation 3200 workstation running SEMPER. The CCD camera allows for numerical reconstruction and accurate correction of distortions so that the accuracy in the reconstructed phase can be about $\pi/100$ radians.[3]

Fig. 1a shows a reconstructed phase image of an O-N-O stacked dielectric structure, where the image intensity is representative of the phase. Whereas a bright field image of this specimen shows very little contrast due to the small difference in atomic scattering factors between the oxide and the nitride layers, the difference in mean inner potential is easily observable. The one-dimensional profile in Fig. 1b shows limited intermixing between the layers, in addition to a thin unexpected layer on the Si substrate. Fig. 2 shows an example of the difference in information content between the amplitude (a) and the phase (b) of an image of a Si_3N_4/Si_3N_4 grain boundary in a Si_3N_4/SiC ceramic composite. These materials are known to have a thin impurity-rich amorphous layer at most grain boundaries, but there has been some question about the difference between the structural width as characterized by high resolution imaging and the chemical width as characterized by spectroscopic mapping.[4] The one-dimensional phase profile in Fig. 2c implies an interface width of about 1.0 nm for this particular example.

The ability to record the phase of the image wave clearly allows for the recovery of additional information about structural and compositional variations in materials. Combining this information with that obtained from other techniques can help to solve some materials problems involving interfaces.[5]

References

1. J. K. Weiss et al, Proc. 49th Annl. Mtg. EMSA (San Francisco Press, San Francisco, 1991) p. 674.
2. A. Tonomura, *Rev. Mod. Phys.* (1987)**59**, 639; S. Frabboni, G. Matteucci, and G. Pozzi, *Ultramicroscopy* (1987)**23**, 29; H. Lichte, in: *Advances in Optical and Electron Microscopy* (1991)**12**, 25.
3. W. J. de Ruijter and J. K. Weiss, *Ultramicroscopy* (1992) submitted.
4. K. Das Chowdhury, R. W. Carpenter and W. Braue, *Ultramicroscopy* (1992) in press.
5. This work was performed at the National Facility for High Resolution Electron Microscopy (NSF grant DMR-8913384) at ASU. Financial support for JKW was provided by the Industrial Associates Program at ASU. The authors would like to acknowledge G. Waytena and K. Das Chowdhury for providing specimens.
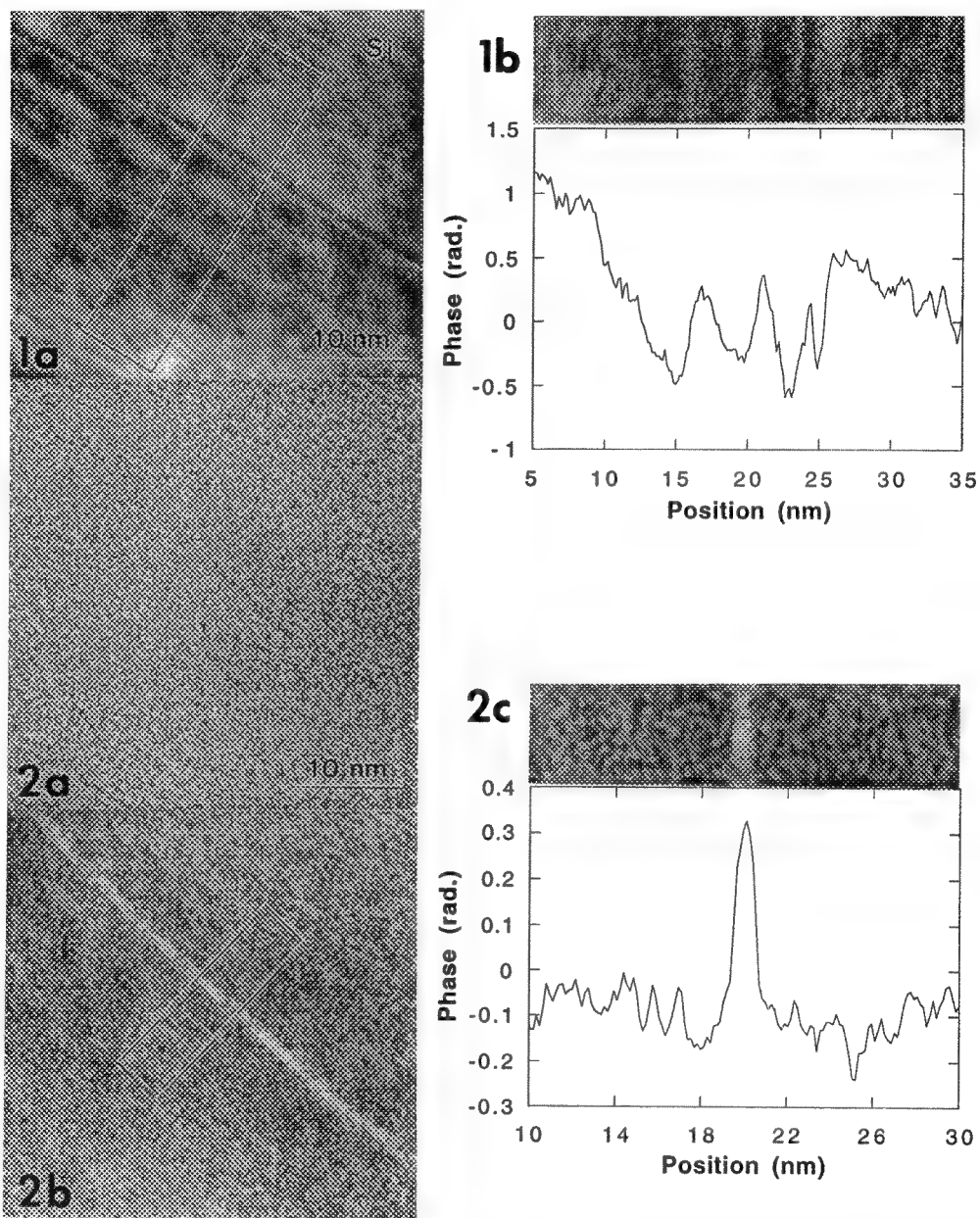
FIG. 1.--Reconstructed phase image (a) and extracted phase profile (b) from $SiO_2/Si_3N_4/SiO_2$ stacked dielectric structure. The one-dimensional profile in (b) is extracted from the boxed area in (a) and is averaged across a 40 pixel-wide area inside the box.

FIG. 2.--Reconstructed amplitude (a) and phase (b) images and extracted phase profile (c) from Si_3N_4/Si_3N_4 grain boundary in Si_3N_4/SiC ceramic. The one-dimensional profile in (c) is extracted from the boxed area in (b) and is averaged across a 40 pixel-wide area inside the box.

IMAGING OF FERROELECTRIC DOMAIN WALLS BY ELECTRON HOLOGRAPHY

Xiao Zhang

Electron Microscopy Facility and Department of Materials Science and Engineering,
The University of Tennessee, Knoxville, TN 37996

Electron holography has recently been available to modern electron microscopy labs with the development of field emission electron microscopes. The unique advantage of recording both amplitude and phase of the object wave makes electron holography a effective tool to study electron optical phase objects.[1] The visibility of the phase shifts of the object wave makes it possible to directly image the distributions of an electric or a magnetic field at high resolution. This work presents preliminary results of first high resolution imaging of ferroelectric domain walls by electron holography in $BaTiO_3$ and quantitative measurements of electrostatic field distribution across domain walls.

A single, high purity tetragonal $BaTiO_3$ crystal oriented on a (001) axis is prepared as a thin film TEM specimen. The electron holography study is conducted in a Hitachi HF-2000 cold field emission 200 keV TEM equipped with a quartz-fiber electrostatic bi-prism.[2] A potential of from 25 to 40 V was applied to the bi-prism resulting in a fringe spacing between 0.5 to 0.37 nm. The interference fringe can be rotated to any direction relative to a feature of interest. The specimen was oriented so as to place the plane of the domain wall, and also a component of the polarization, parallel to the electron beam. The incident current at the specimen is of the order of 0.4 nA, with an illumination angle of about 4.4 μrad. Images are recorded at a magnification of one million times with a exposure time of 4 s.

Figure 1 is a typical hologram over several parallel 90° domain walls. The position of the wall can be viewed from the bending of the interference fringes across the domain wall. The lateral shift of the fringes trend is directly related to the differential phase shift in the corresponding object point. The variations in the phase are due to changes in the electrostatic potential (polarization vector) sampled by the electron beam.[3] The width of the domain wall can, therefore, be measured directly from the onset to the finish of bending for each of the fringes as it crosses the nominal wall position. Measurements on a number of 90° domain walls show that the projected wall thickness is between 2 to 5 nm. These values, as expected, are lower than the TEM results using diffraction contrast, but are in good agreement with theoretical calculation.[4] Figure 2 shows another type of fringe shift. The fringe bending has a sinusoidal type, which seems to be consistent with a Neél type 180° domain wall. The inset in Figure 2 shows a possible configuration of polarization vector changes across the domain wall. Since the phase change between two adjacent fringes is 2π, a quantitative determination of the phase change can be made and the magnitude of the local polarization vector can be found. A measured spontaneous polarization of the value of 1.5×10^{-5} C/cm^2 is obtained with a phase shift of 0.65π, which is close to the measured average bulk value.[3] The shape of the fringe bending also quantitatively displays the variation of the polarization vector across the wall. The agreement between the experimental and predicted variations is close (see Figure 3).[5]

Anomalous fringe bifurcations from some 90° walls are also observed (see Figure 4). The higher phase shifts of the order of 2.5π in those discontinuous phase region suggest a possible accumulation of charged oxygen vacancies to the domain walls.

References

1. A. Tonomura, Rev. Modern Phys., (1987)3, 639
2. G. Möllenstedt and H. Düker, Z. Phys., (1956)377
3. X. Zhang, T. Hashimoto, and D.C. Joy, Appl. Phys. Lett., (1992)6, 784
4. F. Jona and G. Shirane, Ferroelectric Crystals (MacMillan, New York, 1962)
5. V.A. Zhirnov, Sov. Phys. JETP, (1959)822
6. Research sponsored in part by the Laboratory Directed Research and Development Program of Oak Ridge National Laboratory, managed for the Department of Energy by Martin Marietta Energy Systems,
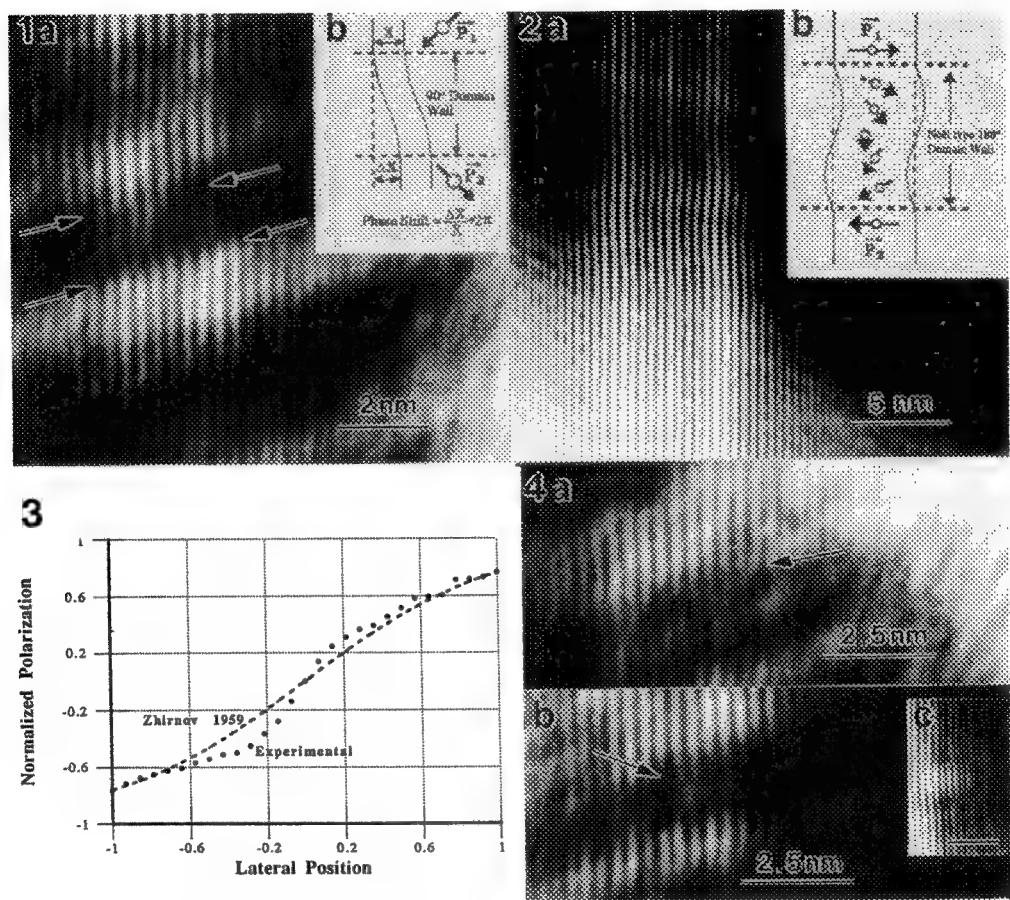
Figure 1. a). Electron hologram with fringe spacing of 3.7 Å, across 90° domain wall in BaTiO$_3$. Edges of wall are shown by pairs of arrows. b). Schematic drawing shows definition of ferroelectric domain wall in electron holographic image.

Figure 2. a). Electron hologram with fringe spacing of 4.6 Å, across possible Neél type 180° domain wall. Fringe shifts shows sinusoidal type. b). Possible configuration of change of polarization vector across wall.

Figure 3. Experimentally determined variation of normalized polarization component P$_z$ across 90° wall (open circles) compared with theory of Zhirnov (dotted line).

Figure 4. Anomalous fringe bifurcations from some 90° domain walls. Fringe spacings are 3.7 Å. a). Y-shape fringe splitting; b). X-shape fringe splitting; c). ϕ-shape fringe splitting. Bar = 3 nm

247

DEFORMATION MECHANISMS AT EPITAXIAL SEMICONDUCTOR INTERFACES STUDIED BY IN SITU TRANSMISSION ELECTRON MICROSCOPY

R. Hull, J.C. Bean and F. Ross

AT&T Bell Laboratories, 600 Mountain Avenue, Murray Hill, NJ 07974

We have studied deformation mechanisms at epitaxial semiconductor interfaces, primarily in the Ge_xSi_{1-x}/Si and $In_xGa_{1-x}As$/GaAs systems, by in-situ annealing of metastably strained films in the transmission electron microscope (TEM) (1-3). This allows direct, real-time, observation and recording of dynamic strain relaxation phenomena such as misfit dislocation nucleation, propagation and interaction mechanisms. This geometry also allows considerable insight into fundamental dislocation physics, as we are able, for example, to accurately quantify dislocation propagation velocities as functions of well-defined effective stresses (in the 10^8 - 10^9 Pa regime)in the epitaxial layers, and to vary dislocation structure and character by varying the orientation of the epitaxial interface (4). Comparison with measurements of dislocation velocities in bulk semiconductors (e.g. 5-7) and with models of dislocation motion via kink propagation (8), allows extension of existing measurements and models to the thin film, high stress regime.

The experimental configuration consists of annealing plan-view TEM samples in a single-tilt Gatan heating goniometer inside a JEOL 2000 FX TEM. Several experimental issues will be addressed in this talk: (i) Accurate measurement of local TEM sample temperature. The goniometer thermocouple (which is welded to the outside of the furnace) may be crudely and routinely calibrated via the melting point of an Al foil. We have also calibrated sample temperature via the Curie transition in Co-Ni alloys, by temperature indicating paints and, most accurately, by subsequent cross-sectional examination of the solid phase epitaxial regrowth of a crystalline/amorphous Si interface which was annealed in the plan-view geometry in the TEM (see Fig.1). (ii) The effect of the electron beam upon dislocation propagation velocities. This may be significant in compound semiconductors, but is negligible in Si and Ge_xSi_{1-x} alloys at the irradiation intensities and energy (200 kV) employed. (iii) Stress relaxation effects in the thinned TEM specimen: to first order we try and minimize these effects by studying very thin epitaxial films and imaging through as thick a sample region as possible (maintaining a film/substrate thickness ratio of <0.1 in the areas imaged), and far from the perforation. We have also attempted to quantify these sample relaxation effects upon our measurements by comparison to dislocation velocities in unthinned regions of the sample, and by finite stress element calculations.

Each of the above experimental issues may be resolved to the point where local sample temperature is known to within +- 30 Kelvin and stress to within 10%. This allows accurate and extensive measurements of dislocation propagation velocities (Figure 2) which yields insight into fundamental dislocation parameters (3). The extremely high stresses (as high as several GPa) in these films can modify the predictions of classical dislocation theory, and novel slip systems and Burgers vectors can be observed (Figure 3).

REFERENCES

(1) R. Hull et al, Phys. Rev. **B40**, 1681 (1988)
(2) R. Hull et al, Proc. of Int. Conf. on Microscopy of Semiconducting Materials, Oxford, England, 1991 (IOP, Bristol, England), p. 497
(3) R. Hull et al, J. Appl. Phys. **70**, 2052 (1991)
(4) R. Hull et al, Proc. Int Symposium on MBE, Anaheim, CA 1991 (Materials Research Society Symposium Proc. Vol. **220**), p. 153
(5) H. Alexander and P. Haasen, Solid State Physics **22** (1968)
(6) M. Imai and K. Sumino, Phil Mag. **A47**, 599 (1983)
(7) A. George and J. Rabier, Revue. Phys. Appl. **22**, 1941 (1987)
(8) J.P. Hirth and J. Lothe , "Theory of Dislocations" (McGraw-Hill, New York 1968)
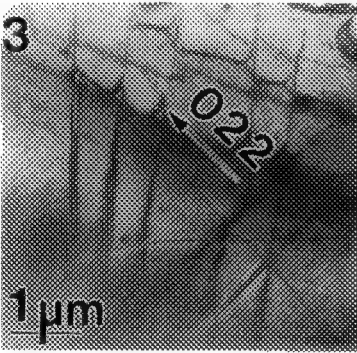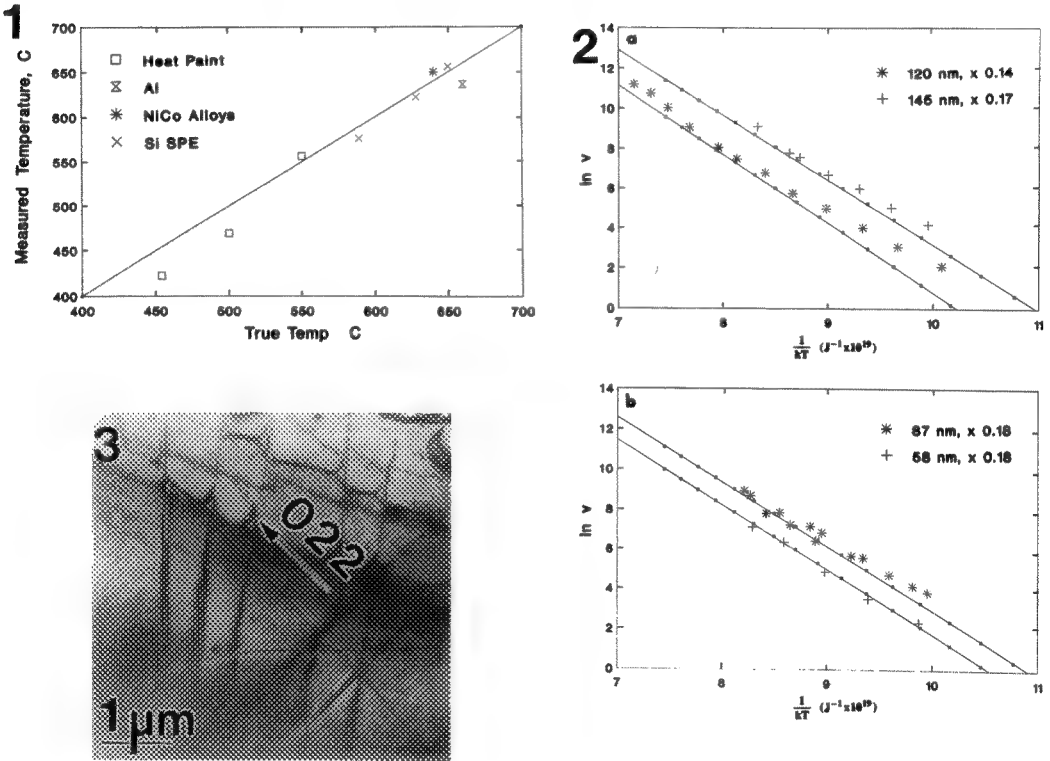
Figure 1: Graph of measured thermocouple reading vs. true temperature calibrated by a number of different techniques for our Gatan single-tilt heating goniometer.

Figure 2: Measured dislocation velocities vs. inverse energy for Ge_xSi_{1-x} alloys buried beneath a 300 nm Si(100) cap. Alloy layer thicknesses (h) and Ge compositions (x) are shown in the legends. v is in Angstrom/sec.

Figure 3: Interfacial misfit dislocations in a $GaAs/In_{0.4}Ga_{0.6}As/GaAs$ (100) heterostructure (alloy layer 20 nm thick). The misfit dislocation grid along orthogonal <011> directions is due to classic <110>{111} slip, whilst the grid along <010> directions is due to <110>{110} slip (9).

249

DEFORMATION OF A [001] Σ13 GRAIN BOUNDARY IN SILICON

Laurent Sagalowicz and William A. T. Clark

Department of Materials Science and Engineering, The Ohio State University, 116 West 19th Avenue, Columbus OH 43210

The interaction between crystal lattice dislocations and grain boundaries has an important influence on the mechanical properties of polycrystalline materials. We describe here a study of the behavior of the Σ13, (510)$_1$, 22.6°/[001] grain boundary in Si, deformed under symmetrical loading. The dissociation of crystal lattice dislocations which interact with this boundary during deformation is far more complicated than simple geometrical models predict.

In a near-exact coincidence site lattice (CSL) boundaries, it is expected that crystal lattice dislocations which interact with the boundary will dissociate into perfect grain boundary dislocations belonging to the DSC lattice[1]. It has been demonstrated, however, that imperfect and partial grain boundary dislocations can also arise. An imperfect dislocation separates two equivalent grain boundary structures which are related by a frustrated symmetry[2] and which both have the same energy. A partial grain boundary dislocation separates two non equivalent grain boundary structures. Fig.1 represents the dichromatic complex obtained when two diamond cubic structures are allowed to interpenetrate in the Σ13 CSL orientation. Three kinds of grain boundary dislocations can be found. b_1, b_2, b_3 are perfect grain boundary dislocations which belong to the DSC lattice, $b_1=1/26[\bar{1}50]_1$, $b_2=1/26[510]_1$, $b_3=1/26[\bar{3}\ 2\ 13]_1$. b_i is an imperfect dislocation, $b_i=1/4[111]_1-1/4[111]_2=1/26[\bar{3}\ 2\ 0]_1$, modulo a DSC vector. This defect separates two structures related by the (001) mirror glide which is present in the diamond cubic structure. b_{3p1} and b_{3p2} are partial dislocations, $b_{3p1}=1/4[111]_1=-1/52[5\ 1\ 13]_1$ and $b_{3p2}=1/4[111]_2=1/52[\bar{1}\ 5\ 13]_1$, modulo a DSC vector. These defects are obtained without allowing any rigid body displacement in the boundary. If a rigid body displacement p is present, the Burgers vector of the imperfect dislocation will become $b_i=1/4[111]_1-1/4[111]_2+(\underline{I} - \underline{W})p$, where $\underline{W}$ is the matrix associated with the (001) mirror glide. The reason for the dependence on the shift can be easily understood; if the two structures separated by the imperfect dislocation are related by the (001) mirror glide, and if one structure exhibits a shift p, the other one will exhibit a shift $\underline{W}p$.[2]

The undeformed sample was examined first, to determine all the defects which can be present in the boundary. Fig.2 is a high resolution image of the grain boundary, for which the beam was aligned parallel to the common [001]$_{1/2}$ direction. The periodicity observed is that of the CSL, and the interface contained a very low density of dislocations[3], indicating the closeness to the exact CSL orientation. α-fringe contrast in CSL reflections was used to determine that there was a 1/8[001]$_{1/2}$ rigid body displacement between the two crystals at the interface[3], which gives rise to an imperfect dislocation with Burgers vector $b_i=1/52[\bar{6}\ 4\ 13]_1$, modulo a DSC vector.

In the deformed sample, four different slip systems were seen to have been activated; [101]$_1$($\bar{1}$11)$_1$ and [101]$_2$($\bar{1}$11)$_2$ which have the highest Schmidt factor (0.47), [011]$_1$($1\bar{1}1$)$_1$ and [011]$_2$($1\bar{1}1$)$_2$ which have the second highest Schmidt factor (0.31). This arises partly because of the very symmetric loading conditions with respect to the grain boundary. The lattice dislocations which enter the grain boundary dissociate into grain boundary dislocations having as line directions the intersections of the slip planes and the grain boundary which are [$\bar{1}$56]$_1$=[156]$_2$ and [$\bar{1}$56]$_1$=[156]$_2$. Fig.3, which was obtained using a common reflection, shows five lattice dislocations, each dissociating into 2 visible grain boundary dislocations. The lattice dislocations marked A and B are in crystal 1 and have Burgers vector 1/2[011]$_1$, those marked C, D and E are in crystal 2 and have Burgers vector 1/2[011]$_2$. Other observations show that these dislocations dissociate into 4 grain boundary dislocations, a decomposition which cannot be explained in terms of DSC dislocations[3]. This decomposition, therefore, involves not only perfect grain boundary dislocations but also imperfect and

partial dislocations, in a reaction such as:

$$1/2[011]_2 \longrightarrow 1/52[\bar{4}\ 6\ 13]_2 + 1/4[001]_2 + 2*1/26[150]_2 \equiv 1/52[\bar{6}\ 4\ 13]_1 + 1/4[001]_1 + 2*1/26[\bar{1}50]_1$$

This reaction involves two imperfect grain boundary dislocations with Burgers vectors $1/52[\bar{6}\ 4\ 13]_1$ and $1/4[001]_1$, and two perfect grain boundary dislocations with the same Burgers vector $1/26[150]1$. It was shown in earlier work[3] that the imperfect dislocations having $1/52[\bar{6}\ 4\ 13]_1$ and $1/4[001]_1$ as Burgers vector can further dissociate into two partial grain boundary dislocations with Burgers vectors close to $1/8[001]_{1/2}$. The lattice dislocations with other Burgers vectors dissociate by similar reactions to produce imperfect dislocations with the same Burgers vectors but different line directions. These imperfect dislocations interact to give the zig-zag line direction observed in fig.3. No dislocation transmission across the interface was observed, which can be explained by the fact that such a symmetric dislocation configuration ensures that the elastic compatibility criteria of the boundary are met without the need to transmit dislocations.

References

1. W. Bollmann, Crystal Defects and Crystalline Interfaces, (Springer-Verlag, Berlin, 1970)
2. R. C. Pond, in Dislocations in Solids, edited by F.R.N. Nabarro, (Elsevier Science Publishers, B.V. 1989) pp. 1-64
3. L. Sagalowicz, R. Beanland and W. A. T. Clark, in Proceedings of the Materials Research society, vol. 238, edited by W.A.T Clark, C.L. Briant, U. Dahmen, (MRS Publishers, Pittsburgh, 1992), in press.
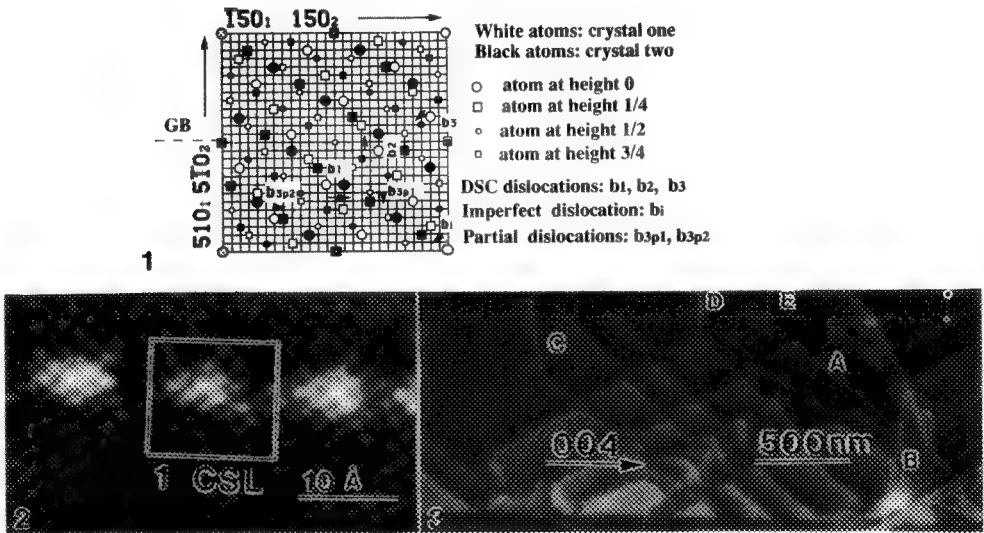
Fig.1-- (001) Dichromatic complex of the $\Sigma13$ grain boundary for the diamond cubic structure showing the different kind of grain boundary dislocations.
Fig.2-- High resolution micrograph of the undeformed grain boundary; the square denotes the CSL. Note the periodicity which is the same as the CSL.
Fig.3-- Dark field micrograph, $g=004_{1/2}$, of the boundary in a deformed sample. The incoming lattice dislocations marked A, B, C, D and E dissociate into four grain boundary dislocations, two of which are visible for this reflection.

HREM STUDY IN Ti/6H-SiC INTERFACE

J.S.Bow,* L.M.Spellman,** M.J.Kim,* R.W.Carpenter,* and R.F.Davis*

*Center for Solid State Science, Arizona State University, Tempe, AZ 85287-1704
**Department of Material Science and Engineering, North Carolina State University, Raleigh, NC 27695-7907

A semiconductor of Ti/6H-SiC with rectifying characteristics was reported recently.[1] That its electrical properties were degraded for 20 min. anneal at 700°C but improved again with subsequent 20 min. and longer anneal was considered to be caused by phase transformation during annealing. The purpose of this study is to identify those phases formed in the annealing process, and to identify those responsible for changing the electrical properties.

A 100 nm Ti thin film was deposited on 6H-SiC by electron beam evaporation in UHV, and subsequent annealing was also done in UHV at 700°C. Cross section TEM specimens were prepared by bonding wafers with Ti-films face to face, grinding, polishing, and then ion milling in a Gatan 600. All TEM observations were performed in an ISI 002B with a 0.18nm resolution at 200KV. HREM images were analyzed by using the SEMPER program.[2]

The as-deposited Ti/SiC was composed of only 6H-SiC with hcp metal Ti layers as reported,[1] and shown in Fig.1. Ti films grew epitaxially on SiC without detectable second phase at the interface. After annealing at 700°C for 20 min., a 10 to 20 nm thick reaction layer was formed from the interface into the Ti film and SiC substrate(Fig.2). The interface between the reaction zone and Ti was rough on a scale of about 10 nm. The major phase of the reaction zone is Ti_5Si_3, which is expected at reaction temperatures from 650° to 750°C.[3] Small islands distributed along the interface of Ti/Ti_5Si_3 and Ti_5Si_3/SiC, the later were similar to that in Ti-Alloy/6H-SiC system,[4] were identified to be cubic TiC phase. formation of TiC at the Ti_5Si_3/SiC interface was due to titanium diffusion to SiC surface, while that at Ti/Ti_5Si_3 interface resulted from carbon diffusion through Ti_5Si_3 layer. Deviations in composition between these two TiCs are thus expected and are under study. The interface between the reaction zone and SiC was amorphized after exposure in the TEM for a period of time, while the Ti/Ti_5Si_3 interface exhibited more resistance to the electron beam. The crystal orientation relationships among these phases are summarized below:

$$(0001)_{SiC} \,/\!/\, (0001)_{Ti_5Si_3} \,/\!/\, (111)_{TiC} \,/\!/\, (0001)_{Ti},$$
$$(1\bar{1}00)_{SiC} \,/\!/\, (21\bar{3}0)_{Ti_5Si_3} \,/\!/\, (1\bar{1}00)_{Ti}, \qquad (1\bar{1}04)_{SiC} \,/\!/\, (002)_{TiC}$$
$$[11\bar{2}0]_{SiC} \,/\!/\, [4\bar{5}10]_{Ti_5Si_3} \,/\!/\, [110]_{TiC} \,/\!/\, [11\bar{2}0]_{Ti}$$

The thickness of the reaction zone did not change appreciably for longer annealing, but the amount of TiC, especially those at the Ti/Ti_5Si_3 interface, was reduced by comparing the Fig.2 and Fig.3. Thus the TiC at Ti/Ti_5Si_3 interface was thought to be the phase which caused high leakage current after annealing.

References

1. L. M. Spellman et al., Mat. Res. Soc. Symp. Proc. 221 (1991), 99.
2. W. O. Saxton et al., Ultramicroscopy 4 (1979) 343.
3. M. Berti et al., J. Appl. Phys. 55[10] (1984) 3558.
4. T.Yano et al., J. Mat. Sci. 23 (1988) 3362.
5. This research was supported in part by NSF grant DMR-8901841, and in part by the Office of Naval Research via Contract N00014-88-K-0341. The microscopy was performed at ASU HREM Facility supported by Arizona State University and NSF-DMR.
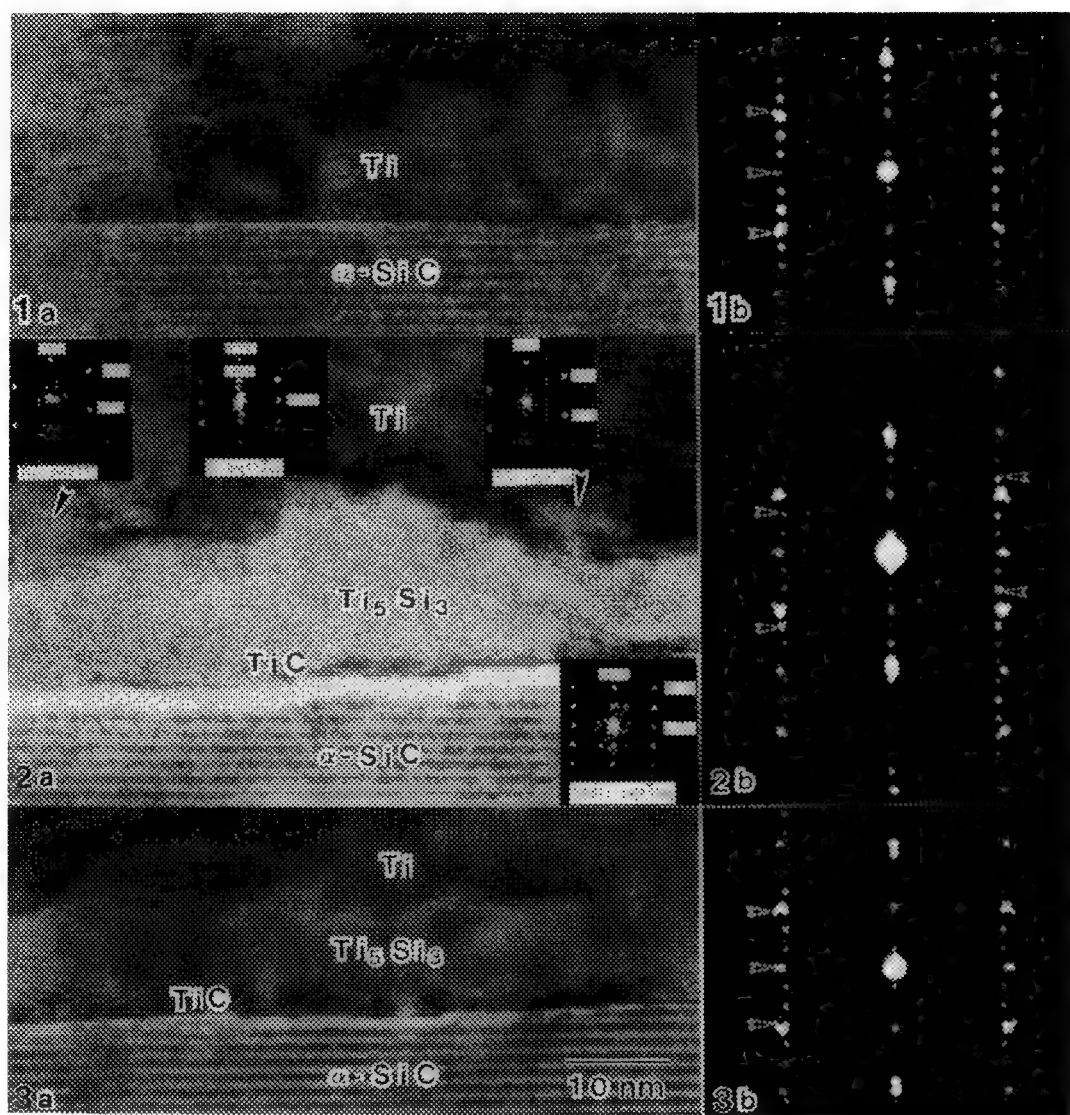
FIG. 1.--(a)HREM image of as-deposited Ti/6H-SiC; (b)SAD pattern shows only Ti (arrowed) and 6H-SiC phases.

FIG. 2.--(a)HREM image of 700°C/20 min.Ti/6H-SiC, and digital diffractions of Ti, TiC and Ti_5Si_3 phase; (b)SAD pattern shows Ti, TiC (arrowed), Ti_5Si_3 and 6H-SiC.

FIG. 3.--(a)HREM image of 700°C/1 h.Ti/6H-SiC; (b)SAD pattern shows Ti, Ti_5Si_3 (arrowed), and 6H-SiC.

MORPHOLOGY AND ATOMIC STRUCTURE OF SEGREGATED GRAIN BOUNDARIES IN Cu-Sb

R. W. Fonda and D. E. Luzzi

Laboratory for Research on the Structure of Matter and the Department of Materials Science and Engineering, University of Pennsylvania, Philadelphia, PA 19104-6272

The properties of polycrystalline materials are strongly dependant upon the strength of internal boundaries. Segregation of solute to the grain boundaries can adversely affect this strength. In copper alloys, segregation of either bismuth or antimony to the grain boundary will embrittle the alloy by facilitating intergranular fracture. Very small quantities of bismuth in copper have long been known to cause severe grain boundary embrittlement of the alloy.[1] The effect of antimony is much less pronounced and is observed primarily at lower temperatures. Even though moderate amounts of antimony are fully soluble in copper, concentrations down to 0.14% can cause grain boundary embrittlement.[2]

Grain boundaries in Cu-Bi have a high propensity to facet along crystallographic orientations.[3,4] This faceting is reversible; the removal or addition of bismuth will reversibly eliminate or produce faceting.[5] The faceted grain boundaries are predominantly $\Sigma=3$ boundaries with $(111)\parallel(111)$ facet planes. Similar faceting is also observed at Cu-Sb grain boundaries. Twins were differentiated from $\Sigma=3$ grain boundaries by the deflection of an intersected grain boundary, which was small for a twin boundary, as well as by high resolution imaging. The atomic structure of the $(111)\parallel(111)$ $\Sigma=3$ boundary in Cu-Bi contains a hexagonal array of bismuth atoms at second nearest neighbor positions within the (111) interfacial plane.[6,7] This arrangement of the large bismuth atoms produces an expansion of the boundary plane, shifting the hexagonal lattice of bismuth atoms adjacent to the remainder of the interfacial plane.

The morphology and atomic structure of $(111)\parallel(111)$ $\Sigma=3$ grain boundaries in Cu-1.5 wt% Sb was examined to compare with the observations in Cu-50 ppm Bi. Since antimony and bismuth are chemically similar, any difference in atomic structure of the boundary will be primarily due to the variation in atomic size. The abundance of $\Sigma=3$ grain boundaries in Cu-1.5% Sb is much lower than observed in Cu-Bi, but these grain boundaries are crystallographically faceted at every heat treatment examined (3, 6, and 24 hrs at 600 °C). The faceted grain boundary planes lie almost exclusively along $(111)\parallel(111)$ (Fig. 1), with small steps out of this plane faceted in a non-consistent orientation.

High resolution electron microscopy was used to examine the atomic structure of $(111)\parallel(111)$ $\Sigma=3$ grain boundaries. Images of this boundary (Fig. 2) differ in two ways from images of a $\Sigma=3$ twin boundary (Fig 3). These are evident at a defocus of approximately -600 Å, where the interfacial plane exhibits bright contrast and is sided by Fresnel fringes. These factors indicate that antimony is highly segregated to the interfacial plane, with a uniform lower concentration elsewhere. There is no observable expansion of this grain boundary, whereas the Cu-Bi $\Sigma=3$ boundary is significantly expanded (Fig. 4). The accumulation of antimony at the $\Sigma=3$ grain boundary evidently does not require the boundary expansion observed in Cu-Bi due to its smaller atomic size. The atomic structure of the $(111)\parallel(111)$ $\Sigma=3$ grain boundaries was analyzed by comparing experimentally obtained images with images calculated using the multislice algorithm over a systematic variation of objective lens defocus.[8]

254

References

1. Voce, E. and Hallowes, A. P. C., *J. Inst. Metals*, **73**, 323 (1947).
2. McLean, D., *J. Inst. Metals*, **81**, 121, (1952).
3. Donald, A., *Phil. Mag.*, **34**, 1185 (1976).
4. Donald, A. M. and Brown, L. M., *Acta Metall.*, **27**, 59 (1979).
5. Ferrence, T. G. and Balluffi, R. W., *Scripta metall.*, **22**, 1929, (1989).
6. Luzzi, D. E., *Philos. Mag. Letters*, **63**, 281 (1991).
7. Luzzi, D. E., Yan, M., Šob, M., and Vitek, V., *Phys. Rev. Letters*, **67**, 1894 (1991).
8. This work is supported by NSF-DMR under 88-19185 and 91-11775.
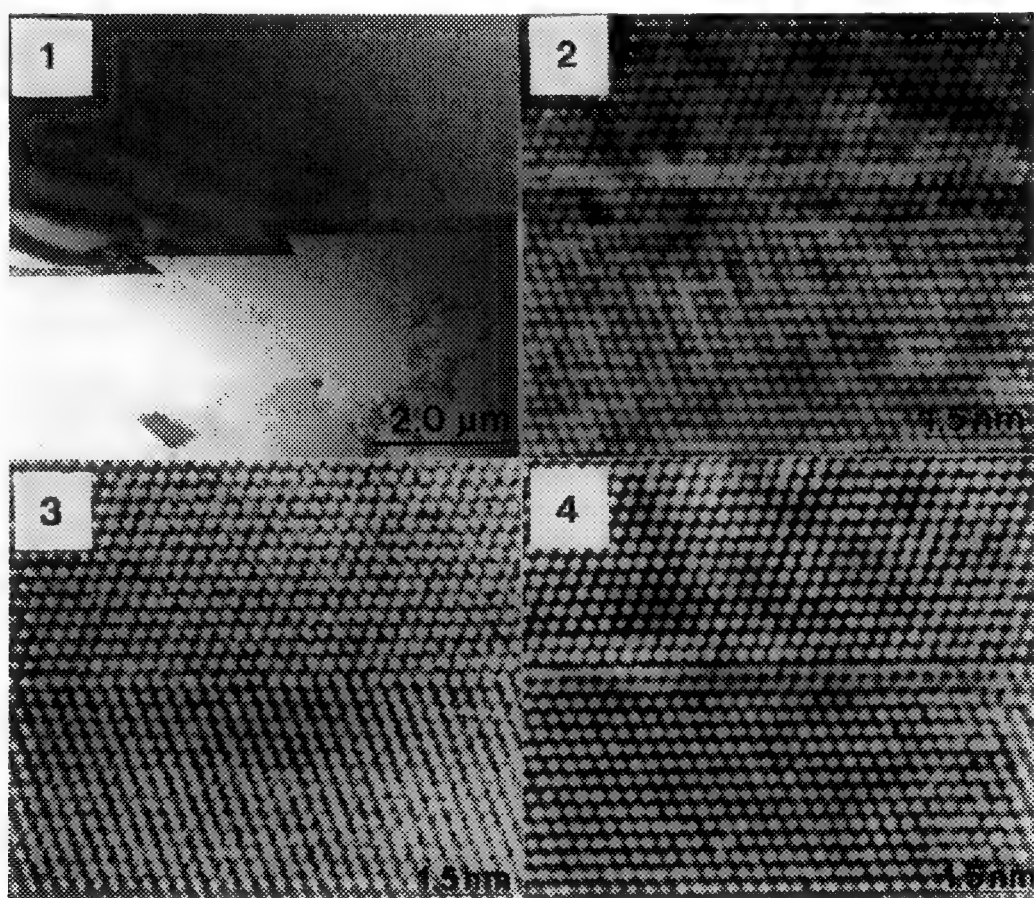
Figure 1.   Faceted $\Sigma=3$ grain boundary in Cu-1.5% Sb.
Figure 2.   The (111)‖(111) facet of a $\Sigma=3$ grain boundary in Cu-1.5% Sb.
Figure 3.   The (111)‖(111) facet of a $\Sigma=3$ twin boundary in Cu-50 ppm Bi.
Figure 4.   The (111)‖(111) facet of a $\Sigma=3$ grain boundary in Cu-50 ppm Bi.

In Situ TEM STUDIES OF AGGLOMERATION OF SUB-NANOMETER Ru LAYERS IN Ru/C MULTILAYERS

Tai D. Nguyen,[1,3] Ronald Gronsky,[2,3] and Jeffrey B. Kortright[1]

[1]Center for X-Ray Optics, MS 2-400, Lawrence Berkeley Laboratory, Berkeley, CA 94720
[2]National Center for Electron Microscopy, Lawrence Berkeley Laboratory, Berkeley, CA 94720
[3]Department of Materials Science and Mineral Engineering, University of California, Berkeley, CA 94720

Nanometer period Ru/C multilayers are one of the prime candidates for normal incident reflecting mirrors at wavelengths < 10 nm. Superior performance, which requires uniform layers and smooth interfaces, and high stability of the layered structure under thermal loadings are some of the demands in practical applications. Previous studies however show that the Ru layers in the 2 nm period Ru/C multilayer agglomerate upon moderate annealing, and the layered structure is no longer retained.[1] This agglomeration and crystallization of the Ru layers upon annealing to form almost spherical crystallites is a result of the reduction of surface or interfacial energy from the amorphous high energy non-equilibrium state of the as-prepared sample through diffusive arrangements of the atoms. Proposed models for mechanism of thin film agglomeration include one analogous to Rayleigh instability,[2] and grain boundary grooving in polycrystalline films.[4-6] These models however are not necessarily appropriate to explain for the agglomeration in the sub-nanometer amorphous Ru layers in Ru/C multilayers. The Ru-C phase diagram shows a wide miscible gap, which indicates the preference of phase separation between these two materials and provides an additional driving force for agglomeration. In this paper, we study the evolution of the microstructures and layered structure via in-situ Transmission Electron Microscopy (TEM), and attempt to determine the order of occurence of agglomeration and crystallization in the Ru layers by observing the diffraction patterns.

The multilayer was prepared by magnetron sputtering. The thickness of each bilayer period is approximately 2 nm, and the Ru layer is nominally 0.8 nm thick. Cross-sectional TEM samples were prepared by mechanical thinning followed by ion beam milling in a cold stage,[3] with the use of M-Bond 610 epoxy for heating experiments. They were studied in a JEOL JEM 200CX AEM equipped with a hot stage single tilt side entry holder, operating at 200 kV. The specimen was loaded such that the tilt direction was perpendicular to the film interface hence allows observation of the multilayer in a direction as close to the cross section as possible. Bright field images and selected area diffraction (SAD) patterns were taken at various temperatures during heating, and at various times while keeping at a constant temperature, 500°C.

The as-prepared multilayer shows flat and continuous layers with quite defined interfaces. This layered structure is stable under thermal heating in the microscope up to approximately 500°C. Figure 1 shows a cross-sectional TEM bright field image of the multilayer and its corresponding SAD pattern taken at 423°C. The SAD pattern shows the [110] spots of the Si substrate, and the finely spaced spots produced by electron scattering from the periodicity of the multilayer. The presence of the high order multilayer diffraction spots provides a good indication of the uniform layers and the layered structure of the multilayer.

After annealing at 500°C for a 10 minutes, the interfaces appear to become sinusoidal with a wavelength comparable to the multilayer period. The Ru layers hence seem to agglomerate into structure similar to that described by the Rayleigh instability, although the layered structure is still apparent, as can be seen in figure 2. Some of the high order multilayer spots are indeed still present in the corresponding SAD pattern, which indicates that the layers are still periodic though not as uniform as before. The SAD pattern also shows a diffuse faint ring at the approximate spacing of the (101) planes of elemental Ru, which indicates either some short range order or some initial nucleation of the crystalline Ru phase. Higher order multilayer diffraction spots in the SAD pattern begin to disappear after about 15 minutes at 500°C, and at the same time, other rings of hexagonal Ru become more visible, confirming the formation of the crystalline Ru phase. Figure 3 shows the multilayer after 25 minutes in the in-situ microscope. The multilayer has almost lost its layered structure, and all but the first order diffraction spots have disappeared. Most of the plate-like Ru grains seen in figure 2 have grown into more spherical structure (arrow A). Some larger Ru grains grow to combine with grains from the adjacent Ru layers and form grains that are larger than the initial multilayer period (B). After approximately 30 minutes, the Ru layers have completely agglomerated into almost spherical grains. The periodicity of the multilayer is destroyed, and accordingly, the remaining multilayer spot in the SAD pattern disappears and the Ru rings become more visible. Figure 4 shows the multilayer microstructures of the sample after annealing at 500°C for 90 minutes and subsequently cooled back to room temperature. The microstructure are not significantly different from that at elevated temperature, and shows Ru grains have of approximately 4 nm in diameter which is approximately twice as large as the initial bilayer period.

This in-situ study suggests that diffusion of the Ru and/or C atoms leads to agglomeration of the Ru layers and subsequently to nucleation of the Ru crystallites, though crystallization and grain growth occur before completion of the agglomeration process. Assuming all interfacial diffusion, which is meaningful because of phase separation in Ru-C, a diffusion coefficient may be approximated. In-situ observation at other temperatures are in process to determine this value. Continuous recording by means of video taping, and in-situ high resolution TEM would be helpful in determining more conclusively the mechanism of this agglomeration.[4]

1. T. D. Nguyen, R. Gronsky, and J. B. Kortright, MRS Proc. 187 (1990) 95.
2. T. D. Nguyen, R. Gronsky, and J. B. Kortright, MRS Proc. 230 (1991) 109, and references within.
3. T. D. Nguyen, R. Gronsky, and J. B. Kortright, J. Elec. Microsc. Tech. 19 (1991) 473.
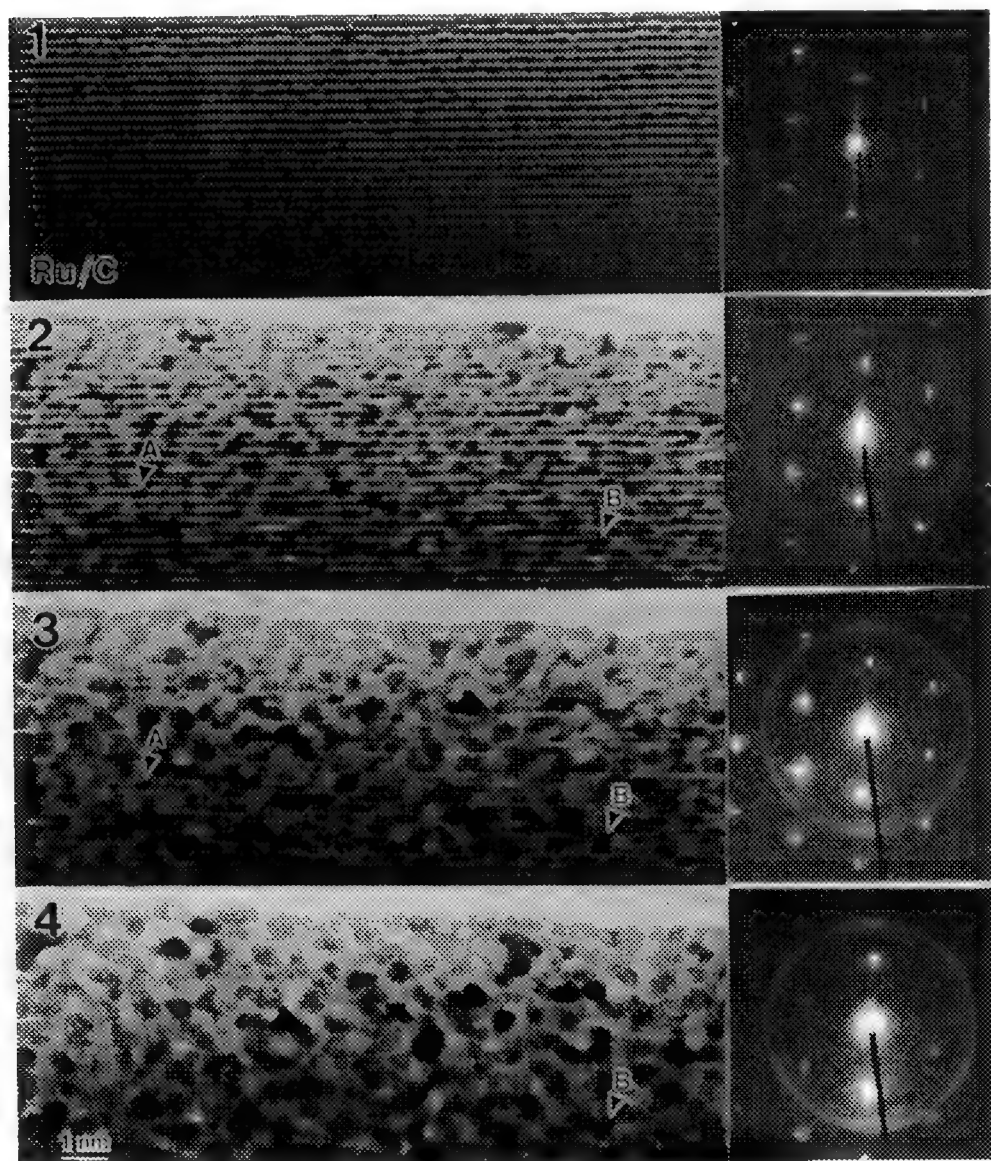
FIG. 1.--Cross-sectional TEM image and diffraction pattern of 2 nm period Ru/C at 423°C.
FIG. 2.--In-situ annealed at 500°C for 10 minutes, showing the Rayleigh instability-like structure.
FIG. 3.--In-situ annealed at 500°C for 25 minutes of same area as in Fig. 2.
FIG. 4.--Same area after in-situ annealed at 500°C for 90 minutes, and cooled to room temperature.

COMPOSITIONAL IMAGING OF Co/Cr MULTILAYER BY HIGH-ANGLE ANNULAR DARK-FIELD MICROSCOPY

J. LIU, Y. CHENG* AND M. B. STEARNS*

Center for Solid State Science, Arizona State University, Tempe, AZ 85287
* Department of Physics, Arizona State University, Tempe, AZ 85287

Magnetic multilayers (ML) have been recently the subject of active research because of their fundamental magnetic behavior (i.e., large magnetoresistance at room temperature and two-dimensional superconductivity etc.) and also because of their potential application as media for perpendicular magnetic recording and information storage. It has been found that the magnetic properties of these ML films strongly depends on their layered structure.[1] Thus it is essential to correlate the growth conditions with the structural, compositional and magnetic properties of the ML films. High resolution electron microscopy (HREM) has proved very useful for providing information about the detailed microstructures of the ML on an atomic scale. But the interpretation of HREM images in terms of chemical modulation across ML films is difficult due to the presence of strong diffraction and phase contrast in HREM images. In this study we have used high-angle annular dark-field (HAADF) microscopy technique to extract compositional information of the e-beam evaporated Co/Cr ML films and to correlate these results with that obtained by HREM.

Co/Cr ML films were fabricated by e-beam evaporation. The detailed description of the fabrication process -es has been reported previously.[1] The Co/Cr ML sample studied here has a bilayer thickness of 7.6 nm Cross-sectional specimens were prepared for electron microscopy observations and the ML were imaged edge-on along the [110] direction of the Si substrate. The HAADF images were obtained with a HB-5 STEM instrument from VG Microscopes, Ld. The microscope has been modified by the addition of an ultra-high resolution pole piece ($C_s = 0.8$ mm). All the HAADF images were acquired digitally.

The inner cut-off angle of the annular detector in a STEM instrument is an important parameter for determining the contrast of ADF images. This is especially true for the study of polycrystalline ML films.[2] Figure 1 shows two ADF images of the same area of a Co/Cr ML sample. These images were obtained with low (1a, ~ 30 mrad) and high (1b, ~100 mrad) inner cut-off angles, respectively. Figure 1a clearly demonstrates that diffraction contrast of Co and Cr crystallites dominates in the low-angle ADF image and the contrast due to compositional variations is obscured. However, this diffraction contrast is suppressed and the atomic number contrast is retrieved in the HAADF image (Figure 1b), clearly revealing the compositional variations across the ML film. Studies have shown that for HAADF imaging of polycrystalline ML films, an inner cut-off angle about 100 mrad or higher has to be used to ensure high atomic-number sensitivity and minimum diffraction contrast.[2] Figure 1b also shows that the compositional roughness of the layers increases with the distance from the substrate. In some regions the Co and Cr atoms appear to be completely intermixed, causing the long range chemical order along the individual layers to be smeared out.

Figure 2 shows a HREM image of the same ML sample. The HREM image reveals that the Co and Cr layers consist of small textured crystallites. In some regions epitaxy between adjacent Co and Cr layers is seen to be present. X-ray analysis showed that coherence existed over ~ 4 to 5 layers.[1] Figure 3 shows a high magnification HAADF image of a relatively good region of the Co/Cr ML film. In order to obtain a quantitative measurement of the compositional profile of the ML film an intensity line scan across several ML layers was obtained, as shown in Figure 4a. This intensity line scan indicates that the HAADF intensity increases linearly with the sample thickness. The intensity ratio between Co and Cr layers is estimated to be ~ 1.25, approaching $(Z_{Co}/Z_{Cr})^2 = 1.27$. After correcting for the thickness effect on the image contrast the compositional profile across the ML layers can be clearly seen in Figure 4b. The interlayer thicknesses seem to be symmetric in this ML system in agreement with the conclusion from a computer analysis of the X-ray spectra.[1,3]

References
1. M. B. Stearns et al., Phys. Rev. B40 (1989) 8256.
2. J. Liu and J. M. Cowley, Ultramicrosc. 37 (1991) 50; J. Liu et al., Ultramicrosc., in press.
3. This work was supported by Shell Development Company and LLNL through the Department of Energy contract No. W-7405-Eng-48 and made use of the ASU Facility for HREM, supported by NSF via grant DMR-8913384.
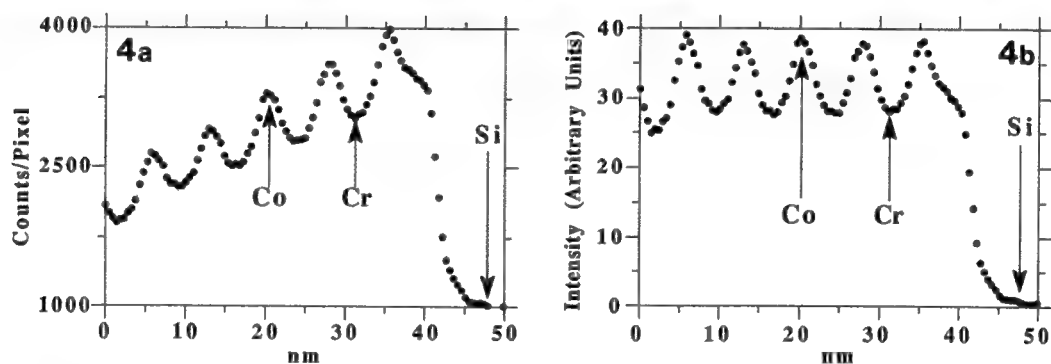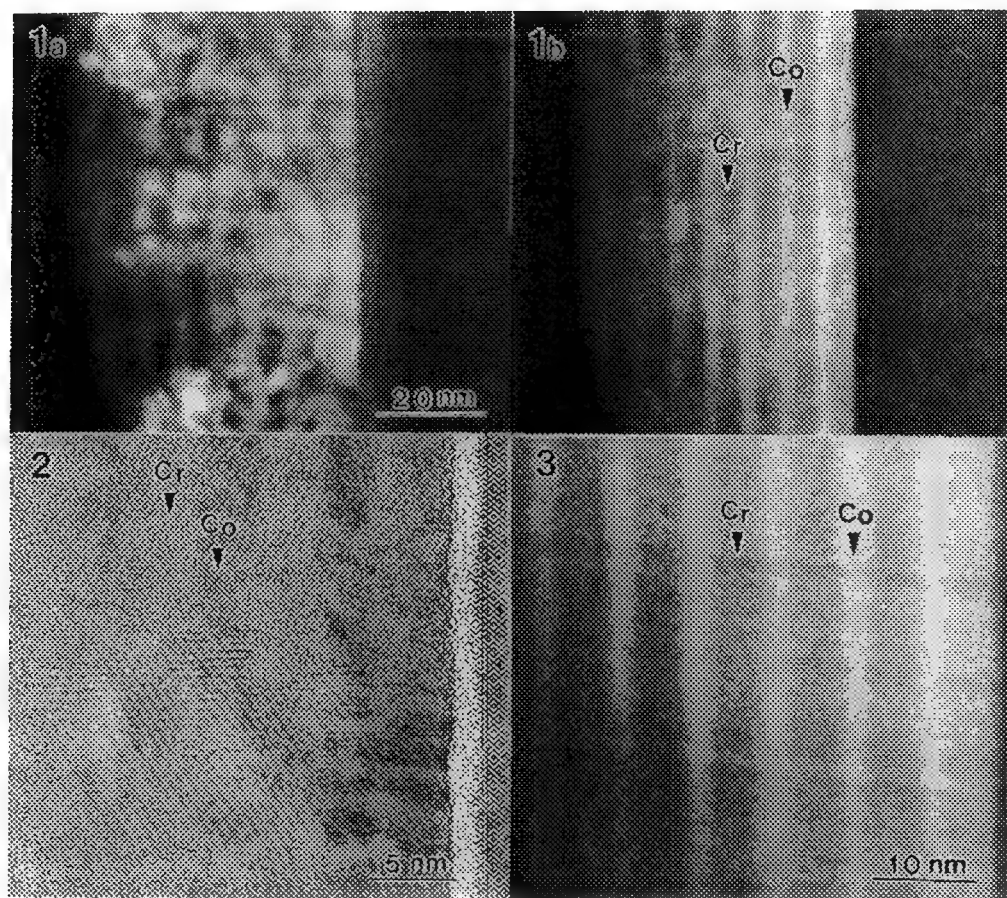
FIG. 1 -- ADF image of Co/Cr ML film obtained with low (a) and high (b) inner detection angles.

FIG. 2 -- HREM image of Co/Cr ML film revealing epitaxial growth in some regions.

FIG. 3 -- High magnification HAADF image of Co/Cr ML film showing atomic number contrast between Co and Cr layers (Z_{Co} = 27, Z_{Cr} = 24)

FIG.4 -- HAADF intensity line scans revealing compositional profile across Co/Cr ML layers.

DEFORMATION EFFECTS ON TRANSGRANULAR CARBIDE PRECIPITATION IN 304 STAINLESS STEELS

A.H. Advani,[+] L.E. Murr, D.J. Matlock, W.W. Fisher, P.M. Tarin, R.L. Miller, C. Ramos, R. J. Romero, J.G. Maldonado and C.M. Cedillo

Department of Metallurgical and Materials Engineering and [+]Institute for Manufacturing and Materials Management, University of Texas at El Paso, El Paso, TX 79968

Plastic deformation is a key variable producing accelerated intergranular (IG) carbide precipitation and chromium-depletion (sensitization) development in stainless steels.[1] Deformation above 20% also produces transgranular (TG) carbides and depletion in the material.[1,2] Research on TG carbides in SS is, however, limited and has indicated that the precipitation is site-specific preferring twin-fault intersections in 316 SS[1] versus deformation-induced martensite and martensite lath-boundaries in 304 SS.[2] Evidences indicating the relation between martensite and carbides were, however, sketchy.[2] The objective of this work was to fundamentally understand the relationship between TG carbides and strain-induced martensite in 304 SS. Since strain-induced martensite forms at twin-fault intersections in 304 SS and the crystallography of the transformation is well understood,[3] we believed that it could be key in understanding mechanisms of carbides and sensitization in SS. A 0.051% C, 304 SS deformed to ~33% engineering strain (40% true strain) and heat treated at 670°C/0.1-10h was used for the research. The study was carried out on a Hitachi H-8000 STEM at 200 kV.

Transgranular carbides were observed to form at deformation regions in 304 SS. Particularly, twin-fault intersections were favored sites for the carbides (Figures 1a,b), as has been noted in 316 SS. However, an analysis of intersections where TG carbides formed did not show the presence of any strain-induced martensite at the locations, which implies that there is no relation between the phases in 304 SS unlike that described previously.[2] This is supported by the fact that TG carbides form at twin-fault intersections in 316 SS, even though no strain-induced martensite forms in 316 SS.[1]

Localized regions consisting of mixed lath (thermal) martensite and recrystallized austenite were also observed to form in the (strained+670°C) treated materials, possibly due to the thermal treatment. Carbides were noted to form on lath martensite or recrystallized austenite boundaries present within these regions, which may refer to the observations reported previously.[2] An example illustration of carbides within a predominantly recrystallized austenitic region shows lattice images of carbides on several boundaries. Detailed views indicate the presence of dislocations within the carbides and at the carbide-matrix interface, and changes in the carbide lattice orientation across a boundary. These may be indicators of key mechanisms of carbide nucleation on grain boundaries in SS. We will focus our future research on a better understanding of the formation of lath (thermal) martensite and recrystallized austenite in 304 SS, and carbide precipitation within these phases in the material.[4]

1. A.H. Advani, L.E. Murr, D.G. Atteridge and R. Chelakara, Metall. Trans., **22A** (1991) 2917.
2. C.L. Briant and A.M. Ritter, Metall. Trans.,**11A** (1980) 2009.
3. L.E. Murr, K.P. Staudhammer, and S.S. Hecker, Metall. Trans., **13A** (1982) 627.
4. Funded by NSF(RIMI) grant HRD-9105065, EPA coop. agreement CR-818296-01-0 through the SW Ctr. for Envir. Res. and Policy, and by DOD grant DN-009, Directorate of Stockpile Mgmt. and GSA grant PF90-018 administered by U.T.El Paso's Institute for Manufacturing and Mater. Mgmt.
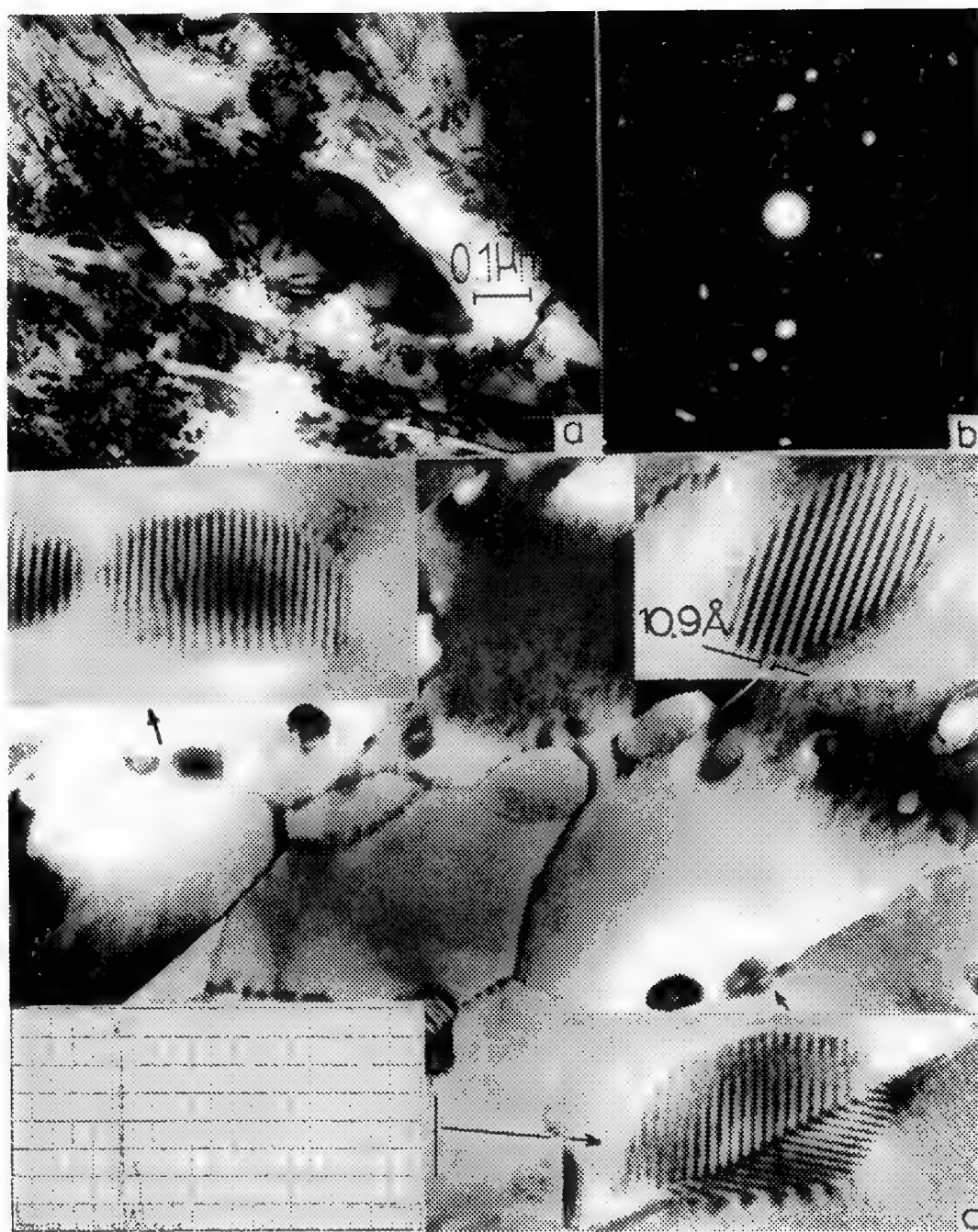
Figure 1. Illustration of carbide formation at twin-fault intersections (a,b), and lattice images and EDS spectra from carbides along (predominantly) recrystallized austenite boundaries (c) in 304 SS.

PROBING MOLECULAR ORGANIZATION OF LIQUID CRYSTALLINE POLYMERS BY ELECTRON AND OTHER MICROSCOPIES

Samuel I. Stupp

Department of Materials Science and Engineering, University of Illinois at Urbana-Champaign, Illinois 61801

Over the past decade many polymers have been synthesized which organize into nematic and smectic mesophases analogous but not identical to those formed by small molecules. It is clear that the phenomenon of liquid crystallinity in polymers is not limited to chains of a specific chemical structure and that self ordering behavior of macromolecules in states of intermediate order is in fact not uncommon. The study of self ordering behavior of polymers into orientationally ordered phases or one dimensional density waves will make important scientific as well as technological contributions. This lecture will discuss a number of problems pertaining to molecular organization in liquid crystalline phases of polymers in which the use of microscopies has played a critical role. The approach is therefore to present the work from a user's perspective emphasizing molecular aspects rather than the techniques themselves. In the first part of the lecture two problems studied by polarized optical microscopy will be discussed. The first one deals with high temperature phase separation of chemically aperiodic polymers into nematic and isotropic phases, forming distinct biphasic patterns. This work has been extremely helpful in understanding the role of molecular flexibility distributions in microphase separation of nematic polymers. Another problem to be discussed is related to surface anchoring of liquid crystalline comb polymers on flat and curved surfaces. The second half of the lecture will discuss new materials developed in our laboratory which may be appropriately described as two dimensional polymers. These supramolecules have the shape of molecular sheets and order macroscopically into smectic phases. On this subject the use of electron microscopy and diffraction has been extremely important in measuring directly the dimensions of these molecular objects and also identifying their self assembly into single crystals. Atomic force microscopy has also made a modest contribution to our understanding of these new materials. A large number of derivatives and model compounds of the two dimensional polymers were studied in our laboratory by electron microscopy and the lecture will describe how this work has helped us understand the structural basis of their synthesis.

References

1. J. S. Moore and S. I. Stupp: Synthesis of a Chemically Ordered Liquid Crystal Polymer. Macromolecules, 21, 1217 (1988).
2. P. G. Martin and S. I. Stupp: The Contrasting Behavior of Chemically Ordered vs. Chemically Disordered Liquid Crystal Polymers. Macromolecules, 21, 1222 (1988).
3. S. I. Stupp, J. S. Moore and P. G. Martin: Chemical Disorder and Phase Separation: A Study of Two Liquid Crystal Polymers. Macromolecules, 21, 1228 (1988).
4. S. I. Stupp, J. S. Moore, P. G. Martin, and J. Wu: Molecular Organization in Nematic Polymers. 1. Biphasic Structures vs. the Nematic Phase, Macromolecules, 24, 6399 (1991).
5. S. I. Stupp, J. S. Moore, and F. Chen: Molecular Organization in Nematic Polymers. 2. Evolution of the Mesophase, Macromolecules, 24, 6408 (1991).
6. S. I. Stupp, S. Son, H. C. Lin, L. S. Li: Two-Dimensional Polymers, ACS Polymer Preprints, 32, 2 (1991).
7. This research was supported by a grant from the Department of Energy, DEFG02-91ER45439 and by a grant from the National Science Foundation NSF-DMR 89-20538, obtained through the Materials Research Laboratory at the University of Illinois.

USE OF LIGHT MICROSCOPY IN THE QUALITATIVE AND QUANTITATIVE STUDY OF LIQUID CRYSTALLINE ORDER

Christopher Viney

Molecular Bioengineering Program, Center for Bioengineering WD-12, University of Washington, Seattle, WA 98195

Light microscopy is a convenient technique for characterizing molecular order in fluid liquid crystalline materials. Microstructures can usually be observed under the actual conditions that promote the formation of liquid crystalline phases, whether or not a solvent is required, and at temperatures that can range from the boiling point of nitrogen to 600°C. It is relatively easy to produce specimens that are sufficiently thin and flat, simply by confining a droplet between glass cover slides. Specimens do not need to be conducting, and they do not have to be maintained in a vacuum. Drybox or other controlled environmental conditions can be maintained in a sealed chamber equipped with transparent windows; some heating/ freezing stages can be used for this purpose. It is relatively easy to construct a modified stage so that the generation and relaxation of global molecular order can be observed while specimens are being sheared, simulating flow conditions that exist during processing.[1] Also, light only rarely affects the chemical composition or molecular weight distribution of the sample. Because little or no processing is required after collecting the sample, one can be confident that biologically derived materials will reveal many of their *in vivo* structural characteristics, even though microscopy is performed *in vitro*.

Microscopic observation in transmission between crossed polars has a long-established qualitative use in identifying and classifying liquid crystalline phases, where observed microstructures (textures) are compared to those in an "atlas" of reference compounds. Applied to a series of compounds with known differences in molecular structure, this type of study can be used to test theoretical models that attempt to predict the molecular and environmental conditions that stabilize liquid crystalline phases. There is continuing controversy as to whether excluded volume effects (entropic) or anisotropic attractive forces (enthalpic) exert the predominant stabilizing influence.[2] The thermotropic phases formed by a series of rigid polytolans $[- (phenyl)_{1 \, or \, 2} - C \equiv C -]$ having different axial ratios are being investigated to establish their sensitivity to changes in excluded volume effects,[3] and the *para- meta-* and *ortho*-fluorinated isomers of the thermotropic polytolan $[F - phenyl - C \equiv C - (phenyl)_2 - C \equiv C - phenyl - F]$ are being used to investigate the effect of changes in anisotropic charge distribution (Figures 1 and 2).

The forces responsible for ordering liquid crystalline molecules produce co-operative alignment that persists over optically resolvable distances. This justifies extrapolation of director topologies characterized at the micron scale, to pictures of order at the molecular scale. For example, the presence of singularities associated with two or (unusually, as in Figure 3) six extinction bands is only compatible with nematic order. The study of textures formed by spider silk secretions offers another example of this type of extrapolation.[4] Silk secretions exhibit biphasic (isotropic+nematic) behavior over only a narrow concentration range (Figure 4), which is a characteristic of athermal lyotropic systems. This observation, together with the fact that the silk secretions only become a single phase nematic at concentrations above 26 vol.%, suggests that the constituent rods have an axial ratio of ~30. This value is inconsistent with the known secondary structure of the molecules, which are not rod-like and do not appear to contain any appropriately rod-like sequences. Also, the variance in scale of the microstructures of different silk secretions are inconsistent with the rods being individual molecules or segments. It appears instead that the rod-like characteristics arise at the quaternary level of structure, therefore depending on the aggregation of molecules. Non-covalent association of protein molecules into rodlike structures occurs elsewhere in nature, for example the "polymerization" of deoxygenated haemoglobin S in cases of sickle cell anemia.

Characterization of liquid crystalline structure by light microscopy is not restricted to observations made with the specimen between crossed polars. Observations in plane polarized light (analyzer removed) and between crossed circular polarizers can be used to confirm the orientation of molecules, as distinct from the orientation of the optical indicatrix.[5] Rheinberg illumination enables a direct and unambiguous determination of the concentration of disclinations in a texture;[6] without compromising resolution, this technique maximizes contrast from the defects themselves.

264

It is anticipated that confocal microscopy will be useful for studying disclination topologies in bulk material, away from anchoring sites at the glass confining surfaces. Attempts to deduce the bulk microstructure from observations between crossed polars are flawed, because light arrives at the objective with a polarization state that is not a simple consequence of interactions occurring only at the in-focus specimen plane.[7]

References

1. W.S. Putnam and C. Viney, Mol. Cryst. Liq. Cryst. 199 (1991) 189.
2. N.V. Madhusudana, in B. Bahadur, Ed., Liquid Crystals, Singapore: World Scientific (1990) Ch.2.
3. C. Viney et al., Mol. Cryst. Liq. Cryst. Lett. 7 (1990) 147.
4. C. Viney, in S.T. Case, Ed., Structure, Cellular Synthesis and Assembly of Biopolymers, Heidelberg: Springer-Verlag (1992) Ch.9.
5. A.H. Windle et al., Faraday Discuss. Chem. Soc. 79 (1985) 55.
6. C.M. Dannels et al., Mol. Cryst. Liq. Cryst. 198 (1991) 341.
7. Tolan compounds were synthesized by Dr R.J. Twieg, IBM Almaden Research Center. Support from ACS-PRF (No. 21300-G7), US Army RD&E Center (Natick, MA) and the Washington Technology Center is gratefully acknowledged.
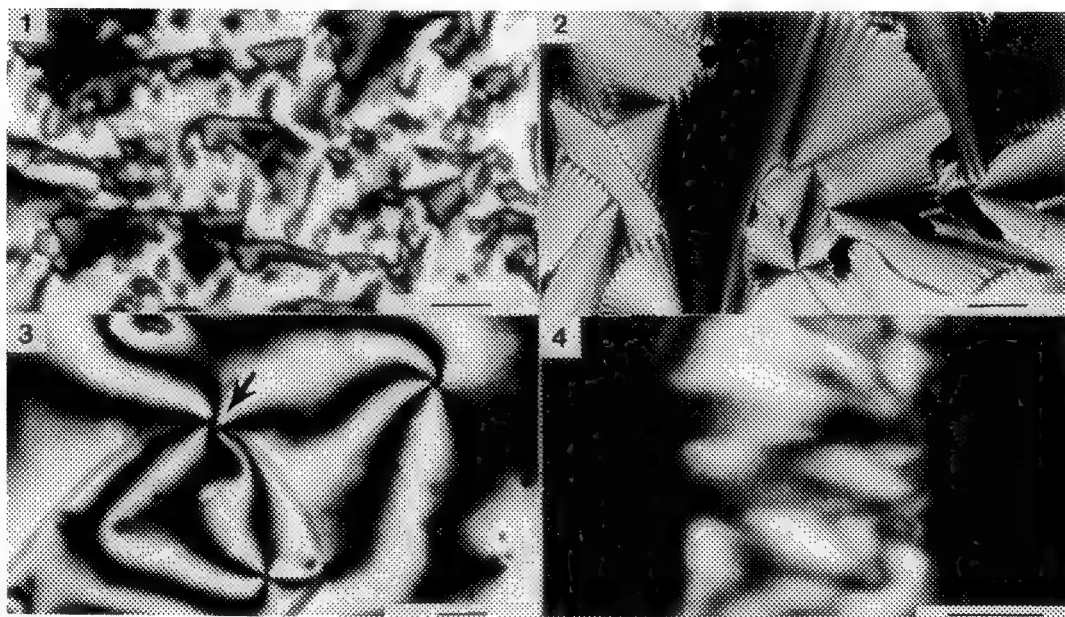
FIG. 1.--*para*-fluorinated isomer of [F - phenyl - C $\equiv$ C - (phenyl)$_2$ - C $\equiv$ C - phenyl - F] is nematic. Crossed polars. Bar = 20 μm.

FIG. 2.--*meta*-fluorinated isomer of [F - phenyl - C $\equiv$ C - (phenyl)$_2$ - C $\equiv$ C - phenyl - F] is smectic. Crossed polars. Bar = 20 μm.

FIG. 3.--Disclination of strength $\pm 3/2$ (arrow) in texture of a thermotropic nematic polytolan. Crossed polars. Bar = 10 μm.

FIG. 4.--Droplet of silk secretion drying between glass slide and cover slip. Concentration increases from left to right. Birefringent region is nematic. Right hand boundary of nematic region is edge of droplet. Isotropic center of droplet lies to left of nematic region, with no evidence of intervening biphasic material. Crossed polars. Bar = 500 μm.

265

LOW–VOLTAGE HIGH–RESOLUTION SEM INVESTIGATIONS OF NOVEL MACROMOLECULAR LIQUID CRYSTALS

W. W. Adams,* D. L. Vezie,** and E. L. Thomas**

*Materials Directorate, Wright Laboratory, Wright-Patterson Air Force Base, OH 45433
**Department of Materials Science and Engineering, M.I.T., Cambridge, MA 02139

The ability to visualize detailed 3-dimensional surface topology with SEM at low voltage and high resolution holds profound promise for analyzing liquid crystal textures, both in polymers and other macromolecular forms. Director textures, domain boundaries, and defects such as inversion walls, disclinations and dislocations can now be easily visualized with this technique. Studies concerning the effects of shear flow and magnetic fields on these defects are currently under way.

Resolution of 4.0 nm at 1.0 keV is now possible with commercial SEM's, which incorporate the latest advances in lens design optimized for low voltage operation, and use high brightness, low energy spread field emission electron guns. The low energy spread of the field emission gun reduces chromatic aberration effects and facilitates successful operation at low keV. Low voltage operation provides dramatically improved image contrast due to the smaller beam/sample interaction volume and also greatly reduces sample charging artifacts.[1] By operating at near crossover conditions, the need for coating nonconducting specimens with a conducting layer of metal or carbon is greatly reduced or eliminated.[2]

Two other advancements in SEM related technology also contribute to new capabilities in analyzing liquid crystal textures: the high resolution sputter coater, which allows the deposition of continuous metal films as thin as 1.0 nm (aids in determining shapes of features at sizes below the secondary electron escape depth), and the frame grabber, a digital image acquisition and analysis system (facilitates fast acquisition of images at high magnification and minimizes scan rate effects in sample charging). We have used the Hitachi S-900 high resolution FEG SEM at low voltage to study carbon and other high performance fibers, thermoplastic films, and single crystals of polyethylene.[3,4] Recently, we have been investigating director texture topologies and defects in liquid crystalline macromolecules including thermotropic nematic polyesters and siloxane based cholesterics.

Figures 1-3 show a thermotropic nematic polyester prepared by the lamellar decoration and methyl amine etch technique described by Hudson, et al.[5] Samples were imaged at 1.0 keV with a very light AuPd coating. Figure 1 shows a s = +1/2 disclination, whereas Figure 2 shows a s = -1/2 disclination. The contrast mechanism in these micrographs is surface topography due to edge effects. The bright regions are the edges of the crystalline lamellae that remain after the sample is etched. The insets in these figures show the molecular orientation or "director" texture and give the topological strength of the disclinations. The director texture is orthogonal to the lamellar texture seen in the micrographs because the polymer chains are orthogonal to the lamellar crystals. Figure 3 is an image of three inversion walls. On each side of an inversion wall the polymer molecules are rotated 180° to each other. Through the use of stereo imaging we have discovered that these inversion walls are actually 3-dimensional, rather than 2-dimensional as always modeled. The inversion walls come out of the plane of the paper, much like the crests of small waves. Figure 4 shows a room temperature fracture surface of a glassy cholesteric siloxane oligomer.[6] Sample was imaged at 0.8 keV with a very light coating of AuPd. Shown is a domain boundary from upper left to lower right. Edge dislocations can be seen within the domain. The fracture surface texture within the domain boundary has a sinusoidal form and is a result of the continuous rotation and translation of the director in the cholesteric phase. The brighter regions are the higher "peaks" of the sinusoidal fracture and the darker regions are the lower "valleys". Presumably, the director is parallel to the tensile axis at the sine wave peaks and perpendicular to the tensile axis at the sine wave valleys. The pitch of this cholesteric sample corresponds to two full periods of the sinusoidal fracture.[7]

References
1. D. C. Joy, Hitachi Instument News, 16 EM Ed., 3, July 1989.
2. S. J. Krause et al, EMSA Proc., 47, 336, (1989).
3. D. L. Vezie and W. W. Adams, J. Mat. Sci. Let., 9, 883, (1990).
4. W. W. Adams and D. L. Vezie, EMSA Proc., 49, 1040, (1991).
5. S.D. Hudson, D.L. Vezie, and E.L. Thomas, Makromol. Chem., Rapid Commun., 11, 657,(1990).
6. T. Bunning, Ph.D. Thesis, University of Connecticut, 1992.
7. Thanks to Steven Hudson, Kevin Schaffer, and Tim Bunning for samples.
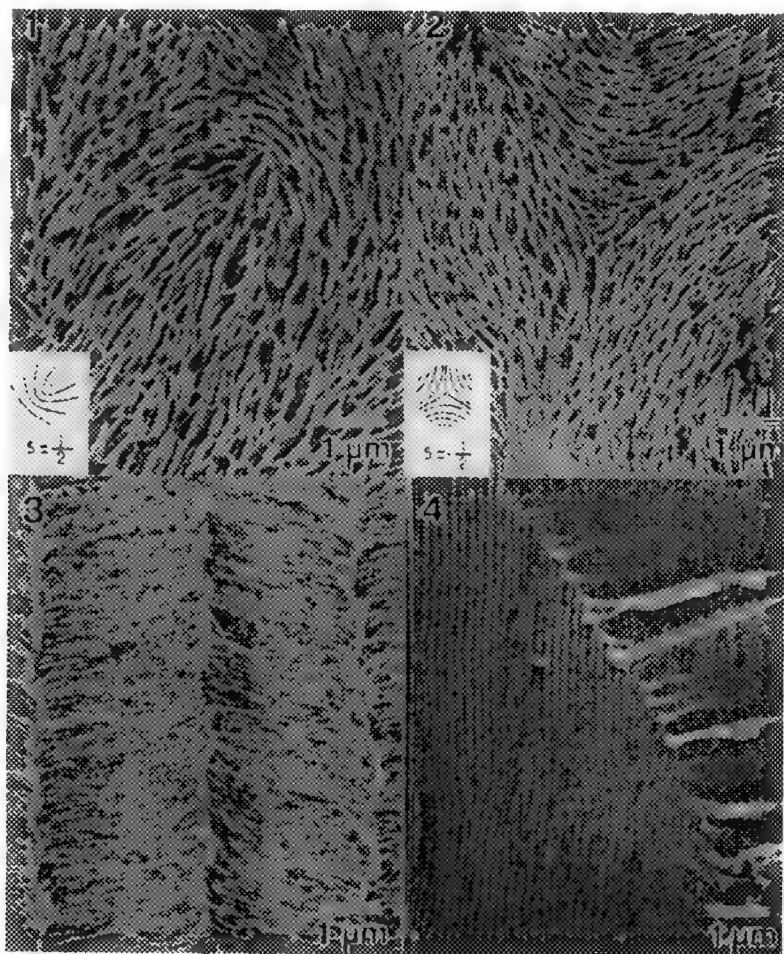
FIG. 1.--Thermotropic nematic polyester showing a disclination of s=+1/2 topological strength.
FIG. 2.--Thermotropic nematic polyester showing a disclination of s=-1/2 topological strength.
FIG. 3.--Inversion walls in a thermotropic nematic polyester. The inversion walls come out of the plane of the paper.
FIG. 4.--Domain boundary in a glassy cholesteric siloxane oligomer. Fracture within the boundary has a sinusoidal form due to the constant rotation and translation of the director.

ATTRACTIVE MODE FORCE MICROSCOPY OF CHIRAL LIQUID CRYSTAL SURFACES

B. D. Terris,[*] R. J. Twieg,[*] C. Nguyen,[*] G. Sigaud,[**] and H. T. Nguyen[**]

[*] Almaden Research Center, 650 Harry Road, San Jose, CA 95120
[**] CRPP/CRNS, Ave. A. Scheitzer, F-33600 Pessac, France

We have used a force microscope in the attractive, or noncontact, mode to image a variety of surfaces. In this mode, the microscope tip is oscillated near its resonant frequency and shifts in this frequency due to changes in the surface-tip force gradient are detected. We have used this technique in a variety of applications to polymers, including electrostatic charging,[1,2] phase separation of ionomer surfaces,[3] and crazing of glassy films.[4]

Most recently, we have applied the force microscope to imaging the free surfaces of chiral liquid crystal films. The compounds used (Table 1) have been chosen for their polymorphic variety of fluid mesophases, all of which exist within the temperature control range of our force microscope. These are all chiral compounds primarily synthesized for their ability to form helicoidal smectic C phases (S_C^*). The typical polymorphism includes a S_C^* phase, a smectic A (S_A) phase, a cholesteric (N*) phase and/or an isotropic liquid (I).

Typical force microscope profiles for compound II, after melting on a clean glass substrate, are shown in figure 1a-d. As it was difficult to scan above the surface relying solely on the van der Waals force, an additional force was provided by applying a small voltage between the tip and sample. We believe the tip was not in contact with the liquid surface as the oscillation amplitude was not dramatically reduced as the tip was brought to its scanning height, as would be expected if the tip entered the liquid.

In the isotropic phase the surface appears uniform (Fig. 1a) and this "flat" surface is preserved upon cooling into the N* phase. The topography changes suddenly in the vicinity of the N*-S_A phase transition (or I-S_A in compound IV). An undulation develops on the surface (Figs. 1b, c), over domains often larger than the area scanned, with different orientations from one domain to the next. The peak-to-peak depth of the corrugation is ca. 5 to 50 nm and the period ranges from 0.5 to 5 μm. As the sample is cooled the period increases and the regular pattern vanishes. No regular topography is observed at lower temperature in the S_A (Fig. 1d) and in the S_C^* phases, although the large surface depressions remain and become farther apart. This corrugation of the S_A surface is detected in all the compounds, although with more difficulty when the temperature range of stability of the stripes is smaller. However a thermal variation could be recorded with sufficient accuracy on compound II which shows that amplitude and in-plane modulation do not vary independently. Upon cooling over a 3 C range the corrugation grows deeper (from 2.5 to 33 nm) and spacing larger (0.63 to 4 μm), but their ratio remains approximately constant at $\cong 6 \times 10^{-3}$.

Since all the materials above are chiral, we propose that the regular stripes result from the pitch of a helicoidal structure, as is the case in some N* and S_C^* textures. However, from the observations on compound IV, which is not N*, we must conclude that this texture occurs in the S_A phase and that the S_A phase in all these compounds has a chiral character.[5] We propose that this phenomenon could be an example of the deformation of a liquid crystalline surface driven by competing alignment forces. This was initially expected by De Gennes for a nematic under a magnetic field [6] and later extended to cholesterics under an homeotropic alignment by Bouligand.[7] The measured value of the depth-to-period ratio is consistent with De Gennes' theoretical estimate.

References

1. B. D. Terris et al., Phys. Rev. Lett. (1989) 63, 2669.
2. F. Saurenbach and B. D. Terris, Trans. of the IEEE-IAS, in press.
3. F. Saurenbach et al., Langmuir, in press.
4. A. C.-M. Yang et al., Macromol. (1991) 24, 6800.
5. J. W. Goodby et al., Nature (1989) 337, 449; J. W. Goodby, J. Am. Chem. Soc. (1989) 111, 8119.
6. P. G. DeGennes, Solid State Commun. (1970) 8, 213.
7. Y. Bouligand, J. Phys. (Paris), (1974) 35, 215.

TABLE 1.--Compounds with optical transition temperatures. Ph: phenyl ring, Me: methyl group

$H(CH_2)_{11}O - Ph - COS - Ph - COO - C{*}HMe - COO(CH_2)_4H$ $\quad$ I
$S_{C^*} - 33\ ^oC \rightarrow S_A - 45\ ^oC \rightarrow N^* - 50\ ^oC \rightarrow I.$
$H(CH_2)_{11}O - Ph - COS - Ph - COO - C{*}HMe - COOCHMe_2$ $\quad$ II
$S_{C^*} - 35\ ^oC \rightarrow S_A - 47\ ^oC \rightarrow N^* - 52\ ^oC \rightarrow I.$
$H(CH_2)_{10}O - Ph - COS - Ph - OOC - C{*}HCl - CHMe_2$ $\quad$ III $\qquad$ F
$S_{C^*} - 48.1\ ^oC \rightarrow S_A - 51.5\ ^oC \rightarrow N^* - 53.6\ ^oC \rightarrow I.$
$H(CH_2)_{18}O - Ph - CH=CH - COO - Ph - COO - C{*}HMe - (CH_2)_6H$ $\quad$ IV
$S_{C^*} - 54\ ^oC \rightarrow S_A - 57\ ^oC \rightarrow I.$
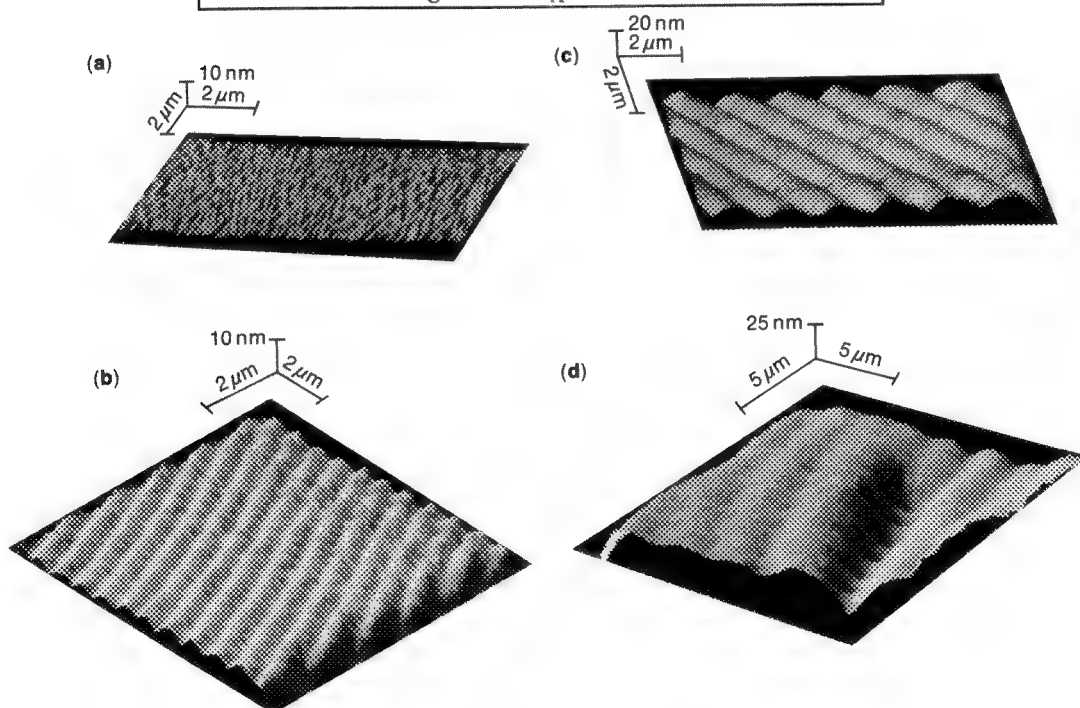
FIG 1.--Force micrographs of compound II in (a) I or N^*, (b)-(c) S_A, (d) S_A near S_C^*

DIMENSIONALITY OF HEXATIC MELTING IN LIQUID CRYSTALS BY IN SITU ELECTRON DIFFRACTION

S.W. Hui*, M. Cheng#, J.T. Ho# and R. Pindak+

*Biophysics Department, Roswell Park Memorial Institute, Buffalo, NY 14263, #Physics Department, State University of New York at Buffalo, Buffalo, NY 14260, and +AT&T Bell Laboratory, Murray Hill, NJ 07974

The theory of melting in two dimensions indicates that it is very different from the melting in three dimensions. An intermediate hexatic phase, with long range orientational but short range translational order, is proposed to exist between two dimensional solid and fluid phases[1]. Because the long range order is limited experimentally by the domain or "grain" size, which is expected to be of sub-millimeter size, selected area electron diffraction is the method of choice for observing orientational order. Free-standing smectic liquid crystal films prove to be a most attractive system in which to verify this theory[2]. However, multilayered liquid crystal samples are not strictly two dimensional systems because of interlayer interaction, their melting characteristics are expected to deviate from that of two dimensional systems. Furthermore, the outer layers may behave differently from the inner ones due to interfacial tension. We have applied low dose electron diffraction to study the effect of dimensionality, or number of layers, on the melting of multilayer organic liquid crystals.

Smectic liquid crystals of n-heptyl-4'-n-pentyloxybiphenyl-4-carboxate (750BC), and mixtures of 25 wt.% of 4-propionyl-trans-(4-n-pentyl)cyclohexane carboxylate (PP5CC) in n-hexyl-4'-n-pentyloxybiphenyl-4-carboxylate (650BC) were used. Free-standing films were formed across a 400 μm diameter hole on an aluminum sample holder. The film thickness was measured by optical reflectance. These free standing films were stable at 30 Torr of pressure in nitrogen, but were not stable in vacuum. Therefore, a differentially-pump environmental stage[3] was used to protect the specimen from the vacuum of the electron microscope. The temperature of the entire stage was regulated to within 0.1°. The electron beam current was limited by a 5 μm second condenser aperture to about 0.1 e/Å^2/sec. The convergence was sufficient to achieve a resolution of 0.01 Å^{-1} on the diffraction plane. A dose of 0.5 e/Å^2 was needed for a typical diffraction recording on Kodak DEF-5 x-ray film.

Electron diffraction patterns of 2 to 6 layers of a mixture of 25 wt% of PP5CC in 650BC in the hexatic-B (Hex-B) phase at 45°C are recorded (Fig. 1), and their azimuthal intensity $I_0\{0.5+C_{6n}\cos[6n(\pi/2 - \chi)]\}$ was analyzed by harmonic scaling[4], by fitting the Fourier coefficients C_{6n} against $C_6^{n+\lambda n(n-1)}$. The parameter λ thus obtained indicated the dimensionality of the system. The value of λ is expected to be 1 for a 2-D system, and 0.3 for a 3-D system. The values were measured to be 1.0, 0.82 and 0.75 for 2, 4 and 6 layer films at 45° respectively, and increased slowly with temperature, until reaching the Hex-B to Smectic-A phase transition of 48.5°, when the pattern became azimuthally isotropic, and the translational correlation length was reduced from about 110 Å to about 20 Å. The proximity of λ to the value of unity for the 2-layer film indicates that the 2-layer film behaves like a true 2-D system. The general decrease of λ for thicker films shows an apparent departure from a 2-D behavior even for a 4- or 6-layer film.

The freezing of thin films of 750BC involved a two step process. The outer layers underwent the Hex-B to Crystal-E (Cr-E) transition at a higher temperature than that for the inner layers. At a lower temperature, the inner layers then transformed into the Cr-E phase. Electron and x-ray diffraction results agreed with calorimetric measurements[5]. An electron diffraction pattern below the surface Cr-E transition temperature (Fig. 2) shows 2 sets of orthorhombic spot patterns of the upper and lower layers superimposing on the hexatic arc patterns of the inner layers. The superposition of these diffraction patterns were global and independent of the size of selected diffraction area, indicating that lateral phase separation were unlikely. These two sets of orthorhombic Cr-E patterns were offset by 2-3° with respect to the director of the Hex-B pattern, to minimize the strain energy of incommensurate lattice. The orientational order measurements by electron diffraction provide valuable information on the characteristics of 2-D melting.

References

1. B.I. Halperin and D.R. Nelson, Phys. Rev. Lett. (1978)41, 121.
2. M. Cheng et al., Phys. Rev. Lett. (1987)59, 1112.
3. S.W. Hui et al., J. Phys. E. (1976)9, 69.
4. A. Aharony and M. Kardar, Phys. Rev. Lett. (1988)61, 2855.
5. R. Geer et al., Phys. Rev. Lett. (1991)66, 1322.
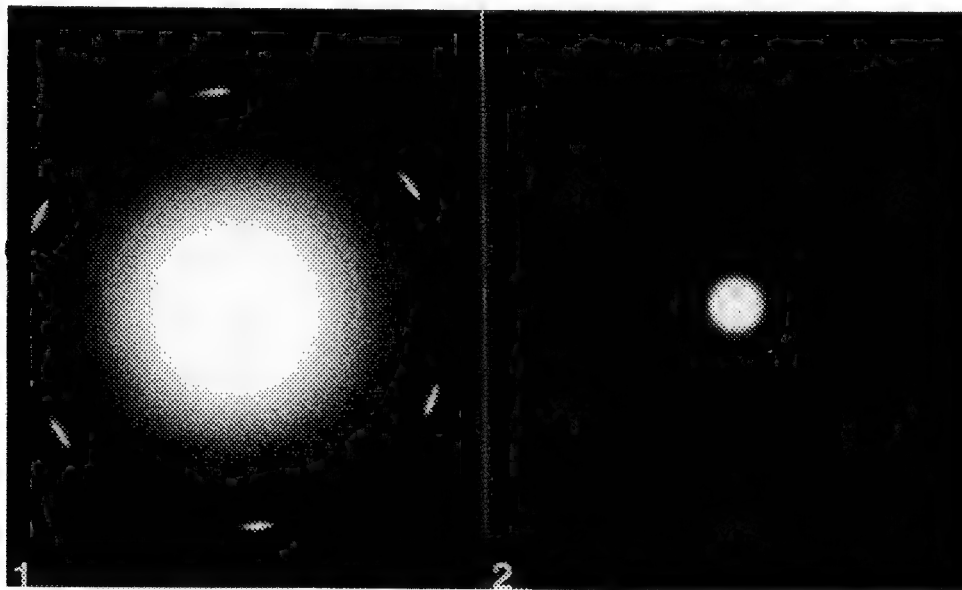
Fig. 1.--Electron diffraction pattern of a thin film of 6 layers of a mixture of 25 wt% of PP5CC in 650BC in the Hex-B phase at 45°C.
Fig. 2.--Electron diffraction pattern of a thin film of 6 layers of 750BC liquid crystal at 64.2°C, showing the twin sets of Cr-E phase diffraction of surface layers and a set of Hex-B phase diffraction of the inner layers.

THE CHIRAL SMECTIC H LIQUID CRYSTALLINE STRUCTURE OF A COMB-SHAPED SIDE-CHAIN POLYMER

L. S. Li and S. I. Stupp

Department of Materials Science and Engineering and Materials Research Laboratory, University of Illinois at Urbana-Champaign, Urbana, IL 61801

The polymer investigated is a comb-shaped polymer with long oligomeric side chains containing a chiral center. The chiral center contains the strongly dipolar nitrile group bound to the aliphatic spacer between aryl units in a stereo-ordered fashion. The chemical structure of the comb polymer is shown below:[1]
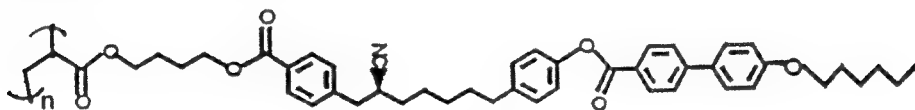
This polymer exhibits two types of liquid crystalline structures at room temperature. When films are prepared by solution casting at 95°C or higher temperatures, films exhibit a chiral smectic E phase[2]. When films are prepared at 77°C using the same technique, films consist of chiral smectic H phase. The morphology and structure of the chiral smectic H phase were studied using a Philips CM-12 electron microscope at 120 KV. It is interesting to see that films prepared at 77°C exhibit a very different morphology from those consisting of chiral smectic E phase. There are many "dome-like" regions in the film which are composed of layers tilted with respect to film's normal(Fig.1). In the thinnest part of the "dome" one observes domains (Fig.2), in which the tilted layers are stacked parallel to each other with the normal to the layer planes in a fixed direction. Different domains of those layer clusters are observed. However, curved layers and stacking faults can also be seen in Figs. 1 and 2. Fig.3 is a selected area electron diffraction pattern taken from a domain of the thinnest part of the "dome". This pattern is similar to that of the chiral smectic E phase (a*b* reciprocal lattice planes). This indicates that there are also orthogonal a*b* lattices perpendicular to the electron beam direction and the c axis (side-chain axis) is parallel to the beam direction. Because the 110 and 200 reflection spots are separated and both of them are distributed with hexagonal symmetry, there must be three different orientations of the orthogonal a*b* reciprocal lattices which are related to each other by rotations of ±60° in each tilted layer. There are many 110 and 200 reflection spots appearing in the electron diffraction pattern and the angle between every two [110]* or every two [200]* is 5.9°. It is therefore possible that the reciprocal lattices in each layer are regularly rotated by 5.9° about the c axis relative to those in the adjacent layer. Fig 4 is a selected area electron diffraction pattern obtained from a tilted sample. This pattern shows not only the 110 and 200 reflections but also 6 small angle reflections, indicating that the period in the normal direction of the tilted layers is very regular and is 51Å. X-ray diffraction results indicate that the period in the side-chain axis direction is 62.6Å and the period in the normal direction of the layers is 51.4 Å. Therefore the side-chain axes are tilted by 34.8° with respect to the normal to the layer planes..The unit cell of the polymer has monoclinic symmetry and its unit cell parameters are,

a=10.06 Å, b=5.35 Å, c=62.6 Å, β=124.8°.

Based on electron microscopy, electron diffraction and x-ray diffraction results the following conclusions can be reached: (1) all the side-chains of the comb polymer are arranged in parallel layers with their axes tilted by 34.8° with respect to the normal to the smectic layer planes and the unit cell of the polymer has monoclinic symmetry, (2) each layer contains three different orientations of the orthogonal ab lattices which are related to one another by rotations of ±60° about

the c axis(the side-chain axis), (3) the orthogonal ab lattices in each layer are regularly rotated about the c axis by 5.9° relative to those in the adjacent layer. These conclusions suggest that the side-chains of the polymer form another type of liquid crystalline structure which may be referred to as a twisted chiral smectic H phase.

References

1. X. J. Hong and S. I. Stupp, Polymer Preprints 30 (1989) 469
2. L. S. Li and S. I. Stupp, Proc. of the XIIth International Congress for Electron Microscopy, Materials Sci. Volume, p. 1100 (1990)
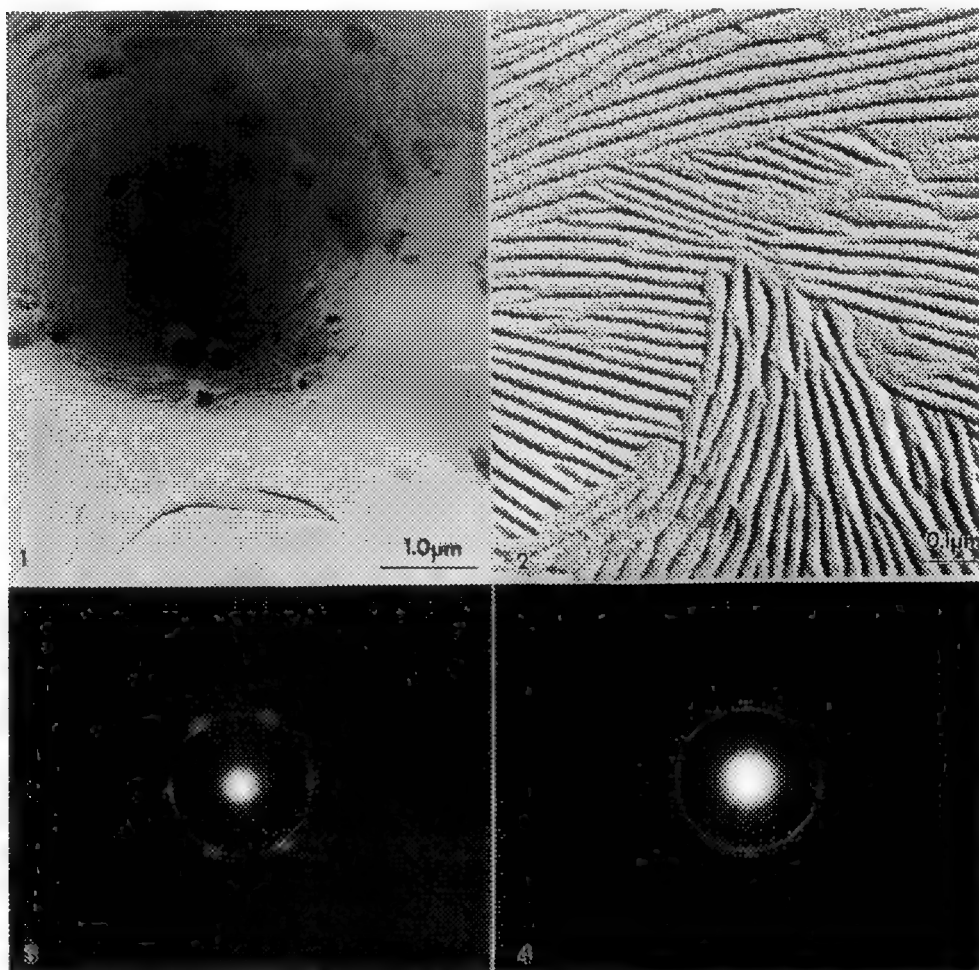
Fig.1.--Electron micrograph of the comb polymer film showing a "dome-like" region.
Fig.2.--Electron micrograph of the thinnest part of the "dome" showing tilted-layer domains.
Fig.3.--Selected area electron diffraction pattern of a domain.
Fig.4.--Selected area electron diffraction pattern showing both the wide-angle and small-angle reflections.

Investigation of Defect Structures of Thermotropic Liquid Crystal Polymers by Optical And Scanning Electron Microscopy

Ding-kuo Ding and Edwin L. Thomas

Department of Materials Science and Eng., MIT, Cambridge, MA 02139

The integer defect structures of semi-flexible thermotropic polyester (MHDT) based on 1,10-decane bisterephthaloyl chloride with methyl hydroquinone were investigated by optical microscopy (OM) and scanning electron microscopy (SEM). Liquid crystals, in general, are characterized by a unit vector called the director, **n**, which indicates the locally preferred orientation of molecules. Different types of defects, which were described by their strength, s, defined by the total change of the orientation of the director around the singularity divided by 2π, are imaged in the director fields. The integer defects of s=±1, in liquid crystal polymers were revealed by OM and SEM using the lamellar decoration technique[1] developed in this laboratory.

A 10 μm thin film on a glass slide was prepared in melt state by blade shearing. This sample was then placed in a hot stage and heated into the isotropic state. The temperature was then quickly dropped to just below the isotropic-nematic transition temperature[2] to create a large number of integer defects (as shown in figure 1) during the transition from the disordered to ordered state. The schlieren textures produced by this temperature-drop defect creation procedure were different each time, i.e. the defects were randomly created. The sign of these defects could be simply determined by rotating the crossed polars, and each defect with four brushes verified the integer defects. The defects form in pairs (negative-positive pair) to lower their energy. This could be confirmed by tracing the brushes which connected adjacent defects. These defect textures were captured by quenching the sample into water at room temperature, then annealing at the temperature 10°C below melting temperature to allow crystallization to proceed. The so formed crystalline lamellae were normal to the director fields[1]. Finally, the sample was etched within 40 wt% methylamine in water and examined by OM and SEM. After examining with OM, the sample was coated with Au and viewed in SEI with a Cambridge Instruments SEM at 5KeV.

Figure 2 shows the schlieren texture of the etched sample in a region containing a s=1 spiral defect and s=-1 defect. The individual integer defect structures shown in figure 3 are more clearerly seen with SEM. The presence of the integer strength defects may be due to the different boundary conditions, one parallel and one normal, on both sides of the sample (Figure 4). The structure of the s=1 defect in thermotropic liquid crystalline polymer (TLCP) was first shown by Vezie[3]. At present, we are able to create many integer defects by quenching the sample from the isotropic state to the nematic state. This defect creation procedure combined with lamellar decoration technique enables high resolution examination of the director field of integer defect in TLCPs.

References
1. E.L. Thomas and B.A. Wood, Faraday Discuss. Chem. Soc. **79**, 229(1985).
2. R.B. Meyer, Mol. Cryst. Liq. Cryst., **16**, 355(1972).
3. D. Vezie, unpublished results.
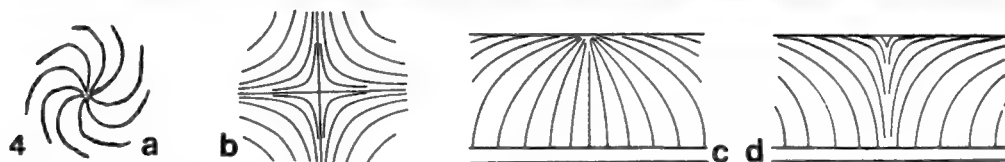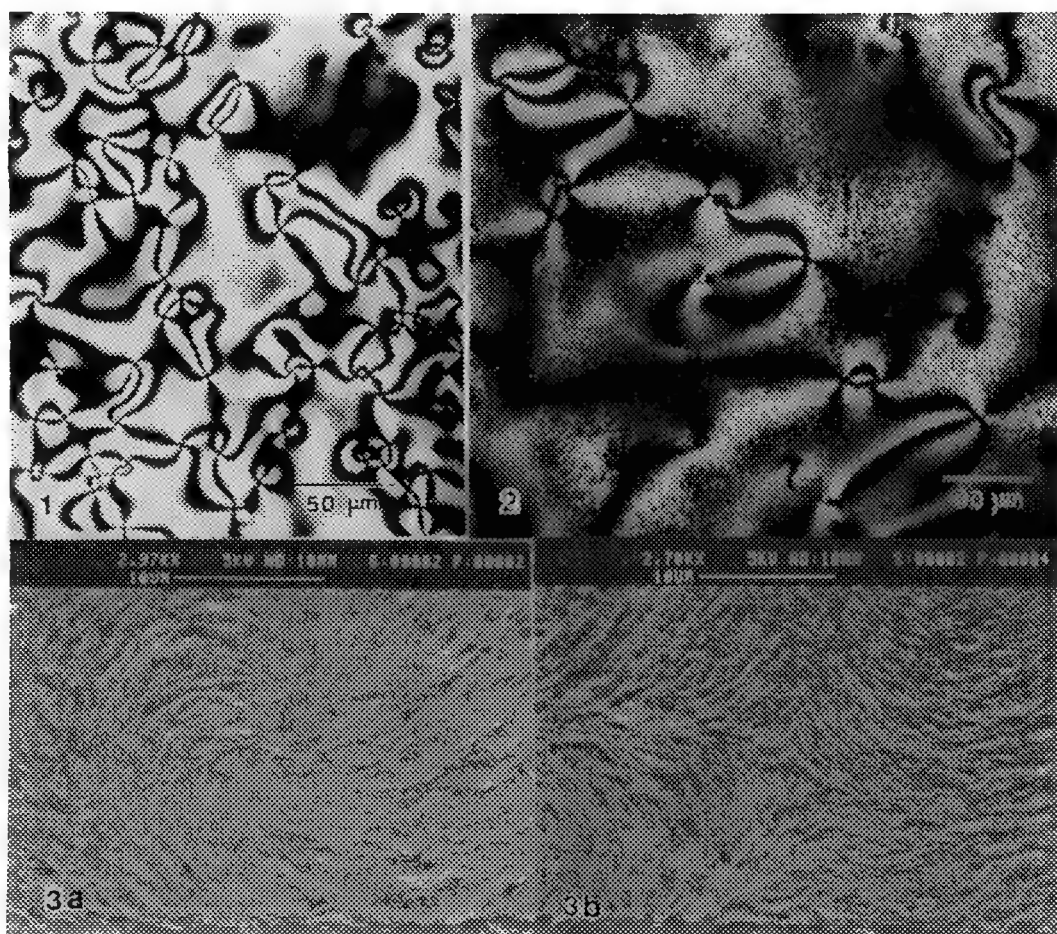
Fig.1 -- OM of schlieren texture of MHDT film created by quenching the sample from the isotropic state (180°C) to the nematic state (160°C). The points with four brushes indicate the presence of integer defects of s=±1.

Fig.2 -- OM of the etched sample from MHDT quenched to room temperature. The director fields of the schlieren texture are directly seen.

Fig.3 -- SEM of the etched sample showing the detailed director fields of a positive spiral defect and negative defect.

Fig.4 -- Schematic of the integer defects structure[2]. (a) and (b) show the top view. (c) and (d) show the side view.

275

EVIDENCE FOR HELICAL STRUCTURES IN POLY(1-OLEFIN SULFONES) BY TEM

George C. Ruben*   and W.H. Stockmayer+

*Depart. of Biological Sciences and +Depart. of Chemistry, Dartmouth College, Hanover, NH 03755

Advances in the techniques of TEM, including the preparation of ultrathin vertically shadowed platinum-carbon (Pt-C) replicas, have allowed the direct recognition of single-chain structural features, such as DNA , pectin helices or polysiloxane polymers.[1] Here we report some observations on the chain conformations of serval poly (olefin sulfones). We find strong evidence for the presence of some helical conformations, which had been inferred for over a decade but could not so far be established by other methods.

Unusual conformational behavior of poly(olefin sulfones) was indicated over twenty-five years ago. Dilute solutions of several poly (1-olefin sulfones), $[-CH_2-CHR-SO_2-]_x$, in non-polar solvents exhibited unexpectedly strong low-frequency dielectric dispersion, with relaxation times typical of rigid tumbling or of the terminal normal mode.[2] In contrast, polysulfones made from olefins with internal double bonds show no low-frequency dielectric loss.[3] To explain these facts, we refer to the crucial experiments of Fawcett and Fee (1982), who prepared terpolymers of 1-hexene, cyclohexene and SO_2 and found that the strength of the low-frequency dielectric relaxation process is a markedly non-linear function of the 1-hexene content.[4] Their result shows unequivocally that the slow process is due to the existence of strongly correlated sequences of longitudinal repeat-unit dipole components. The only plausible rationalization of this behavior is a preference of the chain for helical conformations, and indeed this idea is supported by conformational energy calculations.[5] Unfortunately it has until now not been possible to demonstrate directly the existence of such helices: the polymers do not crystallize,[6] and have random tacticity ;[7] and a polysulfone prepared from an optically active 1-olefin does not furnish conclusive results.[8] All the poly (olefin sulfones), whether or not they exhibit the low-frequency dielectric relaxation, show a higher-frequency process,[9] with a correlation time independent of molecular weight and similar in magnitude to that found by NMR spin-lattice relaxation measurements. It may be remarked that the NMR evidence requires the helical sections of the chain to be conformationally quite mobile.[8] This suggests that any helical conformations imaged may not necessarily be periodic.

TEM images were obtained of fractions of poly (1-tetradecene sulfone), p-C_{14}, and poly (cyclohexene sulfone), p-cC_6, cast from very dilute solutions (0.007% w/v) freeze-dried on a mica surface. The freeze-dried polysulfone molecules from a rapidly frozen solution fell randomly from a subliming solvent matrix onto the mica surface at -150°C and were then vertically replicated with 9±0.3Å Pt-C and held together with 128Å of electron transparent evaporated carbon. The Pt-C coating enlarges the molecular chain diameters by ~5Å making a single polysulfone chain normally 3.8-7Å in diameter 9-12Å in the TEM. Poly (1-tetradecene sulfone) with a mol. wt. of 5.4×10^6 forms short helical regions that show irregular helical turns of 7-18Å and that are 2-8 turns long with helix diameters of 11-17Å [FIG. 1a & 1b]. R= n-$C_{12}H_{25}$ side-chains were not obvious on the helices but a few were visible on extended p-C_{14} molecules [FIG. 1c]. Previously low-frequency dielectric loss peaks in dilute solutions of alternating 1-olefin/SO2 copolymers had shown that these contain strongly correlated sequences of longitudinal repeat-unit electric dipoles which were predicted to be in a helical form. In contrast, poly (cyclohexene sulfone) which does not display low-frequency dielectric loss was predicted to be in a nonhelical form. This compound on mica was a collection of Pt-C coated single chains 10-12Å in diameter with no side-chain projections [FIG. 1d]. A 9.3 Å Pt-C film deposited on mica under the same conditions (-185°C in a 5×10^{-8} torr. vacuum) forms metal chain structures about 5-6Å in diameter [FIG. 1e]. The presence and absence of helical regions in these freeze-dried polysulfones thus reflect their solution conformations.

References
1. G.C. Ruben, J. Electr. Microsc. Tech. 13 (1989) 335.
2. T.W. Bates et al., Trans. Faraday Soc. 63 (1967) 1977.
3. A.H. Fawcett and K.J. Ivin, Polymer 13 (1972) 439;
4. A.H. Fawcett and S. Fee, Macromolecules 15 (1982) 933.
5. M.L. Mansfield, Macromolecules 15 (1982) 1587.
6. M.J. Bowden and H.D. Keith, Eur. Polym. J. 19 (1983) 259.
7. R. Quintero-Arcaya et al., Macromolecules 22 (1989) 3663.
8. R. Bacski, J. Polym. Sci., A-1 5 (1967) 619.
9. S. Mashimo et al., Macromolecules 19 (1986) 682.
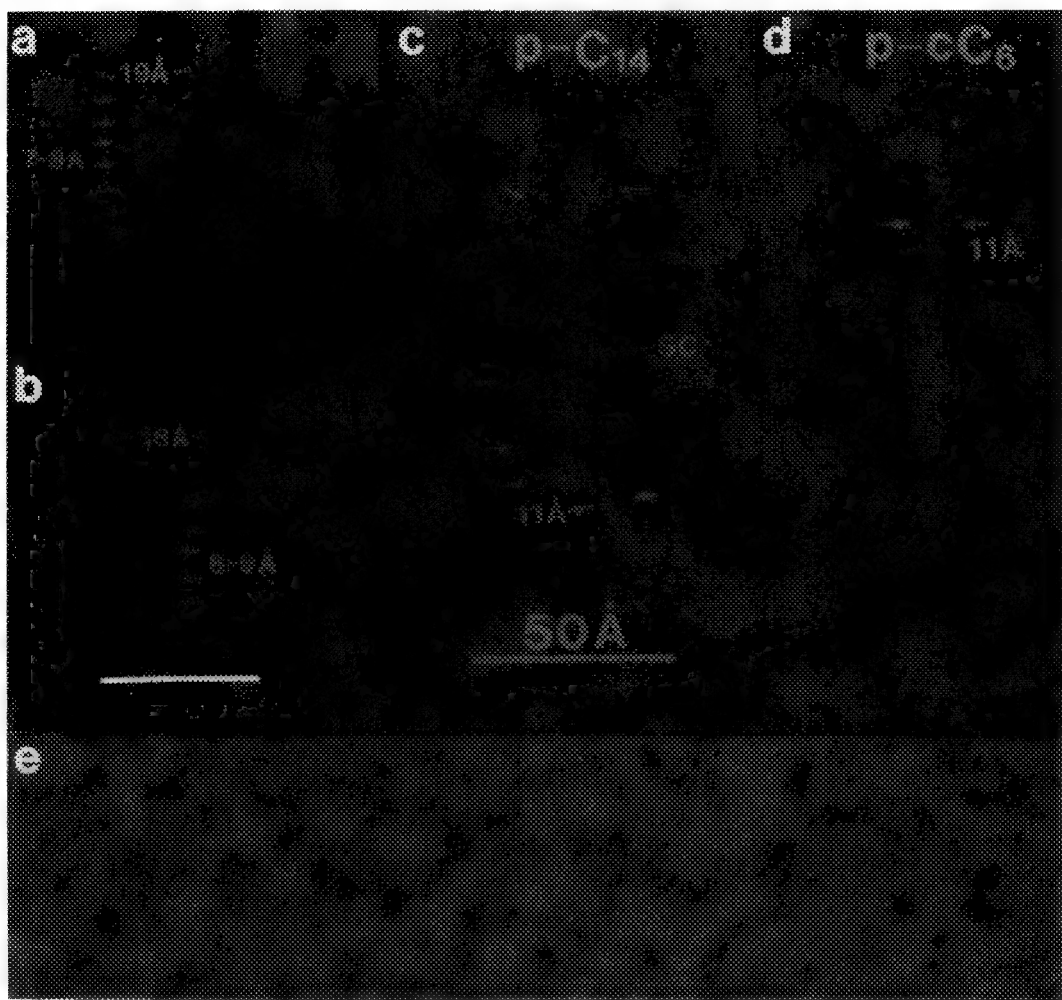
FIG 1. Freeze-dried rapidly frozen solution of (0.007% w/v in CCl₄) was vertically replicated with 9.3Å Pt-C and backed with 128Å of evaporated carbon. The chain diameter of the naked polymer is 3.8-6.4Å and with the Pt-C coating the chain diameter is enlarged to 9-12Å. Distances within the polymer are unchanged by replication. **a)** Helical domain of 7 or 8 turns that are spaced 7-8Å apart. The diameter of the helix is ~14Å (~19Å with 5.3Å of added Pt-C). **b)** Helical domain of 5 or 6 turns that are spaced 8-9Å apart. The diameter of the helix is ~13Å (~18Å with 5.3Å of added Pt-C). 50 Å bar for a &b. **c)** The main chain of p-C₁₄ is approximately 112Å long in this image. The side-chains should be ~17Å fully extended with a 3.8Å diameter. Out of the twenty five possible side-chains, 9-10 side-chains can be detected as side projections that are approximately separated by multiples of 4.4Å. Many of these side chains are either entangled with adjacent side-chains or they are not fully extended. Two side-chains were measured as long as 13-14Å and were also estimated to be ~3Å in diameter (8Å with 5.3Å of added Pt-C). Normal-C₁₂H₂₅ side-chains 4.4Å apart along the main chain could be discerned because the side-chains extend outside the airy disc diffraction limit of 6.6Å. The diameter of the main chain was estimated to be ~6Å (11Å with 5.3Å of added Pt-C). **d)** The nonhelical poly (cyclohexene sulfone) extends for ~140Å along the surface. The diameter of the p-cC₆ in the image varies from 4.3-7Å (9-12Å with 4.7Å of added Pt-C) over this length. There is no evidence of any projections or side-chains on this polymer. **e)** A 9.3Å Pt-C film deposited on mica under the same conditions as **a-d.** Pt-C filaments when present have diameters of the film thickness minus 4Å.[1] The 50 Å bar in **c** is the magn. in **c, d, & e.**

FREEZE-FRACTURE TEM OF THE HELICAL SMECTIC A* PHASE

K.J. Ihn, R. Pindak* and J. A. N. Zasadzinski

Chemical and Nuclear Engineering, University of California, Santa Barbara, CA 93106
* AT&T Bell Laboratories, Murray Hill, NJ, 07974

A new liquid crystal (called the smectic-A* phase) that combines cholesteric twist and smectic layering was a surprise as smectic phases preclude twist distortions.[1] However, the twist grain boundary (TGB) model of Renn and Lubensky[2] predicted a defect-mediated smectic phase that incorporates cholesteric twist by a lattice of screw dislocations. The TGB model for the liquid crystal analog of the Abrikosov phase of superconductors consists of regularly spaced grain boundaries of screw dislocations, parallel to each other within the grain boundary, but rotated by a fixed angle with respect to adjacent grain boundaries. The dislocations divide the layers into blocks which rotate by a discrete amount, $\Delta\theta$, given by the ratio of the layer spacing, d, to the distance between grain boundaries, l_b; $\Delta\theta \approx d/l_b$ (Fig. 1).

The SmA* phase has been observed in 1-methylheptyl 4'-[[(4"-tetradecyloxyphenyl)propioloyl]oxy] bi-phenyl-4-carboxylate (+14P1M7) between 90° C and 94° C.[1] The helical pitch is 0.5 microns and X-ray diffraction has shown that the layer spacing is 4.3 nm, and that the layers are parallel to the pitch axis.[3] Although these observations are consistent with the TGB model, they cannot distinguish between *microscopic* models for the molecular organization. This requires freeze-fracture TEM. To prepare the SmA* phase for TEM, a 0.5 µl drop was heated to the isotropic phase between two copper planchettes. The sandwich was plunged into liquid propane from 92.5° C and fractured and replicated at -170° C.

Fig. 2 shows a typical fracture of the SmA* phase. The surface has a regular asymmetric undulations similar to cholesteric phases.[4] The helical axis is roughly vertical and the pitch is about 0.5 µm. In addition to the undulations, smectic layers are visible at the arrows. They are parallel to the helical axis as predicted by the TGB model.[2] At each trough of the undulating fracture surface (open arrow), the layers are roughly normal to the fracture direction, and the 4.1 spacing (Fig. 4) is consistent with X-ray diffraction. At the crests, the layers are almost parallel to the fracture surface, and the fracture has the typical pattern of a dense array of screw dislocations. These dislocations are oriented normal to the fracture surface, and hence perpendicular to the helical axis, as shown in higher magnification in Fig. 3. The screw dislocations have a Burgers vector of a single layer, which is consistent with the TGB model.

Fig. 4 shows the optical transform of a selected area of Fig. 2. The pairs of strong reflections correspond to the layer spacing and longer spacings in the image. These reflections indicate that the apparent layer spacing changes discontinuously along the helical axis, which is what we would expect for a fracture plane that cuts the discretely rotating blocks of the TGB model of the SmA* phase at an oblique angle to the helix axis. From measurements of the 5 pairs of spots' position in reciprocal space, and their angles, we can determine both the rotation of the layers and the spacing of the screw dislocations. For the TGB model, these angles should be a multiple of the twist angle, $n\Delta\theta \approx nd/l_b$. We find that the twists between layer blocks are 33° ± 3°, 45° ± 3°, 64° ± 2°, and 76° ± 2°, which gives $\Delta\theta = 15° - 16°$. Hence, the spacing between grain boundaries is 15 - 16 nm, consistent with the observed screw dislocation density in Fig. 3. These measurements conclusively show that the TGB model is appropriate for the SmA* phase, and that this phase is the liquid crystal analog of the Abrikosov phase in superconductors.

1. J. Goodby, M. Waugh, S. Stein, E. Chin, R. Pindak, and J. Patel, *Nature*, **337**, 449 (1989).
2. S. R. Renn and T. C. Lubensky, *Phys. Rev. A.*, **38**, 2132 (1988).
3. G. Srajer, R. Pindak, M. Waugh, J. Goodby, and J.Patel, *Phys. Rev. Lett.*, **64**, 1545 (1990).
4. D. Berreman, J. Zasadzinski, M. Sammon, and S. Meiboom, *Phys. Rev. Lett.* **57**, 1737 (1986).

278

TGB PHASE
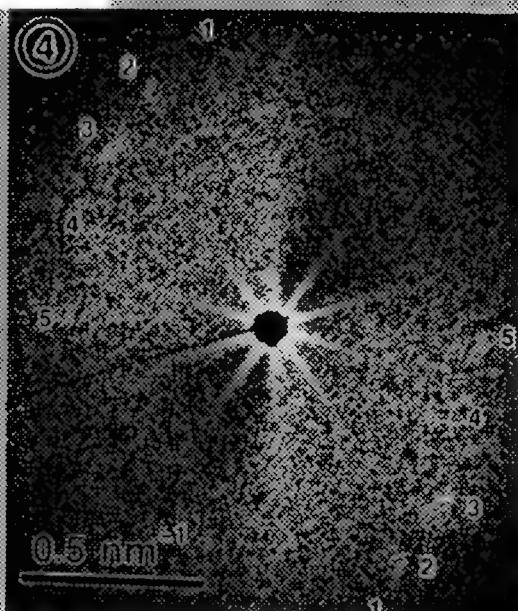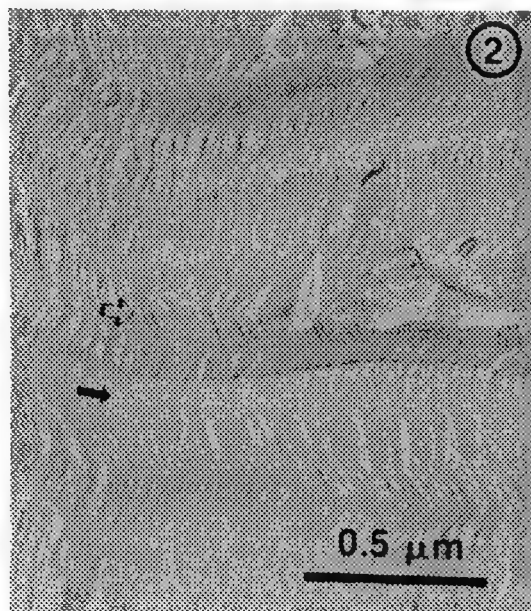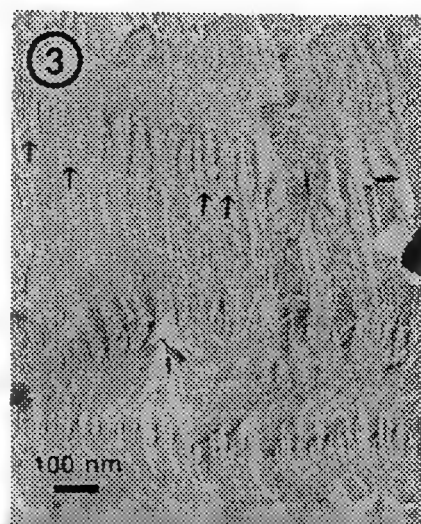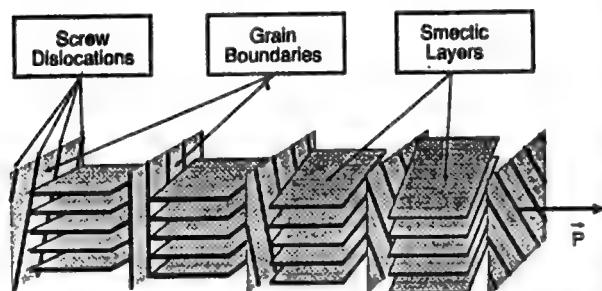
FIG. 1. Schematic representation of the TGB model of the SmA* phase. Blocks of smectic-A layers of spacing d are separated by regularly spaced twist grain boundaries separated by a distance l_b. The angles of the smectic planes separated by a grain boundary differ by $\Delta\theta \approx d/l_b$.

FIG. 2 Freeze-fracture morphology of SmA* phase. At open arrows, layers are normal to the fracture direction and spaced 4.1 nm apart. Full arrows mark the signature fracture pattern of screw dislocations.

FIG. 3 Twist grain boundary of screw dislocations in the SmA* phase. From measurements of the shadow width, these screw dislocations have a Burgers vector of a single layer step.

FIG. 4. Optical diffraction pattern of a selected area near the center of Fig. 2.

TEM STUDY OF Si SURFACES

K. Yagi, H. Sato, K. Kobayashi, Y. Nishiyama and Y. Tanaka

Physics Department, Tokyo Institute of Technology,
Oh-okayama, Meguro, Tokyo 152, Japan

UHV TEM studies of surfaces have been successfully applied in surface science. Low resolution TEM can characterize surface atomic steps, monolayer adsorbate, reconstruction of surfaces and surface structure domains. TED from surfaces of thin films can be used to analyze surface atomic structure. On the other hand high resolution TEM can seen atomic structure of surfaces either in profile or in plan view modes. The profile mode is effective for surfaces with short periods along the beam direction and is sensitive to displacements of surface atoms normal to the surface and along a direction parallel to the surface and perpendicular to the beam direction. Image contrast of high resolution plan view images is very weak except cases of heavy adsorbed atoms on a substrate of light atoms. The present paper shortly reviews recent studies of Si surfaces done with use of a low resolution UHV TEM and high resolution TEM.

Figure 1 reproduces a $(2\bar{2}0)$ dark field TEM image of a thin (111) Si film formed by etching by oxygen. The specimen temperature was around 780°C. A octahedron formed by (111) faces of cubic crystals in the lower right shows crystallographic orientation of the film, which is known by cleavage planes of the crystal from which the sample was formed. Thus, the [112] direction on the electron beam incident surface (denoted i) is to the right.

Most of line images are atomic steps on the i surface and the e (exit) surface. Step down directions are known from the directions of motions of the steps during thinning and are marked by arrow heads. A bright and dark dot image marked by A is a dislocation whose Burgers vector has a component normal to the surface and spiral steps with opposite sense are seen around it. The three fold spiral shows three fold symmetry of the surface and it is well known that the [$\bar{1}\bar{1}2$] step is more stable than the [112] step. Thus, the regular spiral step is said to be on the i surface. Steps which cross the spiral are on the e surface. Surface topography of the film can thus be determined and relative thickness of each part of the film is noted by integer number. It is seen that the image intensity is similar to each other where the thickness is the same.

Another thing to be noted is observations of out of phase boundaries (OPBs marked by O), which appear at steps and extend across the terraces and terminate at the steps on the other side of terraces. In some cases, OPBs make nodes marked N and M on terraces. The contrast across the OPBs is due to difference in relative phases of the 7x7 structures on the i and the e surfaces. It is noted that the OPBs and steps have their own bright and dark contrasts. The origin of these contrasts is considered to be due to the 7x7 reconstucted structure which is under the delatational strain field.

Figure 2 shows a TED pattern from a Si(110) film. The film has a hole with a straight perifery. The pattern shows streaks perpendicular to the $(1\bar{1}1)$ surface through diffraction spots.

Streaks are also at fractional positions (n/7) between streaks from the diffraction spots indicating the 7x7 structure parallel to the

Figure 1
    TEM image of a Si (111) film. Steps on both surfaces are seen (denoted by i and e). Step down directions are indicated by arrow heads.
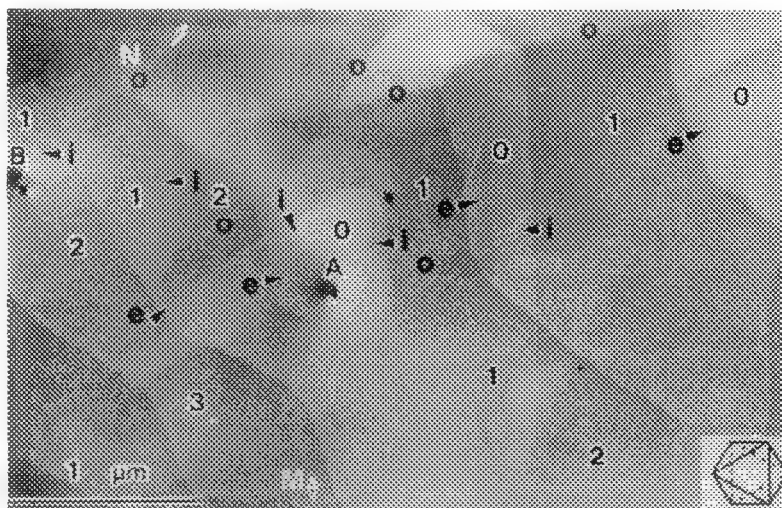
electron beam.
    Figure 3 shows a profile image of a (331) surface. The surface was formed by deposition of few monolayer Ge on a Si(110) film. The image shows surface period of 0.86nm. Recent STM Study of a vicinal surface of Si(111)showed the (331) plane of the 6x4 structure, which has a period of 0.86nm when it is seen along the [110] direction. The present study showed that the similar structure also hold on Ge covered (331) surfaces.
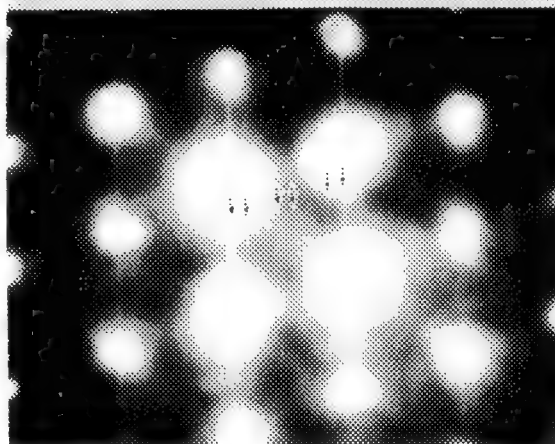
Figure 2
    A TED pattern from a Si (110) film with a (111)7x7 surface edge.

Figure 3
    A profile image of a Ge/Si(331) surface seen along the [110] direction.
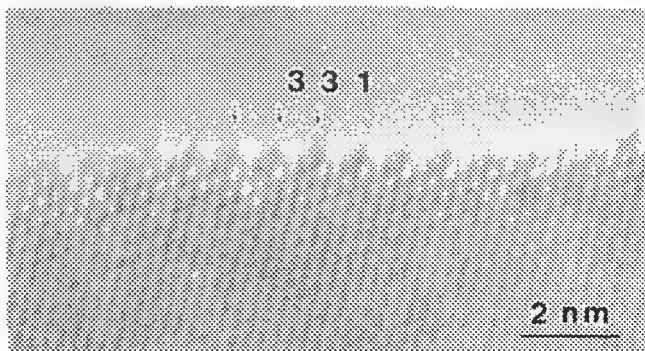
INTENSITY MEASUREMENT OF SURFACE DIFFRACTION SPOTS BY EELS

P. Xu and L. D. Marks

Department of Materials Science and Engineering, Northwestern University, Evanston, IL 60208

With the development of the modern ultra-high vacuum (UHV) transmission electron microscopes, it has become possible to study the surfaces of various materials in a clean environment. Transmission electron diffraction in a plan view geometry is particularly powerful in solving the surface atomic structures, for example Si(111)-7x7[1]. Surface diffraction spots in such a pattern are usually quite strong, readily apparent on a phosphor screen. In addition, these spots are much clearer in an off zone diffraction pattern[1,2]. This paper presents the absolute intensity measurement of the surface spots intensity using an electron energy loss spectrometer.

A silicon (111) surface was prepared by ion-beam cleaning/annealing[3]. A 5x5 surface reconstruction was found after the surface was covered by about one monolayer of Cu-Au and annealed at 600°C[4]. Selected area diffraction patterns are shown in Fig. 1a (near the (111) zone) and 1b (off the zone). Absolute intensity values of the diffraction spots were obtained in a Hitachi UHV H-9000 microscope using a Gatan Parallel Electron Energy Loss Spectrometer (PEELS) interfaced to an Apollo computer. The location of the spectrometer entrance aperture in terms of a position on the phosphor screen was determined and diffraction spots intensities measured after they were moved to this position using dark field tilt controls.

Fig.2 shows some representative PEELS spectra from: (a) the (00) beam in Fig.1a; (b) a bulk (11) spot in Fig.1a; (c) a surface (10) spot in Fig.1a; (d) a (4/5,1) spot due to the 5x5 reconstruction in Fig.1a and (e) a (4/5,1) spot in Fig.1b. The transmitted beam and the bulk (11) beam contain the same amount of plasmon loss intensity (Fig. 2a and 2b). Comparing spectra (d) and (e), it is apparent that near the zone axis there was a strong contribution from the diffuse plasmon scattering around the (11) beam which obscured both the intensity level and clarity of the surface diffraction spots. However, when the specimen was tilted off the zone this plasmon scattering contribution dropped since the intensity of the bulk (11) beam was reduced. This is due to the multiple scattering of the elastic (Bragg) and inelastic (plasmon) events[5].

Table 1 summarizes values of the intensities measured relative to the transmitted beam, integrated over the zero loss peaks. In the near zone pattern, the intensities of the surface spots were found to be of the order of 10^{-4}, which is consistent with multislice simulations[6]. In the off zone pattern, the bulk (11) spot intensity dropped as much as two orders of magnitude while the intensities of the surface spots dropped by about one order of magnitude[7].

REFERENCES
[1] K. Takayanagi, et al. Surf. Sci., **164**, 367 (1985).
[2] D. N. Dunn, et al. Surf. Sci. **260**, 220 (1992).
[3] R. Ai, et al. Ultramicroscopy, **39**, 333 (1991).
[4] P. Xu and L. D. Marks, this volume.
[5] P. Xu, et al. Ultramicroscopy **38**, 127 (1991).
[6] L. D. Marks, Ultramicroscopy **38**, 325 (1991).
[7] This work was supported by the Airforce Office of Scientific Research AFOSR-90-0045.
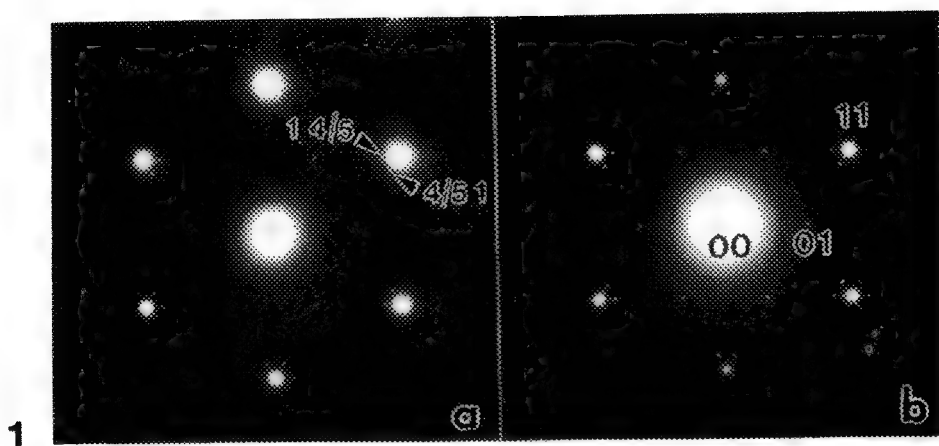
TABLE 1: Intensities of different diffraction spots relative to transmitted beam

Diffraction Spot	Intensity (near the zone)	Intensity (off the zone)
(00)	1	1
(11)	3×10^{-1}	1×10^{-3}
(10)	5×10^{-5}	6×10^{-6}
(4/5,1)	1×10^{-4}	2×10^{-5}
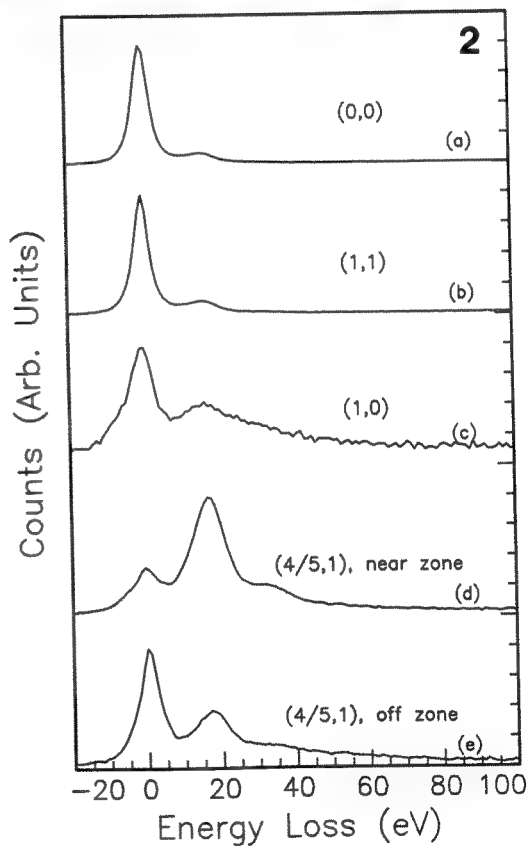
FIG.1: Selected area diffraction patterns of Cu(Au)-Si(111) 5x5 reconstruction, (a) near zone and (b) off zone.
FIG.2: Collection of PEELS spectra as described in text.

CHARACTERIZATION OF CLEAN GALLIUM PHOSPHIDE (110) SURFACES BY REFLECTION ELECTRON MICROSCOPY

M. Gajdardziska-Josifovska, M.R. McCartney and David J. Smith*

Center for Solid State Science, Arizona State University, Tempe, AZ 85287
*Also at: Department of Physics, Arizona State University

The clean (110) surface of GaP has been studied in UHV systems with diffraction and spectroscopy techniques and found to have a 1x1 reconstruction.[1] However, no imaging studies have been reported characterizing the topography of the reconstructed surface. In this work we use reflection electron microscopy (REM) to determine the effects of ion-milling and annealing treatments used to clean the surface. The annealing temperatures for the compound semiconductors are limited by preferential sublimation of one component so we have undertaken heating to higher temperatures to study the surface dissociation and melting processes.

This work was performed on the Philips-Gatan 430 UHV-TEM with in-situ surface preparation and heating capabilities.[2] REM samples were prepared from GaP wafers (from SMM Co. Ltd.) by cleavage along the (110) crystal plane immediately before loading in the microscope. TEM samples from the same source were thinned to perforation using a brominated methanol etch following standard mechanical dimpling. After bake-out, the base pressure in the UHV-section of the microscope was typically 2-5x10^{-9} Torr with additional improvement in the objective lens region provided by liquid-nitrogen-cooled cryofingers. It should be noted that the same vacuum conditions were sufficient to observe the 7x7 reconstruction of the Si (111) surface in this microscope.[3]

Figure 1 shows an REM image and a RHEED pattern of the cleaved surface which remained unchanged by the bake-out of the microscope. The surface has long flat terraces with steps running along (110) directions and the RHEED pattern indicates a bulk terminated surface with some contamination. The surface contamination was removed by ion milling with 1keV Ar ions for 20min during which time the partial pressure of Ar was increased to 2x10^{-6} Torr. RHEED patterns of this surface indicated complete amorphization typical of ion-milled surfaces. The crystal was then annealed to re-establish crystallinity, and the onset of crystallization became visible in the RHEED pattern at 325°C. The crystal was annealed for 4 hrs at 550°C to complete the cleaning cycle.[1] A 1x1 reconstruction was visible in the RHEED pattern both at 550°C and also after cooling to room temperature (rods in Fig.2b). The REM image however showed that the clean surface has much smaller terraces and is in general rougher than the as-cleaved surface. We have also observed the same surface topography and reconstruction from a cleaved (110) surface which was heated to 800°C for 1 min.

Prolonged heating at 800°C resulted in an apparent dissociation of the GaP which has a melting point at atmospheric pressure of 1467°C. This dissociation was evidenced by the appearence of dark features in the REM images from both as-cleaved and ion-milled surfaces. These features appeared to be droplets of a viscous liquid which would coalesce to cover micron sized areas as they moved across the field of view. The motion of this liquid was captured on video from the TV pick-up system. Figure 3 shows an REM image and RHEED pattern from the surface after cooling to room temperature. The areas of the surface not covered by the liquid have somewhat larger terraces than those obtained by annealing at 550°C, and the RHEED pattern indicates that the surface 1x1 reconstruction is still present (as it was at 800°C). On removal from the microscope the bulk REM sample which was originally a translucent yellow color had become covered with shiny metallic droplets. EDS spectra of a transmission sample which had received the same treatment indicated that the droplets were a Ga rich phase.

In conclusion, we have imaged the clean GaP (110) surface for the first time and shown that the ion-milling and annealing treatments which have been used by other researchers to clean the surface also increase the surface roughness. By heating to 800°C we have observed melting and motion of a Ga rich phase on the surface. Those parts of the surface which were not covered by the melted phase were found to be smoother and to maintain the 1x1 reconstruction typical of the clean GaP (110) surface.

References
1. C. B. Duke, A Paton and A. Kahn, *J. Vac. Sci. Tech.* (1984)**A2**, 515.
2. D. J. Smith, J. Podbrdsky, P. R. Swann and J. S. Jones, *Mater. Res. Soc. Symp. Proc.* (1989)**139**, 289.
3. D. J. Smith, M. Gajdardziska-Josifovska, P. Lu, M. R. McCartney, J. Podbrdsky, J. J. Jones and P. R. Swann, *Ultramicroscopy*, submitted.
4. This work was performed at the National Facility for HREM supported by NSF grant DMR89-13384.
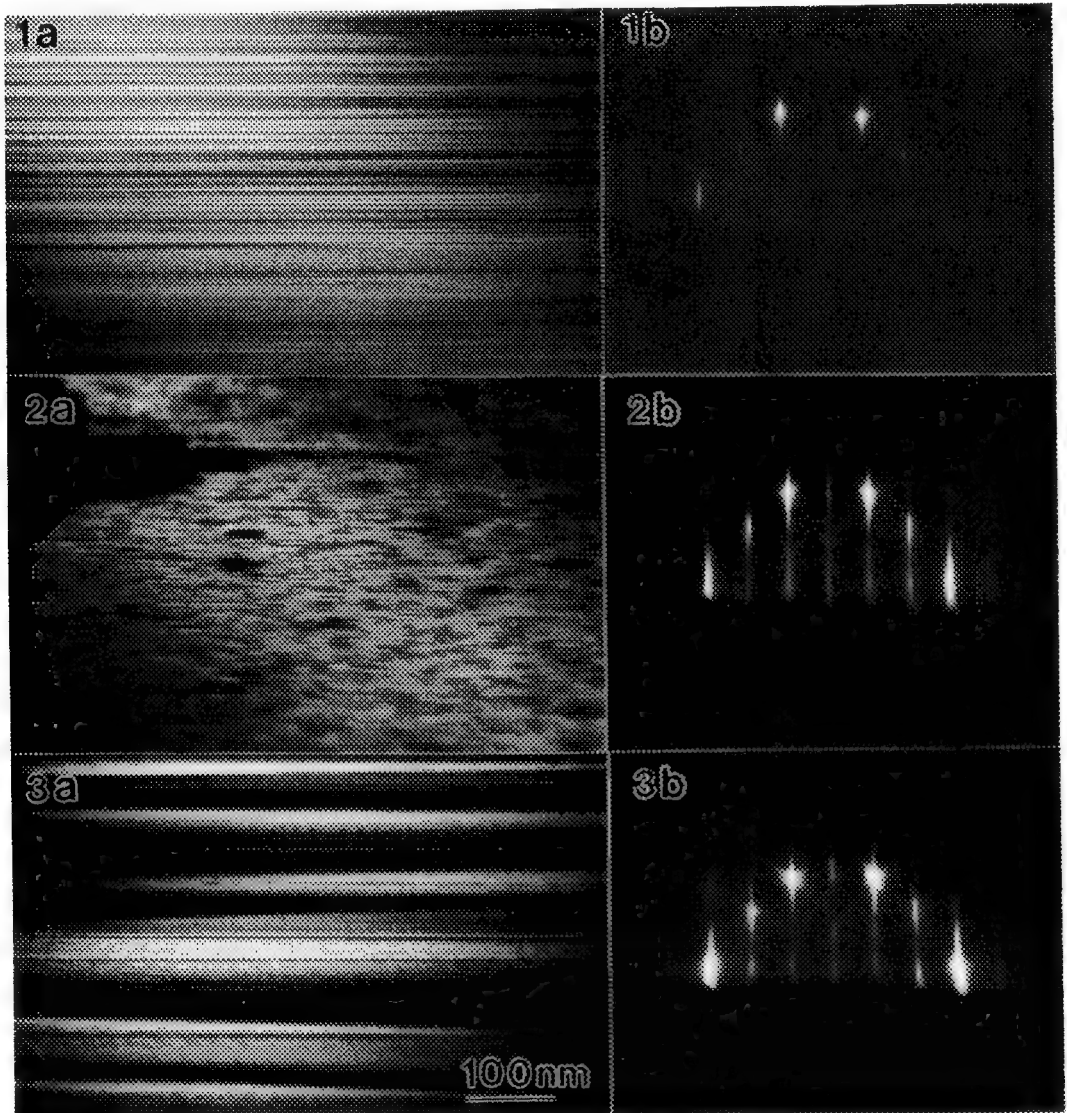
FIG. 1 As-cleaved GaP (110) surface; (a) REM image obtained using (660) specular reflection; (b) corresponding SA-RHEED pattern formed with 100keV electrons.
FIG. 2 GaP (110) surface after ion-milling and annealing to 550°C for 4hr; (a) REM image showing increased surface roughness; (b) SA-RHEED showing rods due to 1x1 reconstruction.
FIG. 3 GaP (110) surface after heating to 800°C for 10min; (a) REM image with flattened clean terraces and dark areas covered by solidified Ga rich phase;. (b) SA-RHEED pattern showing 1x1 reconstruction.

SURFACE REACTIONS OBSERVED BY PHOTOEMISSION ELECTRON MICROSCOPY (PEEM)

H.H.Rotermund

Fritz-Haber Institut der MPG, Faradayweg 4-6, 1000 Berlin 33, FRG

Chemical reactions at a surface will in most cases show a measurable influence on the work function of the clean surface. This change of the work function $\delta\phi$ can be used to image the local distributions of the investigated reaction,.if one of the reacting partners is adsorbed at the surface in form of islands of sufficient size ($\Delta > 0.2\mu m$). These can than be visualized via a photoemission electron microscope (PEEM)[1]. Changes of ϕ as low as 2 meV give already a change in the total intensity of a PEEM picture. To achieve reasonable contrast for an image several 10 meV of $\delta\phi$ are needed. Dynamic processes as surface diffusion of CO or O on single crystal surfaces as well as reaction / diffusion fronts have been observed in real time and space.

As an example a Pt(110) surface covered by a monolayer of CO is exposed to 10^{-4} mbar O_2. Clean Pt will be imaged as bright, while areas covered with CO are reproduced in grey, O covered parts in black, due to the highest work function. Initially no sign of O_2 adsorption can be seen. Only after several thousand langmuir, islands of O will show up, slowly increasing with time as imaged from a video tape in Figure 1. These O islands are at room temperature stable for several hours under ultra high vacuum conditions, after ending the exposure to O_2. Another cycle starting with a 10 langmuir dose of CO, shows the old islands faded, and the O_2 will now not only start its adsorption at the same dislocations in the middle of those islands, but also at the circumferences of the memorized old features as indicated in Figure 2. Probably the CO induced phasetransition from the 1x2 reconstructed surface to the 1x1 structure is responsible for the memory effect.

The PEEM has also been applied for the investigation of spatio-temporal pattern evolution associated with the oscillatory catalytic CO - oxidation on platinum single crystal surfaces[2]. The oscillations can be understood on the basis of the mentioned adsorbate induced (CO) structural change of the surface, which modulates the catalytic activity via the sticking coefficient for O_2. At temperatures around 430 K slowly developing patterns like spirals, or concentric target patterns in a truly two dimensional system dominate the picture, sometimes mixed with oscillations of durations of about 10 s. In Fig.3 a set of 6 images of two spirals with different frequencies imaged at 20 s time interval is reproduced.

At medium temperatures around 480 K much faster growing patterns, including solitons[3], are found, while at temperatures about 550 K fast oscillations occur sometimes involving the whole crystal and showing frequencies of about 1 Hz. A short video of the rich variety of the self sustained spatio-temporal patterns will be shown.

1 W. Engel , M.E. Kordesch, H.H. Rotermund, S. Kubala and A. v. Oertzen
   Ultramicroscopy 36, 148, (1991)

2 S. Jakubith, H. H. Rotermund, W. Engel, A.v. Oertzen and G. Ertl,
   Phys. Rev. Lett.**65**, 3013, (1990)

3 H. H. Rotermund, S. Jakubith, A.v. Oertzen and G. Ertl,
   Phys. Rev. Lett.**66**, 3083, (1991)
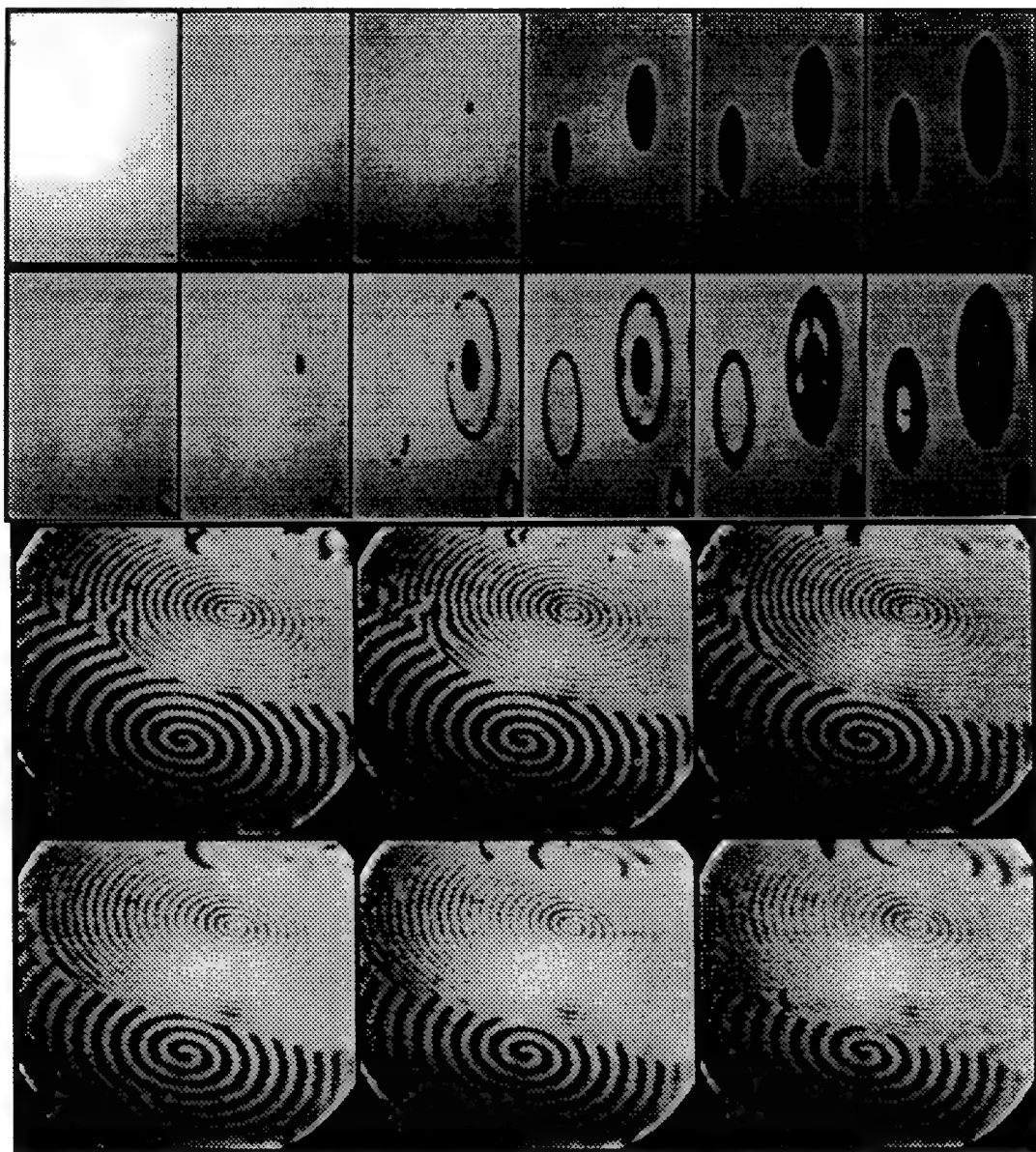
FIG. 1 Image 1 shows an area 260x380 μm of clean Pt(110) surface. Frame 2 is taken after 10 L of CO. Frames 3 to 6 are at 100, 160, 190 and 220 s after the start of dosing at constant 10^{-4} mbar O_2 .

FIG. 2 After stopping the O_2 dosing the completely CO covered Pt still remembers the old O islands, as seen in picture 1. Frames from 2 to 6 are imaged at 5, 45, 55, 65 and 75 s after the start of dosing again with a constant 10^{-4} mbar partial pressure of O_2 .

FIG.3 At $2x10^{-4}$ mbar partial pressure of O_2 and $1x10^{-4}$ mbar partial pressure of CO two spirals with 10 and 5 s rotation are imaged at 20 s intervals.

ELECTRON MICROSCOPY STUDIES OF REDUCTION AND OXIDATION BEHAVIOR OF MODEL HETEROGENEOUS CATALYSTS

Nan Yao, G. D. Meitzner, S. C. Fung, M. M. Disko, S. K. Behal, J. McHenry and J. H. Sinfelt

Exxon Research and Engineering Company, Annandale, New Jersey 08801, USA

Supported metal heterogeneous catalysts, such as $Pt/\gamma-Al_2O_3$, are used for reforming reactions in which saturated hydrocarbons, in petroleum naphtha, are converted to aromatics with a much higher anti-knock quality for automotive fuel[1,2]. Reforming is now one of the most important industrial applications of catalysts[3]. The platinum on alumina catalyst was developed in the 1950s, and remains in use around the world.

The mechanisms of deactivation of alumina-based catalysts are still not well understood, since their deactivation on oil is accompanied, or rapidly followed, by massive carbon deposition which prevents inspection by chemisorption. In order to fully understand the general loss of activity for supported metal catalysts during operation, investigations of the atomic structure and the chemical composition for both working and model catalyst systems have been performed using high resolution transmission electron microscopy (HRTEM). Morphological and chemical changes of small catalytic particles distributed on the top surface of a porous alumina and impregnated within a porous alumina have been compared.

Model $Pt/\gamma-Al_2O_3$ catalysts were prepared for TEM study by the sol-gel method. Porous alumina films were formed by dropping a (0.4m) Boehmite Sol on tungsten TEM grids, then heated in air at 430°C for 12 hours. Platinum was deposited on or impregnated within such alumina supports. One model catalyst was prepared by evaporating platinum onto the support. This yielded 20-50 Å Pt crystallites only on the top surface of the alumina (model A). Another model catalyst was prepared by adsorption of H_2PtCl_6 from an aqueous solution. This yielded 20-50 Å crystallites on the internal surfaces of the alumina, which had an average pore size of 30-50 Å (model B).

Bright field electron micrographs of these fresh catalysts, along with the corresponding electron diffraction patterns and EDXS, are displayed in figure 1(a) (model A) and 1(b) (model B). The diffraction patterns identify the $\gamma-Al_2O_3$ phase in both samples. The behavior of such catalysts was investigated following reduction and oxidation treatment. No obvious change in morphology was observed for either model A and model B catalyst upon pure H_2 treatment at 460°C at 200CC/min flow rate for 3 hours, as shown in figures 2(a) and 2(b). An morphological example of these two model catalysts, after being heated in $Cl_2+O_2+H_e$ (1:6.7:76) at 510°C for 2 hours, then in pure H_2 at 460°C for 1 hour, is displayed in figure 3. Figure 3(a) shows that there was still no obvious change in model A, while the significant change in particle size and distribution took place in model B as shown in figure 3(b). The regeneration treatment of model B yielded a bimodel distribution of extremely small (< 30Å) and extremely large (> 1000Å) Pt particles. This observation suggested a tremendous difference in behavior of Pt crystallites distributed on the top surface or on the internal surface of porous alumina gel. In the later case, the particles experienced much more interaction with the support during the chemical reaction due to occlusion within pores. Further in situ experiments will explore the importance of two or three dimensional diffusion in the dispersion mechanism.

REFERENCES:

1. J. H. Sinfelt, *Adv. in Chem. Eng.*, **5**, 37(1964).
2. F. G. Ciapetta and D. N. Wallace, *Cat. Rev.*, **5**, 67(1971).
3. "Catalysis Looks to the Future", reports from Panel on New Directions in Catalytic Science and Technology, National Research Council (National Academy Press, Washington, D. C., 1992).
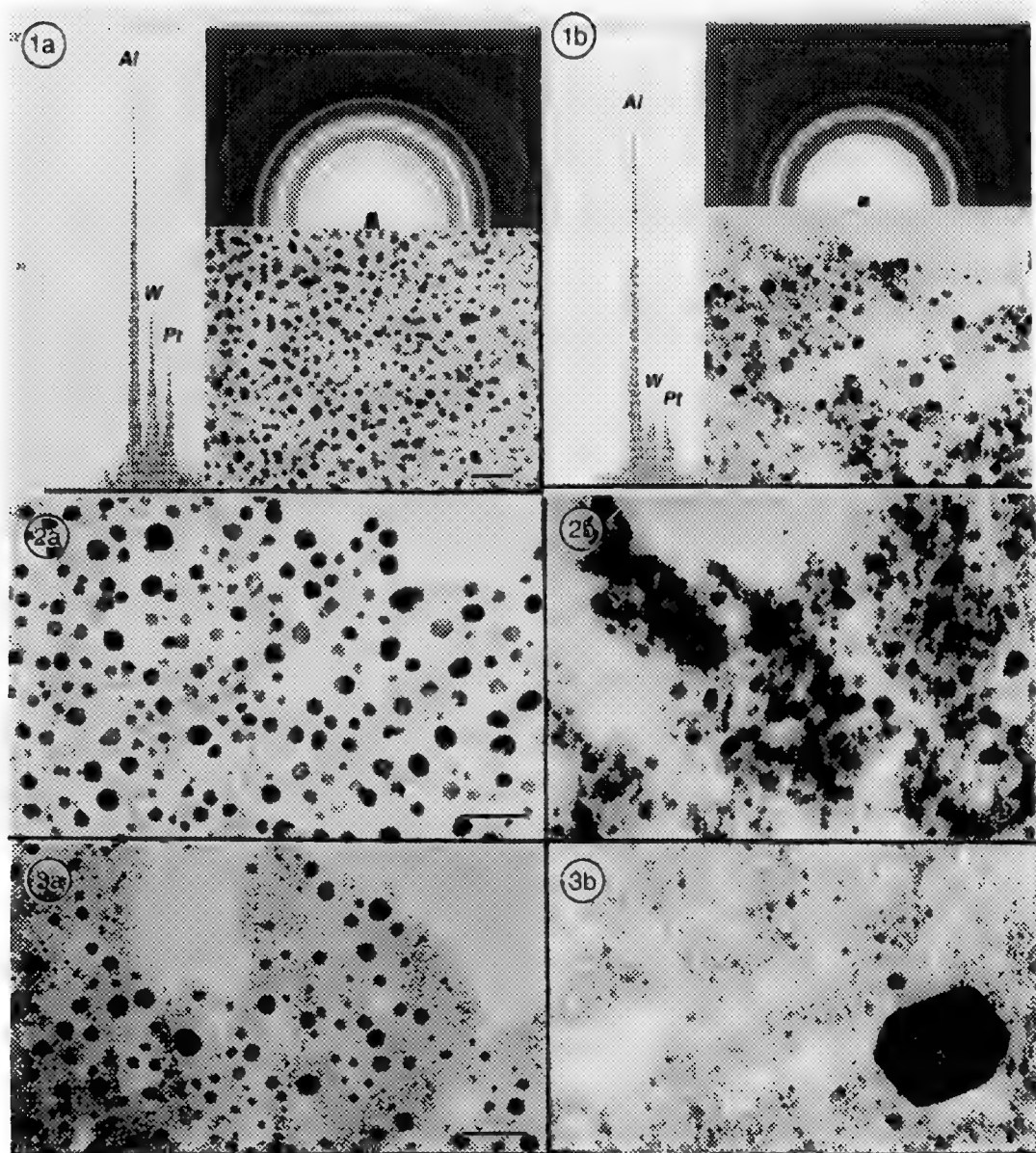
Figure 1 Electron micrographs and diffraction patterns, and EDXS of model A(a) and B(b) supported
Pt catalysts. Porous alumina film was formed on TEM tungsten grid.

Figure 2 Elctron micrograph of Model A (a) and Model B (b) catalysts upon H_2 reduction treatment.

Figure 3 Electron micrograph of Model A (a) and Model B (b) upon oxidation treatment.
(scale bar = 100Å)

ATOMIC SCALE IMAGING OF SURFACES IN UHV

L. D. Marks

Department of Materials Science and Engineering, Northwestern University, Evanston, IL 60208

Electron Microscopy of surfaces can in principle provide information that is not available by other techniques. Arguably the most significant is information about the surface structure simultaneously with the bulk atomic structure. Whereas bulk atomic scale information is now routinely available using standard high resolution imaging techniques, imaging surface with similar resolution has proved far harder. To date the only extensively used technique is profile imaging[1], but this has an inherent scientific problem; the imaged area is so thin that there is great uncertainty about how representative the results are of a bulk surface. For instance, one can conclude almost without ambiguity that any results on large unit cell surface structures will be erroneous since the long range elastic strains will be truncated by the specimen thickness.

The plan view imaging mode has in principle far more power and validity since it avoids the boundary problems that will plague profile imaging. Although there have been tantalizing hints that this is possible at the atomic level[2,3], it has not as yet become a fully developed technique. In addition to technical issues such as how thin a specimen needs to be before the surface signal is swamped by the bulk elastic and inelastic scattering, there are the experimental issues of producing samples of sufficiently high quality[4].

From some of our recent results, it would appear that it is not as hard as might have been thought to obtain atomic scale images from surfaces in plan view, see for instance Fig. 1. In fact, it appears to be as easy (or hard) as obtaining conventional high resolution images. The key appears to be to avoid conditions where the bulk lattice contrast overwhelms the surface information, either by using defoci where the bulk contrast is reduced or minimized (Fig. 1a), aperturing off the bulk diffraction spots (Fig. 1b) or by tilting off the zone axis in order to quench the bulk diffraction (Fig. 1c). Multislice simulations indicate that there should readily be sufficient contrast from thin samples, or even thicker samples when using the higher-order Laue zone 1x1 spots, e.g. Fig. 2.

Interpretation of all (or any) of this information remains unclear, and will be discussed in more detail[5].

References

1. L. D. Marks, Surface Science 139 (1984) 281.
2. G. Nihoul et al., Ultramicroscopy 12 (1983-84) 353.
3. S. Ozawa et al., Mat. Res. Soc. Symp. Proc. 202 (1991) 311.
4. D. Dunn et al, Ultramicroscopy 38 (1991) 333.
5. This work was supported by the Airforce Office of Scientific Research on grant number AFOSR 86-0344 DEF, and draws heavily upon the work of D. Dunn, P. Xu and J. P. Zhang.
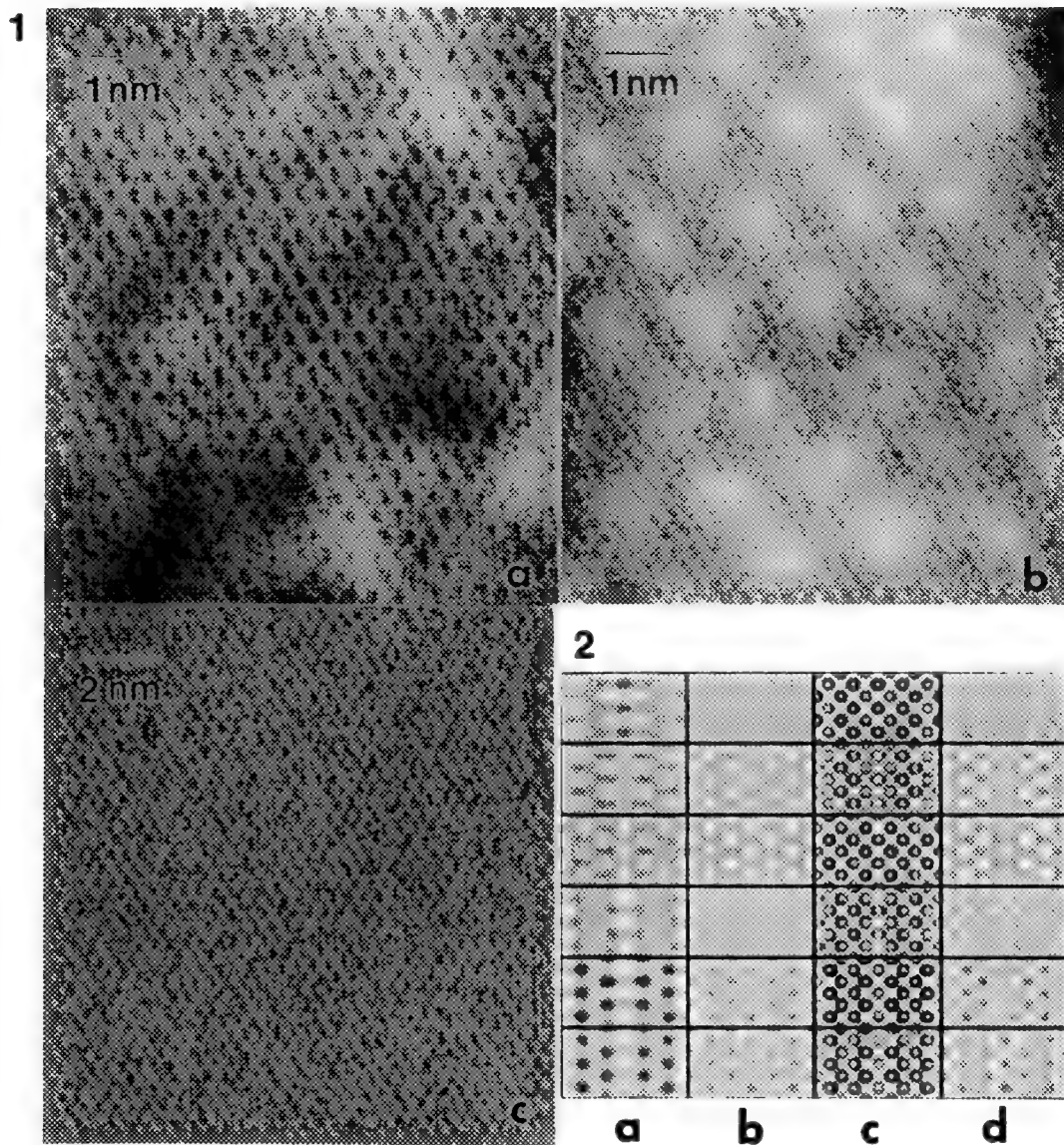
Fig. 1. High resolution images showing the silicon 1x1 lattice (0.31 nm) from a silicon (111) sample with a monolayer Cu-Au coverage as discussed in the text.

Fig. 2. Simulated images for a gold (001) 5x1 surface (top surface) at defoci from 0 to -50 nm in steps of 10nm down for: a) and b) 2.5 and 5.0 nm thicknesses respectively excluding the bulk {200}; c) and d) 2.5 and 5.0 nm thicknesses with a large objective aperture. Excepting a) where the contrast has been enhanced by a factor of 2, the grey scale is the same for all the images and the surface layer is clear in b) and d).

OBJECTIVE-LENS DESIGN FOR HIGH RESOLUTION ULTRA HIGH VACUUM ELECTRON MICROSCOPY

Arno J. Bleeker and J. Murray Gibson

Materials Research Laboratory, University of Illinois,
104 S Goodwin Avenue Urbana, IL61801

Although the main use for Transmission electron microscopy is to study bulk phenomena it is also possible to do surface sensitive experiments with this type of instrument. In order to do reliable surface physical experiments it is necessary to improve the vacuum within the vicinity of the specimen to the Ultra High Vacuum (UHV) level. A number of authors report on such improvements[1,2,3,4] . In most designs the experiments with the sample such as deposition and oxidation are done outside the main microscope column. This means that it is not possible to observe the sample under high resolution conditions during these experiments. The importance of the electron microscope as a surface sensitive instrument can be greatly enhanced if it would be possible to do surface physical experiments in-situ. In that way it would become possible to observe the specimen with high resolution during all kinds of surface processes. In order to be able to do these experiments there must exist a large free space around the sample. In this free space auxiliary equipment such as ion guns and MBE cells can be placed. To further enhance the capabilities of the instrument, analyzing tools such as an Auger spectrometer and SIMS equipment can be attached to the microscope. At the University of Illinois an electron microscope capable of imaging the sample during surface physical experiments is presently under construction. In this machine the objective lens section has been replaced by a large (800 mm diameter and 400 mm high) UHV chamber. The specimen is outside the magnetic field of the objective lens in order to obtain as much free space around the sample as possible thus sacrificing resolution.

In order to do high resolution imaging in an electron microscope the sample has to be immersed in the magnetic field of the objective lens. In this way a short focal length and thus small coefficients of spherical and chromatic aberration can be obtained. The problem encountered is that in most such lenses the sample is situated between the polepieces of the lens which obscure the sample from the rest of the chamber.

In the past research has been done into the properties of so called single polepiece lenses[5] . Since there is only a magnetic circuit present on one side of the sample this type of lens is ideally suited for the use in a UHV microscope. Most times these type of lenses are studied as probe forming lenses in scanning microscopes. Here the high magnetic field at the sample can yield small probe sizes. Also, the magnetic field can be used to extract the secondary and backscattered electrons with high efficiency[6]. Juma *et al.*[7], however, showed that if the single polepiece lens is used as an objective lens it is possible to obtain low coefficients of spherical and chromatic aberration in the transmission mode. The most preferred direction for the electron beam in that case is by entering the magnetic field from the polepiece side. In that way the slowly decreasing field focuses the sample onto the selected area aperture. The advantage of this configuration in a UHV setup is that the sample will face downwards (if we assume that the electrons travel from top to bottom in the microscope column). This means that standard MBE sources can be used for deposition

experiments. Figure 1 shows a schematic view of a setup which incorporates a single polepiece lens in a UHV chamber. Since there is no magnetic circuit underneath the sample there is a lot of space to place auxiliary equipment. The spherical and chromatic aberration of the lens, calculated with MLD[8] are 3.5 and 7.0 mm respectively allowing a resolution of 0.45 nm at 100 keV.

References
1 M.L. McDonald, J.M. Gibson and F.C. Unterwald, Rev. Sci. Instrum. 60, 700 (1989)
2 K. Tagayanagi, K. Yagi, K. Kobayashi and G. Honjo, J. Phys E. 11, 441 (1978)
3 K. Heinemann and H. Poppa, J Vac. Sci. Technol. A4 127 (1986)
4 A.J. Bleeker, Optical and Mechanical design for 1 nm resolution Auger Spectroscopy in an Electron Microscope, Thesis T.U. Delft, The Netherlands (1991)
5 T. Mulvey, Unconventional lens design. In Magnetic electron lenses, ed. P.W. Hawkes Springer Berlin (1982)
6 M. Lenc and I. Mullerova, EUREM 88,Inst. Phys. Conf. Ser. No. 93 Vol 1, 117 (1988)
7 S.M. Juma, M.A.A. Khaliq and F.H. Antar, J. Phys E. Sci. Instrum. 16, 1063 (1983)
8 Magnetic Lens Design cf. B. Lencova and G. Wisselink, Nucl. Instum. and Meth, A298, 56 (1990)
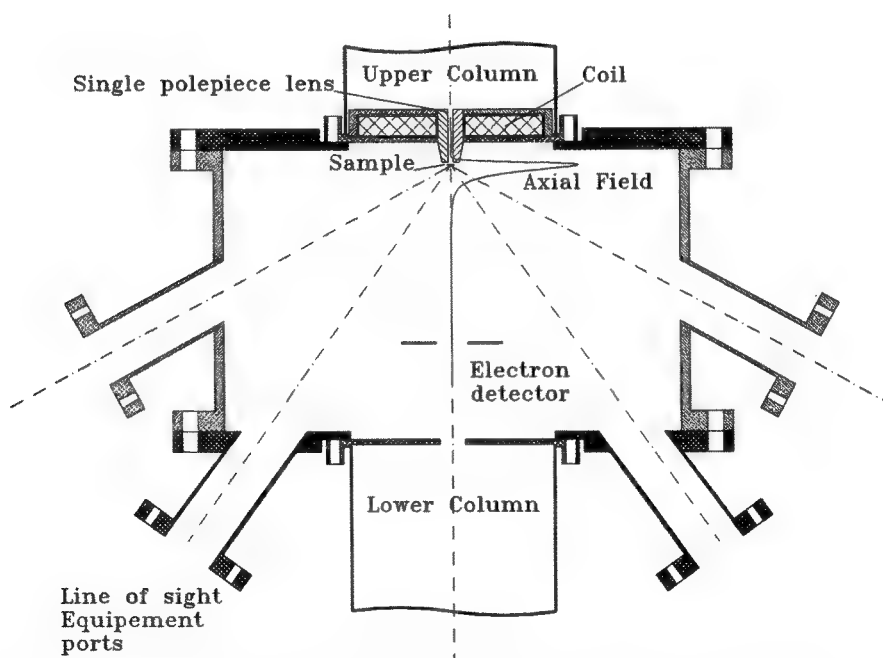
Figure 1. UHV electron microscope setup with a single polepiece objective lens

ELECTRON MICROSCOPY OF SURFACE DYNAMICS

R.M. Tromp

IBM T.J. Watson Research Center, P.O. Box 218, Yorktown Hgt. NY 10598

A proper understanding of the structure and properties of surfaces and interfaces can only be obtained by consideration of the dynamic aspects of their formation and further evolution. In the last few years we have designed and built a Low Energy Electron Microscope (LEEM) for the study of surface dynamics. With an electron energy of only a few eV at the sample a lateral resolution of ~150Å can be obtained, and single height atomic steps can be resolved by phase contrast. Images are obtained at videorate. In this talk I will present results of studies of Ge/Si heteroepitaxial growth, both with and without surfactants, phase transitions on Si(111), 2-D island nucleation and ripening on Si(001), and new step shape phase transitions on Si(001). I will briefly discuss our progress in establishing a new UHV-TEM experiment with in situ surface preparation and diagnostics, such as Molecular Beam Epitaxy, Reflection High Energy Electron Diffraction, Scanning Electron Microscopy, and Auger Electron Spectroscopy.
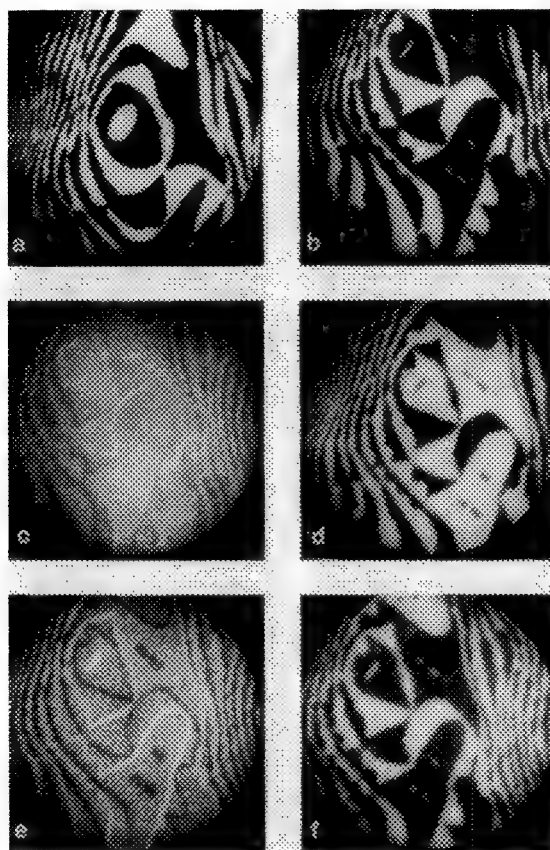
Dark field LEEM images of Ge growth on As terminated Si(001). (a) clean surface, (b) As terminated surface before Ge growth. Approximate Ge coverages: (c) 0.5 ML, (d) 1 ML, (e) 1.5 ML, (f) 2 ML. Field of view is 4 μm. The reversal of contrast at each additional monolayer indicates the layer-by-layer growth mode induced by the As surfactant monolayer. Growth temperature is 630°C.

THE TEMPERATURE STABILITY OF LIGAND STABILIZED GOLD AND BIMETALLIC COLLOIDS

Jan-Olov Bovin

National Center for HREM, Chemical Center, P.O.B. 124, S-221 00 Lund, Sweden

Preparation and characterization of new monodispersed clusters and colloids of different metals are important for use in several applications like catalysis, microelectronics and sintering. The atomic structure of ligand stabilized, 18 nm, gold colloid is important, since they can serve as the core in preparation of bimetallic systems. The recent developments in preparative cluster chemistry[1] have made it possible to make 35 nm bimetallic layered colloids of gold-platinum and gold-palladium. If the colloids should be useful as catalysts, it is important to establish their thermal stability and structure at the elevated temperatures where catalytic reactions take place. The first preliminary results from a high temperature study in an electron microscope with a heating stage are presented here.

The preparation method for the ligand stabilized colloids has been published earlier[1]. The water-solved colloids were collected on holey carbon film and mounted in a heating holder (Hexland environment cell TEM holder). The TEM observations were done in a JEM-2000FX. Due to specimen drift at elevated temperatures, short exposure times (0.1-0.5 s) were used for recording images on photographic film. The photographic films were later digitized and image processed using the SEMPER software. The composition of the edge compared to the whole particle were determined with an EDX-analyzer (Link AN10000), using a beam diameter of about 30 nm, as described previously[1].

The thickness of the ligand shell of the gold colloid was determined by scanning the image contrast over the ligand shell, as shown in the inserted graph (Fig. 1). The distance, 1 nm, between the two Fresnel fringes, of the crystal and the ligand shell was shown to be focus independent. The desorption study of the goldcolloid shows that at 100°C the ligand shell is still 1 nm (Fig. 1), but the image recorded at 150°C shows only one Fresnel fringe and consequently there is no ligand layer (Fig. 2) left at this temperature. The desorption of the ligands occur at 100-150°C, but so far it is not established whether it is a gradual or sudden loss of the layer in this temperature range.

In the case of the Au/Pt system the habitus[1] of the colloids is similar up to about 425°C (Fig. 3). Above 425°C the EDX-analysis of the edges of the colloids approaches the value (approximately 18 at% Au) of the total particle. Around 500°C the habitus of the crystals changes to a more homogeneous shape with visible crystal faces (Fig. 4), and the EDX spectra indicates the same composition all over the crystal.

Heating the Au/Pd colloids from 19°C to 550°C gives another scenario. The ligands are lost at about 100-150°C and small particles down to 2 nm are created on the support. Already between 250°C and 300°C an increase in the Au content can be measured with EDX, but this is followed by a total decrease in Au content. At the same time the small particles start to grow on the support. The crystals at 350°C are homogeneous as indicated by the electron diffractogram in Fig. 5. At 530°C (Fig. 6) crystals of different sizes, some almost pure Au or Pd, can be seen in the same area. The largest ones have a composition of 10 at% Au.

It is clear from this investigation[2] that colloids of Au/Pt and Au/Pd becomes homogeneous alloys at different temperatures and the alloying involves solid state diffusion of atoms. In the case of Au/Pt a single phase should not occur before 1100°C.

References
1. G. Schmid et al, Angew. Chem. Int. Ed. Engl, (1991)30, 874.
2. This work was supported with grants from the Swedish Natural Science Research Council and the Swedish National Energy Administration.
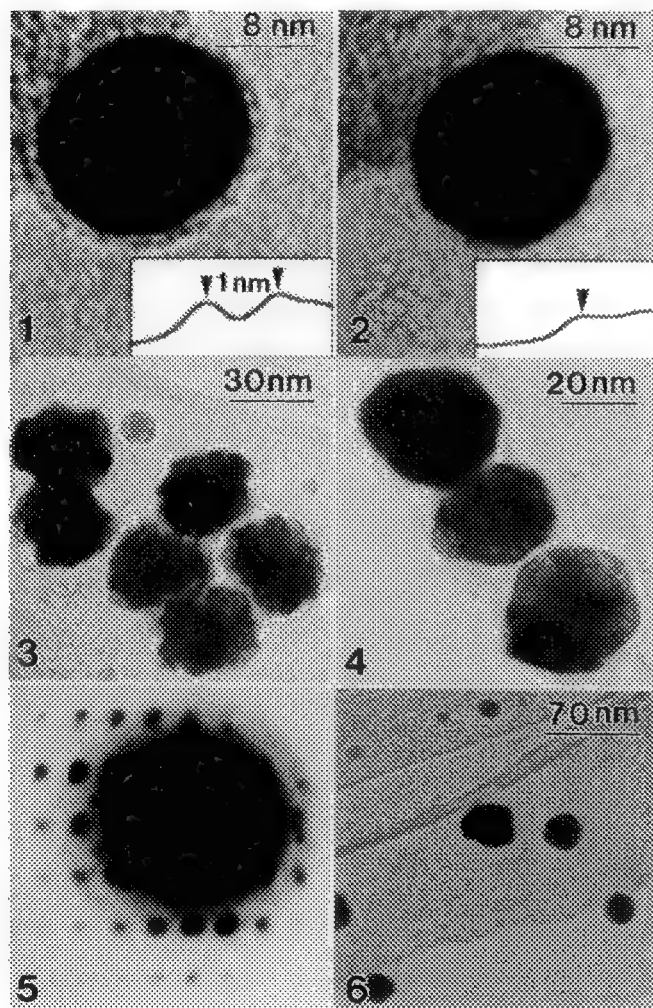
FIG. 1. Au-colloid, recorded at 100°C, showing the ligand shell of 1 nm thickness.
FIG. 2. Au-particle, without ligand shell, recorded at 150°C.
FIG. 3. Au/Pt colloids with small secondary particles recorded at 425°C.
FIG. 4. Homogeneous Au/Pt crystals imaged at 525°C.
FIG. 5. Electron diffraction pattern of a Au/Pd crystal recorded at 350°C.
FIG. 6. Au/Pd particles of different sizes recorded at 530°C.

HIGH-RESOLUTION TEM OF FULLERENES OF DIFFERENT SIZES

Supapan Seraphin and Dan Zhou
Department of Materials Science and Engineering, University of Arizona, Tucson, Arizona 85721

Jun Jiao, Lowell D. Lamb, and Donald R. Huffman
Department of Physics, University of Arizona, Tucson, Arizona 85721

The extraction of macroscopic quantities of the solid phase of the carbon cluster C_{60} by the technique of Krätschmer, Huffman (KH) et.al.[1] has stimulated a large number of investigations into their physical properties. Recently, further developments have led to the extraction from KH-carbon and subsequent mass-spectroscopic characterization of larger clusters C_n, n = 100 to 330, termed giant fullerenes.[2] Of particular interest are studies into the structure of these giant fullerenes. The paper presented here applies the technique of High-Resolution Transmission Electron Microscopy (HRTEM) to an investigation of the structure of the C_{60}, C_{70}, and giant fullerenes, including their transformation under electron beam irradiation. The results show significant differences in the structural response to electron beam irradiation among fullerenes of different sizes.

The samples were prepared by an extraction of KH carbon. Depending on the conditions of preparation and separation, the variety (which differs by numbers of carbon atoms) of fullerenes may change. In this work, crystalline C_{60} and crystalline C_{70} with purity of >99% were obtained by repeated chromatography. TEM samples of C_{60} on holey-carbon grids were produced as vapor deposited thin films, and of C_{70} sample as solution-evaporated platelets. By a recently developed method using a low-boiling-point solvent in a high-pressure high-temperature vessel,[2] giant fullerenes C_n, n = 100 to 330, were extracted as a mixture of different n-values from KH-carbon These specimens were examined at 200 keV with a Hitachi H-8100 TEM that has a structure resolution limit of 0.20 nm, and a C_s value of 0.55 mm.

An HRTEM image of a C_{60} thin film shown in Fig.1 reveals the close-packed configuration of the f.c.c. structure viewed along the <111> zone axis. The leftmost grain shows a 3-fold symmetry which is evident closest to the grain boundary. Across the grain boundary to the right, the orientation of the grain is slightly tilted away from the beam direction resulting in evenly space, one-direction fringes, instead of uniform cross- fringes. Fig. 2 delineates a 2-fold symmetry of the lattice image of the same C_{60} sample when viewed along the <110> orientation. There is strong evidence of electron beam damage. The lattice image of the initial crystal is transformed to one typical of an amorphous phase in 4 minutes. This change is consistent with the results of the electron diffraction patterns which is observed to change from a spot to a ring pattern. The lattice image of a C_{70} crystal prepared by solution evaporation is shown in Fig.3. The image reveals typical defect structures. The stacking of closed-packed layers is faulted as indicated by arrow. Note that the perfect lattices and the faults occur in clusters rather than being uniformly distributed throughout the grains, indicating the existence of short-range order in the C_{70} crystal lattices. Like the crystals of C_{60}, the crystalline phase of C_{70} is transformed into the amorphous phase by electron beam irradiation. Fig.4 shows an overview of a giant fullerene particle. Since the sample contained a mixture of fullerenes of different sizes, i.e. wide range of n values, unique atomic lattice images of the sample were not observed, and no unambiguous statement about the shape of the giant fullerene molecules can be made. However, note the circular features on the grain in the high resolution micrograph of Fig.5. The image shows the characteristic fringes of graphite with the typical layer spacing of 3.4 Å. We speculate that the graphitic features formed as a result of electron beam modification of the giant fullerenes. This result is in significant contrast to the results obtained on C_{60} and C_{70} in which the electron beam transforms the initial crystals into an apparently amorphous phase. The fact that the giant fullerene has more hexagons per molecule than do C_{60} and C_{70} may explain why the giant fullerenes are converted, upon irradiation with the electron beam, to a graphitic phase rather than an amorphous phase. The fact that the structures of the fullerenes are apparently modified by electron beams, and that the result depends on the molecule size, may eventually lead to a means for alteration and tailoring of fullerene molecules.

References:

1. W. Krätschmer, L. Lamb, K. Fostiropoulos, D. Huffman, *Nature*, **347**, 354 (1990).
2. L. D. Lamb, D.R. Huffman, R.K. Workman, S. Howells, T. Chen, D. Sarid, and R.F. Ziolo, *Science*, in press.
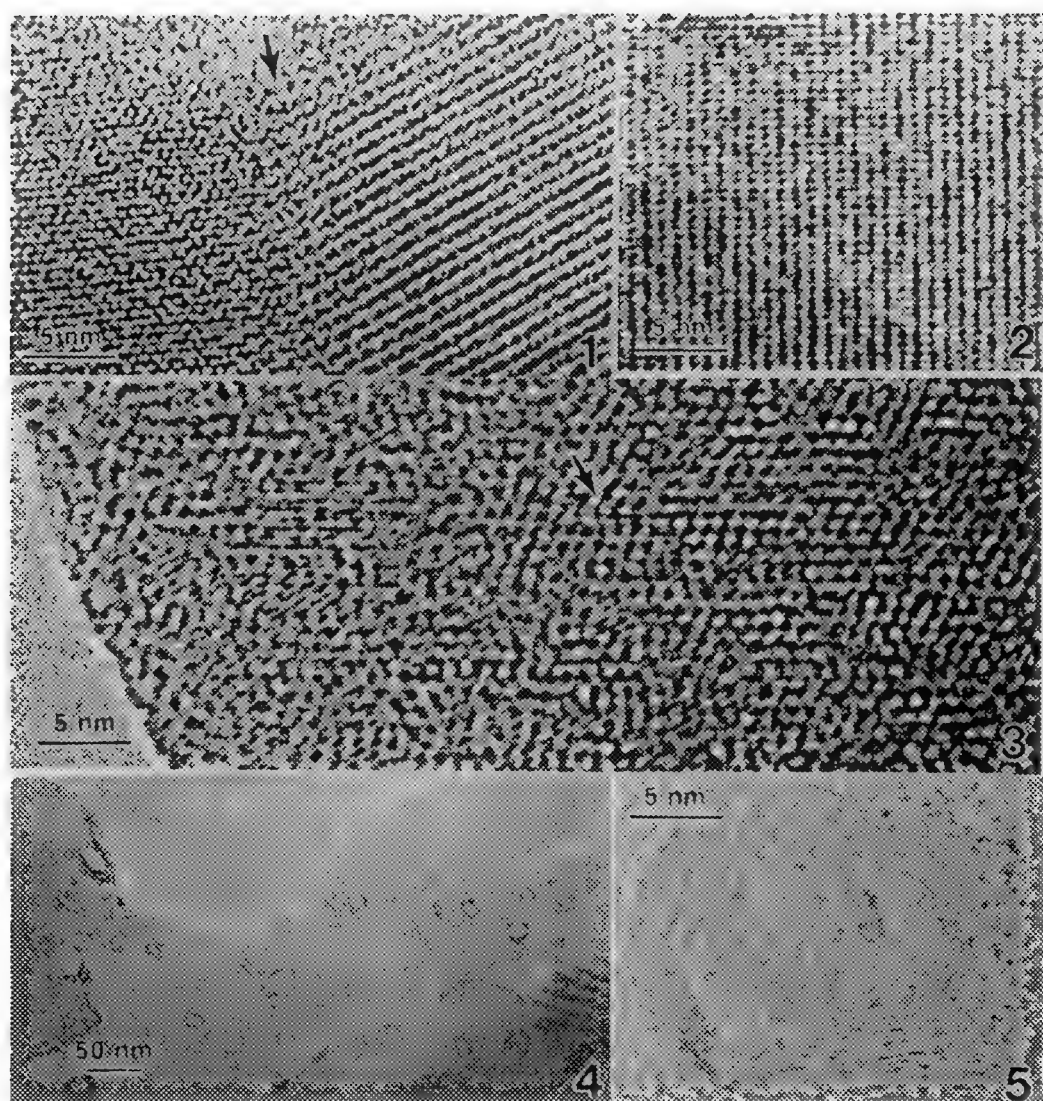
FIG. 1.--Lattice image of <111> C_{60} thin film including a grain boundary (see arrow).
FIG. 2.--High-resolution image of <110> C_{60} thin film.
FIG. 3.--Lattice image of crystalline C_{70}. Arrow indicates stacking fault in crystal.
FIG. 4.--Low magnification overview of giant fullerene platelet.
FIG. 5.--High-resolution image of graphite fringes observed on the giant fullerene crystal in FIG.4 after electron beam irradiation of 4 min.

PLATINUM NANOCLUSTERS IN DOPED GLASSY CARBON: AN ELECTRON MICROSCOPICAL INVESTIGATION

Richard J. Spontak,[*] Michael E. Huston,[†] Nicolas L. Pocard[†] and Matthew R. Callstrom[†]

[*] Miami Valley Laboratories, The Procter & Gamble Company, Cincinnati, OH 45239
[†] Department of Chemistry, The Ohio State University, Columbus, OH 43210

Fabrication of materials which possess a fine dispersion of nanoscale metallic clusters (referred to here as nanoclusters) is of both commercial and fundamental importance. The relatively large surface area of these particulates makes them particularly attractive for applications in molecular catalysis[1] and microelectronics.[2] From a more fundamental viewpoint, they collectively represent structural intermediates between single atoms and crystalline solids. Efforts designed to produce metallic nanoclusters systematically on specific surfaces or in bulk media have relied on a variety of techniques, such as metal evaporation[3] and sol-gel processes,[4] just to name two. Recent efforts[5] have shown that thermolysis of platinum-containing carbon precursors results in Pt(0) nanoclusters dispersed within a stable conductive carbon matrix. These doped materials, at only 1 atom% Pt, exhibit voltammetric responses for H^+ and O_2 similar to those of pure platinum while remaining significantly more stable (presumably due to the rigid matrix). The focus of the present work is to employ transmission electron microscopy (TEM) to correlate the characteristics of these nanoclusters with conditions of preparation.

A series of platinum-doped glassy carbon (Pt-DGC) specimens were prepared at different concentrations of platinum and at different temperatures. In all cases, the process by which these materials were produced is shown in Fig. 1. Poly(phenylene diacetylene) (denoted 1 in Fig. 1) was reacted with ethylene bis(triphenylphosphine)platinum (2) in toluene at 65° C to produce oligomers (3). The oligomers were cast from toluene on sodium chloride substrates and heated to 600° C to produce electron-transparent films of Pt-DGC (4). The rocksalt was dissolved and the thin films picked up on 1000-mesh copper grids. Pt-DGC films heated to 800° C could not be cast onto rocksalt (due to sublimation of the substrate at 800° C). Thick (2 mm) films were subsequently embedded in Spurr's resin and sectioned at ambient temperature with a Diatech diamond knife on a Reichert-Jung FC-4E ultramicrotome. The resultant TEM specimens were picked up on holey copper grids, since the thin sections of Pt-DGC dispersed upon contact with water in the knife trough. Electron micrographs were obtained with a Zeiss EM902 electron microscope, operated at 80 keV and various energy losses, and a Philips CM12 electron microscope, operated at 120 keV.

Figure 2 is a series of bright-field images revealing the presence of Pt nanoclusters in the doped glassy carbons annealed at 600° C on rocksalt. The glassy carbon in the absence of Pt loading is shown in Fig. 2a. If the content of Pt is only 0.6 atom%, discrete nanoclusters are observed (Fig. 2b). An increase to 1.0 atom% Pt results in a higher population density of nanoclusters and larger particles (Fig. 2c). Histogram analysis of these materials indicates that the average nanocluster size is approximately 1.4±0.6 nm (Fig. 2b) and 2.1±0.7 nm (Fig. 2c). Note that selected-area electron diffractograms of these specimens exhibit diffuse rings from amorphous carbon, but do not yield discernible ring patterns for the Pt. When the thermolysis temperature is increased to 800° C, however, the nanoclusters in a 1 atom% Pt system appear to become larger. Figure 3 is a micrograph of this Pt-DGC, in which particulates are observed near the edge of a thin section that apparently cleaved during microtoming. Here, they measure about 3.0±0.6 nm across. In addition to the increase in size, these nanoclusters possess some degree of crystallinity, since electron diffractograms reveal isotropic reflections that correspond to metallic Pt(0). This valence is in agreement with that determined by x-ray photoelectron spectroscopy.[6] A pair of bright-field/dark-field images are presented for comparison in Fig. 4. The bright-field micrograph (Fig. 4a) illustrates both the nanoclusters and the sheath-like morphology the Pt-DGC film assumed upon sectioning. Corresponding bright speckles are observed in the elastic dark-field complement (Fig. 4b), which was recorded with diffraction contrast from the diffractogram. Efforts are currently underway to establish the size at which these nanoclusters are capable of crystallizing.

References

1. S. C. Davis and K. J. Klabunde, Chem. Rev. (1982)82, 153.
2. M. L. Steigerwald and L. E. Brus, Annu. Rev. Mater. Sci. (1989)19, 471.
3. R. W. Siegel, MRS Bull. (1990)15, 60.
4. B. Breitscheidel et al., Chem. Mater. (1991)3, 559.
5. N. L. Pocard et al., J. Amer. Chem. Soc. (1992)114, 769.
6. M. R. Callstrom, work in progress.
7. This work was partially funded by a grant from the National Science Foundation (CHE-9007132).
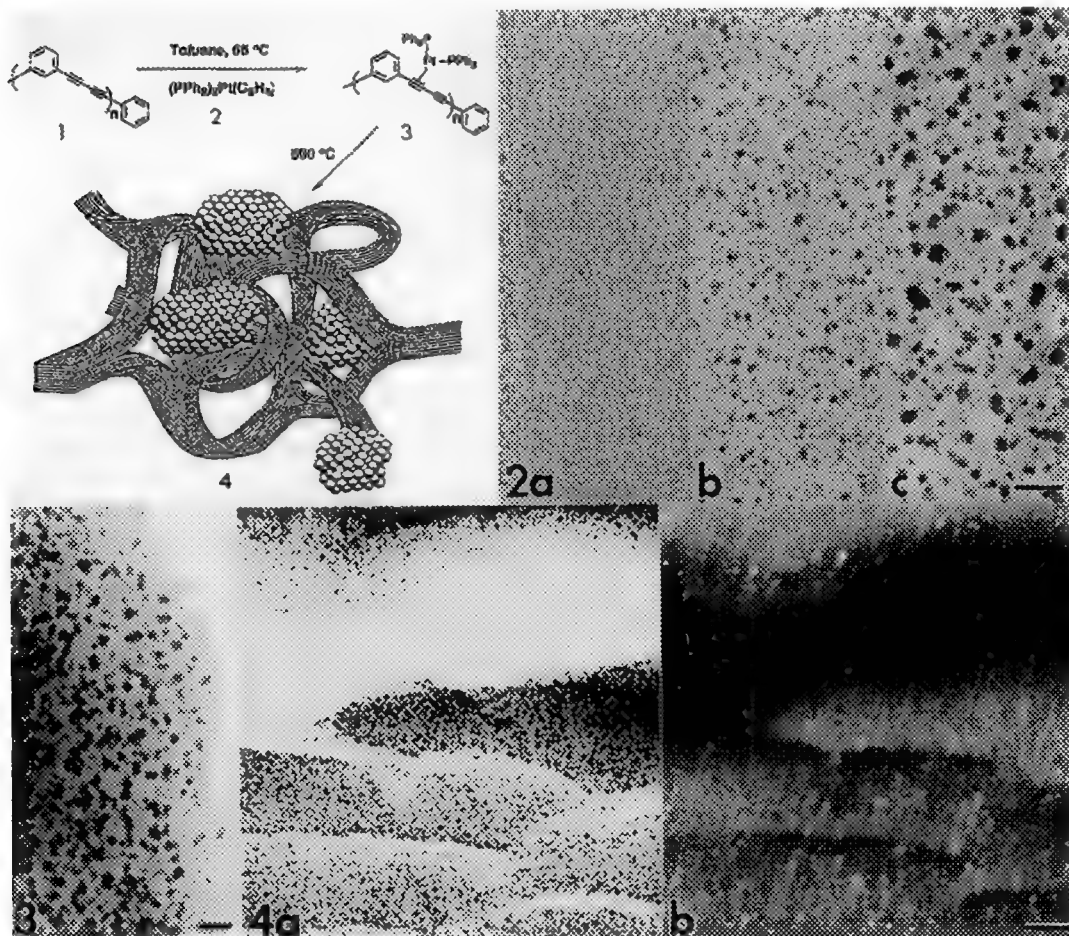
FIG. 1.--Schematic illustration of chemical process responsible for formation of Pt-doped glassy carbon. Reactants (1 and 2) and intermediate (3) are described in text. (4) is conception of Pt nanoclusters in glassy carbon matrix.

FIG. 2.--Micrographs of Pt-DGC demonstrating effect of Pt loading. Platinum concentrations (in atom%) are 0.0 (a), 0.6 (b) and 1.0 (c). Bar = 10 nm.

FIG. 3.--TEM image of Pt nanoclusters in film heated to 800° C. Bar = 10 nm.

FIG. 4.--Bright-field (a) and dark-field (b) images from film annealed at 800° C. Bright speckles in (b) are obtained with diffraction contrast from polycrystalline electron diffractogram. Bar = 50 nm.

301

LOW-DOSE HIGH-RESOLUTION ELECTRON MICROSCOPY OF ZEOLITE MATERIALS WITH SLOW A SCAN CCD CAMERA

M. Pan and P.A. Crozier

Center for Solid State Science, Arizona State University, Tempe, AZ 85287-1704

Zeolite materials are widely used as an important type of catalyst in oil industry. Their catalytic properties and performance are closely related to their unique structures. Use of high resolution electron microscopy (HREM) to characterize structures of zeolite materials has been limited mainly due to the great sensitivity of the framework structures to electron beam irradiation used in the observation[1]. With the recent development in solid state electronics, a new type of image recording device, known as a charge-coupled-device (CCD), has been made possible[2]. Among many of its superior properties, it has been found that the very low noise level present in a slow scan CCD camera offers the possibility of recording high resolution structure images of zeolite materials with very low electron beam dose. The digital storage of CCD images allows on-line image processing to be performed at the microscope, thus making the recording of low dose electron microscope images more efficient. Image processing was also found to be essential in extracting high resolution structure information contained in the noisy low dose HREM CCD images.

The HREM imaging was performed on a JEOL 4000EX electron microscope operated at 400 kV with a point-to-point resolution of 1.7Å. The microscope was equipped with a Gatan 679 slow scan CCD camera which has 1024×1024 pixels; each pixel is 24 μm × 24μm. The low dose images were recorded by use of the smallest spot size at a magnification of 500,000. ZSM-5 zeolite crystals were used in the experiment. The electron dose used to record low dose HREM images was about ~50 e-/Å^2. A real space averaging method[3] was used to reduce the image noise and extract the averaged unit cell structure. The image processing package SEMPER 6 was used in our studies.

Figure 1 shows a 1024×1024 gain-normalized low dose image of a ZSM-5 crystal in the [010] projection. The total electron dose used to acquire this image was about 56 e-/Å^2. The image appears noisy with very low contrast . However the corresponding digital diffractogram (inset) shows reflections out to 2.01 Å. To perform real space averaging, a small motif (shown in fig.2a), containing approximately one unit cell, was arbitrarily chosen from the image in fig.1a. As expected, the cross correlation function (not shown) of the motif with the original image (fig.1a) shows strong periodic intensity peaks, indicating that the image contains periodic structure information of the zeolite despite of the presence of large amount of noise. A total of 290 peaks were found above a given intensity threshold. The correlation function was used to extract the unit cell from the original raw image for subsequent averaging. An averaged unit cell for ZSM-5 was obtained and shown in fig.2b. The averaged image shows a significant improvement in signal-to-noise ratio (SNR) as compared with fig.2a (the fine straight lines in the background of the averaged image are the chicken-wire pattern of the CCD camera). The SNR improves with the square root of the number of superpositions. In addition to resolving the large 10-member rings, the smaller 5- and 6-member rings are clearly seen. The structure model in the [010] projection for ZSM-5 is shown in fig.2c for comparison. The intensities of 6-member rings are clearly different from those of 5-member rings. The inversion symmetry present in the ZSM-5 structure can also be seen in the averaged image as indicated by the arrows in fig.2b.

We have demonstrated the use of a commercially available slow scan CCD camera to perform low dose HREM on ZSM-5 zeolite. At present the main disadvantage is the limited array size (1024×1024 pixels) which restricts the number of unit cells contained in an image. However, under low dose conditions, the slow scan CCD camera has the advantages of very low readout noise and digital storage which allows for immediate evaluation of recorded images on-line, making the image acquisition more efficient. Image processing of low dose HREM CCD images is essential to obtain high resolution structural information[4].

References
1. M.M.J. Treacy and J.M. Newsam, Ultramicroscopy 23 (1987) 411.
2. P.E. Mooney, G.Y. Fan, C.E. Meyer, K.V. Truong, D.B. Bui and O.L. Krivanek, in: Proc. XIIth Intern. Congr. for Elec. Micros., Seattle, WA, Vol.1 (1990) 164.
3. W.O. Saxton and J. Frank, Ultramicroscopy 2 (1977) 219.
4. This work was supported by the HREM Industrial Associates Program at ASU and performed at ASU HREM Facility supported by NSF grant DMR-8913384. We thank Mobil R&D Corp. for providing the zeolite samples.
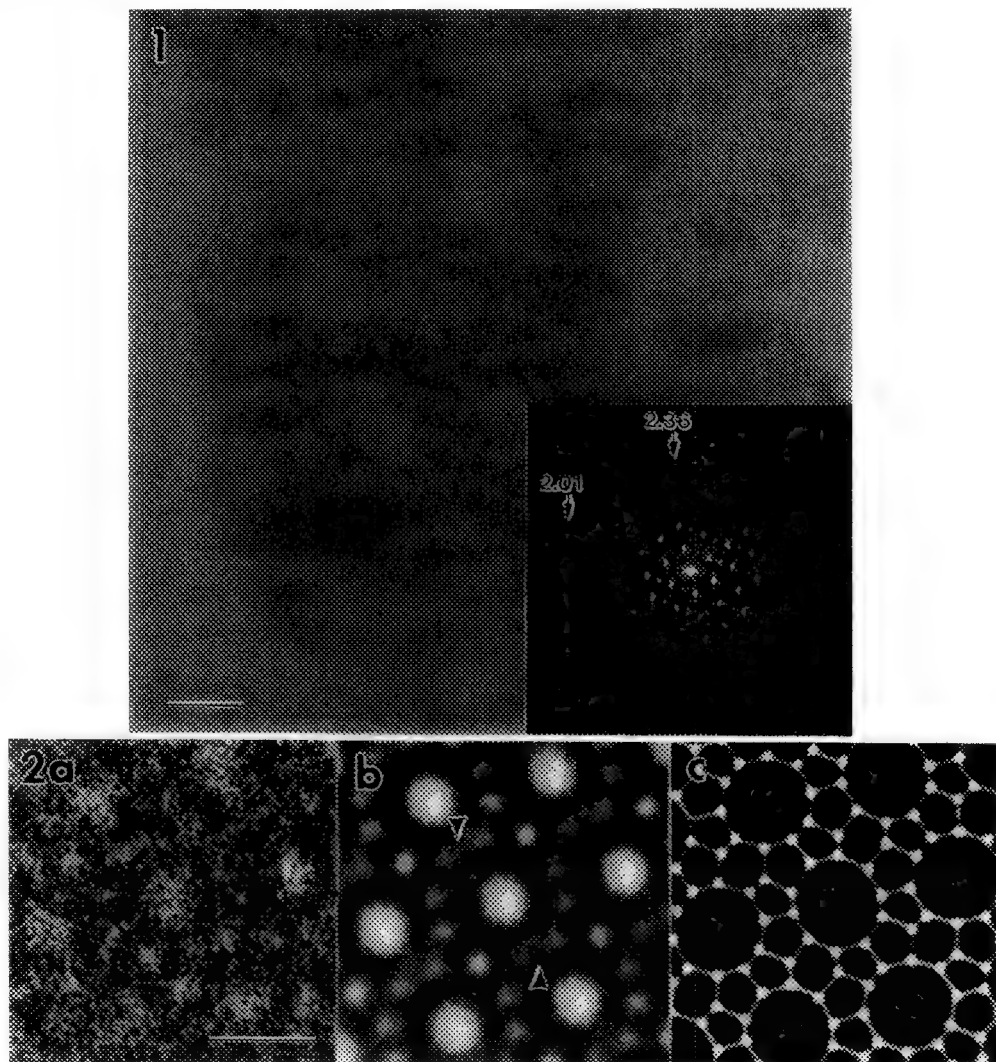
Fig.1 1024 × 1024 gain-normalized HREM low dose image of a ZSM-5 crystal in the [010] projection. The inset is corresponding digital diffractogram showing reflections out to 2.01 Å. Bar = 30Å.
Fig.2 (a) Motif used in real space averaging.(b) motif averaged 290 times. (c) structure model of ZSM-5 zeolite in the [010] projection. Bar = 10 Å.

303

A STUDY ON THE FORMATION OF HYDROTHERMALLY PREPARED BaTiO$_3$ PARTICLES

Fatih Dogan, Jun Liu, Mehmet Sarikaya, and Ilhan A. Aksay

Department of Materials Science and Engineering, Advanced Materials Technology Center, Washington Technology Center, University of Washington, Seattle, WA 98195

BaTiO$_3$ is an important ferroelectric material because of its high dielectric constant. To increase the optical transparency and mechanical strength, it is desirable to produce fine grained BaTiO$_3$. Fine particles can be produced by colloidal processing techniques. In this case, however, it is usually necessary to synthesize monodispersed BaTiO$_3$ particles with a predetermined diameter in a suspension. One widely used method to produce colloidal BaTiO$_3$ particles is by reacting TiO$_2$ particles with Ba(OH)$_2$ in an aqueous solution at a moderately low temperature, i.e., T < 100 °C. Monodispersed particles with a diameter of either about 100 nm or 0.5 μm can be produced this way.[1] It has been suggested that this process is controlled by a diffusion mechanism in which Ba^{2+} ions diffuse into TiO$_2$ particles and a "shell" of BaTiO$_3$ forms on the surface which then advances inward to complete the transformation. According to this hypothesis, the final BaTiO$_3$ particle size is controlled by the initial size of the TiO$_2$ particles through mass balance during the reaction. However, initial TiO$_2$ particle sizes are always much smaller and have a wide size distribution (average particle size about 300 Å). In addition, they are highly agglomerated. Therefore, it is difficult to explain the final monodispersity at diameters of either 100 nm or 0.5 μm. It is desirable to control the size and the surface properties of colloidally prepared BaTiO$_3$ particles and this requires an understanding of the mechanism of particle formation. The goal of this study was to achieve a better insight into the mechanism of BaTiO$_3$ particle formation in colloidal suspensions by a detailed TEM investigation during the formation stages.

In this study, TiO$_2$ particles were first mixed with a Ba(OH)$_2$ solution at 80°C. Then, a small amount of the solution was collected at different times during the reaction process and washed with distilled water by centrifuge. The samples were placed onto TEM grids containing suspended carbon films. Through TEM study it was revealed that BaTiO$_3$ particles were not formed by the mechanism outlined above. Instead, TiO$_2$ first dissolves into the solution and then reacts with Ba^{2+} ions to form nuclei directly from the solution. Subsequently, the nuclei gradually grow to larger particles with rough surfaces. The system usually stabilizes after a long period of time, which allows the particles to sphereodize. This reaction sequence is illustrated in Fig. 1 (a-d). In addition, high resolution electron microscopy on both the TiO$_2$ particles and BaTiO$_3$ particles during the reaction produced no evidence of the presence of surface reaction or shell formation, as hypothesized in the literature based on the diffusion model (Fig. 2). Our observation suggests that there is no direct relationship between the final BaTiO$_3$ and the initial TiO$_2$ particle sizes. Studies are underway to understand why the final particles stabilize at a certain size under certain conditions. The answers to these questions will be helpful in understanding colloidal particle formation, and will provide clues as to how to control particle size and shape in this and other systems prepared by colloidal processing.

1. W. Hertl, *J. Am. Ceram. Soc.*, **71**, 879-883 (1988).
2. Supported by the Air Force Office of Scientific Research under Contract No. AFOSR-91-0040.
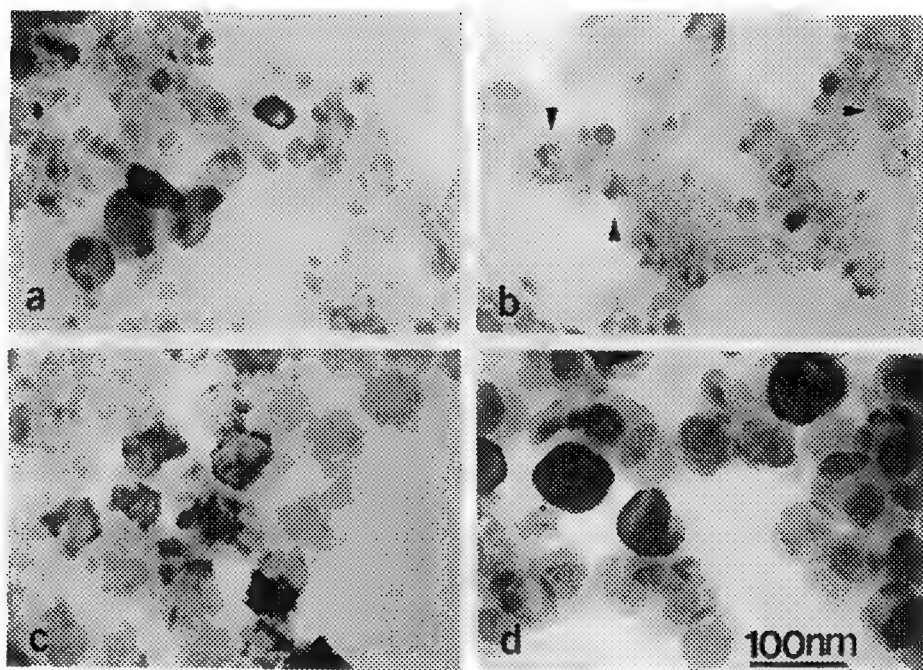
Fig. 1. Sequence of $BaTiO_3$ particle formation: (a) Initial TiO_2 particles. (b) Dissolution of TiO_2 into the solution at t=30 minutes; note that some $BaTiO_3$ nuclei begin to appear (arrows). (c) $BaTiO_3$ particles at t=2 hours. (d) $BaTiO_3$ particles at the final stage.
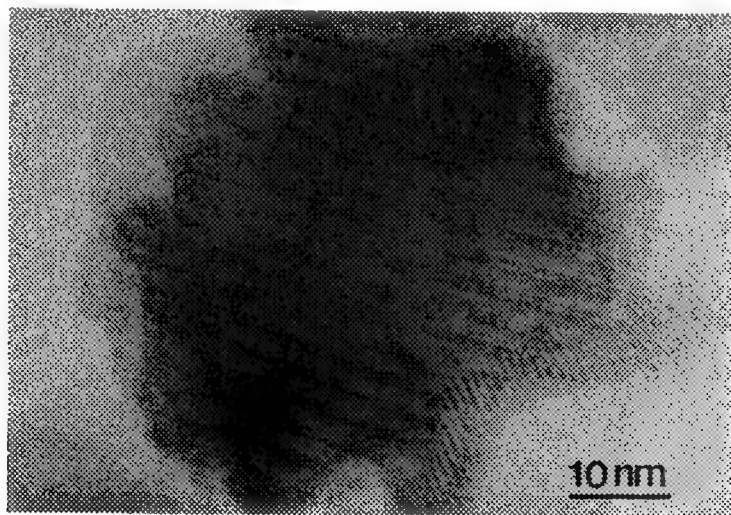
Fig. 2. High resolution image of a $BaTiO_3$ particles formed during the reaction sequence.

305

A STUDY OF THE CRYSTAL NUCLEATION MECHANISM IN SUBMICRON DROPLETS OF PURE ELEMENTS

Louis M. Holzman

Materials Science Program, University of Wisconsin, Madison WI 53706

Liquid-to-crystal nucleation is an important fundamental process to understand as many materials go through the liquid-to-crystal phase transformation in processing. Unfortunately, most previous nucleation experiments have been unable to demonstrate that homogeneous nucleation was the active mechanism and the distribution of heterogeneous nucleants in these systems was unknown, so few concrete conclusions could be reached. In this research, homogeneous nucleation is shown to be operative for the case of submicron droplets of pure silicon and germanium quenched from the melt.

Research on homogeneous nucleation has generally used the method of breaking a large liquid mass into many small droplets (micron-sized) in order to isolate any heterogeneous nucleants present into a small number fraction of the droplets, as Turnbull did in his pioneering investigation of the solidification of mercury.[1] Subsequent research by Perepezko and Rasmussen, however, showed that the nucleation in this case took place heterogeneously.[2]

Electrohydrodynamic atomization (EHD)[3] produces very small droplets (5-200nm) which allows heterogeneous nucleants to be isolated more effectively than previously possible. In this process, the droplets are sprayed from the tip of a molten wire or rod by the application of a large electric field and cool in free flight in the EHD vacuum chamber at rates of 10^5 to 10^7 K/s. At least 10 pure elements have been solidified into the amorphous state using this method.[4] The droplets are sprayed onto a 10 nm thick carbon film, which is mounted on a finder grid so that double counting can be avoided. The droplets are examined using a VG HB501 STEM in normal image mode. The diffraction pattern is observed and the structure and size of individual droplets is recorded.

The mechanism by which nucleation takes place is determined by analyzing the variation of the fraction crystalline versus amorphous droplets with droplet radius. Since the droplet cooling time is dependent on droplet radius for EHD processing and homogeneous nucleation is time dependent, one can easily differentiate between homogeneous and volume heterogeneous nucleation. This can otherwise be a difficult distinction to make.[5] The structure of a large number of droplets (over 1000) must be examined in order to have a statistically significant determination of the mechanism of nucleation. The results for silicon and germanium are displayed graphically in Figs 1 and 2. It is apparent that the best fit of theory with experiment for both silicon and germanium is for homogeneous nucleation (or for homophase impurity nucleation).[6]

Most droplets that were examined were found to be either fully crystalline or fully amorphous. A few examples were found, however, that were partially crystalline and partially amorphous. A silicon droplet of this type can be seen in Fig. 3, along with the diffraction patterns of the amorphous and crystalline regions.

This research has shown that it is possible to demonstrate the existence of homogeneous liquid-to-crystal nucleation in pure elements by using the extreme processing method of EHD atomization. Further research is underway on silicon and germanium to increase the data set so that the results will be statistically conclusive. Also, the experiment is being repeated for vanadium and iron, and from preliminary results, we are confident that at least one of these (V) will exhibit homogeneous nucleation.

1. D. Turnbull, J. Chem. Phys., 20, 411 (1952).
2. J.H. Perepezko and D.H. Rasmussen, TMS-AIME, 9A, 1490 (1978).
3. J.H. Perel et al., Rapid Solidification Processing Principles and Technologies, (R. Mehrabian, B.H. Kear, M. Cohen, eds.) P. 258, Claitor's Publishing Division, Baton Rouge, LA (1978).
4. Y.-W. Kim et al., Acta Metall., 37, 247 (1989).
5. A.J. Drehman and D. Turnbull, Scripta Met., 15, 5433 (1981).
6. D. Turnbull, Progress in Materials Science, Chalmers Anniversary Volume, 269 (1981).
7. The author would like to thank Professors T.F. Kelly and W.N.G. Hitchon for their assistance.
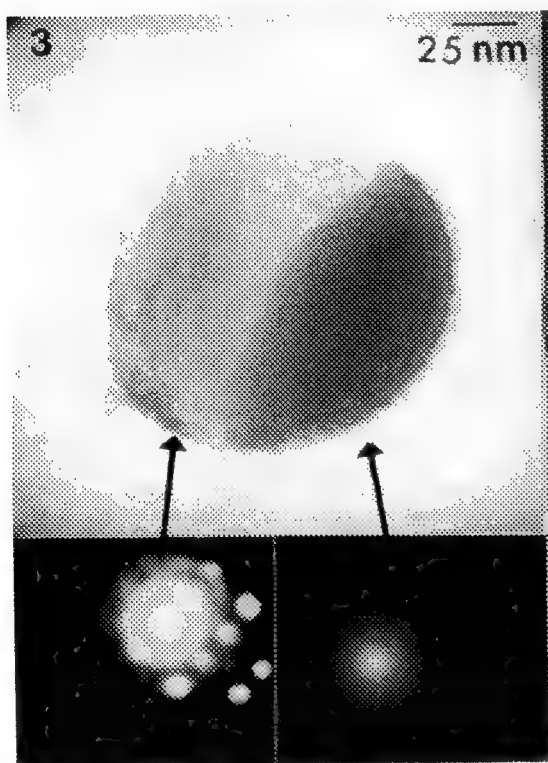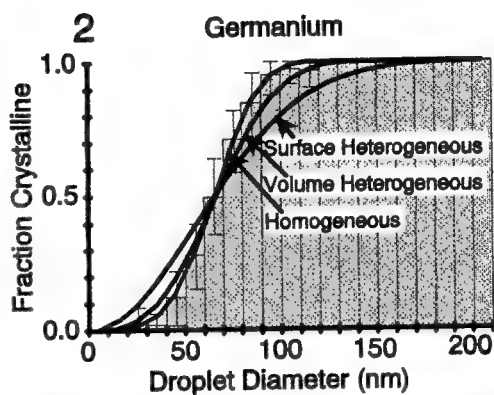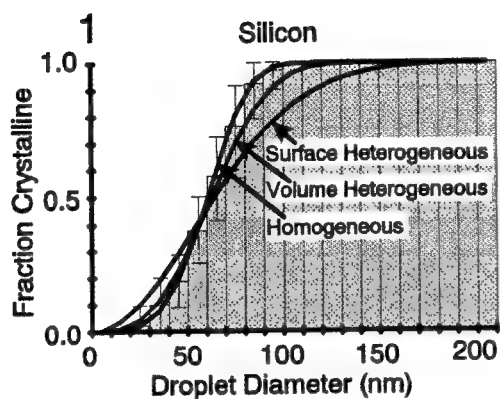
FIG 1.--Comparison between experimental results (histograms) for silicon and best fit for different nucleation mechanisms.

FIG 2.--Comparison between experimental results for germanium and best fit for different nucleation mechanisms.

FIG 3.--STEM image of 122 nm partially crystalline silicon sphere with diffraction patterns.

FIG 4--HRTEM image of silicon sphere.

IMAGING SMALL METAL PARTICLES WITH AUGER ELECTRONS

J. LIU, G. G. HEMBREE[+], G. E. SPINNLER[#] AND J. A. VENABLES[+*]

Center for Solid State Science, Arizona State University, Tempe, AZ 85287
+ Department of Physics, Arizona State University, Tempe, AZ 85287
# Shell Development Company, Westhollow Research Center, P. O. Box 1380, Houston, TX 77251
* Also at School of MaPS, University of Sussex, Brighton BN1 9QH, England

High spatial resolution Auger electron spectroscopy (AES) and scanning Auger microscopy (SAM) have been developed in a UHV scanning transmission electron microscopy (STEM) instrument.[1,2] A resolution < 3 nm has been achieved in SAM images. The application of high resolution AES and SAM to the study of supported catalysts has proved very powerful for extracting chemical information of the surface species.[2] In this paper we report further study of supported metal particles by using high resolution AES and SAM. These experiments were conducted in a VG HB-501S UHV STEM codenamed "MIDAS".[3] Auger electrons were collected from the entrance surface of the sample using a 100 keV probe.

The support materials used in these experiments were MgO smoke crystals and holey-carbon films. The sample was heated to approximately 500° C for 4 hours in the microscope UHV preparation chamber before *in situ* Ag deposition. Pure silver was evaporated onto the MgO/carbon support at room temperature from a Knudsen cell. For high resolution AES and SAM experiments an electron beam of < 0.2 nA, within a probe < 2 nm FWHM, was used. All SAM images and AES spectra were acquired digitally. Figure 1 shows an AES spectrum obtained from an area containing deposited Ag particles and the holey-carbon film support. The total acquisition time for this spectrum was approximately 7 minutes. The carbon KLL and the Ag MNN Auger peaks are revealed clearly. Energy filtered images collected at the Auger peak energy (A) and just above the Auger peak energy (B) were obtained for each element. The full Auger information for such a sample can be extracted by acquiring A and B type images for each element, and can be displayed in various ratio forms. The algorithm (A-B)/(A+B), which produces an elemental specific map, can be obtained by off-line processing of the digitized images. Elemental maps of carbon and silver are shown in Figures 2a and 2b, respectively. The Ag particles are shown dark in the carbon map and they are revealed with bright contrast in the silver map. The signal-to-noise ratio in these elemental maps is much worse than that in the corresponding Auger peak images.

Figure 3 shows a Ag MNN AES spectrum obtained from a small MgO cube deposited with 1.2 ML Ag. The acquisition time for Figure 3 was about 10 minutes. The peak to background ratio in the spectrum is very good because of the high probe energy and very thin specimen used. The oxygen KLL and magnesium KLL AES have also been obtained from small MgO cubes. The Auger peak image of the Ag particles is shown in Figure 4. Ag particles as small as 2 nm in diameter are clearly revealed with high contrast. The diameters of particles comparable to, or smaller than, the probe size cannot be measured reliably from electron micrographs because the intensity profile of the particle is a complicated convolution of the probe, topography and escape depth with the real dimension of the particle. On the other hand, the integrated Auger signal from a small particle, in the absence of image noise, should be independent of the probe size. Thus we can use the integrated intensity as a measure of the particle size provided that a large particle can be used as an internal calibration.[2] In the small particle limit the total number of collected Auger electrons will be proportional to the volume of the particle, and the distinction between "bulk" and "surface" signals is no longer valid. The number of atoms contained in a small particle, N_1, with an integrated intensity I_1 can be estimated from a large particle (subscript 2) as: $N_1 = N_2(I_1/I_2)$. By using this ratio method we estimated that the small particle indicated by A in Figure 4 contains less than 20 Ag atoms. This pushes the minimum detectable mass to less than 3×10^{-21} g for Auger electron spectroscopy.[4]

References
1. G. G. Hembree et al, Appl. Phys. Lett. 58 (1991) 1890.
2. J. Liu et al, Surface Sci. 262 (1992) L111.
3. G. G. Hembree et al, Ultramicrosc. 31 (1989) 111.
4. This work was supported by Shell Development Company and made use of the ASU Facility for HREM supported by NSF grant DMR-8913384.
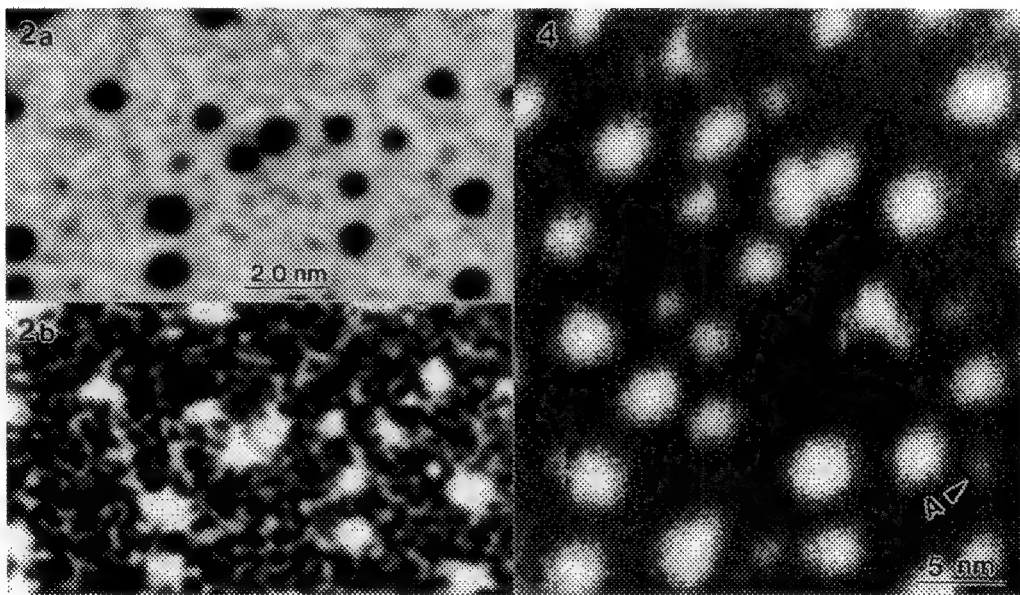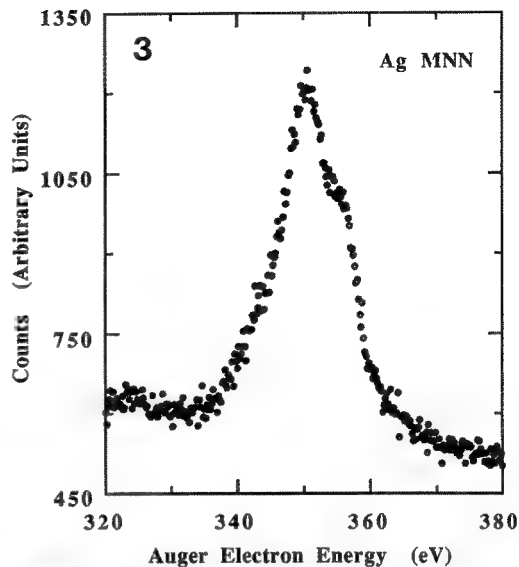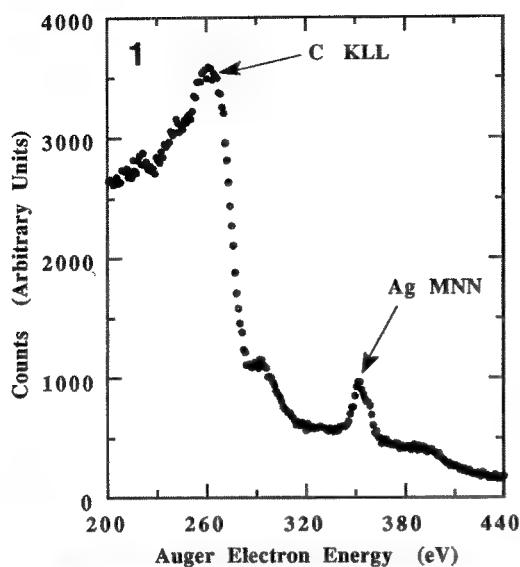
FIG.1 -- AES spectrum obtained from area containing Ag particles and carbon support, revealing C KLL and Ag MNN Auger peaks.

FIG.2 -- Elemental specific maps of carbon (a) and silver (b). Silver particles are shown dark in carbon map and they are revealed with bright contrast in Ag map.

FIG.3 -- Ag MNN AES spectrum obtained from small MgO cube deposited with 1.2 ML Ag.

FIG.4 -- Ag MNN Auger peak image of Ag particles on small MgO cube. Ag particles as small as 2 nm in diameter are revealed clearly.

INVESTIGATION OF VOLUME FRACTION OF OMEGA PARTICLES AND HARDNESS VALUE OF AGED Ti-Mo ALLOY USING DARK-FIELD TEM IMAGING

E. Sukedai and H. Hashimoto

Okayama University of Science, Okayama 700, JAPAN

Investigation about omega phase has been carried out in many alloy systems using X-ray diffraction, electron microscope methods and so on. Volume fraction of aged omega particles seems to be the important factors on the view point of industry, because it influences mechanical properties of alloys. The volume fraction has been investigated using X-ray diffraction[1] and small angle X-ray scattering methods[2]. Except one alloy system, it is very hard to distinguish omega particles using bright field TEM imaging because of strain field in the matrix of alloys and/or around omega particles. However, it is known that using dark field TEM imaging, omega particles in Ti alloys can be seen. This method has other advantageous point; particles of individual omega variants can be seen using isolated diffraction spots from variants. In the present paper, volume fractions of omega variants in Ti-20mass%Mo alloy aged at 623K for 12.6ks, 28.8ks and 100.8ks were estimated using this method and the values were evaluated by considering the strength of alloys aged for these periods.

A plate of Ti-20mass%Mo alloy single crystal having a (10$\bar{1}$) surface was cut, solution heat treated at 1223K for 4.5ks and quenched into water. Specimens for electron microscopy were prepared by an electro-polishing. Dark field images of four omega phase variants were taken using isolated diffraction spots, which were determined by calculating structure factors of each omega variant.

Fig.1 shows dark field images of four omega phase variants in a same area of the specimen aged at 623K for 28.8ks. Incident beams were parallel to [10$\bar{1}$] in (a) and (b), to [31$\bar{1}$] in (c) and to [3$\bar{1}\bar{1}$] in (d). The length along <111> and width of particles can be measured. Fig.2 shows a histogram of volumes of omega particles about one variant. Histograms of other variants were also obtained and the trend was almost same as the one shown in Fig.2. It was noted that the number of particles about 3-5 nm^3 volume was maximum. To estimate the thickness of specimen for measuring the volume fraction of omega particles in the area outlined by white lines in Fig.1, a pair of stereo-micrographs were taken using the isolated spots of one variant; incident beams were parallel to [10$\bar{1}$] and [31$\bar{1}$]. Fig.3 shows the distribution of particles and the thickness of specimen was estimated as a dotted line. The volume fraction of one omega variant can be obtained using this value of thickness and total volume of four omega variants was 7.6%. The volume fractions for aging for 12.6ks and 100.8ks were 1.9% and 10.5%, respectively. It was noted that these values were lower than those obtained using X-ray methods[1,2] about the same composite Ti-Mo alloys aged at 623K for same periods. Then, the present results were evaluated by comparing the hardness values at three stages of aging with the stress which is necessary for dislocations to escape among omega particles based on the precipitation hardening theory. It is assumed that omega particles are distributed homogeneously and Gb is taken as the unit. Fig.4 shows the result and it seems that the volume fraction obtained using dark field TEM imaging explains the trend of increment of hardness value as increasing aging period.

REFERENCES
[1]B.S. Hickmann, Trans AIME. 245 (1969) 1329.
[2]A. Gysler, W Bunk and V Gerold, Z Metallkde., 65 (1974) 411.
[3]E. Sukedai and H. Hashimoto et al., Materials Science and Technology, 8 (1992)3.
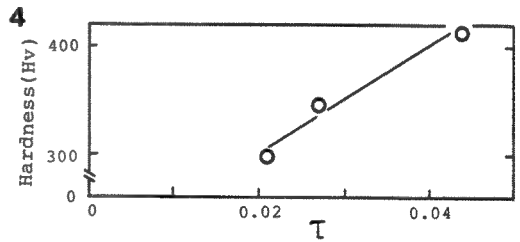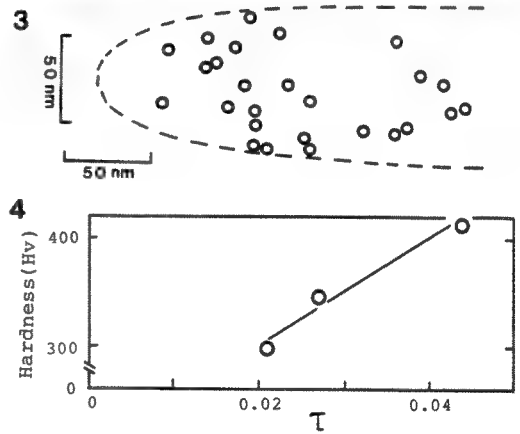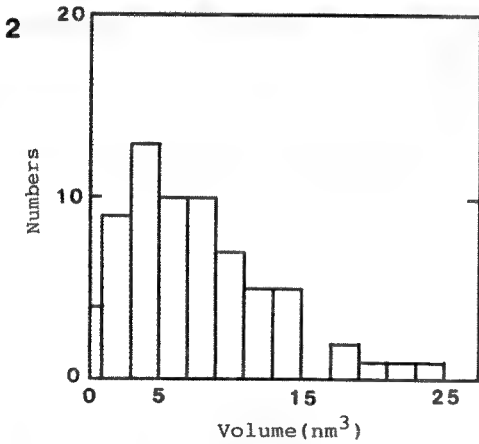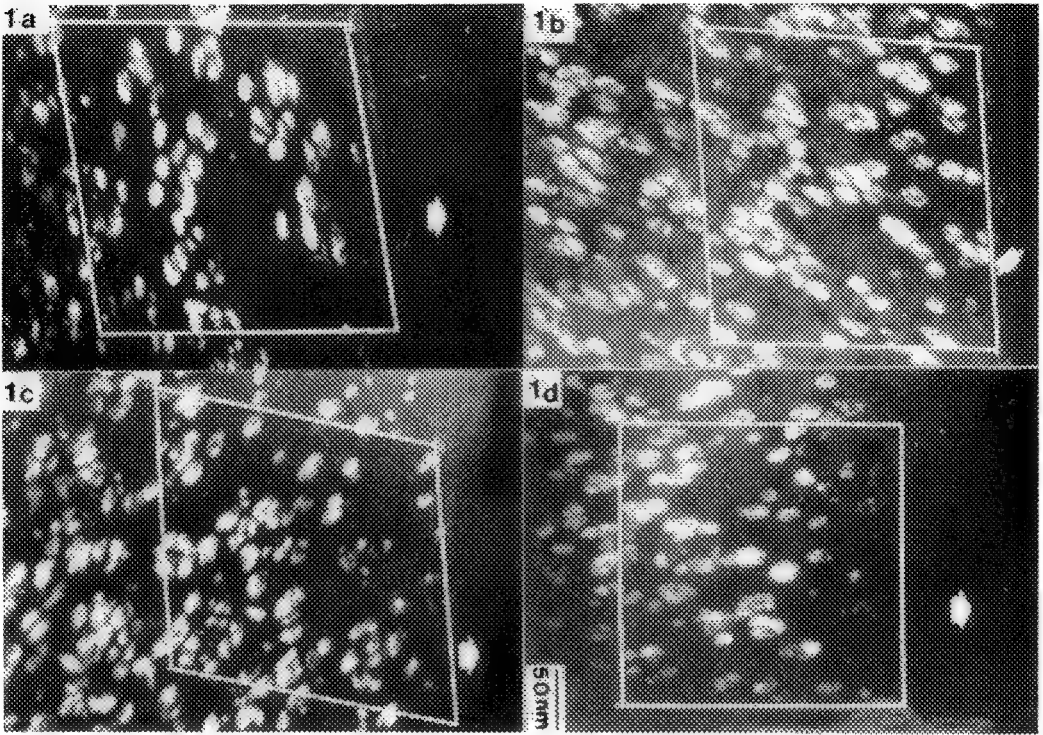
Fig.1. Dark field images of four omega variants at a same place. Incident beams were parallel to [10$\bar{1}$] in (a) and (b), [31$\bar{1}$] in (c) and [3$\bar{1}\bar{1}$] in (d). Arrows show the same point of specimen.

Fig.2. A histogram of volumes of omega particles about one variant.

Fig.3. Distribution of omega particles in a specimen estimated using pair of stereo micrographs: broken line represents cross-section of specimen.

Fig.4. Relationship between hardness value (Hv) and stress (τ) estimated using intervals of omega particles. G b is taken as the unit.

FRACTAL GEOMETRY OF CARBONACEOUS AEROSOL PARTICLES AS DETERMINED USING TRANSMISSION ELECTRON MICROSCOPY

Karen A. Katrinak,[1*] Peter Rez,[3] Paul R. Perkes,[3] and Peter R. Buseck[1,2]

Departments of Geology[1] and Chemistry[2] and Center for Solid State Science,[3] Arizona State University, Tempe, Arizona 85287
*Current address: Energy and Environmental Research Center, University of North Dakota, Grand Forks, North Dakota 58202-8213

Carbonaceous aggregates collected from the aerosol of Phoenix, Arizona have an irregular branched morphology. The aggregates resemble combustion soots and were probably emitted by motor vehicles. Fractal analysis provides a means of quantifying morphologic variations among aggregates and relating these variations to mechanisms of formation. Bright-field transmission electron microscope (TEM) images of 38 individual aggregates were recorded on negatives at magnifications of 15,000 to 200,000. The aggregates have maximum lengths ranging from 0.21 to 2.61 μm and are composed of interconnected spherules, each averaging 26 nm in diameter. The number of spherules in each aggregate ranges from 32 to 1842; the average number is 551. The "nesting squares" method of fractal analysis was applied to digital binary images to calculate the fractal dimension (D) of each aggregate.[1]

The aerosol aggregates were divided into three groups: fractal, non-fractal, and mixed fractal and non-fractal. For the 23 fractal aggregates, D ranges from 1.35 to 1.89. These fractal dimensions are interpretable in terms of cluster-cluster and particle-cluster models, two variations of diffusion-limited aggregation. Many of the aggregates have $1.7 \leq D \leq 1.9$, suggesting cluster-cluster aggregation as the mechanism of formation.[2,3] Aggregates with lower fractal dimensions may form through tip-to-tip models, where electrostatic attraction is used to modify cluster-cluster and particle-cluster aggregation.[4] The 13 aggregates in the non-fractal group were divided into two morphologic types. Those in the first type have complex, branching shapes. Their relatively high density can be explained using the particle-cluster model.[5] Aggregates in the second non-fractal type are covered by coatings that were probably deposited from the ambient atmosphere. The coatings cause the aggregates to appear unusually dense, resulting in classification as non-fractal. The underlying morphology of these aggregates, visible in TEM images, suggests they may be fractal beneath their coatings. The two mixed fractal and non-fractal aggregates each have non-fractal interiors surrounded by an outer fractal region. Their dense centers may have formed through particle-cluster aggregation or by compaction.[6] The low fractal dimensions measured for the outer regions of the aggregates are suggestive of tip-to-tip models.

The range of fractal dimensions indicates that several processes affect the aggregation of carbonaceous aerosols. Process selection appears to be governed by factors other than aggregate size, such as fuel composition and concentration. With sufficient source characterization, it may be possible to use fractal dimensions for aerosol apportionment.[7]

References

1. S.R. Forrest and T.A.J. Witten, J. Phys. A 12 (1979) L109.
2. P. Meakin, Phys. Rev. A 29 (1984) 997.
3. M. Tence et al., J. Physique 47 (1986) 1989.
4. R. Jullien et al., Faraday Discuss. Chem. Soc. 83 (1987) 125.
5. D.A. Weitz and M. Oliveria, Phys. Rev. Lett. 52 (1984) 1433.
6. A. Schmidt-Ott, Appl. Phys. Lett. 52 (1988) 954.
7. This research supported in part by NSF Grant #ATM-9007796.
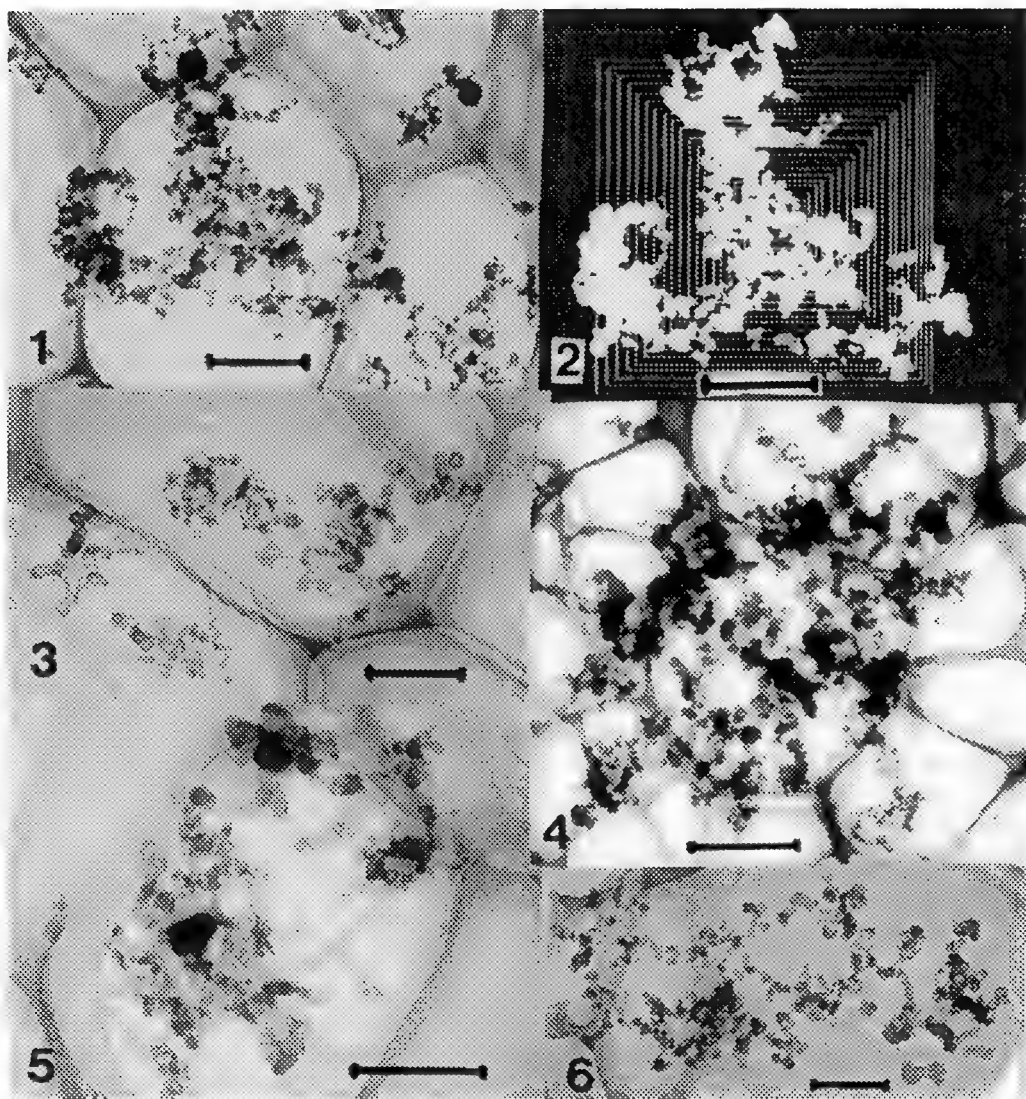
FIG. 1--TEM image of fractal aggregate, with D = 1.4. Bar = 0.5 μm.
FIG. 2--Illustration of "nesting squares" method for fractal analysis, using binary image of aggregate in Fig. 1. Twenty squares are positioned around the center of mass. Bar = 0.5 μm.
FIG. 3--TEM image of fractal aggregate with a shift in D. D = 1.8 in the interior, changing to D = 1.3 at length = 0.2 μm, as measured across the center of mass. Bar = 0.2 μm.
FIG. 4--TEM image of non-fractal, uncoated aggregate. Bar = 0.5 μm.
FIG. 5--TEM image of non-fractal, coated aggregate. The underlying aggregate morphology is partially visible. Bar = 0.2 μm.
FIG. 6--TEM image of aggregate with mixed fractal and non-fractal geometry. The interior portion is fractal, with D = 1.2. At length = 0.3 μm, measured across the center of mass, the geometry shifts to non-fractal. Bar = 0.2 μm.

USE OF FRACTALS TO DESCRIBE MICROSTRUCTURES OF POROUS THICK–FILM PLATINUM ELECTRODES

Steven D. Toteda

Department of Materials Science and Engineering, Whitaker Laboratory #5, Lehigh University, Bethlehem, PA 18015

Zirconia oxygen sensors, in such applications as power plants and automobiles, generally utilize platinum electrodes for the catalytic reaction of dissociating O_2 at the surface. The microstructure of the platinum electrode defines the resulting electrical response. The electrode must be porous enough to allow the oxygen to reach the zirconia surface while still remaining electrically continuous. At low sintering temperatures, the platinum is highly porous and fine grained. The platinum particles sinter together as the firing temperatures are increased. As the sintering temperatures are raised even further, the surface of the platinum begins to facet with lower energy surfaces. These microstructural changes can be seen in Figures 1 and 2, but the goal of the work is to characterize the microstructure by its fractal dimension and then relate the fractal dimension to the electrical response. The sensors were fabricated from zirconia powder stabilized in the cubic phase with 8 mol% percent yttria. Each substrate was sintered for 14 hours at 1200°C. The resulting zirconia pellets, 13mm in diameter and 2mm in thickness, were roughly 97 to 98 percent of theoretical density. The Engelhard #6082 platinum paste was applied to the zirconia disks after they were mechanically polished ($\frac{1}{4}\mu m$ diamond). The electrodes were then sintered at temperatures ranging from 600°C to 1000°C. Each sensor was tested to determine the impedance response from 1Hz to 5,000Hz. These frequencies correspond to the electrode at the test temperature of 600°C.

The sintering conditions and the corresponding changes in the microstructure were monitored with a JEOL 6300F field emission scanning electron microscope. The low-voltage capabilities of the microscope allowed the as-fired platinum film to be imaged at high magnifications without coating, allowing the true surface to be imaged. The surface roughness of the platinum was quantified with the two dimensional fractal[1] dimension, D_2, using a digitizing pad and a computer program written for this purpose. The three dimensional fractal dimension, D_3, was obtained from: $D_3 \approx D_2 + 1$. The use of fractals allowed the microstructural changes to be related to the electrical response of the sensors, supporting recent theoretical treatment.[2]

The change in electrode surface morphology, shown in Figures 1 and 2, affect the impedance response, $Z(\omega)$, of the sensor. The modeling of such sensors generally leads to lumped resistance and capacitance terms, which are macroscopic quantities that tend to loose physical meaning at the molecular level.[3] By observing microscopic changes in the surface of the platinum at various sintering temperatures, the resulting changes in electrical response reveal the physical nature of the limiting mechanisms of the platinum electrodes. Figure 3 gives the impedance data for two extreme experimental conditions, 600°C and 1000°C sintering for five hours. In simplified form, $Z(\omega)$ can be written as $(i\omega C)^{-\alpha}$. The value of α can be extracted from Figure 3 as a structure dependent parameter.[4] This α will increase as the smoothness of the electrode increases.

References:
1. B. B. Mandelbrot, The Fractal Geometry of Nature, New York: W. H. Freeman, (1983) 1.
2. R. de Levie, J. Electroanal. Chem., 281 (1990) 1-21.
3. L. A. Dissado, R. M. Hill, Solid State Ionics, 22 (1987) 331-336.
4. M. M. Gomez, et. al., J. Electroanal. Chem., 317 (1991) 125-137.
5. The author thanks BP America for partial support of this project and Professor C. E. Lyman for helpful discussions.

Sintering	D	Alpha
600 C	2.24	.26
700 C	2.12	.34
800 C	2.04	.40
900 C	2.01	.47
1000 C	2.003	.52
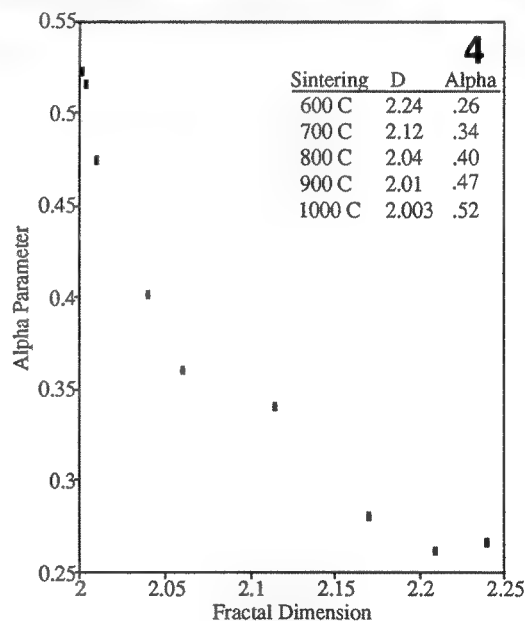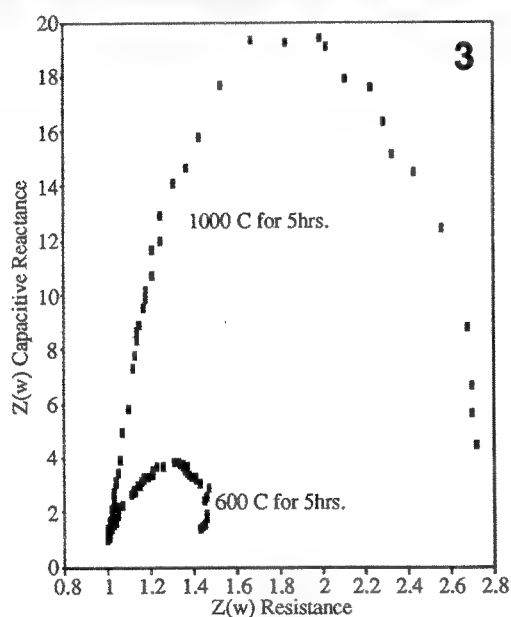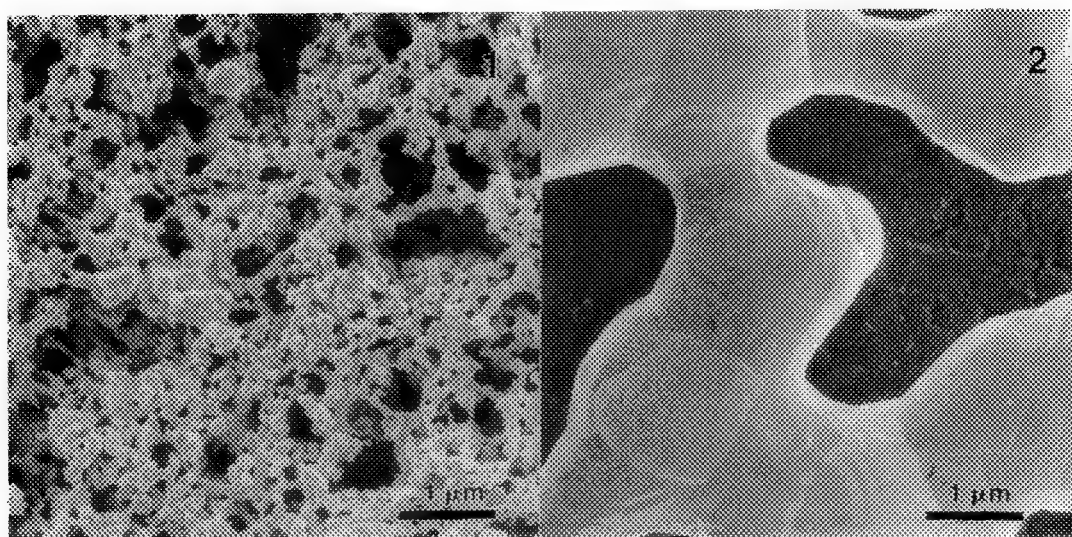
FIGURE 1. Platinum fired at 600°C, showing highly porous microstructure. Calculated fractal dimension is 2.24.

FIGURE 2. Platinum fired at 1000°C, losing high porosity but developing surface orientations. Calculated fractal dimension is 2.003.

FIGURE 3. Impedance data corresponding to the sample sintered at 600°C and 1000°C (normalized). Response changes dramatically with increase in temperature.

FIGURE 4. Value of α corresponding to fractal dimension, D_3, for range of sintering temperatures.

CHARACTERIZATION OF OXIDE FILMS FORMED ON INCONEL 600 AND INCOLOY 800 DURING EXPOSURE TO HIGH-TEMPERATURE WATER

Rafik Allem, Gilles L'Espérance, Francisco Gonzalez[*], Alex M. Brennenstuhl[*] and Mario Caron

Centre for Characterization and Microscopy of Materials (CM^2), Department of Metallurgy and Materials Engineering, École Polytechnique de Montréal, P.O. Box 6079, Station "A", Montréal (Québec), H3C 3A7, Canada

[*] Ontario Hydro Research Division, 800 Kipling Avenue, Toronto, (Ontario), M8Z 5S4, Canada

The structure and composition of oxide films may give an insight into the corrosion resistance of nickel alloys of the type used as tubing in nuclear steam generators. This paper describes the results of a preliminary analytical TEM study aimed at characterizing the surface films formed on Inconel 600 and Incoloy 800 during exposure to high temperature water (300°C).

Alloy coupons were exposed to water at pH 10. pH control was accomplished by additions of either sodium hydroxide or morpholine. Thin foils and extraction replicas were prepared to study the oxide films. Thin electron transparent sections through the oxide/metal interface region were produced using standard techniques[1]. Quantification of the Energy Dispersive and Electron Energy Loss Spectroscopies (EDS and EELS) spectra was carried out using calibration k_{AB} factors and calculated partial cross sections respectively. Identification of crystalline phases was achieved by Focused Beam Electron Diffraction (FBED).

Exposure to high temperature water for both alloys led to the formation of an oxide film which was typically 100 nm thick. High magnification TEM micrographs of cross sections (Fig. 1 and 2) revealed a matrix of small equiaxed grains (10 to 20 nm) and larger submicron crystals with sizes up to 0.5 μm (Fig. 3 and 4) which were either embedded in the film or on the surface. Such submicron crystals were also reported in a recent study[2].

The chemical composition and lattice parameters of the submicron crystals extracted from the oxidized surface of the coupons (Fig. 3) are presented in Table 1. The crystal structure of all the submicron crystals was cubic. The crystals in Inconel 600 were Ni_2O_3 and in Incoloy 800 $NiFe_2O_4$. Such a submicron crystals were observed in thin foils as shown in Figure 4 taken from Incoloy 800. The EELS spectra in the same Figure collected at 300 keV clearly shows the presence of oxygen in the submicron crystal.

The thickness of the oxide film was not uniform and depended on the environment during the exposure. The composition of the film is a function of the type of alloy. EELS data from cross sectional samples showed a chromium/nickel oxide for Inconel 600 and a chromium/iron oxide for Incoloy 800.

It can be concluded that the combination of extraction replics and cross sections are useful complementary approaches for the characterizationn of oxide films in nickel based alloys. This work is presently being continued.

References

1. S. B. Newcomb, C. B. Boothroyd and W. M. Stobbs, J. Microsc. (1985)140, 195.
2. N. S. McIntyre, T. C. Chan and C. Chen, Oxidation of Metals (1990)33, 457.

TABLE 1.--Crystal Structure and Lattice Parameters (in nm) and Chemical Composition (in at. %) as Measured from EDS Spectra Using Calibration k-Factors.

Conditions	Composition (at. %)	lattice (nm)[*]
I-600,NaOH/H_2O	34.0Ni-2.4Fe-0.6Cr-0.7Al-62.3 O	0.436
I-800,NaOH/H_2O	8.1Ni-19.3Fe-0.2Cr-5.2Al-67.2 O	0.834
I-800,NaOH/D_2O	8.4Ni-24.9Fe-0.3Cr-1.7Al-64.7 O	0.831
I-600, Morpholine/H_2O	30.7Ni-5.1Fe-0.6Al-63.6 O	0.418
I-800, Morpholine/H_2O	10.2Ni-21.4Fe-4.3Al-64.1 O	0.831

(*) error bar is 0.007 nm
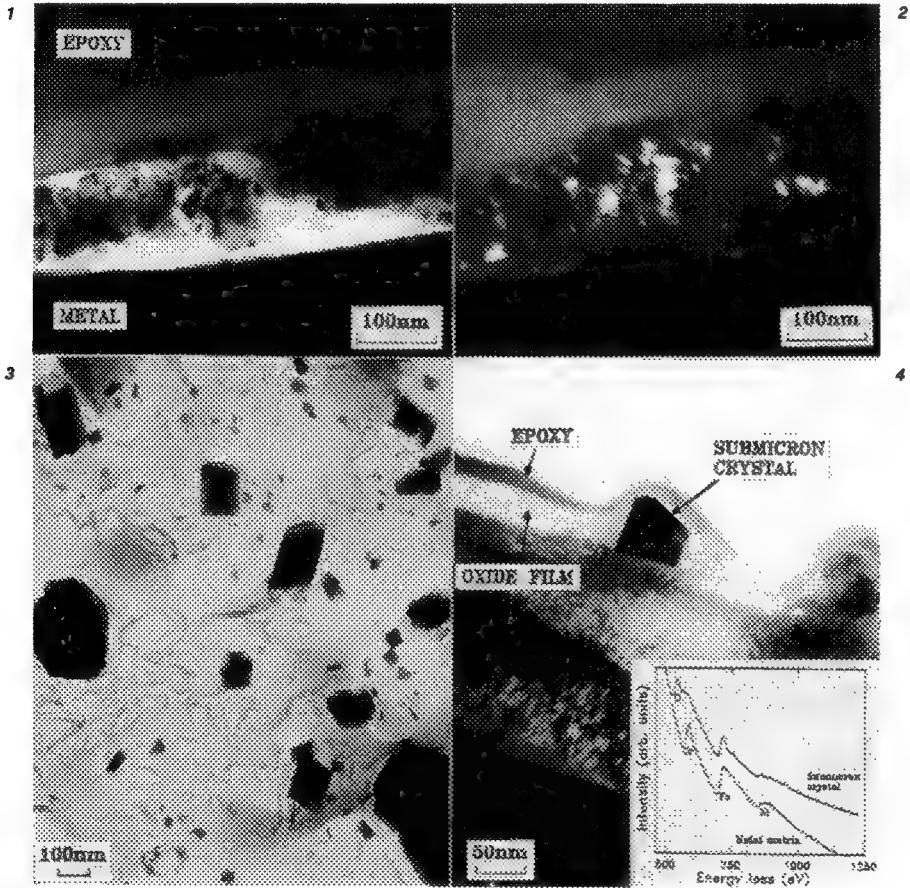
FIG. 1.--Example of High magnification brigh field TEM micrograph of the oxide film.
FIG. 2.--Dark field TEM micrograph showing small grains in the oxide film of Fig. 1.
FIG. 3.--Example of extraction replica TEM micrograph showing submicron crystals.
FIG. 4.--Example of TEM micrograph of Incoloy 800. The EELS spectra are from the metal matrix and submicron crystals like those seen in Fig. 3.

MICROSTRUCTURE AND REACTIVITY OF SMALL METAL PARTICLES: THE ROLE OF Ce ADDITIVES

L. D. Schmidt, K. R. Krause, J. M. Schwartz and X. Chu[*]

[*]Dept. of Chemical Engineering and Materials Science, University of Minnesota, Minneapolis, MN 55455

The evolution of microstructures of 10- to 100-Å diameter particles of Rh and Pt on SiO_2 and Al_2O_3 following treatment in reducing, oxidizing, and reacting conditions have been characterized by TEM. We are able to transfer particles repeatedly between microscope and a reactor furnace so that the structural evolution of single particles can be examined following treatments in gases at atmospheric pressure. We are especially interested in the role of Ce additives on noble metals such as Pt and Rh. These systems are crucial in the automotive catalytic converter, and rare earths can significantly modify catalytic properties in many reactions. In particular, we are concerned with the oxidation state of Ce and its role in formation of mixed oxides with metals or with the support. For this we employ EELS in TEM, a technique uniquely suited to detect chemical shifts with ~30Å resolution.

The microstructure of Rh/Ce on SiO_2 after heat treatments in H_2 and O_2 has been characterized by using TEM, HREM, EELS, and XPS.[1] After initial reduction at 600°C, Rh is present as 50- to 100-Å metal particles while the Ce forms a uniform amorphous film of Ce^{+3} on the SiO_2. After oxidation at 600°C, Rh is oxidized to Rh_2O_3 and spreads over the surface while Ce forms small patches and large (>1000Å) particles of crystalline CeO_2. After reduction of the oxidized microstructure at 600°C, Rh metal returns with a less uniform particle size distribution, while Ce is reduced to Ce^{+3} and structures indicating strong interactions between Ce and Si. In particular, these structures which form only in the presence of Rh are crystalline $Ce_2Si_2O_7$ as confirmed by HREM. The Ce silicate nucleates at Rh particles and spreads over the support as large thin (>1000Å diameter and <50Å thick) single crystal patches as shown in figure 1. After reoxidation at 650°C, both Ce silicate (Ce^{+3}) and CeO_2 were identified using EELS chemical shifts, indicating that the crystalline silicate, once formed, is stable in oxygen. Ce on SiO_2 also showed strong interaction between Ce and Si, but no crystalline species formed after reduction and only small crystalline CeO_2 particles formed after oxidation. Thus, the formation of the Ce silicate and the oxidation of Ce to CeO_2 are catalyzed by Rh.

During reaction, ~100Å diameter Rh metal particles on SiO_2 are found by TEM to be catalytically disrupted by treatment in NO + CO mixtures at ~260°C.[2] Electron diffraction shows that the dispersed Rh is amorphous while XPS shows that the Rh is approximately zero valent in the dispersed state. Continued heating results in irreversible volatilization of the Rh, except for thin rings surrounding the original particles. Subsequent heating in H_2 at 650°C causes the rings to sinter and reform crystalline Rh particles with a lower loading than initially present. Treatment of Rh particles in NO alone at higher temperatures causes similar changes in microstructure as treatment in NO + CO mixtures, whereas CO alone only resulted in slight sintering. Addition of Ce to the Rh causes the disruption to occur more slowly, and the disruption occurs very slowly when Rh is supported on alumina.

The microstructure of Pt on SiO_2 and Al_2O_3 has also been characterized.[3] TEM showed that upon heating Pt alone on SiO_2 in H_2, Pt formed cubic particles while when Pt and Ce were codeposited, the Pt particles were about the same size but no longer had square outlines. The Pt particles tend to shrink or disappear after heating in O_2 at 650°C, and this is much faster without Ce, showing that Ce retards the volatilization of Pt oxides. HREM showed a ~10Å thick amorphous layer on all Pt particles following heating in O_2 when Ce was codeposited as well as a film of crystalline CeO_2. XPS showed that the Pt peak shifted to Pt^{+2} with some metallic Pt still visible when heated in O_2 when Ce was present. No shift was observed in samples without Ce. No Pt oxide was visible using electron diffraction. These observations are all consistent with the formation of a thin amorphous oxide layer

on the Pt particles when heated in O_2 when Ce is also present. Similar microstructures were observed on alumina.

The interactions of catalyst particles with CeO_2 were also studied by examining metal particles supported on CeO_2 submicron spheres. Submicron ceria spheres were prepared by oxidizing sol-gel prepared ceria spherical particles in air at high temperatures. The oxidation and microstructural change of spherical Ce containing particles were studied by transmission electron microscopy. Identical spherical particles were examined after each heat treatment. It has been found that after being heated in air at $450°$ for a few hours the Ce particles turn to be CeO_2 consists of many tiny grains. The spherical particles shrank 50% of its volume. Further heat treatment only increase the grain size in spherical particles while the size of the spheres remain unchanged.

REFERENCES
1. Krause, K. R., Schabes-Retchkiman, P., and Schmidt, L. D., *J. Catal.* **134**, 204-219 (1992).
2. Krause, K. R. and Schmidt, L. D., to be published in *Catal. Lett.* (1992).
3. Schwartz, J. M. and Schmidt, L. D., submitted to *J. Catal.*
4. Chung, W., Chu, X., and Schmidt, L. D., to be published in *J. Amer. Cer. Soc.*
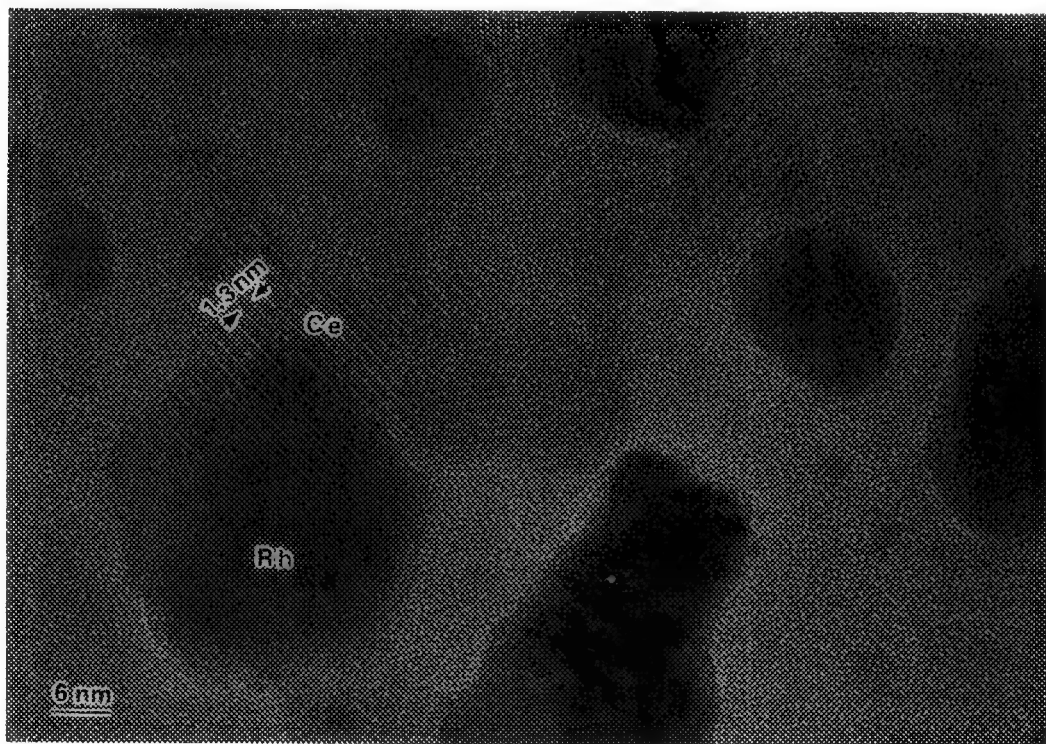
Fig. 1. HREM micrograph taken after second treatment in H_2 showing $Ce_2Si_2O_7$ patch underneath Rh particle. The silicate is only observed in contact with Rh particles.

319

ROTATIONS AND TRANSFORMATIONS IN QUASIMELTING

D. Narayanaswamy and L.D. Marks

Department of Materials Science and Engineering, Northwestern University, Evanston, Il 60208

Morphological fluctuations of a quasimolten particle have been analyzed using high resolution electron microscopy (HREM) to determine the order and relative importance of rotations, translations and morphological transformations.

Small gold particles evaporated onto a holey silicon monoxide support were examined in a conventional 300kV HREM at an electron beam flux of $25A/cm^2$. Single particles were observed over a period of time. The particle behavior was recorded in real time onto a Sony 8mm videotape recorder, at the rate of 30 frames per second, via a Gatan TV camera. The acquired images were further processed using SEMPER software on an Apollo workstation. The image frames were analyzed by employing a data reduction scheme. A basis set of good images were selected from the entire recording, and completely characterized on the lines of earlier workers[1,2]. The set was found to consist of four distinct morphologies in various orientations. Samples of the morphologies isolated are shown in Fig. 1.

The entire videotape was then processed frame by frame by matching all the images with the collected basis set. Cross-correlation filtering with a Gaussian, Fourier filtering and power spectra of single frame images were used to enhance the visibility of any fringes in the particle, for example Fig. 2. In addition to any lattice fringes, the overall particle morphology and facetting of the surfaces were also used. We should note that we were only able to identify the particles about 50% of the time, and included an undetermined classification in the analysis.

The number of image frames corresponding to a particular morphology is shown in Fig. 3. A total of 2849 frames of a single fluctuating particle were used in this analysis. This data indicates that each of the morphologies is approximately equally probable. However, the statistics are as yet too poor to be positive about this.

A much better representation of the data is the trajectory of the particle as a function of time, illustrated in Fig. 4. The figure reveals that the particle stays in essentially the same morphology for extended periods of time, fluctuating slightly and rotating but not transforming. The frequency of rotations is much higher than the frequency of transformations.

One final point about the experimental data. In recent simulations[3] small particles have been found to favor a glassy or amorphous state. This state was considered to be very stable. If such a state existed with a stability period of at least the order of 1/30th of a second, it would have been observable as an amorphous "speckle" image. There was no evidence of such a state in this experiment, which puts an upper limit on the stability of the amorphous states[4].

REFERENCES
1. L.D. Marks and D.J. Smith, J. Cryst Growth. 54(1981)425.
2. D.J. Smith and L.D. Marks, J. Cryst Growth. 54(1981)433.
3. F. Ercolessi et al., Phys Rev Lett. 66(1991)911.
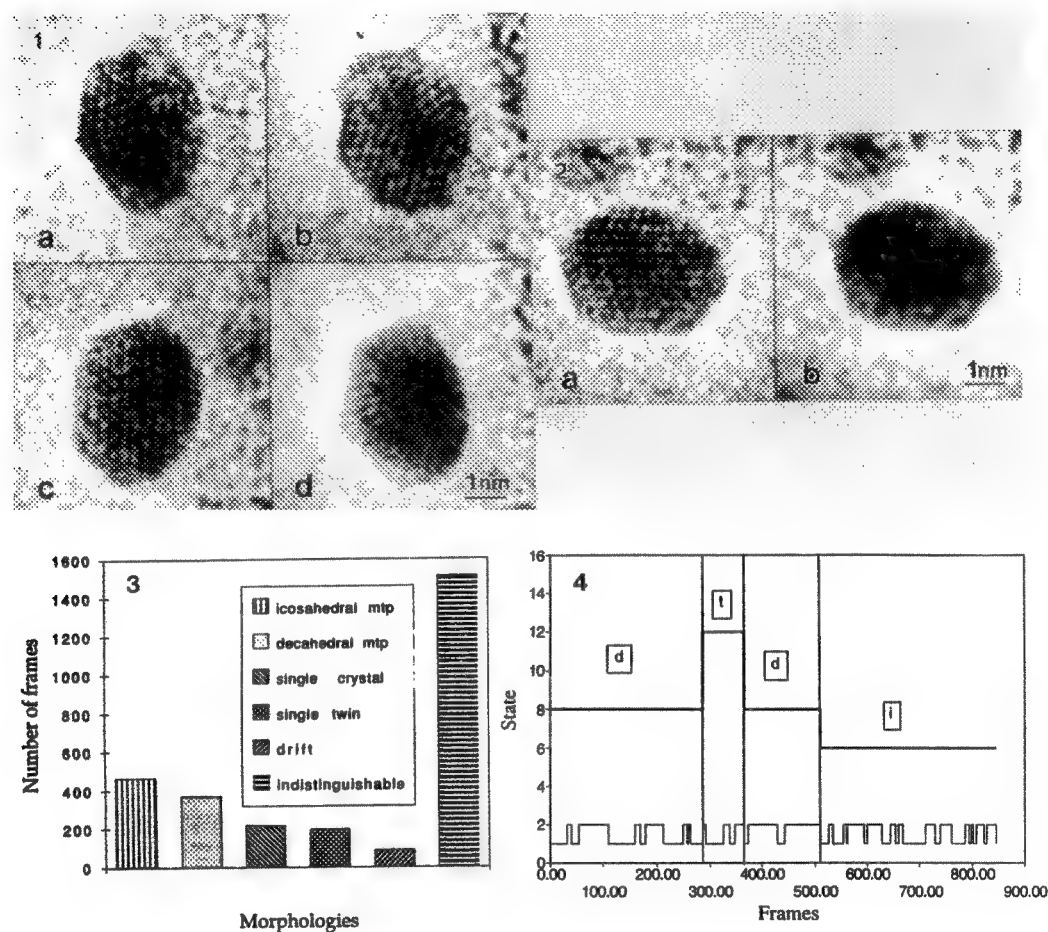
FIG. 1. Sampling of the basis set used to classify the images. (a) Single twin, (b) Asymmetrical decahedral multiply twinned particle (MTP), (c) Single crystal, (d) Icosahedral MTP.

FIG. 2. (a) Represents an unfiltered image and (b) is a processed image.

FIG. 3. Histograms showing total amount of time spent by a 3nm particle in a particular morphology.

FIG. 4. Time sequence comparison of rotational and structural transformations. Arbitrary values have been assigned for the structural states(solid thick line) and the rotations(solid thin line;1,2 states). The labels d,i,t denote decahedral (state 8), icosahedral MTPs (state 6) and single twin (state 12) respectively.

HIGH-RESOLUTION ELECTRON MICROSCOPE (HREM) INVESTIGATION OF MESOPORE FORMATION, ALUMINUM MIGRATION IN USY CATALYSTS

C. Choi-Feng, J. B. Hall, B. J. Huggins, and R. A. Beyerlein

Amoco Research Center, P. O. Box 3011, Naperville, IL 60566

The catalytic properties of ultrastable Y (USY) zeolite are directly influenced by the zeolite destruction which occurs during formation of USY and during subsequent hydrothermal treatment. Previous transmission electron microscope (TEM) studies of hydrothermal aging of neat USY materials and also of USY cracking catalysts have shown 5-50nm defect domains, which were attributed to mesopores.[1-3] Such features are characteristic of extended hydrothermal treatment. It has been suggested that these regions of zeolite destruction comprise the silica source for "healing" the tetrahedral site vacancies left by hydrothermal dealumination. The observations of both homogeneous and inhomogeneous distribution of these mesopores have been reported.[3]

The present data from HREM and analytical electron microscope (AEM) investigations of hydrothermally aged USY materials give clear evidence for an inhomogeneous distribution of mesopores. For neat USY materials, a marked inhomogeneity in mesopore formation was observed among different zeolite grains and within the individual grains. In regions with high defect concentration, mesopores coalesce to form channels and cracks, which ultimately define the boundaries of fractured crystallite fragments. At these boundaries, a dark band is often observed which is highly enriched in aluminum, while within the mesopore itself, aluminum appears to be deficient. These observations have, for the first time, provided insights into the formation and evolution of mesopores, and how these lead to extensive zeolite fracturing. Effects of associated extensive dealumination of USY materials, for example the dark bands, are clearly observed. HREM investigation of a USY cracking catalyst subject to high temperature steam treatment shows similar phenomena. However, inhomogeneities in the distribution of mesopores and in the associated zeolite fracturing appear to be more pronounced compared to the USY neat sieve subjected to a less severe steam treatment. In extreme cases of fracturing, USY grains have broken into small crystallites of dimensions of 20 to 50 nm. This observed dependence of degree of inhomogeneity on the hydrothermal treatment procedures may be attributed to the nonequilibrium nature of the high temperature steam-induced processes which characterize accelerated deactivation procedures in the laboratory.

Comparison with previous TEM results for age-separated equilibrium catalyst from a commercial fluid cracking unit (FCU) shows clear differences.[4] For an "old" catalyst fraction, defects are less inhomogeneously distributed, and the small crystallites remaining are not demarcated by fracture boundaries, indicating different microscopies of deactivation for the slower catalyst deactivation.

References

1. F. Maugé, et al, in B. Imelik, et al, Ed., Catalysis by Acids and Bases, Amsterdam: Elsevier (1985) 91.
2. V. Patzelová and N. I. Jaeger, Zeolites (1987)7, 240.
3. P. Gélin and T. Des Courières, Appl. Catal. (1991)72, 179.
4. R. A. Beyerlein, et al, in Fluid Catalytic Cracking II, ACS Symposium Series 452, Washington D.C.: American Chemical Society (1991), 109.
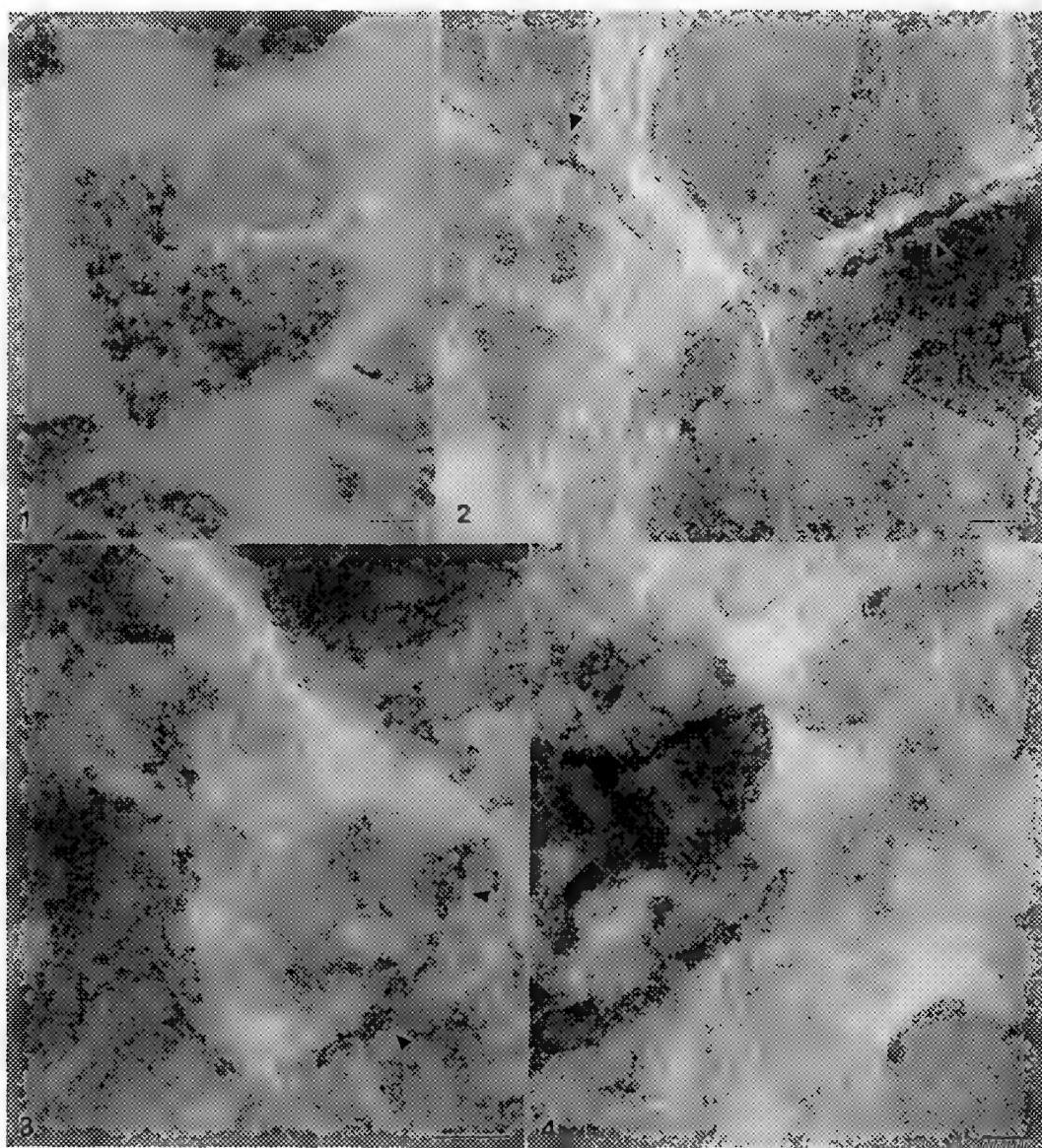
FIG. 1.--TEM image of steam/acid treated neat USY sieve. Many mesopores are seen distributed inhomogeneously among and within grains. Channels have formed from coalescence of mesopores in regions with high mesopore concentration. Bar = 0.2 μm.

FIG. 2.--HREM image of steam/acid treated neat USY sieve. Cracks (indicated by arrows) are formed from coalesced mesopores. Al enriched dark bands are seen along fracture boundaries. Bar = 50 nm.

FIG. 3.--HREM image of USY grains in steam treated USY catalyst. Inhomogeneous distribution of mesopores is apparent. Al enriched dark bands are visible along fracture boundaries (indicated by arrows). Bar = 50 nm.

FIG. 4.--HREM image of steam treated catalyst showing extreme case of USY fracturing. There are many crystallites as small as 20 nm, which have broken away from originally single USY grain. Bar = 20 nm.

IN SITU TRANSMISSION ELECTRON MICROSCOPY OF SILICON OXIDATION

J. Murray Gibson, F.M. Ross[+] and R.D. Twesten

Department of Physics, University of Illinois, Urbana, IL 61801

[+] AT&T Bell Laboratories, Murray Hill, NJ 07974

Oxidation is an important process in materials science. Silicon oxidation is particularly relevant for electronic device fabrication, but it also provides a model system. We report here the use of in-situ TEM for the examination of the microstructural details of the oxidation process.

Two techniques have proved effective in this analysis:

1) Quantitative analysis of transmission electron diffraction patterns from ordered surface structures.

The scattering of electrons by an ordered monolayer at the surfaces of a thin foil can be accurately viewed as a kinematical process. For example, the maximum amplitude of scattering by the Si(111) 7x7 surface is of order $A = 10^{-2}$ at 100 kV incident energy. Double scattering by the surfaces should be of order A^2, that is two orders of magnitude smaller. This allows quantitative investigation of surface structure using conventional diffraction analysis techniques, such as patterson functions[1] and fourier difference maps[2]. We use these methods to reveal the initial interaction of oxygen with the Si surface, noting that oxygen breaks bridging bonds[2], rather than tying up dangling bonds.

The limitations on validity of the kinematical approximation will be discussed. These arise primarily from double diffraction with "bulk" Bragg reflections[3]. Full dynamical simulations, including surface and bulk effects, could be used to improve agreement[4].

2) Surface-Sensitive Bragg Reflections

These can be used to image steps both on clean surfaces and at buried heterointerfaces. Originally observed by Cherns[5], these reflections can be viewed as reciprocal lattice spikes penetrating into the zero-order Laue Zone from a higher order Laue Zone. Intensity is observed at this position because of the abrupt termination of the crystal, so that these are called "crystal truncation rods" in X-Ray diffraction[6]. Since the deviation parameter for a first-order Laue zone reflection is equal to the reciprocal lattice interlayer spacing, images show thickness fringes with periodicity equal to one unit cell. Therefore, single atomic steps are observed, as in figure 1.

324

We have used these images to observe the etching and oxidation processes on Si (111). The kinetics of step motion during high temperature etching can be obtained from dynamic images and used to gain insight into the Si/O reaction. During formation of a buried oxide at lower temperatures, the progress of the interface can be viewed dynamically. These unique views of the motion of a true heterointerface give insight into the fundamental mechanisms of oxidation.

Figure 1: A 1/3 422 Dark Field Image from a Clean Si (111) Foil, showing atomic steps on both surfaces as black-white contrast boundaries.

[1]K. Takayanagi, Y. Tanashiro, S. Takahashi and M. Takahashi, Surf. Sci. 164, 367 (1985).

[2]J.M. Gibson, Surf. Sci. 239, L531 (1990).

[3]Y. Tanishiro and K. Takayanagi, Ultramic. 27, 1 (1989).

[4]K. Takayanagi, private communication.

[5]D. Cherns, Phil. Mag. 30, 549 (1974).

[6]S.R. Andrews and R.A. Cowley, J. Phys. C 18, 6427 (1985).

325

SURFACE STUDIES WITH A UHV-TEM

David J. Smith[*], M. Gajdardziska-Josifovska and M.R. McCartney

Center for Solid State Science, Arizona State University, Tempe, AZ 85287
[*]also at: Department of Physics, Arizona State University, Tempe, AZ 85287

The provision of ultrahigh vacuum capabilities, as well as in situ specimen treatment and annealing facilities, makes the transmission electron microscope into a potentially powerful instrument for the characterization of surfaces. Several operating modes are available, including surface profile imaging, reflection electron microscopy (REM), and reflection high energy electron diffraction (RHEED), as well as conventional transmission imaging and diffraction. All of these techniques have been utilized in our recent studies of surface structures and reactions for various metals, oxides and semiconductors with our modified Philips-Gatan 430ST high-resolution electron microscope.[1]

Of major concern in any TEM surface study is the level of the ambient vacuum at the specimen: in the confined space of the objective lens pole-piece area, particularly with a liquid-nitrogen-cooled cryofinger in operation above and below the sample, an accurate measurement is unavailable in our case. The criterion we have therefore taken as evidence for an adequate vacuum has been the existence of the well-known 7x7 reconstruction of the Si {111} surface. Figure 1 shows a RHEED pattern from this surface which was recorded from a freshly cleaved bulk silicon sample at room temperature following in situ cleaning at 1200°C. Similar vacuum conditions were prevalent for most of the other observations reported here.

The RHEED and REM techniques provide direct links with traditional surface science methods since they involve the observation of bulk samples. Indeed, it can be very illuminating to form REM images from surface(s) that have been characterized by RHEED. For example, we have observed (100) surfaces of MgO bulk crystals to investigate the effects of in situ annealing, especially for temperatures above 900°C when Ca impurities are expected to segregate to the surface.[2] More recently, we have used REM to study the reconstructed (110) surface of GaP, in particular to establish the influence of ion-milling and annealing treatments on the surface topography,[3] and we have also followed morphological changes in Si {111} surfaces after various heat treatments.

Conventional transmission imaging, which includes surface profile imaging, can take full advantage of the high-resolution capabilities of the electron microscope to provide surface information down to the atomic scale, including the documentation of dynamic events occurring in real-time at elevated temperatures. For example, we have observed that a reversible phase transformation of the CdTe (100) surface from a 2x1 Cd-rich reconstruction to a 3x1 Te-rich phase occurs at a temperature of about 200°C.[4] With the assistance of image simulations, it was possible to distinguish between various models for the structure of the reconstructed surfaces. Rearrangements of different CdTe surfaces have been observed, and recorded directly onto videotape, using an online TV image pickup and recording system. In the case of Ag single crystals, the effects of heat treatment, including the onset of surface melting, have been followed. Surface damage of rutile crystals induced by the incident electron beam, and the effect of subsequent annealing, have been studied.[5] Figure 2 shows a high-resolution image of a (100) MgO single crystal following intense electron irradiation: note that the rectangular holes formed as a result of electron-beam-induced damage processes are strongly facetted on {001} planes. Similar facetting has been observed for MgO crystals irradiated in other projections.[6]

References

1. D.J. Smith et al., Mater. Res. Soc. Symp. Proc., 139(1989)289
2. M. Gajdardziska-Josifovska et al., Proc. 49th. Ann. Meet. EMSA (1991) pp.624-625
3. M. Gajdardziska-Josifovska et al., these proceedings
4. P. Lu and D.J. Smith, Surface Science, 254(1991)119
5. M.R. McCartney and D.J. Smith, Surface Science, 250(1991)169
6. This work was conducted at the National Facility for HREM at Arizona State University supported by NSF Grant DMR-89-15584
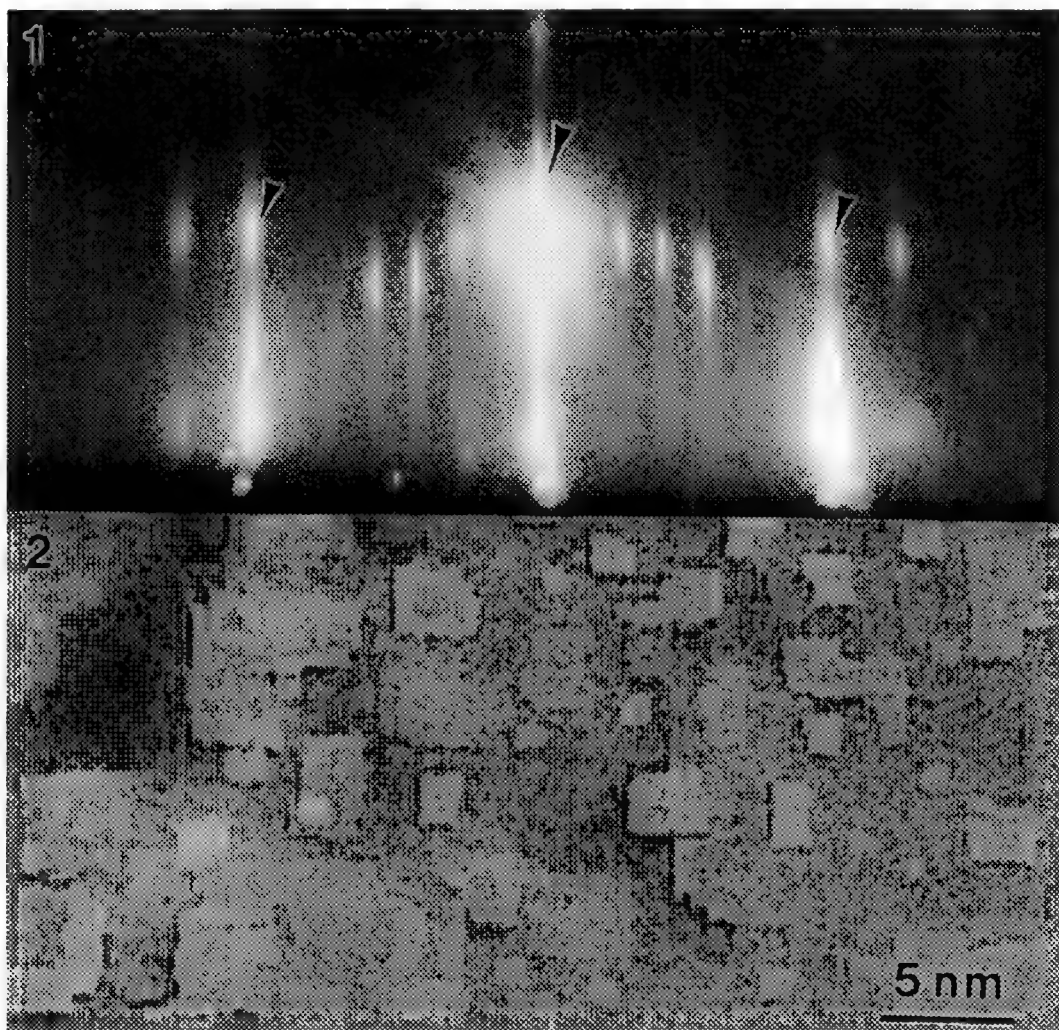
FIG. 1   Reflection high-energy electron diffraction pattern from Si {111} surface. Rods with 1/7 the separation of the fundamental   reflections (arrowed) confirm the 7x7 reconstruction.
FIG. 2   High-resolution image showing the facetted nature of electron-beam-induced sputter pits in [100] orientated crystal of MgO.

UHV-TEM IMAGING AND DIFFRACTION STUDY OF CU-AU ON SI(111)

P. Xu and L. D. Marks
Department of Materials Science and Engineering, Northwestern University, Evanston, IL 60208

It has been demonstrated that ultra-high vacuum transmission electron microscopy is a powerful technique in solving surface atomic structures[3]. During some recent work while we were testing surface imaging modes using the Si(111)-7x7 surface, we accidentally contaminated the surface by sputtering copper and some gold from the specimen holder onto the silicon. This paper presents the results of transmission electron diffraction and imaging studies of this surface.

Experiments were performed in a Hitachi UHV H-9000 300 keV electron microscope with a stable operation pressure of 1×10^{-10} Torr. Attached to the microscope is a UHV surface science chamber for *in situ* sample preparation[4]. A thin sample of silicon (111) (P doped to 80 ohm-cm) was mechanically polished, dimpled, and ion-beam thinned before being transferred into the surface science chamber. The sample was then ion beam sputter cleaned using 3-4 Kv argon ions and annealed to about 600°C using an electron gun (4-5 Kv, 2-3 Ma). Later tests indicated that the ion gun was not centered around the 3 mm disk and a part of the sample surface was covered by the sputtered materials from the sample holder. EDX results from a Hitachi HF-2000 analytical microscope showed that the deposited layer consisted of about 70% Cu and 30% Au.

Fig.1 shows a selected area diffraction pattern from an area with 5x5 reconstruction, strong diffraction spots due to the reconstruction are located at the positions $m(4/5,1)$, $n(1,4/5)$ (where m and n are integers) and all the other symmetry position. A simple structure model can be constructed directly from the diffraction pattern as was done in Ref.3 and a schematic drawing is shown in Fig.2: a close packed fcc layer of Cu(Au) with a unit cell dimension of 3.5 Å (which is very close to the copper lattice constant) rotated 3.5° or -3.5° with respect to the silicon lattice. We can rule out any subsurface stacking fault, as in the Si(111)-7x7, since these would lead to strong diffraction spots at positions such as (4/5, 0). The absence of any other strong diffraction indicates that any additional 2-D structural variations has to be small. The existence of the two domains was clearly demonstrated by the uneven intensities of the m and n family of diffraction spots in Fig.1b which also contained a $\sqrt{3} \times \sqrt{3}$ R30° reconstruction.

Fig. 3 shows a bright field image of the 5x5 reconstruction with domains on the order of 50-100 nm in size. These domains are separated by boundaries in the {110} direction. High resolution imaging of the surface structure[5] indicated some small local disorder and this is consistent with the fact that the surface diffraction spots (Fig.1) are more diffused than the ones in the Si(111)-7x7[6].

REFERENCES
[1] K. Takayanagi, et al. Surf. Sci., **164**, 367 (1985).
[2] L. D. Marks, et al. Nature, **303**, 316 (1983).
[3] K. Takayanagi, et al. Appl. Surf. Sci., **41/42**, 337 (1989).
[4] R. Ai, et al. Ultramicroscopy, **39**, 333 (1991).
[5] L. D. Marks, this volume.
[6] This work is supported by the Airforce Office of Scientific Research AFOSR-90-0045.
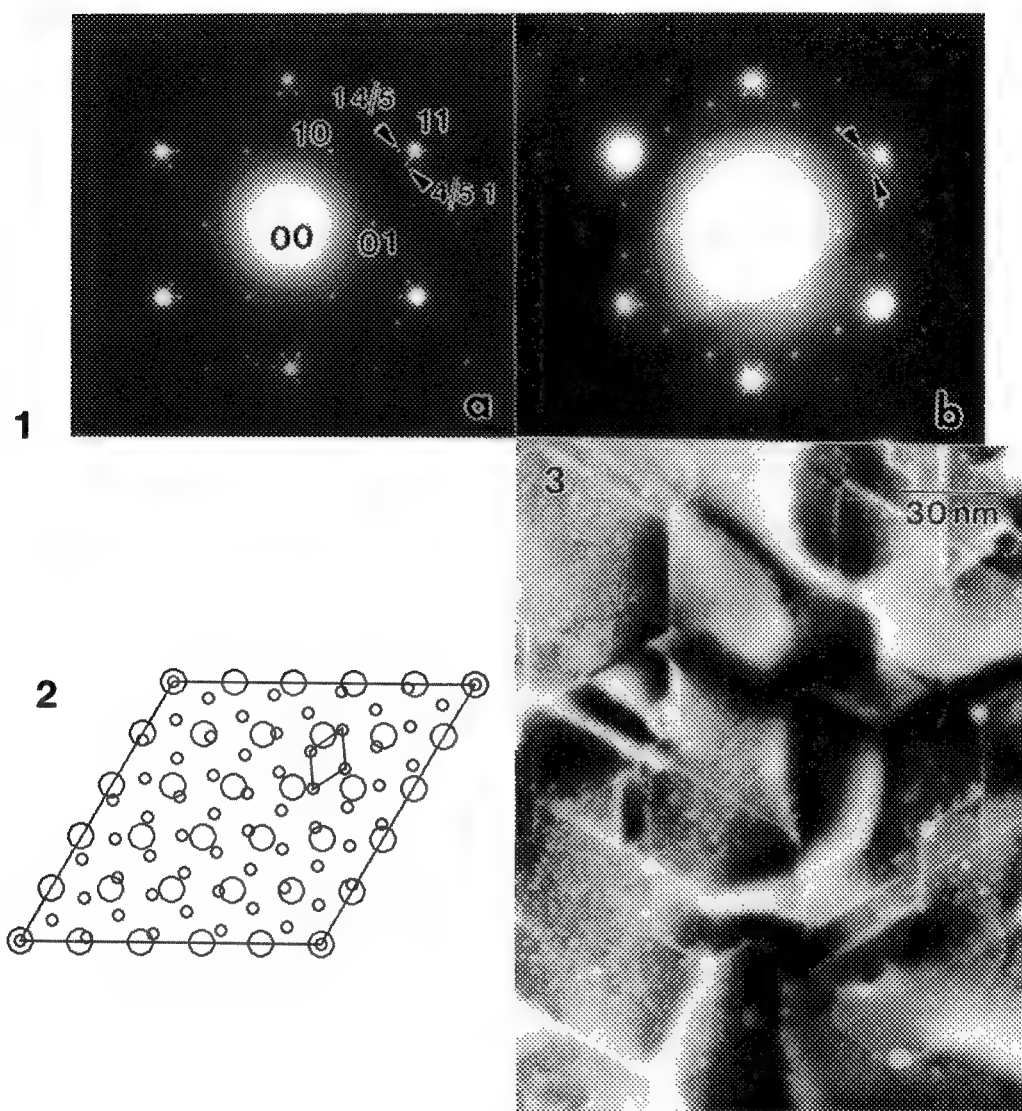
FIG 1. SAD patterns of (a) Cu(Au)-Si(111) 5x5 and (b) 5x5 plus √3x√3 R30° reconstructions.

FIG 2. Schematic drawing of Cu-Si(111) 5x5 structure model. Small circles are Cu, big ones are Si.

FIG 3. Bright field image of 5x5 reconstruction showing domains.

SULPHUR—INDUCED RECONSTRUCTION ON Cu$_3$Au (110) SURFACE

Yi Huang and John M. Cowley

Department of Physics, Arizona State university, Tempe, Arizona 85287

Sulphur is a common impurity in metals and alloys. The segregation of sulphur to the surface and interface has major effects on the chemical and mechanical properties of the materials. The structure of the sulphur adsorbed surface and its behavior at raised temperature have great practical and theoretical significance. Cu$_3$Au is a typical ordering alloy whose bulk structure and properties have been extensively studied. Recently its clean surfaces have also been studied by many authors[1-5]. These make Cu$_3$Au a good material for studying the behavior of sulphur on surface, but, as we know, the impurity-adsorbed surfaces of this alloy have not been investigated very much. No work on the sulphur-adsorbed surfaces has been done.

In the present work the sulphur adsorbed Cu$_3$Au(precise composition Cu$_{71.7}$Au$_{28.3}$) (110) surface has been studied with Reflection High Energy Electron Diffraction (RHEED) and Auger Electron Spectroscopy (AES). The experiments are carried out in a UHV chamber with base pressure of 2×10^{-10} mbar. The surface is cleaned with the conventional ion milling-heating cycling procedure. After about 20 cycles all other impurities are eliminated; but some sulphur keeps appearing on the surface. The amount of sulphur on the surface is then controlled by annealing the sample for different times and/or at different temperatures. The sulphur concentration is measured with AES. The periodicity and the symmetry of the surface mesh is determined by RHEED.

At least fiv different reconstructed phases have been observed on the sulphur adsorbed Cu$_3$Au (110) surface. With respect to the disordered clean surface 1x1 structure the reciprocal meshes of these phases exhibit symmetries of p(2x2), p(2x3), p(4x2), p(3x2) and c(2x4), respectively. Fig.1-4 are RHEED patterns of four of these phases and the reciprocal meshes derived from these patterns. Lower part of Fig.5 shows how these phases occur in different ranges of sulphur concentration. Because pure sulphur can not be studied in UHV due to its high partial pressure, and the preparation of a clean surface of sulphur compound with known composition is very difficult, if is not impossible, we have not been able to obtain the relative Auger sensitivity of Au and Cu vs Sulphur. Probably due to the same reason we failed to find these sensitivity data in the literature. Therefore here we use the relative intensity ratio I$_S$/I$_{Au}$ of S LVV (152eV) and Au NVV (69eV) lines instead of the percentage to represent the sulphur coverage on the surface. It can be seen from Fig.5 that the surface structure depends on the sulphur concentration of the surface; when sulphur concentration increases the structure changes in a sequence of p(2x2), p(2x3), p(4x2), p(3x2) and c(2x4); there are overlap between phases; in the sulphur-rich region the p(3x2) and c(2x4) coexist in a wide range. The upper part of Fig.5 shows how the ratio I$_{Cu}$/I$_{Au}$ changes with increasing sulphur coverage. The quantity ln(I$_{Cu}$/I$_{Au}$) increases with ln(I$_S$/I$_{Au}$) in a linear form. The fact that the ratio I$_{Cu}$/I$_{Au}$ increases with the sulphur concentration indicates that copper atoms tends to move from inside of the crystal to the surface to react and combine with sulphur atoms. The linear form implies that the S atoms are associated with Cu atoms on the surface in a constant configuration.

Heating experiments have been done to find out how the reconstructed phases behavior at high temperature. These phases are stable at relatively low temperatures(<430 °C). Some of the transition temperatures are very close to the clean surface disorder temperature. The (0,1/3) spots of the p(2x3) phase disappear at lower temperature than the (1/2,0) spots, suggesting that the transition has two separate steps.

References: 1. H. C. Potter and J. M. Blackly, *J. Vac. Sci. Technol.* 12 (1975) 635.
2. S. F. Alvarado et al, *Z. Phys.* B66 (1987) 103.
3. S. Krummacher et al, *Z. Phys.* B75 (1989) 235.
4. E. G. McRae et al, *Surf. Sci.* 238 (1990) L481.

5. Y. Huang, G. G. Hembree and J. M. Cowley, in preparation
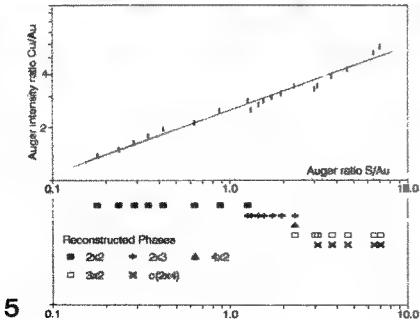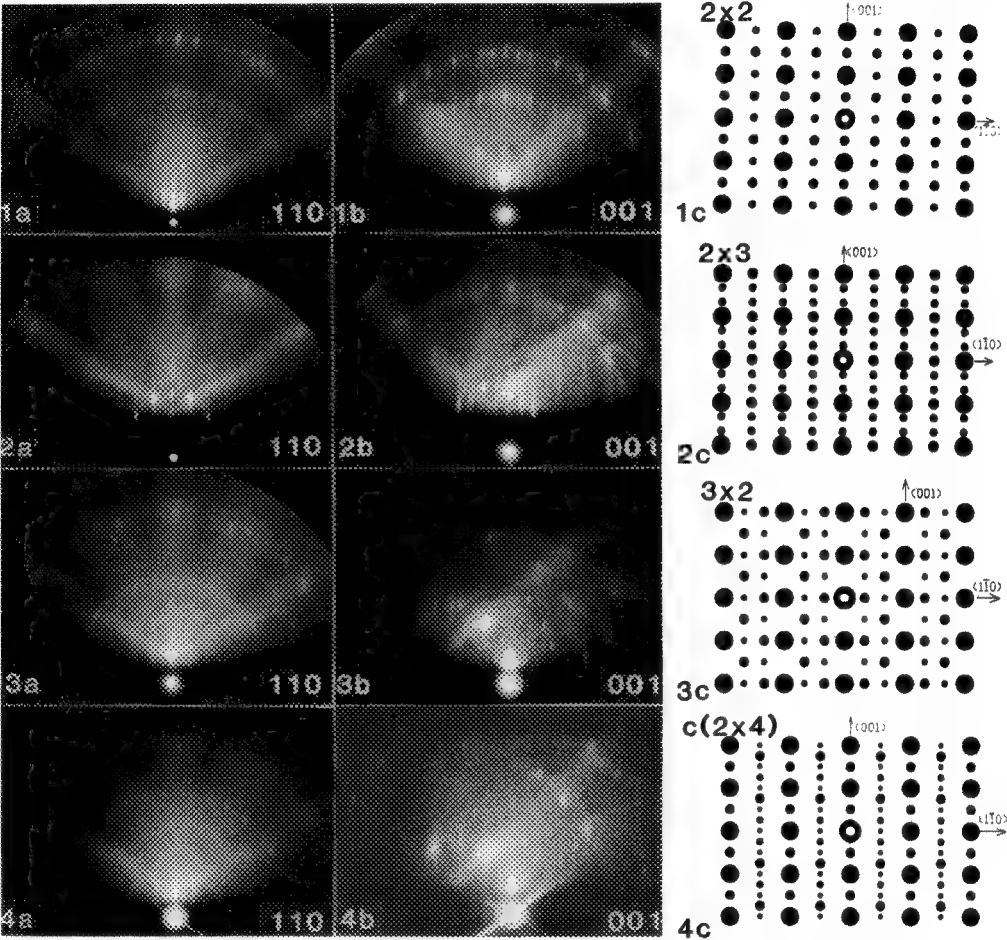
Fig.1-4: a),b) [110] and [001]RHEED patterns of p(2x2), p(2x3), p(3x2) and c(2x4) reconstructed surface phases, respectively; c) reciprocal meshes of reconstructed surface phases derived from these patterns.

Fig.5: Lower part shows sulphur concentration regions in which reconstructed phases occur; upper part illustrates how ratio I_{Cu}/I_{Au} changes with surface sulphur concentration.

331

STRESS-INDUCED STRUCTURES ON SURFACES OBSERVED USING SCANNING TUNNELING MICROSCOPY AND LOW-ENERGY ELECTRON MICROSCOPY

Ellen D. Williams, R.J. Phaneuf and N.C. Bartelt

Department of Physics, University of Maryland, College Park, MD 20742-4111

W. Swiech and E. Bauer

Physikalisches Institut, Technische Universitat Clausthal, D-3392 Clausthal-Zellerfeld, Germany

Elastic stresses play a well-known and important role in the structure of thin films during growth.[1] However, elastic effects can also greatly influence surface morphology of the substrate. One source of this influence, as has long been recognized is the elastic interactions between steps on surfaces.[2] More recently, Marchenko[3] has shown that surface stress can stabilize finite-size structures in surfaces, such as facets. Traditionally surface morphologies such as steps and facets have been measured by low-energy electron diffraction. However, the more recent development of ultra-high vacuum compatible microscopic techniques such as scanning tunneling microscopy, reflection electron microscopy, and low-energy electron microscopy, now make it possible to image steps and facets directly to obtain information about sizes and size distributions. This information in turn makes it possible to test the influence of stress on surface morphology directly.

We have found rich evidence of the influence of stress in the structures observed on vicinal surfaces of Si(111). Our previous studies of silicon surfaces have shown that silicon has an interesting orientational phase diagram, which results in a diversity of surface morphologies depending on the surface orientation[4]. For the purposes of this presentation, it is sufficient to note that above 850°C, the step structure on surfaces misoriented by 1-12 ° from the (111) plane is a stable array of uniformly spaced single-layer height steps. However, upon cooling through the temperature at which the surface reconstructs to form a 7x7 periodicity, the step structure changes dramatically. For surfaces misoriented toward (down-staircase) the [21$\bar{1}$] direction, the steps rearrange to form a mixture of single- and triple-layer height steps.[5] However, if the misorientation is toward the [$\bar{2}$11] direction , the surface becomes orientationally unstable and breaks up into facets of (111) orientation and regions of higher vicinality.[6]

We have investigated the mixtures of step heights using STM and high-resolution low-energy electron diffraction[7] at the University of Maryland, and the formation of facet structures using LEEM[8] at the University of Clausthal.[9] The samples used were commercially obtained silicon wafers, which were cleaned in UHV using standard techniques that have been shown to allow equilibration of the step structure.[4-7] The STM measurements were made at room temperature. Since surface mobility on these samples is extremely limited below about 700°C, the structures observed by STM are thus quenched structures characteristic of a much higher temperature. The high-resolution LEED and low-energy electron microscopy measurements were made as a function of temperature, allowing characterization of the equilibrium structures through the reconstructive transition, as well as direct measurements of the kinetics of step rearrangements.

The LEED measurements of the mixtures of single- and triple-height steps reveal a well defined periodicity in the step structure, distinctly different than what would be expected for a random mixture of steps.[10] STM measurements were made over large areas, allowing statistics for hundreds of steps to be compiled. From these measurements, it was possible to

determine directly whether this periodicity is due to a well-defined sequence of singles and triples. In fact it is not: the correlation functions of the positions in the STM sequences are exactly as would be expected for a random sequence. However, the STM data revealed that the distribution of step-step spacings is quite narrow and has an unexpected characteristic. Terraces bounded by two triple-height steps are approximately 1.3 times as large as those bounded by a single- and a triple-height step, which are in turn approximately 1.3 times as large as those bounded by two single-height steps. This can be shown to be consistent with steps which are interacting elastically. The strength of the elastic interaction between two step of heights h_1 and h_2 is directly proportional to $h_1 h_2$[11]. An analysis of the ground state configuration of mixed-height steps incorporating this behavior shows that the ratios of the step-step separations which we have measured should be $\sqrt[3]{3} = 1.44$, in surprisingly good agreement with the observation.

The LEEM measurements of the faceting transition were made during a quench of 4°C below the transition temperature. The qualitative nature of the facet formation is in excellent agreement with Mullins' predictions[12]. The facets nucleate at a small rate (approximately 1 in 5s in a 3μm field of view), and then grow rapidly (approximately 1000Å/s) in the direction parallel to the step edges. In the direction perpendicular to the step edges, however, all growth stops nearly immediately after the nucleation event, yielding a final facet width of approximately 700Å. This is quite surprising as one would expect a nucleated phase to grow without limit, until hindered by encounter with neighboring domains. The observation of a preferred size for the facets suggests an energetic preference for that size. Such a possibility was predicted by Marchenko[3] for facets on the surface of an elastic medium, The surface stress for the Si(111) surface reconstructions have been investigate both theoretically[13] and experimentally.[14] The necessary elastic contribution to stabilize the facets at the size observed is quite consistent with the known values of the surface stress.

The role of surface stress has been observed through direct measurements of the morphology of Si substrates. The morphologies can be quite complex, which has serious implications for use of the surfaces for growth and in etching. Furthermore, as the work of Webb and co-workers[15] has demonstrated, there is the interesting potential to use stress as a method for modifying substrate morphology.

References

1   J. H. van der Merwe, Phil. Mag. (1982) **A 45**, 127.
2   J. M. Blakely and R.L. Schwoebel, Surf. Sci. (1971) **26**, 321.
3   V.I. Marchenko, Sov. Phys. JETP (1981) **54**, 606.
4   E.D. Williams and N.C. Bartelt, Science (1991) **251**, 393.
5   R.J. Phaneuf and E.D. Williams, Phys. Rev. B (1990) **41**, 2406.
6   R.J. Phaneuf, E.D. Williams and N.C. Bartelt, Phys. Rev. B (1988) **38**, 1984.
7   J. Wei, *et al.* (1992) to be published
8   W. Telieps and E. Bauer, Ultramicroscopy (1985) **17**, 57.
9   R.J. Phaneuf, et al., Phys. Rev. Lett. (1991) **67**, 2986..
10   P.R. Pukite, C.S. Lent, and P.I. Cohen, Surf. Sci. (1985) **161**, 39
11   P. Nozieres, Lectures given at the Beg-Rohu Summer School (unpublished, 1989).
12   W.W. Mullins, Philos. Mag. (1961) **6**, 1313
13   D. Vanderbilt, Phys. Rev. Lett. (1987) **59**, 1456.
14   R.E. Martinez, W.M. Augustyniak and J. Golovchenko, Phys. Rev. Lett.(1990) **64**, 1035.
15   F.K. Men, W.E. Packard and M.B. Webb, Phys. Rev. Lett (1988) **61**, 2469.
16   Different aspects of this work have been supported by DOD, NSF (INT-8822564), ONR (N00014-91-J-1401), and Volkswagen.

MICROSTRUCTURES OF CAVITY SURFACES IN SILICON

D. M. Follstaedt, S. M. Myers, W. R. Wampler, and H. J. Stein

Sandia National Laboratories, Albuquerque, NM 87185

Helium is insoluble in most materials and forms "bubbles" when it is ion implanted into them. The microstructures of the cavities formed when Si is implanted with He and annealed are of interest for several basic materials science investigations: luminescence of porous structures, stabilities of atomic surfaces and H attachment to Si bonds on the internal cavity surfaces. Such cavities can allow new "surface-science"-type investigations to be conducted, such as the recent determination of the Si-H bond strength $(2.5 \pm 0.2$ eV)[1]. We have used cross-section TEM at 200 kV to characterize the cavities formed when (001) Si is implanted with 1×10^{17} He/cm^2, 30 keV, at room temperature and then annealed at 700 or 800°C. The enhancement of internal surface area relative to the wafer surface is quantified, and faceting of the cavities is used to infer the relative stabilities of Si surfaces.

Specimens were made by cutting along <110> directions, epoxying implanted surfaces together, coring through the interface, and slicing disks for thinning. The disks were polished to 100 μm thickness; final polishing was done parallel to the epoxy line to avoid chipping micron-size pieces out of the fragile cavity layer below the implanted surface. The disks were dimpled with 1 μm diamond paste using a stainless steel wheel until red light was transmitted through the specimen, followed by a felt wheel until amber light was transmitted. The specimen was then ion-milled on both sides with 4.5 keV Ar at 15° incidence until break-through.

Figure 1 shows the surface layer in the thinnest area next to the hole for a specimen annealed 10 hours at 800°C. The specimen is tilted off the [110] cross-section orientation to the Bragg angle of a {111} reflection to produce strong contrast from thickness fringes. The thicknesses at the center of the dark contours correspond to $(2n-1)/2$ ξ where ξ is the {111} extinction distance in Si (76 nm)[2]. These contours indicate the thickness at several positions and allow the number of cavities and cavity area to be measured per unit area of the implanted (001) surface. Stereo measurements at different tilt angles gave the vertical separation between pairs of cavities and provided lower limits on the thicknesses which agree with those determined with the contours. Observations at the thinnest area around the hole, which was amorphized by the Ar ion milling, suggest that ~5 nm of amorphous material may be present in addition to the crystalline thickness measured with the contours.

The cavities can be seen in Fig. 1, but are better characterized by tilting further off the [110] zone axis to avoid diffraction contrast. By underfocussing the instrument, the cavity contrast is enhanced by Fresnel fringes. Figure 2 is such an image extending from the implanted surface through the cavity layer. The depth and width of the cavity layer are in good agreement with the projected range $(R_p = 0.28$ μm) and width $(\Delta R_p = 0.09$ μm) of the He distribution predicted by TRIM simulations[3] for 30 keV He in Si. After annealing for 10 hours at 800°C, however, other work predicts that the He has probably vacated the cavities[4]. By measuring the diameters of all the cavities in such an image and knowing the thickness, the ratio of internal surface area to the (001) surface area can be obtained. Values obtained for several thicknesses between 0.5-2.0 ξ were in good agreement and show no systematic trend with thickness or position. The average areal ratio was 4.8 ± 0.7.

Counting cavities and measuring their areas was more difficult for specimens annealed 1/2 hour at 700°C because of overlap of cavity images in thicker areas. From averages of several measurements with {111} and {220} contours, an areal ratio of 7.5 ± 1.5 was obtained. Using 0.7×10^{15}/cm^2 for the average density of monohydride bonds on {100} and {111} surfaces, the maximum amount of bound H is calculated to be 5×10^{15} H/cm^2, which is somewhat lower than that observed $(9 \times 10^{15}$ H/cm$^2)$[1]. Fourier transform infared spectroscopy shows the presence of Si-H bonds on {111} and {100}, in agreement with the faceting observed with TEM (below).

After annealing 10 hours at 800°C, many cavities exhibited faceting as seen in Fig. 2; a lesser degree of faceting is observed for 700°C. The most prevalent facets are {111} planes; a lesser amount are (001). A few faceted cavities are symmetric like the one indicated in Fig. 3; it shows {111} facets which round into the (001) plane. The three-dimensional cavity shape is thus inferred to be essentially an octahedron truncated by cube faces. Close examination of Fig. 3 shows a small facet between the {111} planes, indicating that {110} facets slightly truncate the cavity also. We tentatively identify the low energy surfaces of Si to be (in order of increasing energy): {111}, {100}, and {110}.
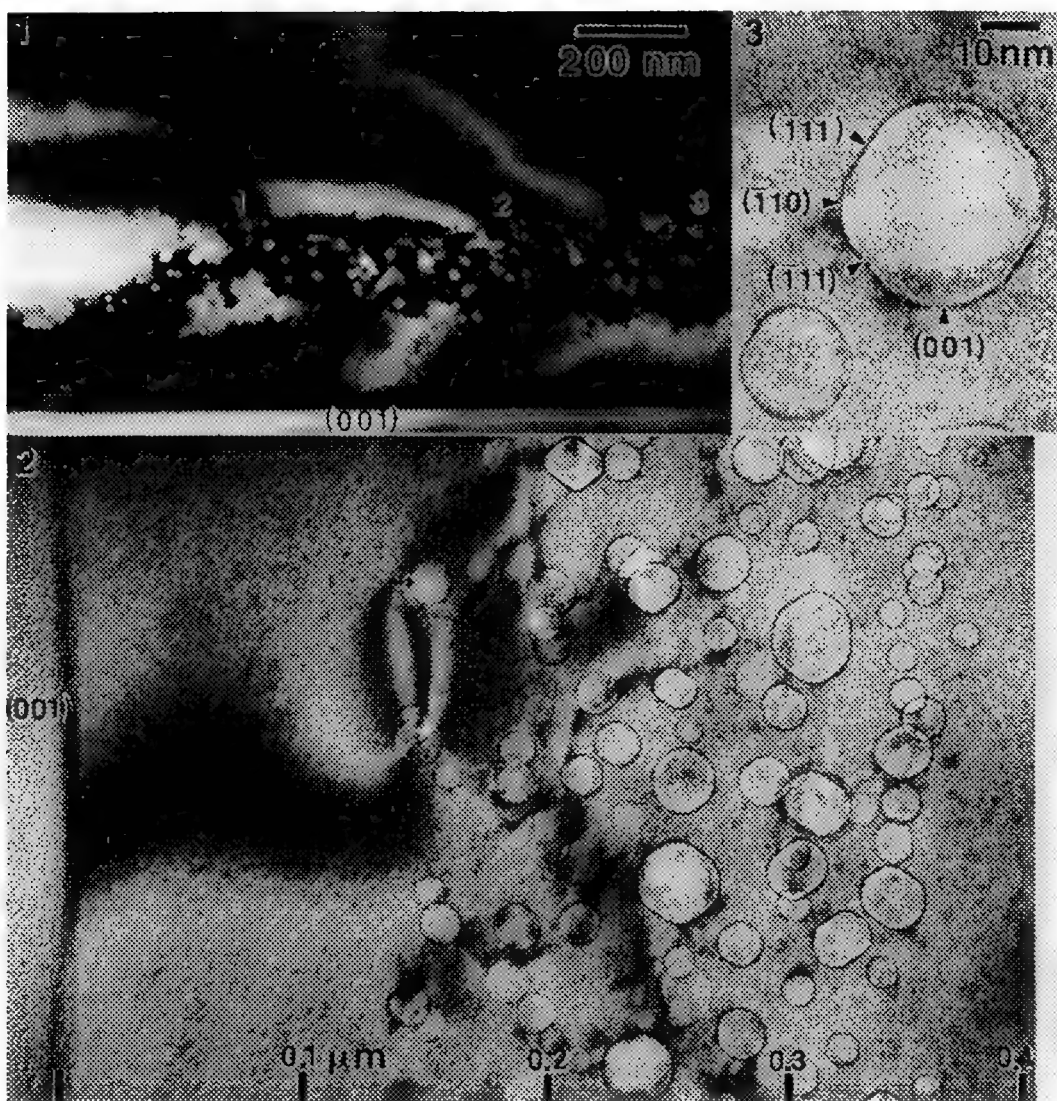
FIG. 1.--[110] cross-section image with (1,-1,1) thickness contours (1,2, and 3) in the cavity area.
FIG. 2.--[110] cross-section image of cavities beneath the (001) implanted surface; tilted off [110] axis and imaged at -420 nm defocus below minimum contrast.
FIG. 3.--Higher magnification image of a cavity; defocus: -150 nm below minimum contrast.

References

1. S. M. Myers, D. M. Follstaedt, H. J. Stein and W. R. Wampler, Phys. Rev. B 45, 3914 (1992).
2. P. Hirsch, A. Howie, R. B. Nicholson, D. Pashley and M. J. Whelan, Electron Microscopy of Thin Crystals (R. E. Krieger Publishing Co., Huntington, NY, 1977), pp. 102 and 416.
3. J. F. Ziegler, J. P. Biersack and U. Littmark, The Stopping and Range of Ions in Solids (Pergamon Press, New York, 1985).
4. C. C. Griffioen, J. H. Evans, P. C. DeJong and A. Van Veen, Nucl. Inst. Meth. B27, 417 (1987).

IMAGING MICRO-TWIN DISTRIBUTIONS IN AS-GROWN CVD DIAMOND FILMS WITH TEM

Z.L. Wang*, L.L. Horton, R.E. Clausing, L. Heatherly and J. Bentley

Metals and Ceramics Division, Oak Ridge National Laboratory, Oak Ridge, TN 37831-6376;
* and Dept. Materials Science and Engineering, The University of Tennessee, Knoxville, TN 37996-2200

Fractured edges of diamond films grown by chemical vapor deposition (CVD) have been examined directly in a conventional transmission electron microscope (TEM) without thinning [1,2]. An important advantage of the fracture specimen preparation technique is that the microstructures in the diamond grains at the growth face can be characterized directly by bright-field (BF) and dark-field (DF) TEM imaging and diffraction. Additionally, the topography of the same region can be directly determined from secondary electron (SE) images available in the same TEM.

Diamond films with thicknesses of approximately 75 μm were grown with a hot filament system on a silicon substrate at 930-935ºC in a mixture of hydrogen, methane (0.5%) and carbon monoxide (4%) gases. The as-grown surface morphology consisted of 2 to 3-μm-diam grains with (001) top facets, each surrounded by four {111} facets (Fig. 1). TEM analysis has shown the core volume bounded by the (001) top facet and orthogonal {110} is free of micro-twins. The remaining volume around the core, bounded by {111} facets, is filled with micro-twins. Thus, the volumes filled with and free from micro-twins terminate with {111} and (100) facet surfaces, respectively [1,2]. However, the "boundary" separating the two regions does not appear sharp, and there is clearly no twin boundary, as confirmed by the selected area diffraction (SAD) patterns (Fig. 2).

Diamond films, of approximately 50 μm thickness grown at 1100-1120ºC in a mixture of hydrogen and methane (0.75%) without CO, have a different surface morphology, but again consisting of {111} and {100} facets. Some narrow facets are identified at the intersection of two large facets (arrowed in Fig. 3). When viewed along [110] in TEM, non microtwinned perfectly crystalline (p) regions are separated by twin boundaries from microtwinned regions (t), as seen from the relative rotations of the <110> convergent beam electron diffraction patterns (Fig. 4). With SE imaging, the correspondence between grain facets and the associated micro-twin distribution in TEM images can be determined (Figs. 5 and 6). Each region seems to terminate with different facet, so that the film appears less textured than the film shown in Figs. 1 and 2.

A clear difference between the two diamond films examined above is that twin boundaries do not exist in the former but do exist in the latter. The presence of twin boundaries allows {111} surface facets to exist and micro-twinned material to grow in the midst of other material growing without micro-twins from {100} facets, thus complicates surface morphology. The twin boundary separates these two regions. The cause of the twin boundary is not clear. More detailed studies are in progress [3].

1. Z.L. Wang, J. Bentley, R.E. Clausing, L. Heatherly and L.L. Horton, Proc. 49th Ann. Meet EMSA (1991) pp. 956.
2. Z.L. Wang, J. Bentley, R.E. Clausing, L. Heatherly and L.L. Horton, Applications of Diamond Films and Related Materials, Y. Tzeng, M. Yoshikawa, M. Murakawa and A. Feldman eds., Elsevier Science Publishers (1991) pp. 489-494; J. Materials Research, to be submitted (1992).
3. This research was sponsored by the ORNL exploratory studies program and by the Division of Materials Sciences, U.S. Department of Energy, under contract DE-AC05-84OR21400 with Martin Marietta Energy Systems, Inc.

FIG. 1.--SEM image showing topography of diamond film examined by TEM in Fig. 2.
FIG. 2.--[110] DF TEM image with SAD inserts of fractured diamond grain from film shown in Fig. 1.
FIG. 3.--SEM image showing topography of diamond film examined by TEM in Figs. 4 and 6.
FIG. 4.--[110] BF TEM image with SAD inserts of a fractured diamond grain from film shown in Fig. 3.
FIG. 5.--SEM image showing topography of diamond grain from film shown in Fig. 3.
FIG. 6.--[110] DF TEM image with SAD inserts from region indicated in Fig. 5.

5 μm

0.2 μm

5 μm

0.2 μm

2 μm

0.2 μm
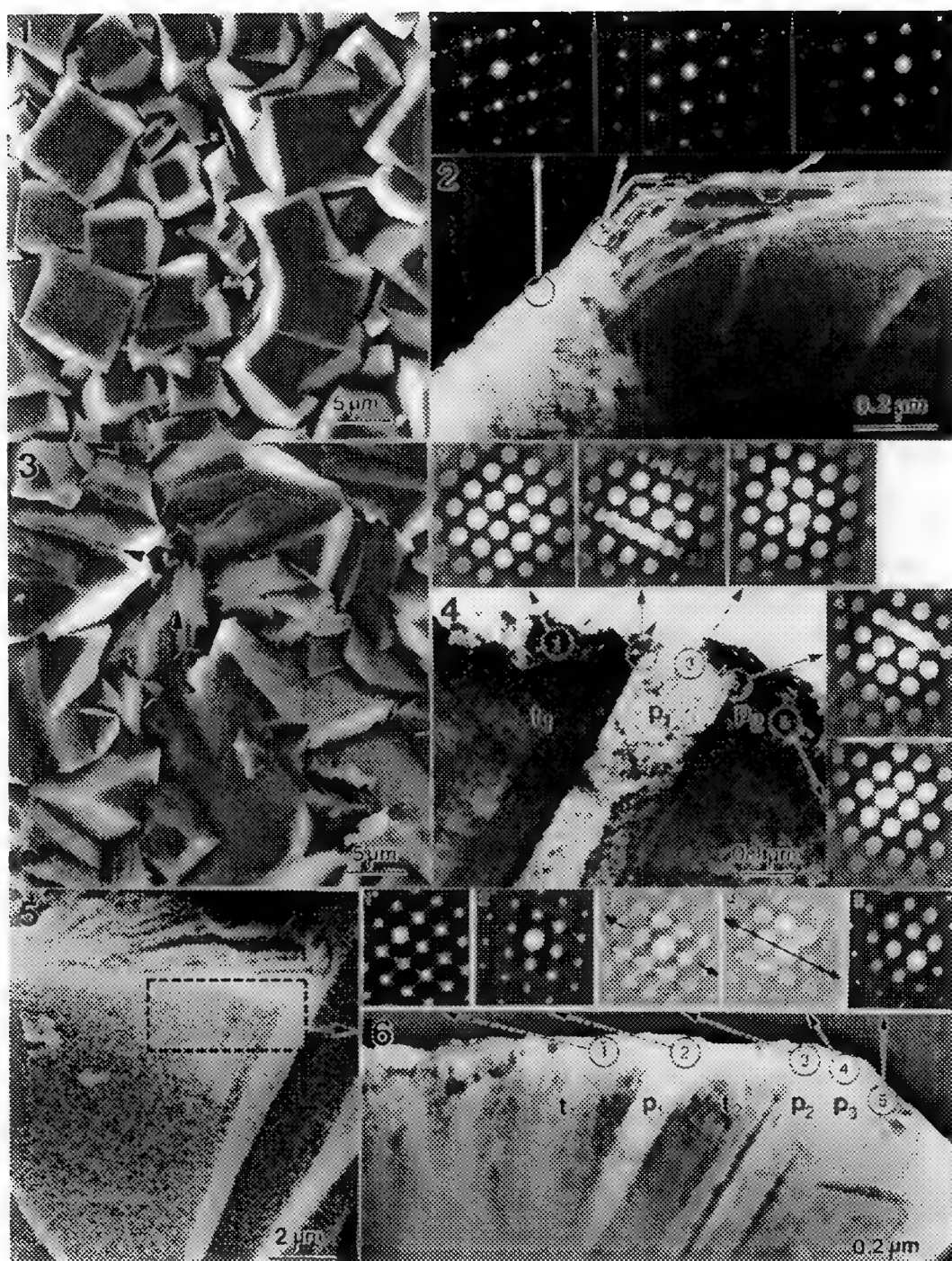
THE CRYSTALLIZATION OF THIN-FILM CERAMICS

J. M. Schwartz[*], L.F. Francis[*], L.D. Schmidt[*], and P.S. Schabes-Retchkiman[**]

[*]Dept. of Chemical Engineering and Materials Science, University of Minnesota, Minneapolis, MN 55455
[**]Instituto de Fisica, U.N.A.M., Apdo. Postal 20-364, México, D.F. 01000, Mexico

Ceramic thin films and coatings are of interest for electrical, optical, magnetic and thermal barrier applications.[1] Critical for improved properties in thin films is the development of specific microstructures during processing. To this end, the sol-gel method is advantageous as a versatile processing route.[2] The sol-gel process involves depositing a solution containing metalorganic or colloidal ceramic precursors onto a substrate and heating the deposited layer to form a crystalline or non-crystalline ceramic coating. This route has several advantages, including the ability to create tailored microstructures and properties, to coat large or small areas, simple or complex shapes, and to more easily prepare multicomponent ceramics.[3] Sol-gel derived coatings are amorphous in the as-deposited state and develop their crystalline structure and microstructure during heat-treatment. We are particularly interested in studying the amorphous to crystalline transformation, because many key features of the microstructure such as grain size and grain size distribution may be linked to this transformation.

We have used TEM along with EELS, XPS and XRD to investigate the microstructural evolution of $PbTiO_3$ thin films from a sol-gel precursor. TEM grids were prepared to support deposited thin ceramic films at high temperatures by vacuum evaporating ~300Å of Si on Formvar coated gold TEM grids. The grids were then heated in O_2 at 800°C to oxidize the Si to amorphous SiO_2 and remove the Formvar. Platinum was also vacuum deposited on some parts of the grids; a heat-treatment in H_2 at 650°C was used to disperse the Pt film into particles. This preparation enabled us to examine the effects of Pt particles on the crystallization of the $PbTiO_3$ film. Sol-gel precursor solutions were prepared by the method of Budd et al.[4] Dilute, partially hydrolysed solutions (0.1 M, 1 mole H_2O per mole of Pb) were spin cast (2000 rpm) directly onto the silica coated TEM grids. The microstructures of the *same areas* were monitored after repeated sequential heating at different temperatures using TEM and EELS .

Figure 1 shows the microstructure evolution of a thin film prepared on a silica coated grid that did not contain dispersed Pt particles. The same sample was examined after drying at room temperature (fig. 1A), heating for 30 minutes at 400°C (fig. 1b), heating for 30 minutes at 500°C (fig. 1c), and heating for 30 minutes at 600°C (fig. 1d). Electron diffraction shows no crystallization in samples treated below 500°C. After heating at 500°C, some crystallization had occurred, but crystallization was apparently not complete. Heating the sample at 600°C increased the sharpness and intensity of the rings in the electron diffraction pattern. Intermediate stages between the amorphous, granular structure after drying (fig. 1a) to the final crystallized state (fig. 1d) show features that may be associated with phase separation or development of porosity with removal of residual organics from the film.

The effect of dispersed Pt particles on crystallization of thin film $PbTiO_3$ is shown in figure 2. The bright field image (fig. 2a) from a sample heated at 600°C appears to show patches of $PbTiO_3$ grains surrounding each Pt particle. The corresponding dark field image (fig. 2b) obtained from diffraction rings of both Pt and $PbTiO_3$ confirms this observation. $PbTiO_3$/Pt patches are illuminated in the dark field image. The platinum particles may serve as nucleation centers for thin film crystallization. Further research is in progress to study the microstructural evolution of the ceramic films and the effect of Pt and other nucleating agents on microstructure development.[5]

References

1. D.R. Uhlmann and G.P. Rajendran, in L.L. Hench and D.R. Ulrich, Eds., Ultrastructure

Processing of Advanced Ceramics, New York: John Wiley & Sons (1988) 241-253.
2. C. J. Brinker and G.W. Scherer, Sol-Gel Science: The Physics and Chemistry of Sol-Gel Processing, New York: Academic Press (1990).
3. H. Dislich, in L.C. Klein Ed., Sol-Gel Technology for Thin Films, Fibers, Preforms, Electronics, and Speciality Shapes, Park Ridge, New Jersey: Noyes Pub. (1988) 50-79.
4. K. D. Budd et al., Brit. Ceram. Proc. (1985) 36, 107.
5. This research was partially sponsored by NSF under Grants CBT-882745 and INT-90000511, and CONACyT (Mexico)-NSF. J.M.S. acknowledges support from an Amoco Fellowship. The help of L. Rendon in the HREM is appreciated.
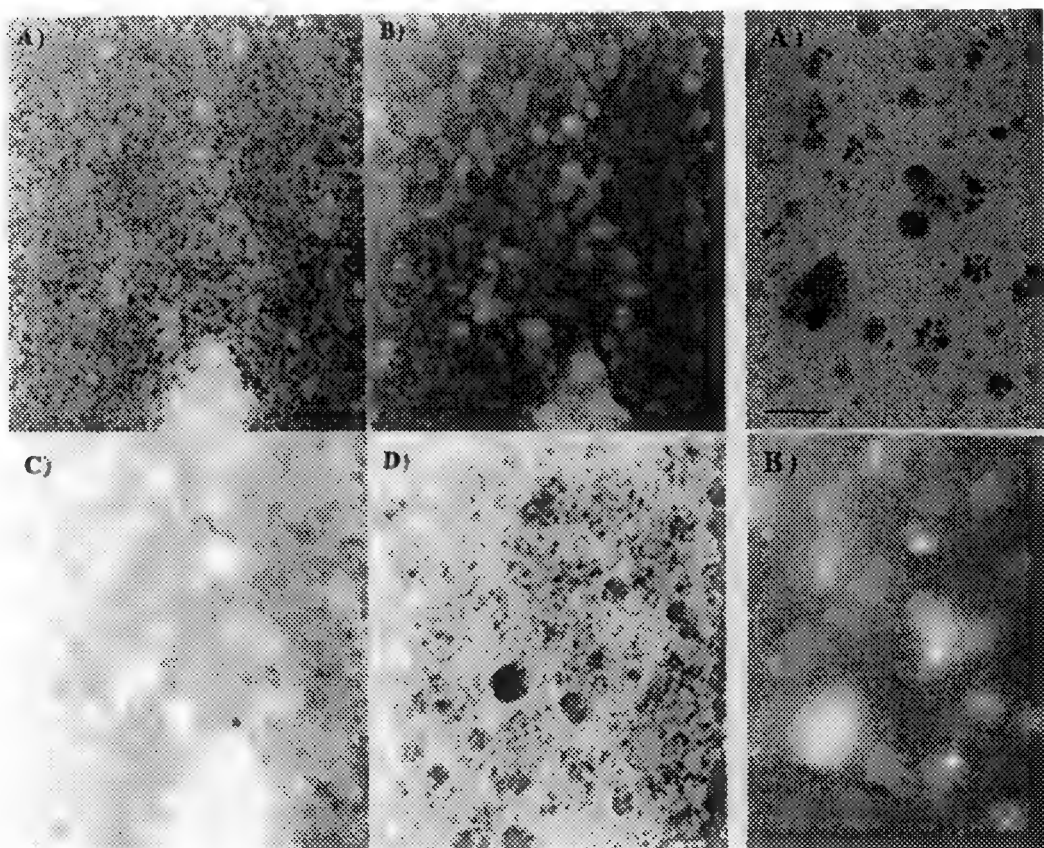
FIG. 1.--Bright field images showing evolution of PbTiO$_3$ microstructure after drying (A), and heating to 400°C (B), 500°C (C), and 600°C (D). Bar = 500Å.
FIG. 2.--Bright field (A) and dark field (B) images of PbTiO$_3$ microstructure after heating to 600°C with Pt codeposited. Bar = 500Å.

IMAGING DISLOCATION SHEAR BAND IN SAPPHIRE

S. J. Chen

Department of Geology, University of California, Davis, CA 95616

The deformation of sapphire at low temperatures and high strain rates produces basal twins and dislocation activity in various slip planes which appear as distinctive shear bands, where the dislocations line up in a row (figure 1). The most common shear band is in the basal plane (the lower band in figures 1a through 1c) and is made up of partial dislocations of the type $1/3<\bar{1}010>(0001)$. These dislocations are all associated with the same stacking fault and the sum of three of these faults returns the structure to perfect stacking. The faults can be distinguished in bright field in the {$10\bar{1}4$} reflections (figure 1b) and clearly, in the lower band, the stacking fault disappears when three dislocations have traversed.

Sapphire is a rhombohedral ($R\bar{3}C$) structure which can be straightforwardly envisaged as a hexagonal close packing of oxygen with additional interspersed layers of aluminum ions. The oxygen layers are completely dense but the aluminum sites are only two thirds full, resulting in a hexagonal arrangement of holes. The unit cell of sapphire is six oxygen layers thick because there are three different ways in which the aluminum layers are oriented in the structure. It is these three alternatives that are related to each other by translations of the $1/3<\bar{1}010>$ type which is the stacking fault that is observed in the basal plane. Hence the stacking faults in the lower shear band in figures 1a through 1c are the translations of the aluminum sublattice and the three fold dislocation sequence brings the lattice back into registry.

Dislocation shear bands have also been also observed in face centered cubic metals and it has for a long time been assumed that microstructures of this type are caused by rapid dislocation generation at sources such as the Frank-Reed type. There is also another possibility and that is that the dislocations are the beginning of a twin. In this case the $1/3<\bar{1}010>$ dislocations would glide on adjacent planes and it has been shown (Chen and Howitt 1992) that the basal twinning mechanism in sapphire from $1/3<\bar{1}010>$ dislocations is, in some respects, quite similar to that from $1/6<\bar{1}12>$ dislocations which produce the {111} twin in the FCC structure.

Since the spacing of the oxygen layers in the basal plane of sapphire is greater than 0.2 nm it is possible to resolve this question using high resolution imaging and it is clear from the micrograph in figure 2 that the dislocations are in fact on adjacent planes and are indeed more characteristic of the beginning of a twin than a dislocation pile up.

References

1. Chen S. J. and Howitt D. G. submitted to Acta Metall
2. Support for this work was provided by the U.S. Department of Energy, Office of Basic Energy Sciences under contract no. DE-AC07-761D01570 and contract no. DE-AC07-761D01570. This work was done as part of a collaborative effort with Dr Mike Mills and Dr George Thomas at Sandia National Laboratories.
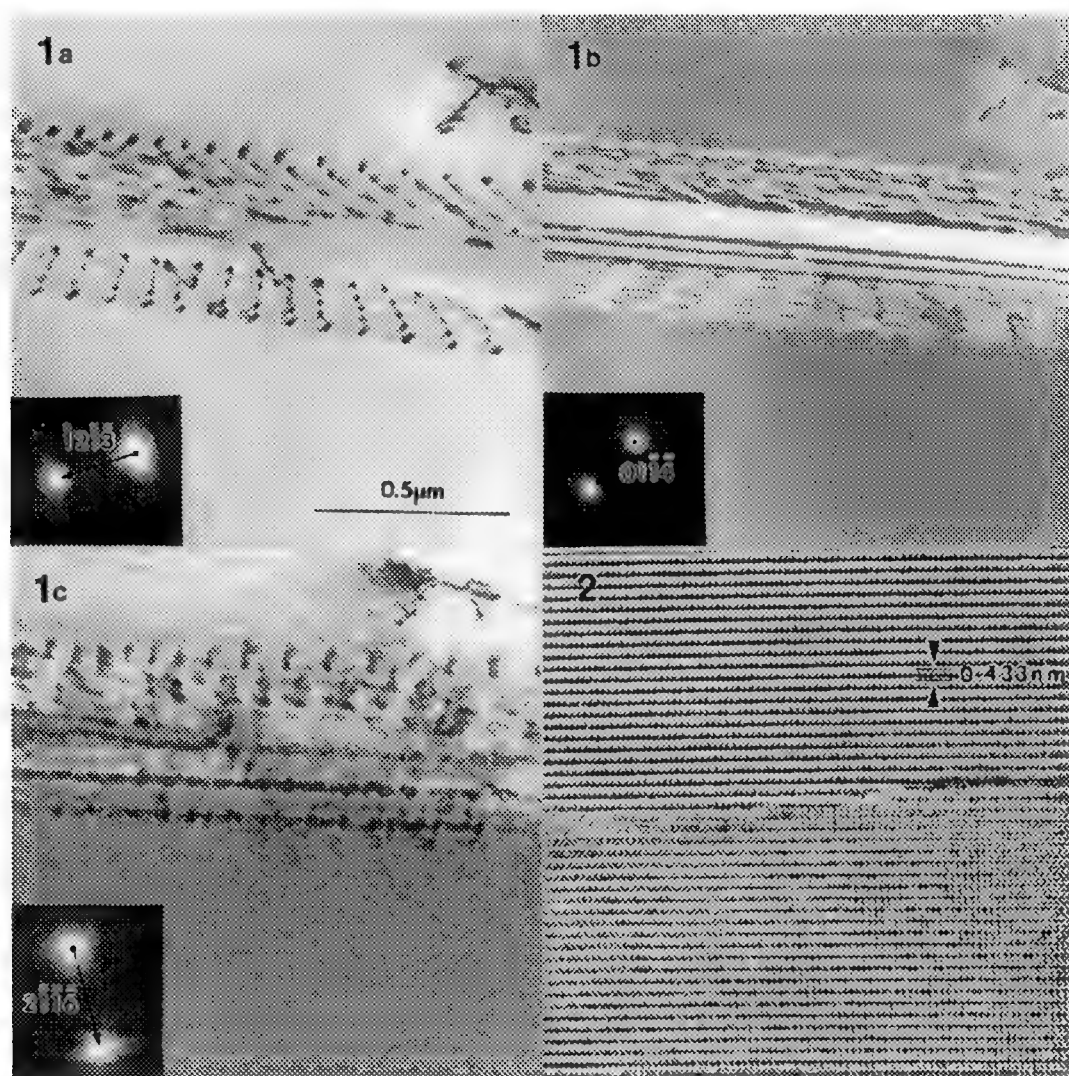
FIG. 1(a,b and c): Diffraction contrast images from the $1/3[01\bar{1}0]$ dislocations and the associated stacking faults.
FIG. 2: A high resolution image of the shear band orthogonal to the basal plane.

DISLOCATION LOOPS IN α-SILICON NITRIDE SINGLE CRYSTALS

H. Suematsu, J. J. Petrovic* and T. E. Mitchell

Center for Materials Science and *Materials Science and Technology Division, Los Alamos National Laboratory, Los Alamos, New Mexico 87545

Silicon nitride(Si_3N_4) is well known to be a most promising ceramic material for high temperature structural applications. It has high strength even at 1200°C and its fracture toughness is about 5 to 7 MPa·m$^{1/2}$. Si_3N_4 has been manufactured on mass production lines as the compressor rotor for turbo chargers. For high temperature use, it is important to know the deformation characteristics of the material and the role played by dislocations and other defects. However, research on the nature of defects in Si_3N_4 has been limited considering the importance of Si_3N_4[1,2]. In this study, we have examined defects in single crystals of Si_3N_4.

The Si_3N_4 single crystals were grown by chemical vapor deposition(CVD) by Union Carbide Coating Service as a modification of the normal CVD process described previously[3]. The crystals were several mm in size and were found to have the α-Si_3N_4 structure from Laue x-ray diffraction patterns. Samples for transmission electron microscopy(TEM) were cut from the crystal and thinned with diamond paste followed by Ar ion beam milling. The samples were examined by TEM in a Philips CM-30ST microscope operated at a voltage of 300kV.

Fig.1 shows a bright field image of the Si_3N_4. A high density of dislocation loops is seen. The loops are rather small with an average diameter of 30nm. The circular shape of the loops becomes clearer if weak beam dark field imaging is used(Fig.2). In some loops, stacking fault contrast can be seen, indicating that the loops are faulted. Fig.3 shows a high resolution electron micrograph of a loop imaged along the [1$\bar{1}$01] zone axis. The loop is seen in the middle of the figure as a distorted region which is essentially on a straight line so that the loop is approximately edge on. Fig.4 shows a higher magnification image of the partial dislocation at one end of the loop and the accompanying stacking fault. The distortion around the fault is restricted to atomic dimensions, again confirming that the loop is edge on. The habit plane is thus found to be (12$\bar{3}$1). From a Burgers circuit analysis, the loop is interstitial type and the Burgers vector is almost perpendicular to the habit plane. The most easily measured component of the Burgers vector is 1/9[11$\bar{2}$0] but there could be components in the two orthogonal directions. However, the loops were found to display minimum contrast with $g = 1\bar{1}00$ and so the Burgers vector is likely to be 1/9[11$\bar{2}\ell$] where ℓ could be 3, as discussed below.

Interstitial dislocation loops on the {10$\bar{1}$0} plane have been reported in Si_3N_4 following neutron irradiation but this was in the β-structure[1]. Of greater relevance are the observations of More[2] who also analysed loops in polycrystalline α−Si_3N_4 prepared by CVD and reported that they had 1/3<11$\bar{2}$3> Burgers vectors and {$\bar{1}\bar{1}$21} habit planes. However, fault contrast was also seen and this is inconsistent with 1/3<11$\bar{2}$3> which is a perfect lattice vector. Perhaps a better assignment would be 1/9<11$\bar{2}$3> which would then be consistent with the analysis described above. The habit plane is still different but this was found to be variable in the present study in any case. The nature of the Burgers vectors and habit planes of the loops in CVD Si_3N_4 are still under investigation, as are their origin and significance[4].

References
1. T. E. Mitchell and R. A. Youngman, Radiation Effects 74 (1983) 267.
2. K. L. More, Proc. Annual EMSA Meeting 49 (1991) 936.
3. O. Ünal, J. J. Petrovic and T. E. Mitchell, J. Mater. Res.7(1992)136.
4. This work is supported by the US DOE-OBES.
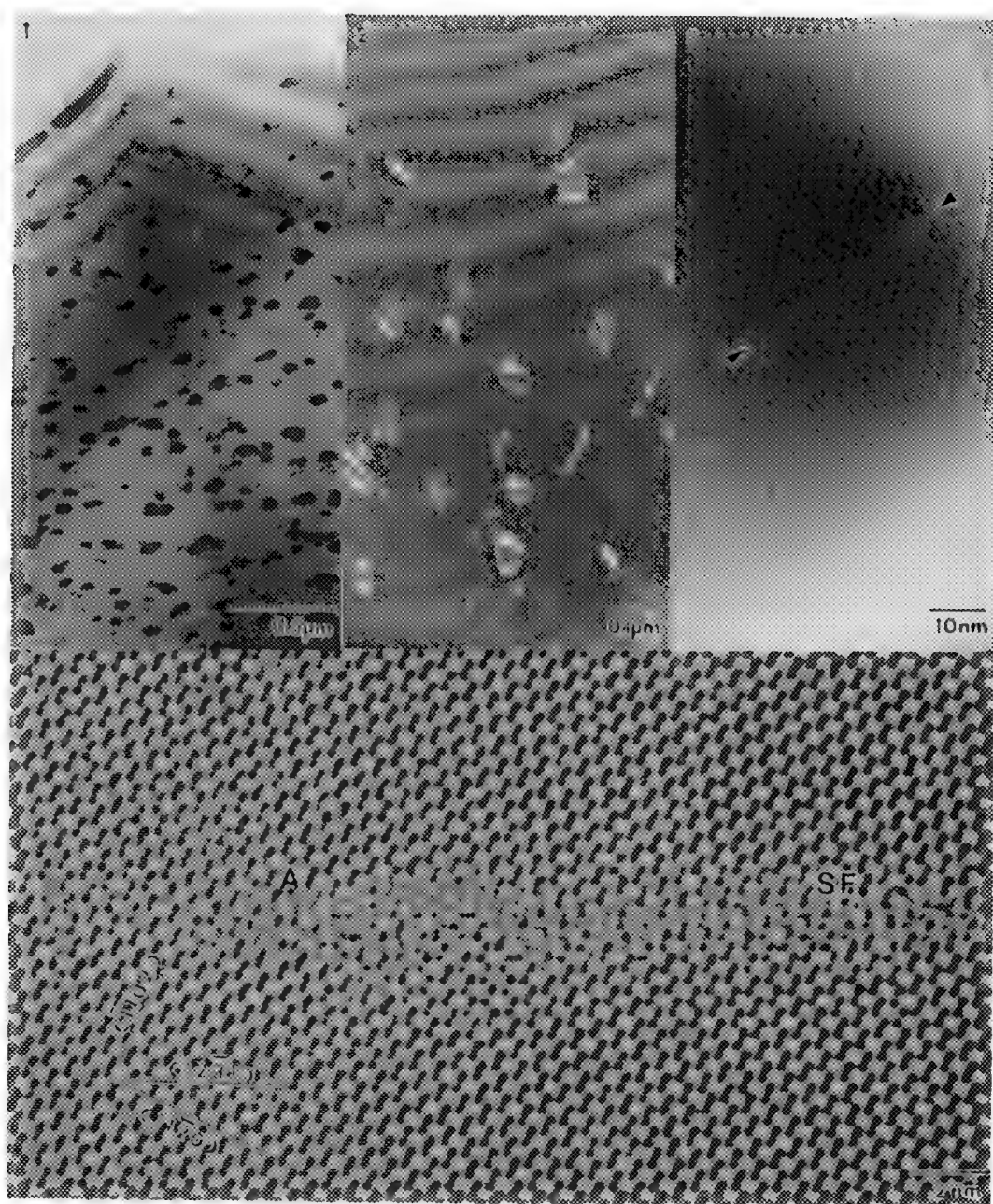
Fig.1 Bright field image of loops in the Si$_3$N$_4$ single crystal.
Fig.2 Weak beam dark field image of the loops.
Fig.3 High resolution image of a loop(arrowed).
Fig.4 The loop in Fig.3 at higher magnification. A is a edge-on partial dislocation and SF is a stacking fault.

ANALYTICAL ELECTRON MICROSCOPY OF REACTION–BONDED SiC

K Das Chowdhury, R. W. Carpenter and W. Braue*

Center for Solid State Science, Arizona State University, Tempe, AZ 85287-1704, *German Aerospace Research Establishment, D5000, Cologne 90, Germany

Research on reaction-bonded SiC (RBSiC) is aimed at developing a reliable structural ceramic with improved mechanical properties. The starting materials for RBSiC were Si, C and α-SiC powder. The formation of the complex microstructure of RBSiC involves (i) solution of carbon in liquid silicon, (ii) nucleation and epitaxial growth of secondary β-SiC on the original α-SiC grains followed by (iii) $\beta > \alpha$-SiC phase transformation of newly formed SiC. Due to their coherent nature, epitaxial SiC/SiC interfaces are considered to be segregation-free and "strong" with respect to their effect on the mechanical properties of RBSiC. But the "weak" Si/SiC interface limits its use in high temperature situations (1). However, few data exist on the structure and chemistry of these interfaces (1-3). Microanalytical results obtained by parallel EELS and HREM imaging are reported here.

Planar TEM specimens of a commercially available RBSiC were made by conventional mechanical thinning, dimpling and Ar-ion-milling. HREM was performed in JEOL 4000EX operating at 400KeV with a point to point resolution of 0.17nm. A Philips 400ST/FEG microscope fitted with a Gatan 666 parallel EELS detector was used for chemical analysis. ELS spectra were collected at 1 ev/ch and an acceptance half angle of 13 mrad. A liquid nitrogen stage was used to eliminate specimen borne contamination.

HREM analysis of Si/SiC interfaces showed that these interfaces were free of any resolvable amorphous layer (fig.1). The SiC was in <1-2 1-3> orientation and Si was in g=<111> two beam condition. Good planar matching between the Si and SiC grain with periodic misfit was observed in fig.1. Every fourth Si{111} fringes matched with every fifth {0 1-1-1} SiC fringes. This is due to the fact that four Si{111} interplanar spacing is approximately equal to five SiC {0 1-1-1} interplanar spacing. Therefore the interface may be considered as consisting of a periodic array of edge dislocations. The interface also contained small approximately 1 nm steps. This good matching probably indicates that the residual Si is nucleating on the SiC grains. No amorphous layer was observed in SiC grain boundaries.

Figure 2a shows an HREM image of a second phase inclusion in an SiC grain. These inclusions showed regions of graphite in random orientation (fig.2b) and amorphous phase (region B in fig.2a). This amorphous phase was preferentially ion-milled, creating a hole in the middle of the inclusion. EELS analysis showed the amorphous phase contained Si, C and O. Some areas in the graphite rich regions of the inclusion contained a fairly large amount of Ca with traces of oxygen (fig. 2c). Second phase inclusions in sintered α-SiC reported elsewhere (2) showed periodic distribution of graphite and an oxygen rich amorphous phase in the inclusion.

The origin of the oxygen containing inclusions is of interest, since we could detect neither oxygen nor amorphous layers in Si/SiC or SiC/SiC interfaces. We presume that oxygen was present on the surface of the Si powder particles. When the solid plus liquid synthesis reaction occurred, the oxygen went into solution in Si(l) along with C. Oxygen solubility in Si(s) and SiC(s) is very small. During SiC precipitation and grain growth a few particles high in O content precipitated on mobile α-SiC surfaces and became entrapped in SiC grains. During subsequent cooling these particles precipitated graphite and a Si and O rich amorphous phase (4).

REFERENCES

1. J. N. Ness and T. F. Page, Proc. of the 21st University Conf. on Ceramic Science (1985) 22-23, 347.
2. W. Braue and R. W. Carpenter, J. Mat. Sci., (1990) 25, 2943.
3. S. R. Nutt, D. J. Smith, H. J. Kim and R. F. Davis, Appl. Phys. Lett. (1987) 50 (4), 203.
4. This research was supported by the US Dept. of Energy, Basic Energy Sciences (DE-FG02- 87ER 45305) and performed in the NSF/ASU HREM Facility.
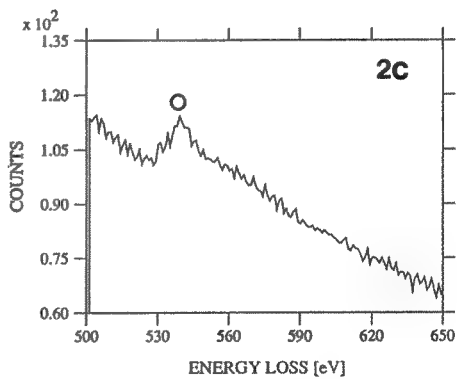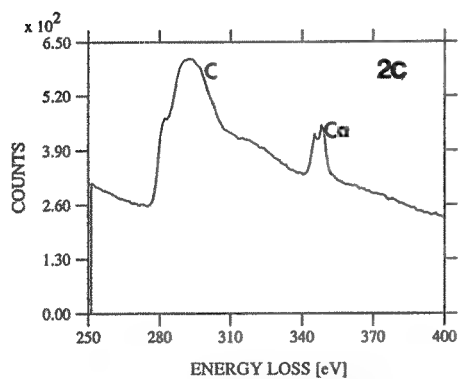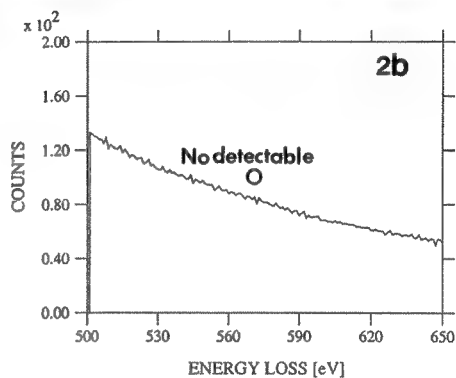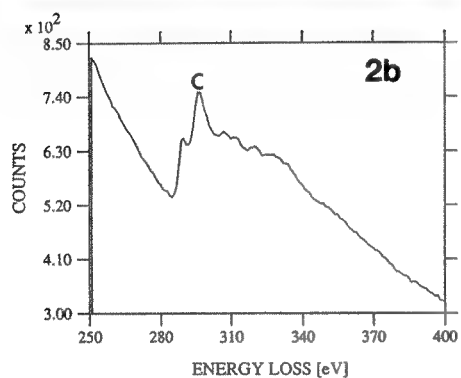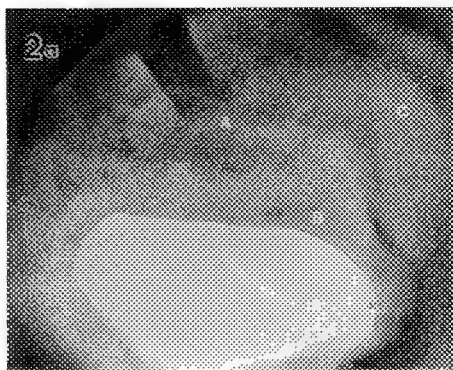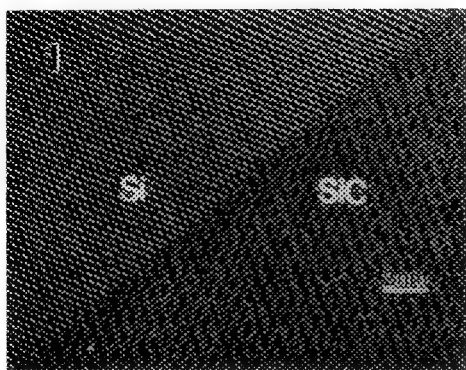
Fig.1 HREM image of Si/SiC boundary indicating no interfacial layer.
Fig.2 Second phase inclusion in α-SiC (a) HREM image (b) EELS spectrum taken from the region A in (2a) (c) EELS spectrum taken from region C in (2a)

CHARACTERIZATION OF IRON-IMPLANTED SILICON CARBIDE

J. Bentley, L. J. Romana, L. L. Horton, and C. J. McHargue*

Metals and Ceramics Division, Oak Ridge National Laboratory, P. O. Box 2008, Oak Ridge, TN 37831-6376.
*Now at: The University of Tennessee, Knoxville, TN 37993

As part of extensive fundamental studies of ion-implanted ceramics,[1] analytical electron microscopy (AEM) has been used to characterize [0001] single crystal 6H α-silicon carbide implanted at room temperature with 160 keV ^{57}Fe ions to fluences of 1, 3, and 6×10^{16} ions/cm^2. AEM was performed at 100 kV with a Philips EM400T equipped with a field emission gun, a 6585 STEM unit, an EDAX 9100/70 energy dispersive X-ray spectrometer (EDS), and a Gatan 666 parallel-detection electron energy loss spectrometer (PEELS).

A micrograph of a cross-sectioned specimen implanted with 6×10^{16} ions/cm^2 is shown in Fig. 1. The implanted region extending to 195 nm from the surface is amorphous, as confirmed by convergent beam electron diffraction (CBED) patterns (insets), and contains iron at levels easily detectable by EDS (Fig. 2). The 15 nm lattice fringes of the edge-on 6H basal planes in the substrate provide an unambiguous depth calibration scale. The transition layer at the end of the ion range exhibits the expected strain contrast. The depth profile of the implanted iron was measured by EDS line scans perpendicular to the implant surface; the mean of three of these scans is shown by the filled symbols in Fig. 3. The integrated iron profile agrees with the expected 6.0×10^{16} ions/cm^2 only if the density of the amorphous SiC is equal to that of its crystalline forms, rather than the 20% lower density reported earlier.[1]

In order to search for evidence of iron clustering, a plan-view specimen sectioned to near the peak iron deposition (confirmed by EDS) was examined. Iron-rich precipitates or clusters with diameters >2 nm would have been clearly visible with the high magnification annular dark-field Z-contrast and through-focus phase-contrast (Fig. 4) imaging employed, but no precipitates or clusters were observed. Information about the bonding of the iron was obtained from examination of the electron energy loss fine structure for the iron L_{23} edge. Fig. 5 shows a comparison of the fine structure for this edge in spectra measured with PEELS for the plan-view Fe-implanted SiC specimen and for metallically-bonded-iron in type 304 stainless steel. The "white lines" at ~711 and ~724 eV in the spectrum from Fe-implanted SiC are broader and of much lower intensity relative to the contribution from the continuum states (the region above ~735 eV) than those in the spectrum from the stainless steel. Comparisons with additional Fe compounds are planned but the preliminary results suggest that the iron in the SiC is not primarily metallically-bonded. This supports the conclusion of conversion electron Mössbauer spectroscopy data that the iron is in covalently bonded sites.[2]

In an attempt to promote the deposited iron to change its form or distribution, a cross-sectioned AEM specimen was annealed in-situ. No changes, such as clustering of the Fe, were observed after annealing at up to 550°C, but at 600°C the amorphous layer began to crystallize. The transformation began in the middle of the layer and proceeded in a direction parallel to the original surface (see Fig. 6). The crystallized material was cubic β-SiC that was heavily twinned normal to the $<111>_\beta$ growth direction. Similar in-situ annealing of Cr-implanted polycrystalline SiC by Sklad et al.[3] achieved only slight epitactic regrowth from the substrate at up to 1100°C. Bohn et al. showed that annealing at 1500°C was necessary for complete epitactic regrowth in Cr-implanted SiC, but some recovery at 650°C was indicated in Raman spectra.[4] The iron profile in the crystallized material was measured by EDS line scans (open symbols, Fig. 3). Some redistribution of the Fe is noticeable in the lowered and broadened profile. The local variations in the Fe signal are much greater than fluctuations from counting statistics and may indicate precipitation of the iron. However, the high defect density and specimen thickness preclude reaching any firm conclusions from the image. The possibility of rejection of the iron to the foil surfaces also has to be considered.[5]

1 C.W. White, C.J. McHargue, P.S. Sklad, L.A. Boatner, and G.C. Farlow, Mat. Sci. Rep. 4 (1989) 41-146.
2 C.J. McHargue, A. Perez, and J.C. McCallum, Nucl. Inst. and Meth. B59/60 (1991) 1362-5.
3 P.S. Sklad, P. Angelini, C.J. McHargue, and J.M. Williams, Proc. Ann. EMSA Meet. 42 (1984) 416-7.
4 H.G. Bohn, J.M. Williams, C.J. McHargue, and G.M. Begun, J. Mater. Res. 2 (1987) 107-116.
5 Research sponsored by the Division of Materials Sciences, U.S. Department of Energy under contract DE-AC05-84OR21400 with Martin Marietta Energy Systems, Inc.
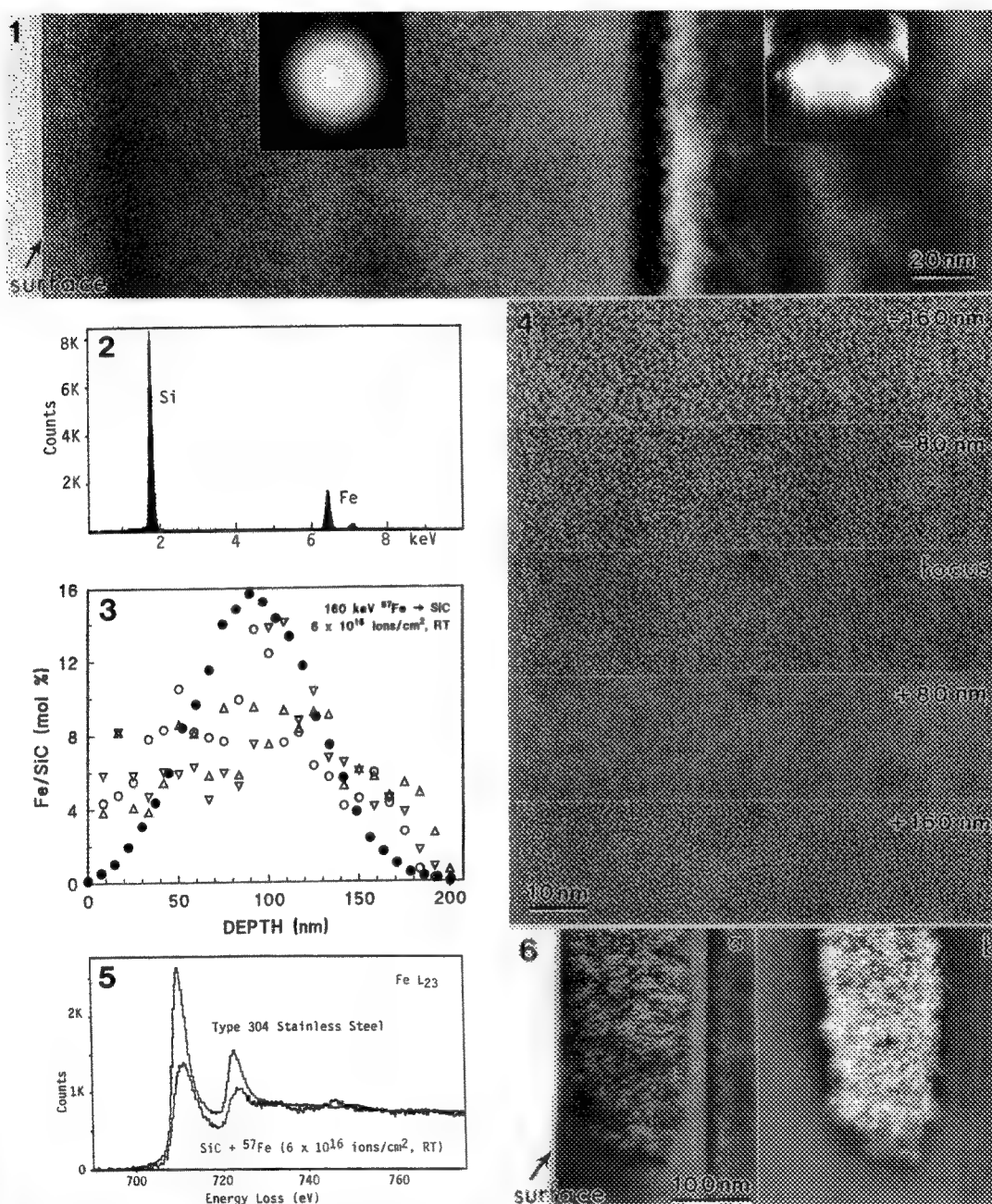
FIG. 1.--Micrograph (with inset CBED patterns) of cross-sectioned SiC implanted with 6×10^{16} Fe ions/cm^2.
FIG. 2.--Energy dispersive X-ray spectrum from center of implanted region.
FIG. 3.--Fe depth profiles measured by EDS; ● as-implanted; ○ △ ▽ after 600°C in-situ anneal (3 data sets).
FIG. 4.--Through-focus-series phase-contrast images of plan view specimen sectioned to 80 nm.
FIG. 5.--PEELS fine structure of Fe L_{23} edge for Fe-implanted SiC and type 304 stainless steel.
FIG. 6.--(a) Bright-field and (b) dark-field images of crystallized region in SiC annealed in-situ at 600°C.

IN-SITU OBSERVATIONS OF THE BEHAVIORS OF FERROELECTRIC DOMAINS IN BaTiO$_3$ UNDER APPLIED ELECTRIC FIELDS WITH TRANSMISSION ELECTRON MICROSCOPY (TEM)

Feng Tsai, Victoria Khiznichenko, and J. M. Cowley

Center for Solid State Science and Department of Physics and Astronomy, Arizona State University, Tempe, AZ 85287-1704

The previous studies on the behaviors of ferroelectric domains under applied electric fields were made by a number of researchers, e.g. Merz[1] and Little[2] on bulk BaTiO$_3$ crystals with optical microscopy. It was suggested that under the applied electric field the new antiparallel domains nucleated and grew[1] and 90° and 180° domains nucleated and grew sidewise[2]. However, those results and conclusions were obtained from the experiments on large bulk crystals with optical microscopy of relatively lower magnification and resolution. TEM is a very powerful tool in the study of crystal structure and defects and may provide a new interpretation to the study of microdomains of hundred angstroms in thin ferroelectric films with a higher magnification and resolution and may be combined with electron diffraction[3,4,5]. However, no reference has been found that an in-situ TEM study of the behaviors of ferroelectric materials under applied electric fields has ever been made.

The present paper introduces an in-situ study of the behaviors of ferroelectric domains and domain boundaries in BaTiO$_3$ under applied electric fields in a conventional TEM. The samples are ceramic BaTiO$_3$ provided by Valpy-Fisher, Inc. and BaTiO$_3$ single crystals grown with Remeika method. The specimens are dimpled and then Ar ion-milled. Gold is evaporated to form two parallel electrodes on both sides of the specimen, as shown in Fig.1. The electrodes are so made that they are parallel with a gap of 0.2 mm-0.5 mm. The electric field is perpendicular to the specimen plane and can be roughly estimated as E=V/d, presuming the electric field is uniform, where E is the electric field, V is the applied voltage on the two electrodes and d is the spacing between the electrodes. Thin edges without evaporated gold are used for the observation of the domain nucleation and movement. A specimen holder is specially designed for applying an electric field on the specimen with a DC power supply during the TEM observations. TEM observations are made on a 120 kV Phillips 400T conventional TEM with a vacuum pressure better than 3×10^{-7} torr .

Fig.2(a) is the image of an area with 90° a-a domain boundaries under an electric field about 3 kV/cm and Fig2(b) is the selected area diffraction(SAD) pattern of the same area. It can be noticed that when the electric field is applied, the original 90° a-a domain boundaries are not moved by the electric field but instead, many small new domains of about submicron sizes are nucleated on the old a-a boundaries, as indicated in Fig.2(a). The new domains have boundaries with fringes along [010] direction when observed along [001] direction, which suggest that they might be 90° a-c domain boundaries. The SAD pattern shows an extra spot beside the splits due to 90° a-a domains, as indicated in Fig.2(b). The analysis of reciprocal lattice nets of tetragonal BaTiO$_3$ in Fig.2(c) shows that the split of diffraction spots due to "c" domains nucleated in 90° a-a domain crystal can be differentiated from those of a-a domain configurations, especially for high index reflections. From the SAD pattern of the same area, in Fig.2(b), the ratio of lattice constants corresponding to the split of presumable "c" domains are 0.996, which basically fits the theoretical value 1 in analysis in Fig.2(c). It is then confirmed that the "c" domains nucleate under the applied electric field. The new "c" domains have certain sizes under an electric field and do not change with time at a certain electric field but grow larger as the electric field increases. It is suggested that in this case the polarization vectors of the "c" domains take the direction of the applied electric field. The observation is different from the previous observations made on bulk BaTiO$_3$ in which the sidewise boundary movement were observed[1,2] because the electric field is applied perpendicular to the 90° a-a domain boundaries. However, the mechanism that new domains nucleate and grow should be the same under an electric field. Since polarization vectors of 90° domains are 45° to their boundaries, the sidewise movement of domain boundaries is the consequence of domain growth under an electric field. When the electric field is removed, the new "c" domains do not disappear but keep their positions, sizes and shapes. It is also found that "a" domains in the areas deposited with Au electrodes are stable under applied electric fields. Neither the domain boundaries are moved, nor the new "c" domain are nucleated.

REFERENCES
1.W. J. Merz, Phys. Rev. 95(1954)690
2. E. A. Littles, Phys. Rev. 98(1955)978
3. M. Tanaka and G. Honjo, J. of Phys. Soc. Jpn., 19(1964)954
4. M. Verwerft, G. van Tendeloo, J. van Landuyt and S. Amelinckx, Ferroelectrics, 97(1989)5
5. L. A. Bursill and J. Peng, Ferroelectrics, 70(1986)191

SPECIMEN HOLDER

[001]

Au ELECTRODES

+

−

2c

(1 1 0)

(1 0 0)

O

a*

a₂

c*   a₁   c (1-1 0)
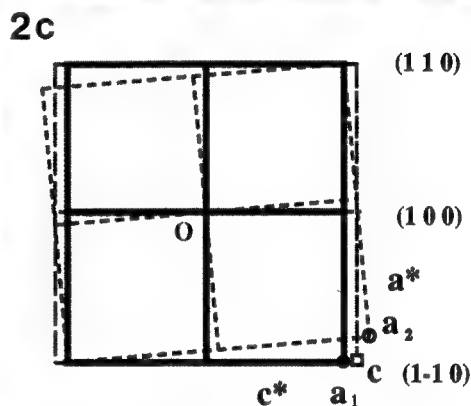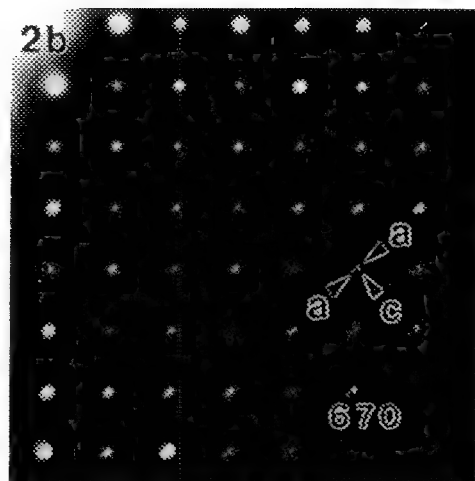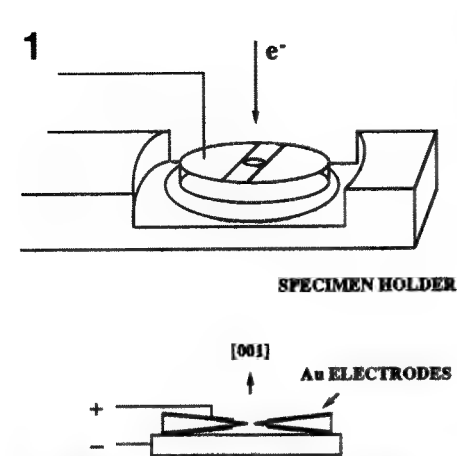
Fig.1. The design of the electrodes on specimen for applying electric field in TEM.

Fig.2(a)the bright image of BaTiO₃ with 90° a-a domain boundaries imaged along [001] direction under applied electric field along [001] direction about 3 kV/cm. The original 90° a-a domain boundaries are not moved. The new "c" domains grow on the 90° a-a domain boundaries; (b)the diffraction spots in SAD pattern show the corresponding splits of new "c" domains; (c) analysis of reciprocal lattice nets of "a"-"a"-"c" domain configuration.

349

THEORY AND PRACTICE OF ENERGY-FILTERED ELECTRON DIFFRACTION USING THE HB5 STEM[1]

L.C. Qin, A.J. Garratt-Reed and L.W. Hobbs

Department of Materials Science and Engineering
Massachusetts Institute of Technology
Cambridge, MA 02139

Electron diffraction patterns obtained in TEM have long been an important part of microstructural characterizations. Certain materials, such as crystalline silicas, are amorphized in the fast electron beam of the TEM, and their aperiodic (metamict) structure is of interest[2]. For amorphous materials, both elastically and inelastically scattered electrons contribute to the diffuse diffraction pattern. Analysis of aperiodic structure, however, requires intensity data from only elastically scattered electrons, and it is therefore it is necessary to obtain energy-filtered electron diffraction patterns[3]. With the energy-filtered electron diffraction technique, the background intensity that is mainly due to inelastically scattered electrons is removed. This makes possible the derivation of radial distribution functions (RDFs) from collected electron diffraction intensity data for uniform aperiodic structures.

For a multiple component system, the diffraction intensity from a uniform structure can be expressed as[4]

$$I(s) = N \sum_{uc} f_j^2 + N f_e^2 \sum_{uc} K_j \int_0^\infty 4\pi r^2 [\rho_j(r) - \rho_e] \frac{\sin(2\pi s r)}{2\pi s r} dr \qquad (1)$$

where $I(s)$ is the intensity; $s = 2\sin(\frac{\Theta}{2})/\lambda$ is the scattering vector with Θ being the scattering angle and λ the electron wavelength; f_j is the atomic scattering amplitude for atomic species j; N is the number of chemical units within the scattering volume of the thin specimen, and K_j are the proportionality constants that relate the atomic scattering amplitudes f_j with a mean value f_e.

Defining the averaged RDF $G(r)$ as a superposition of partial radial distribution functions $\rho_j(r)$ as

$$G(r) = 4\pi r^2 \sum_{uc} K_j [\rho_j(r) - \rho_e] , \qquad (2)$$

$G(r)$ can then be deduced from the experimental electron intensity data by

$$G(r) = 8\pi r \int_0^\infty s i(s) \sin(2\pi s r) ds \qquad (3)$$

where

$$i(s) = (\frac{I(s)}{N} - \sum_{uc} f_j^2)/f_e^2 . \qquad (4)$$

Energy-filtered electron diffraction intensity data have been collected with an HB5 scanning transmission electron microscope (STEM), which has an energy-loss spectrometer with energy resolution of about 2 eV, in either the selected area diffraction mode or the micro-diffraction mode. In the selected area diffraction mode, parallel incidence can be obtained and the energy-filtered electron diffraction data are collected at the spectrometer as the electron beam is scanned across a range of incident angles. In this mode, a relatively large area is illuminated, and this gives a quite good signal/noise

ratio. In the micro-diffraction mode, on the other hand, the stationary incident beam illuminates a small area of the specimen, which guarantees that the scattered electrons collected are from the small volume being analyzed, and the exit electrons are scanned across the spectrometer by a post-specimen scanning coil (Grigson coil). In the selected area diffraction mode, the angular resolution is limited by the finite size of the collector aperture; but in the micro-diffraction mode, since a convergent beam is used, the angular resolution is limited by the finite beam divergence. The data are recorded in either analog form or digital form. In digital acquisition, the data are transmitted to computers for deducing the RDFs using the algorithms mentioned above.

As examples for application of the technique, figure 1(a) shows the experimental $I(s)$ vs s data which were obtained from vitreous silica (v-SiO$_2$) and quartz amorphized by fast electron irradiation (in situ), respectively. The data presented here were collected using analog output, and the diffraction patterns were recorded on Polaroid films and digitized manually. The camera length for the metamict quartz was calibrated by using the Bragg reflections from adjacent crystal lattice. The reconstructed RDFs for both materials are given in Figure 1(b), which are found to be different from each other at medium range. The difference reflects differences in their atomic structures, as the two have undergone different routes to reach the final aperiodic states. Phosphate glasses have been similarly investigated[5].

References
1. Research supported by DOE under Grant DE-FG02-89ER45396.
2. M.R. Pascucci, J.L. Hutchison and L.W. Hobbs, Radiation Effects (1983) 74, 219.
3. J.F. Graczyk and S.C. Moss, Rev. Sci. Instrum. (1969) 40, 424.
4. B.E. Warren, X-Ray Diffraction, (1990: Dover Publications Inc.).
5. A.N. Sreeram, L.C. Qin, A.J. Garratt-Reed and L.W. Hobbs, these Proceedings.
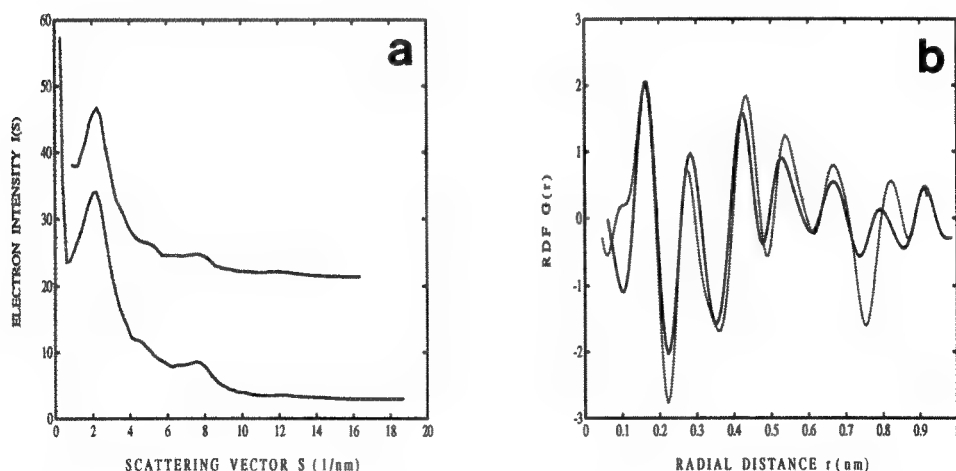
Figure 1: Energy-filtered electron diffraction patterns and reconstructed RDFs for two aperiodic silicas. (a) Zero-energy loss electron intensities $I(s)$ vs scattering vector s for vitreous silica (top) and metamict quartz (bottom). The intensity is in arbitrary units. (b) Reconstructed RDFs $G(r)$ vs r for vitreous silica (dotted line) and metamict quartz (solid line).

ANALYTICAL ELECTRON MICROSCOPY STUDY OF REACTED SURFACE LAYER OF BOROSILICATE NUCLEAR WASTE GLASSES

L.M. Wang*, S.A. Kaser*, R.C. Ewing* and J.K. Bates†

*Department of Geology, University of New Mexico, Albuquerque, NM 87131
†Chemical Technology Division, Argonne National Laboratory, Argonne, IL 60439

Analysis of the reacted surface layer of borosilicate glass is important to the understanding of the long term nuclear waste glass reaction process. The objective is to assess the simulated nuclear waste glass/water reaction pathway by identifying new crystalline phases that appear on the glass surfaces during the reaction. The results can be used to validate models generated to predict long-term performance of the nuclear waste glass under a range of conditions.[1]

In this study, extensive scanning electron microscopy (SEM) with qualitative energy dispersive x-ray spectroscopy (EDS) analysis, quantitative analytical and high resolution transmission electron microscopy (AEM and HRTEM) have been performed on two 202U glasses which were reacted in saturated water vapor for 14 and 23 days, respectively. In order to study the microchemical and microstructural changes with increasing depth from the reaction surface, TEM specimens were prepared in cross-section using the ultramicrotomy slicing technique similar to that described by Bates et al.[1] In this process, small chunks containing the reacted surface layer and a thin layer of glass were first broken off from the sample surface and each of these chunks was then embedded in resin to form a block. Finally, thin sections, approximately 90 nm thick, were microtomed from these blocks and were transfered to copper mesh grids covered by holey carbon films for observation. AEM and HRTEM analyses were accomplished using a JEOL JEM-2000FX microscope attached with a Noran/TN-5500 EDS system at the University of New Mexico.

Fig. 1 is a SEM micrograph obtained from the surface of the 202U glass reacted in saturated water vapor at 200°C for 14 days. The micrograph shows that a primary layer of clay and several other secondary phases have formed on the reacted glass surface. According to their morphology and the qualitative chemical analysis, the primary alteration layer and three secondary phases could be roughly identified even before AEM study.[2] These phases are: a smectite primary layer with "honeycomb" morphology; well-developed cubo-octahedral zeolites; diaphanous uranium silicates, calcium silicate rosettes and flakes. Fig. 2 is a cross-sectional TEM bright-field micrograph taken from the same sample as in Fig. 1. The entire thickness of the primary reaction layer (smectite) and all the three secondary phases shown in Fig. 1 can be observed in this micrograph. The composition and structure of the primary alteration layer and the secondary phases have been carefully studied with AEM and HRTEM. Many EDS spectra have been collected across the thickness range of the primary layer, no systematic compositional change was detected. The HREM images of the smectite layer (as the one shown in Fig. 3) have the typical curved lattice fringes of clay minerals and from which 0.47 nm and 1.4 nm lattice spacings have been measured (the 0.47 nm spacing was calibrated using the inner ring of the selected area electron diffraction pattern). AEM and HRTEM results confirmed that the primary alteration layer is smectite and further suggest it is probably nontronite–a mineral in the smectite clay group. The AEM data show the weight percentage ratio of uranium oxide to silicon oxide in the uranium silicate crystals is about 70 times of that in the bulk glass. The formation of this uranium-rich phase may limit the ultimate loss of uranium from the glass. Also, several crystals of calcium hydrate have been observed during AEM analyses. One unique feature of the smectite primary layer on the sample reacted for 23 days is that it consists two sub-layers which are separated by a very obvious interface. Small U-Ti-O particles (~30 nm in dimensions) were found on the interface between the two sub-layers of smectite. Finally, a high temperature silica polymorph, tridymite has also been observed on top of the smectite layer.[3]

References
1. J.K. Bates et al., Argonne National Laboratory report ANL-90/40 (1991).
2. J.E. Welton, SEM Petrology Atlas,Tulsa: The American Assoc. of Petroleum Geologists (1984).
3. This work is supported by U.S. DOE, Office of Environmental Restoration and Waste Management under contract W-31-109-ENG-38.
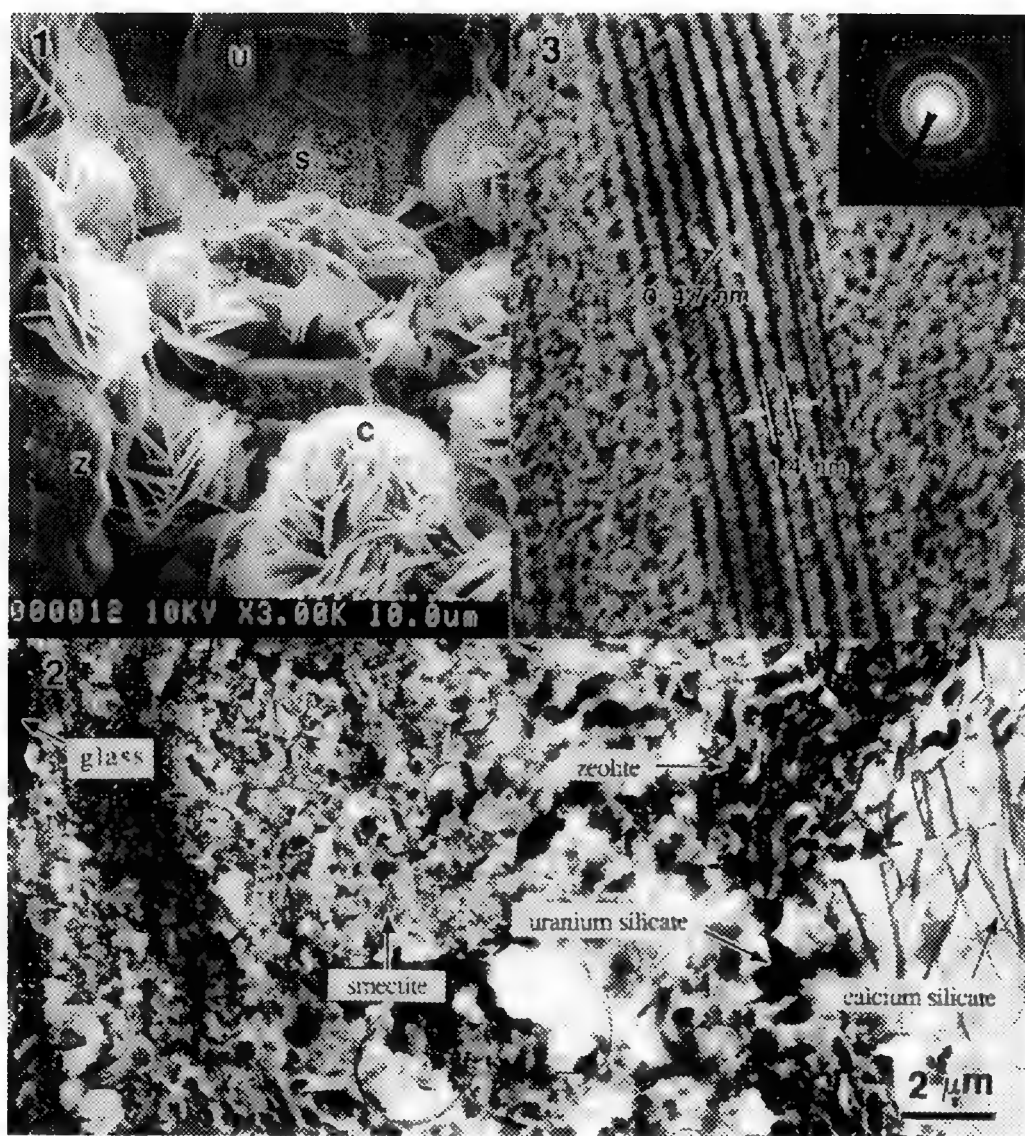
FIG. 1.--SEM micrograph showing the primary reaction layer and secondary phases on the surface of a 202U glass sample which was reacted in saturated water vapor at 200°C for 14 days. Letters marked on the micrograph represent: S–smectite (primary layer); Z–zeolite; C–calcium silicate; and U–uranium silicate.

FIG. 2.--Cross-sectional TEM micrograph showing the entire reacted depth range of the sample shown in Fig. 1. The glass/reaction layer interface is on the left, and the top surface of the layer is on the right (note, all the phases shown in Fig. 1 can be found in this micrograph).

FIG. 3.--HRTEM image of the crystalline smectite layer formed on the surface of 202U glass after reaction with saturated water vapor at 200°C for 14 days. The insert is a selected area electron diffraction pattern from the smectite layer. The inner ring in the pattern arises from the 0.47 nm spacing lattice planes.

TEM CHARACTERIZATION OF THE α' AND β PHASES IN POLYCRYSTALLINE DISTRONTIUM SILICATE (Sr₂SiO₄)

Y. J. Kim, J. L. Shull and W. M. Kriven

Department of Materials Science and Engineering, University of Illinois at Urbana-Champaign, Urbana, IL 61801

Two polymorphs, α' and β, are known to be major phases in pure distrontium silicate (Sr_2SiO_4) at atmospheric pressure.[1] Fully dense pellets were fabricated by sintering chemically prepared powders in the temperature range of 900° to 1400°C for 1 to 5 hours. Their phases and microstructures were studied by TEM. At lower sintering temperatures such as 900°C, the major phase was orthorhombic α' (space group, *Pmnb*). The euhedral α' grains had a size of about 1 μm diameter (Fig. 1a). As the sintering temperature increased, the amount of monoclinic β phase (space group, $P2_1/n$) tended to increase. These β grains were usually irregular and twinned on $\{100\}_\beta$ or $\{001\}_\beta$ planes. Concentration of the electron beam on the grains gave rise to a disappearence of twins (Fig. 1b).

SADP's from the α' grains showed an incommensurate modulation along the $\underline{b}^*$ direction. In the $[001]_{\alpha'}$ orientation, the modulation was almost commensurate, with satellite reflections located at ~1/3 of the principal reflections (Fig. 2a). When the specimen was tilted to the $[102]_{\alpha'}$ orientation, the number of satellite reflections increased (Fig. 2b). This modulation could be interpreted in several different ways, one of which suggested that the satellite reflections around $\{0k0\}$ were extinct, when k is even, in the $[001]_{\alpha'}$ orientation. In this case the modulation vector, $\mathbf{q}$, would be about 0.3 $\underline{b}^*$. A previous study reported $\mathbf{q} = 0.303 \pm 0.005$ $\underline{b}^*$.[2] SADP's from the twinned β grains also showed a similar incommensurate modulation along the $\underline{b}^*$ direction. Fig. 3a shows the $[100]_\beta$ SADP, which is almost identical to the $[001]_{\alpha'}$ SADP except for the appearance of $\{010\}_\beta$ principal reflections in the former. The $[110]_\beta$ SADP of the same area (Fig. 3b) did not display any modulations, but $\{001\}_\beta$ twinned reflections were observed (arrowed). Because of complications and variations of the modulated structures of both the α' and β phases in samples processed under different conditions, further study is needed, particularly in conjunction with the transformation mechanism between the α' and β phases.

References

1. M. Catti *et al.*, Acta Cryst. (1983) B39, 674.
2. R. L. Wither *et al.*, J. Physics (1987) C20, 1653.
3. This research was supported by Air Force Office of Scientific Research through a URI Grant AFOSR-90-0174.
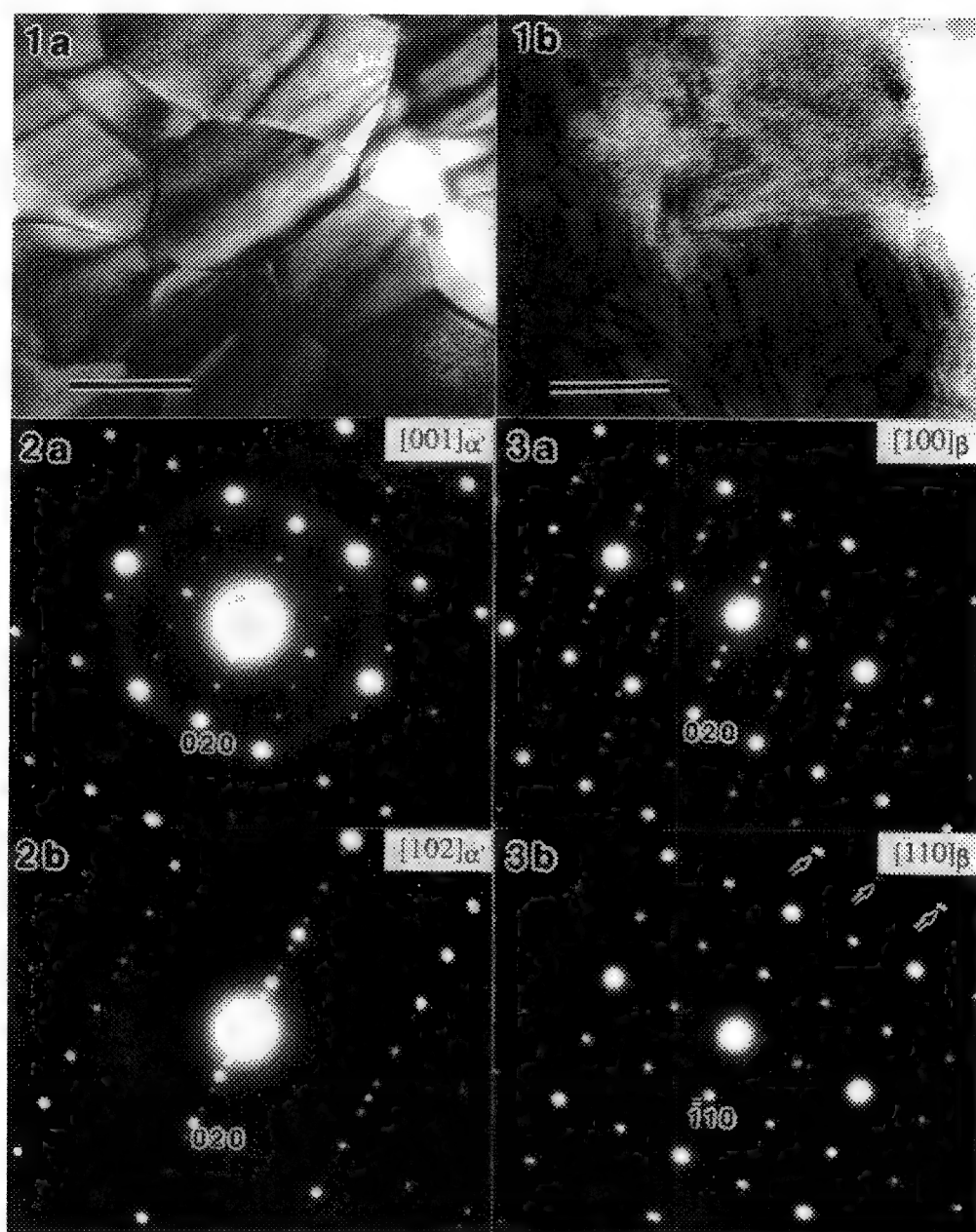
Fig. 1. (a) Euhedral α' grains and (b) twinned β grains. Bar = 1 μm.

Fig. 2. SADP's from an α' grain showing an incommensurate modulation:
(a) $[001]_{\alpha'}$ and (b) $[102]_{\alpha'}$

Fig. 3. SADP's from a twinned β grain: (a) $[100]_\beta$ showing an incommensurate modulation and (b) $[110]_\beta$ with $\{001\}_\beta$ twinned reflections (arrowed).

USE OF BACKSCATTERED ELECTRON IMAGE INTENSITY SIGNALS TO CALCULATE THE WATER/CEMENT RATIO OF CONCRETE

R. J. Lee, A. J. Schwoeble, Yuan Jie

RJ Lee Group, Inc., 350 Hochberg Road, Monroeville, PA 15146

Water/Cement (W/C) ratio is a very important parameter affecting the strength and durability of concrete. At the present time, there are no ASTM methods for determining W/C ratio of concrete structures after the production period. Existing techniques involving thin section standard density comparative associations using light optical microscopy and rely on visual comparisons using standards and require highly trained personnel to produce reliable data. This has led to the exploration of other methods utilizing automated procedures which can offer a precise and rapid measurement of W/C ratio. This paper discusses methods of determining W/C ratio using a scanning electron microscope (SEM) backscattered electron image (BEI) intensity signal and x-ray computer tomography.

Known W/C ratio standards must be prepared using the cement type of the concrete to be examined. There are two very important conditions to be considered for minimizing measurement error. The system parameters (for example, brightness and contrast levels) must be constant and the same for each sample and the BEI signal must be stable for the entire measurement time period. The signal should be monitored over an extended time period to ensure the beam intensity remains constant, as illustrated in Figure 1. In this study, the BEI intensities of five standard W/C ratio samples ranging from 0.35 to 0.55 were measured (50 fields per sample) using a quartz grain BEI image intensity as a normalizing factor at the beginning and end of each data set. Then the average BEI intensity was calculated to obtain the ratio of image intensity of quartz to paste. The W/C ratios of the standard samples were calculated using the following equation:

$$(W/C)_x = A + \frac{Y_o - Y_x}{\tan \alpha}$$

Where: A = Ratio of backscattered image intensity from initial point; Y_o = Ratio of backscattered image intensity of standard paste/quartz; and Y_x = Ratio of backscattered image intensity of paste/quartz in sample (see Figure 2). A typical BEI image of a quartz grain used for calibration is seen in Figure 3. A BEI image of an area in the paste of a W/C ratio standard is shown in Figure 4. The correlation of known W/C ratio standard samples to BEI intensity measurements is highly correlated to expected results and that has shown much promise based on this early experimental work. Further studies are being conducted on other cement types.

X-ray computer tomography was another investigative technique used to examine five W/C ratio standard mortar samples in a joint venture project with IDM Corporation.[1] A density scan was performed utilizing a cobalt 60 gamma-ray source and energy levels of 1.17 and 1.33 MeV. Figure 5 is a graph produced from taking eleven density scans through each sample. Densities were determined by volume displacement in water and these values (g/cm^3) appear along the X-axis. The values along the Y-axis are the densities, in arbitrary units, as determined by the scan. The box-whisker format allows us to examine the veracity of using CT-generated data for determining some critical physical parameters of cement paste and mortar.

For additional information, thin sections made from these samples were used for SEM analysis. Figure 6 is a graph showing the ratio of the backscattered image intensity of the cement paste to the quartz and indicates the expected linear relationship between the samples. The sample with the lowest W/C (Sample CT 1) exhibits the greatest backscattered intensity, and there is an inversely proportional relationship between this intensity and increasing water to cement ratio.

References

1. R. J. Lee, E. A. Draper, "Advanced Methods of Concrete Characterization," MRS, Boston, MA (1991).
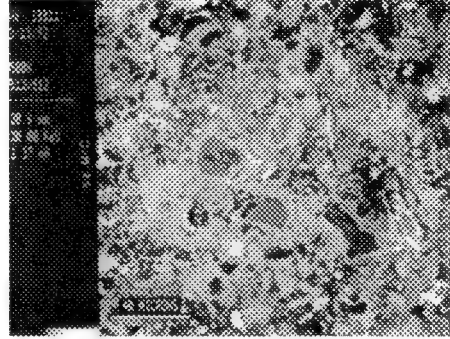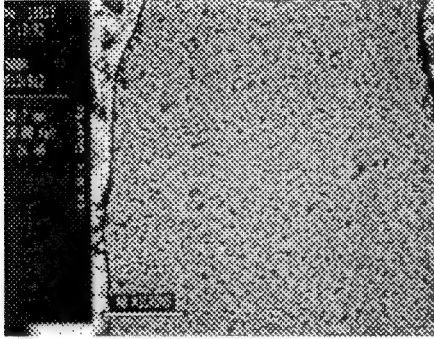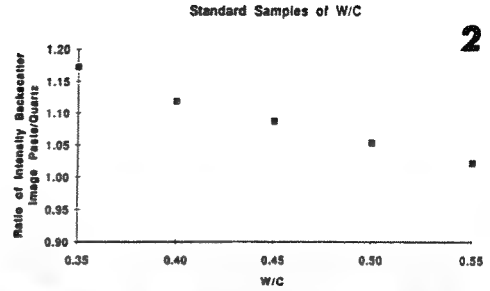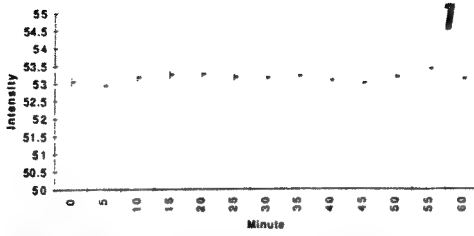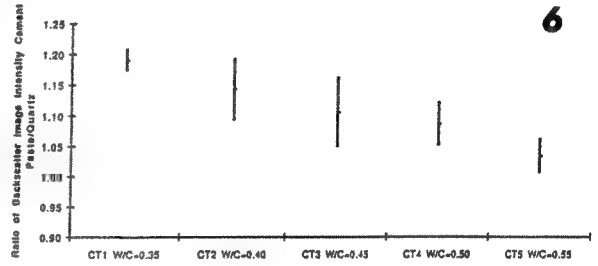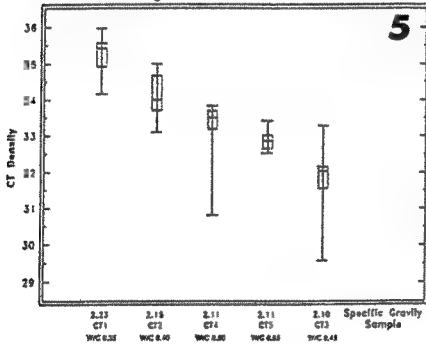
Figure 1. Stability of BEI Signal Over Extended Time Period
Figure 2. Standard Samples of W/C Ratio
Figure 3. Typical Backscattered Electron Image of Quartz Grain Used as a Normalizing Factor
Figure 4. Backscattered Electron Image of Cement Paste
Figure 5. Graph Produced from Density Scans Using X-Ray Computer Tomography
Figure 6. Ratio of Backscattered Image Intensity of Paste/Quartz

STRUCTURE OF STACKING FAULTS IN PYRITE USING TEM TECHNIQUES

Raja Subramanian and Kenneth S. Vecchio

Department of Applied Mechanics and Engineering Sciences, University of California-San Diego, La Jolla, CA 92093

The structure of stacking faults and partial dislocations in iron pyrite (FeS_2) have been studied using transmission electron microscopy. Pyrite has the NaCl structure in which the sodium ions are replaced by iron and chlorine ions by covalently-bonded pairs of sulfur ions. These sulfur pairs are oriented along the <111> direction. This covalent bond between sulfur atoms is the strongest bond in pyrite with Pa3 space group symmetry. These sulfur pairs are believed to move as a whole during dislocation glide[1]. The lattice structure across these stacking faults is of interest as the presence of these stacking faults has been preliminarily linked to a higher sulfur reactivity in pyrite[2]. Conventional TEM contrast analysis and high resolution lattice imaging of the faulted area in the TEM specimen has been carried out.

The bright field (BF) images of the stacking faults in pyrite have been obtained using different g-reflections under two-beam dynamical conditions. They are presented in Figure 1(a-d). The contrast analysis of the stacking faults and partial dislocations which bound these faults are given in Table 1.

TABLE 1.
Contrast analysis of stacking faults and dislocations in Figure 1.

g-reflection	partial dislocations contrast	g· a/2 [110]	stacking fault fringes contrast	g·[0,0.27,1/2]
331	invisible	0	visible	1.31
2̄20	invisible	0	visible	-0.54
1̄11	visible	-1	visible	0.23
02̄2	visible	-1	visible	0.46
220	visible	2	visible	0.54

The partial dislocations enclosing a stacking fault showed identical contrast for a given g-reflection. These partial dislocations have the Burger's vector, b = a/2 [110] and the stacking faults lie on (001) planes. In Figure 1(a) the double-headed arrow lies along the (010) traces of another set of stacking faults. The arrowheads in Figure 1(a) indicate small regions of Moire fringe contrast due to deposition of pyrite layers produced during ion milling of the TEM sample. The two sets of stacking faults are in contrast in Figure 1(c).

In Table 1, the displacement vector R = [0,0.27,1/2] on (001) plane[3] has been used to analyze the contrast of the stacking faults. The displacement vector is of particular type on the (001) plane due to the fact that [010] and [100] directions are not equivalent in a (001) plane. At the stacking fault interface, the fault would break half of the Fe-S first neighbors bonds(d_{Fe-S} = 2.26A) to create S-S bonds (d_{S-S} = 2.15A). The orientation of these bonds would be close to <111> similar to in the pyrite lattice[4].

High resolution lattice image of the (001) stacking fault obtained using axial illumination is shown in Figure 2. The simulated image of the stacking fault on the (001) plane in the pyrite lattice is shown in Figure 3 for R = [0, 0.27, 1/2], and in Figure 4 for R = [0.27, 1/2, 0]; both simulations are at Scherzer defocus. The collapse of the lattice across the fault by the removal of the Fe atom layer can be seen in these images. The simulation in Figure 3 using R = [0, 0.27, 1/2] produces the best match of the faulted region atom positions.

References

1. L. V. Goethem et al., American Mineralogist, 63, 548, 1978.
2. S. Pollock, R. Graham, and K.S. Vecchio, unpublished research.
3. H. S-Long and S. Pouyan, J. Mat. Sci. Letters, 6, 1238, 1987.
4. P. M. Fagot et al., Phil. Mag. A, 38, 353, 1978.
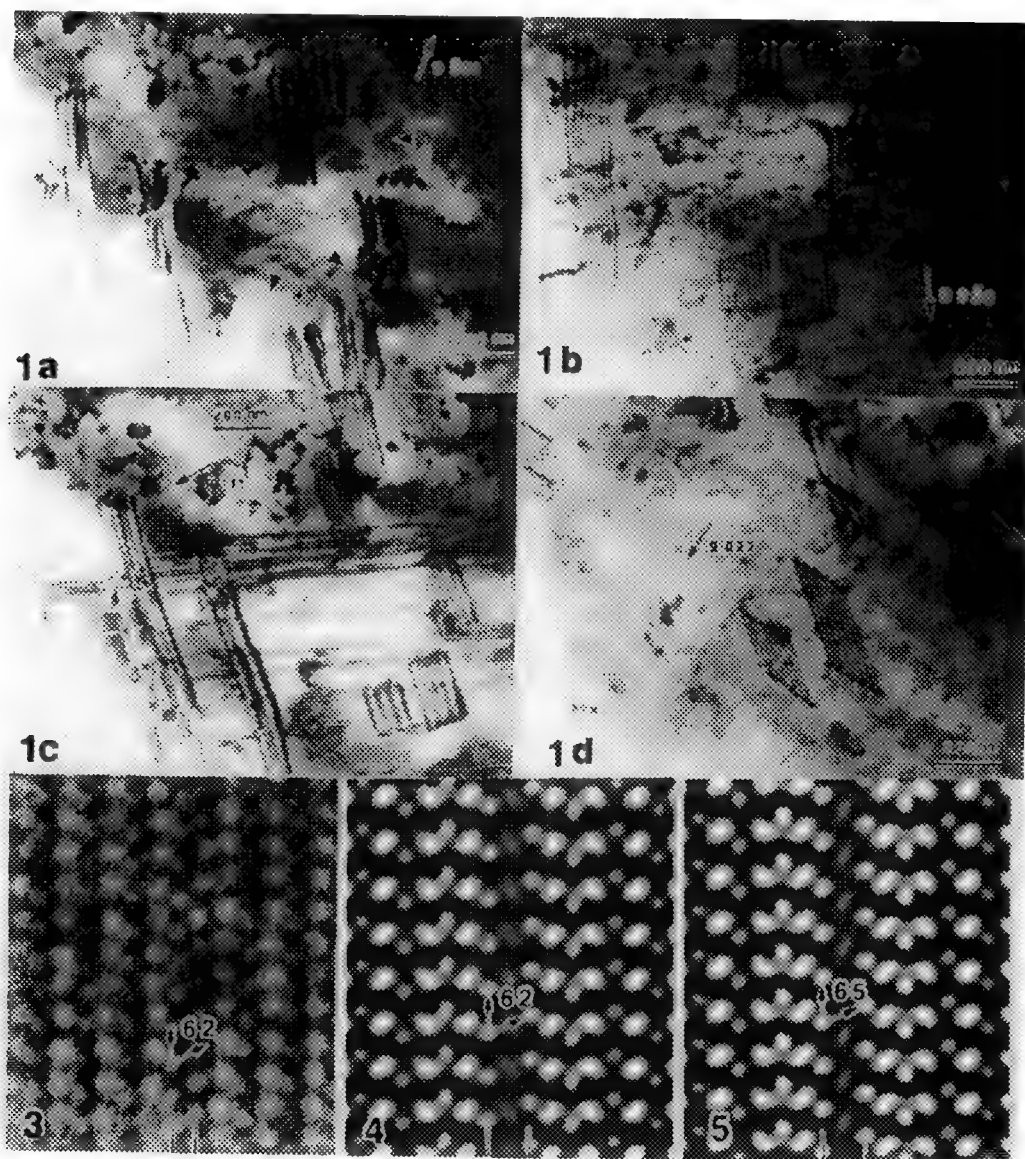
FIG. 1.--BF images of stacking faults in pyrite using (a) g=331, (b) g=2$\bar{2}$0, (c) g=$\bar{1}\bar{1}$1, (d) g=0$\bar{2}$2.
FIG. 2.--(001) lattice image of stacking fault in pyrite.
FIG. 3.--Simulated image of stacking fault on (001) plane, defocus = -75.2nm, and R =[0, 0.27, 1/2].
FIG. 4.--Simulated image of stacking fault on (001) plane, defocus = -75.2nm and R =[0.27, 1/2, 0].

OBSERVATION OF FERROELECTRIC DOMAIN BOUNDARIES IN BaTiO$_3$ WITH REFLECTION ELECTRON MICROSCOPY(REM)

Feng Tsai

Center for Solid State Science and Department of Physics and Astronomy, Arizona State University, Tempe, AZ 85287-1704

The earlier work of transmission electron microscopy(TEM) on ferroelectric domains have been concentrated on the studies of domain configurations and contrast theory[1,2]. Scanning electron microscopy(SEM) is also used to study ferroelectric material surfaces and has revealed various domain boundaries on the chemical-etched surface of BaTiO$_3$[3]. However, the method is destructive and largely dependent on the etching technique. Reflection electron microscopy (REM) has recently been developed to study crystal surfaces[4], especially the surface defects such as surface steps and emerging dislocations[5]. This paper presents the observation of 90° domain boundaries in BaTiO$_3$ single crystal with REM and concentrates on the contrast of 90° domain boundaries.

The samples used in this work are BaTiO$_3$ single crystals grown with Remeika method. Thin plates with {100} surface are selected to prepare for REM experiments. The surfaces to be observed in REM are (100) cleaved surfaces from large thin plates at elevated temperatures (about 130°C). An 120 kV Philips 400T conventional TEM is used to study the surface of BaTiO$_3$.

It is necessary to define the domain configurations in terms of REM. Fig.1(a) and (b) are schematic comparisons of imaging of a 90° a-a domain boundaries in TEM and REM and a 90° a-c domain boundary in TEM and REM, respectively. The "a", "c" domains denote that the polarization vectors of domains are perpendicular or parallel to the direction of the surface normal, as shown in Fig.1(a) and (b). By simply rotating the specimen 90° so that the incident electron beam strikes the surface with a small glancing angle, as shown in Fig.1(b), a group of 90° domain boundaries can be defined. Usually, various domain configurations may exist, the reflection-diffraction spots will be split due to the twinning of 90° domains on {110}planes. Such splittings can be observed in the reflection-diffraction pattern, as shown in Fig.2, a reflection-diffraction pattern of BaTiO$_3$ (100) surface. As only a small area is illuminated by the incident electron beam, the reflection-diffraction spots are split into two parts corresponding to the domains on either sides of the boundary. Fig.3(a) and (b) are the REM images of a 90° a-c domain boundary with the two splittings of (14 1 0). It is found that either domains can be strongly excited by a slight deflection of the electron beam and that the contrast of domains are related to the deviations from Bragg diffraction condition, and predominantly, surface resonance conditions. The domain boundary appears as a bright line in this case and the contrast is related to the strain field around the domain boundary. It can be noticed that the boundary is slightly bent and has some dents. It is suggested that the bending may be related to the strain field or interaction with other domain boundaries. However, the other possibility is that it is an artifact from REM of an uneven surface. On the cleaved surfaces of BaTiO$_3$, various domain boundaries may exist, as well as various kinds of surface defects which may produce various contrasts under electron illumination. Only those 90° a-c domain boundaries which are nearly parallel to the electron beam direction can be imaged, while the others may exist but are confused by the contrasts of the surface defects and the foreshortening effects. By rotating the crystal azimuthally so that the incident electron beam strikes the crystal surface along [110] direction, the 90° a-a domain boundaries can be observed, as shown in Fig.4(a) and (b). It can be seen that the domain boundary appears as a straight line at about 40° to the the incident electron beam direction due to the foreshortening effect. It is also found that the 90° domain boundaries move under electron illumination and stop moving eventually, especially at the beginning of observation. It is suggested that it may be related to the charging or discharging of the surface. No evidence has been found that the 180° domain boundaries were observed in REM. The reasons are probably that the contrast due to the failure of Friedel's law is not enough to show the 180° domains and the contrasts of surface defects can easily confuse the observation.

REFERENCE

1. M. Tanaka and G. Honjo, J. of Phys. Soc. Jpn., 19(1964)954
2. Y. H. Hu, H. Chan, Z. X. Wen and M. P. Harmer, J. Am. Ceram. Soc., 69(1986)594
3. R. Le Bihan and M. Maussion, Ferroelectrics, 7(1974)307
4. Osakabe, Y. Tanishiro, K. Yagi and G. Honjo, Surf. Sci., 97(1980)393
5. L. M. Peng and J. M. Cowley, Ultramicro., 26(1988)261
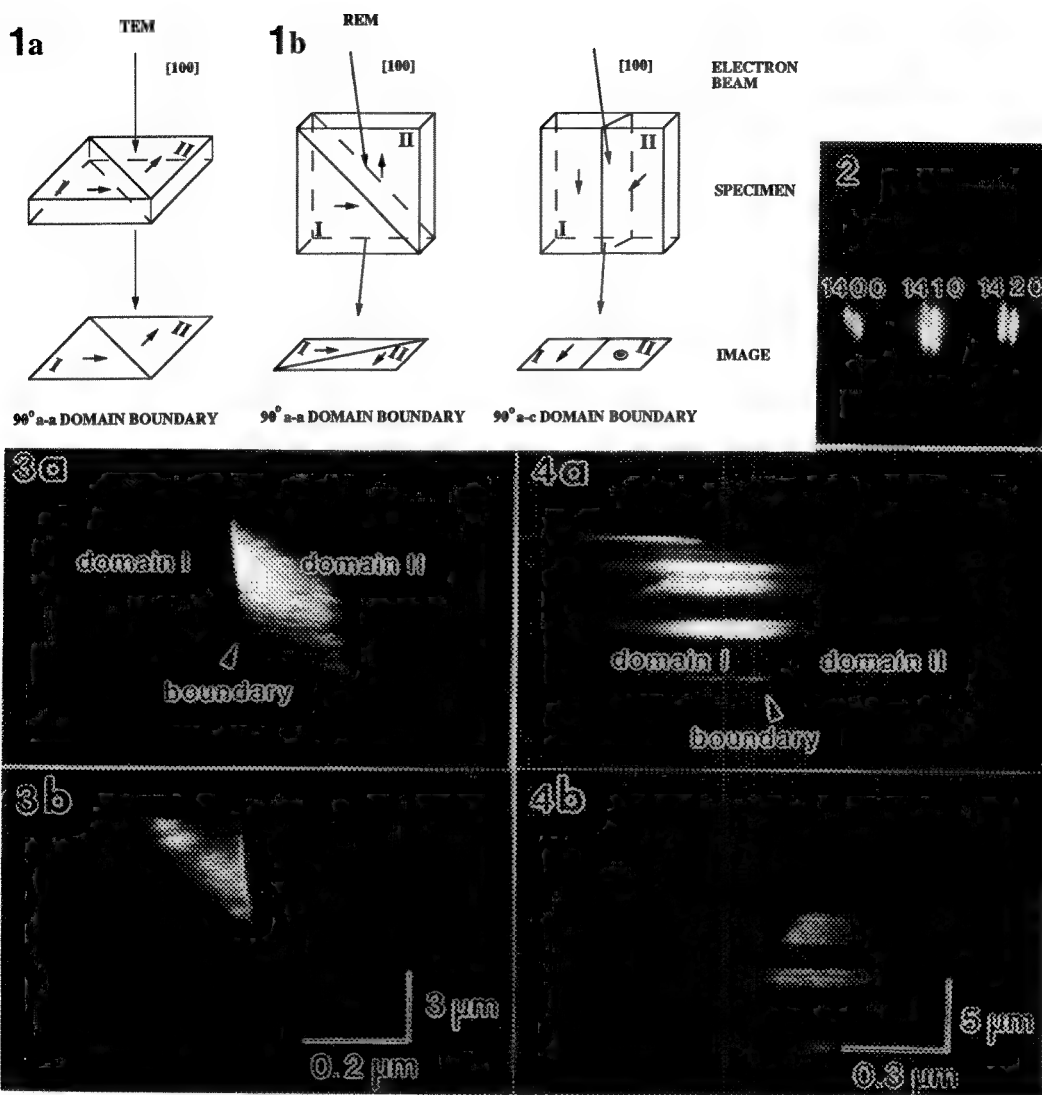
Fig.1(a) is the schematic comparison of a 90° a-a domain boundary in TEM and REM; (b)a 90° a-c domain boundary in REM; (c) a reflection-diffraction pattern from BaTiO$_3$ (100) surface.

Fig.2. A reflection-diffraction pattern from BaTiO$_3$ (100) cleaved surface showing the spot splittings.

Fig.3. REM images of a 90° a-c domain boundary on the BaTiO$_3$ (100) surface along [100] direction;(a)the domain on one side of the boundary is strongly excited; (b) a slight tilt of the electron beam excites the domain on the other side due to the surface resonance and deviation from Bragg diffraction conditions.

Fig.4. REM images of a 90° a-a domain boundary on the BaTiO$_3$ (100) surface along [110] direction;(a)the domain on one side of the boundary is strongly excited; (b) a slight tilt of the electron beam excites the domain on the other side due to the surface resonance and deviation from Bragg diffraction conditions.

CRYSTALLIZATION OF BARIUM HEXAFERRITE

Chung-kook Lee, Yolande Berta and Robert F. Speyer

New York State College of Ceramics at Alfred University, Alfred NY 14802

Barium hexaferrite ($BaFe_{12}O_{19}$) is a promising candidate for high density magnetic recording media due to its superior magnetic properties.[1,2] For particulate recording media, nano-sized single crystalline powders with a narrow size distribution are a primary application requirement. The glass-crystallization method is preferred because of the controllability of crystallization kinetics, hence, particle size and size distribution.[3,4] A disadvantage of this method is the need to melt raw materials at high temperatures with non-reactive crucibles, e.g. platinum. However, in this work, we have shown that crystal growth of barium hexaferrite occurred during low temperature heat treatment of raw batches.

An aqueous solution of $BaCl_2$, H_3BO_3, Na_2CO_3, and $Fe(NO_3)_3 \cdot 9H_2O$ reagent chemicals was prepared corresponding to the mole ratio of 0.313 BaO–0.258 B_2O_3–0.100 Na_2O–0.330 Fe_2O_3. The solution was heated in an alumina crucible to 300°C, holding for 30 minutes in an air atmosphere to obtain the powder form. The powder was heated to 750°C at 10°C/min, and then cooled with no holding. The final powder was obtained by leaching out the soluble matter with an aqueous solution of acetic acid. For TEM analysis, the magnetic particles were embedded in a thin layer of Formvar (polyvinyl formal), picked up on copper mesh grids and carbon coated.

The XRD (X-ray diffraction) pattern for the powder before and after leaching is shown in Fig. 1. The only residual phase detected after leaching was barium hexaferrite. The TEM microstructures in Fig. 2 show that the hexagonal single crystals were ~ 200 to 600 nm in diameter, with an aspect ratio of ~ 7.0. Most particles had a cavity in the center which is interpreted to be a leached-out precursor phase. This phase acted as a heterogeneous nucleation site for crystal growth of $BaFe_{12}O_{19}$. For this leaching to have occurred, the precursor phase or the stress field surrounding it had to have been exposed to the acetic acid. It would then follow that one dimension of the precursor phase and the thickness of the $BaFe_{12}O_{19}$ phase would have been approximately the same. As implied by the shape of the particle, preferred crystal growth occurred along the basal plane of the hexagonal structure. It is not certain if the precursor phase adopted the hexagonal structure since, as can be seen in Fig. 2 (b) and (c), the shapes of the precursor sites are not regular.

At the boundary where the two growing crystals mutually impinged there would be a lattice mismatch. Fig. 2 (c) shows that a large crystal had grown at the expense of the small crystal. Such particles, which grew from more than one precursor phase, would in time grow to a single large crystal, irregularly shaped. This phenomenon should be avoided for data storage applications.

Several improvements are in progress, focusing on proper heat treatments which should homogenize particle size and shape, and cause a uniform distribution of precursor phases.

References

1. M.P. Sharrock, *MRS Bull.*, (March,1990)15[3], 53.
2. D.E. Speliotis, *IEEE Trans. Magn.*, Mag-23(1987), 3143.
3. H. Yokoyama, JARECT, V. 15, *Recent Magnetics for Electronics*, ed. by Y. Sakurai, (1984) 187.
4. B.T. Shirk and W.R. Bussem, *J. Am. Ceram. Soc.*, (1970)53[4], 192.
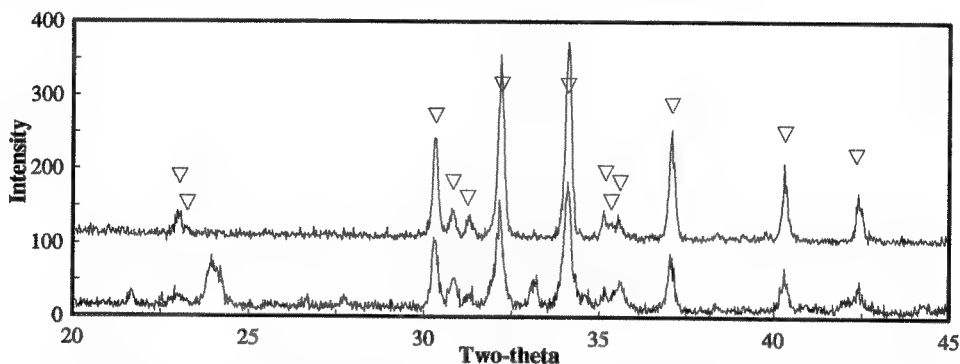
Figure 1. XRD intensity versus 2θ of heat treated samples at 750°C. Lower trace: before leaching; upper trace: after leaching. $\triangledown$: $BaFe_{12}O_{19}$ (JCPDS: 27-1029).
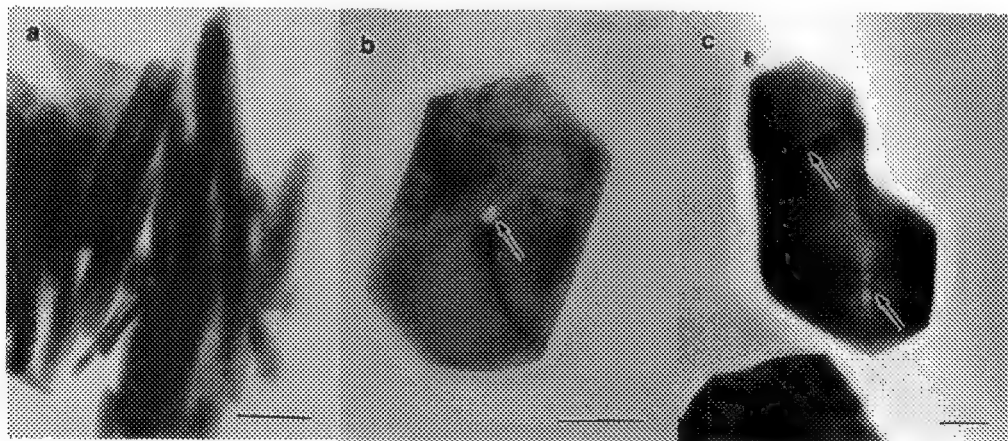
Figure 2. TEM microstructures of $BaFe_{12}O_{19}$ particles after leaching. (a) agglomerate of particles, (b) volume occupied by dissolved precursor phase (arrow) and (c) particle with two nucleation sites (arrows). Bar: 100 nm.

OBSERVATION OF FROZEN HYDRATED OIL SANDS FINE TAILINGS: FREEZING EFFECTS AND INTERPARTICLE FORCES

R.J. Mikula, W.W. Lam, C. Payette, and V.A. Munoz

Fuel Processing Laboratory, CANMET, Energy, Mines and Resources Canada, P.O. Bag 1280, Devon, Alberta, T0C 1E0

It is well known that kaolinite clay platelets can align positive edges with negative faces to build a so called "card-house" structure. Although kaolinite is a major component of oil sands fine tailings or sludge, this idealized structure is unlikely due to the presence of other components. The modification of the ideal card house suggested by Scott et al[1] is more likely to exist in sludge. Freeze fracture preparation and subsequent direct observation of frozen hydrated samples in an electron microscope were used to characterize the morphology and composition of oil sands sludges, in order to directly determine the interactions between the various components. In these cryogenic techniques, the rate of freezing is critical in minimizing the creation of artifacts.[2-5]

After sublimation of the freeze fracture surface water layer, a distinct structuring of the solids in sludge can be noted as illustrated in Figure 1. The structure shown in Figure 1 is, in fact, typical of artifacts which can be generated during the freezing process: namely ice crystal formation and physical movement of fine particles and concentration of solute along ice crystal boundaries.[6,7] However, there is some evidence that suggests it is in fact representative of the actual interparticle relationships in oil sands sludge. Figure 2 shows a sludge sample which was sheared in a blender just before being freeze fractured. In this case, one can see some structuring but on a much smaller distance than when the sludge is undisturbed before being frozen and fractured (Figure 1). Figure 3 shows an extreme case of structure breakdown after shearing, with the previously aligned clay particles now completely randomized. This further decrease in edge to edge structure relative to Figure 2 was achieved by increasing the shear and minimizing the time between shearing and sample freezing.

If the structure observed is due only to freezing effects, one would expect the morphology to be similar regardless of sample handling history. The micrographs discussed in this paper represent many different samples and many fields of view and are meant to generally represent the morphology of the samples discussed. Although the details of the features observed may be due to the freezing process, the differing behaviour of settled and sheared sludges suggests that the structures observed after freezing are at least modified by the original sludge morphology if not directly representative of it. Therefore, even if the micrographs discussed do not represent sludge structuring, it seems clear that they are somehow related to sludge structural properties and/or interparticle interactions. The sludge structure observed is not present in model systems which would be expected to show structure if it was simply due to freezing artifacts and the ability to degrade the structure with shearing also indicates that one might be directly or indirectly observing the sludge structure. Although artifact formation in the freeze fracture of oil sands sludge cannot be ruled out entirely, there appears to be features in sludges which can be attributed to a card house type of structure. The relatively long range structuring observed in settled sludges but not in sheared systems indicates that orientation of the solids is occurring which can account for the stability of oil sands sludges and their extremely slow consolidation rates. And indeed, even if the effect is simply an artifact of the freezing process, it might still be possible to utilize the method in an empirical way to characterize sludges.

References

1. J.D. Scott et al., Applied Clay Science, 1, 1985, 207-218.
2. K.R. Miller et al., Journal of Ultrastructure Research, 82, 1983, 123-133.
3. J. Lepault and J. Dubochet, Journal of Ultrastructure Research, 72, 1980, 223-233.
4. J. Dubochet et al., Journal of Microscopy, 128(3), 1982, 219-237.
5. A.W. Robards and U.B. Sleytr, Vol. 10 of Practical Methods in Electron Microscopy,
   A.M. Glauert, editor, Elsevier, 1985.
6. T. Nei, Journal of Microscopy, 99(2), 1973, 227-233.
7. J.I. Fukasawa and K. Tsujii, Journal of Colloid and Interface Science, 125(1), 1988, 155-161.
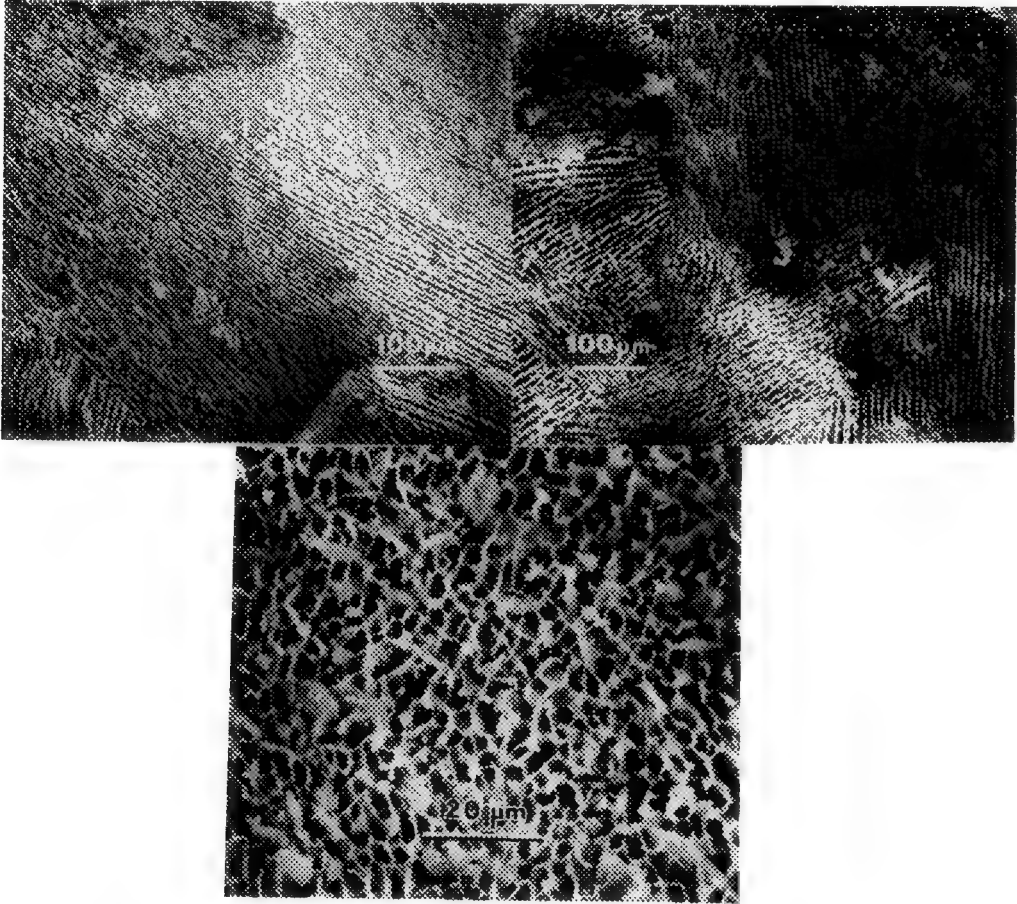
FIG. 1.--SEM micrograph of sludge after sublimation of water showing evidence of an ordered, card house type of structure.

FIG. 2.--SEM micrograph of structuring, but on a shorter range, of a sheared sludge.

FIG. 3.--SEM micrograph of completely disordered sludge produced from a sample which was highly sheared and by minimizing the time between sludge shearing and the freeze fracture step.

MICROSCOPIC VERSUS PROCESS PARAMETERS IN HEAVY–OIL UPGRADING

V.A. Munoz, R.J. Mikula, C. Payette, and W.W. Lam

Fuel Processing Laboratory, CANMET, Energy, Mines and Resources Canada, P.O. Bag 1280, Devon, Alberta, Canada, TOC 1EO

The transformation of high molecular weight components present in heavy oils into useable liquid fuels requires their decomposition by means of a variety of processes. The low molecular weight species produced recombine under controlled conditions to generate synthetic fuels. However, an important fraction undergo further recombination into higher molecular weight components, leading to the formation of coke. The optical texture of the coke can be related to its originating components. Those with high sulfur and oxygen content tend to produce cokes with small optical texture or fine mosaic, whereas compounds with relatively high hydrogen content are likely to produce large optical texture or domains. In addition, the structure of the parent chemical components, planar or nonplanar, determines the isotropic or anisotropic character of the coke. Planar molecules have a tendency to align in an approximately parallel arrangement to initiate the formation of the nematic mesophase leading to the formation of anisotropic coke. Nonplanar highly alkylated compounds and/or those rich in polar groups form isotropic coke. The aliphatic branches produce steric hindrance to alignment, whereas the polar groups participate in cross-linking reactions.

Process parameters such as heating rate, final temperature, pressure, and hydrodynamic conditions control the rate of the reactions that initiate the formation of coke. Therefore, changes in the process parameters can produce a different type of coke from chemically identical originating components. This allows one to use microscopic data to monitor process conditions by analyzing the coke morphology and composition.

Figure 1 depicts a typical mesophase stage during the formation of anisotropic coke. The mesophase precipitated from the isotropic phase (I) in the form of spheres (S) due to surface tension effects. The growth and coalescence of these spheres (C) leads to the formation of large anisotropic domains. Figure 2 shows anisotropic domains (D) brought about by the relatively undisturbed coalescence of mesophase spheres. The increased pressure caused by evolution of gases during the decomposition of the feed produced a dramatic deformation of the mesophase in the direction of the gas flow, generating long and narrow anisotropic domains (L). Figure 3 illustrates the effect of changes in the reactor pressure and residence time. An increase in pressure produced elongated anisotropic domains (E) while a reduction in pressure allowed the formation of large anisotropic domains (D). The low reflectance isotropic area (I) contains many small anisotropic spheres in the early stage of formation. These characteristics are indicative of shorter residence time than areas (E) and (D).

The formation of isotropic coke has not been studied as thoroughly as the formation of the anisotropic coke. Figure 4 shows that isotropic coke also evolves from the coalescence of spheres, which demonstrates that the viscosity of the intermediate stage is low enough to allow the formation of spheres due to surface tension effects.

The complementary use of microscopic techniques such as optical, infrared, electron, and confocal laser microscopy provides unique data that allows one to monitor changes in the process parameters during heavy oil upgrading which in many cases could not be detected by conventional solid and liquid analysis of the products. The combined data and thorough characterization of the process can have a significant impact in achieving more efficient production of liquid fuels from heavy oil.
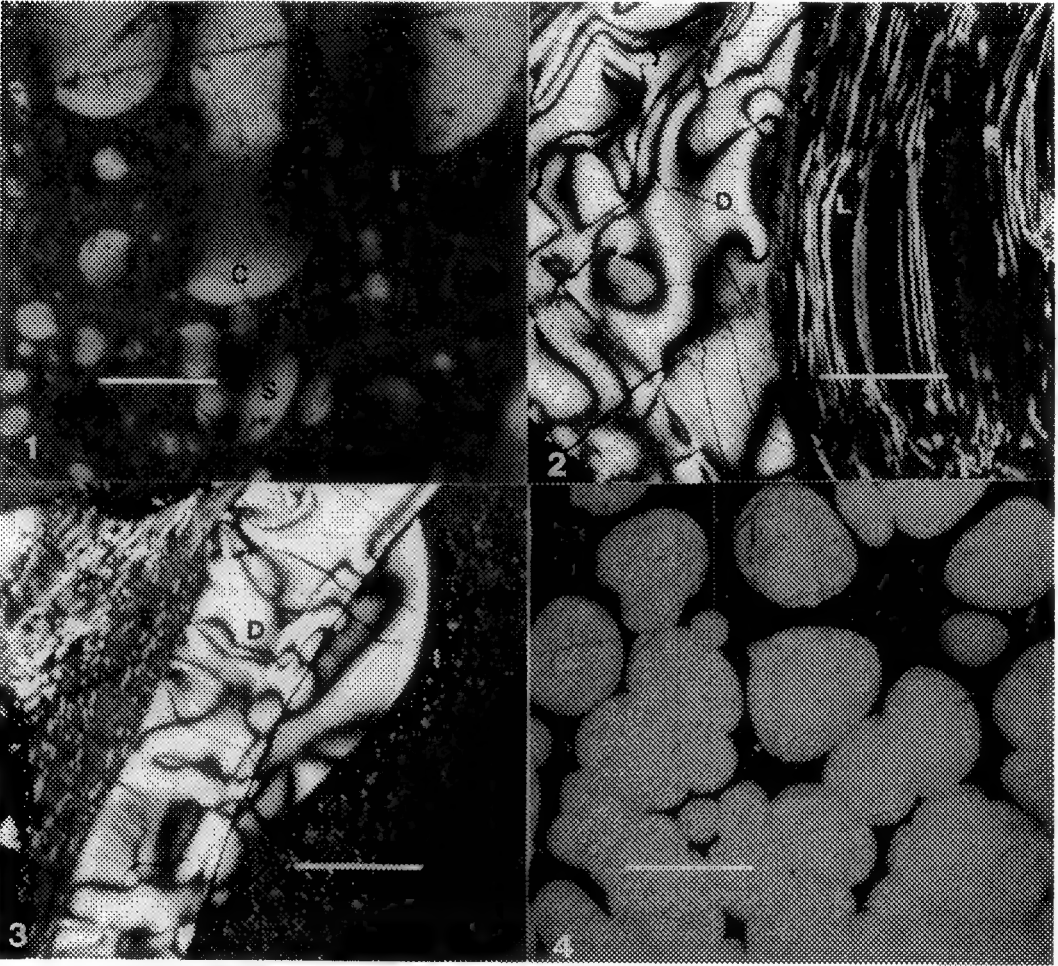
FIG. 1.--Mesophase spheres (S) and coalescence spheres (C) included in an isotropic matrix (I). Bar = 10 μm.
FIG. 2.--Anisotropic domains (D) fused to long and narrow anisotropic components (L). Bar = 50 μm.
FIG. 3.--Elongated anisotropic coke (E), anisotropic domains (D), and isotropic phase (I). Bar = 50 μm
FIG. 4.--Isotropic spheres during coalescence. Bar = 50 μm

FLOTATION OF ATHABASCA OIL SANDS: MICROSCOPICAL DETERMINATION OF STRUCTURE OF BITUMINOUS FROTH

W.W. Lam, C. Payette, V.A. Munoz, R.J. Mikula, and J. Tyerman*

Fuel Processing Laboratory, CANMET, Energy, Mines and Resources Canada, P.O. Bag 1280, Devon, Alberta, T0C 1E0

*Syncrude Research Ltd., P.O. Box 5790, Edmonton, Alberta, T6C 4G3

The extraction of bitumen from oil sands involves the flotation process where the initial separation of the oil phase, or the bituminous froth, from the inorganic solids and water occurs. However, the froth obtained has high solids concentration and water, which produces problems in downstream operations. Concurrently, some of the oil reports to the tailings, with economic and environmental impact.

Flotation can be considered to be a physical-chemical separation process which depends on the selective adhesion of air to the desired component (bitumen) in order to separate it from the water and solids. The feed to the flotation process is an oil-in-water emulsion with relatively high solids. At some point in the separation vessel, this emulsion inverts and becomes a water-in-oil emulsion and forms the bituminous froth. Understanding this inversion process will help in maximizing water and mineral matter drainage from the bitumen product, leading to an improvement in bitumen extraction from oil sands. As well, the partitioning of solids can be understood by studying their wettability with the froth and thus determining whether or not these solids report to the tailings, or are carried upward by attachment to air bubbles in the flotation cell.

The physical chemistry of oil sands processing has been studied,[1,2] and the effect of ionic strength and surfactant concentration in the aqueous phase have been modelled.[3] However, the physical structure of the froth has not been determined quantitatively, largely because the froth samples are labile, and a sampling method which would unequivocally give bubble and droplet sizes representative of the process streams has not been demonstrated. Recently, microscopy has been shown to be a useful tool in emulsion characterization[4-6] and is being developed for the study of froth from extraction units and pilot-scale plants.

The general features of the froth from both the batch extractor and pilot-scale plants were found to be similar. Figure 1 is a SEM micrograph of a frozen-hydrated primary froth sample. Identification of the air, oil, and water phases is based on the morphology and the x-ray spectra; and also from the study of simpler systems such as air in dry bitumen and water in bitumen. The air/water interface can be distinguished clearly in Figure 1. At high magnification, this interface is shown to consist of oil droplets of <1 μm (Figure 2). The identification of oil is based on the sulphur signal from the x-ray spectra, taken from one of the micron-sized droplets, at 10 and 15 kV (Figures 3 and 4, respectively). These oil droplets may have been stabilized by the presence of clays, shown by the Al and Si peaks in Figure 4. Once the three phases are identified, the more quantitative studies can be undertaken using combined SEM and image analysis.

References
1. E.C. Sanford, Can. J. Chem. Eng. (1983)61, 554.
2. K. Takamura and D. Wallace, J. Can. Pet. Technol., (1988)27, 98.
3. L.L. Schramm and R.G. Smith, Can. J. Chem. Eng., (1987)65, 799.
4. R.J. Mikula, in "Emulsions. Fundamentals and Applications in the Petroleum Industry", L.L. Schramm, ed. Adv. in Chem. Series 231, ACS, Washington, 1992, pp. 79-129.
5. R.J. Mikula, Colloids Surf., (1987)23, 267.
6. R.J. Mikula, J. Colloid Interface Sci., (1988)121, 273.
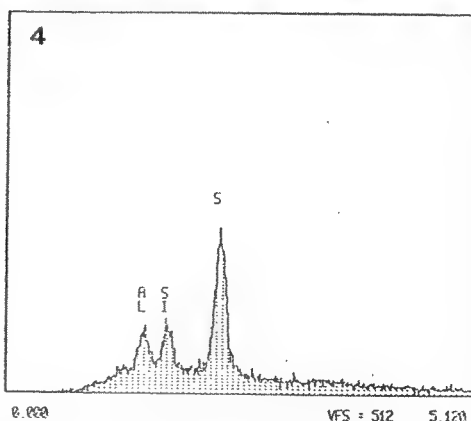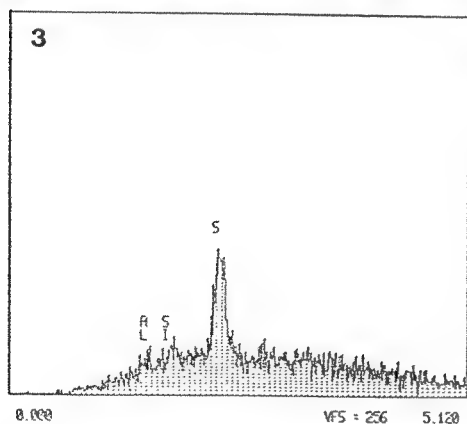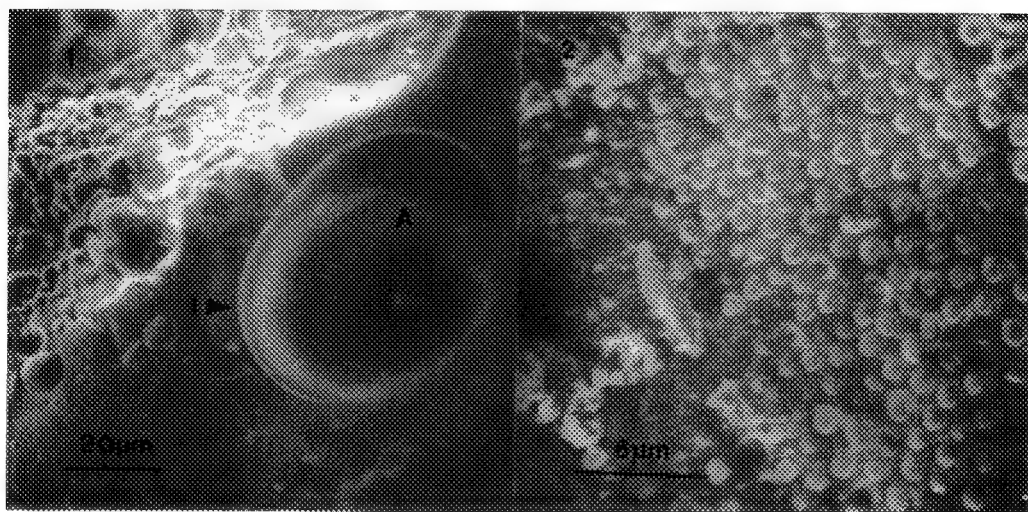
FIG. 1.--SEM micrograph of a frozen-hydrated primary froth. A=air bubble. I=air/water interface. Bar = 20 μm.
FIG. 2.--SEM micrograph of the froth at air/water interface. Bar = 6 μm.
FIG. 3.--X-ray spectrum of oil droplets at air/water interface (10 kV, 200 s).
FIG. 4.--X-ray spectrum of oil droplets at air/water interface (15 kV, 200 s).

OBSERVATION OF FERROELECTRIC DOMAIN BOUNDARIES IN PZT(52/48) WITH TRANSMISSION ELECTRON MICROSCOPY(TEM)

Feng Tsai and J. M. Cowley

Center for Solid State Science and Department of Physics and Astronomy, Arizona State University, Tempe, AZ 85287-1704

Lead zirconium titanates(PZT) are ferroelectric materials of considerable current interest because their potential for applications in memory devices and electrooptics has drawn the attention of industry. The performance of the devices made of PZT largely depends on the behaviors of ferroelectric domains and domain boundaries. TEM has been proved to be a very powerful tool in the study of ferroelectric domains and domain boundaries in ferroelectric materials[1,2,]. It is suggested that around the domain boundaries in $BaTiO_3$ there is a distribution of lattice distortion and strain field[3]. However, few references have been found on the study of ferroelectric domains and domain boundaries in PZT materials by TEM.

The present paper introduces the TEM study of ferroelectric domains and domain boundaries in PZT(52/48). The samples are PZT(52/48) ceramics provided by Valpy-Fisher, Inc. The specimens are dimpled and Ar-ion milled at 3 kV. Thin edges with 90° a-a domain boundaries are tilted to [001] orientation and used to carry out TEM and HREM observation. TEM observations are performed on an 120 kV Phillips 400T conventional TEM and a 400 kV JEM 4000EX high resolution TEM.

It is found that in the low resolution images, 90° a-a domains have the configuration of thin plates of a-domains within the big a-domain substrate having the polarization vector of 90° to them, as shown in Fig.1(a). It can be noticed that the domains are several hundreds Å wide and can be slightly bent. This observation is different from other observations of PZT by TEM[3] and may suggest that the shapes and configurations of domains are related to the ferroelectric transitions[4].The selected area diffraction(SAD) pattern showed that the angle of the tilt of the lattice planes across the domain boundaries is about 2.8^o, in Fig.1(b). The c/a ratio calculated from that value is 1.04. No significant electron irradiation effect has been noticed. But, a surface decomposition layer seems to exist due to the previous ion milling. A high resolution image along [001] direction shows the lattice fringes of tetragonal structure of the PZT, as shown in Fig.2(a). The tilt of the lattice planes across the domain boundary can be seen in the image along [100] or [010] direction and is estimated about 1°, which is much smaller than the value obtained from the SADP of a large and thick area. It is suggested that the lattice distortions are very dependent on the local configuration of domain boundaries and that in very thin films the strain field or lattice distortion can be partially relaxed. A region of dark diffuse contrast along the domain boundary can be seen and interpreted as the deviation of the lattice planes from the Bragg condition, as indicated in Fig.2(a). It is suggested that a strain field exist around the domain boundaries. It is also found that the boundary shifts sideway to the adjacent (110) planes. Such observation coincides with the low magnification observation that the boundaries can be slightly bent. Since no kinks of boundaries have been observed, it is assume that the shift occurs on (100) or (010) planes[4]. Fourier analysis of the regions including 25x25 unit cells, (b) centered at the domain boundary and (c) well away from the domain boundary gives the diffractograms from the two regions. It is noticed that the diffraction spots from the domain boundary region are diffused showing that the variation of the lattice fringe spacings is large,which indicates a lattice distortion existing in the domain boundary.

REFERENCES

1. M. Tanaka and G. Honjo, J. Phys. Soc. Jpn, 19, 6(1964)954
2. L. A. Bursill and J.Peng, Ferroelectrics, 70(1986)191
3. M. L. A. Dass, U. Dahman, G. Thomas, T. Yamamoto and K. Okazaki, IEEE 6th International Symposium on Applications of Ferroelectrics, (1986)146
4. M. E. Lines and A. M. Glass, Principles and Applications of Ferroelectrics and Related Materials, Clarendon Press, Oxford, 1977
5. F. Tsai, V. Khiznichenko and J. M. Cowley, submitted
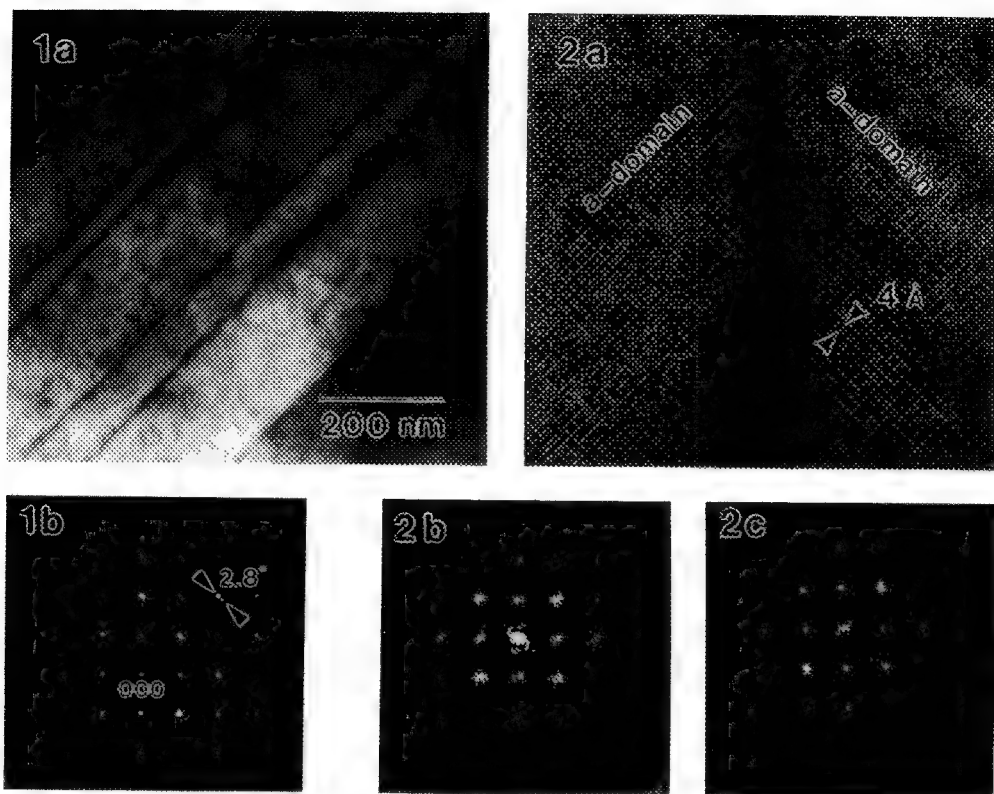
Fig.1(a) Low resolution image of 90° a-a domain boundaries in PZT(52/48) imaged along [001] direction; (b) the selected area diffraction pattern from the same area.

Fig.2.(a) High resolution image of 90° a-a domain boundary showing the tilt of lattice fringes about 1° across the domain boundary and the dark diffuse contrast of the domain boundary. Fourier analysis gives the diffractograms of the areas: (b)from domain boundary of about 25x25 unit cells; (c) away from the domain boundary of about 25x25 unit cells, which show that a lattice distortion exist in the vicinity of 90° domain boundary.

PHASE CHANGES DURING HEAT TREATMENT OF ELECTRODEPOSITED WO_3, MoO_3 AND V_2O_5

G. Veilleux, A. Guerfi, R. G. Saint-Jacques and Lê H. Dao

INRS-Énergie et Matériaux, Institut national de la recherche scientifique, C.P. 1020, Varennes, Québec, Canada J3X 1S2

Many transition metal oxides have been studied in the last two decades. By an appropriate chemical or electrical means, ions can be inserted into the structure of these oxides with minimal structural changes. This process known as coloration can easily be reversed. This reversible mechanism is of particular interest in applications such as battery and fuel cell electrodes, chemical sensors, electrochromic displays and catalysts [1].

In this study, films of three transition metal oxides (WO_3, MoO_3, V_2O_5) were prepared by electrodeposition [2]. The morphology and the structure of these films were analyzed by transmission electron microscopy (TEM) in their as-deposited states and after heat treatment in ambient air up to 500 °C. Previous measurements made by differential scanning calorimetry (DSC) showed exothermic peaks corresponding to phase changes. The temperature values determined at those peaks were then chosen as specific treatment temperatures.

As shown in Fig. 1A, as-deposited WO_3 films consist of fine particles agglomerated in more or less dense packs with an amorphous structure. Films heated to 390 °C begin to transform to the hexagonal WO_3 phase (a=7.298 Å, c=7.798 Å). It has been shown that this change corresponds to the dehydration of the films [3]. Fig. 1B shows a film at 410 °C after complete transformation. From 430 °C, a triclinic WO_3 phase (a=7.309 Å, b=7.522 Å, c=7.678 Å, α=88.81°, ß=90.92°, γ=90.93°, JCPDS #32-1395) is observed (Fig. 1C).

As-deposited MoO_3 films are very thin and uniform films having an amorphous structure (Fig. 2A). Transformation upon heating in air begins at 250 °C and is completed at 350 °C. Monocrystalline regions having an orthorhombic structure corresponding to the dehydrated MoO_3 phase (a=3.96 Å, b=13.86 Å, c=3.70 Å) have been observed (Fig. 2B). Anhydrous MoO_3 with these parameters has been reported by Günter [4].

Fig. 3A shows an as-deposited V_2O_5 film which is characterized by a fine-grained polycrystalline orthorhombic structure (a=11.51 Å, b=3.559 Å, c=4.371 Å, JCPDS #9-387). The film morphology consists of a large number of interlaced fibres. The fibrous nature of these films is altered at temperature higher than 150 °C and disappears totally above 250 °C, although the structure remains identical. As shown in Fig. 3B, heating at 350 °C produces the monoclinic V_6O_{13} phase (a=11.92 Å, b=3.68 Å, c=10.14 Å, ß=100.9°, JCPDS #27-1318). This transformation has also been reported by Tilley et al. [5] after heating single crystals of V_2O_5 in vacuum at 400 °C.

References

1. C. M. Lampert, Solar Ener. Mater. 11 (1984) 1.
2. A. Guerfi and Lê H. Dao, J. Electrochem. Soc. 136 (1989) 2435.
3. B. Gerand, G. Nowogrocki, J. Guenot and M. Figlarz, J. Solid State Chem. 29 (1979) 429.
4. J. R. Günter, J. Solid State Chem. 5 (1972) 354.
5. R. J. D. Tilley and B. G. Hyde, J. Phys. Chem. Solids 31 (1970) 1613.
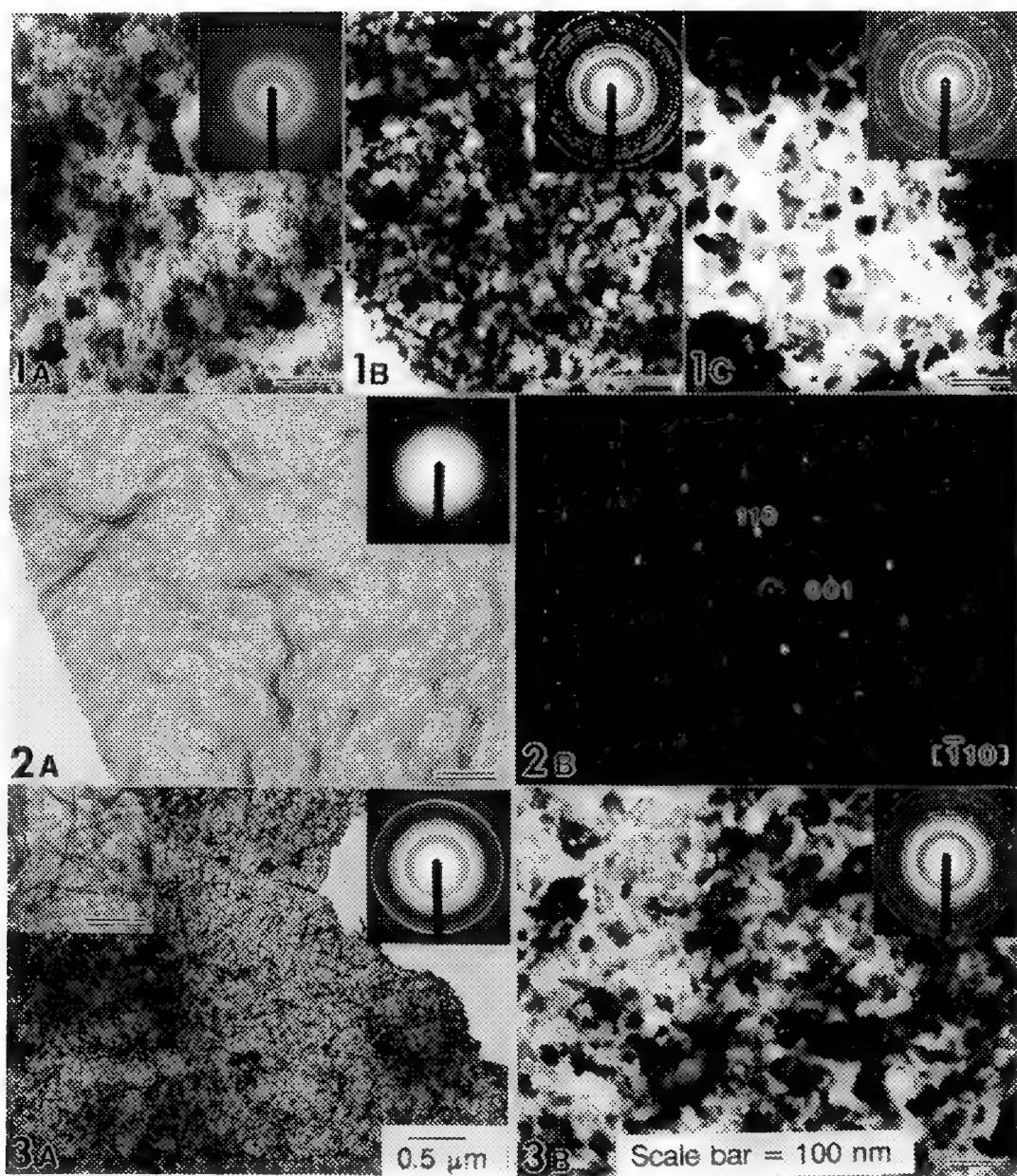
Fig. 1 Micrographs and SAD patterns (inset) of tungsten trioxide (WO_3) at A) room temperature, B) 410 °C, C) 430 °C.

Fig. 2 Micrographs and SAD patterns (inset) of molybdenum trioxide (MoO_3) at A) room temperature, B) 350 °C.

Fig. 3 Micrographs and SAD patterns (inset) of vanadium pentaoxide (V_2O_5) at A) room temperature, B) 350 °C.

HREM STUDY OF HETEROEPITAXIAL INTERFACES IN THE Ni.50Co.50O/Al2MgO4(100) SYSTEM

W. Cao and G. Thomas

Department of Materials Science and Mineral Engineering and National Center for Electron Electron Microscopy, Lawrence Berkeley Laboratory, University of California, Berkeley, CA 94720

Epitaxial CoO/NiO multilayers and alloys have been produced which show interesting structural and magnetic properties[1,2]. Typically, epitaxial films are grown either by chemical vapor deposition or evaporation. However, sputtering can also yield high quality epitaxial films[2]. The structure of the substrate and the interface of the film/substrate are critical factors to determine the quality of the epitaxial film. The CoO/NiO epitaxial films on the α-Al2O3 had been studied extensively in our previous work[2,3]. In this paper, the heteroepitaxial interface in the Ni.50Co.50O/Al2MgO4 is studied by using high resolution electron microscopy. Transmission electron microscopy was performed using the JEOL-200CX and JEOL-ARM1000 microscopes at the National Center for Electron Microscopy, Berkeley.

On Al2MgO4 (100), a Ni.50Co.50O epitaxial film with the (100) orientation is formed. The Ni.50Co.50O has the NaCl structure with intermediate value of the lattice parameter (.420nm)[3] between that of NiO and CoO. Al2MgO4 also has cubic symmetry with eight molecules in the unit cell and a lattice parameter a=.808nm. In both of these structures, the oxygen ions form a fcc lattice and correspond to an average interatomic oxygen planar spacing of .210 and .202nm for each of these lattices. Thus the lattice misfit between the film and substrate is about 3.8%. Fig.1a is an electron diffraction pattern of the substrate along the <001> direction in which basic vectors in the reciprocal lattice are the (220) and (2̄20) as shown by the small square. Fig.1b is a composite electron diffraction pattern of cross sectional Ni.50Co.50O/Al2MgO4 along <001> direction where the large square is the pattern only from the film. The orientation relationship is given :

$$<001>_{film}//<001>_{substrate}$$
$$(100)_{film}//(100)_{substrate}$$

Fig.2 is a low magnification TEM micrograph of cross-sectional sample. Fig.3 is a high resolution electron image of the Ni.50Co.50O/Al2MgO4 interface .The interface can be easily detected if we notice that the (200) reflections of the film and (220) reflections of the substrate are dominant in this image. The interface is not straight, but rather faceted. The lattice misfit dislocations are found at the interface as shown by arrows. The projected Burgers vector is determined to be $1/2<010>_{film}$ from the HREM image. Hence, it is likely that the actual Burgers vector is $\mathbf{b}=1/2<110>_{film}$ as these are lattice dislocations in fcc crystals. According to the simple theory, the average distance between two misfit dislocations is given by $D=d_1 d_2/d_1-d_2 =5.3nm$, where d_1 and d_2 are the (200) plane spacing of Ni.50Co.50O and (400) plane spacing of Al2MgO4, respectively. This agrees well with the direct measurement from the image in which the spacing of two misfit dislocations is about $D=27d_1=5.6nm$.[4]

Reference

1.M.Takano, T. Terashima and Y.Bando, Appl.Phys.Lett.,51(3),205(1987)
2.M.J. Carey et al, J. Mater. Res., Vol.6, No.12, 2684(1991)
3.W. Cao, G. Thomas, M.J. Carey and A.E. Berkowitz, Scripta Metal., 2633(1991)
4. We would like to acknowledge M.J. Carey and Professor A.E. Berkowitz, UCSD, for their donation of the sample. This researsh is sponsored by the NSF under contracts No. DMR-8707241 and facilities at NCEM used in this work are supported by the director, office of Energy Research, office of Basic Energy Sciences, Materials Sciences Division, U.S. Department of Energy under contract No. DE-AC03-76SF00098.
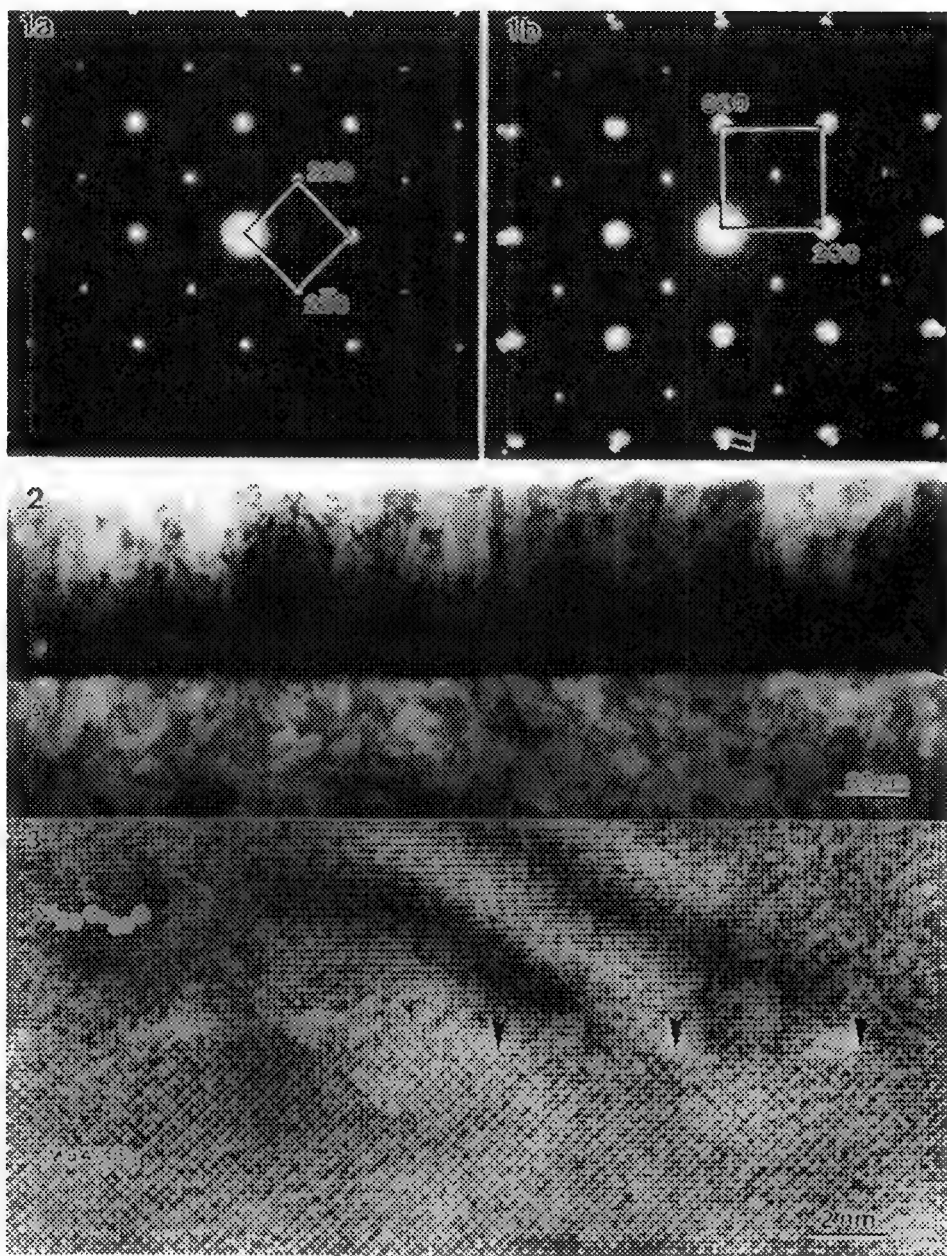
Fig.1 Electron diffraction patterns of a cross-section sample a) Al_2MgO_4 substrate[001] only and b) both substrate [001] and $Ni_{.50}Co_{.50}O$

Fig.2 Low magnification image of $Ni_{.50}Co_{.50}O/Al_2MgO_4$ interface

Fig.3 HREM image of the $Ni_{.50}Co_{.50}O/Al_2MgO_4$ interface

EELS FINE STRUCTURE ANALYSIS OF RADIATION DAMAGE OF V_2O_5

Xiwei Lin and Vinayak P. Dravid

Department of Materials Science and Engineering and, Center for Catalysis and Surface Science, Northwestern University, Evanston, IL 60208

The oxides of maximum valence transition metals have been extensively studied in view of their useful physical and chemical properties. Vanadium pentoxide is one such compound which exhibits important catalytic properties, but is sensitive to electron beam irradiation[1]. Vanadium pentoxide has the orthorhombic symmetry and the structure is built from deformed octahedra with a longer and weak V-O bond along the c direction. Consequently, V_2O_5 is a layered structure with (001) cleavage plane, and the oxygen atoms located at the cleavage plane can be easily lost during the electron beam irradiation. In this paper we present time resolved parallel detection EELS study of radiation damage of V_2O_5 with a 200 kV cold field emission analytical electron microscope (HF-2000). Samples of V_2O_3 and VO_2 are also analyzed for comparison. The EELS spectra were obtained with a spectrometer dispersion of 0.1 eV per channel in TEM image mode using probe sizes of 20-50 nm. The beam current recorded by a picoammeter connected to the screen was calibrated by the direct measurement with a Faraday cup for the calculation of electron dosage.

Figure 1 shows a series of PEELS spectra from a V_2O_5 particle. The energy scale is calibrated by assigning the edge threshold energy of vanadium L_3 to be 517.65 eV as determined by x-ray absorption spectroscopy (XAS)[2]. The low-loss spectra containing the metal $M_{2,3}$ edges did not exhibit significant variation with radiation dosage. However, significant changes occur in L_{23} core-loss spectra with irradiation.

At the beginning, both L_3 and L_2 edges of vanadium have a low-energy shoulder which disappears as the dosage increases, and the peaks become narrow. In a period of 64 seconds, the L_3/L_2 intensity ratio increases from 0.92 to 1.05, and the positions of L_3 and L_2 peaks shift to slightly lower energies by about 0.90 eV. For many transition element oxides, the L_3/L_2 intensity ratio is a reliable measure of oxidation state of the cation[3,4]. Thus, our observations are consistent with reduction of oxidation state of vanadium from +5 to lower value as a function of dosage. The ELNESs of O-K edges are very sensitive to the irradiation. O-K edge consists of three peaks: the first one located at 528.5 eV which falls down quickly and disappears in the last spectrum, the second one at 534.3 eV in the first spectrum and shifts to 535.5 eV in 64 seconds of irradiation, the third one at 546.2 eV, the position of it does not change during irradiation, but the intensity drops down a little.

Fig.2 is a montage of EELS spectra from various oxides of vanadium with its oxidation state changing from +3 (in V_2O_3) to +5 (in V_2O_5). It also shows that the L_3/L_2 intensity ratio increases as the oxidation state of vanadium decreases. Comparing radiated V_2O_5 spectra with those of V_2O_3 and VO_2, it can be recognized that radiation damage of V_2O_5 is induced by electron stimulated desorption of oxygen[5].

REFERENCES
1. H.J. Fan & L.D. Marks, Ultramicroscopy (1989), Vol. 31, p.357.
2. C.D. Wagner et al., Handbook of X-ray Photoelectron Spectroscopy (1979, Physical Electronics Division, Perkin-Elmer Corporation, Eden prairie, Minnesota).
3. J.H. Rask et al., Ultramicroscopy (1987), Vol. 21, p.321.
4. O.L. Krivanek & J.H. Paterson, Ultramicroscopy(1990), Vol.32, p.313.
5. This research is supported by a seed grant by the Center for Catalysis and Surface Science (CCSS), Northwestern University.
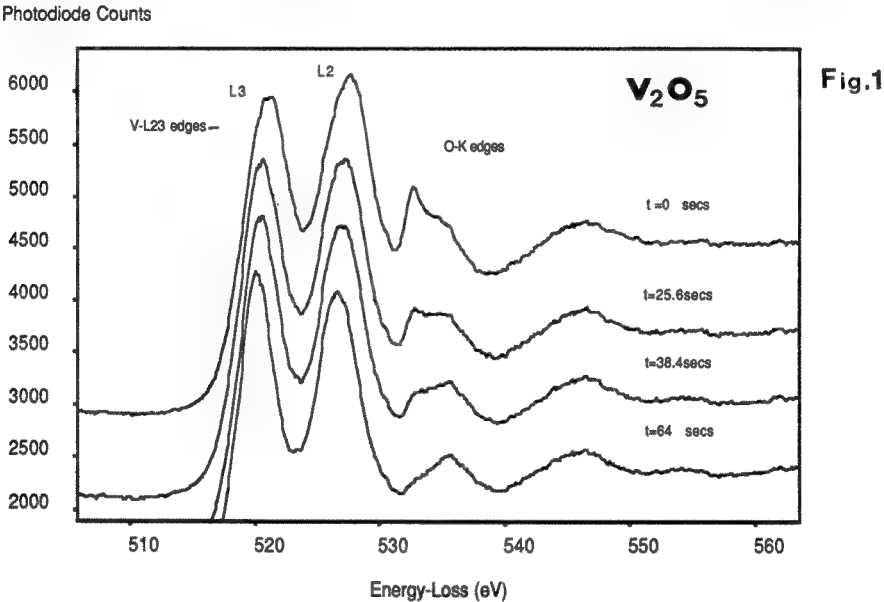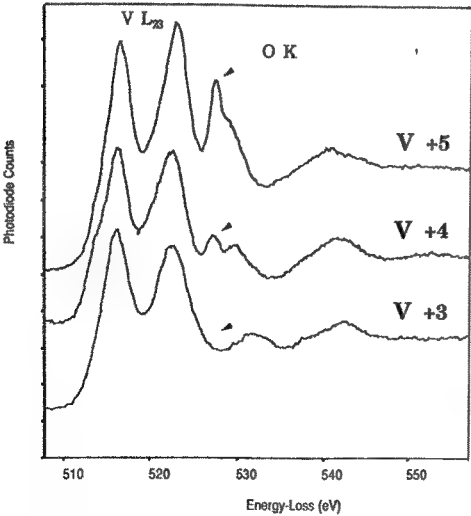
Figure 1: Time resolved PEELS core loss speactra from V_2O_5. Prolonged beam exposure results in: (i) increase in L_3/L_2 intensity ratio (ii) shifting of L_3 and L_2 to lower energy and, (iii) shifting of O-K edge towards higher energy.

Figure 2: Montage of PEELS core loss spectra from various vanadium oxides, exhibiting notable differences in spectral shape/intensities due to variations in oxidation state of vanadium.

377

HRTEM OBSERVATIONS ON ELECTRON IRRADIATION DAMAGE IN F-APATITE

M. Cameron*, L.M. Wang†, K.D. Crowley*, and R.C. Ewing†

*Department of Geology, Miami University, Oxford, OH 45056
†Department of Geology, University of New Mexico, Albuquerque, NM 87131

Radiation damage in crystalline phases with the apatite structure is of interest in the biomedical, geoscience, and materials science communities. Phases close to hydroxyl apatite $[Ca_5(PO_4)_3OH]$ in composition are volumetrically the most significant in dental enamel and bone.[1] Natural apatites with variable halogen compositions $[Ca_5(PO_4)_3(F,OH,Cl)]$ are used by geoscientists to place constraints on the thermochronologic conditions under which portions of the Earth evolved.[2] Rare-earth-silicate isomorphs of these naturally occurring apatites are also of interest because they may be actinide hosts in ceramic nuclear waste forms.[3]

The susceptibility of apatite to electron irradiation damage has been noted by researchers in a variety of TEM studies.[4,5] In such studies the effects of electron beam damage must be clearly delineated from primary structural features in order to interpret the TEM images. In this study, we have documented *in situ* the damage evolution induced by electron irradiation in naturally-occurring, hexagonal fluor-apatite from Durango, Mexico. The samples were polished, oriented (c-axis parallel to the foil normal) sections of single crystals that were ion-milled to perforation. Observations were made at 200 keV using a JEOL JEM-2000FX analytical electron microscope at the University of New Mexico.

Modification of the apatite microstructure was evident in less than one minute of irradiation with a 200 keV electron beam. The perfect (undamaged) HRTEM image shown in Fig. 1 could only be obtained in the initial moments (within 30 seconds). Most noticeable in the initial stages of beam damage were discrete, evenly distributed light-colored areas. Some of the areas were completely facetted with boundaries defined by {110} or {100} forms; others were only bounded or not bounded by any straight edges (Fig. 2). We interpret the light-colored regions as areas of lower mass, reflecting displacement and migration (or even sublimation) of weakly bounded fluorine and perhaps calcium from their sites within the apatite structure. With continued exposure to the electron beam, these areas coalesced by elongation – commonly in directions parallel to the {110} or {100} lattice planes. Ultimately the damaged, light-colored areas formed a complex labyrinth with channels or voids 5 nm in diameter (Fig. 3). Concomitant with the formation of this distinctive pattern was the development of Moiré patterns, throughout the crystal matrix between the labyrinthian channels (Fig. 4). These Moiré patterns mark the crystallization sites of randomly oriented CaO crystals. With continued irradiation, some CaO crystals intrude upon the labyrinth of voids produced during earlier stages of the damage process. Experiments completed to date have not revealed any significant instability of CaO under further electron irradiation. The microstructural modifications were accompanied by systematic changes in selected area electron diffraction patterns. Notably the diffraction maxima associated with crystalline apatite decrease in intensity, and powder rings that match the pattern of CaO form and increase in intensity as the irradiation dose increases (Fig. 5). No new phosphorus-bearing or fluorine-bearing phases were identified by electron diffraction techniques.[6]

References
1. R.Z. LeGeros & J.P. LeGeros, in Phosphate Minerals (Ed. J.O. Nriagu & P.B. Moore), Springer Verlag (1984) 351.
2. K.D. Crowley et al., Fission Track Analysis: Theory & Applications, Geol. Soc. Amer. Shortcourse (1989).
3. W.J. Weber, J. Mater. Res.6 (1991) 1334.
4. D.G.A. Nelson et al., Rad. Effects Lett. 68 (1982) 51.
5. E.F. Bres et al., Ultramicroscopy 35 (1991) 305.
6. This work was supported by NSF grant EAR-9192379 (MC), NSF grant EAR 8517621 (KDC & MC), and DOE/BES grant DE-FG04-84ER45099 (RCE).
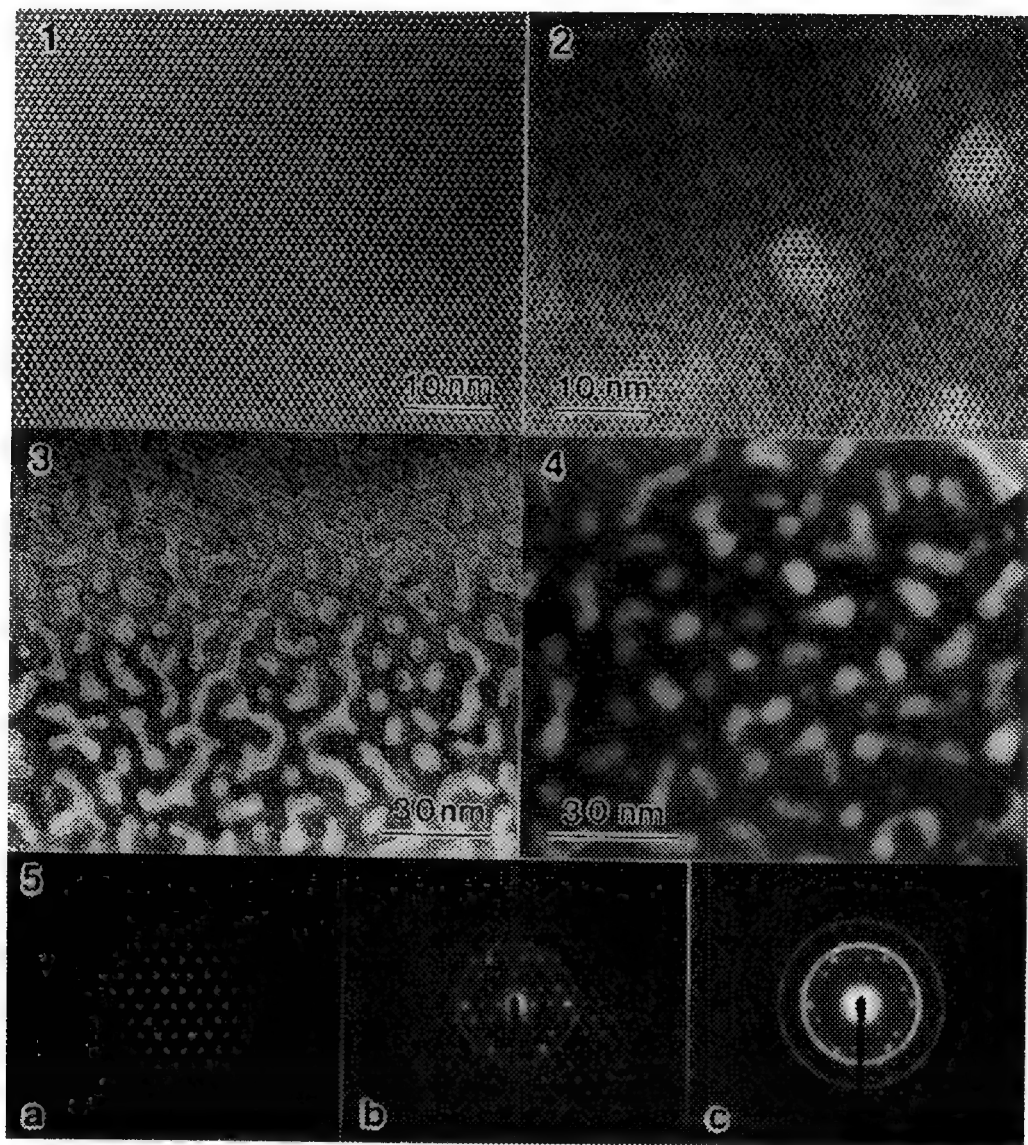
FIG. 1.--HRTEM image of undamaged $Ca_5(PO_4)_3F$ (F-apatite, [001] zone).

FIG. 2.--Early stage of the electron irradiation damage in F-apatite.

FIG. 3.--HRTEM image of F-apatite taken after five mimutes of 200 keV electron irradiation. A labyrinth of voids has formed.

FIG. 4.--HRTEM image of F-apatite taken after ten minutes of 200 keV electron irradiation showing the formation of CaO (manifested by the Moiré fringes) in addition to the voids.

FIG. 5.--Selected area electron diffraction patterns showing the progressive fromation of CaO crystals in F-apatite during electron irradiation (all of the rings in (b) and (c) can be indexed exactly with the cubic CaO structure).

DIRECT OBSERVATION OF MONOMER IMAGE OF POLY(P-XYLYLENE) CRYSTAL

Weiping Zhang and Edwin L. Thomas

Department of Materials Science and Engineering, Massachusetts Institute of Technology, Cambridge, MA 02139

Poly(p-xylylene) (PPX) single crystals have been studied recently with high-resolution electron microscopy (HREM) by two groups (1,2). The resolution achieved to date is 0.26 nm for the α-form and 0.25 nm for the β-form. Polymer crystals are generally very sensitive to electron irradiation since the molecular chains become crosslinked or are decomposed (chain scission) in a short time upon electron irradiation. Individual chain stems in a polymer crystal can be resolved in micrographs if the electron beam is introduced into the crystal along the chain axis. Obtaining structural images from different crystal orientations is very useful in three dimensional reconstruction. Most HREM studies on polymer crystals have focused on taking images along the polymer chain direction. The present work demonstrates that monomer images can be obtained from other directions, and a 0.18 nm resolution is achieved for α-form PPX crystals at room temperature.

Single crystals of PPX (Parylene N, Union Carbide, Mw = 500,000) were prepared following the self-seeding technique described previously (2). Under these conditions, the crystal thickness of monolayer α-form is 12 nm as measured by shadowing a sample with chromium. HREM is performed at 200 kV on an Akashi 002B electron microscope, equipped with a minimum dose system and a Gatan image intensifier system connected to a video monitor. High-resolution images were taken at a magnification of 98,000. The micrographs were examined on an optical bench, and selected areas of the good images were enlarged by a magnification of 3, then scanned with an Optronics P-1000 microdensitometer with a 25 μm aperture. The images were then filtered using the SEMPER image processing system on a Micro Vax II/GPX workstation with the VMS 4.5 operating system. The windows used are parallelograms with sides 0.1 times the corresponding base vector length. The crystal structure of α-form PPX is monoclinic (space group C2/m) with a = 0.592, b = 1.064, c = 0.655 nm and β. = 134.7^{o}. Original HREM image and electron diffraction pattern (insert) (a), its optical diffraction pattern (b) and digitally filtered image (c) of α-form PPX single crystal taken along the [102] direction are shown in Fig. 1. The $(20\bar{1})$, $(24\bar{1})$ and (060) reflections, corresponding to resolutions of 0.28, 0.19 and 0.18 nm respectively, are indicated by arrow heads in (b); and the black ellipses in (c) correspond to the monomer column projections shown in Fig. 2(b). Fig. 2 shows the schematic two-dimensional projections of the α-form PPX crystal structure along different directions: (a) [001], (b) [102] and (c) [010]. Circles represent carbon atoms, dark black lines the side view of aromatic rings and hydrogen atoms are omitted. In (c), the polymer chains marked by 1 and 3 are at $b = 0$ or 1 level, and the chain denoted by 2 at the $b = 1/2$ level. The angle between the aromatic planes and the [001] direction is about 14°, and that between the planes and the [102] direction is approximately 11°. This makes the aromatic rings in (b) about 20% narrower than those in (a) along the vertical direction of the figure. A centered orthogonal planar lattice is formed in Fig. 2(a), and a simple orthogonal one in Fig. 2(b). The individual monomer projection in Fig. 2(a) and (b) is very similar, but a closer packing appears in (b). In the first case, the image is formed by the monomers of the same chain stem; in the latter, the image is formed by monomers of different chain stems. They both are similar to molecular images of small molecular organic crystals. To verify the applicability of the electron density projection approximation in this study and to demonstrate the differences under different resolutions, [102] high-resolution images of α-form PPX crystal with a thickness of 12 nm and at Scherzer focus were simulated using the Multislice program package from the Arizona State University facility for HREM. The result proves that electron density projection approximation can be applied in this study. It can be claimed that an individual dark region in Fig. 1(c) corresponds to a monomer column in the crystal as illustrated in Fig. 2(b). Combined with data from other orientations, similar results can be used for three dimensional crystal structure determination.

References:
1. Isoda, S., Tsuji, M., Ohara, M., Kawaguchi, A. and Katayama, K. Polymer 1983, 24, 1155.
2. Pradere, P. and Thomas, E.L. Phil. Mag. 1989, 60, 177.
3. Financial support from the National Science Foundation by a NSF grant DMR 89-07433 and AFOSR 91-0078 is gratefully acknowledged. We also thank Dr. D.L. Dorset for use of his microdensitometer.
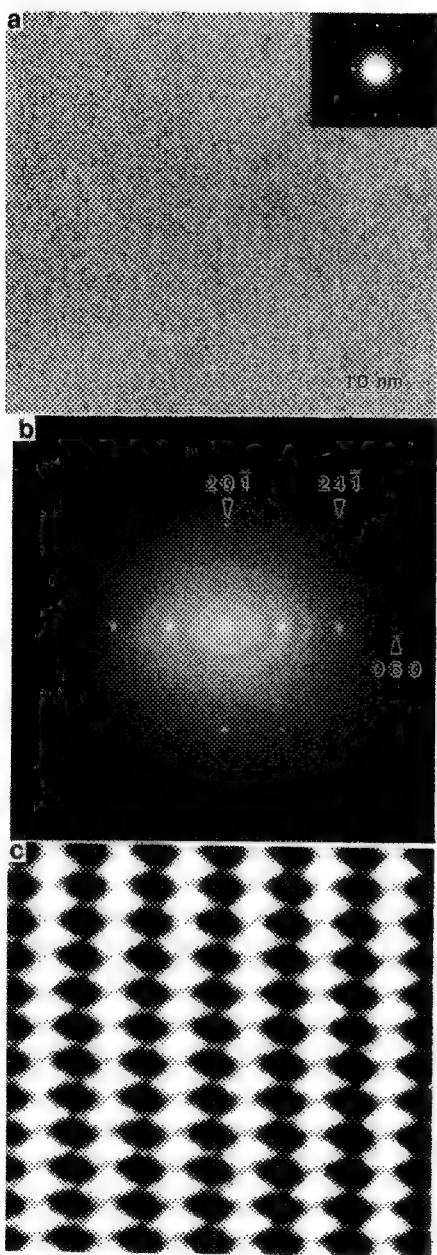
FIGURE 1
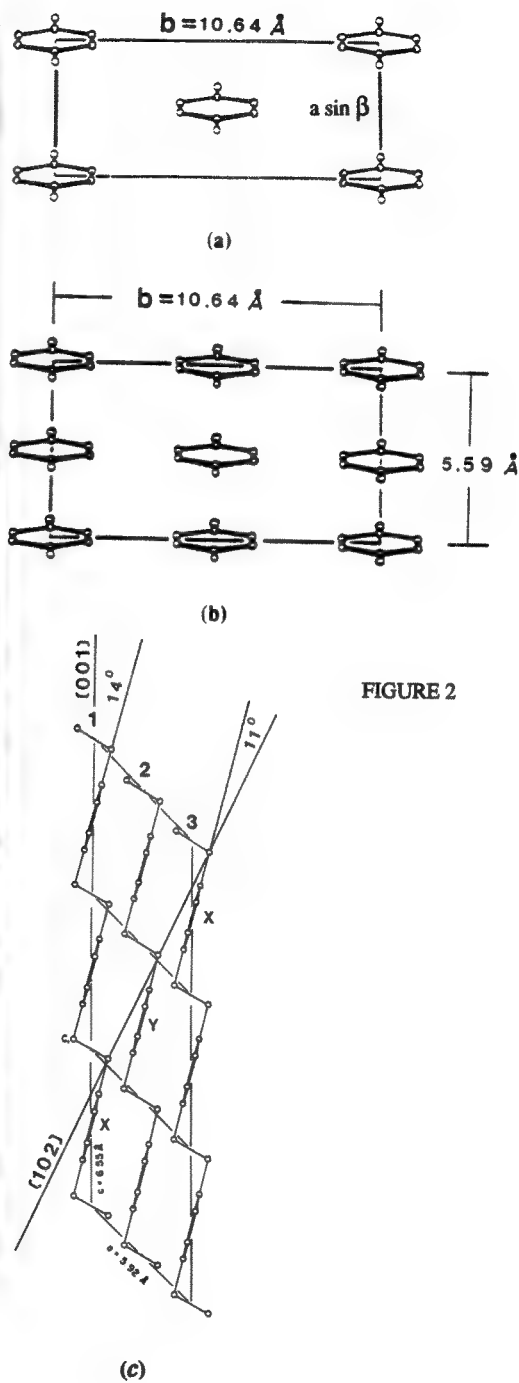
FIGURE 2

QUANTITATIVE ESTIMATION OF ELECTRON BEAM IRRADIATION DAMAGE OF POLYETHYLENE SINGLE CRYSTAL USING IMAGING PLATE

T. Oikawa,* D. Shindo,** J. Kudoh,*** S. Aita* and M. Kersker****

*JEOL Ltd., 1-2 Musashino 3-Chome, Akishima, Tokyo 196, Japan
**Institute for Materials Research, Tohoku University, Katahira, Sendai 980, Japan
***Computer Center, Tohoku University, Katahira, Sendai 980, Japan
****JEOL (U.S.A.) Inc., 11 Dearborn Road, Peabody, MA 01960

The degree of electron beam irradiation damage is estimated from the intensity fading of diffraction spots and the lattice spacing increase of the specimen. Previously, qualitative estimatin of the damage was made for beam-sensitive specimens, e.g., polymers[1] and biomolecules.[2] In the present study, the degree of irradiation damage was estimated by quantitative measurement of the intensity of electron diffraction patterns, using the Imaging Plate (IP). Polyethylene single crystal, which is a typical material for polymers, was used as a specimen.

The instrument used was the TEM-IP system,[3] a PIXsysTEM based on the JEM-2010 200kV TEM. Specimen temperature was kept at room temperature. Data analysis was carried out by standard software on the PIXsysTEM and by a newly-developed "background subtraction program for electron diffraction patterns,"[4] in order to eliminate the background intensity of the diffraction spots. This is because the background intensity is considered as due to multiple scattering in the crystal and scattering in the support film.

Figure 1 shows electron diffraction patterns and their intensity distributions obtained by the IP at 200kV. The electron dose rate was 1 electron/($nm^2 \cdot sec$) and a shutter speed of 0.1 sec was used because a higher-time-resolution exposure was required. Figure 1(a) shows a pattern from a fresh crystal. It is seen that the many diffraction spots from the center beam to higher-order diffraction spots, were well recorded. Figure 1(b) shows a pattern taken from the same crystal but after giving an electron dose (Qs) of 600 electrons/nm^2. The intensity distribution along the line in the pattern is shown on a logarithmic scale in absolute electron intensity.

Figure 2 shows a series of diffraction pattern changes with increasing electron dose. The lower patterns are the original prints. The upper ones are perspective drawings of the intensity distribution of 110 reflection in the patterns, obtained after background subtraction. Various intensities of diffraction spots from weak to strong reflections, ware measured with high precision by this method.

Since the IP has superior characteristics such as high sensitivity, wide dynamic range and linear sensitivity, the higher intensity of the diffraction spots and the lower intensity of the halo and background are recorded simultaneously in a single image. After recording the image, the intensity was measured quantitatively using the IP's linear sensitivity. Also, its high sensitivity allows high shutter speeds at very low electron dose rates.

1. K. Kobayashi and K. Sakaoku, Proc. Symposium on "Quantitative Electron Microscopy" (Washington D. C.) (1964) 359.
2. Y. Fujiyoshi et al., Proc. IIth Int. Cong. on EM (Kyoto) (1986) 1829.
3. T. Oikawa et al., J. Electron Microsc., 39 (1990) 437.
4. D. Shindo et al., (Proceeding of this Meeting).
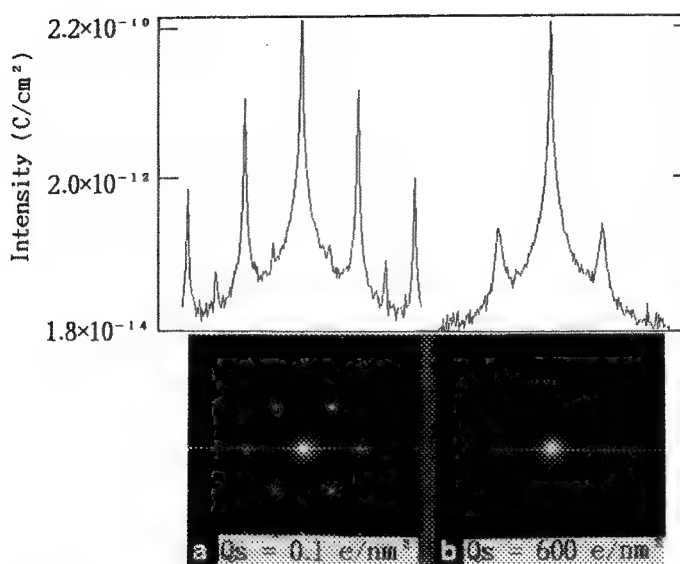
Fig.1 Electron diffraction patterns of polyethylene single crystal and their intensity distribution (at 200 kV and room temperature).
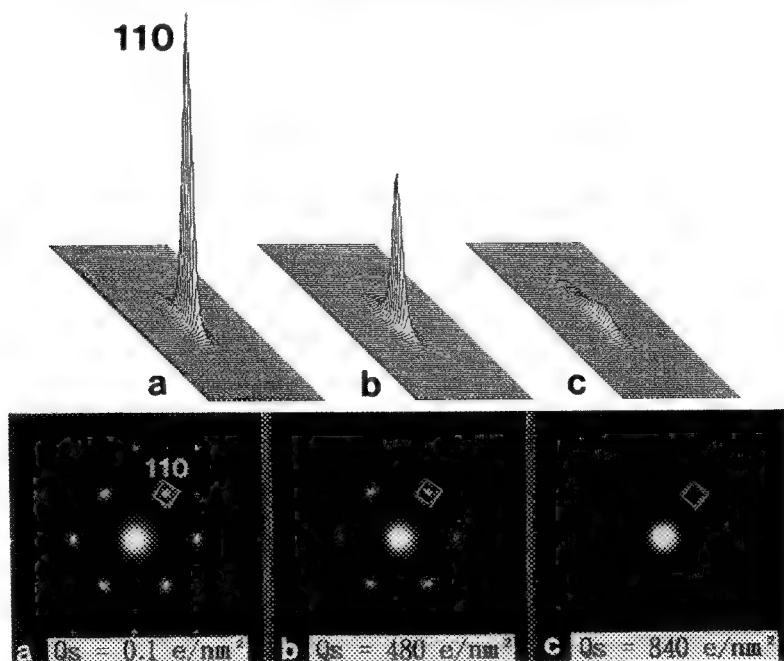
Fig.2 Electron diffraction patterns of polyethylene single crystal taken at varying electron doses, Qs.
Upper patterns: Perspective drawings of the background subtracted intensity distribution of 110 reflections in the patterns.
Lower patterns: Original prints.

383

MORPHOLOGICAL STUDIES OF LINEAR (AB)n MULTIBLOCK COPOLYMERS AND THEIR BLENDS

Richard J. Spontak, Steven D. Smith and Arman Ashraf

Miami Valley Laboratories, The Procter & Gamble Company, P.O. Box 398707, Cincinnati, OH 45239

Block copolymers are composed of sequences of dissimilar chemical moieties covalently bonded together. If the block lengths of each component are sufficiently long and the blocks are thermodynamically incompatible, these materials are capable of undergoing microphase separation, a weak first-order phase transition which results in the formation of an ordered microstructural network.[1] Most efforts designed to elucidate the phase and configurational behavior in these copolymers have focused on the simple AB and ABA designs. Few studies[2] have thus far targeted the perfectly-alternating multiblock $(AB)_n$ architecture. In this work, two series of neat $(AB)_n$ copolymers have been synthesized from styrene and isoprene monomers at a composition of 50 wt% polystyrene (PS). In Set I, the total molecular weight is held constant while the number of AB block pairs (n) is increased from one to four (which results in shorter blocks). Set II consists of materials in which the block lengths are held constant and n is varied again from one to four (which results in longer chains). Transmission electron microscopy (TEM) has been employed here to investigate the morphologies and phase behavior of these materials and their blends.

Concentrated solutions (5% wt/v) of each copolymer or copolymer/homopolymer blend were prepared in toluene and cast into Teflon molds. After slow solvent evaporation over the course of at least three days, the resultant films were heated to above 100° C to remove residual solvent. The assemblies were encapsulated under argon and heated for one week at 170° C to promote thermodynamic equilibrium. Then, 50 nm TEM specimens were obtained by microtoming normal to the film surface at –100° C. Sectioning was performed with a Diatome 35° cryodiamond knife on a Reichert-Jung FC-4E cryoultramicrotome. The isoprene microphases were preferentially stained with OsO_4 vapors for 90 min. Micrographs were obtained with a Zeiss EM902 electron microscope, operated at 80 keV and an energy loss of 50 eV.

Figure 1 illustrates lamellar morphologies in the three copolymers constituting the upper and lower limits of the two series described above. Well-oriented lamellae are observed in the 60K/60K and 15K/15K diblock copolymers (Figs. 1a and 1b, respectively), for which n=1. In Fig. 1c, the corresponding octablock copolymer (n=4) possesses eight 15K dalton blocks and exhibits lamellae which remain oriented over relatively small grains. The additional interconnectivity of blocks in this material clearly produces additional defects in the morphology and results in less long-range order and enhanced microstructural isotropy. The lamellar periodicity (D) has been determined from each set of copolymers and is presented as a function of n in Fig. 2. In both cases, D(n) is found to decrease monotonically with n. This behavior is not surprising for Set I, since the block sizes decrease with increasing n. However, this functional relationship in Set II indicates that the blocks contract the microphases as n is increased.[3] These experimental observations are in agreement with recent theoretical predictions,[4] which attribute the contraction in Set II to an extended configuration of the 2n–2 middle blocks.

A 50/50 blend of the copolymers presented in Figs. 1a and 1c results in the mixed morphology seen in Fig. 3. Despite the fact that both materials are chemically identical, they macrophase separate and remain insoluble to a large extent due to differences in architecture and block length. Macrophase separation is commonly encountered when block copolymers are blended with high-molecular-weight homopolymers incapable of solubilizing into the microphases. Figure 3 reveals that the lamellae of the 60K/60K diblock copolymer are oriented normal to the interphase between the macrophases, thereby reflecting the shared chemical moieties in both materials. Blends of one Set I copolymer (n=3) with high- (112K) and low- (9.5K) molecular-weight PS result in the morphologies shown in Figs. 4a and 4b, respectively. In the former, the copolymer and homopolymer macrophase separate, as described above. The 9.5K PS, on the other hand, is observed from Fig. 4b to partially solubilize the PS microphases of the copolymer. Due to the configurational restriction of the middle blocks, however, the lamellae are incapable of swelling

384

appreciably (as they do in diblocks[5]). Consequently, regions in which individual lamella abruptly end in pools of PS are rich in intermediate structure (e.g., micelles). Such regions can be conceptualized as diffuse interphases between the copolymer and homopolymer. These interphases would not exist in diblock/homopolymer blends due to the flexibility of the copolymer but arise in these $(AB)_n$ copolymers as a result of the multiblock architecture.

References

1. F. S. Bates, Science (1991)251, 898.
2. N. M. Patel, Macromolecules (1988)21, 2689.
3. S. D. Smith et al., Phys. Rev. Lett. (submitted).
4. J. M. Zielinski and R. J. Spontak, Macromolecules (1992)25, 653.
5. K. I. Winey et al., Macromolecules (1991)24, 6182.
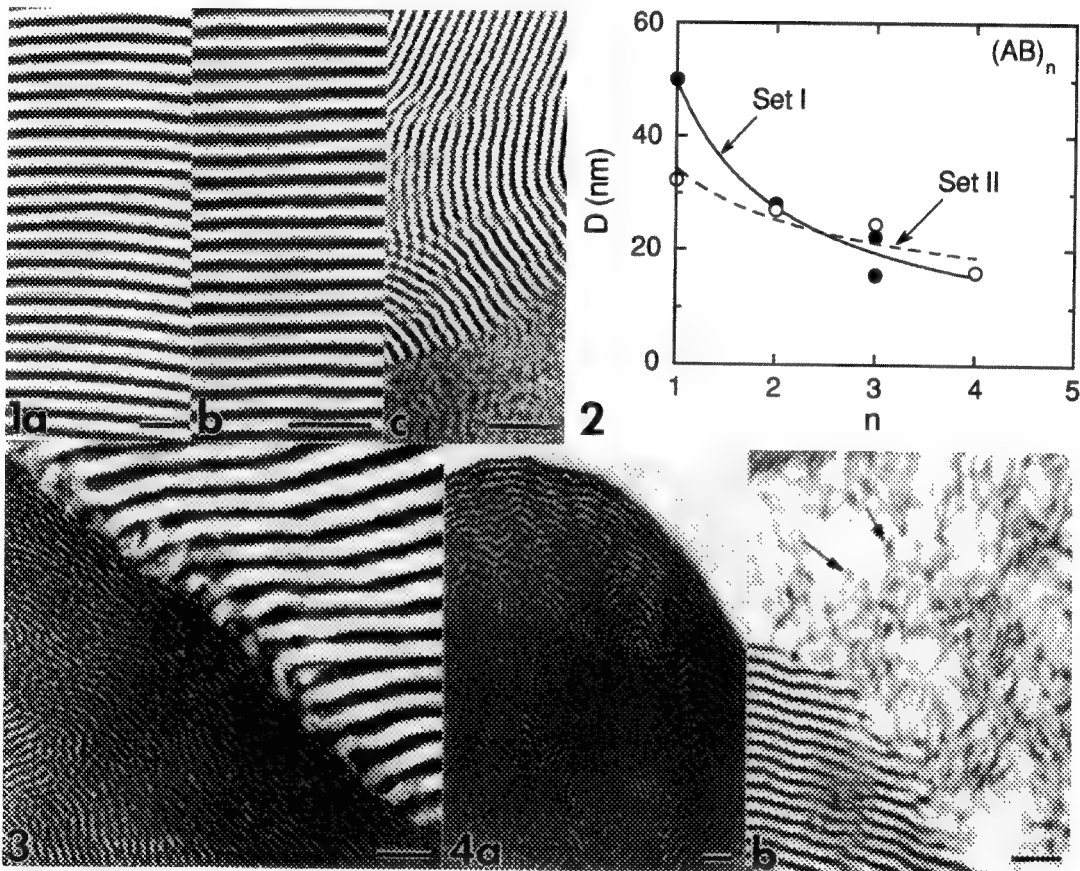
FIG. 1.--Transmission electron micrographs of lamellar morphologies in pure multiblock copolymers: (a) 60K/60K diblock, (b) 15K/15K diblock, and (c) $(15K/15K)_4$ octablock. Bars = 100 nm.

FIG. 2.--Functional relationship of microdomain periodicity, D(n), obtained from TEM images. Set I is denoted by (●), and Set II by (o). Lines are power-law fits to data and reveal that $D \propto n^{-a}$.

FIG. 3.--TEM image of macrophase-separated morphology in 50/50 blend of 60K/60K diblock and $(15K/15K)_4$ octablock copolymers. Bar = 100 nm.

FIG. 4.--Micrographs of $(20K/20K)_3$ hexablock copolymer blended with equal masses of (a) 112K PS and (b) 9.5K PS. Note disordered micelles (arrows) in (b). Bars = 100 nm.

LOW-ENERGY ELECTRON BEAM LITHOGRAPHY: MONTE CARLO SIMULATION AND EXPERIMENT

T.J. Stark[1], Z. J. Radzimski[2], P.A. Peterson[1], D.P. Griffis[2] and P. E. Russell[1]

[1] Materials Science and Engineering, [2] Analytical Instrumentation Facility, North Carolina State University, Raleigh, NC 27695-7916

Recent advances in electron optical systems which allow reduction of electron beam voltage while maintaining sufficiently small spot size and high current density have opened new possibilities for electron beam lithography. The main advantage of low beam energy lithography is a reduction of backscattered electrons and, consequently, the reduction of problems associated with proximity effects. The other advantages of this technique are reduction in the dose required to modify a resist and minimization of substrate damage caused by energetic electrons. Proper electron energy must be chosen at which the beam deposits its energy mainly within the resist film with minimal penetration into the substrate. Monte Carlo simulation programs have been used widely to predict the scattering interactions and thus the area of proximity effects. Rutherford cross section for angle scattering and Bethe energy loss have been commonly used in Monte Carlo modeling. However, low energy lithography (<5keV) requires a more accurate approach based on Mott cross sections for scattering and a more precise formula for energy loss replacing the Bethe law which is invalid below 1 keV energy.

The Monte-Carlo programs used in this work are based on earlier single scattering programs developed by Shimizu, Myklebust, and Joy and their co-workers [1]. They use Rutherford or Mott cross sections for scattering and Love's energy loss formula [2]. The programs were modified to provide a simulation of the electron beam interactions with thin multilayer structures [3]. The programs can be applied to structures with internal variations in composition or density and/or surface irregularities. The optimum beam energy can be estimated by analyzing the total energy losses in the resist layer (see example in Fig. 1 for PMMA layer on Si substrate). More precise information can be obtained from the energy loss distribution as a function of depth. An example is given in Fig. 2 for 500Å PMMA layer. The evaluation of proximity effects can be done by simulation of a series of exposure as shown schematically in Fig. 3 for 500Å PMMA layer. Fig. 3 a shows the effective dose which results from a series of line exposures 10, 20, 40, 80 and 320 nm wide with 10 nm steps. Figure 3b illustrates the overlap of line exposures separated by 10, 20 and 40 nm spaces.

The goal of this work is to illustrate how Monte-Carlo methods are used to determine the optimal electron beam exposure conditions to be used in electron beam lithography processes. Three different examples of low energy beam lithography have been demonstrated experimentally. In the first case, a thin layer of electron beam sensitive resist (PMMA) has been exposed [4]. The second was the patterning of thin SiO_2 layers through a direct write process [5] and the third was formation of thin metal (Pd) lines as a result of electron beam radiation of palladium acetate (Pd-Ac)[6]. SEM micrographs of thin lines exposed in PMMA and from Pd-Ac are shown in Fig. 4a-b, respectively.

Thus, it has been shown that the Monte-Carlo method can provide accurate predictions for electron beam exposures for a wide variety of materials. Various experimental examples illustrate the feasibility of low energy beam lithography.

References
1. D. C. Joy, J. Microscopy (1987) **147**, 51.
2. J. C. Russ , Z. J. Radzimski , A. Buczkowski , L. Maynard , J. Comput. Assist. Microscopy, **2** (1), 53.
3. G. Love, M. G. Cox, V. D. Scott, J. Phys. D: Appl. Phys. (1977) **10**, 7.
4. P.E.Allen, D.P.Griffis, Z.P.Radzimski, P.E.Russell, J. Vac. Sci. Technol.(1992), to be published.
5. T.J.Stark, T.M.Mayer, D.P.Griffis, P.E.Russell, J. Vac. Sci. Technol. (1991), **B9**(6), 3475.
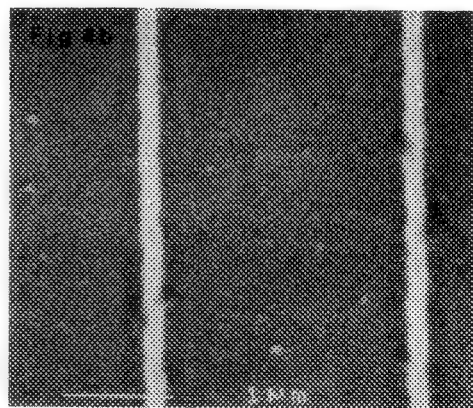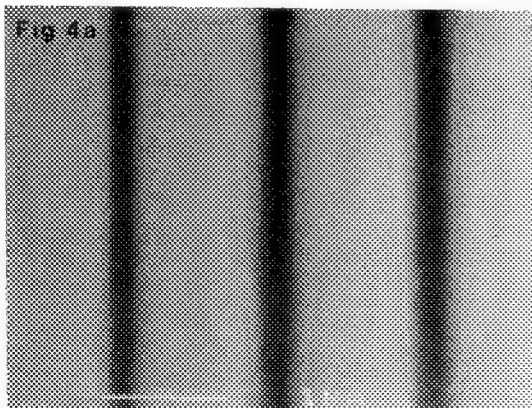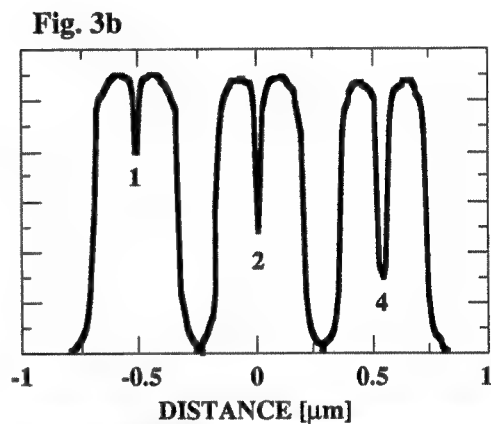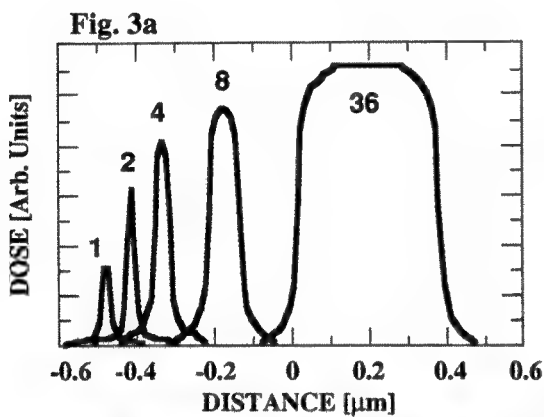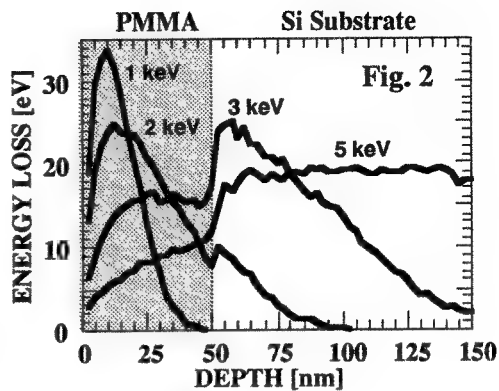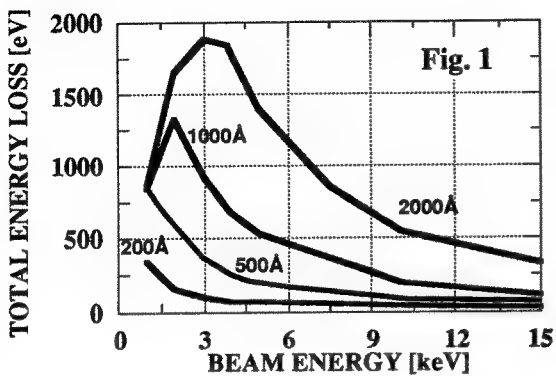
Fig. 1 Total energy loss in the PMMA layer as a function of primary beam energy (Resist layer thickness - parameter).

Fig. 2 Depth distribution of energy loss for a 500Å PMMA layer on Si substrate (Primary beam energy - parameter).

Fig. 3 Effective dose in PMMA layer from a) isolated lines and b) lines with narrow spaces.

Fig. 4 SEM examples of thin lines obtained using low energy beam lithography: a) 3500Å PMMA on Si - 3keV exposure) and b) 2000Å PdAc on Si - 4keV exposure.

IRRADIATION DAMAGE IN OHAP STUDIED BY HREM

Shulin Wen, Jingwei Feng and D.J. Smith+

Shanghai Institute of Ceramics, Chinese Academy of Sciences, 1295 Dingxi Rd.,
Shanghai, CHINA
+Center for Solid State Sciences, Arizona State University, Tempe, Arizona

Hydroxyapatite (OHAP) with chemical composition $Ca_{10}(PO_4)_6(OH)_2$ is a very promising biomaterial. OHAP has been found to be incorporated in bone and tooth tissue. Both sintered OHAP compact implant and OHAP-coated implant are used as prostheses in surgery [1]. Recent irradiation damage studies [2-4] show that very complicated physical and chemical process may occur to both the synthetic OHAP and natural OHAP (human enamel), during the electron irradiation in TEM analysis. So the irradiation damage investigation is very important for TEM study of OHAP.

Present work indicated that during the observation at 200-400 keV, all of the OHAP material, even with quite different processing, might undergo such a chemical reaction as $OHAP \to Ca_3(PO_4)_2 + Ca_4P_2O_9 + CaO + H_2O$. In the meanwhile, some mechanisms of irradiation such as keV-energy dependent damage, structural orientation-dependent damage, been-induced diffusion damage which causes outgrowths at surfaces, recrystallization or forms new phase, were found in our materials.

In comparison of human enamel with synthetic OHAP, no irradiation damage has been observed at 100 keV for the synthetic one as shown in Fig.1. However, the irradiation damage has observed for the human enamel crystals. This shows that the structure in synthetic OHAP may be stronger than that in natural OHAP (human enamel) probably due to different impurity and processing.

With irradiation energy getting higher than 100 keV, the damage in synthetic OHAP would start. Present work indicated that the synthetic OHAP material was damaged with the production of white patches as shown at area A in Fig.2. These white patches has been proved to be subsurface voids. The anisotropy of the void formation mechanism is most like due to a higher mobility at [001] direction than any other direction. And this is probably the right reason for high patches density being observed at [001] zone direction and for no white patches being observed at [100] zone direction (see Fig.3).

After a prolonged irradiation at 400 keV, some new crystallite as seen at A in the Fig.4 would form at the crystal surface. The index of the lattice in the area A indicated that it is CaO crystallite. This overgrown crystal seems to form from atomic diffusion on the terraces of the surface in the specimen. However, with even longer electron irradiation at 200keV, the similar overgrown crystallite could not observed. This shows that the atomic diffusion on the terrace in the surface for forming the overgrown crystallite needs higher keV energy than 200 keV. However, the atomic diffusion within crystal in specimen for moving voids (compare Fig.5 and Fig.6) were easily realized with a prolonged irradiation only at 200 keV.

Reference

[1] M. Jarcho, Clin. Orthop. 157(1981)259.
[2] Wen Shulin, Electron Microsc. Review, 2(1989)1.
[3] Huaxia Ji and P.M. Marquis, Journal of Materials Science Letter, 10(1990)132.
[4] E.F. Bres, J.L. Hutchison, et al.,Ultramicroscopy, 35(1991)305.
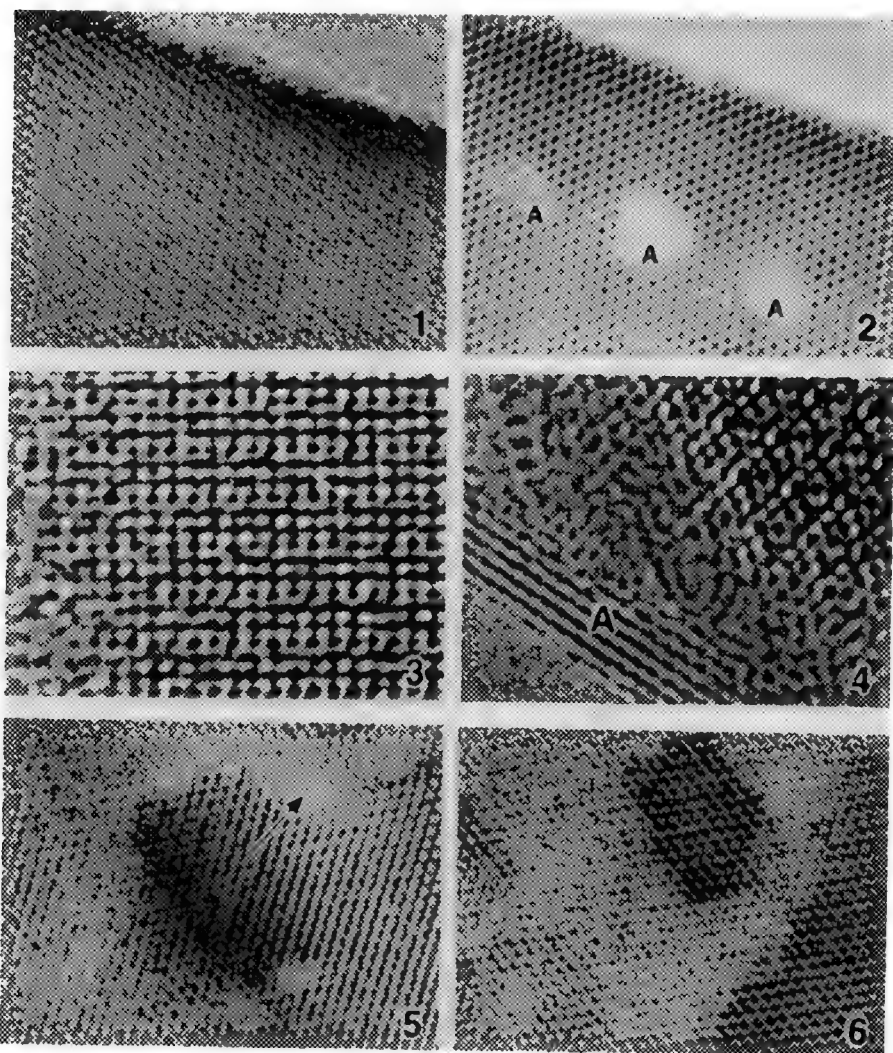
FIG.1--Lattice image of OHAP in [001] zone axis at 100 keV.
FIG.2--Lattice image of same area as Fig.1 but with an irradiation at 200 keV.
FIG.3--Lattice image of OHAP in [100] axis with a prolonged irradiation at 400 keV.
FIG.4--Lattice image of OHAP in [001] axis with a prolonged irradiation at 400 keV.
FIG.5--Lattice image of OHAP in [001] zone axis at 200 keV.
FIG.6--Lattice image of same area as Fig.5 but with a prolonged irradiation.

THE SEARCH FOR A 'MATERIALS SCIENCE' KNIFE IN ULTRAMICROTOMY

Tom Malis

Metals Technology Laboratories (MTL), CANMET, 568 Booth St., Ottawa, Canada K1A 0G1

Specimen preparation problems in analytical electron microscopy relating to phase differences, specimen geometry or microanalytical requirements have spurred increasing usage of diamond knife sectioning.[1] Since many of these materials are quite hard and/or tough, many material scientists assume (hope?) that there must be a knife specifically designed for 'hard' materials. The fact that such a knife has not been developed is due to the fact that conventional (biological) knives have performed so well, with somewhat vague recommendations to use a 35° knife angle for reduced section compression, 45° for general usage and 55° for very hard materials such as embedded catalyst particles.[1]

New knives of all three angles, and a 45° histo-knife [2](intended for low-quality biological sections > 200nm) were used to section materials of varying difficulty - an Al alloy, embedded BN fibers, a SiC particulate-reinforced Al composite and embedded particles (2-20μm) of rapidly-solidified FeNdB intermetallic.[2] Section thickness and oxide layer thickness were measured in the TEM via EELS.[3]

A first series of tests on the 3 regular knives had involved sectioning the same Al and BN blocks (facet size about 0.1mm square) for over 200 40nm thick sections under the same conditions. All sections were quite acceptable and no major differences were observed in section compression, section or oxide layer thickness, section deformation or knife appearance (undamaged but probably starting to wear).[3]

As thickness was increased in this study, curling frequency increased, with the 35° knife performing best (Fig 1a). Increasing the facet edge from 0.1 to 0.8mm demonstrated that all knives could produce 40nm sections which were remarkably free of major curling (Fig 1b,c), with thickness within +/-10% across the entire section. Tests on the extremely hard FeNdB powder produced only particle fragments with all 3 knives, moreover the 35° knife suffered severe damage, the 45°, moderate damage, and only the 55° knife escaped relatively unscathed. This trend was consistent with an earlier 45°/55° comparison using fine-grained sintered WC of similar hardness, where the 45° knife suffered noticeably more damage than the 55° knife but produced marginally thinner section fragments.[4] On the other hand, the SiC particle retention in the Al composite sections was noticeably superior with the 55° knife (Fig 2).

The most surprising results were obtained with the histo-knife since, at about half the price of regular knives, it might be assumed to possess an inferior edge for hard materials as well as soft materials. However, useful 40nm sections were produced from all of the materials studied. The only observeable visual difference was what might be termed 'continuous knife marks' (Fig 3 - as opposed to the scattered knife marks produced by regular knives after usage). Even for the worst of the Al sections, these marks (about 100nm wide, with thickness varying about +/-20%) did not interfere with section usage, although the sections sometimes parted along these lines (Fig 1c). The measured section thickness in Al was consistently closer to the set thickness than for regular knives and the oxide layer was much thinner. Sections of the BN fibers (Fig.4) were much closer to the set thickness, sections from the regular knives having been almost double that of the set thickness.[1,3] Sections up to a micron thick were produced with the histo-knife (seldom attempted in regular knives due to fear of diamond fracturing) and some that were quite flat. Finally, the histo-knife produced by far the best sections of the FeNdB powder (Fig 5) with no noticeable damage to the knife edge. Though these results are promising, they are only preliminary tests, and further testing is required if the histo-knife is to be a 'materials science' knife.[4]

References

1. T.F. Malis and D. Steele, Spec. Prep. for TEM of Materials II, Mat. Res. Soc. Symp. 199 (1990) 3.
2. Knives supplied courtesy of Diatome U.S.
3. D. Steele and T. Malis, Spec. Prep. for TEM of Materials III, Mat. Res. Soc. Symp.(1991).In press.
4. T. Malis and H. Gnaegi, unpublished work.
5. The author thanks G. Williams for the production of sections and D. Steele for useful discussions.
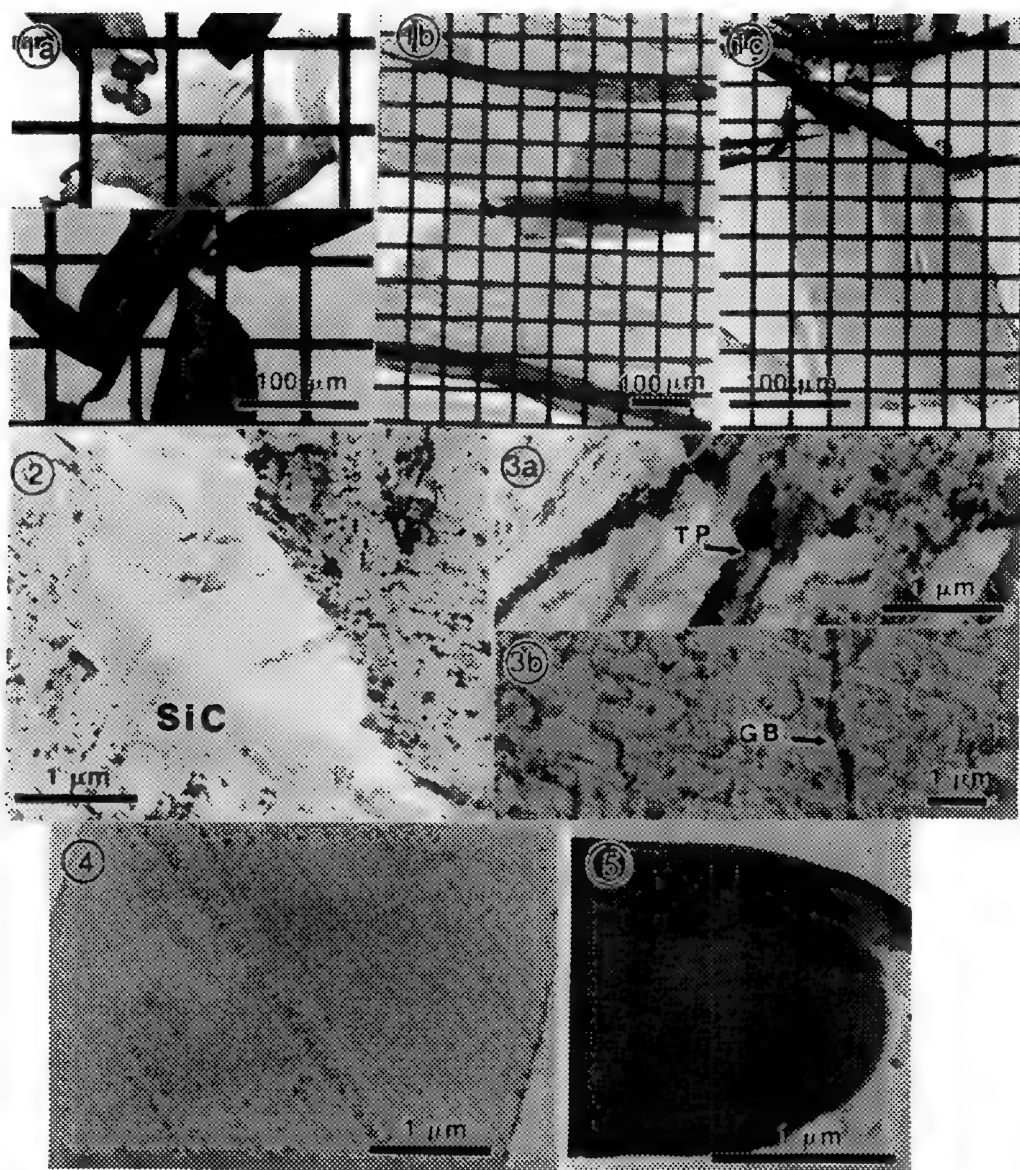
Fig 1 a) Reduced curling of 200nm thick sections, 35° (upper) vs 45° (lower). b) Very large 40nm Al sections, 45° knife, minor folding. c) Similar section, histo-knife, some tearing along knife marks.
Fig 2 Section fragment of Al-SiC composite (breakup due to weak metal-ceramic bond) showing significant retention of SiC, hence of metal-ceramic interface. 55° knife, 40nm thick.
Fig 3 Typical sectioning deformation in Al using a) 45° regular knife (note triple point-TP), t~40nm, b) histo-knife, t~200nm (note grain boundary (GB) and high density of knife marks).
Fig 4 BN fiber sectioned along fiber axis, histo-knife, t~35nm (set at 40nm). Note fine knife marks.
Fig.5 FeNdB particle, t~35nm (set at 40nm). Particles up to 20 μm in diameter were sectioned.

IDENTIFICATION OF POLYMER PHASES IN ELASTOMER BLENDS

P. SADHUKHAN

Central Research Laboratories, Bridgestone/Firestone, Inc. Akron, Ohio 44317

Elastomers are composed of natural rubber and synthetic polymers. They are generally blended to produce rubbers with certain "designing properties" (Shaffer, et al., 1985), including high resilience, tensile strength and elongation, resistance to tear, flexing, freezing and abrasion and low permanent set. The analytical procedures used for the identification and characterization of these polymer blends range from a simple color or flame test to more sophisticated technique like electron microscopy. Over the years, transmission electron microscopy has become the principal technique of direct visualization and subsequent characterization of phase separation and domains in polymer blends. The standard specimen preparation has been to perform cryo-ultramicrotomy on solid blend materials at liquid nitrogen temperature (Andrews et al., 1967) followed by staining with osmium tetroxide (Kato, 1966) to enhance differential contrast between the polymers in these blends. Without prior knowledge of the chemistry between the polymers and osmium, it is difficult to identify them under the TEM.

Polymers of reasonable equal viscosity in blends may undergo phase separation and generate small particle sizes and continued polymerization produce phase inversion. Dispersed phase morphology prior and after the phase inversion enables identification of the individual phases in blends. Three polymer blends, namely, NR/BR, NR/SBR and NR/EPDM have thus been chosen for such phase identification studies. The morphologies were selectively varied by a change of the blend composition in the ratios of 80/20, 50/50 and 20/80. All blends were heterogeneous showing distinct domains of dispersed phase in continuous matrix at 80/20 and 20/80 compositions (Figs. 1-3). At 50/50 composition, they form co-continuous phases. It has thus been possible to identify the respective phases in 50/50 composition by observing the complimentary grey levels of the dispersed phases in the 80/20 and 20/80 blends.

References

1. O. L. Shaffer, V. Dimonie, M. S. El-Aasser and J. W. Vanderhoff, Proc. 43rd Ann. Conf. EMSA (1985) 82.

2. E. H. Andrews, M. W. Bennett and A. Markham, J. Polym. Sci. (1967)5, 1235.

3. K. Kato, J. Polym. Sci. (1966)B4, 35.
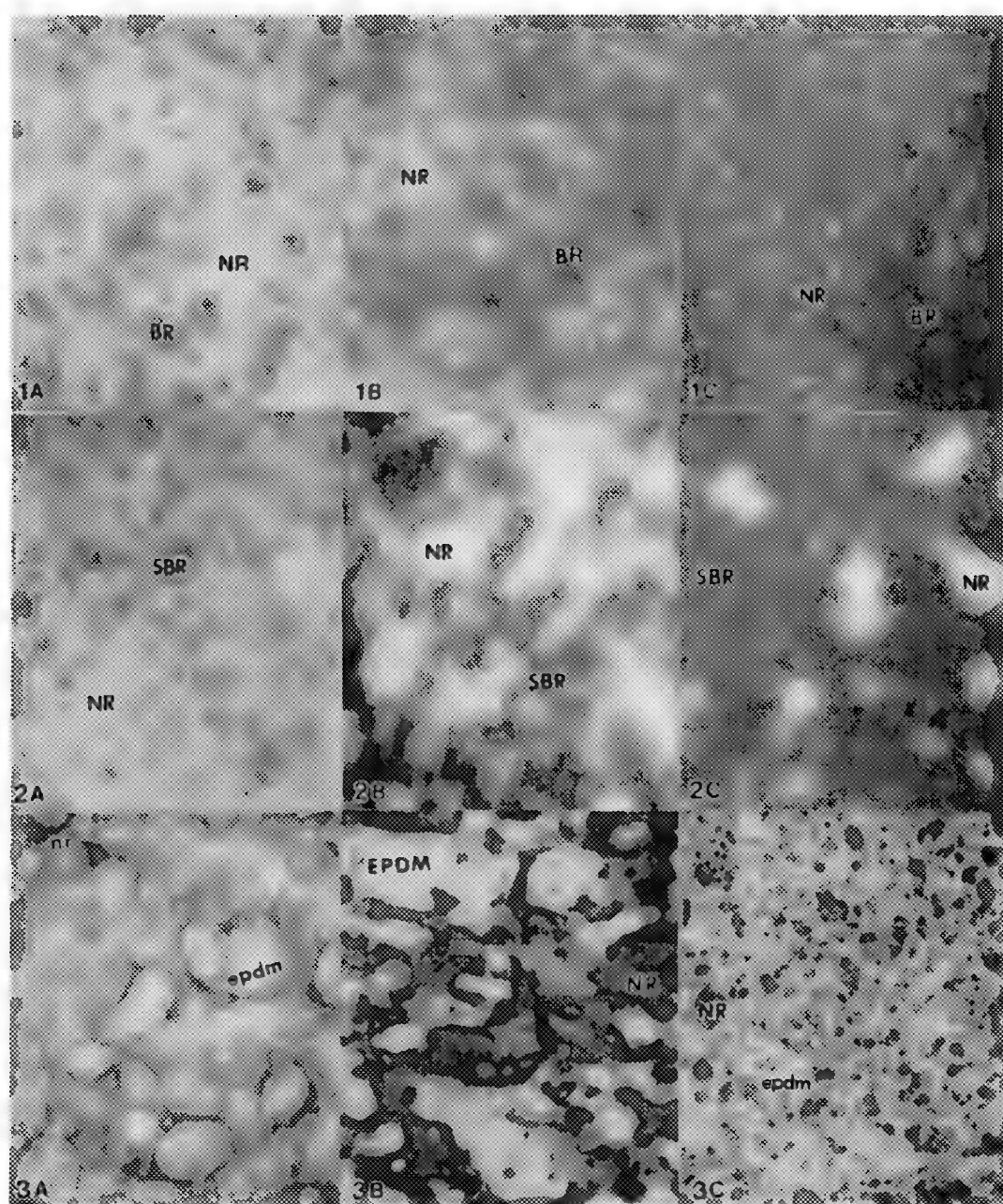
Fig. 1: NR/BR   :80/20(A) ; NR/BR   :50/50(B) ; NR/BR   :20/80(C)
Fig. 2: NR/SBR :80/20(A) ; NR/SBR :50/50(B) ; NR/SBR :20/80(C)
Fig. 3: NR/EPDM:80/20(A) ; NR/EPDM:50/50(B) ; NR/EPDM:20/80(C)

1.0μm

ION THINNING OF TEM CROSS SECTIONS UNDER BEAM SWITCHING CONTROL

R. Alani, R.G. Harper and P.R. Swann

Gatan Research and Development, 6678 Owens Drive, Pleasanton, CA 94588

Ion milled, cross sectional TEM specimens are used extensively to study the microstructure of multilayered materials. Unfortunately, it is difficult to get all the layers in a cross section equally electron transparent because usually they mill at different rates and have different atomic numbers. Differential thinning can be minimized by milling at low angles so that the slow milling layers protect the fast milling layers from the ion beam[1]. However, even at low angles uneven milling can still occur when the ion beam travels along the multilayer interface (glue line). This problem can be partially overcome by using a shield to cut off the ion beam in these directions[2]. However, this solution is not completely satisfactory because material sputtered from the edge of the shield can contaminate the specimen. A better solution[3], is to rock the specimen over a range of angles while the ion beam is centered approximately about the perpendicular to the glue line. With this method there is a possibility of uneven milling at both ends of the rocking angle where the beam is stationary for a short period during the change in direction of specimen rotation. Another solution, which is reported here, is to rotate the specimen continuously in the normal way and to switch off the ion beam as it passes by along the specimen glue line.

The Gatan precision ion polishing system (PIPS™) was chosen as a base instrument for testing the beam switching control, because its ion guns are able to deliver stable ion beams after passing through rapid on/off cycles. The design, construction and performance of the PIPS™ which is a dedicated low angle (4°) ion milling unit with high thinning rate, has been described elsewhere[4]. The experimental system consists of a sector speed control which rotates the specimen at two different angular speeds: 1 rpm to 6 rpm (adjustable) for the slow sector and 12 rpm for the fast sector and an electronically controlled switch which turns the ion beam on or off almost instantly at selected angular positions in the specimen rotation cycle. The sector speed control is programmed so that specimens always come to rest in the same orientation when they are raised into the airlock position. This feature allows the glue line to be oriented correctly with respect to the ion beam switching device when the specimen is lowered into the working position.

In order to determine the thinning capabilities of the new beam switching system, a multilayered Si based wafer was mounted in G1 epoxy, cross sectioned and dimpled to <5μm thickness and ion polished in the PIPS™ on a single side specimen post using one ion gun at 5KeV. The milling angle was 4°, the slow and fast sector speeds were 2rpm and 12 rpm, respectively and the angular range of the slow (beam on) sector perpendicular to the glue line was 60°. The specimen surfaces were milled sequentially under beam switching control. The total milling time was about 30 minutes. Fig. 1 shows a TEM micrograph of the ion polished specimen taken at 120 KeV. It can be seen that under beam switching control all the layers (a thick tungsten-titanium nitride layer sandwiched between two thinner layers of tungsten-titanium alloys) are electron transparent. These layers have much slower thinning rates than Si substrate and the G1 epoxy, as well as having much higher atomic numbers. All the regions including the G1 epoxy and the Si substrate are labeled.

References

1. R. Alani, J.S. Jones and P.R. Swann, MRS Symposium Proceedings Vol. 119, 85, (1990)
2. U. Helmersson and J.E. Sundgren, J. Elec. Micr. Tech. Vol.4, 361 (1986)
3. F. Shaapur and K.A. Watson, Proc. on Symposium W, MRS Fall Meeting (1991), to be published
4. R. Alani and P.R. Swann, Proc. on Symposium W, MRS Fall Meeting (1991), to be published
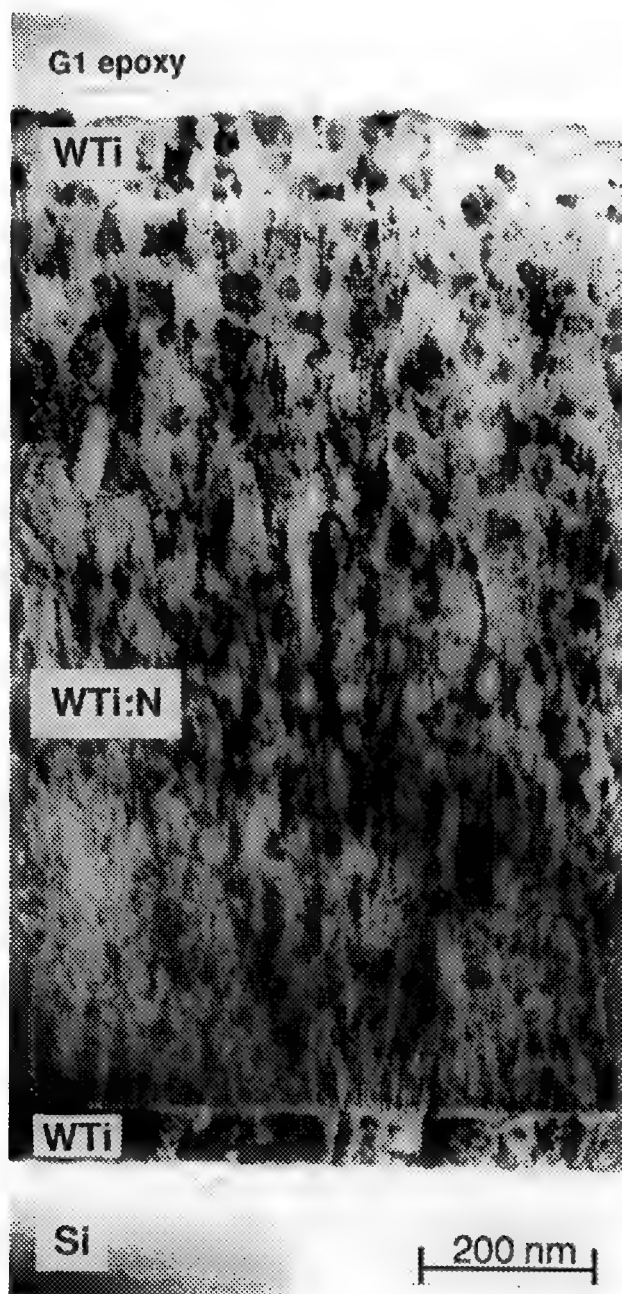
Figure 1. TEM image of a cross section through WTi/WTi:N/WTi layers on a Si wafer. Uniform thinning was achieved by ion milling at low angles in the PIPS™ under beam switching control.

EFFECTS OF ARGON ION SPUTTERING ON ZIRCONIUM AND TITANIUM

G.J.C. Carpenter*, J.A. Jackman* and J. McCaffrey**

*Metals Technology Laboratory, CANMET, 568 Booth St., OTTAWA, Canada K1A 0G1
**Division of Microstructural Sciences, NRC, OTTAWA, Canada K1A 0R8

Argon ion sputtering is widely used in the final thinning stage for the preparation of thin foils for transmission electron microscopy. During a recent study of a titanium alloy, we observed that ion-beam thinning resulted in specimens that appeared in the electron microscope to have become severely damaged. Similar microstructures had been observed previously in zirconium, thinned in this manner [1]. Because ion-beam sputtering takes place on the atomic scale, it seemed unlikely that gross distortion of a thin foil could have been caused *directly* by the sputtering process. A more detailed study has therefore been made of this phenomenon.

The materials used were zirconium of iodide purity and a Ti-6%Al-4%V alloy, both in the annealed condition. The intrinsic microstructures were examined in thin foils prepared by jet electropolishing. Specimens for ion thinning were first dimpled by jet electropolishing to a thickness of ~20µm at the centre of each 3mm disc. Argon-ion thinning to perforation was carried out in the following systems: (a) an Ion Tech Microlap Mark 2, operated with gun angles of 15° and (finally) 12°, and (b) an MFKI (Hungary) thinning unit, used with a retarding field on the specimen, giving an effective beam angle of ~4°. The microstructures of the electropolished specimens were typical of annealed Zr and Ti-Al-V, with a low dislocation density. Some needle-shaped γ-zirconium hydrides, 1~3µm in length, were present in the zirconium specimens, whilst the Ti alloy consisted mainly of the α-phase, together with smaller grains of the β-phase.

In the case of the ion-milled Zr, the degree of specimen damage depended upon which sputtering unit was used. With the Ion Tech unit, a "blister" appeared in the centre of the 3mm disc prior to perforation. The height of the blister was observed to increase to ~200µm by the time perforation occured. Examination in the TEM revealed a highly defected microstructure, containing a very high density of dislocations (fig. 1a) and, occasionally, fine twins. It was surmised that such a large strain might be caused by the accumulation of hydrogen in the specimen, because hydride formation occurs with a substantial volume increase and hydrogen is the only element that can diffuse over distances of tens of micrometers at relatively low temperatures. The presence of significant hydrogen was readily shown using SIMS. PEELS spectra, obtained from random areas of the specimen, showed that the first plasmon peak occurred at an anergy, $E_p=19.5(+/-0.1)eV$ (fig.1b), consistent with the ε-hydride[2], which is found at the hydrogen-rich side of the phase diagram. This conclusion was confirmed using convergent beam microdiffraction.

In contrast, the specimen thinned in the MFKI unit showed no visible evidence for blister formation and appeared to have thinned normally. However, TEM examination showed that significant changes had in fact occurred, such that a lenticular phase was present and the matrix contained a high dislocation density (fig. 1c) and occasional fine-scale twinning. EELS spectra from the lenticular phase gave $E_p=18.2eV$ (fig.1d), consistent with the γ-hydride[3]. The Ti alloy was substantially more resistant to hydrogen absorption: the Ion Tech specimen contained a high dislocation density plus occasional lathes of γ-hydride, whilst that thinned in the MKFI unit was relatively undamaged.

Two mechanism are suggested by which Zr and Ti could absorb hydrogen during ion-beam sputtering. It is possible that hydrogen or moisture in the vacuum chamber is absorbed onto what is essentially a clean and reactive specimen surface and dissolves more rapidly than it is removed by the sputtering process. Alternatively, hydrogen or moisture may be present as impurities in the argon-ion beam, so that energetic hydrogen or hydrogen-containing ions may be implanted below the surface, diffusing into the bulk to form hydride. Certainly, the chemical affinity between Zr or Ti and hydrogen is strong and the diffusion rate of hydrogen in these metals is high, particularly as some beam heating probably occurs. A marked difference in microstructures was observed for the two thinning units, using nominally the same purity argon and similar pumping systems. It appears that the lower hydrogen absorption in the case of the MFKI unit may be related to the grazing angle

of incidence of the ion beam, which results in a more shallow implant, or to its higher sputtering rate, which limits the time available for inward diffusion of the hydrogen.

References
1. E. Silva, J.W. Robinson and D.O.Northwood, Proc. The Microscopical Society of Canada, Ed. J.R. Parsons (Imperial Press, Canada, 1983) 56.
2. O.T. Woo and G.J.C. Carpenter, submitted for publication.
3. O.T. Woo and G.J.C. Carpenter, Scripta Met. 20 (1986) 423.
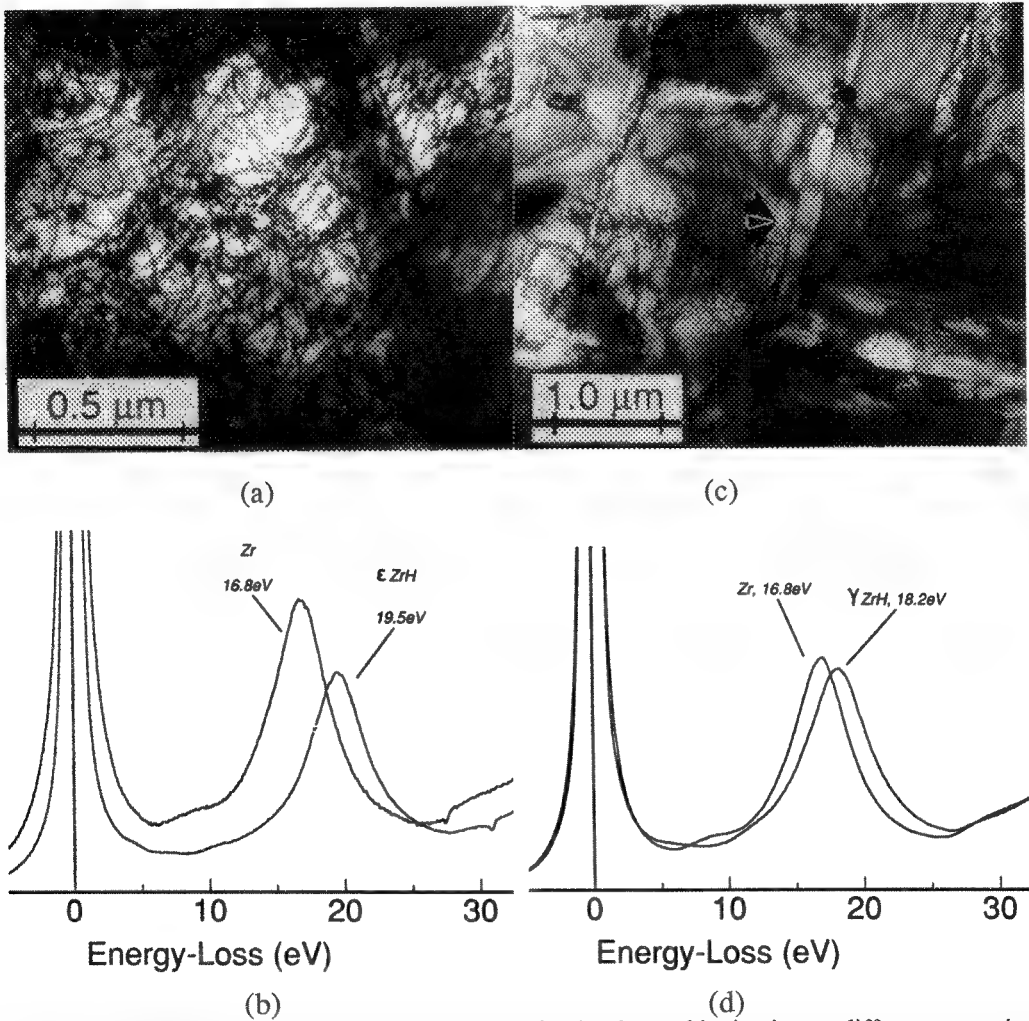
Figure 1. Microstructures observed in zirconium, after ion-beam thinning in two different sputtering systems, together with hydride analyses using the first plasmon peaks from PEELS spectra; (a) and (b) Ion Tech Microlap Mk. 2, (c) and (d) the MFKI unit.

OBSERVATIONS ON THE PRECIPITATES IN STEELS BY EXTRACTION REPLICA TECHNIQUE USING THE POTENTIOSTATIC ETCHING METHOD WITH A NON-AQUEOUS ELECTROLYTE

Shin-hwa Park, Ki-hwan Kim, Byung-ryang An

Technical Service Center, Research Institute of Industrial Science and Technology, Pohong P.O. Box 135, South Korea

Quantitative analysis of the precipitates of the steel is necessary in order to improve mechanical properties of the steel, because the precipitates in steels play an important role on the grain growth, recrystallization, and precipitation hardening. Recently, in-situ scanning electron microscope(SEM) observations on the precipitates with potentiostatic etching method in non-aqueous electrolyte have been reported.[1-2] We applied the potentiostatic etching method for the preparation of the extraction replica.

The potential-current curves of various standard compounds such as TiC, TiN, B_4C, BN, VC, VN, and NbN were obtained with potentiostat in the 10%Acetylacetone-1%Tetramethylammonium-chloride-Methanol(10% AA) solution. We also observed the potential-current curves of commercial steels(3% Si-steel and stainless steel) and the residues exracted from 3% Si-steel. The samples(mixture of 30mg of standard compound and 100mg of carbon electric conductive paint) were painted on a platinum plate. The plate was used as an anode for the measurement of the potential-current curve.[3] The extraction replica was prepared as usual.[4] To separate precipitates from the matrix the suitable potential of the first and second etching was selected from the potential-current curves. The phase of the standard compounds was identified by X-ray diffraction analysis. The result of the 3% Si-steel prepared in a non-aqueous solution was compared with the ones obtained in an acid(2% Nital) and in an aqueous(5%Sodiumcitrate-1%KBr-0.5%KI-H_2O) solution.

As shown in Figure 1 steel samples were dissolved under -50mV with respect to saturated calomel electrode(SCE) in 10% AA. While most of compounds in precipitates were dissolved over +400mV with respect to SCE. Therefore, there was a wide range of potentials in 10% AA, at which the matrices were electrolyzed but the precipitates were not. The results from the 3% Si-steel with different etching solutions are as follows: The sulfides were dissolved partially in the 2% Nital(Figure 2). The large artifacts were introduced in the replica when the 5%Sodiumcitrate-1%KBr-0.5%KI-H_2O solution was used(Figure 3). On the other hand a clean replica was obtained in 10% AA(Figure 4). Being applied the potentiostatic etching method to the large precipitates in a stainless steel, we could get a good replica for transmission electron microscpoe(TEM) observation. Results are shown in Figure 5 and 6. In Figure 5, the coarse TiN precipitates larger than 5μm formed from the melt of stainless steel could be obtained by this method. Large M_2C and $M_{23}C_6$ precipitates on a grain boundary were also identified in Figure 6.

References

1. J. J. Lee, S. W. Jung, D. H. Lee, Research Report, 0148A, Research Institute of Science and Technology, (1991), 1.
2. F. Kurosawa and M. Saeki, J. of the Iron and Steel Inst. of Japan, (1990)4, 43.
3. O. Kammori, I. Taguchi and A. Ono, J. of the Japan Inst. Metals, (1969)33, 403.
4. P. J. Goodhew, " Thin foil preparation for electron microscopy", Ed. A. M. Glauret, Elsvier, Amsterdam, (1985), 159.
5. This research was supported by a grant from the RIST, Pohang, Korea, No. 1154H.
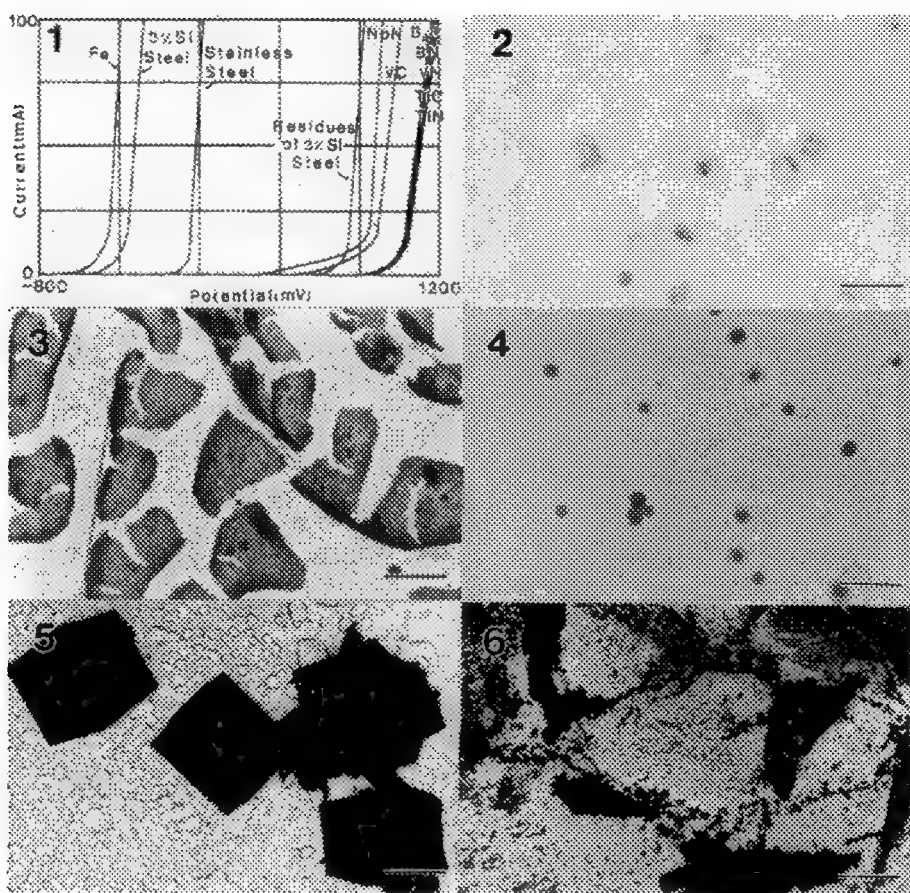
Figure 1. Potential-current curves of steels, the residue of 3% Si-steel, and various standard compounds in 10% AA solution.

Figure 2. Carbon extraction replica showing that the sulfide precipitates of 3% Si-steel were partially dissolved in 2% Nital solution. Bar=0.2μm.

Figure 3. Carbon extraction replica showing large artifacts introduced during sample preparation in 5%Sodiumcitrate-1%KBr-0.5%KI-H₂O solution. Bar=2μm.

Figure 4. Carbon extraction replica obtained in 10% AA solution without any defects. Bar=0.2μm.

Figure 5. Carbon extraction replica of large TiN precipitates formed from the melt of stainless steel. Specimen prepared in 10% AA solution. Bar=2μm.

Figure 6. Carbon extraction replica of large M₂C and M₂₃C₆ on the grain boundary of stainless steel. Specimen prepared in 10% AA solution. Bar=5μm.

PREPARATION AND EXAMINATION OF Y-BA-CU-O WIRE SECTIONS

A. Zanota*, D. Perry*, E.P. Kvam*, D. Balkin [†], and P. McGinn[†]

*Materials Engineering, Purdue University, West Lafayette, IN 47907
[†]Center for Materials Science, Electrical Engineering, University of Notre Dame, Notre Dame, IN 46556

The electrical properties of directionally solidified $YBa_2Cu_3O_7$ wires have been shown to be as good as or better than any other bulk-form materials in many situations.[1] However, the microstructural defects, including subgrain, stacking fault, and dislocation contents of these materials have not been well-characterized, in part because of the difficulty of preparing specimens for TEM examination.

A new technique has been developed to prepare these wires for TEM examination. The wires were less then .7mm in diameter, making handling of cross-sections difficult. Further, adhesion of evaporated films, electroplated films,[2] and epoxies to the wires was so poor that the wire sections would either shed the films completely, or fall out of the epoxy even when several hundred microns thick. To avoid this problem, a coating technique which adhered tightly to the wire surface was needed.

The solution which was devised was to rapidly immerse the wires into an Al - 30% Cu eutectic alloy melt at temperatures of 520 to 550°C. Each immersion step involved manually plunging the wire into the melt, then rapidly retracting it to be cooled. The process was repeated sequentially to build up a total diameter of 2.5-3.0mm, typically requiring 7 to 12 immersions. The total time at the melt temperature was thus about 10 seconds.

This process resulted in a good bond between the wire and embedding matrix, presumably aided by reactions occurring at the melt/wire interface. The samples could readily be handled for preparation for examination in either transverse or longitudinal cross section. Preparation steps began with sectioning on a diamond saw, and grinding to about 200μm. One face was then flat-polished, and that face epoxied onto a Cu grid. Dimpling proceeded from the opposite face until the wire was 5 to 15μm thick, at which point final preparation for TEM was done by Ar-ion milling with LN2 cooling. Typical conditions were to begin at 6keV and 18° tilt, and finish at 3-4keV and 10° tilt. The only problems encountered in the entire process were at the ion milling stage. The metal was observed to mill much more rapidly than the wire, and gaps gradually opened between the metal and wire. However, even when these existed at over 70% of the interface, the bond held together. This problem was circumvented by adding epoxy 'dots' at the interface once gaps began to appear.

Figure 1 illustrates an embedded wire (1a) and a dimpled specimen of approximately 5-10μm (1b). Most notable is the fact that the wire/matrix bond, although the wire is partially broken and with a significant portion of the metal matrix lost during dimpling, is still intact.

The microstructures of the wires have not yet been fully characterized. Figure 2 is from the transverse cross section shown above, and illustrates some of the significant features observed. First, the dominant structure on a TEM scale of observation is the subgrain structure of about 2 to 5μm width in the **c** direction. The adjacent platelets were seen to have slight misalignments, and the interface between them was very near the common (001) surface. These platelets, and the corresponding selected area diffraction pattern, are shown in 2 (a) and (b), viewed nearly along <100> / <010>. Also visible in the images is a wide grain boundary region, presumably of Cu-O. Within the platelets can be seen fringe images resulting from {110} twinning, and (001) stacking faults of the 1/6[031] type. Further investigations in these materials are underway to fully characterize the microstructural aspects of these and other directionally solidified wires.

References
1. P. McGinn, W. Chen, N. Zhu, L. Tan, C. Varansi, and S. Sengupta, Appl. Phys. Lett., 59(1) (1991) p.120
2. T.F. Kelly, M.R. Libera, and J.B. VanderSande, MRS Symp. Proc. Vol. 115 (1987) p.205
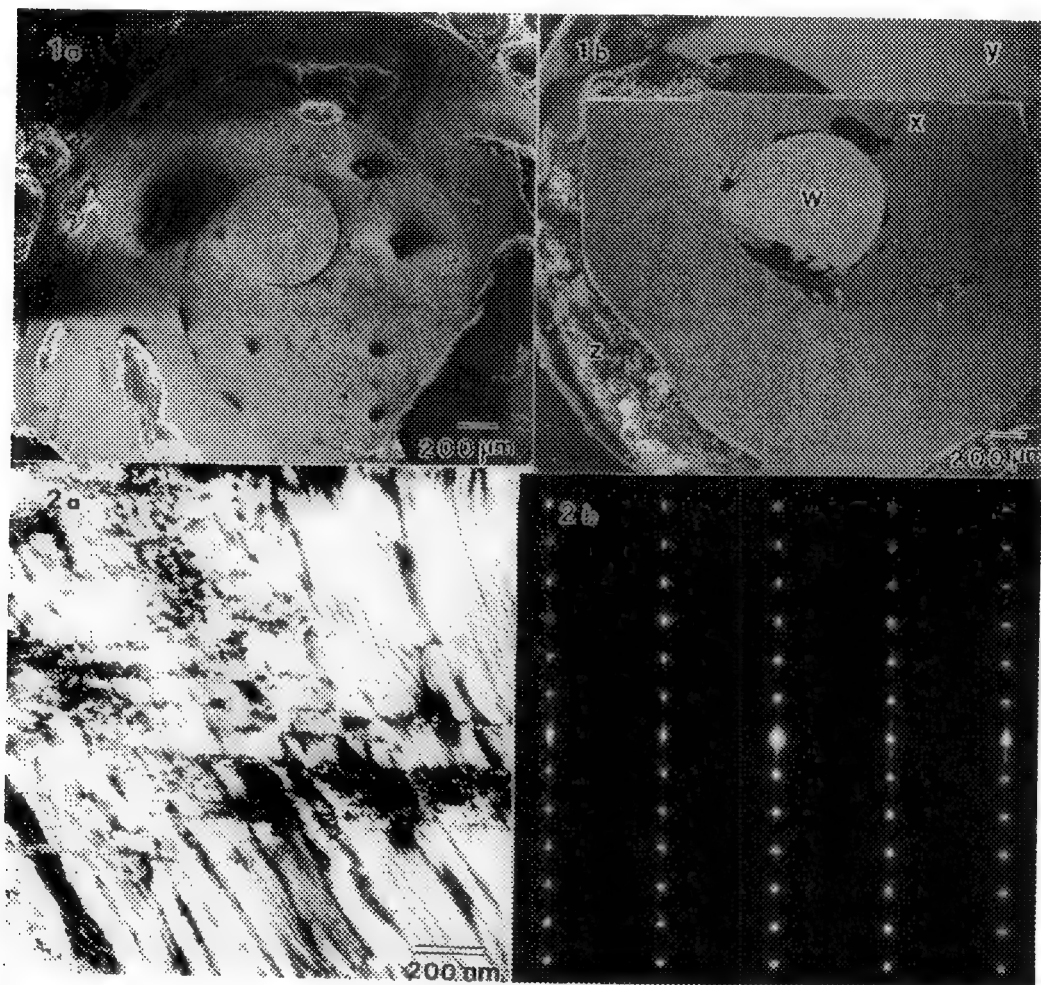
FIG. 1 Cross-Section SEM of $YBa_2Cu_3O_7$; (a) 0.54mm wire after embedding and sectioning, and (b) 0.69mm wire approximately 5-10μm thick ready for milling; w: wire; x: Al-Cu alloy; y:grid; z: epoxy.
FIG. 2 Cross-Section TEM of $YBa_2Cu_3O_7$; (a) platelets showing microstructural defects, and (b) TEM diffraction pattern along <100> / <010> from area shown in 2(a).

CROSS-SECTION TEM SAMPLE PREPARATION OF Ti-6Al-4V / SCS6 (SiC) FIBER–REINFORCED COMPOSITES

Warren J. Moberly* and Scott Apt**

*Department of Materials Science & Engineering, Stevens Institute of Technology, Hoboken, NJ 07030
**UES, Air Force Materials Laboratory, WRDC/MLLM, Wright-Patterson AFB, OH 45433-6533

Titanium-based metal matrix composites (MMC) and titanium aluminide intermetallic matrix composites (IMC) have been selected for future aerospace structural applications. The mechanical integrity of these composites are dictated by the thermodynamic stability of the fiber / matrix interface and deformation that occurs at the interface. The thermal processing incurred during hot-isostatic-pressing (HIP) results in the formation of intermetallic phases, with detrimental mechanical properties, at the interface [1, 2]. In addition, the thermal processing results in residual stresses due to the mismatch in coefficient of thermal expansion (CTE) between the Ti-based matrix and the SiC fiber. In some cases the thermal stresses are sufficient to cause yielding in the matrix, and/or lead to fatigue from the thermal cycling that will be incurred during application [3].

The continuous-fiber-reinforced composites considered in this study have been acoustically monitored during tensile deformation in order to determine when (and how many) fiber fragmentation occurs [4]. X-ray photographs acquired after deformation help locate where the individual fiber fragmentation events occur. One goal of this TEM analysis is to observe the constrained deformation that occurs in the matrix region surrounding a fractured fiber as a consequence of load transfer. (Other results of the deformation at the interfaces of these composites are discussed in a separate paper presented at this EMSA conference and in additional reports [5].)

Since it is desirable to measure the extent of deformation present in the composite, TEM sample preparation must not allow for artifacts in measuring dislocation densities. High voltage electron microscopy is used to observe thicker samples and ascertain that dislocations are not lost to free surfaces in the TEM thin foil. TEM samples have been acquired by first cross-sectioning the composite with a diamond saw. Samples are subsequently ground to a thickness of 0.15 to 0.2 mm, using 600 grit SiC grinding paper for a final finish. Due to the SiC fibers resistance to grinding, as compared to the Ti-Al matrix, the TEM sample must be polished flat using diamond paste and a flat dimpling wheel. A round dimpling wheel and 1 μm diamond paste is then used to produced a local dimple in the TEM sample [6]. Selective location of the dimple enables particular regions of the interface to be studied. When the dimpled region is less than 25 μm thick, it is possible to transmit visible light (red) through the outer crystalline regions of the chemically-vapor-deposited SiC fibers (see FIG.1). If a fiber fragmentation event has occurred within the cross-section of the TEM sample, then such a fracture will be visible with this transmitted illumination. Since the tensile specimens pulled to 19% elongation undergo hundreds of fiber fragmentation events, the statistical chance of sectioning through a fracture is quite reasonable. These TEM cross-section samples should not be dimpled to a thickness below 10 -15 μm (where yellow light is transmitted through the SiC fibers) as the fibers will then be subject to being pushed out of the matrix. During ion milling the crystalline regions of the SiC fibers and the Ti-Al matrix etch at a faster rate than the intermetallic phases (titanium carbide and titanium silicide) that exist at the interface. Thus it is possible to produce TEM samples which have been thinned to electron transparency in the α Ti grains which neighbor much of the circumference of a fiber (see FIG.2). It is also possible to produce thin area for TEM imaging (especially for HVEM imaging) in all matrix grains that exist between closely spaced fibers (see FIG.5).

Although most reports of interfacial reactions between Ti alloys and SiC have indicated the formation of titanium silicide as well as titanium carbide [1, 2, 7], many regions of the interfaces in these composites had no Ti-Si layer. When the titanium silicide layer is present, electron diffraction characterized it as having a hexagonal structure. In addition, these results exhibit different relative sizes of the titanium silicide and titanium carbide grains, as well as the relative thicknesses of each layer, as compared to other researchers. Overall, the extent of intermetallic phase formation at the interfaces of these composites is less than has been reported, possibly as a result of a lower HIPing temperature.

References
1. C. G. Rhodes & R.S. Spurling, *Recent Advances in Composites*, ASTM, Philadelphia, 1985, p.585.
2. E. L. Hall, A. M. Ritter & N. Lewis, *General Electric Technical Report* #90CRD173, (1990).
3. G. S. Daehn & G. Gonzalez-Doncel, Metall. Trans., 1989, 20A, p.235.
4. I. Roman & S. Krishnamurthy, in preparation.
5. W. J. Moberly, AFOSR-SFRP report published by Research Development Corporation, 1991.
6. J. C. Bravman & R. Sinclair, J. Electron Microsc. Tech., 1984, 1, p.53.
7. Jones, C., C. J. Kiely & S. S. Wang, J. Mater. Res.,1989, 4, p.327-335.
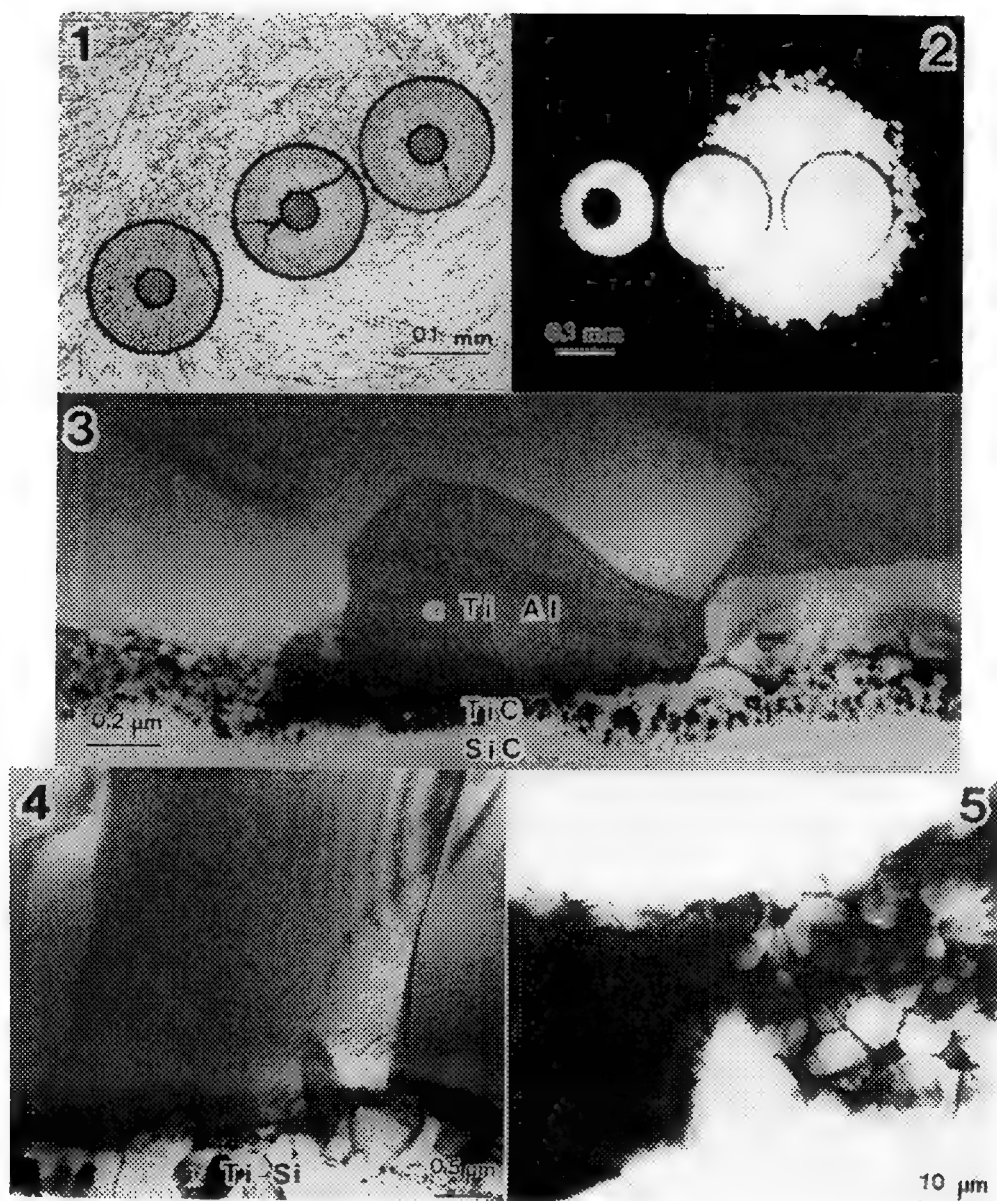
FIG.1.--Optical micrograph acquired with transmitted and reflected illumination, of cross-sectioned and partially-dimpled TEM sample from Ti-6Al-4V / SiC fiber-reinforced composite. The cracks in the SiC fibers are indicative of fiber-fragmentation having occurred during 19% tensile elongation of composite. FIG.2.--Optical micrograph (transmitted illumination) of TEM cross-section composite sample after ion milling. The interface region has been thinned to electron transparency, and the SiC fiber and surrounding Ti matrix has been removed. FIG.3.--TEM bright field micrograph of interface region of composite, depicting α grains of Ti alloy abutting fine TiC grains which formed during hot-isostatic-pressing (@ 1200°C). FIG.4.--TEM BF micrograph of composite interface region which includes more typical titanium silicide grains between TiC layer and α Ti grains of matrix. FIG.5.--TEM BF micrograph of matrix α grains (and β phase along grain boundaries) between fibers, after 1/2% tensile deformation.

TEM SAMPLE PREPARATION OF TRANSPARENT POLYCRYSTALLINE ALUMINA: CORRELATION BETWEEN OPTICAL MICROSCOPY AND TEM IMAGES

K.J. Ostreicher and C.M. Sung
GTE Laboratories Incorporated, 40 Sylvan Road, Waltham, MA 02254

Since the discovery of the Lucalox process, a considerable amount of research effort has been devoted to locating both impurities and additives in transparent polycrystalline alumina (PCA). The control of grain growth and porosity by introducing dopants such as MgO and Y_2O_3 has been shown to directly affect the strength and transmittance properties of the material[1,2]. The presence of impurities or dopants in excess of their solubility limits leads to precipitation in the bulk and along grain boundaries. It is essential that TEM sample preparation be controlled so as not to introduce damage or pull-out of second phases as artifacts. Since optical microscopy is readily adaptable to monitoring the mechanical preparation of materials it becomes a good method to obtain information concerning grain size and shape, grain orientation relationships, and porosity[3]. The purpose of this study is to describe such a sample preparation process and demonstrate its usefulness in allowing effective correlation of optical microscopy and TEM results.

Bright-field, dark-field and differential interference contrast are used to determine the amount of material removal necessary to eliminate damage from preceding steps. Samples are mounted in a fixture such as the Acustop* which maintains surface flatness and allows for calibrated removal of material. The mechanical preparation can be summarized as follows: i) A 20 μm diamond-resin bonded wheel is used with water to flatten the sample surface; ii) 6 μm diamond dispersed onto a Petrodisc* and lubricated with DP-Lubricant Blue* is used to remove 40 μm of material as determined by optical microscopy; iii) 3 μm diamond on a Pellon (Pan-W) cloth is used with DP-Lubricant Blue to remove 15-20 μm of material; iv) 1 μm diamond on a Pellon cloth is used with DP-Lubricant Blue to remove 10 μm of material; v) 1 or 0.5 μm diamond on a DP-Nap cloth is used to final polish the sample for 1 minute using DP-Lubricant Red*. A typical PCA surface after 20 μm grinding and final 1 μm polishing is shown in Figures 1a-1b. The remaining side of a 3 mm disc is prepared by grinding with 3 μm diamond on a phosphor/bronze dimpling wheel followed by polishing using 1 μm diamond on a Pellon cloth covered wheel and final polishing using 1 μm diamond on a DP-Nap covered wheel. At the completion of these steps the sample is ≈5 μm thick. Final thinning is performed using dual Ar+ ion milling (15° incidence, 5 kV, 0.5 mA/gun). Energy dispersive X-ray spectroscopy (EDXS) analyses were performed using a Philips 400T STEM: accelerating voltage of 120 keV, sample tilt of 12°, and 20% dead time. Backscattered electron (BSE) images were obtained at 40 keV using a STEM unit .

PCA materials which have been prepared using the above procedure were analyzed using optical microscopy to investigate grain size, porosity, and possible second phases since these features are enhanced as a result of milling. In principle, the presence of grain boundaries in anisotropic materials can be recognized using crossed polarized light due to the contrast between grain orientations. Dark field optical microscopy was useful for displaying porosity, Figure 2. Areas analyzed by optical microscopy were examined and compared using AEM. Such a correlation of an optical dark-field image to BSE and bright-field images is shown in Figures 3a-3c. EDXS and convergent beam electron diffraction patterns were used to confirm the presence of YAG phase (e.g. bright contrast in the BSE image, identified as "Y") and spinel $(MgAl_2O_4)$[4], identified as "S" in bright-field STEM image.

In summary, damage resulting from grinding/polishing process can be removed by use of the procedure outlined above which maintains sample flatness and allows for calibrated removal of damaged material. The process is efficient and assures consistently high quality results. The sample can be observed during the preparation and after ion milling by optical microscopy to obtain information regarding grain size and shape as well as porosity. It was often not possible to

distinguish pores from second phases (e.g. 1-0.5 μm in diameter) in the optical images and therefore TEM was used to examine and characterize the identical areas.

References

1. R.C. McCune, W.T. Donlon, and R.C. Ku, J. Am. Ceram. Soc., 69(1986), C-196.
2. J.G.J. Peelen, Materials Science Research, Plenum Press, vol. 10, 1975, p443.
3. M. Calvo, E. Gautier, and A. Simon, J. Mat. Sci., 26(1991), 1236.
4. C. Sung, K. Ostreicher, G. Wei, and W. Rhodes, Presented in ACers 93rd Annual Meeting, 1991.
* These items are products of Struers Inc.
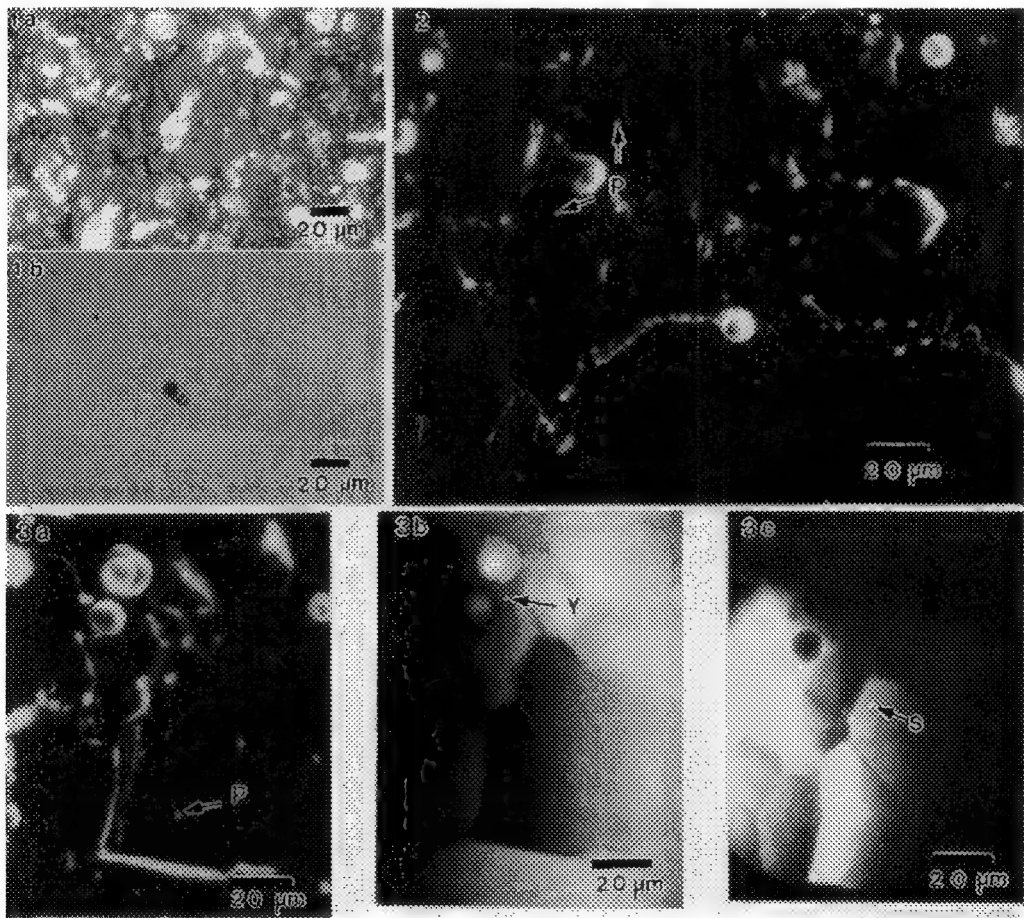
FIG. 1a. Reflected- polarized optical image of PCA after grinding with 20 μm diamond.
FIG. 1b. Reflected-polarized optical image of PCA after 1 μm diamond polish.
FIG. 2   Optical dark-field image of PCA showing pores "P".
FIG. 3   (a) Optical dark-field image, (b) BSE image, (c) BF-STEM, showing YAG (Y) and Spinel (S) phases as confirmed by EDXS and CBED.

QUANTITATIVE MEASUREMENT OF SURFACE ROUGHNESS OF TEM SPECIMENS

J. Zhang, K.H. Olsen and K.A. Schoessow

Memory Technology Group Laboratories, 3M Company, St. Paul MN 55144

The thickness and the local thickness variation of thin film specimens are critical parameters for many types of AEM analysis. The local thickness variation of the thin film specimen can be estimated from the surface roughness of the specimen. TEM specimens of most materials, especially multi-phase materials, have rough surfaces as observed by secondary electron imaging. However, there is little quantitative assessment of the surface roughness because of the difficulty of specimen thickness measurement. In this study, surface roughness of TEM specimens prepared using chemical etching, electropolishing, and ion beam thinning was measured using a direct phase detecting optical interferometer.[1,2] This interferometer gives a quantitative three dimensional map of the surface topography with a depth resolution of ~0.7 nm by converting digitized light intensity at each point of a 1024x1024 array into the optical path difference using the *three-measurement algorithm*.[3] The horizontal resolution of the interferometer (~340 nm) is limited by optical diffraction and is poor by the TEM standard. The quantitative information obtained by the interferometer is complimentary to the secondary electron imaging in STEM or FEG SEM for characterizing TEM specimen surfaces.

Fig. 1a is a grey scale 3-D perspective of the surface of a single crystal Si TEM sample. (The interferometer usually shows 2-D height contour and 3-D perspective using the thermal scale which gives a much clearer view of the surface topography.) The sample (3 mm diameter disc) was ion milled using a Gatan IBT at 5 kV with a 15° incident angle. A topography similar to fish-scales is observed on the surface. The typical peak-to-valley distance for this sample is about 70 nm. The line scans along the radius of the sample disc show saw-tooth shaped profiles with the steeper side of the teeth towards the center of the disc (see Fig. 1b). A SEM image of this sample is shown in Fig.2. The topography in the SEM image is identical to that observed optically. No fine structure can be seen on these fish-scales indicating a relatively smooth surface which provides very small contrast for secondary electron imaging. The surface topography described above is typical for ion beam thinned specimens. The Si sample ion milled with a 12° incident angle shows a similar surface topography. The Si specimens prepared by chemical etching have a smoother surface. Fig.3 is a 3-D perspective of a Si surface etched by a HF:HNO$_3$=1:20 solution. In this case, the typical P-V distance is less than 2 nm. However, the surface topography formed by chemical etching is sensitive to the crystal orientation, etching time, and initial smoothness of the surface.

Fig.4 shows a 3-D perspective of the surface of a Fe-15%Ni alloy specimen. Ni-rich precipitates of >100 nm wide are present in this alloy. The TEM specimen was electropolished using a double-jet polisher. Interferometry reveals small bumps about 30 nm higher than the average sample surface. The size and shape of these bumps suggest that they are the precipitates. A 3-D perspective of the surface of this sample after 1 hour ion milling is shown in Fig.5. The familiar fish-scales topography, with typical P-V distance of 50 nm, is again observed and the small bumps have disappeared.

In summary, a typical surface topography similar to fish-scales is observed in ion beam thinned specimens. The P-V distance is typically 50 to 100 nm for the normally used IBT conditions. For the Si and the Fe-Ni alloy specimens investigated, chemical etching and electropolishing yield a smoother surface than ion beam thinning.

References
1. C.L. Koliopoulos, Ph.D dissertation (1981) University of Arizona.
2. J.C. Wyant et al., Appl. Optics (1975)**14**,2622.
3. D.M. Perry et al., J. Inst. Electronic & Radio Eng. (1985)**55**, 145.
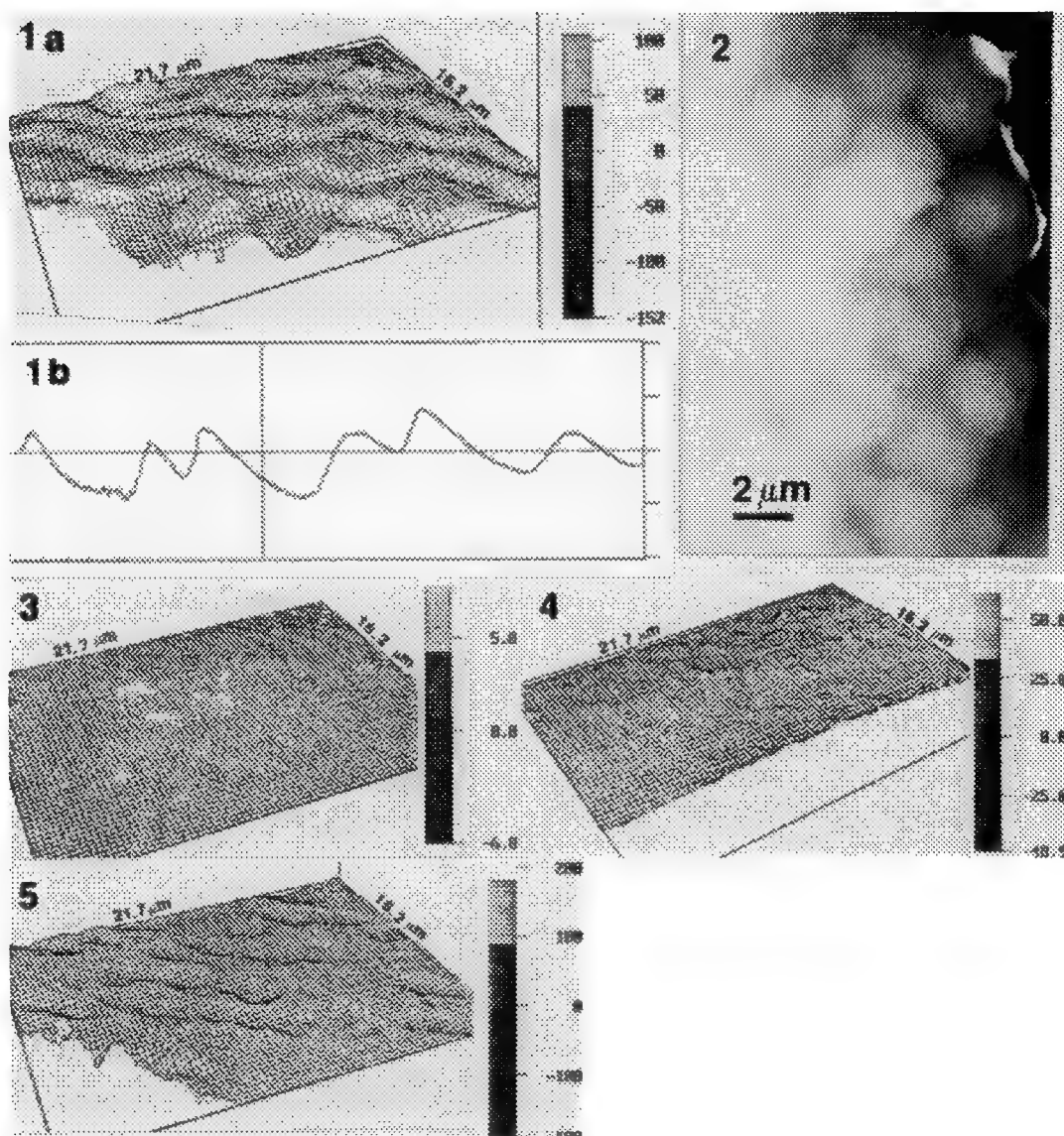
Fig.1 a) 3-D perspective of Si(100) surface ion milled at 5 kV and 15°. Lower left corner is hole at center of 3 mm disc. b) line scan from hole edge (left side) inward. Vertical scale -100 nm to 100 nm. Vertical scales in all other figures are in nm.

Fig.2 SEM secondary electron image of Si sample shown in Fig.1.

Fig.3 3-D perspective of Si(100) surface chemically etched.

Fig.4 3-D perspective of Fe-15%Ni alloy double-jet electropolished. Edge: lower right.

Fig.5 3-D perspective of Fe-15%Ni alloy first double-jet electropolished and then ion milled for one hour at 4 kV and 13°. Edge: lower left corner.

FREEZE-DRIED DISPERSIONS FOR AUTOMATED SCANNING ELECTRON MICROSCOPE ANALYSIS OF INDIVIDUAL SUBMICRON AIRBORNE PARTICULATES

Karen A. Katrinak, David W. Brekke, and John P. Hurley

Energy and Environmental Research Center, University of North Dakota, Grand Forks, North Dakota 58202-8213

Individual-particle analysis is well established as an alternative to bulk analysis of airborne particulates. It yields size and chemical data on a particle-by-particle basis, information that is critical in predicting the behavior of air pollutants. Individual-particle analysis is especially important for particles with diameter < 1 μm, because particles in this size range have a disproportionately large effect on atmospheric visibility and health.

Automated scanning electron microscopy allows hundreds to thousands of individual particles to be imaged and analyzed using energy-dispersive x-ray spectrometry and image analysis. A minimum of operator effort is required to achieve a statistically significant characterization of the sample. Submicron particles are difficult to analyze using automated techniques because their small size places them near the imaging and analytical detection limits of the conventional scanning electron microscope.

We have developed a sample preparation method to optimize the conditions for automated analysis of submicron particles. The method involves freeze-drying a small amount of dispersed particles onto a substrate of vitreous carbon. Vitreous carbon is used because its exceptionally smooth surface allows unambiguous identification of small particles. Freeze-drying allows a uniform separation of particles to be achieved.

Approximately 10 μg of particulate sample is suspended in 5 mL of purified propanol, to which a drop of dilute organic dispersant has been added. The propanol was first purified by filtration through a 0.05 μm-pore polycarbonate filter. The suspension is vibrated ultrasonically for ten minutes to break up any loosely attached particles. Two to five drops of the suspension are placed on a clean piece of vitreous carbon measuring 15 x 10 x 3 mm. The sample assemblage is lowered into liquid nitrogen to freeze the particles and propanol into place. After the sample has cooled completely, it is removed from the liquid nitrogen and placed on top of a brass disk measuring approximately 25 mm in diameter and 12 mm in height. The brass disk was previously cooled in liquid nitrogen and serves as a heat sink to prevent overly rapid thawing of the sample. The sample and brass disk are positioned in the bell jar of a vacuum evaporator unit. Thawing under vacuum allows the propanol to evaporate gradually from the sample while preserving a constant spacing between particles. A vacuum of approximately 0.07 Pa is maintained during thawing.

The sample appears dry after approximately 30 minutes, but must remain under vacuum for an additional 60 to 90 minutes to allow its temperature to rise sufficiently to prevent condensation upon removal from the chamber. After removal, samples are coated with a 20 nm-thick layer of vacuum-deposited carbon to improve conductivity.

The freeze-dry dispersion method was tested using size-fractionated coal fly ash samples. Inspection in the scanning electron microscope shows that many individual submicron particles are present (Fig. 1). In some instances several submicron particles are fused together to form aggregates (Fig. 2). Such aggregates are common in fly ash and probably form at elevated temperatures prior to emission.[1,2] It would not be desirable to break up these aggregates, as this would alter the size distribution of the original sample.

The freeze-dried dispersions are suitable for scanning electron microscope analysis. Low accelerating voltage (7 kV) is preferred to keep the excitation volume within the particles and to improve imaging. Secondary electron imaging and derived binary images are used to locate and measure the size of each particle. X-ray spectra acquired for 25 seconds at 300 pA are sufficient to identify the elemental composition of each particle. The use of a low accelerating voltage results in decreased detection efficiency for many metals but is sufficient for most fly ash samples. The size and chemical data together are useful in identification of particle types characteristic of the sample.

References

1. A. Hazrati, Surf. Interface Anal. 13 (1988) 142.
2. N. Kaufherr and D. Lichtman, Environ. Sci. Technol. 18 (1984) 544.
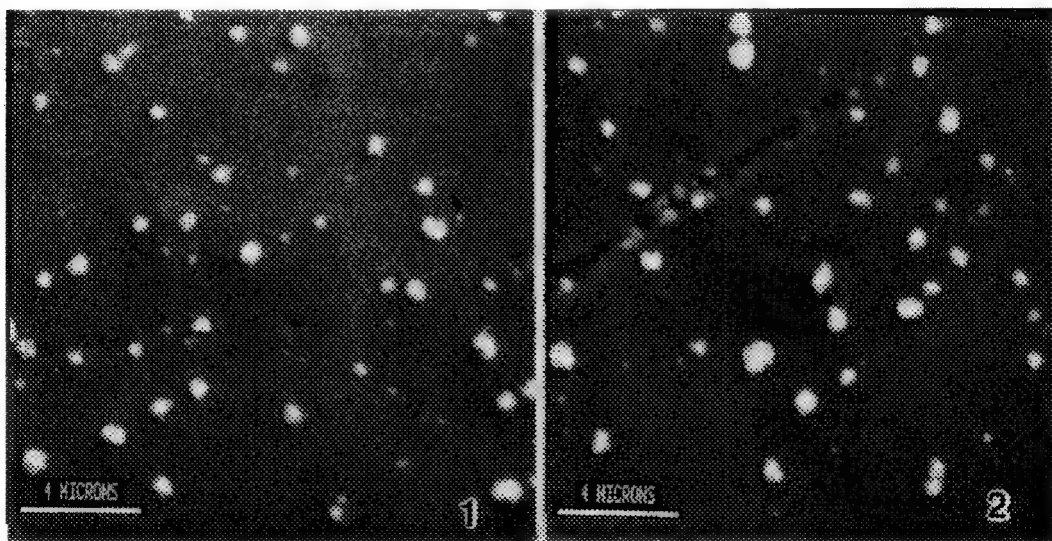
Fig. 1. Secondary electron image of freeze-dried dispersions showing numerous submicron particles. The particles are predominantly sodium sulfate.
Fig. 2. Secondary electron image of a different area in the same sample preparation, showing submicron and supermicron particles. The larger particles appear to be aggregates of submicron particles.

MOUNTING OF SPECIMENS FOR SEM WITH THE COMMON GLUE GUN

Leo Barish

Albany International Research Co., 777 West Street, Mansfield, Massachusetts 02048

Specimens are usually attached to SEM studs by means of either sticky tape, adhesives, or melts. The use of sticky tape is very convenient and fast; unfortunately, the bonds formed are not strong or stable. In addition, it is difficult to attach large, irregular shaped specimens with tape. Adhesives, usually solvent-based, can form strong bonds; however, for the satisfactory operation of the coater and the SEM, the solvent must be evaporated completely which can take considerable time.

Melt adhesives can set up strong bonds very quickly and there is available a commercial melt adhesive mounting kit; however, the procedure for its use is cumbersome. When using this kit, the adhesive is first melted onto thin aluminum plates, which are then cooled and placed aside. When ready for the attachment of the specimen, a plate is heated to remelt or soften the adhesive; the specimen is then adhered to the surface. After cooling, the plate with the attached specimen is clamped onto a special SEM stud.

Mounting with melts using the common glue gun is quicker and more convenient. The general procedure is very simple: the melt is extruded from the nozzle directly onto the surface of a stud. While the adhesive is still molten or soft, the specimen is applied to it, forming a strong bond very quickly. Because the melt hardens so quickly, it is feasible to hold and fix the specimen in the desired position without the need of clamping. If desired, the specimen can be easily repositioned by softening the adhesive with the hot nozzle of the glue gun.

Several glue gun adhesives were examined with FTIR; all appeared to be derivatives of a copolymer of polyethylene and polyvinyl acetate. The temperature at the nozzle of conventional glue guns was found to be 180-195°C which could cause damage to heat-sensitive specimens. Fortunately, there has recently become available so-called low temperature glue guns and adhesives; the nozzle temperature of one was measured at only 106°C. There has been no evidence found of degassing of the melt adhesives in either the sputter coater or the SEM.

A few examples in which the mounting specimen was expedited by use of the glue gun will be illustrated.

Large, irregularly shaped objects are often difficult to secure to studs. By use of the glue gun, a fragment of coral was mounted easily by holding it in the desired position in contact with a drop of molten adhesive (Figure 1).

A discontinuous, porous specimen can often be susceptible to charging even though it is heavily sputter coated. The path from the surface to ground can be so tortuous that conduction is inadequate and a charge can build up. Using melt adhesive, a smooth, direct path can be constructed over the walls of the specimen so that after sputter coating, a direct, conductive path is formed. Figure 2 shows a low density felt in which melt adhesive was formed around the walls, improving grounding.

The glue gun can also be used in mounting granular or powdered specimens. A drop or smear of melt adhesive is deposited onto a stud. The granular or powdered material is adhered to the adhesive by sprinkling or by being dipped. It is desirable that the particles should adhere well, but should not be submerged or depressed visibly below the surface of the adhesive. The degree of penetration of the particles can be controlled by the consistency of the adhesive. Figure 3 shows relatively large particles of sodium chloride which were mounted on adhesive which was quite molten. If very small particles were mounted in that way,

410

they would be submerged excessively. For such small particles, it is better to let the adhesive cool to the point in which it is hard but still slightly sticky. Such a cooled adhesive was used to mount cornstarch particles as shown in Figure 4.
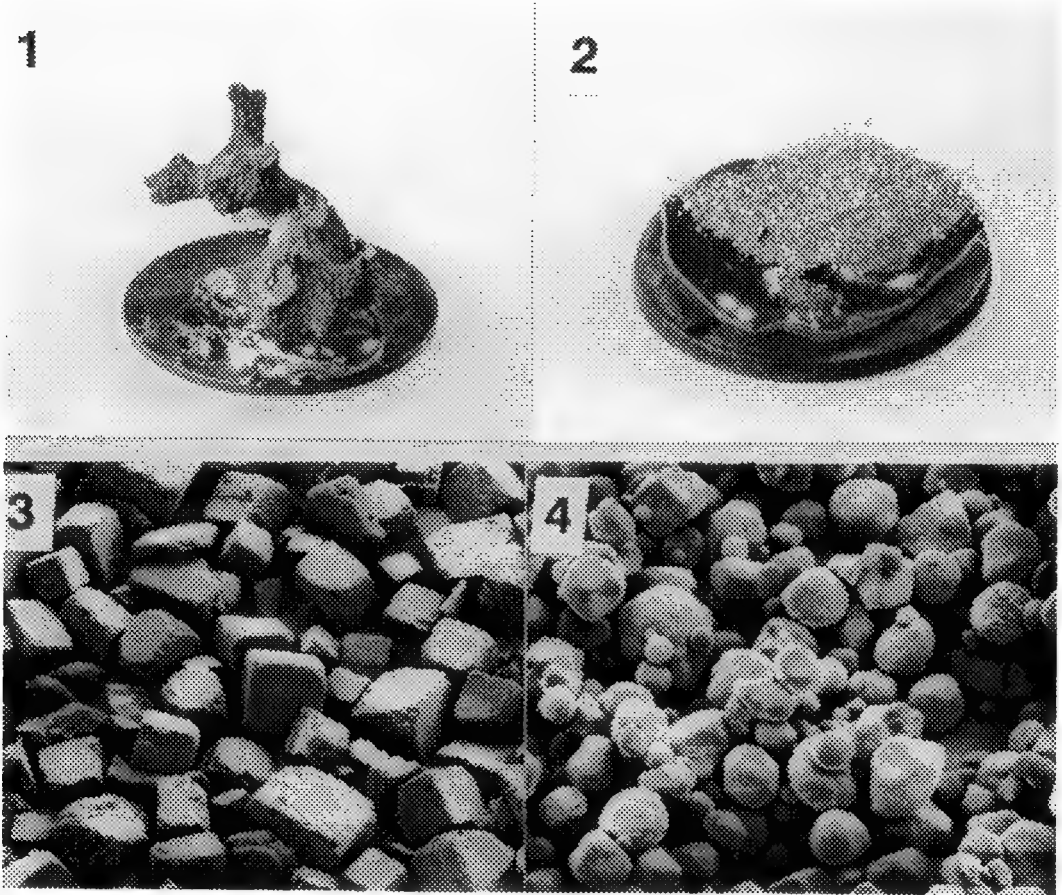
FIG 1.--Irregularly shaped coral mounted on stud with melt adhesive.

FIG 2.--Loose felt mounted on stud with walls of melt adhesive to minimize charging.

FIG 3.--Sodium chloride crystals mounted on highly molten melt adhesive.

FIG 4.--Cornstarch particles mounted on slightly sticky melt adhesive.

PROSPECTING FOR GOLD IN A VG STEM

G. L. Shoemaker, W. M. Sherman*, R. H. Duff, and D. R. Rothbard

BP Research, 4440 Warrensville Center Road, Cleveland, Ohio
* Now at Allied Signal Aerospace Co., South Bend, Indiana

A calcined pyritic gold ore concentrate was examined using both ion-milled and ultramicrotomed samples to determine the distribution of gold and the porosity of the matrix supporting the gold. Examinations of the same specimen prepared by different techniques yielded complementary information about the overall characteristics of the material.

Figure 1 is a secondary electron image (SEI) of a piece of roasted pyritic ore. The particles are highly porous with morphology suggesting that the iron pyrite (FeS_2) particles virtually exploded when labile sulfur was released during oxidative calcination. The particles produced by this process are not large enough to permit ordinary solid specimen preparation techniques. Therefore, a compacted bar of material was made by compressing the powder with a binder to form a disk which was subsequently impregnated with epoxy in a PARR bomb under isostatic pressure of a few thousand psi. From this dense material two types of specimen were prepared, one by diamond knife ultramicrotomy and the other by standard thin foil techniques. For the latter, the sample was sliced with a diamond saw, core-drilled into 3mm disks, polished to about 100μm, dimple ground, and Argon ion milled to perforation. This yielded specimens which show the porosity and connectivity of the iron oxide frameworks formed during calcination. Figure 2 is a 10,000X annular dark field (ADF) image of an ion-milled particle taken with a VG HB501 STEM. The channel structures evident in this image are easily related to the SEI image in Figure 1. Figure 3 is a 200,000X ADF image which illustrates the connectivity of individual iron oxide crystallites that form the skeletal structure. This sample was electron transparent only near the central perforation and did not have a large usable area. Also, the outer surfaces of the particles may have been milled away during specimen preparation and therefore it is not easy to determine where the remaining structures were located in the original particles.

A second sample was prepared by microtoming a piece of the compacted disk with a diamond knife ultramicrotome. Figure 4 shows a representative area of the microtomed sample with a section of most of one particle visible in the central area (and a grid bar on the right). In general, the microtomed sections provided a much larger thin area that could be searched for gold particles. Also, the outer boundaries of the particles are preserved with this technique. However, it is more difficult to visualize connectivity in the microtomed sections and to relate the images to SEI micrographs such as Figure 1 because the sections are randomly oriented, two dimensional slices through three dimensional networks.

With patience, several small particles of gold in the size range of 3 to 8nm were located on pieces of the iron oxide matrix in the microtomed sections. The search was aided by the Z-contrast characteristics of the ADF image. Particles were positively identified using ultrathin window EDS in the STEM. Figure 5 shows a 3nm gold particle on a piece of the iron oxide matrix. Figure 6 is an EDS spectrum from this particle. EDS mapping was not useful for locating gold particles primarily because large areas could not be searched in reasonable time periods. Bright field TEM or STEM images also were of limited value due to amplitude and phase contrast effects which confused the images. Overall, SIMS was the most reliable technique for locating general areas of gold concentration in polished cross sections[1], but SIMS spatial resolution was not good enough to image individual gold particles. Only the VG STEM with its ADF imaging and small, high current electron probe proved capable of locating and obtaining useful spectral data from individual gold particles in the iron oxide matrix.

1.   S. R. Bryan, J. D. Stephens, J. H. Gibson, D. R. Rothbard, 7th Int. SIMS Conf., 1989, Monterey, CA.

2.   Dr. J. D. Stephens aided in sample preparation and interpretation.
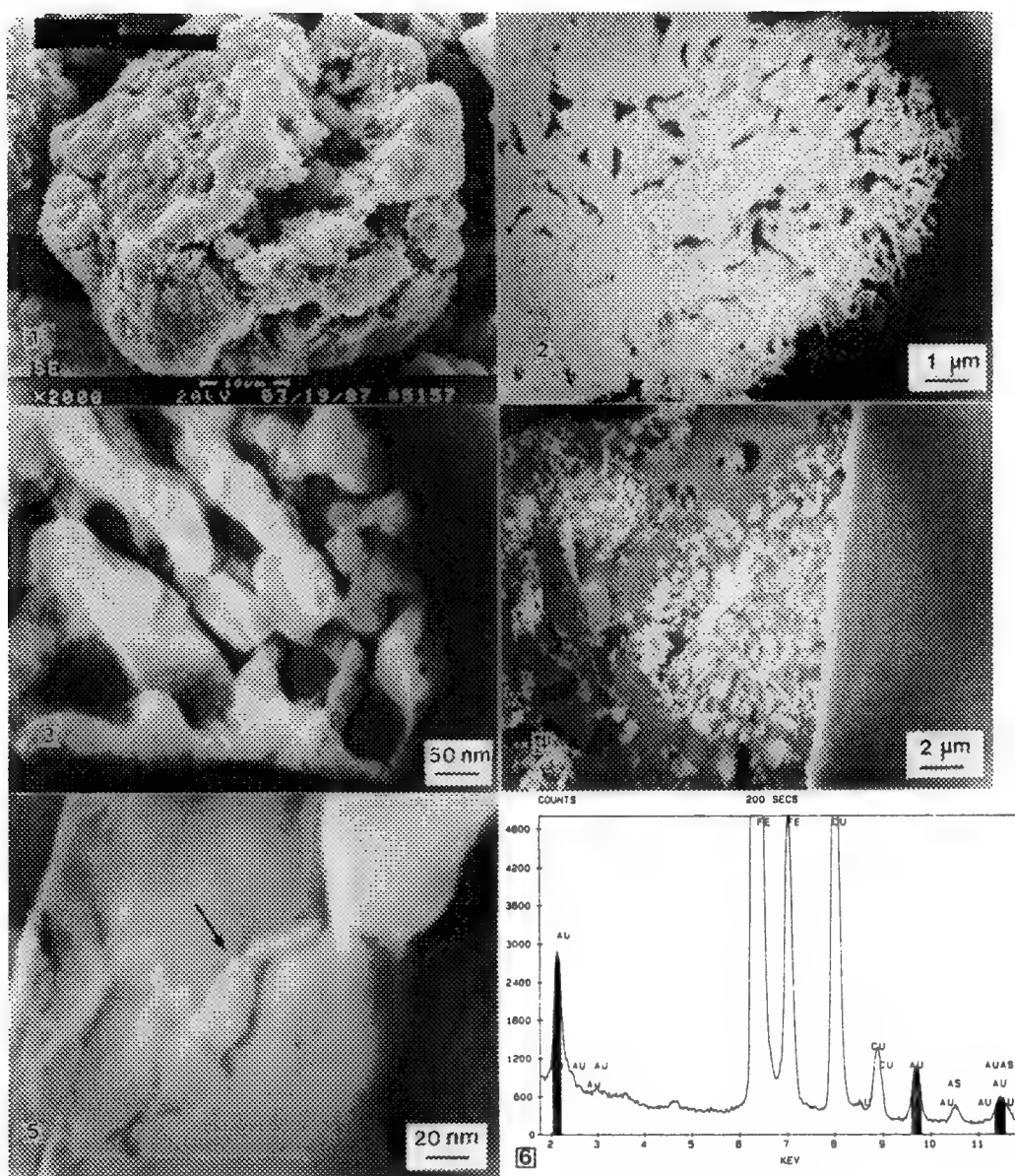
Figure 1.   Secondary electron image illustrating the exploded nature of the roasted grains.
Figure 2.   STEM ADF image of an ion milled grain.
Figure 3.   STEM ADF image showing fused iron oxide crystallites.
Figure 4.   STEM ADF image of a grain in the microtomed thin section.
Figure 5.   STEM ADF image of a 3nm gold particle (arrow) on iron oxide matrix.
Figure 6.   EDS spectrum from the 3nm particle in Figure 5.

413

HIGH-RESOLUTION VIDEO-ENHANCED LIGHT MICROSCOPY

E. D. Salmon

Department of Biology, University of North Carolina, Chapel Hill, NC 27599-3280

Video-enhanced differential interference contrast (VE-DIC) methods can produce high contrast images of isolated macromolecular complexes and cellular fine structures invisible by eye or photographic recording methods through the light microscope (1, 2, 3). Objects 10 nm - 20 nm wide, much smaller than the wavelength of green light, can be seen at high contrast, although lateral resolution is limited by the Abbe diffraction limit (about 200 nm for 550 green light through objective NA = 1.4). In addition, VE-DIC microscopy can produce thin optical sections through transparent thick specimens with z-axis resolution less than 200 nm (3). We have been developing this technology to provide video assays (30 frames per sec) of the dynamics of individual molecular complexes. Applications include measurement of the polymerization kinetics of individual 25 nm diameter microtubules in living cells (4) and in reconstituted preparations (5), the assembly of individual polymers of sickle cell hemoglobin in vitro (6), the translation of mechanochemical enzymes like dynein and kinesin along individual microtubules in vitro (7) and the movements of individual sister kinetochores during mitosis (8). Lateral movements of diffraction limited images of spherical particles can be tracked with 1 nm precision (9). We have used a semi-automatic version of the Gelles tracking algorithm to measure the movements of individual kinetochores and centrosomes in living cells at 1 sec intervals with 100-200 nm precision (8).

Achieving high resolution and high contrast VE-DIC images requires selection of both optical and video components of the imaging system with the highest transmission efficiency and maximum signal to noise characteristics. Practical aspects of implementing VE-DIC microscopy will be discussed along with applications demonstrating techniques for manipulating unresolved objects using micromanipulation, UV microbeam irradiation (10), and perfusion chambers (12). The optical and electronic principles used to obtain high contrast images in VE-DIC also apply to other contrast modes of bright field light microscopy including polarization, reflection interference contrast, oblique illumination, single side-band edge enhancement, and labeled molecular complexes with 20 nm - 50 nm gold particles (1,3).

1.   Salmon, et al., 1989, Biotechniques 7:624.
2.   Walker et al., 1990, In Optical Microscopy for Biology, New York: Wiley Liss, p. 395.
3.   Inoué, 1989, Methods in Cell Biology 30:85.
4.   Cassimeris et al., 1989, J. Cell Biol.
5.   Walker et al., 1988 J. Cell Biol. 107:1437.
6.   Samuel et al., 1990, Nature 345:833.
7.   Walker et al., 1990, Nature 347:780.
8.   Salmon et al., 1991, In Proceedings of the 49th meeting of the Electron Microscopy Society of America, G. W. Bailey, ed.., San Francisco Press, p. 238.
9.   Gelles et al., 1988, Nature 331:450.
10.   Walker et al., 1989, J. Cell Biol. 108:931.
11.   Walker et al., 1991, J. Cell Biol. 114:73.
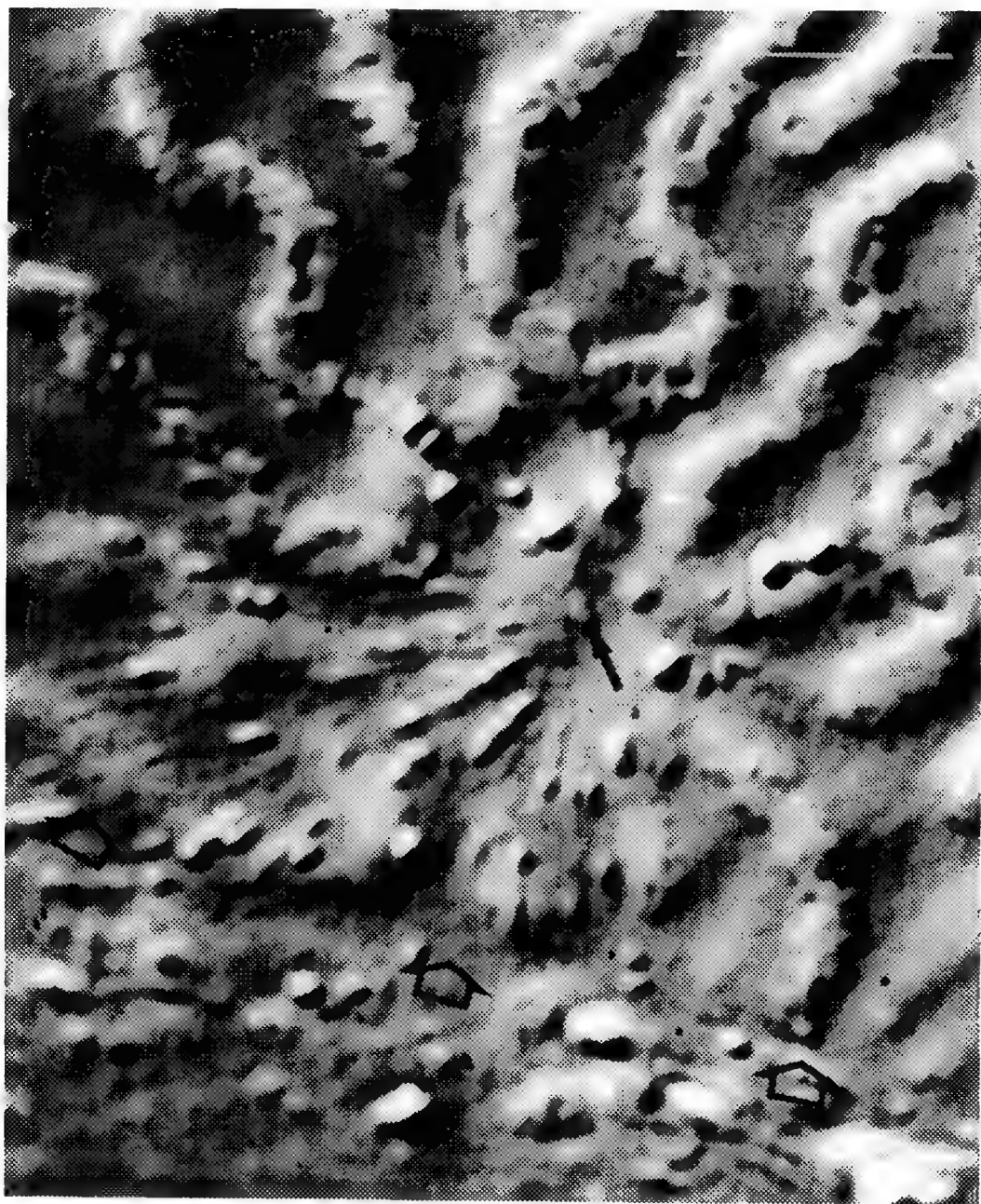
Figure 1.   VE-DIC micrograph of chromosome arms and a centrosome-aster complex at the edge of the nucleus in a prophase newt lung cell in culture. Small arrow marks the position of a centriole at the center of the centrosome while the large arrows mark the out-of-focus edge of the nucleus.   Time-lapse video sequences show rapid translocation of particles along the aster microtubule array.   Scale = 5 μm

415

4-DIMENSIONAL, HIGH-RESOLUTION IMAGING OF LIVING CELLS

Shinya Inoué

Marine Biological Laboratory, Woods Hole, MA 02543

This paper reports progress of our effort to rapidly capture, and display in time-lapsed mode, the 3-dimensional dynamic architecture of active living cells and developing embryos at the highest resolution of the light microscope. Our approach entails: (A) real-time video tape recording of through-focal, ultrathin optical sections of live cells at the highest resolution of the light microscope; (B) repeat of A at time-lapsed intervals; (C) once each time-lapsed interval, an image at home focus is recorded onto Optical Disk Memory Recorder (OMDR); (D) periods of interest are selected using the OMDR and video tape records; (E) selected stacks of optical sections are converted into plane projections representing different view angles ($\pm$4 degrees for stereo view, additional angles when revolving stereos are desired); (F) analysis using A - D.

Technical improvements that we have made to date include: (1) ultrathin optical sectioning, with high lateral image resolutions and rapid image capture, achieved by use of digitally enhanced video imaging in polarized light and DIC microscopy using high NA, strain-free Plan Apochromatic objective lenses coupled with matched aperture, rectified condenser illuminated via light scrambler; (2) computer-controlled movements (synchronized to video-image acquisition) of fine-adjustment stepper motors, that permit vibration-free, differential slewing of the condenser and objective lenses to maintain a constant background in focus while the objective focuses reproducibly through the specimen imbibed in aqueous medium (with 0.1 μm accuracy of focal repeat); (3) computer algorithms for converting stacks of optical sections into plane projections stored onto OMDR for stereo viewing at selectable playback speeds.

So far we have been able to: (a) obtain clean, very high resolution, revolving stereo images of Golgi-stained neurons reconstructed from a stack of 81 trans-illuminated, serial optical sections recorded stepwise at 0.5-μm focal intervals; (b) convert stacks of 4 to 6 through-focal images of diatom frustules and dividing sea urchin zygotes imaged in rectified polarization and DIC microscopy into stereo pairs; (c) use the system in Fig. 1A to capture through-focal DIC images through a 30-μm depth of developing sea urchin (*Lytechinus variegatus*) zygotes in ca. 1 sec., repeated at ca. 5-sec. intervals (Fig. 1B) over many hours.

The revolving stereo images of neuron, which include views at right angles to the original direction of observation, clearly show the detailed arrangement of the neuronal spines that arise from the dendrites, including the 3-dimensional bending of the 0.1-μm-diameter neck of each spine. The image of the diatom frustule complements the stereo images similarly reconstructed from a series of some 40 optical sections captured in the reflection contrast mode with confocal microscopy. The sequential through-focal images of the developing sea urchin zygote show the tortuous course of the astral rays linking the female pronucleus and male centrosome and explain the non-linear movement of the pronucleus towards the centrosome; display for the first time, the thread-like mitotic chromosomes throughout anaphase in the first and second zygotic division in *L. variegatus*; clarify the topology of the telophase nuclear envelope within which a tunnel is formed around the spindle remnant by the fusing karyomeres.

We are working to improve the algorithm used to convert the stack of through-focal images into plane projections so that stacks of 30 to 60, rather than a few, DIC and pol images of live zygotes can be converted into clear projections for stereo viewing. Once this problem is solved, we will be able to obtain high-resolution, 4-dimensional images (three spatial dimensions plus time) that allow detailed stereo observations of actively dividing cells and developing embryos. Furthermore, by reducing the conversion time for generating tilted projections to one or two seconds, the dynamic stereo images will be available for analysis even during time-lapse recording, allowing for immediate modification of experimental parameters as warranted.
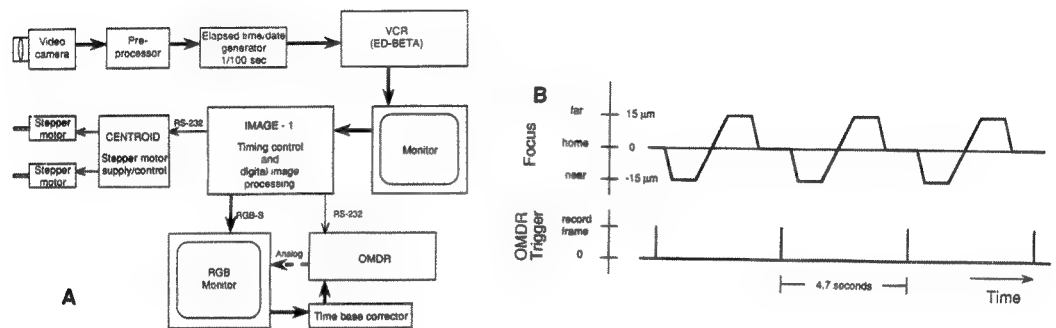
Fig. 1. A) Schematic of video and control systems for the 4-dimensional image data acquisition system. The pre-processed video microscope image is recorded continuously onto an ED-Beta VCR (500-TV-line resolution). This signal, digitally processed, is then recorded one frame per cycle to the Optical Memory Disk Recorder (OMDR) according to the sync pulses (Fig. 1B) generated by the central processor--controller, Image-1. Image-1 also governs, through the Centroid unit, the movement of the stepper motors that drive the objective lens and condenser focus. B) Upper curve: focusing movement of objective and condenser lenses. Lower curve: recording pulses for the OMDR. [From ref. 1, with permission.]

References

1. Inoué, S., A. Stemmer, T.D. Inoué and R.A. Knudson. 1991. High-resolution, 4-dimensional imaging of early development in *Lytechinus variegatus*. *Biol. Bull.*, 181: 336-337.
2. Supported by NSF grant DCB-8908169 and NIH grant R37-GM31617.

MULTIMODE LIGHT MICROSCOPY AND FLUORESCENCE-BASED REAGENTS AS TOOLS FOR THE STUDY OF CHEMICAL AND MOLECULAR DYNAMICS OF LIVING CELLS AND TISSUES

D. L. Taylor

Center for Light Microscope Imaging and Biotechnology, Carnegie Mellon University, 4400 Fifth Avenue, Pittsburgh, PA 15213

Cells function through the complex temporal and spatial interplay of ions, metabolites, macromolecules and macromolecular assemblies. Biochemical approaches allow the investigator to define the components and the solution chemical reactions that might be involved in cellular functions. Static structural methods can yield information concerning the 2- and 3-D organization of known and unknown cellular constituents. Genetic and molecular techniques are powerful approaches that can alter specific functions through the manipulation of gene products and thus identify necessary components and sequences of molecular events. However, full knowledge of the mechanism of particular cell functions will require direct measurement of the interplay of cellular constituents. Therefore, there has been a need to develop methods that can yield chemical and molecular information in time and space in living cells, while allowing the integration of information from biochemical, molecular and genetic approaches at the cellular level.

The renaissance and revolution in the use of the light microscope in biomedical research has yielded both new reagents and machine-vision light microscopes that enable researchers to explore the chemical and molecular dynamics in living cells and tissues. We have developed the multimode light microscope workstation that combines the following modes of light microscopy into the same automated microscope: video-enhanced contrast, 6 color fluorescence, ratio imaging, uncaging illumination, 3-D by computational methods, and photobleaching/activation. A standard inverted microscope has been modified to maximize the light throughput and to gain computer control of three camera ports, excitation and emission wavelength selection, presence or absence of selected optical components, selection of transmitted light, epi-illumination or laser light path, shutters, x,y,z-stage controls and environmental controls for a cell chamber. The experimenter can thus switch between microscope modes or operating conditions through a program or directly through the computer keyboard. This capability allows an experiment to be planned and executed without the need for the experimenter to interact with the myriad of microscope controls. Furthermore, a complex data set involving

multiple modes of microscopy can be acquired, processed and displayed automatically.

We have developed two classes of protein fluorescent analogs to define the temporal-spatial signalling and contractile response of cells stimulated with growth factors. The simplest fluorescent analogs are proteins that have been labelled covalently with fluorescent probes, while maintaining biochemcial and functional activity. When incorporated into living cells they report the distribution and dynamics of the protein during cell activity. The second class of fluorescent analogs are proteins or peptides that are designed as "optical biosensors" of chemical or molecular activity. Environmentally sensitive fluorescent probes are attached in specific locations to report chemical or molecular changes in the labelled molecule. A simple fluorescent analog of myosin II, one of the cellular motors responsible for movements, permits the analysis of contractile activity in cells. An optical biosensor of calcium binding to calmodulin, MeroCam, defines when and where in the cell that calmodulin is activated by binding calcium. In addition, an optical biosensor of myosin regulatory light chain phosphorylation is under development. The combined use of specific reagents and advanced machine-vision light microscopes will play a major role in defining cell functions.

VIDEO MICROSCOPIC MEASUREMENTS OF DIFFUSION AND FLOW IN CULTURED KIDNEY CELLS

Kenneth R. Spring*, Peter M. Bungay+, Jean-Yves Chatton*, Bruno Flamion^O, Carter C. Gibson*, Peter J. Harris†

*Laboratory of Kidney and Electrolyte Metabolism, NIH, NHLBI, Bethesda, MD 20892
+ Biomedical Engineering and Instrumentation Program, NIH, ^O Free University of Brussels, Brussels, BELGIUM, † University of Melbourne, Melbourne, AUSTRALIA

New, optical microscopic techniques were developed to study the composition, fluid flow patterns and restrictions to diffusion in the fluid filled spaces surrounding renal epithelial cells. The prevailing theoretical model for the mechanism of isosmotic fluid transport by epithelia, the standing osmotic gradient hypothesis[1], predicts gradients in ion composition as well as significant restrictions to the diffusion of small solutes within the lateral intercellular spaces separating epithelial cells. Key questions about the validity of the model arise from uncertainties about the values for the hydraulic water permeability of the cell membranes and the lack of data about the composition of the fluid filling the lateral intercellular spaces. This presentation will describe measurements of the local composition, geometry and diffusion coefficients within lateral intercellular spaces of cultured renal epithelia and in the lumen of isolated, perfused renal tubules.

Preparations were illuminated by means of an acousto-optically controlled laser and visualized with an image intensified video camera as previously described[6]. The spaces between the epithelial cells were filled with fluorescent dye by first loading the cells and allowing the dye to be transported out of the cell interior and into the lateral intercellular space by the organic anion transporter present in certain renal epithelia in tissue culture. Madin Darby canine kidney cells (MDCK) exhibit an organic anion transporter located on the basolateral cell membrane[4] which moves organic anions from the cell interior to the lateral intercellular spaces adjacent to the tissue. A variety of organic anions are transported, and it has already been shown (Harris, Chatton, Spring, unpublished observations) that MDCK cells transport the anionic, pH-sensitive dye, BCECF, into the lateral intercellular spaces. The accumulation of the dye occurred best when cells were grown on glass coverslips. The dye was loaded into the spaces by pulsing the perfusion solution with 4 μM of the acetoxymethyl ester of BCECF (BCECF-AM) for 30 seconds. The dye entered the cells by diffusion, the acetoxymethyl ester linkage was cleaved by intracellular esterases and the anionic form of BCECF was produced. Over the next 15-20 minutes, this organic anion was recognized by the transporter and translocated across the basolateral membrane into the lateral intercellular space where it accumulated in very high concentrations (50-100 times that of the original perfusate). Thus cell pH could be measured while the dye was still in the cells and lateral intercellular space pH determined once the dye had been transported out of the cell.

Localization of pH differences to a small region requires some additional analytical capabilities. Because the light emitted from a fluorescent object goes in all directions, fluorescence microscopic images are contaminated by out-of-focus signals arising from the focal planes above and below the one of interest. It is necessary to optically or computationally subtract the contributions of out-of-focus signals to produce an accurate estimate of the signal in a defined

region along the optical axis of the microscope. We used a digital deblurring method, the nearest neighbors algorithm, to remove the out-of-focus signal from optical sections of the dye-filled spaces. Three dimensional reconstructions of these deblurred images revealed that the spaces were arranged into a series of folds oriented along the apical-to-basolateral axis of the cells. Analysis of the unmodified or deblurred images failed to demonstrate any gradients in pH or dye concentration within the spaces.

Fluorescence recovery after photobleaching (FRAP) was used to measure the rate of fluid flow in the lumen of isolated, perfused renal medullary collecting duct tubules[2] and to determine the diffusion coefficient of BCECF within the lateral intercellular spaces of MDCK cells. Diffusion coefficients were measured by the video FRAP technique[3] adapted to the linear geometry required by the tissue architecture. The dye filling a small area of the lateral intercellular space was bleached by an intense pulse of laser light (~33 mW at 488 nm) focused to a slit by a cylindrical lens. The rate of diffusion of unbleached dye from adjacent regions into the bleached area was recorded and analyzed. Diffusion of the bleached dye from the bleached zone and diffusion of unbleached dye into the zone during the bleach pulse were modelled mathematically. No restrictions to the free diffusion of BCECF were detected within the lateral intercellular spaces of MDCK cells.

Measurement of renal tubular fluid flow rate was accomplished by bleaching a region of the lumen of an isolated medullary collecting duct that was perfused with a fluorescent dye (fluorescein sulfonate). A rectangular slit in the illumination path produced a sharply defined region in which the dye could be bleached with a brief (~20 msec) pulse of intense laser light. The replacement of bleached dye by convection gave a direct measure of the linear velocity of flow through the tubule lumen when the intensity of the lumen was monitored by lower level illumination and detected with a photomultiplier tube (2kHz sampling frequency). This method enabled rapid sequential measurement of the dye concentration in the tubule lumen from the fluorescence intensity as well as the fluid flow rate from the FRAP data. Combination of the fluorescence measurements with differential interference contrast transmitted light imaging[5] enabled concomitant measurements of the cell volume changes accompanying alterations in perfusate composition. The application of these light microscopic techniques to renal epithelia has enabled measurements of the water permeability of the cell membrane and of the entire epithelium in the same tissue at virtually the same time, a prerequisite for determination of the pathways for fluid movement across epithelial tissues.

REFERENCES

1. J.M. Diamond and W.H. Bossert, J.Gen. Physiol. (1967)50, 2061.
2. B. Flamion et al., Biophys. J. (1991)60, 1229.
3. H-G. Kapitza et al., Proc. Nat. Acad. Sci. (1985)82, 4122.
4. R.J. Lowy and K.R. Spring, J. Membr. Biol. (1990)117, 91.
5. K.R. Spring, in B. Herman and K. Jacobson, Ed., Optical Microscopy for Biology, NY:Wiley-Liss (1990)513.
6. K.R. Spring and P.D. Smith, J. Microsc. (1987)147, 265.

THE DYNAMICS OF LOCAL CHEMICAL CHANGES UNDERLYING WHITE-CELL CHEMOTAXIS MEASURED WITH DIGITAL IMAGING MICROSCOPY

F.S. Fay*, R. Brundage**, K. Perry* and S.H. Gilbert*

*   Department of Physiology, Univ. of Mass. Medical School, Worcester, Massachusetts
**   Department of Biology, University of Pennsylvania, Philadelphia, Pennsylvania

The ability of cells to polarize and move towards or away from a chemical stimulus is a fundamental property of virtually all cell types at some stage in their development. This process is important for biological processes ranging from morphogenesis, to wound healing, to the attack by leukocytes of invading organisms in our body. Despite the importance of this phenomenon, surprisingly little is known regarding the mechanism whereby an external chemical gradient is converted into an intracellular gradient of 2° messengers, how the local chemistry of the cell is compared and how the result of that comparison gives rise to the polarized organization of the cell and the resulting directional migration of the cells. In order to obtain insights into this fundamental cellular process, we have been investigating the local chemical changes underlying the response of newt eosinophils to chemoattractants. This cell system is particularly well suited for asking such questions as the cells are large (30 microns wide, 70 microns long), thereby facilitating micro-injection of various fluorescent compounds as well as the imaging of local differences in the concentration of important species involved in responses to chemoattractants. Furthermore, these cells respond in seconds to gradients of serum chemoattractants, thereby facilitating an analysis of the sequence of events linking the gradient of chemoattractant to the generation of local chemical signals ultimately leading to the polarization and directed migration of these cells.

In order to assess these local chemical changes we have developed a digital imaging microscope system uniquely adapted for this problem. The microscope uses a slow scan cooled CCD to measure with high efficiency and low noise the fluorescent signals at multiple excitation and emission wavelengths generated by one or several fluorescent probes injected into these cells. The system is capable of acquiring a series of such images with no more than 100 msec. intervals between images in a 2- or 3- image series, thereby diminishing the contribution of motion artifacts to the data set. The optics of the microscope have also been altered so as to simultaneously record phase contrast images of the cell at video rates in the far red portion of the spectrum, thereby allowing correlation of local chemical changes with the local activity of the cells. Software has been developed for analyzing these images, providing the ability to automatically track individual cells within an image as well as to utilize two or three wavelength image sets to calculate the local concentration of specific ions or molecules for which a ratiometric indicator (s) has been injected into the cell. The program automatically thresholds the image, excluding pixels for which the certainty of the resulting calculation falls below a level pre-determined by the investigator.

Using these methods we have found that exposure of cells to chemoattractant causes an initial large and transient rise in $[Ca^{2+}]$, that returns to a fluctuating value somewhat greater than rest. Associated with the initial rise and subsequent fall in $[Ca^{2+}]$,

422

the cell flattens and polarizes and ultimately begins to move. The onset of migration is coincident with the formation of a $[Ca^{2+}]$ gradient, with the $[Ca^{2+}]$ at the rear being higher than in the front. Periodic increases in $[Ca^{2+}]$ are observed in cells during chemokinesis in response to the addition of chemoattractant to the bath and these $[Ca^{2+}]$ spikes are often associated with turns of the cells. The spikes in the $[Ca^{2+}]$ begin with a rise in $[Ca^{2+}]$ in the rear of the cell. The new lamellipod formed as a cell changes its direction of polarization and locomotion is most often the region with the lowest $[Ca^{2+}]$ during a spike or the region that has the briefest rise in $[Ca^{2+}]$ during the spike. A similar rear to front $[Ca^{2+}]$ gradient is observed in cells migrating in response to a gradient of chemoattractant generated by ejecting serum from a micropipette. Similarly, in such cells when the pipette is repositioned to cause the cell to turn, the $[Ca^{2+}]$ rises, and as the cell repolarizes and heads in a new direction, a new gradient of $[Ca^{2+}]$ forms parallel to the new cell axis with the front of the cell having the lower $[Ca^{2+}]$, the rear having the higher concentration.

Polarization of the cell in response to chemoattractant is associated with an increase in average $[Ca^{2+}]$ but the greatest increase in calcium occurs in the rear of the cell presumably the region being least stimulated by chemoattractant. This suggests that somehow the mechanism that is responsible for transducing the chemoattractant signal to a change in $[Ca^{2+}]$ involves a sign reversal within the cell. One possible mechanism whereby this sign reversal might take place would be if the chemoattractant produced two 2° messengers that had an opposite effect on Ca^{2+} homeostasis; one acting to cause a rise in $[Ca^{2+}]$, the other a fall in $[Ca^{2+}]$. Such a pair of 2° messengers produced in response to chemoattractant might give rise to the observed $[Ca^{2+}]$ gradient if the 2° messenger producing a rise in Ca^{2+} has a longer range of action than the 2° messenger having the opposite effect. This pair may be IP_3 and DAG, with IP_3 causing release of Ca^{2+} from internal stores and DAG acting to stimulate protein kinase C which in turn might act to inhibit processes responsible for increasing $[Ca^{2+}]$. In order to begin to test this hypothesis, we have studied the effects of modulating protein kinase C activity on Ca^{2+} homeostasis and the behavior of single newt eosinophils. We find that activation of protein kinase C causes $[Ca^{2+}]$ to fall. In addition, using inhibitors of protein kinase C, we find that $[Ca^{2+}]$ changes in response to stimulation with chemoattractants are accentuated. These results support the role of protein kinase C in providing a negative feedback on Ca^{2+} signalling in eosinophils in response to chemoattractants. The observed gradients of $[Ca^{2+}]$ as well as the postulated gradients of IP_3 and protein kinase C activity are likely of considerable importance in organizing and regulating the local activities of cytoskeletal elements thought to be important in the polarization and directed migration of these and other cells. The relationship between the observed gradients in 2° messengers and these cytoskeletal changes will be discussed.

423

OPTICAL TWEEZERS AS A TOOL TO STUDY CELLULAR FUNCTION

Steven M. Block

Rowland Institute for Science, 100 Cambridge Parkway, Cambridge MA 02142 USA
and Department of Cellular & Developmental Biology, Harvard University, Cambridge
MA 02138

A single beam gradient force optical trap[1-3], or "optical tweezers", exerts forces on microscopic dielectric particles using a highly focused beam of laser light, and can achieve stable, three-dimensional trapping of such particles (for a review, see ref. 4). Using an infrared laser, calibratable forces in the piconewton (pN) range can be easily generated without causing significant damage to living biological specimens. Optical tweezers work through the microscope, without mechanical intrusion within sealed preparations, and can even reach directly inside transparent cells or organelles. Because it is formed by light, an optical trap can be controlled with very high spatial and temporal precision. Its characteristic size (i.e., its "grasp") is approximately equal to the wavelength of light, but it can be used to capture and/or manipulate objects ranging in size from ~20 nm to ~100 mm. Biological preparations (*e.g.*, cells, vesicles, organelles) or small particles (*e.g.*, latex or silica microspheres, perhaps carrying reagents coupled to their surfaces) can be held, maneuvered, or released at will. Already, researchers have begun to contemplate experiments that were practically impossible just a few years ago. Some possibilities include: (1) the sorting and isolation of cells, vesicles, organelles, chromosomes, *etc.*; (2) the direct measurement of the mechanical properties of cytoskeletal assemblies, membranes, or membrane-bound elements; (3) measurement of the tiny forces produced by mechanoenzymes; (4) establishing cell-cell contacts, or measuring receptor-ligand interactions; (5) studying cellular rheology on the micrometer scale; (6) doing cellular microsurgery, membrane fusion, and building novel cellular (or noncellular) structures; (7) capturing and maintaining fragile biological structures away from vessel surfaces, in order to study them in isolation under optimal viewing conditions; (8) and much more![2-15] The principles by which optical tweezers work will be explained, and a videotape illustrating a number of experimental uses will be shown.

1. A. Ashkin, J.M. Dzeidzic, J.E. Bjorkholm, and S. Chu, Optics Lett. (1986) 11:288-290.
2. A. Ashkin and J.M. Dzeidzic, Science (1987) 235:1517-1520.
3. A. Ashkin, J.M. Dzeidzic, Nature (1987) 330:769-771.
4. S.M. Block, *in* J.K. Foskett & S. Grinstein, eds. Nonivasive Techniques in Cell Biology, New York: Wiley-Liss. Modern Rev. Cell Biology series (1990) 9:375-402.
5. S.M. Block, D.F. Blair, and H.C. Berg, Nature (1989) 338:514-518.
6. S.M. Block, L.S.B. Goldstein, B.J. Schnapp, Nature (1990) 348:348-352.
7. A. Ashkin, J.M. Dzeidzic, Proc. Natl. Acad. Sci. USA (1989) 86:7914-7918.
8. Shepherd, G.M.G., D.P. Corey, and S.M. Block, Proc. Natl. Acad. Sci. USA (1990) 87:8627-8531.

9. M.W. Berns, W.H. Wright, B.J. Tromberg, G.A. Profeta, J.J. Andrews, and R. J. Walter, Proc. Natl. Acad. Sci. USA (1989) 86:4539-4543.
10. H. Liang, H., W.H. Wright, W. He, and M.W. Berns. Exptl. Cell Res. (1991) 197: 21-35.
11. A. Ashkin, K. Schuetze, J.M. Dzeidzic, U. Euteneuer, and M. Schliwa. Nature (1990) 348:346-348.
12. M. Edidin, S.C. Kuo, M.P. Sheetz, Science (1991) 254:1379-1382.
13. S. Seeger, S. Manojembashi, K.-J. Hutter, G. Futterman, J. Wolfrum, and K.O. Greulich. Cytometry (1991) 12:497-504. See other articles in this issue by Visscher & Brakenhoff; Block, Blair, & Berg; Steubing *et al.*, Bakker Schutt *et. al.*
14. Svoboda, K., Schmidt, C.F., and S.M. Block, Biophysical Journal (1992, *in press.*)
15. D.F. Kucik, S.C. Kuo, E.L. Elson, and M.P. Sheetz, J. Cell Biol. (1991) 114:1029-1036.
16. This work was supported by the Rowland Institute for Science.

Use of optical tweezers to arrest a swimming spirochete
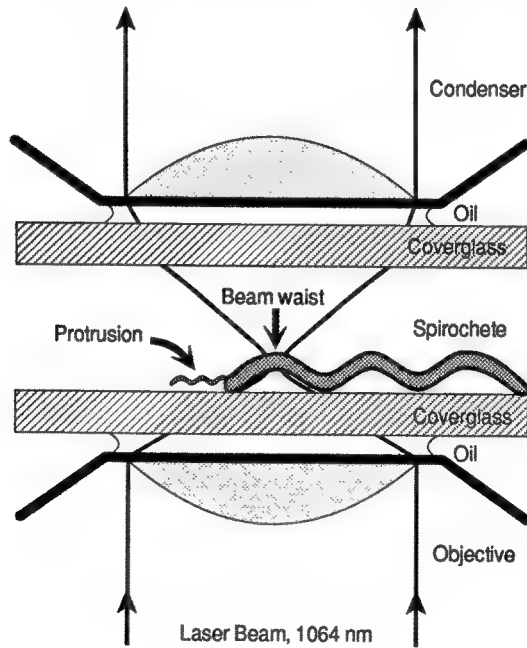
Inverted microscope, detail

Fig. 1. A Cartoon illustrating the geometry of cell capture by optical tweezers.

425

ANALYZING REACTIONS OF SINGLE MECHANOENZYME MOLECULES BY LIGHT MICROSCOPY

Jeff Gelles

Graduate Department of Biochemistry and The Center for Complex Systems, Brandeis University, Waltham, MA 02254

Mechanoenzymes are enzymes which use a chemical reaction to power directed movement along a biological polymer. Such enzymes include the cytoskeletal motors (e.g., myosins, dyneins, and kinesins) as well as nucleic acid polymerases and helicases. A single catalytic turnover of a mechanoenzyme moves the enzyme molecule along the polymer a distance on the order of 10^{-9} m. We have developed light microscope and digital image processing methods to detect and measure nanometer-scale motions driven by single mechanoenzyme molecules.[1-3] These techniques enable one to monitor the occurrence of single reaction steps and to measure the lifetimes of reaction intermediates in individual enzyme molecules.[3-5] This information can be used to elucidate reaction mechanisms and determine microscopic rate constants. Such an approach circumvents difficulties encountered in the use of traditional transient-state kinetics techniques to examine mechanoenzyme reaction mechanisms.

The use of this approach is illustrated by our studies on the kinetics of transcription of DNA by single molecules of *E. coli* RNA polymerase.[3] Previously, analysis of the movement of RNA polymerase on the DNA template had been limited to the study of the population-averaged properties of large ensembles of enzyme molecules.

To analyze transcription by single polymerase molecules, we adsorb purified ternary transcription complexes (consisting of RNA polymerase, a linear DNA template, and the nascent RNA transcript) to a glass coverslip at < 1 μm^{-2} surface density. The upstream end of the template is labelled for microscopy with a 40nm diameter colloidal gold particle (Figure 1A). Brownian motion of the DNA-tethered gold particle is recorded by video-enhanced differential interference contrast light microscopy. During transcriptional elongation, the length of the segment of DNA linking the particle to the coverslip increases due to the movement of the DNA through the polymerase. The lengthening of the tether results in an increase in the range of particle Brownian motion (Figure 1B). The range of particle motion is quantitated (with a precision < 10 nm r.m.s. at 0.4 Hz) by measuring with a non-linear curve-fitting algorithm the width of time-averaged images of the moving particle. The position of the polymerase on the DNA template can be calculated from the measured range of particle motion using an empirically or theoretically determined calibration factor.

We are currently using this method to study the mechanisms of transcriptional elongation and of the processes which regulate it. The method may prove valuable for mechanistic studies of other enzymes that interact with nucleic acids.[6]

References

1. J. Gelles et al., Nature 331(1988)450.
2. B.J. Schnapp et al., Cell Motil. Cytoskel. 10(1988)47.
3. D.A. Schafer et al., Nature 352(1991)444.
4. S.M. Block et al., Nature 348(1991)348.
5. D. Colquhoun and A.G. Hawkes in B. Sakmann and E. Neher, Eds., Single Channel Recording, New York:Plenum Press (1983)135.
6. Work in the author's laboratory was supported by The Lucille P. Markey Charitable Trust, The Searle Scholars Program, and the NIH.
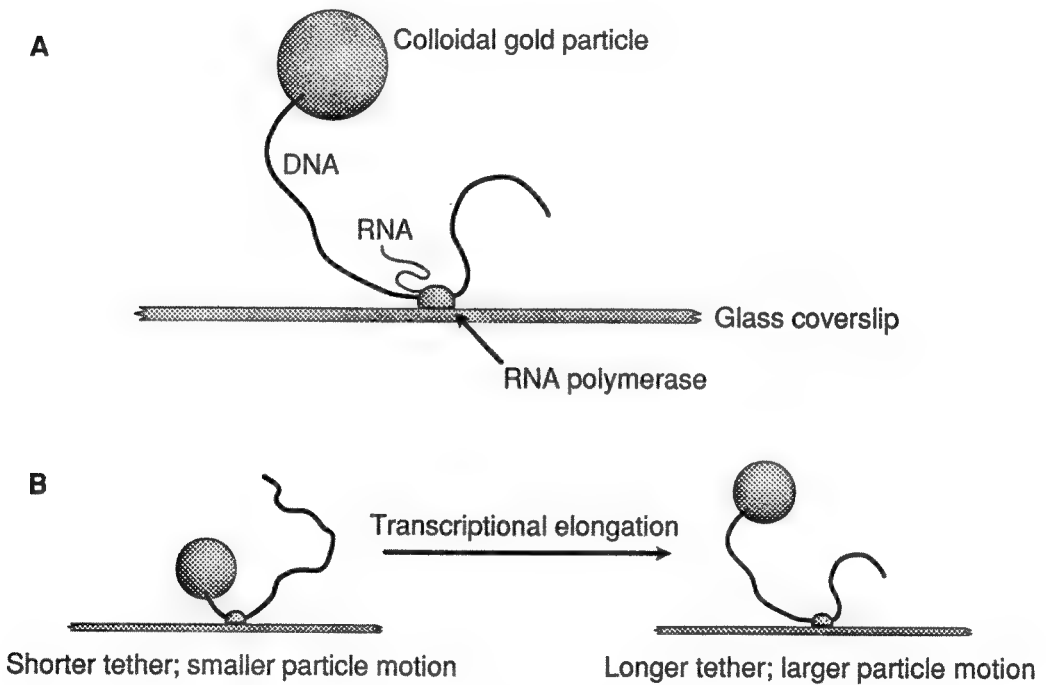
Fig. 1.--Light microscope specimen for observing transcriptional elongation by a single RNA polymerase molecule using the method of Ref. 3. (A) Specimen composition. A stalled transcription complex, consisting of RNA polymerase, DNA template, and nascent RNA transcript, is immobilized by non-specific adsorption of the polymerase to a glass coverslip. The upstream end of the template, which is linked to a biotin moiety, is labelled with a 40nm diameter streptavidin-conjugated colloidal gold particle. (B) Effect of transcriptional elongation on specimen geometry and on particle Brownian motion.

LAMELLIPODIA, STRESS FIBERS AND THE ACTIN CORTEX OF MOTILE CELLS: THEIR STRUCTURE AND DYNAMIC INTERACTION STUDIED BY VIDEO DIC MICROSCOPY AND CORRELATED ELECTRON MICROSCOPY

Julian P. Heath and Bruce F. Holifield

Depts. Pediatrics (CNRC) and Cell Biology, Baylor College of Medicine, Houston, TX 77030

We have used high resolution video differential interference contrast (VDIC) light microscopy and correlated electron microscopy to examine the spatial and functional relationships between actin structures in the lamellipodia, adhesion plaques, stress fibers and the dorsal cortical actin microfilament sheath (DCMS) of cultured motile fibroblasts. Fibroblasts were examined on a Zeiss Axiophot using a 1.3NA 100x plan objective and 1.4 NA condenser and imaged with a Dage CCD camera. Contrast-enhanced images were recorded on a Panasonic S-VHS time-lapse recorder.

The actin in the lamellipodium of motile fibroblasts is organized into a criss-cross network of filaments interspersed with small bundles or ribs (Figure 1). Ribs are continually moving laterally through the advancing lamellipodium. Adhesion plaques form at the bases of ribs as previously described.[1] In fixed cells we noted a link between the ends of stress fibers and arcs in the leading lamella (Figure 2). Using VDIC, we have shown for the first time the sequential steps in stress fiber formation and growth: an actin stress fiber is initiated at the rib base and elongates centripetally coordinately with the rearward flow of the dorsal actin cortex of the lamella (Figure 3). A result of this interaction is that the flow of the dorsal cortex is restrained leading to deformation and folding of the lamellar cortex. As the stress fiber grows, this fold develops into an arc (Figure 3). Figures 4 and 5 are sections through the lamella; each shows an arc at the region of insertion of stress fibers into the DCMS.

Our findings are consistent with a model of a continuous rearward flow of actin through the leading edge of a moving cell. Actin filaments are assembled at the tips of the lamellipodium and flow, or are pulled, rearwards becoming reoriented and incorporated into the DCMS. An adhesion plaque fixes a point in this rearward flowing system appearing to draw out filaments from the DCMS. Arcs are regions where stress fibers insert into the dorsal cortex.[2]

(1) Izzard, C.S. (1984) Cell Motility and Cytoskeleton 10:137-142
(2) Supported by NSF DCB-8820262 and USDA/ARS Cooperative agreement 58-6250-1-003

Fig. 1. Lamellipodium of phalloidin-stained cell showing criss-cross network of actin filaments and actin ribs.
Fig. 2. Association between proximal ends of stress fibers and an arc (arrowheads) in the leading lamella.
Fig. 3. Time lapse sequence of DIC images showing a lamellipodium (L), a newly formed adhesion plaque (arrowhead) and an elongating stress fiber (arrow). The site of stress fiber insertion into the DCMS appears first as a dark focal deformation (arrow); this deformation develops into a small arc (arrow). Further back in the lamella several stress fibers are seen inserting into a well-developed arc (asterisk).
Fig. 4. Horizontal section of lamella showing region of association of an arc and stress fibers (SF). Note filaments passing between the arc and stress fibers (arrows).
Fig. 5. Vertical section showing an arc and DCMS filaments in cross section. The arc is a prominent deformation of the DCMS. The arrowheads mark segments of oblique stress fibers (SF) rising to meet the dorsal cortex.

Figure 1

Figure 2

Figure 3 (20 03 17, 20 03 29, 20 03 48, 28 04 15)

Figure 4 (SF, Arc)

Figure 5 (DCMS, Arc, SF)
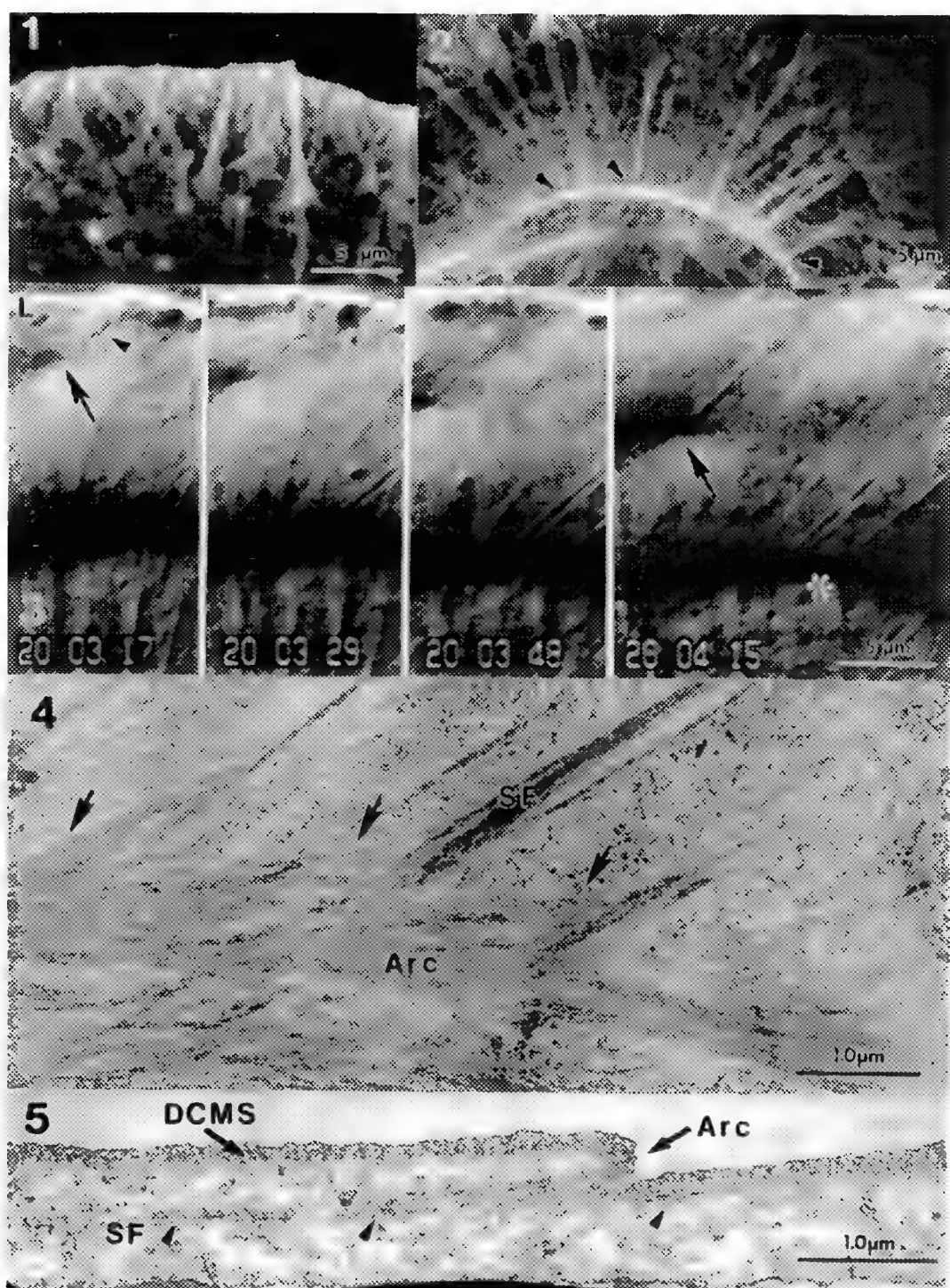
ELECTRON CRYSTALLOGRAPHY OF MEMBRANE PHOSPHOLIPIDS

Douglas L. Dorset

Electron Diffraction Department, Medical Foundation of Buffalo, Inc., 73 High St., Buffalo, NY 14203

Membrane phospholipids are notoriously difficult to crystallize to sample sizes suitable for collection of single crystal X-ray intensity data, accounting for the relatively few crystal structures which have been reported to date. At the 24th Annual EMSA meeting, Parsons and Nyburg[1] suggested that the enhanced scattering of electrons by matter be exploited to obtain single crystal electron diffraction patterns from the more readily available microcrystalline preparations, an example of which was shown in a subsequent paper[2]. For almost 20 years we have investigated the utility of such intensity data for *ab initio* crystal structure analysis.

Two types of crystallization can be carried out to give orthogonal views of the molecular packing. The easiest preparation, from a dilute solution in some organic solvent, crystallizes layers where the molecular long chains are more or less perpendicular to the lamellar surface. (The exact tilt value for the chain axes can be determined in a RHEED experiment[3].) Because of slight elastic bends and the long unit cell spacing in the electron beam direction[4], only the structure of the acyl (or alkyl) chain methylene subcell packing can be determined from the electron diffraction intensities[5]. This restriction, nevertheless, has permitted some chain packing structures to be solved which had not been previously found in X-ray structure determinations. Such structures can be determined by interpretation of Patterson maps[6] but they also represent the first instance where so called "direct phasing" methods have been successfully applied in electron crystallography[7]. Also the first high resolution, low dose electron micrographs of paraffin monolamellar crystals[8] demonstrated how such methylene subcell packings can be visualized directly at 2.5Å resolution.

The second type of crystallization involves an epitaxial orientation onto an organic substrate such as naphthalene[9,10], a procedure shown to be effective for orienting numerous polymethylene chain compounds[11] so that the chain axes parallel the major crystal face. Unfortunately phospholipids oriented this way are actually paracrystalline with curvilinearly distorted lamellae[12] so that the most useful diffraction intensities are the so called "lamellar reflections", analogous to the X-ray diffraction study of oriented multilamellar samples. Data from such samples can be used for *ab initio* determination of the bilayer profile. At first, one-dimensional Patterson maps were interpreted to determine the projected conformation of the phospholipid headgroup[13]. As suggested also in an earlier analysis of lamellar X-ray data[14], a molecular model was constructed from a similar X-ray crystal structure, and this was translated along the unit cell to find a minimum of the crystallographic R-factor. The layer structures of four different headgroup classes were thus analyzed from electron diffraction intensity data[15-18].

A more direct method of structure analysis was suggested in the analysis of high resolution, low dose electron micrographs which diffract on the optical bench to 6Å resolution[19]. After directly determining the crystallographic phases of the first 7 (00ℓ) reflections from the computed image transform, evaluation of Σ_1- and Σ_2-three phase structure invariants[20] was shown to provide phase values for the other data out to ca 3Å resolution. Indeed, such direct

phasing was later shown to be remarkably robust by itself[21]. More recently, model studies[22] have shown direct phasing to be suitable for analyzing many types of lipid bilayer structures and density modification procedures are useful for phase refinement. Since the positions of individual atoms are not resolved, a figure of merit evaluating the smoothness of the density function[22,23] is shown to be useful for identifying the correct crystallographic phase set.

While initial results are quite promising, further work is necessary to remove the deleterious effect of multiple scattering to the observed data, which particularly affects the success of phase refinement[23]. Also better orientation procedures most be found to remove the paracrystalline disorder to the sample.

1. D. F. Parsons and S. C. Nyburg, J. Appl. Phys. (1966) **37**, 3920.
2. D. F. Parsons, Canad. Cancer Conf. (1967) **7**, 193.
3. D. L. Dorset, EMSA Bulletin (1990) **20(1)**, 54.
4. J. M. Cowley, Acta Cryst. (1961) **14**, 920.
5. D. L. Dorset, Ultramicroscopy (1983) **12**, 19.
6. D. L. Dorset, Biochim Biophys Acta (1976) **424**, 396.
7. D. L. Dorset and H. A. Hauptman, Ultramicroscopy (1976) **1**, 195.
8. F. Zemlin, E. Reuber, E. Beckmann, E. Zeitler and D. L. Dorset, Science (1985) **229**, 461.
9. J. C. Wittmann and R. St. J. Manley, J. Polym. Sci.-Polym Phys. Ed. (1978) **16**, 1891.
10. D. L. Dorset, J. Phys. Chem. (1990) **94**, 6854.
11. D. L. Dorset, J. Electr. Microsc. Techn. (1989) **11**, 298.
12. J. R. Fryer and D. L. Dorset, J. Microsc. (Oxford) (1987) **145**, 61.
13. D. L. Dorset, J. Electr. Microsc. Techn. (1987) **7**, 35.
14. P. B. Hitchcock, R. Mason and G. G. Shipley, J. Mol. Biol. (1975) **94**, 297.
15. D. L. Dorset, A. K. Massalski and J. R. Fryer, Z. Naturforsch. (1987) **42a**, 381.
16. D. L. Dorset, Biochim. Biophys Acta (1987) **898**, 121.
17. D. L. Dorset, Biochim. Biophys Acta (1988) **938**, 279
18. D. L. Dorset and W. P. Zhang, Biochim Biophys Acta (1990) **1028**, 299.
19. D. L. Dorset, E. Beckmann and F. Zemlin, Proc. Nat. Acad. Sci. USA (1990) **87**, 7570.
20. D. L. Dorset, Ultramicroscopy (1991) **38**, 23.
21. D. L. Dorset, Biophys J. (1990) **58**, 1077.
22. D. L. Dorset, Biophys. J. (1991) **60**, 1356.
23. D. L. Dorset, Biophys J. (1991) **60**, 1366.
24. Research supported in part by a grant from the Manufacturers & Traders Trust Company.

THE STRUCTURE OF MEMBRANES AND MEMBRANE PROTEINS EMBEDDED IN AMORPHOUS ICE

Uwe Lücken and Joachim Jäger

Electron Microscopy Department, Fritz-Haber-Institut der Max-Planck-Gesellschaft
Faradayweg 4-6, W-1000 Berlin 33, Federal Republic of Germany

TEM imaging of frozen-hydrated lipid vesicles has been done by several groups[1-5] Thermotrophic and lyotrophic polymorphism has been reported. By using image processing, computer simulation and tilt experiments, we tried to learn about the influence of freezing-stress and defocus artifacts on the lipid polymorphism and fine structure of the bilayer profile. We show integrated membrane proteins do modulate the bilayer structure and the morphology of the vesicles.

Phase transitions of DMPC vesicles were visualized after freezing under equilib-rium conditions at different temperatures in a controlled-environment vitrification system. Below the main phase transition temperature of 24°C (Fig. 1), vesicles show a facetted appearance due to the quasicrystalline areas. A gradual increase in temperature leads to melting processes with different morphology in the bilayer profile. Far above the phase transition temperature the bilayer profile is still present. In the band-pass-filtered images (Fig. 2) no significant change in the width of the bilayer profile is visible.

A tilt experiment (Fig. 3) performed with the same vesicles exhibits a flattening effect during the freezing process. Analysis of the change in diameter of vesi-cles 11-17 perpendicular to the tilt axes provides a fairly good basis for judging the amount of flattening and, as a bonus, the thickness of the ice layer.

This flattening effect may be responsible for the appearance of the lipid vesicle reconstituted with Na/K-ATPase as shown in Fig. 4. The stress on the vesicle led to an eruption. One has to consider that the integral membrane protein may weaken the bilayer structure. We never found such protrusions in images of pure lipid vesicles. Vesicles which may not be disturbed by the flattening sometimes show surface modulation, as reported in Ref. 5 and shown in Fig. 5.

Does the bilayer profile change with defocus? To address this question we per-formed a computer simulation of a lipid vesicle. As input image an ideal projec-tion of a lipid vesicle was used. The contrast transfer function was applied for different defoci, and results in the corresponding output images are shown in Fig. 6. The appearance of the bilayer profile does change with defocus. Inter-pretation of the width of the bilayer and the fine structure should only be made after correction for the contrast transfer function or by visualization close to focus, as performed with the EM 902 and shown in Fig. 7. The zero-loss filtering affords the possibility of imaging in very thick ice layers close to focus.

References

1. J. Lepault et al., Biochim. Biophys. Acta 820 (1985) 315.
2. Y. Talmon et al., J. Microsc. 141 (1986) 375.
3. P. M. Frederik et al., J. Microsc. 153 (1989) 81.
4. P. K. Vinson et al., J. Colloid Interf. Science 142 (1991) 74.
5. W. Helfrich and B. Kloesgen, Springer Proceedings in Physics 52 (1990) 2.

Fig. 1.   DMPC vesicle equilibrated above 34°C and below 3°C, the main phase
           transition temperature (T_m = 24°C) before freezing.
Fig. 2.   Band-pass-filtered images retaining frequency components from 1.5 to 6 nm.
           Vesicles were equilibrated at 3°C, 24°C, 29°C and 34°C before freezing.
Fig. 3.   Tilt experiment with DMPC vesicles equilibrated at 30°C before freezing.
Fig. 4.   Lipid vesicles with reconstituted Na/K-ATPase embedded in thin ($\sim$ 50 nm)
           amorphous ice.
Fig. 5.   Lipid vesicles embedded in a thick (> 150 nm) layer of amorphous ice.
Fig. 6.   Computer simulation of a lipid vesicle and application of the contrast
           transfer function at (a) Δ = 0, (b) Δ = -1, (c) Δ = -10, (d) Δ = -30.
Fig. 7.   Frozen-hydrated electron spectroscopic images of reconstituted CF_1F_0-ATP-
           synthase taken at (a) Δ = -1.5, (b) Δ = -7, with zero-loss filtering.

433
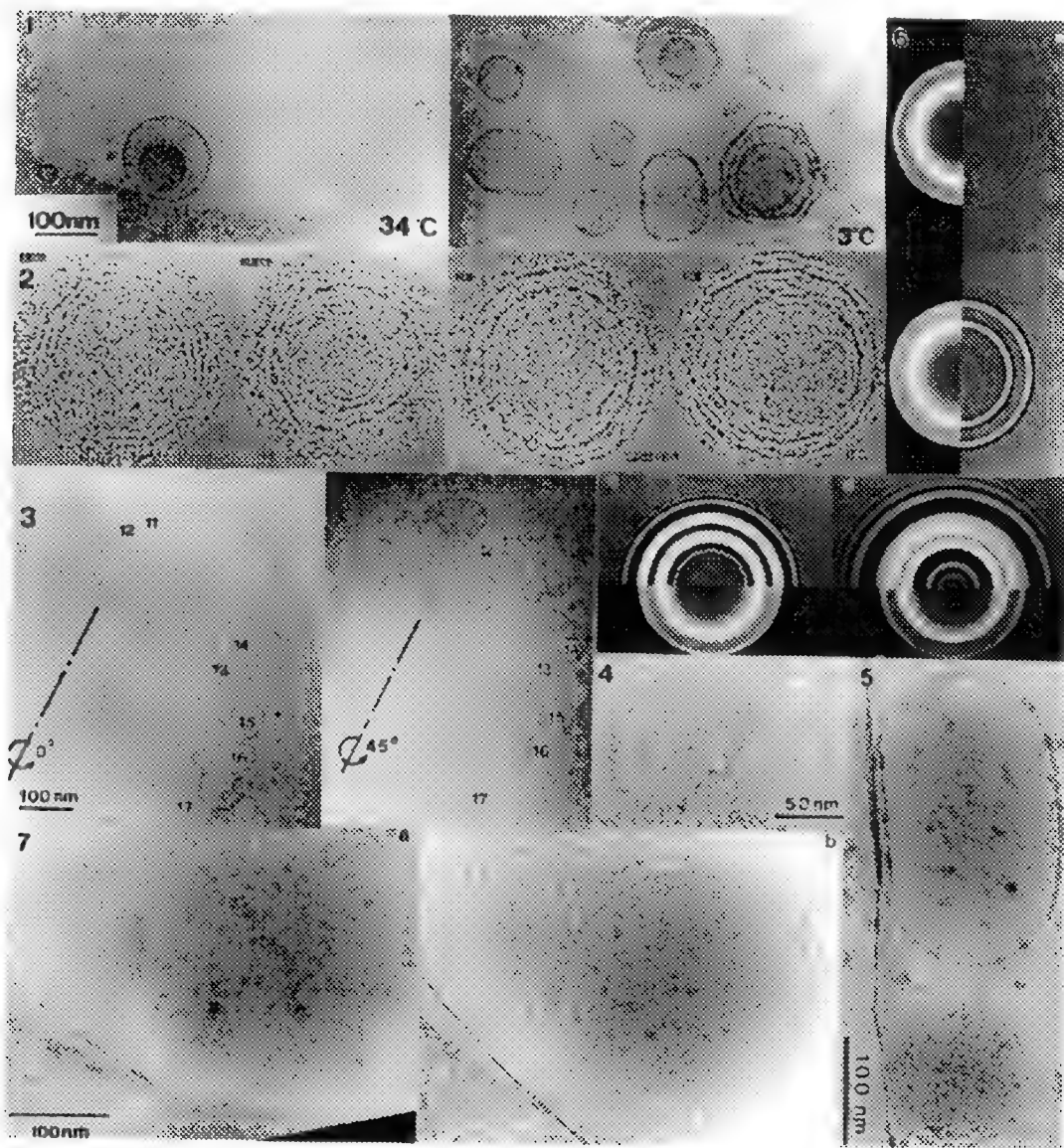
HIGH-RESOLUTION THREE-DIMENSIONAL COULOMB POTENTIAL MAP OF PHOE PORIN

Bing K. Jap, Thomas N. Earnest, Peter Walian and Kalle Gehring

Cell and Molecular Biology Division, Lawrence Berkeley Laboratory, University of California, Berkeley, CA 94720

PhoE porin is an outer membrane, pore-forming channel with selectivity for the transport of phosphate-containing compounds and negatively charged solutes. We have reconstituted this membrane protein with lipids to form highly coherent, 2-dimensional crystalline patches. Diffraction patterns and images of trehalose embedded crystalline patches were recorded using a JEOL 100B electron microscope, which is equipped with a field emission gun and a cold stage that was operated at about -120° C. A complete 3-dimensional (3-D) diffraction data set to a resolution of 2.8 Å and a number of high resolution images at tilt angles ranging from 0 to 60 degrees were collected. A high resolution projection map at 3.5 Å resolution and a 3-D map at 6Å, showing the detailed structural architecture of this protein, have been published.[1,2]

We report here the high resolution 3-D map of PhoE porin to a resolution of 3.4 Å determined by electron crystallography together with the utilization of the non-crystallographic symmetry that exists in our crystal. A 3-D map at 4.2 Å resolution was first reconstructed. At this resolution, the phase values along the lattice rods were fairly well sampled by our high resolution images. The map was then refined at this resolution by the use of non-crystallographic symmetry. In the refinement cycles the diffraction amplitudes were used as the constraint, and the phases that have high reliability were initially kept unaltered. After several cycles of refinement, all phase values up to the given resolution limit were then allowed to vary. The refinement of 3-D map was extended gradually to 3.4 Å resolution with the use of our 3-D diffraction data set and the phase values from our images. This was done by incremental inclusion of diffraction amplitudes and the phase information from the limited number of images. A partial model was then constructed from the map at 3.4 Å resolution; the model included a large fraction of β-sheet strands, as well as the structures for features which displayed strong density. The phase refinement was repeated but with inclusion of this partial model in a protocol of phase refinement and extension using phase combination by addition of Hendrickson-Lattmann coefficients which included filling in the missing cone information with the calculated structure factors and phases from the model, in addition to solvent flattening and averaging about the non-crystallographic three-fold axis.

Figure 1 shows the central 8Å-section of the 3-D map at 4.2 Å resolution before and after phase refinement with averaging about the non-crystallographic three-fold axis. The refined map gives, even at this resolution, some indication of the orientation of β-strands in the β-sheet wall that is located away from the three-fold symmetry axis. Our 3-D map suggests that the β-strands are tilted about 35 degrees from membrane normal. Near the three fold symmetry axis, the orientation of the β-strands is not clear. The β-sheet wall near the three fold symmetry axis is somewhat shorter than the wall further away from the axis. Within the cylinder, the substructure, which is located further away from the three-fold symmetry axis, spans almost the entire width of the membrane, and this substructure defines the channel itself. The channel appears to converge as it traverses the membrane. This is consistent with our earlier 3-D map of negatively stained samples. A strong, rod-like density, which is located within the cylinder and oriented normal to the membrane plane is also clearly visible. The refined 3-D map at 3.4 Å resolution (Fig. 2) shows the orientation of most of the β-sheet strands clearly, but the density of β-strands near the three-fold symmetry region remains less well-defined. Densities of presumed bulky side-chains become clearly visible, especially those of the β-strands further away from the three-fold axis. The substructure within the cylinder shows also a greater structural detail, and some of the density can now be easily interpreted.[3]

References

1. B.K. Jap *et al.*, J. Struct. Biol. (1990)103, 57.

2. B.K. Jap *et al.*, Nature (1991)350, 167.
3. This work was supported by the Office of Health and Environmental Research, US Department of Energy, under contract no. DE-AC03-76SF00098 and by National Institutes of Health Program Project grant GM 36884.
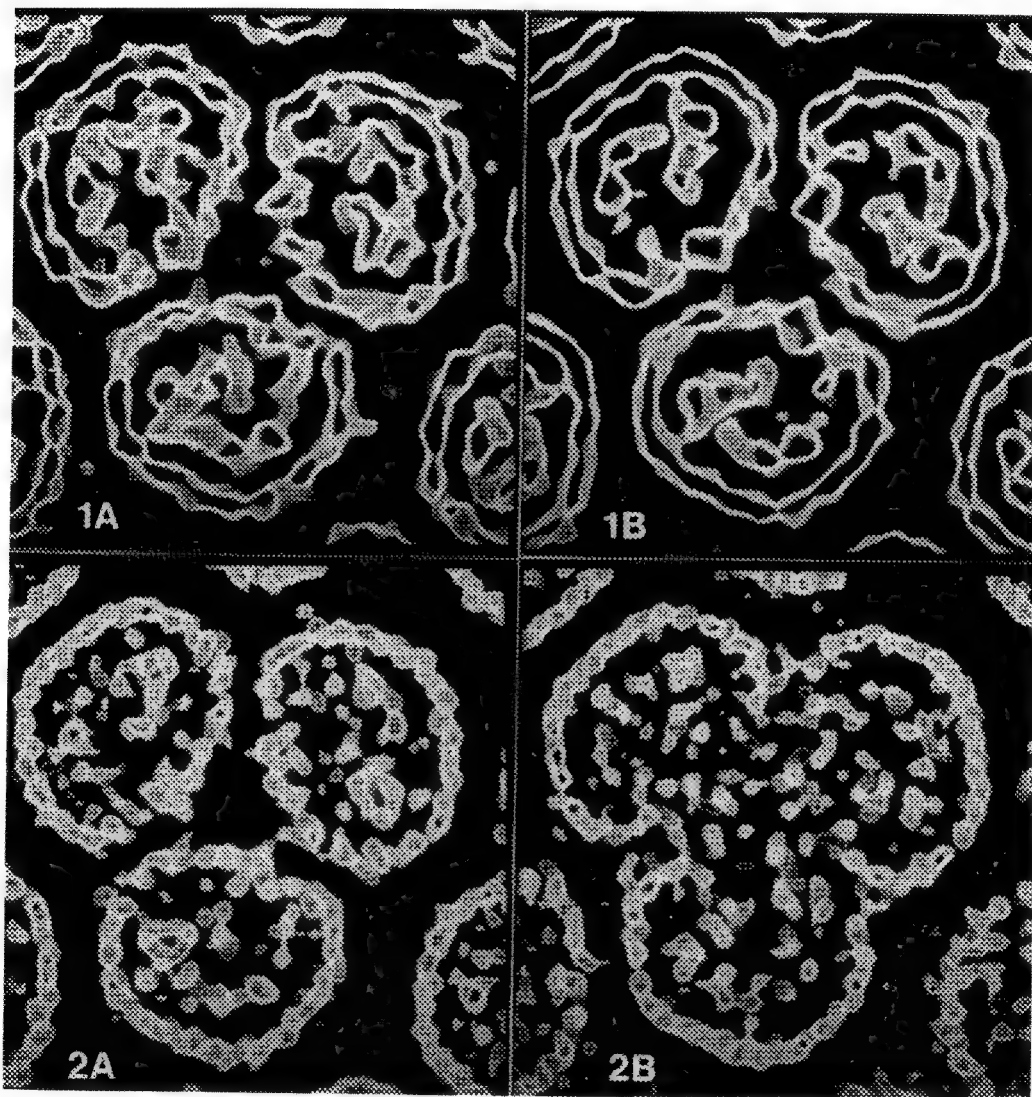
FIG. 1. The central 8Å-section of our 3-D map of PhoE porin at 4.2 Å resolution. (a) The map obtained before phase refinement. (b). The map reconstructed after several cycles of molecular averaging about the non-crystallographic three-fold axis. The refined map is less noisy and shows more defined β-strand structure.

FIG. 2. Sections of 3-D map at 3.4 Å which is obtained after phase refinement with inclusion of the partial model and filling in the missing cone, as well as molecular averaging and solvent flattening. (a) 8Å-section above the middle of the membrane and (b) same section thickness below the middle of the membrane.

ELECTRON CRYSTALLOGRAPHIC STUDIES ON *E.COLI* - EXPRESSED VARIANTS OF BACTERIORHODOPSIN

Alok K, Mitra, Larry J. W. Miercke, Mary C. Betlach, Richard F. Shand[*], and Robert M. Stroud

University of California San Francisco, Dept. of Biochemistry and Biophysics, San Francisco CA 94143-0448,[*]Dept. of Biological Sciences, Northern Arizona University, Flagstaff, AZ 86011

Bacterorhodopsin (BR) is an integral membrane protein present in the purple membrane (PM) of *Halobacterium halobium*[1] where it is arranged in a highly ordered 2-dimensional hexagonal P3 lattice. BR contains a single retinylidene chromophore bound via a protonated Schiff base to Lys-216 and functions as a light-driven proton pump. Upon absorption of a photon, BR cycles through a series of photointermediates resulting in a vectorial pumping of a proton from the intracellular side to the extracellular side. Site-directed mutagenesis[2-4] has identified residues whose substitution affects the chromophore environment in BR and those that are involved in the proton transport. Specifically Asp-85, Asp-212, and Arg-82 are involved in the proton release pathway, whereas Asp-96 is involved in Schiff base reprotonation.

To help establish the role of altered residues in the photoreaction cycle, it is necessary to characterize any changes in structure in addition to function. We have used wild-type, *E.coli*-expressed bacteriorhodopin fusion protein (e-BR) containing 13 heterologous residues[5], and its variants in particular Asp-85-Asn, Asp-96-Asn and Arg-82-Gln to understand bR function[6]. The 3-dimensional structure of bR at 3.5Å in-plane by ~ 10Å perpendicular to the membrane plane has been determined from electron imaging[7]. With the resulting phases, any changes in structure can now be characterized in three dimensions by difference Fourier methods using accurately determined electron diffraction amplitudes. Initially, the degree of structure change can readily be quantitated in projection by using in-plane electron diffraction amplitudes and phases[8-9]. We have shown that changes in projected electron density due to as little as two to three carbon atoms are identifiable by Fourier difference mapping[10].

Using the *E.coli*-expressed purified protein in a single detergent we have obtained two-dimensional crystals by reconstitution in *Halobacterium halobium* lipid milieux[6]. These crystals (typically 3-5µ in diameter) are trigonal, as in purple membrane and show high-resolution electron diffraction pattern from glucose-embedded patches. Fig. 1 describes the method developed for obtaining such large 2-dimensional crystals. These crystals are in general twinned, with domains of bR molecules organized in twinned lattices consistent with the P3 symmetry. We apply a scheme for the analysis of the twins, detwinning, and removal of the effects of the specimen tilt to extract projection amplitudes[10] . Fig. 2 compares, as a function of resolution, averaged amplitude data from crystals of e-BR and those for PM. The similarity of the two profiles show that the structure of e-BR and BR in PM are very close agreeing with the implications from functional studies on e-BR in liposomes[6]. This establishes that such 2-dimensional crystals are appropriate for high-resolution investigations on the structures of interesting e-BR variants. Towards this end we have recently crystallized the Asp-96-Asn mutant. An electron diffraction pattern from a 2-dimensional crystal for this mutant is shown in Fig. 3. Quantitative analyses of the high-resolution data from the crystals from the mutant protein and its comparision to those already obtained from e-BR crystals will be presented.[11]

References

1.W. Stoeckenius and R.A. Bogomolni, Annu. Rev. Biochem. (1982)51, 587.
2. T. Mogi et. al. Proc. Natl. Acad. Sci. USA. (1988)85, 4148.
3. L. J. Stern and H.G. Khorana J. Biol. Chem.(1989)264, 14202.
4. B. J. Butt et. al. EMBO J.(1989)8,1657.
5. R. F. Shand et. al. Biochemistry (1991),30, 3082.
6. L. J. W. Miercke et. al. Biochemistry (1991)30, 3088.

7. R. Henderson et. al. J. Mol. Biol.(1990)213, 899.
8. S. B. Hayward and R. M. Stroud. J. Mol. Biol. (1981)151, 491.
9. J. M. Baldwin et. al. J. Mol. Biol. (1988)202, 585.
10. A. K. Mitra and R. M. Stroud. Biophys. J.(1990)57, 301.
11. Supported by N.I.H. grants GM32079 to R.M.S. and GM31785 to M.C.B. and National Research Service award 5T32CA09043 to R.F.S.

Fig. 1

Fig. 2

Fig.1. Protocol for obtaining large 2-dimensional trigonal crystals of *E-coli*-expressed wild-type and mutant bacteriorhodopsin.

Fig.2. Comparision of the extracted electron-diffraction amplitudes determined from e-BR crystals (average of 4 data sets, shaded diamonds) and those for PM (open squares) as a function of resolution.
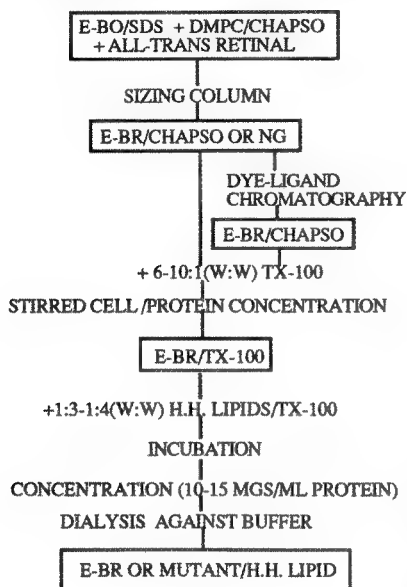
Fig.3 High-resolution electron diffraction pattern from a glucose-sustained e-Asp-96-Asn-BR crystal after subtracting contribution from inelastic scatter. The pattern is from two major crystalline domains oriented by an angle of 8° The circular arcs represent 3.1 Å resolution.
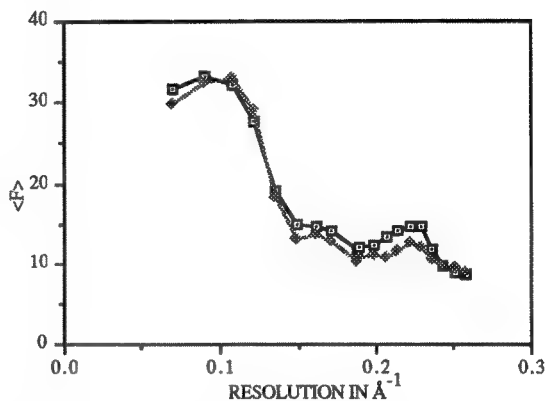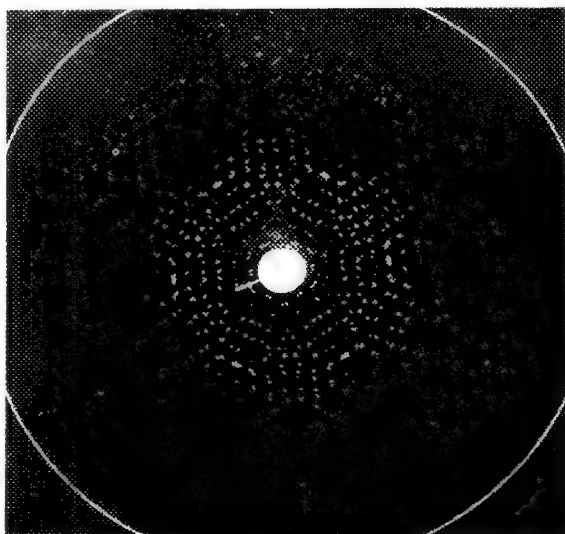

437

TWO-DIMENSIONAL PORIN OMPF-LIPID CRYSTALS: A COMPARISON OF ELECTRON MICROSCOPY AND X-RAY DATA

C. Henn[1], A. Hönger[1], S. Cowan[2], J.P. Rosenbusch[3] and A. Engel[1]

[1]M.E. Müller-Institute, [2]Department of Structural Biology and [3]Department of Microbiology, Biocenter, University of Basel, CH-4056 Basel, Switzerland

In *Escherichia coli* *(E.coli)* cells porins represent a major component of the outer membrane. Embedded in the lipid bilayer, these channel forming proteins facilitate the diffusion of solutes up to a mass of 600 Da. Porins OmpC, OmpF and PhoE exhibit a high sequence homology, whereas the sequence of LamB, the maltose channel, is different. Nevertheless, all *E.coli* porins have pronounced common features: (i) the wall of the cylindrical channel is in a β-sheet conformation with the antiparallel β-strands running at approximately 45 degrees;[1,2] (ii) functional porins exist as trimers, and (iii) voltage-induced conductance steps of OmpC, OmpF and PhoE are triplets of the monomeric channel closure step.[3,4] In addition, *E.coli* porins share many features with porins from other species such as *Rhodobacter capsulatus*, whose porin structure has been solved to atomic resolution.[2]

We have investigated the formation of two-dimensional (2-D) porin OmpF-lipid crystals under different conditions (Fig. 1a,b) to gain insight into the assembly process. Depending on the lipid used, different crystallographic packing arrangements can be induced. With the structure of OmpF porin available,[5] the lipid-protein and protein-protein interactions in these 2-D crystals can now be studied by molecular modeling. As a first step, we tested the correlation of low-resolution (2 nm) data from electron microscopy with the OmpF structure from X-ray crystallography. To this end, the atomic scale map was bandwidth-limited and surface-rendered at 1 and 2 nm resolution. One side of the membrane (Fig. 2a,b) is compared with the surface relief (Fig 2c) reconstructed from freeze-dried, metal-shadowed OmpF-dimyristoyl phosphatidylcholine (DMPC) crystals.[6] The other side of the OmpF porin trimer (Fig 3a,b) is compared with the 3-D map [7] from negatively stained reconstituted 2-D porin OmpF-DMPC crystals (Fig. 3c).

As illustrated by Figs. 2 and 3, the X-ray structure corroborates data previously found by electron microscopy techniques.[6,7]

1. R.A. Pauptit et al., J. Struct. Biol. (1991) **107**, 136
2. M.S. Weiss et al., Science (1991) **254**, 1627
3. L.K. Bühler et al., J. Biol. Chem. (1991) **266**, 24446
4. B. Dargent et al., EMBO J. (1986) **5**, 773
5. S. Cowan et al., (in preparation)
6. A. Hönger et al., J. Struct. Biol. (1990) **103**, 185
7. A. Engel et al., Nature (1985) **317**, 643
8. This research was supported by grant No. 31-25684.88 of the Swiss National Foundation for Scientific Research and the M.E. Müller Foundation.
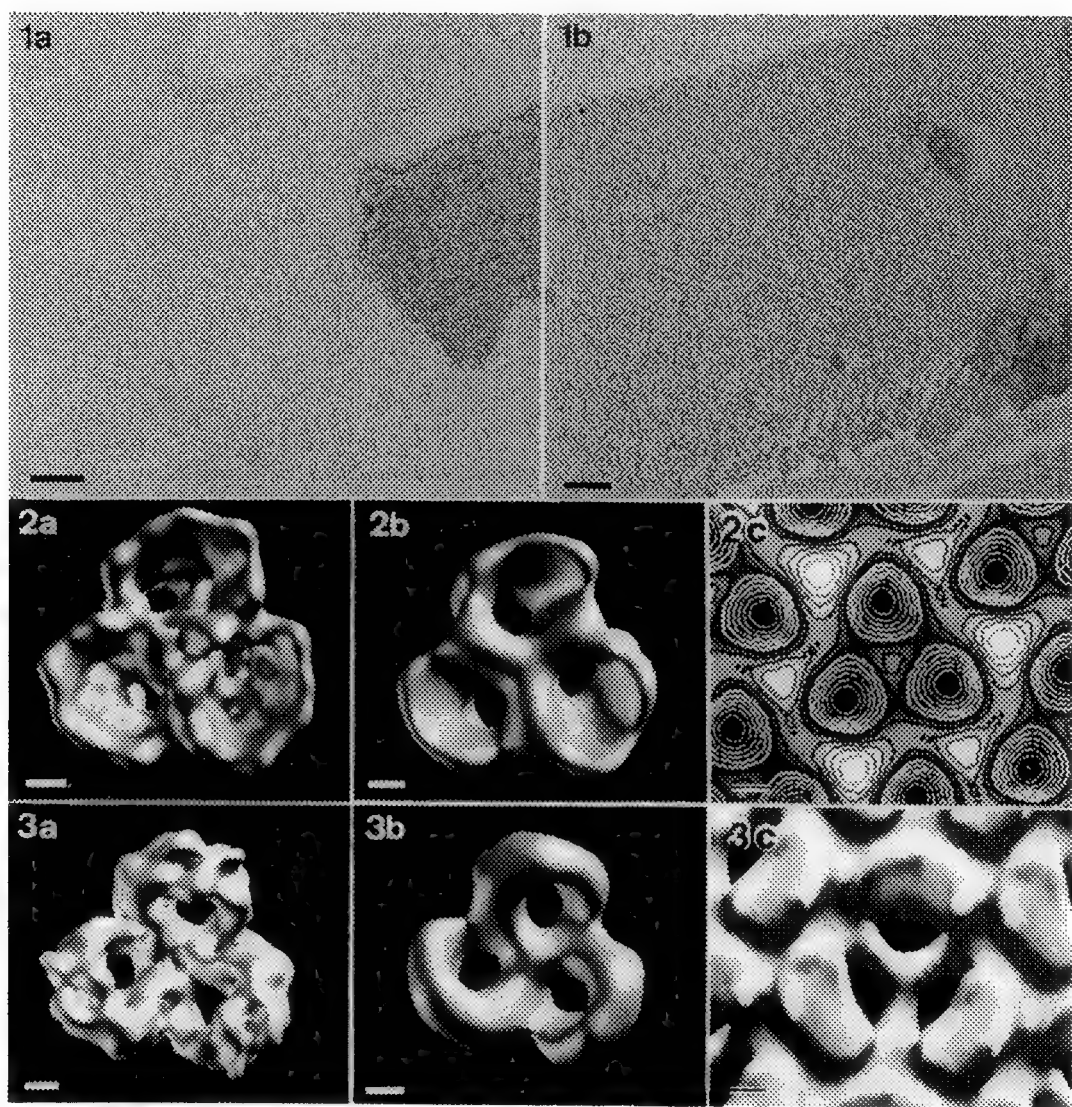
Fig.1: 2-D porin-lipid crystals: a) after negative staining and b) after freeze-drying and metal shadowing. Scalebars = 100 nm

Fig.2: Surface rendered density map of the OmpF trimer, calculated from atomic structure data: a) at 10 Å resolution and b) at 20 Å resolution, both contoured to 100 % of the molecular mass. c) Surface relief reconstructed from freeze-dried, metal-shadowed OmpF-lipid 2-D crystals. Scalebars = 1 nm.

Fig.3: a) and b) Surface rendered OmpF trimers analogous to Fig. 2, but viewed from the other side of the membrane. c) Rendering of the 3-D map from negatively stained reconstituted 2-D porin-lipid crystals. Scalebars = 1nm

STRUCTURE OF CRYSTALLINE VDAC, THE VOLTAGE-GATED CHANNEL IN THE MITOCHONDRIAL OUTER MEMBRANE

X.W. Guo,[*] P.R. Smith,[+] M. Radermacher,[*] C.A. Mannella[*]

[*]Wadsworth Center for Laboratories and Research, New York State Dept. of Health, Empire State Plaza, Albany, NY 12201-0509; and Depts. of Biomedical Sciences and Physics, State Univ. of New York at Albany; [+]Dept. of Cell Biology, New York Univ. School of Medicine.

The voltage-gated, mitochondrial channel, VDAC, is formed by a 31-kDa outer-membrane polypeptide. Crystalline arrays of this channel, produced by phospholipase A_2 treatment of *Neurospora crassa* mitochondrial outer membranes, consist of groups of 6 channels repeated on a parallelogram ("oblique") lattice (a=13.3nm, b=11.5nm, γ=109°). These membrane crystals are polymorphic, i.e. lateral contraction is triggered by a polyanion which also decreases VDAC's gating potential.[1] Projection images of unstained, frozen-hydrated VDAC arrays indicate that lattice contraction is accompanied by changes in the distribution of protein away from the hexameric repeat unit.[2]

We have undertaken 3D reconstruction of VDAC arrays embedded in aurothioglucose, correlation averages of which typically show resolution of 1.3 nm (Figs. 1,2). Sets of projection images of arrays tilted 60°, 45 or 30°, and 0° have been recorded by minimal dose electron microscopy and correlation averages computed with the SPIDER system.[3,1] Twenty-two projections of tilted oblique arrays (representing 44 projections with p2 symmetry applied) have been used to compute a 3D reconstruction using the MDPP system.[4] Fig. 3 is a projection down the z-axis of the reconstructed VDAC crystal, showing reasonable agreement with the axial projection of Fig. 1. Figs. 4-8 are five 1-nm-thick slices through the reconstruction normal to the z-axis. The six dark (aurothioglucose-filled) pores extend through the central 5 nm of the reconstructed volume, with most of the stain confined to a 3 nm slab in the center of the bilayer. The six pore lumens are normal to the membrane plane and show no evidence of merging, as do the channels in the bacterial porin trimer.[5] Similar 3D reconstruction of contracted arrays is underway to determine if lattice contraction correlates with changes in the shape of VDAC's lumen.

In the projections of Figs. 1-3, the dark pore lumens are bounded by several subsidiary density maxima (two are indicated "a" and "b" in Figs. 1 and 3), not seen in projections of conventionally negatively stained crystals. In the reconstruction (Figs. 4-8), these elongated features are seen to result from superposition of densities on both sides of the membrane array. The nature of these features, some of which penetrate well into the interior of the membrane, is uncertain. They may represent minor grooves in the structure that are filled with aurothioglucose or segments of the VDAC protein that form part of (and/or reside inside) the channel lumen.[6]

References:

1. C.A. Mannella, X.W. Guo, Biophys. J. 57(1990)23.
2. X.W. Guo, Proc. 12th ICEM Congress 1(1990)100.
3. J. Frank et al., Ultramicroscopy 6(1981)343.
4. P.R. Smith et al., Comp. Appl. Biosci. 7(1991)501.
5. A. Engel et al., Nature 317(1985)643.
6. Supported by NSF grant 89-16315.
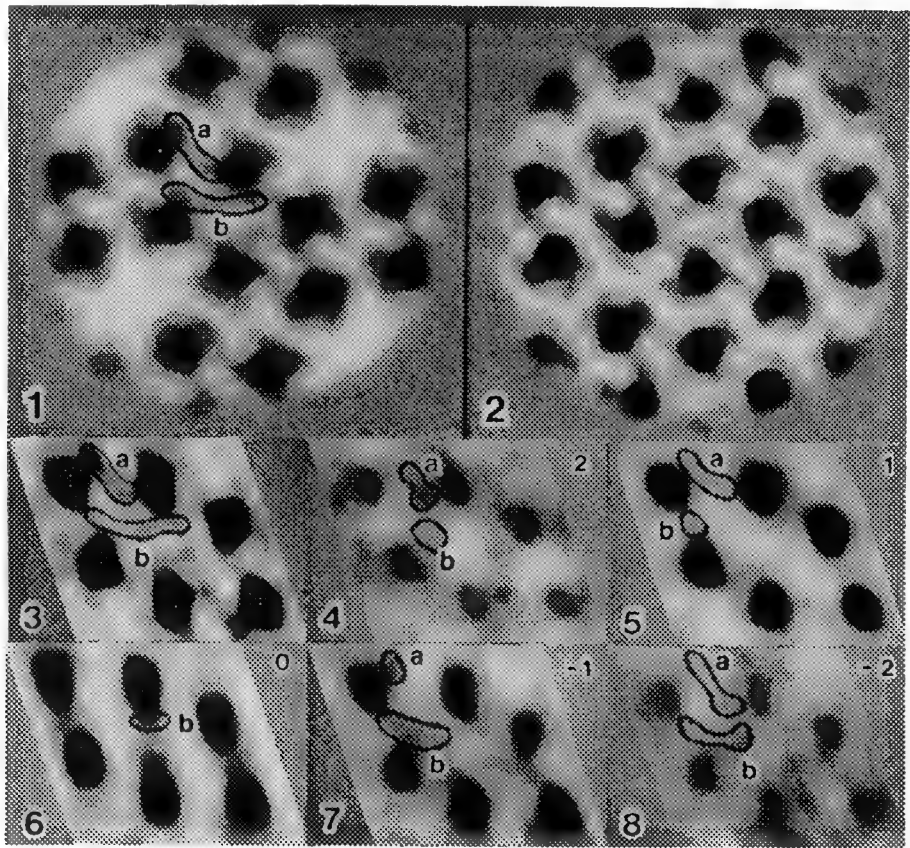
Figs. 1,2 Correlation averages of oblique (1) and contracted (2) arrays of VDAC, embedded in aurothioglucose.
Fig. 3 Projection through the reconstructed oblique VDAC array.
Figs. 4-8 1-nm-thick slices through the array parallel to the membrane plane. Numbers in upper right are the distance in nm of the center of each slice from the center of the volume.

441

DIVERSITY IN GAP JUNCTION STRUCTURES

Gina E. Sosinsky

Rosenstiel Basic Medical Sciences Research Center, Brandeis University, Waltham, MA 02254-9110

Gap junctions are the specialized regions between two adjoining cells responsible for regulated communication. The morphological unit of the gap junction is composed of 12 copies of the connexin molecule. Six connexins form a hexamer in each cell membrane called a connexon and two connexons pair across the two cell membranes of coupled cells to form gated channels [1]. Although other proteins are found in enriched gap junction preparations, it is generally accepted that the gap junction structures are formed from a family of connexin proteins. The connexins are named according to their DNA deduced molecular weights, e.g. Cx32 for the 32kDa liver major connexin and Cx26 for the 26 kDa liver minor connexin [2]. Within a given tissue, several connexins are often found and different connexins are often found within the same junctional plaque [3]. These connexins contain both conserved and variable domains in their primary amino acid sequences, with the major differences occuring in the sequence and size of the cytoplasmic C terminus. The most conserved regions of the compared sequences are in the transmembrane and gap portions of the proteins. Determination of the sequences of the connexin proteins and correlation of information on antibody binding, proteolytic cleavage and chemical reactivity have led to a model where the C- and N- termini are located at the cytoplasmc surface and four α-helical segments of the protein cross the membrane.

Gap junctions are isolated by membrane purification followed by detergent or alkali extraction as membrane plaques containing quasi-crystalline hexagonal arrays of thousands of connexons. These membrane plaques are subject to several kinds of disorder or variation: 1) lattice disorder, 2) structural polymorphism due to changes in the basic appearance of the connexon unit during preparation for electron microscopy, 3) disorder in the cytoplasmic domains which are thought to be flexible and therefore invisible in electron micrographs analyzed by Fourier methods, and 4) variability in connexin composition. The first three variations have been recently reviewed[4], the last is relatively new in light of the recent discovery of additional connexin proteins.

Mass mapping by scanning transmission electron microscopy (STEM) is the most direct method of stoichometric analysis. The number of elastically scattered electrons in images obtained from the STEM is proportional to the molecular weight of the object. STEM micrographs (in collaboration with the Brookhaven STEM Facility) have been recorded from both mouse and rat liver gap junctions. In rat liver plaques, the connexin composition is approximately 1:20 Cx26:Cx32 (as judged by SDS- PAGE) whereas in mouse liver gap junctions, it is 1:2 Cx26:Cx32. By measuring the mass of individual connexons, it should be possible to determine if they are homo-dodecamers or hetero-dodecamers of Cx32 and/or Cx26. There are two likely outcomes: connexons could contain all Cx26 and all Cx32 (theoretically, 384 kD versus 312 kD for total protein weight) or contain varying proportions of Cx26:Cx32. In the first case, the population of masses should be bimodal whereas in the second, the mass distribution would be continuous.

1. Bennett, M.V.L. and Goodenough, D.A. (1978), Neurosci.Res.Program Bull., 16, 375-486.
2. Beyer, E.C., Goodenough, D.A., and Paul, D.L. (1988) in Modern Cell Biology, 7, Gap Junctions (Hertzeberg, E.L., and Johnson, R.G. eds.), Alan R. Liss, Inc. New York, 167-175.
3. Zhang, J.-T. and Nicholson, B.J. (1989), J.Cell Biol., 262, 7751-7763.
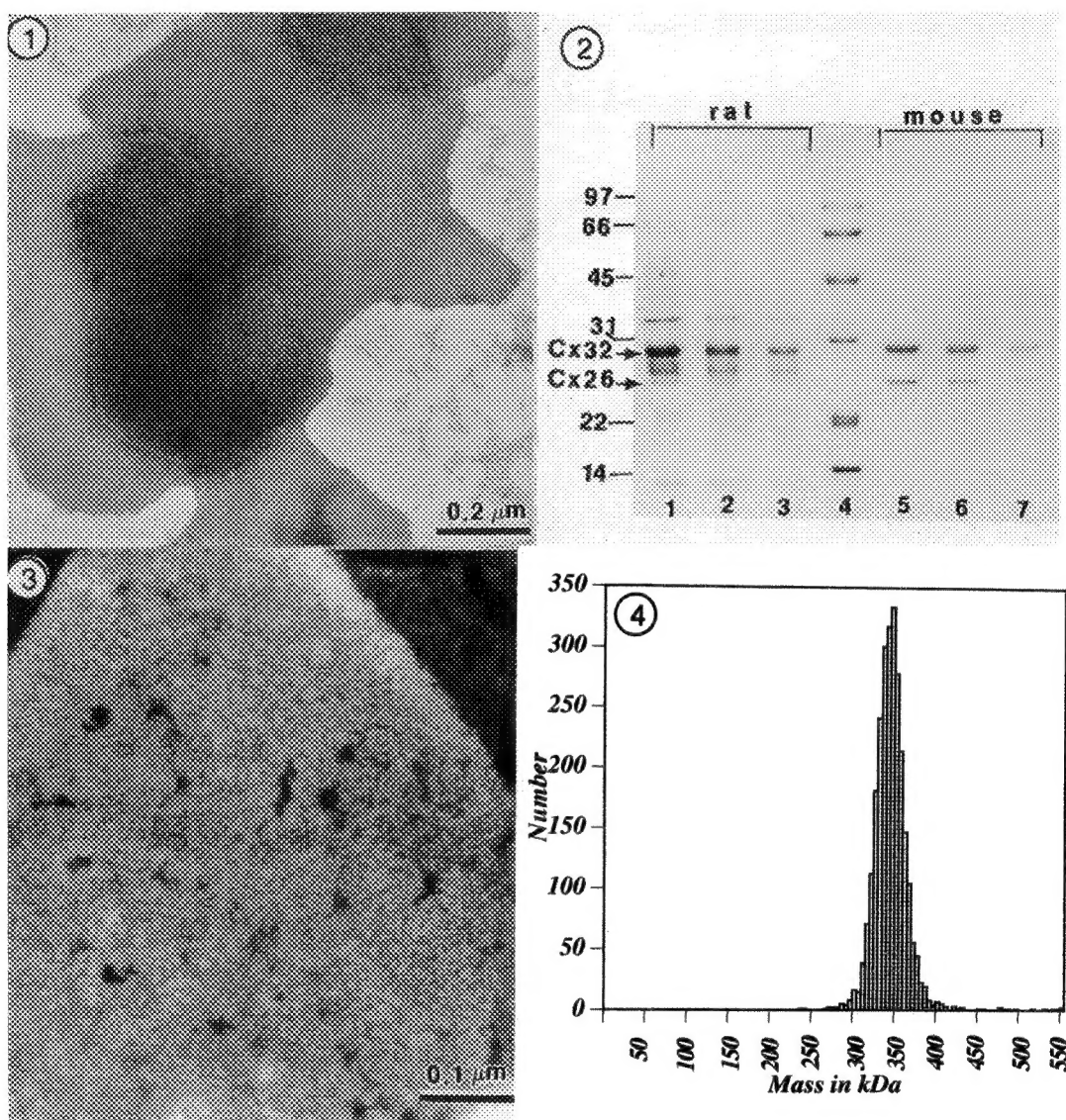4. Sosinsky, G.E. (1992), Electron Microsc. Review, 5, 59-76.

Fig. 1 Conventionally imaged uranyl acetate stained mouse liver gap junctions. At the resolution of these images, the connexon structure in the mouse liver junctions is indistinguishable from rat liver junctions in spite of the greater proportion of Cx26 present in mouse gap junction preparations.

Fig. 2 Coomasie stained SDS-PAGE of a rat liver gap junction preparation (lanes 1-3) and a mouse liver gap junction preparation (lanes 5-7). The two connexins, Cx32 and Cx26, are marked and are evident in the mouse preparation. Lane 4 contains standards for molecular weight calibration.

Fig.3 STEM micrograph of a freeze-dried mouse liver gap junction. Because the individual connexons are visible, cross-correlation image processing techniques may be used to identify the centers and determine the mass distribution across the whole junctional plaque.

Fig. 4 Histogram of the masses of the connexons in Fig. 3. The mass distribution for the ~2600 connexons is unimodal, indicating that connexons may contain a mixture of Cx32 and Cx26.

443

STRUCTURE IN THREE DIMENSIONS OF H,K-ATPase BY ELECTRON MICROSCOPY AND IMAGE PROCESSING

Manijeh Mohraz, Sonal Sathe, and P.R. Smith

Department of Cell Biology, New York University School of Medicine,
550 First Avenue, New York, NY 10016

H,K-ATPase is an integral protein of the plasma membrane of parietal cells in the gastric mucosa. It is believed to constitute the pump responsible for secretion of acid into the stomach. It utilizes energy from ATP hydrolysis to transport H^+ out of the cell and K^+ into the cell against an H^+ concentration gradient of one million-fold. The catalytic subunit (M_r 110,000) of H,K-ATPase shows striking sequence homology to those of other ion-transporting ATPases. The enzyme has a second subunit, a glycoprotein of ca 300 amino acids, which is homologous to the β subunit of the Na,K-ATPase.

H,K-ATPase was isolated in protein-rich membrane vesicles from gastric glands of hog stomachs.[1] Formation of two-dimensional crystals was induced in suspensions of the enzyme by phospholipase A_2, which had proved successful in crystallization of the Na,K-ATPase[2,] as well as by phospholipases C and D.

Electron micrographs of negatively stained specimens showed ordered arrays of various morphologies: long tubes or rods, basic sheets, multi-stacked sheets, and vesicles. Several types of these crystals would form concurrently in a given suspension. Image processing indicated that the packaging of the protein molecules in all crystal forms was identical to that of the basic sheet. Most of the crystalline fragments were extremely large (some more than 2 um in diameter), and their optical diffraction patterns indicated that they were also very well-ordered.

The unit-cell parameters were: a=b=10.3 nm, ɣ=90⁰. Image processing employed conventional techniques.[3] Computer filtrations of projection

images showed that there were four molecules (two sets of dimers) in the unit-cell, related by a four-fold rotational symmetry. However, systematic absences in the diffraction patterns of the crystalline sheets seemed to indicate that the lattice had $p2_1$ symmetry. This packing was quite different from those of the Na,K-ATPase[4] and Ca-ATPase[5] where there were only two molecules in the unit-cell, packing with p2 symmetry.

Tilt series were recorded from negatively stained specimens of the enzyme at tilt angles 15, 30, 45, 50, 55, and 60 degrees. A preliminary three-dimensional reconstruction from one tilt series of a basic sheet has been performed at a resolution of about 2.0 nm. Reconstruction from other tilt series and refinement of the structure is in progress.[6]

References

1. G. Saccomani et al., Biochim. Biophys. Acta, 465 (1977)311.
2. M. Mohraz et al., J. Ultrastruct. Res. 93(1985)17.
3. Aebi et al., J. Cell Biol. 91(1981)340.
4. M. Mohraz et al., J. Cell Biol. 105(1987)1.
5. K.A. Taylor et al., J. Mol. Biol. 187(1986)417.
6. This work was supported by NIH Grant GM-35399 and BRSG SO7 RR05399-29 to MM. We thank Marcia V. Simpson for recording the tilt series.

TRANSIENT DNA-PROTEIN COMPLEXES TRAPPED AND STUDIED BY CRYO-ELECTRON MICROSCOPY

Edward P. Gogol[*], Mark C. Young[§] and Peter H. von Hippel[§]

* Program in Molecular and Cell Biology, Mail Station FO 3.1, University of Texas at Dallas, P.O. Box 830688, Richardson, TX 75083, and   § Institute of Molecular Biology, University of Oregon, Eugene, OR 97403

Replication of an organism's genome is a complex process which involves the coordination of multiple enzymatic activities to perform both the work of template-directed DNA synthesis as well as numerous necessary associated duties. Even the central function of DNA synthesis requires the interaction of multiple protein subunits or subassemblies to achieve the rate and fidelity observed *in vivo*. The enzymatic activity of the DNA polymerase, which in simple organisms is a single polypeptide, is enhanced by a set of accessory proteins which dramatically increases its processivity on the DNA template. As a first step in obtaining a structural understanding of the assembly and function of the multiple protein subunits required for DNA replication, we have directly visualized the complexes formed by the accessory proteins with DNA cofactors, and explored the conditions required for their formation.

The replication system which we have examined is that of bacteriophage T4, a simple and well-characterized set of proteins encoded by the T4 genome.[1] This system contains all of the critical activities demonstrated in more complex organisms, but in a relatively simpler form, and hence serves as a useful model for the mechanism of replication. The DNA polymerase of T4 is the product of gene 43 (gp43), and the accessory proteins consist of gp44, gp45, and gp62. The set of the three accessory proteins, in the presence of Mg^{++} and ATP, form distinctive bar-like structures associated with appropriate DNA cofactors, as visualized by cryo-electron microscopy (cryo-EM).[2] All three of the accessory proteins are required to obtain these structures, and the addition of the T4 single-stranded DNA binding protein gp32 increases the number of these complexes. ATP hydrolysis by the DNA-stimulated ATPase activity of gp44 is absolutely required for the formation of these structures. Stopping ATP hydrolysis results in loss of the structures within seconds, the minimum time required to prepare a cryo-EM specimen. Use of cryo-EM has proven critical in this study, in that the complexes are temporally transient, and continual ATP hydrolysis is required to maintain a population of them. The very rapid vitrification of cryo-EM specimens has permitted appropriate conditions to be maintained until the moment of their preservation.

Preliminary experiments with incompletely purified mixtures of DNA suggested that complexes associated with only some cofactors.[2] We have examined the DNA cofactor requirements for the formation of these complexes, in hopes of determining the mechanism by which the structures are formed. Double-stranded plasmid DNA was prepared in three different forms: supercoiled, nicked at a single site, and gapped with 100-300 bases of single-stranded DNA. No complexes were seen in the presence of the intact, supercoiled DNA (figure 1A). In contrast, numerous complexes were associated with the nicked DNA, both individually and in clusters (figure 1B). Even more complexes were visible, under identical conditions, with the gapped DNA cofactor (figure 1C). The stimulation of the gp44 ATPase by these three DNA cofactors parallels the appearance of the structures (data not shown). Linear blunt-ended DNA fragments were prepared from each of the three states of the plasmid, and gave the same pattern of complex formation, although many fewer complexes were visualized with the linear cofactors than with the parent circular plasmids.

These results lead us to postulate a model for the formation of these protein complexes with DNA, shown schematically in Figure 2. The accessory proteins in solution associate at nicks or single-stranded gaps in the DNA, bind the DNA, and possibly rearrange upon ATP hydrolysis. The presence of long clusters of the complexes, even on cofactors with a single nick, indicates that they translocate along the DNA, probably by one-dimensional diffusion, forming clusters whose size and